International Cryogenics Monograph Series
Series Editor: Klaus D. Timmerhaus · Carlo Rizzuto

Steven W. Van Sciver

Helium Cryogenics

Second Edition

Springer

International Cryogenics Monograph Series

For further volumes:
http://www.springer.com/series/6086

Steven W. Van Sciver

Helium Cryogenics

Second Edition

Springer

Steven W. Van Sciver
Florida State University
Field Laboratory
Tallahassee, FL 32310, USA
vnsciver@magnet.fsu.edu

ISBN 978-1-4419-9978-8 e-ISBN 978-1-4419-9979-5
DOI 10.1007/978-1-4419-9979-5
Springer New York Dordrecht Heidelberg London

Library of Congress Control Number: 2011942902

To Mary, Travis and Courtenay

Preface First Edition

At least 10 years have elapsed since a comprehensive monograph concerned with the broad subject of cryogenics has been published. During this time a considerable quantity of research and development has been carried out in the field of cryogenics. Furthermore, there has been a certain degree of redirection of effort within the field, mostly driven by the variety of new applications, ranging from superconductive magnet systems to microelectronics. Greater emphasis is now being placed on low-temperature cryogenics, particularly that of liquid helium. Until now cryogenic books have provided a broad survey of materials and fluid properties over the entire cryogenic regime, $T \lesssim 120$ K. This approach does not allow sufficient detail in any particular area to bring the reader to the current level of understanding in the subject. In addition, the behavior of helium has been lumped with that of other cryogenic fluids, although the properties of helium are in many cases quite unique. As a result, a clear relationship has not been established between the fundamental understanding of helium fluids and their potential applications.

The present book has been written to fill this void. The approach is to survey the field of cryogenics, specifically as it pertains to helium fluids. This approach is more specialized than that contained in previous cryogenics books. Furthermore, the level of treatment is more advanced and a certain knowledge of fundamental engineering and physics principles has been assumed. Unlike previous books on liquid helium, the present treatment contains both engineering and physical descriptions. The goal throughout the work is to bridge the gap between the physics and engineering aspects of helium fluids to encourage their use and enhance their usefulness in low-temperature systems.

The content of the book is based on a course first offered at the University of Wisconsin–Madison. Students who register for this course are almost exclusively at the graduate level. As a result, a reasonable background knowledge of physics and engineering has been assumed. Recommended prerequisites include a working knowledge of thermodynamics and statistical physics, heat transfer and fluid mechanics, and elementary solid-state physics. Without this background, the reader

may find it necessary to review one or more of these subjects. A number of useful references are given at the end of the book.

The material contained in this book is divided into nine chapters. Chapter 1 introduces the basic principles of cryogenics, including a discussion of applications. Chapter 2 describes the properties of materials at low temperatures, concentrating on solids. This is not only a useful background review but it also introduces some fundamental physics, which is used in later chapters. Chapter 3 introduces helium as a classical fluid, concentrating on its physical aspects as they can be described using classical models. Chapter 4 then discusses helium as a quantum fluid, emphasizing the theory and experimental evidence associated with superfluidity. Chapter 5 turns to the engineering problem of heat transfer in superfluid helium, and how the fundamental understanding of helium introduced in Chapter 4 can be used to describe its characteristics. Chapter 6 concentrates on the problem of heat transfer in pool boiling normal helium. Chapter 7 extends the discussion of helium to fluid flow, including heat transfer and pressure drop. Chapter 8 discusses the thermodynamic aspects of liquefaction and refrigeration systems, including a discussion of actual refrigeration systems in use today. Finally, Chapter 9 summarizes some special topics of interest to both helium cryogenics and related disciplines. The goal here is to survey a few very specific areas of helium cryogenics and related disciplines which, although slightly outside the main scope of the text, are still important in low-temperature applications.

Throughout the writing of this book, I have received considerable assistance and encouragement from colleagues, students, and friends. Their support should not go unrecognized. I would like to particularly give thanks to two of my students, D. Scott Holmes and John G. Weisend II, for their critical review of the partially completed manuscript and for assisting in developing problems. A number of colleagues read sections of the manuscript and made substantive suggestions on improvements to be made. They are Drs. A. F. Clark, F. R. Fickett, and V. Arp, all of the National Bureau of Standards; Dr. L. Dresner, Oak Ridge National Laboratory; Prof. O. E. Vilches, University of Washington; Prof. J. T. Tough, Ohio State University; and Prof. R. F. Barron, Louisiana Tech University. Their help is greatly appreciated. The conversion of my handwritten version to a readable typewritten text was due to the efforts of Ms. Kay Ewers. This task was certainly second only to the actual writing in terms of the amount of effort involved. Production of the graphics must be credited to Ms. Helga Fack and her staff. Finally, I would like to acknowledge the indirect help that my family has provided in terms of encouragement and willingness to forego some leisure activities so that time could be devoted to the effort of writing this book. In retrospect, it has been worthwhile.

Madison, WI, USA Steven W. Van Sciver

Preface Second Edition

A lot of cryogenic development has occurred in the 25+ years since the first edition of *Helium Cryogenics* (1986) was published. The field has seen the completion of the Large Hadron Collider (LHC) in Geneva, Switzerland with its associated enormous helium cryogenic refrigeration system. Numerous superconducting fusion engineering projects have been completed and the International Thermonuclear Experimental Reactor (ITER) is under development. Also, a variety of space-based cryogenic instruments have been successfully launched, many of which have contained hundreds of liters of liquid helium in a near zero-g environment. On a different plane, one of the most notable related developments has been the discovery of and now applications for high temperature superconductors (HTS). This field has impacted cryogenics in a fundamental way encouraging the development of cryogenic systems in the intermediate temperature regime (20–80 K). This along with other applications such as space-based instruments has brought about a broad and sustained effort at small scale cryocooler R&D with the most prominent being that of pulse tube coolers.

The author has also aged over this period with the associated gains of experience and somewhat different perspective on the subject. Given these changes and the opportunity to incorporate them into a new edition, it seemed a good time to undertake such a project. Before you is the result of this effort. Hopefully, it will be viewed to be a significant improvement over the first edition and a useful addition to the library of scientists and engineers interested in the field of low temperature science and technology.

This edition of *Helium Cryogenics* has undergone considerable revision and updating. Since the first edition was written prior to the widespread availability of word processing, the first task was to convert the available hard copy to electronic form. This task was ably assisted at FSU by Ms. Lindsay Hardy. Once the author had access to a revisable document, the real work began. Much of the updating was accomplished during the author's sabbatical leave from FSU, which was spent as a Visiting Erskine Fellow in the Mechanical Engineering Department at the University of Canterbury in Christchurch, New Zealand in fall (spring in the southern

hemisphere) 2010. Without that opportunity it would have been very difficult to carry out the project. Also, the author received help and suggestions from a number of colleagues. Valuable suggestions and comments on the first draft were provided by Dr. Dogan Celik, Dr. David Hilton, Ernesto Bosque and Mark Vanderlaan of FSU, Prof. John Weisend II of Michigan State University, Dr. Ting Xu of Oak Ridge National Laboratory, Prof. Andrew Rowe of the University of Victoria and Prof. John Pfotenhauer of the University of Wisconsin.

The resulting second edition has been reorganized with several additions and a few deletions. Chapters 1 through 3 have been revised to include a few new sections and updated data. After that the book has undergone a major reorganization. Since Chap. 3 concerns helium as a classical fluid it seemed appropriate to move the classical transport properties of fluid mechanics and heat transfer to occupy the next two chapters, Chaps. 4 and 5. Chapter 6 (formerly Chap. 4) then concerns helium as a quantum fluid. This is followed by Chap. 7 (He II Heat and Mass Transfer). For those familiar with the first edition, a most notable change is in the expanded and enhanced discussion of He II heat and mass transfer owing to the considerable research advances in the interim. Chapter 8 is again about liquefaction and refrigeration of helium and has been updated considerably from the first edition including more discussions on cryocoolers and He II refrigeration technology. Chapter 9, now titled "He^3 and Refrigeration Below 1 K", concentrates on the properties and applications for the rare isotope of helium. Finally, a new Chap. 10 has been created that incorporates a few special topics that do not fit easily within the content of the first nine chapters. These include cryogenic insulation, helium adsorption and magnetic refrigeration. The other generally noticeable enhancement is that the questions and problems at the end of each chapter have been expanded and revised. Also, within each chapter there are more short examples to illustrate the theory for the reader.

This text has been used in a course primarily taught for graduate students in the Mechanical Engineering Department at the FAMU-FSU College of Engineering. It has also been used as a supplement to numerous short courses taught by the author at various locations around the world. Through this process, many of the detailed explanations have been clarified and supplemented. It is my hope that you will find *Helium Cryogenics*, *Second Edition* to be a worthy improvement and a valuable asset for your research and development activities.

Tallahassee, FL, USA Steven W. Van Sciver

Contents

Symbols

Symbols	SI units
A	area, m^2
	Schottky specific heat coefficient, J K/kg ion
	^{3}He viscosity coefficient
A_{GM}	Gorter–Mellink parameter, m s/kg
a	absorptivity
	coefficient of turbulence buildup, $W^{3/2}/m^{3/2}$
	radius, m
	van der Waals gas coefficient, m^6 kPa/$kmol^2$
	vortex core radius, m
	Zeeman ordering parameter
B	magnetic flux density, T
	second virial coefficient, m^3/kg
	vortex interaction parameter
	^{3}He thermal conductivity coefficient
B_J	Brillouin function
b	coefficient of expansion
	impact parameter, m
	van der Waals gas coefficient, m^3/kmol
	coefficient for flow through porous media
C	circulation, m^2/s
	cost, $
	heat capacity, J/K, J/m^3 K, J/mol K
	specific heat, J K/kg
	third virial coefficient, m^6/kg^2
c	sound velocity, m/s
	surface wave speed, m/s
D	density of states
	diameter, m
	thermal diffusivity, m/s

(continued)

Symbols	SI units
	fourth virial coefficient, m^9/kg^3
d	diameter, m
	film thickness, m
	number of atomic layers
E	binding energy, J
	energy flux, J/m^2
	electric field, V/m
	internal energy, J
	radiant energy flux, W/m^2
	Young's modulus, N/m^2
e	charge of electron, coulombs
	specific internal energy, J/kg
	spectral energy density, W/m^3
F	force, N
Fo	Fourier number
f	bubble detachment frequency, s^{-1}
	Fermi-Dirac distribution function
	force per unit length, N/m
	Maxwell-Boltzmann distribution function
f_F	Fanning friction factor
f^1	He II heat conductivity function, W^3/m^5 K
G	specific mass flux, kg/m^2 s
Gr	Grashof number
g	degeneracy
	Landé g-factor
	specific Gibbs potential, J/kg
	gravitational acceleration, m/s^2
	He II heat conductivity function fitting factor
g_{peak}	He II heat conductivity function pressure factor
H	Hamiltonian
	height, m
	magnetic field, A/m
h	heat transfer coefficient, W/m^2 K
	hydrostatic head, m
	Planck's constant, J/K
	specific enthalpy, J/kg
	He II heat conductivity fitting function
h_{fg}	heat of vaporization, J/kg
J	exchange interaction
	particle collision term
	total angular momentum quantum number
j	momentum flux, kg/m^2 s

(continued)

Symbols	SI units
I	current, A
K	numerical constant
K_D	permeability, m^2
K_v	He II forced convection parameter
k	expansion parameter
	thermal conductivity, W/m K
	wave number
k_B	Boltzmann constant, J/K
L	length, m
	Lorenz number
	orbital angular momentum quantum number
l	mean free path, m
M	magnetization, A/m
	molecular weight, kg/kmol
M_{HeII}	He II heat exchanger coefficient
m	mass, kg
	(dot) mass flow rate, kg/s
	electron spin quantum number
m_{HeII}	He II heat exchanger coefficient
N	number of particles
N_0	Avogadro's number, mol^{-1}
Nu	Nusselt number
n	number density, m^{-3}
	statistical distribution
P	momentum, kg m/s
	perimeter, m
	polarization
	refrigeration power, W
Pr	Prandtl number
p	Pressure, Pa
Q	heat rate, W
q	heat flux, W/m^2
q_c	critical quality
q_{st}	isosteric heat, J
R	gas constant, J/mol K
Ra	Rayleigh number
Re	Reynolds number
r	radius, m
S	entropy, J/K, J/m^3 K, J/mol K
	slip ratio
	spin quantum number
	vortex line dimension, m

(continued)

Symbols	SI units
s	specific entropy, J/kg K
T	temperature, K
t	reduced temperature
	time, s
	transmission coefficient
U	attractive potential, J
	average approach velocity, m/s
	overall heat transfer coefficient, W/m^2 K
u	velocity component, m/s
V	volume, m^3
v	velocity, m/s
	specific volume, kg/m^3
	velocity component, m/s
v_F	Fermi velocity, m/s
W	work, J
w	Bénard convection parameter
	specific work, J/kg
	width, m
X	boiling heat transfer correlation coefficient
x	molar concentration
	coverage
	expansion circuit flow fraction
	position coordinate, m
y	position coordinate, m
	yield in a liquefier
Z	collision number, m^{-3} s^{-1}
	integrated heat conductivity function, $W/m^{5/3}$
	impedance
	partition function
z	fugacity
	position coordinate, m
	compressibility factor

Greek letters

α	accommodation coefficient
	linear thermal expansion coefficient, K^{-1}
	porosity
	Kapitza conductance parameter, W/m^2 K^n
	void fraction
β	bulk expansivity, K^{-1}
	condensation coefficient
	geometrical factor in Poiseuille flow
	He II fin coefficient

(continued)

Symbols	SI units
	$1/k_BT$
η	efficiency
	phase shift
θ	angle
Θ	reduced temperature
Θ_D	Debye temperature, K
κ	compressibility, Pa^{-1}
	transient heat transfer parameter, W^4 s/m^8
λ	wavelength, m
μ	viscosity, N s/m^2
	chemical potential, J
	roton mass, kg
μ_s	isentropic expansion coefficient, K/Pa
μ_J	Joule Thomson expansion coefficient, K/Pa
μ_B	magnetic moment
μ_0	permeability constant
ν	frequency, s^{-1}
	kinematic viscosity, m^2/s
ξ	coherence length, m
π	reduced pressure
ρ	density, kg/m^3
	resistivity, Ωm
ρ_B	electrical contact resistivity, Ωm^2
σ	electrical conductivity, $(\Omega m)^{-1}$
	Kapitza conductance parameter, W/m^2 K^4
	Lennard-Jones potential parameter, J
	scattering cross section, m^2
	Stefan–Boltzmann constant, W/m^2 K^4
	stress, Pa
	surface tension, J/m^2
γ	coefficient of the electronic specific heat, J/mol K^2
	reduced velocity
	specific heat ratio
	statistical parameter
	He II heat exchanger coefficient
γ_C	Curie constant, K
γ_G	Grüneisen parameter
Δ	roton energy gap, J
δ	thickness, m
	level splitting in Stark effect, J
	vortex line spacing, m
ε	emissivity

(continued)

Symbols	SI units
	energy level, J
	Lennerd-Jones potential parameter, J
τ	reduced temperature
	time, s
Φ	potential, J
	wave function
	reduced equation of state
φ	standing pressure, N/m
	azimuthal angle
χ	magnetic susceptibility
	vortex interaction parameter
ψ	wavefunction
	parameter in He II cylindrical heat transfer
Ω	collision integral
	thermodynamic probability
ω	angular frequency, s^{-1}
	tortuosity

Subscripts

a	acceleration, absorbed
B	Bohr
Bo	Boyle
b	bath, black body
bp	boiling point
C	cold, Curie
c	critical
c1	lower critical
c2	upper critical
CL	classical
D	Debye
e	electronic, expansion, emitted
eff	effective
exp	experimental
F	Fermi, Fanning
f	final state, film
fb	film boiling
fc	forced convection
G	Grüneisen
GM	Gorter Mellink
g	gas
gen	generation
gr	gravitational
H	hot, constant field

(continued)

Symbols	SI units
h	hydraulic, constant enthalpy
i	initial state, incident
ic	internal convention
int	internal
inv	inversion
j	Joule–Thomson
K	Kapitza
k	index
L	vortex line, liquid
LJ	Lennerd-Jones
l	liquid
m	maximum
n	normal, normal fluid, index
nc	normal fluid critical
ns	normal-superfluid
p	constant pressure, proton
ph	phonon
pl	constant pressure liquid
R	reversible, recovery
r	roton, reduced, radiant
s	superconducting, superfluid, sound, constant entropy, surface, substrate
sat	saturated
sc	superfluid critical
st	isoteric
T	constant temperature, thermal de Broglie
t	transmitted, total
tt	turbulent
u	ultimate
v	constant specific volume
y	yield
λ	lambda point
$\perp$	perpendicular component
0	ambient, ground state, first
1	first excited state, first
2	second
3	of ^{3}He, third
4	of ^{4}He, fourth
Superscripts	
*	critical, normalized parameter, effective
-	average
·	time derivative

(continued)

Symbols	SI units
A	acoustic mismatch
c	critical
m	empirical power law
n	empirical power law
p	phonon radiation, empirical power law
q	empirical power law
r	empirical power law
α	empirical power law
β	empirical power law

Chapter 1
Cryogenic Principles and Applications

Cryogenics is generally referred to as the science and technology of producing a low-temperature environment for applications. The word cryogenics has its origin in the Greek language where "kryos" means frost or cold and "gen" is a common root for the English verb to generate. Strictly speaking, cryogenics means to produce cold, yet the term has developed a more general connotation over years of usage by engineers and scientists. Today, the word cryogenics is associated with the production and study of low-temperature environments with a cryogenic engineer being a person who specializes in these areas. The expertise of a cryogenic engineer can vary considerably within this discipline. For example, he or she may be concerned mostly with heat transfer aspects of low-temperature fluids such as liquid hydrogen or helium or alternatively may be a specialist in methods of producing low temperatures such as various refrigeration technologies. Expertise in cryogenic engineering is in demand in a wide variety of technical fields including advanced energy production and storage technologies, transportation and space programs, and a wide variety of physics and engineering research efforts. As a result, the field is very interdisciplinary consisting of essentially all engineering fields focused on low temperature technology.

Over the years, the word cryogenics has developed several common usages. A cryogenic fluid is one that is used in the production of cold, while cryogenic machinery is the hardware used in achieving low-temperature environments. At first it would appear that all machinery and fluids used in cooling would be identified as cryogenic. However, it is generally accepted that the word cryogenics is reserved for those processes that take place below about 120 K. This distinction is somewhat arbitrarily established as it represents the point where permanent gases such as N_2, O_2, Ar and methane (CH_4) begin to liquefy. Sometimes cryogenics is used in reference to higher temperature processes such as cryo-preservation or cryo-surgery; however, these topics are outside the present discussion and therefore will not be considered as part of traditional cryogenics.

S.W. Van Sciver, *Helium Cryogenics*, International Cryogenics Monograph Series,
DOI 10.1007/978-1-4419-9979-5_1,

1.1 Temperature Scale

Assuming it is possible to refer to a range of temperature as being the cryogenic regime and that the range spans from absolute zero to about 120 K, one might ask the following question: "Why all the excitement over a range of temperature spanning only about a hundred kelvin?" The answer to this question lies in the thermodynamic description of the temperature scale.

One normally thinks of the process of producing low temperatures as reduction of entropy, where the entropy is a state function defined as,

$$s = \int_0^T \frac{dQ_R}{T} \tag{1.1}$$

with T being the absolute temperature and the entropy is taken to be identically zero at absolute zero. The third law of thermodynamics states that as absolute zero is approached, not only does the entropy of a system go to zero, but the entropy change associated with an adiabatic process must also go to zero. In other words, the lower the absolute temperature the more difficult it is to obtain a unit temperature decrease. Among other phenomena, this principle manifests itself in the thermodynamic efficiency of refrigerators decreasing with temperature.

It is therefore often more meaningful to identify temperature as having a logarithmic rather than linear scale. On a logarithmic temperature scale, the cryogenic range occupies a very large portion of achievable temperatures. Plotted in Fig. 1.1 is the temperature scale with the range of physical phenomena superimposed.

It should be immediately clear that cryogenic temperature range occupies nearly half of the achievable temperatures. From the physical point of view, this range is interesting for the large number of phenomena that occur within it. A few examples of these include: phase changes of many common elements, magnetic ordering, solid-state transformations, and the quantum effects including the onset of superconductivity and superfluidity.

A subfield of cryogenics is identified with the most permanent of all gases, helium. Although helium is a fairly rare element, there is probably more known about low temperature helium than any other fluid with the possible exception of water. Helium has a number of important applications in welding and lighter than air vehicles, but of greater interest to the present discussion is its use as a low temperature coolant. The refrigeration and liquefaction of helium are somewhat specialized fields because of the extremely low temperatures involved. However, the existence of low temperature helium enables a wide variety of technological applications. It is also a fluid with extremely interesting physical properties. These topics will be discussed in later sections.

The field of helium cryogenics spans a smaller range of temperature than classical cryogenics in part because the critical point of the most common isotope,

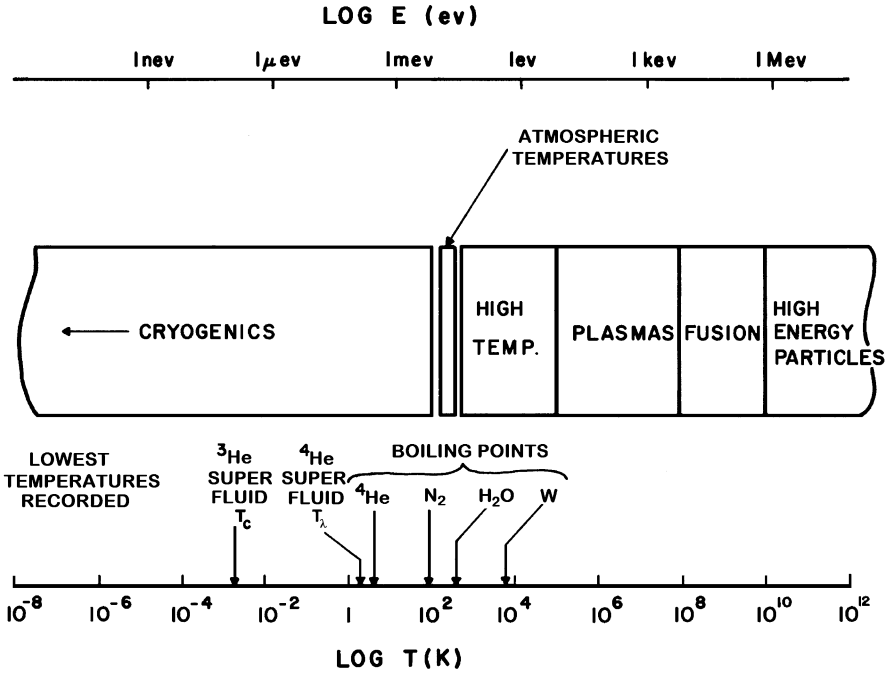

Fig. 1.1 Logarithmic temperature scale with superimposed physical phenomena. Note that $E = k_B T$ and 1 eV is equivalent to 11,609 K

^{4}He, is only 5.2 K. However, one of the more unique features of helium is that it does not solidify except under an external pressure exceeding 2.5 MPa (~25 atm) at low temperatures, thus allowing fluid properties to be studied to as low a temperatures as physically possible. At the present time the minimum achievable bulk temperature for liquid helium (in this case, the rare isotope ^{3}He) is below 100 μK. The technology of achieving these ultralow temperatures is special and relevant primarily to fundamental studies of condensed-matter and astrophysics. Since the emphasis of this book is on the technological applications of helium cryogenics, the phenomena associated with ultralow temperatures are not considered in much detail. Thus, helium cryogenics as described here emphasizes the range of temperature where the fluid has large scale potential applications as a coolant, 1 K $\lesssim T \lesssim$ 10 K. In Chap. 9 we will consider helium cryogenics for temperatures below 1 K both in terms of the technology of achieving these temperatures as well as the physical phenomena that occur in this range. However, it is important to keep in mind that this regime is only accessible through the use of the rare isotope of helium (^{3}He).

1.2 Historical Background

Research and development into the field of cryogenics began more than 100 years ago. Perhaps the most significant discovery in that time frame was the realization that common fluids such as air and water have similar behavior when cooled to temperatures near their respective critical points. In the early 1860s, substantial theoretical and experimental evidence was put forth identifying the concepts of phase separation and critical phenomena [1]. These ideas, which are mostly taken for granted today, form essential background to the understanding and application of the liquefaction and refrigeration processes.

To summarize phase separation and critical phenomena, reference is made to a useful general figure (Fig. 1.2) showing the states of matter when temperature T is plotted versus entropy S. Here the critical temperature T_c is the maximum of the two-phase coexistence region, which for obvious reasons is often refer to as "the dome".

As a rule of thumb, the normal boiling point T_{nbp} of a liquid is about $T_c/2$, although there is considerable deviation from this rule particularly for cryogenic fluids like helium where $T_{nbp}/T_c \approx 0.8$.

Three major scientific developments in the late nineteenth century provided the essential framework for the successful liquefaction of helium and thus the beginning of helium cryogenics. The first of these occurred during the study of low temperature O_2 in 1877 by two separate investigators in Europe, Cailletet in France and Pictet in Switzerland. Each of these workers demonstrated the concepts of liquid–vapor coexistence in permanent gases near their normal boiling point. Furthermore, Pictet's method used the cascade principle to produce liquid O_2,

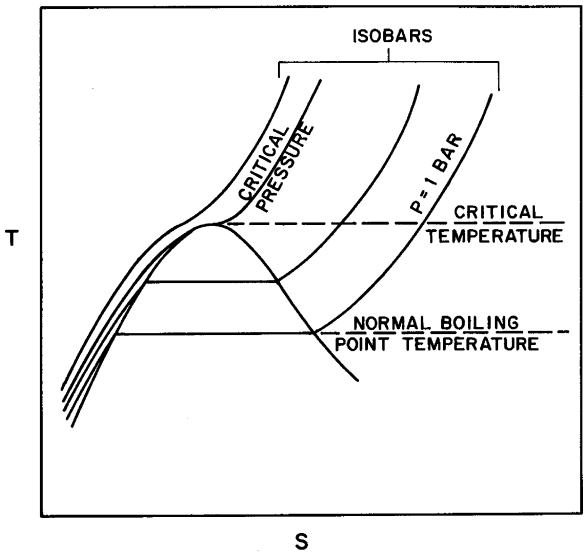

Fig. 1.2 Typical temperature-entropy diagram for a pure substance

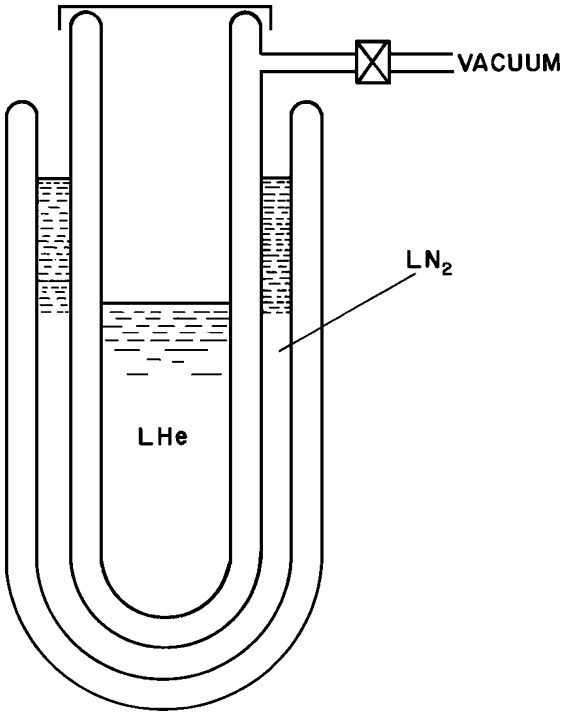

Fig. 1.3 Schematic of an early dewar vessel for containing liquid helium. The outer liquid nitrogen dewar provides a thermal radiation intercept

where gases are successively cooled to lower temperature by exchanging heat with a higher normal boiling point liquid. This method is later used in the first successful liquefaction of helium by H. K. Onnes.

The second major development occurred in 1892 when Sir James Dewar of the Royal Institution in London introduced the vacuum insulated flask as a storage container for liquid cryogens. His concept, which consisted of a glass double-walled vacuum vessel with inner walls silvered to reduce thermal radiation heat transfer, finally allowed collection of a significant quantity of liquid cryogen. A drawing of a simple "dewar" vessel that could be used for liquid helium is shown in Fig. 1.3. In this case, liquid nitrogen shielding is provided to reduce further the thermal radiation heat leak.

The dewar is essential for the storage of liquid helium because of the fluid's extremely small latent heat. Modern liquid helium dewars are significantly more sophisticated than that shown in Fig. 1.3, but they still use vacuum and highly reflective surfaces to achieve efficient thermal insulating systems.

Sir James Dewar made the final development that led the way to the liquefaction of helium when he demonstrated the use of a Joule-Thomson valve to produce liquefaction of hydrogen, the last of the permanent gases with boiling points above that of helium. It is particularly significant that Dewar employed a Joule-Thomson valve, which produces essentially an isenthalpic expansion, because this method also can be used in the production of liquid helium. With liquid hydrogen available

(with a normal boiling point $T_{nbp} = 20.4$ K), it became possible to consider liquefying helium by a combination of the cascade principle and Joule-Thomson expansion. The chief remaining difficulty was that helium gas was a rare commodity around 1900.

It took another 10 years for helium to be successfully liquefied. At the time, two laboratories were vying to be the first to accomplish the task: Sir James Dewar's lab in London and H. Kamerlingh Onnes lab at the University of Leiden. For a variety of technical reasons, the Onnes group came out on top in the competition successfully achieving liquefaction of helium in 1908. At that time their total helium inventory in their lab was only 360 STP gaseous liters (equivalent to about 0.5 liquid liter), and yet as a result of this early success the Leiden rapidly became the world-wide center of liquid helium research. Among the achievements attributed to Onnes' group are included the discovery of superconductivity in many of the elements.

For the next 30 years, production of liquid helium and its associated research and applications were limited primarily to a few specialized laboratories. Researchers actively investigated the properties of materials as well as those of liquid helium down to temperatures below 1 K. Included among their discoveries are: superfluidity in ^{4}He, identification of numerous superconducting materials, and the use of magnetic cooling to achieve temperatures below 1 K. At the same time, researchers envisioned large-scale applications of helium cryogenics but lacked the motivation and resources to develop these technologies.

In the 1940s commercial development of hydrogen and helium liquefaction equipment began, owing to a large extent to the efforts of Prof. Samuel Collins of MIT and the Arthur D. Little Company. For the first time, laboratories could purchase helium liquefaction plants and liquid helium become available on the open market. Liquid helium research became more widely practiced. This point in time marked the beginning of large-scale cryogenic engineering, which required individuals skilled at design and handling of cryogenic equipment. At first, military and space applications led the field. Later major thrusts in applications of superconductivity began to dominate low temperature applications. As a result of this growth, helium cryogenic engineering has developed into a substantial discipline.

Since the development of commercial helium refrigerators, major progress has been made on the two fronts of research and development. In basic research, the ready access to large quantities of liquid helium has freed the researchers to push toward lower temperatures. Milestones in this progress must include: the development of ^{3}He-^{4}He dilution refrigeration technology permitting continuous cooling in the millikelvin temperature range; the approach to submillikelvin temperatures using techniques such as Pomaranchuk cooling and nuclear demagnetization; and the discovery of superfluidity in ^{3}He at about 2 mK.

Commercial development has also progressed substantially since the 1940s. Larger and larger liquefiers and refrigerators are being produced. Huge helium liquefaction plants with capacities in the 1,000s of liters/hour operate in various parts of the world separating helium from its primary source in natural gas wells. Supplying liquid helium for superconductivity applications has similarly increased

in scale and sophistication. Installations like the Large Hadron Collider particle physics experiment at CERN in Geneva, Switzerland now have fully automated refrigeration plants in the multi-kW range supplying liquid as well as cold gas helium to a variety of thermal loads within the accelerator facility. In addition to these larger-sized refrigerators, there has also been broad and extensive development of small stand-alone refrigerators, or cryocoolers, with cooling capacities in the 1–100 W range for cooling a wide variety of low-power applications including superconductors and infrared detectors.

Overall, helium cryogenics has now evolved into a well-established discipline providing the environment for a wide range of technologies. What is in store in the future? Trends include development of a wider range of standard products both from the very small refrigerators to the largest ones. New demands are being placed on the systems being produced: higher thermodynamic efficiency, greater reliability, and cleaner operation, and lower cost. Considerable research is aiding this progress and new technologies such as applications of high temperature superconductors are putting special demands on helium cryogenic systems. There continues to be unique and challenging applications that require low temperatures and cryogenic facilities. Thus, there is a steady demand for engineers and scientists with cryogenic engineering skills.

1.3 Applications for Cryogenics

As motivation to the discussion of the properties and production of low-temperature fluids, it is useful to identify the major applications for cryogenics technology today. Some of these are commercial enterprises, while others are still primarily in the stages of research and development. It is possible to separate these applications into at least six major categories:

1. Storage and transport of gases
2. Separation of gases
3. Biological and medical applications
4. Altering material properties by reduced temperature
5. Electronics
6. Superconductivity

Large-quantity storage and transport of gases are best achieved with the help of cryogenics. It is much more efficient from the standpoint of total weight, to transport cryogenic fluids in the liquid state rather than as a pressurized gas. Furthermore, the gases evolved from a storage dewar can maintain a lower impurity content than is common in high-pressure gas storage. There are a number of examples where cryogenic storage and transport are widely practiced. At relatively high temperatures, liquid natural gas (LNG) is transported on a large scale in tanker ships containing over 100,000 m^3 of liquid. Liquid oxygen is stored in large quantities for applications in steel production as well as to provide high-purity

gaseous oxygen supplies for hospitals. Another major application for cryogenic storage and transport is in liquid fuel rockets where LO_2 and LH_2 are common propellants. Even helium is often transported in the liquid state. This is not only because many users do not possess the necessary liquefaction equipment but also to save weight for transportation.

The separation of gas mixtures such as air or natural gas is a commercial enterprise in which cryogenics plays a major role. By using the physical properties of adsorption, that is, the tendency for gases to condense on cold surfaces, it is possible to separate gas mixtures by differences in their adsorption rates. This procedure is used commonly in extracting O_2 and N_2 from air, for purification of LNG or separation of rare gases such as Ne or He. Related to gas separation is the technology of cryopumping, where the physical process of adsorption provides a mechanism for clean, oil free, high-speed pumping systems. For this process to be effective, the pumping surfaces must be well below the critical temperature of the gas to be pumped.

Biological and medical uses for cryogenics are extensive. In these applications the goal is to store, modify, or destroy a biological structure by reducing its temperature. Storage of cellular structures in liquid nitrogen is a common practice, the largest of these being the storage of blood plasma. Other examples of this technology include storing cattle semen for artificial insemination and the preservation of food. Apart from cellular storage, medicine is making increasing use of cryogenics. In a procedure known as cryosurgery, selected areas of tissue are frozen and removed with less difficulty or trauma to the patient than by conventional surgical methods. Such techniques are commonly experienced by almost anyone who has visited a dermatologist.

The basic properties of materials change as the temperature is reduced and these effects are used in several engineering applications of cryogenics. A good application for material property variation is in the recycling industry. Cryogenic recycling uses low temperatures to separate materials. The approach takes advantage of differential thermal contraction and the increased brittle nature of materials at low temperatures. There are numerous examples of composite materials that can be recycled by this method. Thermal contraction can also be used in the construction of mechanical structures. The assembly of a close tolerance connection can be facilitated if one of the components is first cooled in a cryogenic fluid to make it slightly smaller. In these applications there is little need to reduce the temperature below the normal boiling point of liquid nitrogen because very little thermal contraction occurs below this temperature.

Besides mechanical properties, low temperatures also are used to change electrical properties of materials. One of the major applications of this process is in the cooling of detectors and other electronic sensors. The low temperature reduces the thermal noise and provides an isothermal environment for the sensor. Examples of devices that use low temperatures include infrared detectors for everything from night vision equipment to large-scale astrophysical science experiments.

The technology of superconductivity warrants special attention as an application that depends on cryogenics. The largest-scale application of superconductivity is in

magnet technology. At present, superconducting magnets are an integral part of high-energy physics accelerators, magnetic fusion confinement systems, energy storage, magnetic levitation, whole-body magnetic resonance imaging (MRI) scanners as well as specialized research magnets. Additionally, RF particle accelerators us superconducting Nb cavities that must be cooled to low temperature ($T \sim 2$ K) to achieve the required performance. Most of these systems operate at low temperature ($T < 10$ K) and thus require fairly complex helium refrigeration systems.

The discovery and development of high temperature superconductors has significantly impacted the development of cryogenic systems. Large-scale HTS superconducting applications such as are proposed for the power industry are now contemplated to operate at significantly higher temperatures, $T > 30$ K. Small-scale applications of HTS are also being developed many of which only require a few watts of cooling. These applications have had a major impact on the development of small-scale, intermediate temperature refrigeration systems. The development of cryocoolers for such applications has been an active thrust area of the field in recent years.

1.4 Thermodynamic Laws

Thermodynamic principles and concepts are of fundamental importance to the field of cryogenics. Thermodynamics forms the basis for calculations of the properties of cryogenic fluids as well as the performance of refrigeration and liquefaction systems.

There are three basic laws of thermodynamics that apply to all systems and are of particular interest to the discussion here. Although it is assumed that the reader is familiar with these laws through a previous course in thermodynamics, for completeness and commonality of notation a review of the subject is presented here. For further details, the reader should consult one of many thermodynamics text books.

1.4.1 First and Second Laws of Thermodynamics

The first law of thermodynamics involves conservation of energy in a closed system. Consider two thermodynamic states characterized by their internal energy, E_i and E_f. If we connect these two states by an adiabatic path, that is a process taking the system from one thermodynamic state to another without the production or absorption of heat, the work W needed is exactly equal to the change in the internal energy. This statement can be considered a definition of work; that is, work done on an adiabatic system is equal to the increase in the potential energy.

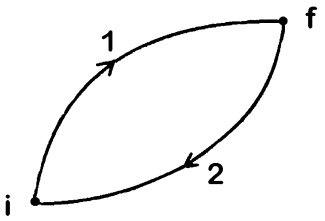

Fig. 1.4 Adiabatic paths between two thermodynamic states

On the other hand, if the process is not adiabatic, an amount of heat Q is produced during the process and conservation of energy demands that the amount of extra heat be included in the total amount of work done. This statement leads to the mathematical formulation of the first law of thermodynamics which is written,

$$Q = E_f - E_i + W \tag{1.2}$$

It is important to keep in mind that the internal energy is a state function and its change only depends on the initial and final points of a path in thermodynamic space. This is to be compared to the heat and work functions which are path dependent.

Now consider a cyclic process where a system in question is taken from the initial state through the final state and back to the initial state by some other path. This process, shown schematically in Fig. 1.4, may be a heat engine or a cycle used to refrigerate a cryogenic fluid. The principal distinction between an engine and a refrigerator is with the sign of the work process. Since the cycle closes on itself, the change in internal energy (ΔE) around the cycle is zero and the first law (1.2) demands that the difference between the heat and work for the two paths must be equal in magnitude but opposite in sign. For the entire cycle, the sum of the heat and work must be identically zero. However, the amount of work that must be done to accomplish the cycle is proportional to the enclosed area in Fig. 1.4. The larger the area, the more work that is done per cycle and in turn the larger amount of heat that must be generated.

Before discussing the other thermodynamic laws, it is useful to go into a little more detail about the work as part of a thermodynamic process. To make the first law into a more useful form for application, the initial and final states can be brought arbitrarily close together resulting in the differential form of the first law,

$$dQ = dE + dW \tag{1.3}$$

For a thermodynamic process, the differential work term dW in (1.3) can take on several forms, dependent on what type of system is of interest. Of particular interest to cryogenics are:

Liquid–gas system:

$$dW = p\,dV \tag{1.4a}$$

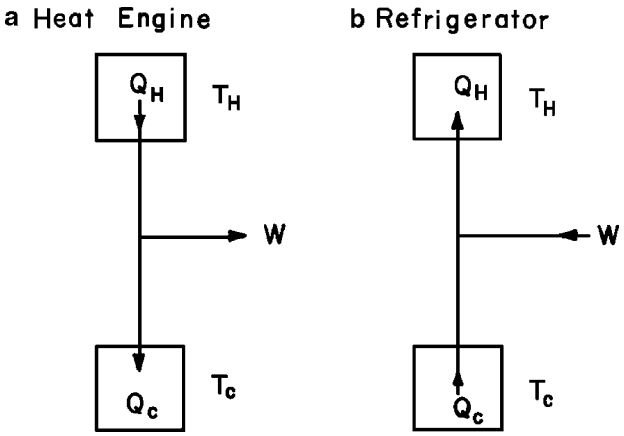

Fig. 1.5 Schematics of a heat engine and a refrigerator

Magnetic system:

$$dW = -\mu_o \mathbf{H} \bullet d\mathbf{M} \tag{1.4b}$$

Electric system:

$$dW = -\mathbf{E} \bullet d\mathbf{P} \tag{1.4c}$$

The *pdV* work term is the most common since most refrigerators use gas cycles. However, magnetic refrigerators have special applications, which will be discussed in later sections. Note that the latter two differentials are vector quantities dependent on the direction of the applied fields, while the *pdV* product is directionally independent. Fortunately, it is a rare occurrence for more than one type of work to be important in a particular system or process. The differential form of the first law is preferred in process calculations as the process variables usually change continuously within the cycle.

Moving on, the second law of thermodynamics is concerned with the conversion of heat into work and the efficiency with which this can take place. The second law works in concert with the first law to describe correctly the behavior of an ideal thermodynamic process. The second law is often defined in terms of heat engines and their performance of work [1]:

> *It is impossible to construct an engine that does work while exchanging heat with only one reservoir.*

Thus, according to the second law, any engine that performs work must have at least two reservoirs. By analogy, a refrigerator, which is simply an heat engine running in reverse, also requires two reservoirs; the low temperature one from which heat is absorbed and the high temperature one into which heat is rejected. Schematic configurations of a heat engine and a refrigerator are shown in Fig. 1.5.

The attached subscripts refer to the hot (H) and cold (C) reservoirs. Note that the engine supplies work while the refrigerator requires work to complete the process.

The combined first and second law therefore require an engine or refrigerator to operate between two reservoirs at different temperatures. For an engine, the thermodynamic efficiency η for such a process is given in terms of the work output W divided by the heat input, Q_H.

$$\eta = \frac{W}{Q_H} = \frac{Q_H - Q_C}{Q_H} \tag{1.5}$$

Note that we have used the first law for the thermodynamic cycle to replace W with $Q_H - Q_C$, which explicitly shows why η must always be less than unity. It is apparent that an efficiency of unity can never be achieved because the second law requires two reservoirs and Q_C is always finite.

For a refrigerator, the important quantity to optimize is the coefficient of performance (COP), which is defined as the ratio of the heat extracted from the low temperature reservoir to the work done on the system,

$$COP = \frac{Q_C}{W} = \frac{Q_C}{Q_H - Q_C} \tag{1.6}$$

Thus the COP is just the inverse of the efficiency. For the case of an engine, the work done is given by the area enclosed by the cycle and the heat is expelled at T_C. On the other hand, for a refrigerator, the heat is expelled at $\mathrm{T_H}$ and the cycle uses the work to extract heat at T_C.

The entropy S is a state function that is commonly used in cryogenic systems because it better defines the process variable that one is trying to minimize. For example, the most efficient process available for refrigeration is isentropic, $\Delta S = 0$ and this is only achievable if the processes are fully reversible. On the other hand, if the process is done irreversibly (such as Joule-Thomson isenthalpic expansion) or with exchange of heat, then $\Delta S > 0$ and there is entropy generated. The Clausius theorem, which is part of the second law, refers to the entropy associated with a closed cycle. If such a cycle follows reversible paths, the Clausius theorem states that the entropy change through the cycle is identically zero.

Like all thermodynamic variables, entropy also has a definition based on statistical mechanics. The statistical definition of entropy is associated with order in the system. The greater the order the lower the entropy. Thus, a condensed liquid is in a lower entropy state than its coexisting vapor. Normally, the solid state of a substance is in a lower entropy state than the liquid state because the crystal periodicity implies a more ordered system. In a magnetic system, if the spins are all aligned with the applied magnetic field they are more ordered and in a lower entropy state than if they are randomly oriented. This would suggest that if absolute zero were attainable, the system would be completely ordered, i.e. all the spins would be aligned and the solid would be perfectly periodic. Helium is an exception to this general rule, as will be discussed later, because of its quantum nature the lowest entropy state of helium is liquid.

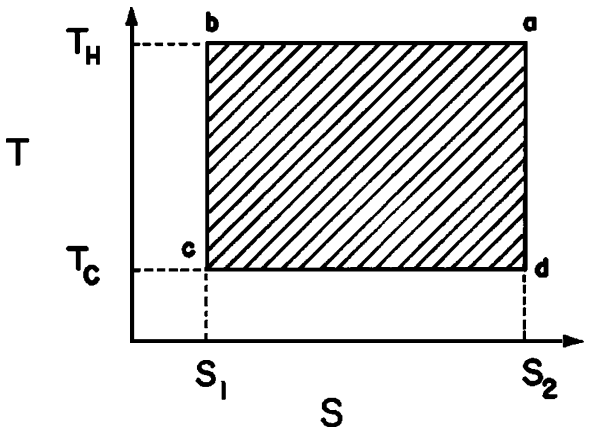

Fig. 1.6 Carnot cycle

In statistical mechanics, the definition of entropy evolves from introduction of a thermodynamic probability function Ω, which is a measure of the occupation of the states in the thermodynamic system. Entropy is given mathematically by a function of this probability,

$$S = k_B \ln \Omega \tag{1.7}$$

where k_B, is the Boltzmann constant equal to 1.38×10^{-23} J/K molecule. Incidentally, other state functions of the system are also defined in terms of Ω. The statistical definition of entropy leads to a natural physical understanding of absolute zero temperature. At absolute zero, the system is in a ground state with the probability of that state being occupied at unity. Consequently, the probability function is equal to unity ($\Omega = 1$) and by the definition in (1.7) $S_0 \equiv 0$.

A useful application of the entropy concept is obtained by considering a Carnot refrigerator. The Carnot cycle is shown schematically by the four-step process in Fig. 1.6. The first step in the cycle takes the thermodynamic system isothermally (at constant temperature) from (a) to (b), decreasing the entropy from S_2 to S_1. This process could be for example the isothermal compression of a gas at high temperature. The second step is an isentropic process (constant entropy) that reduces the temperature of the system from T_H to T_C, taking it from (b) to (c). The third step then heat exchanges with the low-temperature reservoir, a process (c) to (d) that takes place isothermally. Finally, the cycle is completed by an isentropic return to the original point (a). Since the Carnot cycle is reversible the work done is equal to the area enclosed by the cycle. The amount of heat absorbed from the low-temperature reservoir is $Q_C = T_C \Delta S$ and the heat ejected in the hot reservoir is $Q_H = T_H \Delta S$. Therefore, for a Carnot cycle the ratio of Q_C to Q_H is simply the ratio of absolute temperatures,

$$\frac{Q_C}{Q_H} = \frac{T_C}{T_H} \tag{1.8}$$

From (1.6), it is easy to show that the *COP* of a Carnot refrigerator is,

$$COP = \frac{T_C}{T_H - T_C} \tag{1.9}$$

The ideal Carnot refrigerator is used as a comparative standard for practical refrigeration systems. Any real refrigeration system operates at a fraction of Carnot performance due to the non-ideal nature of the processes involved in the cycle.

1.4.2 Third Law of Thermodynamics

The unattainability of absolute zero, the third law of thermodynamics, has fundamental significance in numerous aspects of cryogenics. Since the difficulty in achieving low temperatures increases as the temperature is decreased, cryogenics, by definition, is an attempt to fight this thermodynamic law. Additionally, the third law helps us understand the behavior of thermodynamic variables as absolute zero is approached. For example, considering an isothermal change in pressure in a liquid–gas system, we can express the entropy change as

$$S(T,p) - S(T,0) = -\int_0^p \left(\frac{\partial V}{\partial T}\right)_p dp \tag{1.10}$$

an expression obtained by integrating one of Maxwell's relations [1]. Similarly, for a magnetic system, an isothermal change in magnetic field leads to the following expression:

$$S(T,H) - S(T,0) = \mu_0 \int_0^H \left(\frac{\partial M}{\partial T}\right)_H dH \tag{1.11}$$

where M is the magnetization of the material. By combining (1.10) and (1.11) with the third law of thermodynamics a statement can be made about the behavior of V and M as absolute zero is approached. Specifically, since ΔS approaches zero as $T \rightarrow 0$, both the volume and magnetization must approach constant values.

In addition to the above conventional statement of the third law and unattainability of absolute zero, the Nernst-Simon statement concerns itself specifically with entropy change [1]:

> *Entropy change associated with an isothermal reversible process in a condensed system approaches zero as $T \rightarrow 0$.*

Since the Nernst-Simon statement deals only with the entropy change, the absolute entropy of a system at $T = 0$ must be a universal constant. It can be shown further that this constant can arbitrarily be set identical to zero.

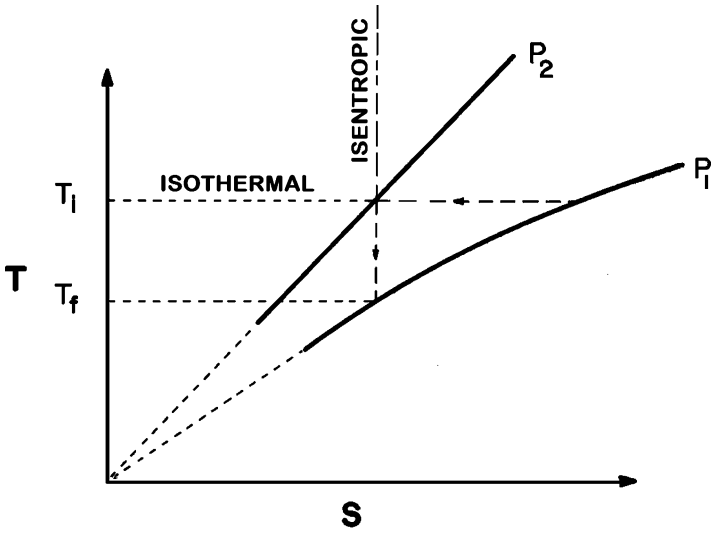

Fig. 1.7 Schematic *T*-*S* diagram showing isothermal and isentropic properties

The unattainability of absolute zero can be demonstrated by a number of examples. One useful example is based on the Nernst-Simon statement of the third law ($\Delta S \rightarrow 0$). Consider the schematic *T*-*S* diagram in Fig. 1.7 showing two isobars (constant pressure curves). For this type of system, it is fairly straightforward to achieve cooling and reduce the temperature by performing a constant entropy (isentropic) expansion from T_i to T_f. It would appear possible to extend this procedure toward absolute zero by a repeated application of isothermal compression from p_1 to p_2 and subsequently isentropic expansion from p_2 to p_1. However, the third law states that $\Delta S_0 = 0$ so the two isobars must approach the same value of the entropy at $T \rightarrow 0$. Thus, it should take an infinite number of steps to reach absolute zero by this process.

These concepts are integral to the processes and properties that make up cryogenic systems. In engineering systems operating near room temperature, it is common to treat many of the process variables as constants or at least as simple functions of temperature. These kinds of simplifications are generally not suitable for cryogenic system analysis as will become clear in subsequent sections of this book.

Questions

1. Why is it more efficient to store and transport industrial gasses as cryogenic liquids?
2. What are the principal differences between a heat engine and a refrigerator?
3. What does the third law of thermodynamics tell us about the heat capacity of a solid as T approaches 0 K?

4. Show that the thermodynamic definition of entropy leads to a logarithmic temperature scale.
5. Compare T_b/T_c for some common cryogenic fluids. Comment on the relative values.

Further Readings

1. Absolute Zero, Public Broadcasting Special: http://www.pbs.org/wgbh/nova/zero/about.html
2. R. de Bruyn Ouboter, Superconductivity: Discoveries during the Early Years of Low Temperature Research at Leiden, *IEEE Trans. on Magnetics*, **Vol. Mag-23**, 355 (1987).
3. K. Mendelssohn, *Quest for Absolute Zero*, World University Press, 1966.
4. R. G. Scurlock, *History and Origins of Cryogenics*, Oxford Science Publications, 1992.
5. T. Shachman, *Absolute Zero and the Conquest of Cold*, Houghton Mifflin Co. New York, 1999.
6. K. D. Timmerhaus and R. P. Reed, *Cryogenic Engineering: Fifty Years of Progress*, Springer, New York, 2007.
7. M. W. Zemansky, *Heat and Thermodynamics*, McGraw Hill, New York, 1968.

Chapter 2
Low-Temperature Materials Properties

Before delving into the fluids and processes associated with helium cryogenics, it is important to first have a working knowledge of the relevant properties of other materials at low temperatures. This knowledge is valuable in part because materials have behavior that must be taken into account when considering the problems of refrigeration, heat transfer, or storage of low temperature helium. In addition as seen in subsequent chapters, many of the properties of helium are understood in terms of physical models that were primarily developed to treat the properties of different materials at low temperatures.

The study of material properties at low temperatures continues to be an active field of research. Current investigations include studies of the properties of materials at ultralow temperatures, $T \approx 1$ mK, new materials such as alloys and composites as they depend on external variables such as temperature, pressure and magnetic field, and new types of investigation on traditional materials. Much of this work is fundamental in nature. On the other hand, since many material properties play an important role in the design and construction of low-temperature systems, it is essential to have a thorough knowledge of their behavior.

The present chapter is a survey of those properties that are of greatest importance to cryogenic applications. Included in the discussion are the behavior of state properties such as the internal energy and heat capacity, thermal expansion or contraction, transport properties including the electrical and thermal conductivities, and finally mechanical properties. The discussion concentrates on solid elements and alloys. The special properties of superconductors will also be included although the discussion is brief due to space limitations. Most of the descriptions are based on either thermodynamic or solid-state physics principles. More extensive discussions of these topics may be found in textbooks on the relevant subjects [1, 2]. In addition, for applications there are a number of property databases [3, 4] and books [5, 6] that collate available experimental data and can be useful in analysis and design.

S.W. Van Sciver, *Helium Cryogenics*, International Cryogenics Monograph Series,
DOI 10.1007/978-1-4419-9979-5_2,

2.1 Heat Capacity

The heat capacity is a fundamental state property of matter. It represents the amount of energy needed to raise the temperature of a known quantity of a material one degree. The heat capacity per unit mass is called the specific heat. In cryogenic systems, the heat capacity of a material is integral to numerous calculations including: the dynamics of cooling devices from superconducting magnets to sensors, thermal energy storage, dynamic thermal loading on refrigeration systems, and transient heat transfer.

As with many physical properties, the heat capacity is defined in terms of other thermodynamic state variables. In particular, it can be written as a derivative of either the entropy S or internal energy E. Because these state functions are described in a liquid–gas system in terms of an equation of state relating pressure p, temperature T, and specific volume v, one variable usually must be held constant in the definition of the heat capacity or specific heat. For example, the constant volume heat capacity is written in terms of a derivative of the entropy or internal energy as,

$$C_v = T\left(\frac{\partial S}{\partial T}\right)_v = \left(\frac{\partial E}{\partial T}\right)_v \tag{2.1}$$

while the constant pressure heat capacity may be written

$$C_p = T\left(\frac{\partial S}{\partial T}\right)_p = \left(\frac{\partial E}{\partial T}\right)_p + p\left(\frac{\partial v}{\partial T}\right)_p \tag{2.2}$$

It is also possible to define the heat capacity with other external variables held constant. For systems where magnetic properties are of importance, C_H or C_M may be used to designate the heat capacity at constant applied magnetic field or magnetization. This topic is of particular interest in magnetic cooling systems and is discussed in Chap. 10.

A useful relationship between C_p and C_v is obtained from thermodynamic expressions and is given by

$$C_p - C_v = -T\left(\frac{\partial v}{\partial T}\right)_p^2 \left(\frac{\partial p}{\partial v}\right)_T = \frac{Tv\beta^2}{\kappa} \tag{2.3}$$

where $\beta = \frac{1}{v}\left(\frac{\partial v}{\partial T}\right)_p$ is the volume expansivity and $\kappa = -\frac{1}{v}\left(\frac{\partial v}{\partial p}\right)_T$ is the isothermal compressibility.

An extensive amount of experimental data exists for the heat capacity of solids at low-temperatures. For simple solid materials such as metals and crystalline insulators, there is a very good match between experiment and theory. For example, measurements near and above room temperature give close correspondence with

the classical model of harmonic oscillators due to DuLong and Petit for which the heat capacity is equal to $3N_0k_B = 3R$, where N_0 is Avogadro's number = 6.023×10^{23} molecules/mole and k_B is Boltzmann's constant = 1.38×10^{-23} J/molecule K. The gas constant $R = 8.31$ J/mol K. This classical model is based on the equipartition of energy which assigns $\frac{1}{2}k_BT$ to each of the three kinetic energy and three potential energy degrees of freedom in the three-dimensional solid.

At low temperatures, there is markedly different behavior according to the type of solid considered. Over most of the cryogenic range for crystalline solids, the dominant temperature dependence is proportional to T^3. At very low temperatures, $T \lesssim 10$ K, crystalline insulators maintain the T^3-dependence while metals have heat capacities that become linearly proportional to temperature as $T \to 0$. Non-crystalline amorphous materials also have a heat capacity is proportional to T^n where $n \sim 3$. Finally, the difference between C_v and C_p becomes negligible as $T \to 0$ for all solids. This fact can be used in conjunction with (2.3) to show that the volume expansivity, β, must also go to zero at very low temperatures.

2.1.1 Lattice Heat Capacity

Two relatively simple theories are available to describe the general behavior of the heat capacity of metals and crystalline insulators over the entire temperature range of interest [1]. The first such theory is based on the energy contained in the quantized lattice vibrations or phonons that exist in a solid. For most solids, except metals at very low temperatures, this phonon contribution to the heat capacity dominates.

To calculate the phonon heat capacity, we begin with an expression for the internal energy E_{ph} of an ensemble of phonons as a function of their characteristic frequencies ω,

$$E_{ph} = \frac{h}{2\pi} \int D(\omega) n(\omega) \omega d\omega \tag{2.4}$$

In this case, $D(\omega)$, the phonon density of states, describes the fraction of phonons that occupy a particular energy level characterized by its frequency ω. The function $n(\omega)$ is the statistical distribution function, which for phonons obeying Bose-Einstein statistics, is given by [7],

$$n(\omega) = \frac{1}{e^{h\omega/2\pi k_B T} - 1} \tag{2.5}$$

with $h = 6.63 \times 10^{-23}$ J s is Planck's constant. The model-dependent choice in the theory is included in the selection of the proper density of states function, $D(\omega)$. This problem can be quite complicated depending on the detailed nature of the excitations within the solid. Fortunately, many materials at least approximately obey the simplifying assumptions inherent in the Debye model.

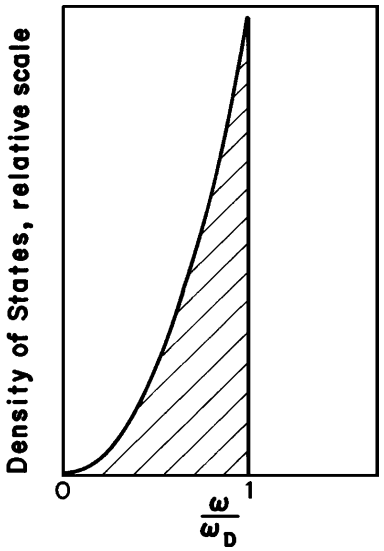

Fig. 2.1 Density of states $D(\omega)$ versus ω for the Debye model for a constant phonon velocity

The Debye model assumes that the density of states is described by a continuum of levels up to the characteristic frequency ω_D, referred to as the Debye frequency. The density of states is then proportional to ω^2 and is shown schematically in Fig. 2.1.

Inserting the Debye density of states and distribution function into the equation for the internal energy of the phonons, (2.4), a nearly closed-form solution for this quantity is obtained,

$$E_{ph} = 9RT\left(\frac{T}{\Theta_D}\right)^3 \int_0^{x_D} \frac{x^3}{e^x - 1} dx \tag{2.6}$$

where $x = h\omega/2\pi k_B T$, $x_D \equiv \Theta_D/T$. The Debye temperature Θ_D is defined in terms of the maximum phonon frequency, ω_D, see Fig. 2.1. The Debye temperature is characteristic to a particular material and has a simple form,

$$\Theta_D = \frac{hc}{2\pi k_B}\left(6\pi^2 \frac{N}{V}\right)^{1/3} \tag{2.7}$$

where c is the speed of sound in the material and N/V is the number of molecules per unit volume. In real materials, the Debye temperature may be a function of more variables than just the number density as described in (2.7), so the above description is only an approximation [1].

The heat capacity in the Debye model can be calculated directly from differentiation of the internal energy, (2.6), with respect to temperature

$$C_{ph} = 9R\left(\frac{T}{\Theta_D}\right)^3 \int_0^{x_D} \frac{x^4 e^x}{(e^x - 1)^2} dx \tag{2.8}$$

The definite integration within (2.8) can be easily performed numerically once Θ_D is known. However, one can obtain considerable insight be studying the limiting form of C_{ph}, which can be checked by evaluating (2.8) at either high or low temperatures relative to Θ_D.

In the high temperature limit, $x_D \ll 1$, the exponentials within the integral may be expanded as $e^x \sim 1 + x$ and simply integrated leading to a constant value for C_{ph}

$$C_{ph} = 3R \; for \; T \gg \Theta_D \tag{2.9}$$

which is the classical Dulong-Petit limit. Note that the heat capacity per mole is constant in this range and on the order of 25 J/mole K. On the other hand, at low temperatures, $x_D \gg 1$, the upper limit of the integral may be taken to be infinite, which makes the exponential terms dominant. The result leads to constant value for the definite integral and a cubic temperature dependence for the heat capacity,

$$C_{ph} = \frac{12\pi^4}{5} R \left(\frac{T}{\Theta_D} \right)^3 \text{ for } T \ll \Theta_D \tag{2.10}$$

which accurately reproduces the cubic temperature dependence of the heat capacity observed for many materials at low temperatures. Thus, a measurement of the heat capacity of a solid at low temperature is one way of determining the Debye temperature. Note that (2.10) indicates that low Debye temperature materials will have relatively larger heat capacities at low temperature, which is technically significant for refrigeration.

The simplicity of the Debye model and the dominance of the phonon contribution to the heat capacity over most of the relevant temperature range makes it a useful tool for approximate calculations in cryogenics. One can simply tabulate the C_{ph} and E_{ph}/T in terms of T/Θ_D as is shown graphically in Fig. 2.2. These are universal forms for the Debye phonon heat capacity and internal energy in Joules/mole K that depend only on the value of Θ_D. For most solid materials, the Debye temperatures range from 100 to 1,000 K with examples listed in Table 2.1. This simple analysis is usually accurate to within 20%.

Example 2.1

Using the Debye model, Fig. 2.2, estimate the change in internal energy of a 1 kg copper block when it is cooled from 300 to 80 K.

Molar weight of copper is 0.0635 kg/mol. Thus, 1 kg = 15.75 mol.
The Debye temperature of copper is 343 K (see Table 2.1).
At 300 K, $T/\Theta_D = 0.87$ and at 80 K, $T/\Theta_D = 0.23$

From the graph, E_{ph}/T (300 K) ~ 15 J/mol K; and E_{ph}/T (80 K) ~ 6 J/mol K
Thus, the internal energy is dominated by its 300 K value. For the 1 kg copper block,

$E_{ph} \sim [15 \text{ J/mol K} \times 300 \text{ K} + 6 \text{ J/mol K} \times 80 \text{ K}] \times 15.75 \text{ mol} = 63 \text{ kJ}$.

Note: This problem could also be solved numerically by integration of (2.8).

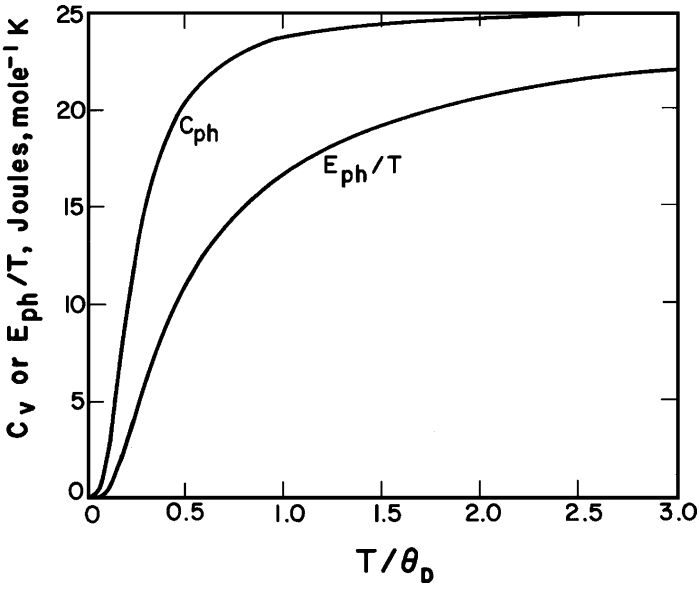

Fig. 2.2 Debye specific heat and internal energy functions

Table 2.1 Debye temperatures for common elements in cryogenics [1]

Element	Θ_D (K)
Al	428
Au	165
Cd	209
Cr	630
Cu	343
Fe	470
Ga	320
Hf	252
Hg	71.9
In	108
Nb	275
Ni	450
Pb	105
Sn	200
Ti	420
V	380
Zn	327

2.1.2 Electronic Heat Capacity

For metals at low temperatures, $T < 10$ K, there is an additional significant contribution to the heat capacity due to the energy contained in the conduction electrons. Fortunately, as with the phonon contribution, the electron contribution to the heat capacity can also be approximately described by a simple theory. The free-electron model treats the conduction electrons as a non-interacting gas of spin ½ particles. Thus, as in the case of the Debye model, the internal energy of the electron gas E_e is written in terms of the density of states $D(\varepsilon)$ [1],

$$E_e = \int D(\varepsilon) f(\varepsilon) \varepsilon d\varepsilon \tag{2.11}$$

where ε is the electron energy used as a variable in this case instead of frequency in the Debye model. The density of states in the free-electron model is written,

$$D(\varepsilon) = \frac{V}{2\pi^2} \left(\frac{m}{2\pi^2} \right)^{3/2} \varepsilon^{1/2} \tag{2.12}$$

Since electrons are spin ½, they must obey Fermi-Dirac statistics, which means that each energy level can have no more than one electron. The Fermi – Dirac distribution function is [7],

$$f(\varepsilon) = \frac{1}{e^{(\varepsilon - \mu)/k_B T} + 1} \tag{2.13}$$

where μ is the chemical potential, which is approximately equal to the Fermi energy, ε_f, at low temperatures [1].

The free-electron model defines the Fermi energy ε_f in terms of the total number of free electrons per unit volume, N_e/V

$$\varepsilon_f = \frac{h^2}{8\pi^2 m_e} \left(3\pi^2 \frac{N_e}{V} \right)^{2/3} \tag{2.14}$$

where m_e is the mass of an electron equal to 9.11×10^{-31} kg. Thus, the Fermi energy only depends on the number density of electrons. One can also define a characteristic temperature, called the Fermi temperature, $T_F = \varepsilon_F / k_B \sim 10^4$ K.

Ordinarily and certainly in cryogenics, the electron temperature in a metal is far below the Fermi temperature so that only a small fraction of the electrons near the Fermi surface contribute to the thermal properties. Because $T \ll T_F$, the electrons in a metal generally are referred to as a degenerate Fermi gas. For a degenerate Fermi gas the internal energy (2.11) can be simply evaluated. The electronic contribution to the heat capacity then turns out to be linearly proportional to the absolute temperature,

$$C_e = \gamma T \tag{2.15}$$

Table 2.2 Coefficient of the electronic specific heat for various metallic elements of technical interest [1]

Element	γ(mJ/mol K^2)
Ag	0.646
Al	1.35
Au	0.729
Cr	1.40
Cu	0.695
Fe	4.98
Ga	0.596
Hg	1.79
In	1.69
Nb	7.79
Ni	7.02
Pb	2.98
Sn	1.78
Ti	3.35
V	9.26
Zn	0.64

where $\gamma = \frac{1}{3}\pi^2 D(\varepsilon_F)k_B^2$ is sometimes called the Sommerfeld constant with $D(\varepsilon_F)$ being the electron density of states evaluated at the Fermi energy (2.14). The Sommerfeld constant has been measured for many metals and some typical values are listed in Table 2.2. To give a rough idea of the importance of the electronic contribution to heat capacity, one should note that for copper the electron and phonon contributions are equal at about 3.8 K.

2.1.3 Heat Capacity of Special Materials

The above general trends in the heat capacity of solid materials are fairly universal. However, they do not describe all materials and the usefulness of the Debye and free electron models is limited. In other cases, the knowledge of the heat capacity of materials is more empirical.

Figure 2.3 is a plot of the specific heat of a variety of materials used in cryogenics [6]. Note that these materials display similar trends in C_p to the theory discussed above. The pure metals (Fe, Cu, Al, Be) show a linear dependence at low temperatures ($T < 10$ K) followed by a transition region where C_p is proportional to T^3 and finally appproach a near constant value above 100 K. The metallic alloys (stainless steel, brass) generally do not display the linear region due to a smaller contribution by free electrons otherwise their behavior is similar to that of pure metals. Non-metals (Pyrex, glass resin) show only a T^n dependence ($n \sim 3$) at low temperatures due to the dominance of the phonon excitations.

Also, there are certain special materials that have anomalous low temperature heat capacities that are unique and also significant for cryogenic applications.

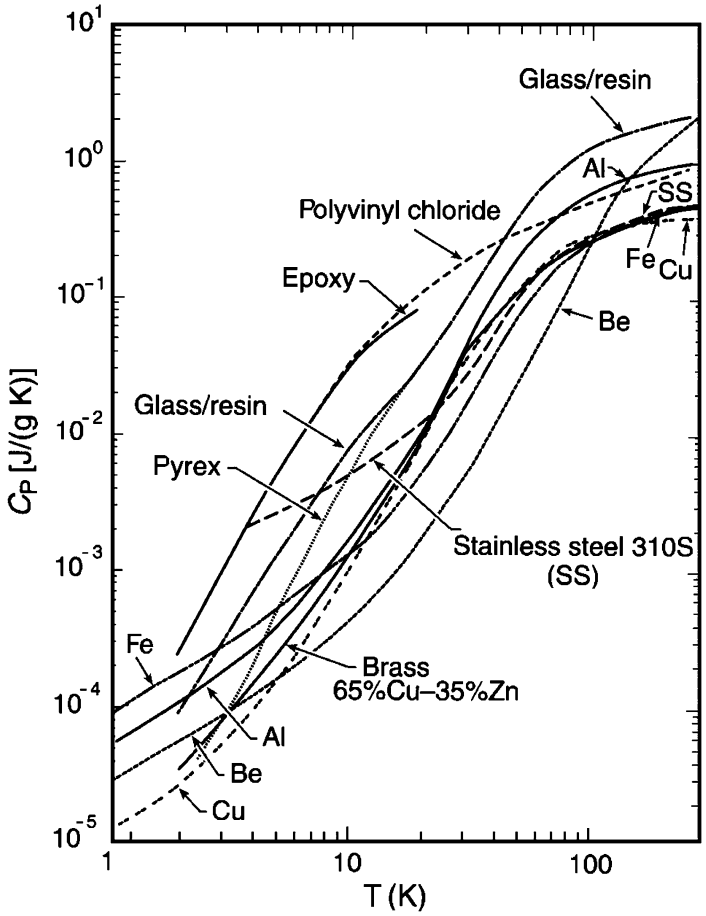

Fig. 2.3 Specific heat capacity of technical materials used in cryogenics (Reprinted from Ekin [6])

One such class of materials are those that undergo magnetic ordering transitions at low temperatures. These transitions produce a large peak in the specific heat, see Fig. 2.4. Most of these materials consist of rare earth compounds where the magnetic ions such as gadolinium (Gd^{++}) undergo ordering at low temperatures. These materials are useful as thermal capacity stores in low temperature cryocooler regenerators, a topic discussed in that context in Chap. 8. They are also used in magnetic refrigeration where the order – disorder transition can be driven by application of a magnetic field. This topic is discussed in Chap. 10.

Finally, superconducting materials undergo phase transitions with a discontinuity in the heat capacity at the onset of the superconducting state, $T = T_c$. Below T_c, the heat capacity of a superconductor decreases rapidly below that of the normal state, particularly at very low temperatures where the phonon contribution is small.

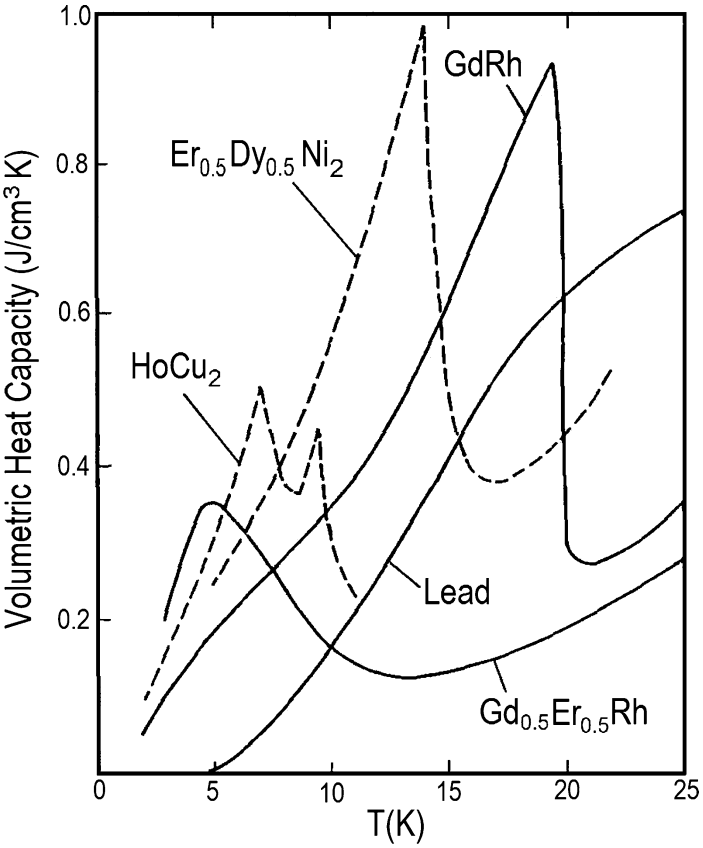

Fig. 2.4 Volumetric specific heat to metallic compounds with low temperature phase transitions (Reprinted from Nageo, et al [8])

This behavior has to do with the very nature of superconductivity, a topic that is discussed further in Sect. 2.5.

2.2 Thermal Contraction

All materials experience a change in physical dimension when cooled to low temperatures. This effect, normally referred to as thermal contraction in the field of cryogenics, is typically on the order of a few tenths of a percent change in volume in most materials between room temperature and liquid helium temperatures. Although the effect is not large in absolute magnitude, it can have a profound impact on the design of engineering devices operating in a low-temperature environment. The thermal contraction coefficients of different materials vary by as much as an order of magnitude. Furthermore, since most devices constructed to

operate in cryogenic systems are fabricated at room temperature out of a number of different materials, one of the major concerns is the effect of the differential thermal contraction and the associated thermal stress that may occur when two dissimilar materials are bonded together. Differential contraction is especially important to the design of low temperature vacuum seals, structural supports, and electrical insulation systems. Thus, it is of considerable importance to understand this behavior of technical materials. There are a number of good reviews in the literature on this subject [9–12].

The thermal contraction or expansion has a thermodynamic definition, which can be combined with other state properties to make predictions of the details of the properties of materials at low temperatures. For liquids and gases, the most meaningful form to consider is the volume expansivity defined as,

$$\beta = \frac{1}{V}\left(\frac{\partial V}{\partial T}\right)_p \tag{2.16}$$

where β is in general a function of temperature. For solids, where the changes in individual dimensions may be different due to anisotropic effects, the linear thermal expansion coefficient,

$$\alpha = \frac{1}{L}\left(\frac{\partial L}{\partial T}\right)_p \tag{2.17}$$

is a more appropriate and common factor to consider and is the value that is tabulated in the literature. For isotropic materials, $\alpha = 1/3\beta$ to first order. For many common solids near room temperature, the linear expansion coefficient is approximately constant.

In a solid, the thermal expansion is caused by anharmonic terms in the restoring potential between the individual molecules. Recall that the Debye model assumes that a solid is comprised of a set of harmonic oscillators. Therefore, the Debye model in its simplest form does not predict the existence of thermal expansion. Anharmonic terms in the interaction potential are what cause the non-zero β. For molecules in a solid, the anharmonic terms can be represented as variations in the Debye temperature Θ_D with the specific volume. This variation may be written,

$$\gamma_G \equiv -\frac{d(\ln \Theta_D)}{d(\ln V)} \tag{2.18}$$

where γ_G is referred to as the Grüneisen coefficient, values of which for a few elements are listed in Table 2.3. The Grüneisen coefficient, which is nearly constant over a temperature range down to $T \approx \Theta_D/5$, can be used along with other thermodynamic properties to calculate the thermal expansion coefficient,

$$\alpha = \frac{\gamma_G C_v \kappa}{3v} \tag{2.19}$$

Table 2.3 Values for the Grüneisen coefficient y_G for common elements [1]

Element	y_G
Ag	2.40
Al	2.17
Cu	1.96
Fe	1.6
Ni	1.88
Pt	2.54

where κ is the isothermal compressibility. For metals at low temperatures, $T < \Theta_D/25$, the dominant temperature dependence of α is in the specific heat, $C_v \approx \gamma T + \beta T^3$.

At low temperatures, the expansion coefficient is far from linear and actually approaches absolute zero with zero slope, a fact that can be understood in terms of thermodynamics. In (2.3), the difference between the constant volume and constant pressure heat capacity is shown to be proportional to the square of the volume expansivity β. Since according to the Third Law of Thermodynamics, the quantity $(C_p - C_v)$ must go to zero as $T \rightarrow 0$, it follows that β also must do so. This effect makes sense physically because the harmonic terms would be expected to dominate the interatomic potential at such low temperatures.

Because of the nonlinear nature of α and β, it is often more useful to have the integrated thermal contraction for the purpose of design. Figure 2.5 displays the integrated linear contraction of a number of common materials used in cryogenic applications [6]. Note that metals typically have total contractions in the range of 0.5% or less with the lowest value being for Invar, which is a special metal designed to have a low value of α. Polymers such as epoxy or Teflon contract about three times as much as metals and can have a total contraction between 300 and 4 K as high as 2%. Some amorphous materials, particularly Pyrex, have nearly zero or sometimes negative thermal contraction coefficients.

Composite materials often can have their thermal contraction predicted based on a linear combination of the two individual materials, taking into account the elastic modulus of each constituent. This approach to estimating the thermal contraction of a composite is referred to as the rule of mixtures. However, composite materials are frequently anisotropic by design, which makes their linear contraction coefficients dependent on the internal structure and orientation of the component materials. A clear example of this behavior can be seen in the structural material, G-10, which is a composite of epoxy and fiberglass. In this case, the thermal contraction of the composite depends on the volume ratios of the two materials and the orientation of the fibers within the composite. For example, the integrated $\Delta L/L$ from 300 to 4.2 K is about 0.25% for G-10 in the fiber direction (wrap) and about 0.75% normal to the fiber direction.

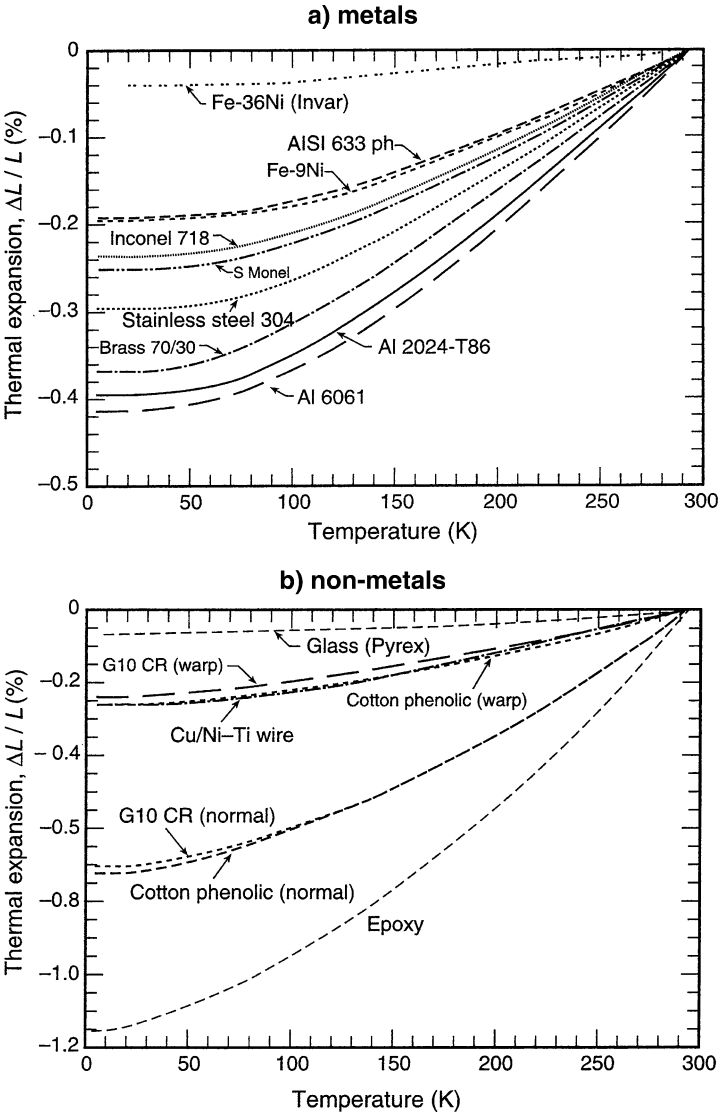

Fig. 2.5 Total thermal expansion/contraction for materials commonly used in cryogenics: (**a**) metals; (**b**) non-metals (Reprinted from Ekin [6])

2.3 Conductivities: Electrical and Thermal

The electrical and thermal conductivities are non-equilibrium transport properties that determine, among other things, the heat generated due to current flow or the heat flow due to a temperature difference. In general, the electrical and thermal conductivity of pure metals is higher than that of alloys, which is why pure copper,

aluminum and silver are common electrical conductors or thermal conduction straps in cryogenic systems. On the other hand, insulating materials and composites do not carry electrical current at all and for the most part have lower thermal conductivities, which makes such materials best for thermal and electrical insulating supports. Some special crystalline insulators have high thermal conductivities that are useful for electrical insulating connections that require good thermal contact.

2.3.1 Electrical Resistivity of Metals

Near room temperature, the electrical resistivity of most pure metals decreases monotonically with temperature following an approximately linear relationship. This trend is the result of electron–phonon scattering and is the dominant temperature-dependent contribution to the resistivity $\rho(T)$. At low temperatures, the resistivity trends to a constant value, which is approached when the metal is near liquid helium temperature. The constant value of low temperature is referred to as the residual resistivity ρ_0 and is strongly dependent on the purity and amount and distribution of lattice imperfections in the metal. Generally, these two effects are additive, obeying what is known as Matthiessen's rule that the total resistivity is the sum of two contributions,

$$\rho = \rho_0 + \rho(T) \tag{2.20}$$

As an example of the behavior of electrical resistivity consider Fig. 2.6, which is a plot of $\rho(T)$ for various purities of copper, defined in terms of the residual resistivity ratio [RRR $= \rho(273\ \text{K})/\rho\ (4.2\ \text{K})$]. The more pure and defect free the metal, the higher its RRR value. It should also be noted that the temperature at which essentially constant resistivity is obtained decreases with increasing purity. The other point of interest in the figure is that the high-temperature ($T \approx 300$ K) resistivity is essentially independent of RRR, consistent with the dominance of electron–phonon scattering. This universal form for the resistivity of pure metals makes them very useful as temperature sensors. For example, platinum resistance thermometers are often preferred for accurate measurements in the intermediate temperature regime (30–300 K) where their sensitivity, dR/dT, is roughly constant. The electrical resistivity is one of the easiest properties to measure and as a result $\rho(T)$ is known and tabulated for many elements and alloys of interest [13–18].

The theoretical interpretation of electrical conductivity of metals associates the loss mechanism with scattering processes between the electrons and the lattice. Considering a low-frequency transport of electrical current in a metal, we can relate the conductivity to the mean scattering time, $\tau \approx l/v_F$, where l is the mean free path between electron scattering events and $v_F = (2E_f/m)^{1/2}$ is the Fermi velocity. Elementary theory of electrical conductivity gives σ as,

$$\sigma = \frac{ne^2\tau}{m_e} \tag{2.21}$$

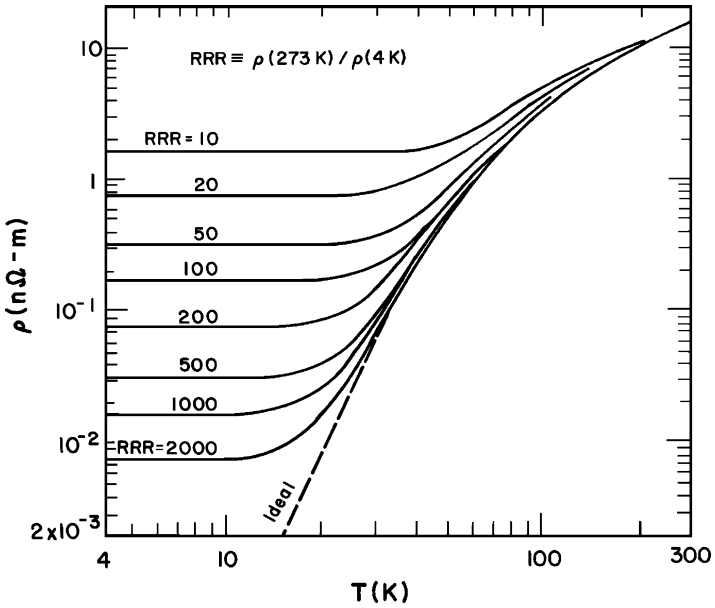

Fig. 2.6 Electrical resistivity versus temperature of differing purities of copper, $\rho(273\ \mathrm{K}) = 15.45\mathrm{n}\Omega\ \mathrm{m}$ (Reprinted from Powell and Fickett [13])

where $n = N_e/V$ is the number of conduction electrons per unit volume and m_e is the electron mass.

As mentioned above, there are two principal types of electron-lattice scattering that determine the magnitude of the electrical conductivity. For fairly high temperatures, $T \approx \Theta_D$, the dominant mechanism is due to electron scattering by quantized lattice vibrations, phonons. A simple way to see the temperature dependence of this effect is to relate the magnitude of the phonon scattering with the mean square displacement of the molecules in the lattice, $<x^2>$. In a simple harmonic solid, this quantity is proportional to $k_B T$, the thermal energy of the lattice. Assuming that the electrical resistivity is proportional to the magnitude of phonon scattering, near room temperature the resistivity of metals should also be proportional to T, a fact borne out at least approximately by the data.

For low temperatures, $T << \Theta_D$, the phonon scattering decreases with T giving way to scattering dominated by lattice imperfections. In this domain the resistivity approaches a temperature-independent value determined primarily by the amount of impurities and imperfections in the lattice. For metallic elements, a few parts per million of impurities can have a profound effect on electron transport as can the amount of cold work generated imperfections. At the lowest temperatures with the purest samples, the mean free path of the electrons can become very large approaching the sample size, such that scattering off the surface of the sample can contribute a size effect dependence to the resistivity.

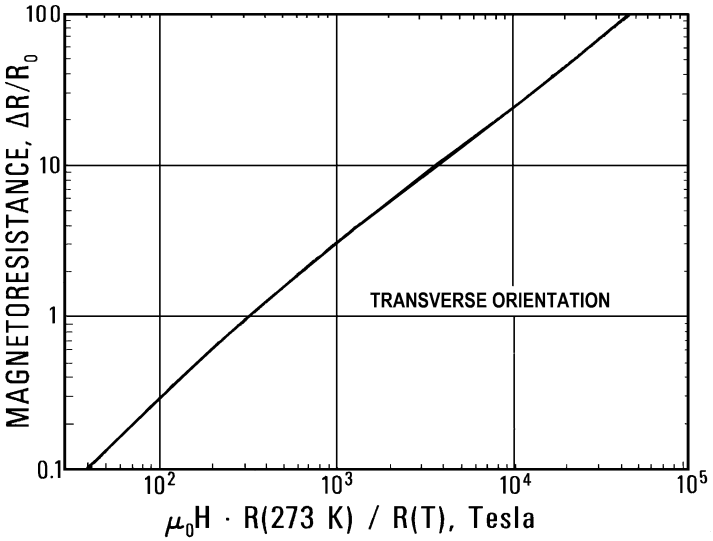

Fig. 2.7 Kohler plot for magneto-resistance of copper (Reprinted from Fickett [19])

At intermediate temperatures, $T \approx \Theta_D/3$, the resistivity varies smoothly between the two regions. Many metals have a roughly T^5 dependence in this regime which can be attributed to the phonon population being proportional to T^3 and the probability of scattering through large angle having a T^2 dependence. The resistivity is therefore proportional to the product of these two factors.

2.3.2 Magneto-Resistance in Metals

The electrical resistivity of pure metals generally increases with applied magnetic field. This effect is most significant for pure metals at low temperatures because of their relatively long mean free paths for electron scattering. Physically, magneto-resistance comes about from the fact that the electrons in the metal are deflected from a straight path in the presences of an applied magnetic field. Since the deflected path will have a greater opportunity for the electrons to scatter, the electrical resistivity would be expected to increase monotonically with applied magnetic field. The magnitude of the effect depends on the type of metal, its purity and the magnitude and orientation of the applied magnetic field.

No simple theory is available for calculating the magneto-resistance of a particular metal. However, a considerable amount of data exists and correlations are available for calculating the magnitude of the effect in common metals. For copper, the magneto-resistance is often tabulated in terms of what is known as a Kohler plot [19], shown in Fig. 2.7. To utilize this plot one needs to know the RRR = $\rho(273\ \text{K})/\rho\ (4.2\ \text{K})$ of the copper sample, the applied magnetic field ($\mu_0 H$), in this case transverse to the axis of the sample, and the desired operating temperature.

Table 2.4 Electrical resistivity of various technical alloys (units of nΩ-m) [3, 14]

Alloy	10 K	20 K	50 K	100 K	200 K	300 K	RRR
AL 5083	30.3	30.3	31.3	35.5	47.9	59.2	1.95
AL 6061-T6	13.8	13.9	14.8	18.8	30.9	41.9	3
304 SUS	490	491	505	545	640	720	1.46
BeCu	56.2	57	58.9	63	72	83	1.48
Manganin	419	425	437	451	469	476	1.13
Constantan	461	461	461	467	480	491	1.07
Ti-6%Al-4%V	1,470	1,470	1,480	1,520	1,620	1,690	1.15
PbSn (56-44)	4.0	5.2	16.8	43.1	95.5	148	37
Pt	–	0.367	7.35	28	69.2	107	290

From this information, one can calculate the magneto-resistance contribution to the total value of RRR, which in turn allows determination of the effective resistivity of the metal. However, it is important to keep in mind that this is an approximate correlation and only suitable for copper. By contrast, magneto-resistance measurements on pure aluminum do not yield a similar universal correlation. In general, the magneto-resistance makes the largest contribution to the resistivity at high field and low temperatures for pure metals.

Example 2.2

For an applied magnetic field of $\mu_0 H = 10$ T, calculate the effective RRR for a sample of copper, which has a RRR = 100 at $\mu_0 H = 0$.

In this example, the product, $\mu_0 H \times RRR = 1{,}000$ T. Using the Kohler plot for transverse magnetic field, Fig. 2.7, the magneto-resistance contribution can be estimated to be $\Delta R/R_0 \approx 3$. This value must be added to the resistance of the metal at zero field, which makes the ratio $R_{10}/R_0 \approx 4$. Thus, the sample has approximately the same electrical resistivity as a RRR = 25 sample on zero background field. The resistivity of copper at 273 K is 15.6 nΩ-m [3]. This means that the resistivity of the copper at liquid helium temperature and $B = 10$ T should be $\rho \sim 0.62$ nΩ-m, which compares reasonably well with tabulated data, which gives a value of 0.56 nΩ-m for these conditions.

The electrical resistivity of metallic alloys is generally higher than that of corresponding pure metals. Also, the temperature dependence of the resistivity of alloys is much weaker. Mostly these effects are due to the large amount of lattice imperfection scattering that occurs in concentrated alloys. The electrical resistivity of a variety of metallic alloys is given in Table 2.4. Note that the RRR for most of these metals, which varies from approximately unity for Constantan (Cu57% Ni43%) and Manganin (Cu84%Mn12%Ni4%) to 2 or 3 for aluminum alloys and over 30 for PbSn solder is considerably smaller than that of pure metals. Also, the room temperature resistivity can be very high up to two orders of magnitude greater than that of pure metals. Both of these features make alloy metals particularly useful for heaters and instrumentation leads in cryogenic applications.

2.3.3 Electrical Conductivity of Semiconductors

Semiconductors have electrical resistivities that typically range from 10^{-4} to 10^{7} Ω-m, which is many orders of magnitude higher than that of most metals ($\rho \sim 10^{-8}$ Ω-m). However, in the case of semiconductors, the low conductivity is due more to the limited number of charge carriers that exist than impurity or phonon scattering. Semiconductors possess properties that are dependent on the existence of an energy gap E_g in the electron density of states. Unlike pure metals, which do not have an energy gap, the number of conduction electrons in a semiconductor varies exponentially with temperature roughly as,

$$N_c \sim e^{-\frac{E_g}{k_B T}} \tag{2.22}$$

This exponential dependence dominates the resistivity leading to an increasing value as the temperature decreases. Such variation can be quite strong with the resistivity increasing over several orders of magnitude between room temperature and liquid helium temperature with the exact variation depending on the details of the semiconductor.

Pure semiconductors are insulators at absolute zero because the electrons cannot be excited above the energy gap, see (2.22). To overcome this limitation, the conductivity of a semiconductor can be increased by doping it with impurities that introduce additional charge carriers. Small concentrations of impurities can change the conductivity of a semiconductor by several orders of magnitude. Due to the strong temperature dependence of their resistivity, semiconductors are most commonly encountered in cryogenic applications as temperature sensors with high negative temperature coefficients. For example, high levels of sensitivity at liquid helium temperatures can be achieved using doped germanium as a sensor.

2.3.4 Thermal Conductivity of Metals

The thermal conductivity is a material property that determines the temperature gradient across a substance in the presence of a heat flow. In all materials there are several contributions to the thermal conductivity k. For metals, the principal conduction mechanisms are electronic and lattice, with the electronic contribution being dominant for pure metals. The electronic thermal conductivity can be understood by a similar model as used for electrical conductivity.

By analogy to the process of electrical conductivity, the behavior of k can be understood in terms of a kinetic theory model for gases of electrons and phonons [20]. Such simple models work very effectively to explain the limiting behavior of the thermal conductivity. In particular, the thermal conductivity may be written,

$$k = \frac{1}{3} C v l \tag{2.23}$$

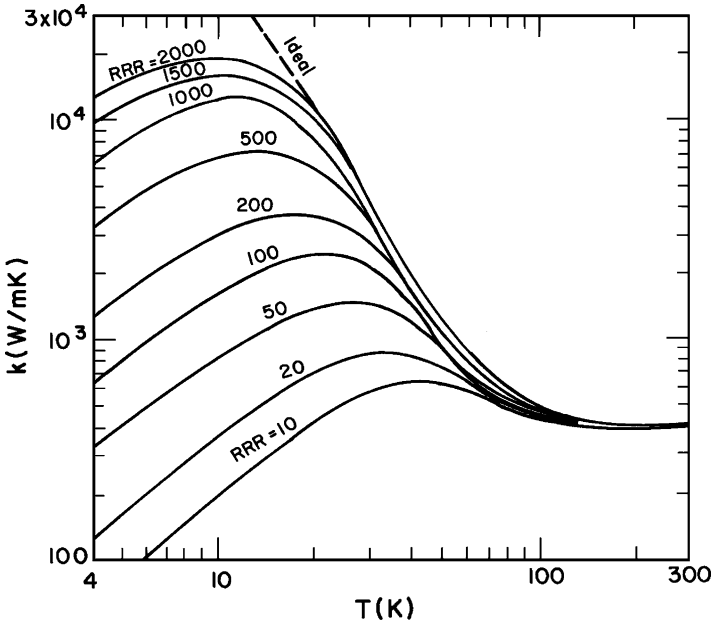

Fig. 2.8 Thermal conductivity versus temperature of differing purities of copper (Reprinted from Powell and Fickett [13])

where C is the heat capacity per unit volume, v is the characteristic speed, and l is the mean free path. Using the free-electron model, the electronic contribution to the thermal conductivity can be calculated by inserting the electronic specific heat, (2.15), and the Fermi velocity, $v_F = (2\varepsilon_F/m)^{1/2}$, into (2.23). Thus,

$$k_e = \frac{\pi^2 n k_B^2 T \tau}{3m} \tag{2.24}$$

where τ is the mean scattering time identical to that considered for electrical conductivity. At high temperatures, $T > \Theta_D$, $\tau \approx T^{-1}$ due to the increase in the lattice vibrations so that the thermal conductivity approaches a constant value. At low temperatures, τ is approximately constant, since impurity scattering dominates there, implying the thermal conductivity should be proportional to T. As an example, Fig. 2.8 shows plots of the thermal conductivities of copper analogous to Fig. 2.6 for the electrical resistivity. The limiting behavior near room temperature gives a near constant value $k = 401$ W/m K. With decreasing temperature, the thermal conductivity rises through a maximum that depends on the purity of the sample followed by a linear region ($k \sim T$) at the lowest temperatures. This system is entirely consistent with the simplified theoretical picture.

Since the electronic thermal and electrical conductivities in pure metals have similar scattering processes, a correspondence clearly should exist between these

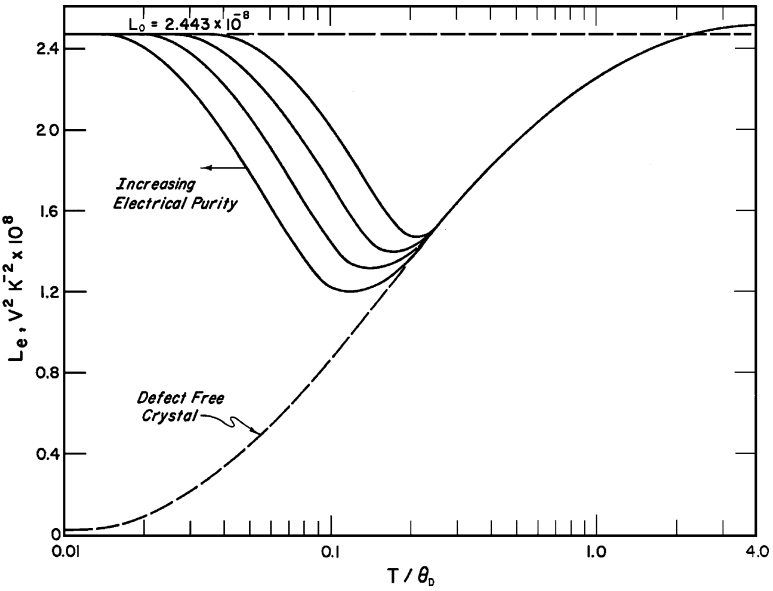

Fig. 2.9 Electronic Lorentz ratio for pure metals and defect-free metals (Reprinted from Sparks and Hurst [21])

two properties. The Wiedemann-Franz Law generally assumes that for metals the ratio of the thermal conductivity and electrical conductivity is a function of temperature only. Furthermore, for the free-electron model, this ratio is a simple expression,

$$\frac{k_e}{\sigma} = \frac{\pi^2}{3}\left(\frac{k_B}{e}\right)^2 T = L_0 T \tag{2.25}$$

where the quantity $L_0 = (\pi^2/3)(k_B/e)^2 = 2.45 \times 10^{-8}$ W Ω/K^2 is the free electron Lorenz number. L_0 is totally independent of material properties and temperature.

Experimental evidence indicates that the Wiedemann-Franz Law works only at temperatures near room temperature and at very low temperatures ($T \ll \Theta_D$) [21]. This fact is related to the asymmetry imposed on the Fermi surface when it is subjected to a thermal gradient resulting in the transport of electrons. At intermediate temperatures, the experimentally defined Lorenz ratio ($L = k/\sigma T$) is almost always less than L_0. The amount of deviation is strongly dependent on the purity of the sample, with the less pure having a smaller deviation. The overall behavior of the Lorenz ratios with sample purity are plotted in Fig. 2.9. Considerable effort has been applied to understanding these effects, the details of which are beyond the scope of the present discussion.

2.3.5 *Lattice Thermal Conductivity*

The lattice contribution to the thermal conductivity of metals, semiconductors and insulators is also understood in terms of kinetic theory although the thermal carrier in this case is a phonon gas of lattice vibrations. It is still possible to apply (2.23) although the heat capacity must be that due to the lattice, C_{ph}, which as we have discussed above is proportional to T^3 at low temperatures. Also, v is the speed of sound and l is the phonon mean free path. Most insulators and semiconductors have thermal conductivities that are several orders of magnitude lower than that of common pure metals. At high temperatures their behavior is complicated by the details of the phonon density of states, but generally the thermal conductivity decreases monotonically with temperature. At low temperatures, where scattering times become approximately independent of temperature, the thermal conductivity decreases more rapidly, approaching zero as T^n where $n \approx 3$.

The thermal conductivity of some technical materials are shown in Fig. 2.10 and listed in Table 2.5. Because the list includes a wide variety of alloys and amorphous insulators, a considerable range in values is displayed. These contain only a limited number of technically interesting materials, indicating that an area of continuing research is the determination of thermal conductivities of new materials. This need is particularly evident with the growing use of composite materials for low temperature applications.

Because the thermal conductivity of most materials used in cryogenic systems varies with temperature, it is often necessary to integrate the thermal conductivity over the temperature range of interest to obtain a total or integrated value,

$$\bar{k}(T_1, T_2) = \int_{T_1}^{T_2} k(T) dT \tag{2.26}$$

which has units of W/m. If the temperature dependence of k is known, it is straightforward to obtain $\bar{k}$ for a particular temperature range. One can then calculate the total heat flux, Q by multiplying the integrated thermal conductivity by the area to length ratio, A/L.

Example 2.3

Estimate the integrated thermal conductivity for BeCu between 1 and 300 K.

Looking at Fig. 2.10a, the thermal conductivity of BeCu is nearly linear on the log-log plot and therefore can be represented as $k \sim aT^n$, where it can be shown that $n = 1.1$ and $a = 0.4$ W/m K^{1+n} as determined from the data. It then follows that the integrated thermal conductivity is,

$$\bar{k} = \int_1^{300} aT^n dT = \frac{a}{n+1} T^{n+1} \Big|_1^{300} = 0.19\left[300^{2.1} - 1^{2.1}\right] = 30,300[W/m]$$

Note that in this case, integrated thermal conductivity is mostly determined by the upper temperature.

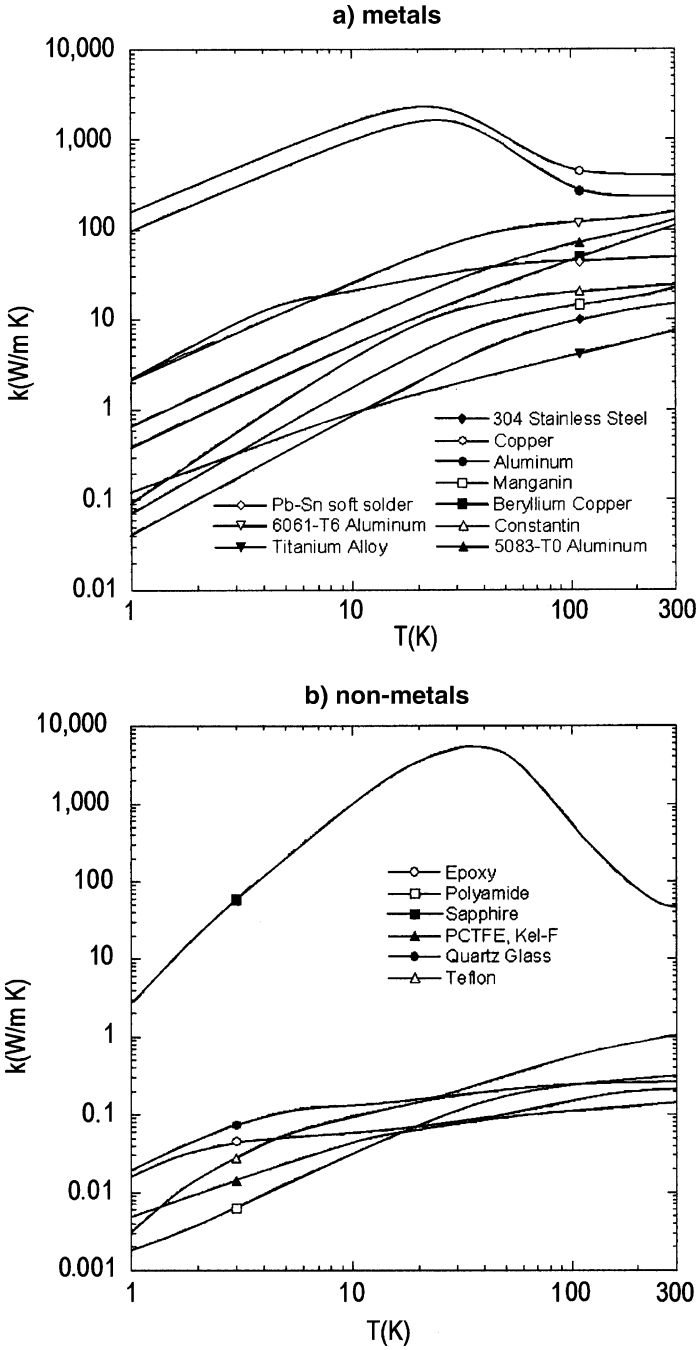

Fig. 2.10 Thermal conductivity of various materials used in cryogenics: (**a**) metals; (**b**) non-metals [3]. Symbols are used as identifiers for each material

Table 2.5 Conductivity of various technical alloys (units are W/m K) [3]

Alloy	10 K	20 K	50 K	100 K	200 K	300 K
AL 5083	30.3	30.3	31.3	35.5	47.9	59.2
AL 6061-T6	23.8	50.1	100	120	135	160
304 SUS	0.77	1.95	5.8	9.4	13	14.9
BeCu	5.1	10.3	24	44.5	79.5	112
Manganin	1.7	4.1	10.1	14	17.2	22
Constantan	3.5	8.7	18.1	20	22.8	24.9
Ti-6%Al-4%V	0.87	1.5	2.6	4	5.9	7.7
PbSn (56-44)	20	28.5	40.7	45	48	51

2.3.6 Contact Resistance

Thermal and electrical contact between materials is a topic of considerable importance in cryogenics and yet it is only qualitatively understood. Contract resistance occurring at conductor joints in magnets or other high power applications can lead to undesirable electrical losses. Poor thermal contact at the interface of a heat strap can significantly decrease the efficiency of a thermal link in a conduction cooled system. Thermal contact is also critical in the mounting of sensors for accurate temperature measurement, where failure to carefully consider this issue can lead to erroneous results. Thus, it is important to have a basic understanding of this topic for a wide variety of cryogenic system designs.

Whenever two materials are joined together for the purpose of transporting heat or electrical current a localized resistance occurs at the boundary. The magnitude of this resistance depends on a number of factors, including the properties of the bulk materials, the preparation of the interface between the two materials, whether there are bonding or interface agents present, and external factors such as the applied pressure.

The electrical contact resistance is of greatest interest in the production of joints between high purity metals such as copper, where its value can contribute or even dominate the overall resistance of an electrical circuit. Generally, the contact resistance in pure metals has a temperature dependence that scales with the properties of the bulk material, displaying among other traits a purity dependent RRR. For electrical contacts between pure metals without bonding materials like solder, the value of the electrical contact resistance decreases with applied pressure normal to the joint interface. This tendency results from an increase with pressure in the effective contact area between the two bulk samples. To understand this effect, consider that the two surfaces have microscale roughness due to how the surfaces were prepared. As the pressure is increased normal to the surfaces, the asperities tend to mechanically yield and deform increasing the effective area of contact. As the bulk material has high conductivity, the contact resistance is mostly due to the constriction of current flow that occurs at the small contact points [22]. As the contact pressure is increased, the amount of constriction for current flow decreases, thus reducing the contact resistance.

Figure 2.12 is a graphical summary of the measured electrical contact resistivity for various unbonded samples as a function of applied pressure [23]. To obtain the

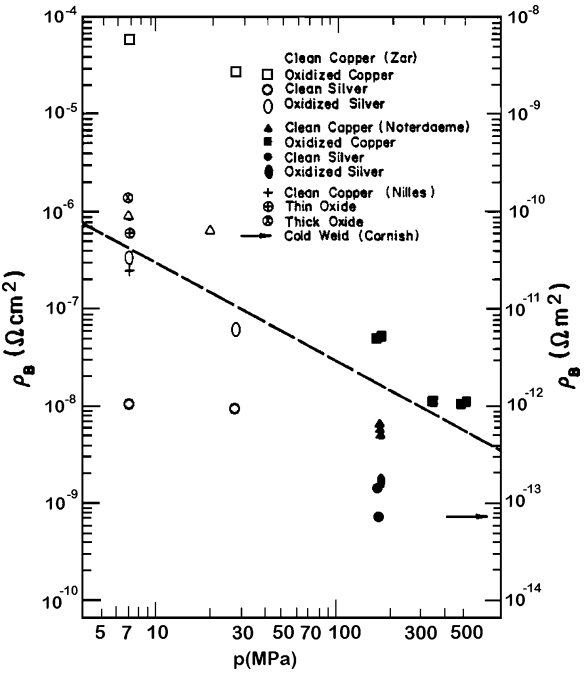

Fig. 2.11 Summary of low temperature electrical contact resistance versus pressure. *Dashed* line is the fit (2.27) [23]

contact resistance, the contact resistivity should be divided by the contact area, $R_B = \rho_B/A$. There are two things to observe in these results. First, at a particular contact pressure, there is still a wide variation in the contact resistivity, a result that is probably due to variations in sample preparation, treatment and oxidation. Second, the contact resistance generally decreases with applied pressure. The line in the graph is a rough correlation for the contact resistivity,

$$\rho_B \sim 3/p \tag{2.27}$$

where p the pressure is in Pa and ρ_B is in Ω-cm^2. This result is at least qualitatively consistent with the expected increase in area with contact pressure.

For thermal contact resistance, there are two cases to consider. First is the thermal contact resistance between metals, which would be expected correlate with the electrical contact resistance much as with bulk metals. This correlation is approximately correct for contacts between identical metals. However, if the contact is between dissimilar metals or if there are solders or other interface metals involved, the thermal contact resistance can no longer be scaled with ρ_B. This latter point is particularly significant at low temperatures where many soldiers are superconducting (Fig. 2.12).

For thermal contact resistance between non-conducting materials, the fundamental limit even for ideal contacts is the mismatch in the phonon transport across the interface [24]. Since the phonon spectra for the two materials are not the same there is an impedance mismatch that leads to a resistance occurring within roughly

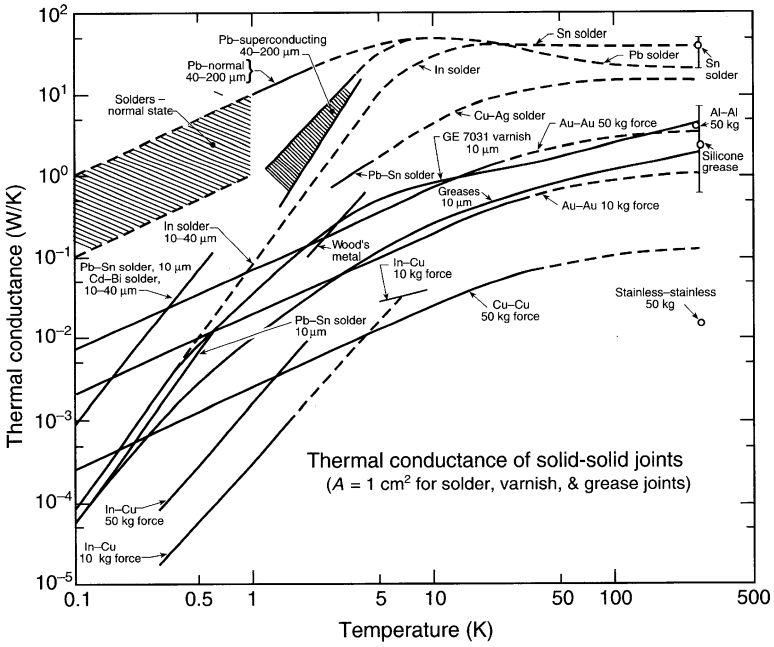

Fig. 2.12 Thermal contact conductance as a function of temperature for a variety of contact preparations and conditions. The contact assumes a 1 cm^2 area. Data compiled by Radebaugh [25] (Reprinted from Ekin [6])

one phonon wavelength of the interface. This effect is known as Kapitza conductance and is also important for heat transfer in liquid helium, a topic that will be revisited in Chap. 7. Overall, the theory of Kapitza conductance predicts a heat transfer coefficient ($h = 1/R$),

$$h_K = \left(\frac{16}{15}\frac{\pi^5 k_B^4}{h^3 c^2}\right) T^3 \tag{2.28}$$

where c is the speed of sound. Note that the speed of sound is proportional to the Debye temperature, so that low Θ_D materials would be expected to have higher thermal conductances than materials with high Debye temperature. For most solids, the factor in parentheses is on the order of 1 kW/m^2 K^4. Overall, (2.28) places an upper bound on the magnitude of the thermal contact conductance for insulating contacts. Real contacts between non-ideal surfaces are more complex and their understanding is thus more qualitative.

For joints between real materials, the interface is irregular with intermittent points of contact. In this case, the thermal contact conductance is more determined by the constriction resistance at the asperities similarly to the electrical contact resistance in metals. Thus, particularly for deformable materials without bonding agents, the thermal contact conductance should increase with interface pressure.

Experimentally, this correlation is born out with the thermal contact conductance increasing with pressure as,

$$h \approx ap^n \tag{2.29}$$

where n $\approx$ 1 and a is an empirical coefficient [23].

Thermal contact conductance varies over a wide range depending on whether the contact is insulating or conducting. Figure 2.12 displays a compilation of data for low temperature thermal contacts [25]. Some general trends can be observed. First, the thermal contact conductance values at low temperatures can range over six orders of magnitude, depending on materials and surface preparation. This large range is mostly due to variations of actual contact area and surface preparation. Second, contacts that are bonded with solder of similar agents that fill the asperities generally have higher thermal conductances than bare contacts. However, the bonding agents can also contribute to the interface resistance particularly if the bond region is thick or electrically insulating. In the low temperature region (T < 5 K), most of the data correlate with a power law, $h \sim T^n$, but there are two distinct characteristic behaviors. Pure metal-metal contacts have a temperature dependence that correlates with that of the bulk metal. Thus, at low temperature $h \approx aT$, with the coefficient of proportionality being mostly determined by sample purity and contact pressure but varying between 10^{-1} and 10^{-3} W/cm^{2}K^2. On the other hand, if the contact is bonded with solder or indium, the conductance can be much higher, but at low temperature such contacts may become superconducting. As discussed in the next section, metallic superconductors have lower thermal conductivities than in the normal state with $k_s \sim T^3$, so that the thermal conductance can in principle be reduced by introduction of bonding agents. Finally, if the interface is between two non-conducting materials, then electron transport is non-existent and the thermal conductance is generally lower following the correlation scaling with the bulk thermal conductivity, $h = aT^n$, where $n \sim 3$. However, in some special cases involving crystalline insulators, such thermal conductances can be very high as is seen with the bulk materials, see Fig. 2.10.

2.4 Mechanical Properties

The mechanical properties of materials are also very important to consider when designing cryogenic systems. Most cryogenic systems require mechanical supports to carry the loads between ambient temperature and low temperature components. Thermal transport through structural supports often significantly contribute to the overall low temperature heat load. Since the thermal conductivity of a structural material determines the heat load and the structural properties determine the required dimensions of the support, both the structural and thermal properties must be considered when designing and optimizing structural components in cryogenic systems.

The two properties that are most often of interest in a mechanical system are the stress $\sigma = F/A$ within the material and the modulus of elasticity $E_y = \sigma/\varepsilon$, where ε is the linear material strain, dx/x. These material properties enter into calculations such as mechanical deflection and failure modes in mechanical structures.

Table 2.6 Yield stress σ_y of several materials (units are MPa) [26, 27]

Material	σ_y (0 K)	σ_y (80 K)	σ_y (300 K)
304L-SS	1,350	1,300	1,150
6061-T6 Al	345	332	282
OFHC-Cu (Annealed)	90	88	75
Cu + 2 Be	752	690	552
Brass (70% Cu, 30% Zn)	506	473	420
Inconel X-750	940	905	815
G l0 – CR	758	703	414
Teflon	130	65	20

Table 2.7 Ultimate stress of several materials (units are MPa) [26, 27]

Material	σ_u (0 K)	σ_u (80 K)	σ_u (300 K)
304 L-SS	1,600	1,410	1,200
6061-T6 Al	580	422	312
OFHC Cu (annealed)	418	360	222
Cu + 2 Be	945	807	620
Brass (70% Cu, 30% Zn)	914	804	656
Inconel X-750	1,620	1,496	1,222
G-10 – CR	758	703	414
Teflon	194	86	21

Most structural materials are characterized in terms of their uniaxial stress limits. Typically, the yield stress of a material, σ_y, is defined as the load that creates a 0.2% permanent deformation; however, this definition is sometimes not meaningful particularly if one is considering a brittle material. The yield stress sometimes refers to the load that produces a distinct change in the slope of the stress–strain curve. In any case, for the design of structural components in systems, it is advisable to stay well below the specified yield stress of the material in use; typically to a maximum stress not exceeding $2/3\sigma_y$. Furthermore, in an application involving cyclic loading, this design value must be de-rated even further to take into account the failure associated with repeated application of load.

The ultimate stress σ_u, represents that level of stress necessary to cause failure of a particular material under tensile load. In ductile materials, the ultimate stress is considerably greater than σ_y and can be associated with substantial permanent deformation. On the other hand, brittle materials have $\sigma_y \simeq \sigma_u$. Composite structural materials such as fiberglass epoxy have even more complex behavior.

For most common structural materials, the yield and ultimate stresses increase with decreasing temperature. The magnitude of this increase varies from around 10% in some metallic alloys to over 100% in polymeric materials. The increase in strength is seen to result from the reduced thermal excitations within the lattice, which inhibits the spread of dislocations. Listed in Tables 2.6 and 2.7 are respectively the yield and ultimate stress values for several materials commonly used in cryogenic applications. Values listed are typical and considerable variation can occur depending on the treatment and form of the particular materials. More detailed tabulations can be found from several sources in the literature [4, 6].

Table 2.8 Young's modulus E_y of several materials (units are GPa) [26, 27]

Material	E_y (0 K)	E_y (80 K)	E_y (300 K)
304 -SS	210	214	199
6061-T6 Al	78	77	70
OFHC-Cu (annealed)	139	139	128
Cu + 2 Be	134	130	118
Brass (70% Cu, 30% Zn)	110	110	103
Inconel(X-750)	252	223	210
G-10-CR	36	34	28
Teflon	0.7	2.8	4

Table 2.9 Figure of merit (σ/k) for several different structural materials (units are MPa-m-K/W)

Material	σ/k (4 K)	σ/k (80 K)	σ/k (300 K)
304 ss	6,000	160	80
6061 T6 AL	36	3	2
G-10	12,000	1,600	500
Brass	150	9	3
Copper	2	2.5	3

The modulus of elasticity, or Young's modulus E_y, represents the change in stress level needed to cause a unit change in strain while the material is in the elastic region. Thus, Young's modulus is simply the slope of the stress–strain curve for small values of strain. As with the yield and ultimate stresses, Young's modulus also increases with decreasing temperature. A list of typical values for technical materials is shown in Table 2.8. Unlike the limiting stress values, Young's modulus is not as strongly affected by material treatment and form.

Before leaving the subject of structural materials, it is worth mentioning a method for determining the relative merits of different materials for structural applications. In the simplest example, a figure of merit (FOM) can be constructed based on the ratio of the allowable stress to the thermal conductivity (FOM $= \sigma/k$) of a particular material. Thus, high FOM materials have high strength and low thermal conductivity, such as stainless steel or certain fiberglass composites (G-10). On the other hand, a low FOM material would have high thermal conductivity and low strength, *e.g.* pure metals like aluminum and copper.

Table 2.9 shows the figure of merit for several different materials as a function of temperature. Note that the highest FOM is for G-10 composite due to its relatively high strength. On the other hand, clearly pure copper is not suitable for structural applications.

2.5 Superconductivity

Superconductivity occurs in a large number of elemental metals, alloys and now in several classes of ceramic materials. This effect, which manifests itself as an absence of electrical resistivity along with an expulsion of magnetic flux, was first observed by H. Kamerlingh Onnes in 1911 as part of an investigation of

the electrical resistance of pure metals at low temperatures. First performing such experiments with mercury, Onnes observed a sharp transition from the normal resistive state to one which had immeasurably small electrical resistance at a temperature near the normal boiling point of helium, $T \approx 4.2$ K. This new state, termed by Onnes as "supraconductive," has been the subject of much fundamental theoretical and experimental research in the many years since its discovery [28].

In the 1960s, high-field superconductive materials, mainly as Nb_3Sn and NbTi, were discovered spawning a lot of activity in high current technical applications [29]. In particular, superconductive magnets began to be developed for a wide range of applications for everything from particle accelerators to magnetic resonance imaging instruments. On a smaller scale, the high current densities in these materials made possible superconductive electronics for sensors and computers. Therefore, it is important to note that much of the interest in helium cryogenics is brought about by the existence of these materials and their applications.

Late in the 1980s, the field of superconductivity was drastically changed with the discovery of a new class of layered compounds that display superconductivity at high temperatures, near the boiling point of liquid nitrogen. Today, these materials, commonly referred to as high temperature superconductors (HTS), are actively being studied for all sorts of applications as well as for their fundamental physical properties. Their success still depends on cryogenic systems, but due to their higher operating temperatures, more effort is being placed on the development of cryogenic refrigeration in the range from 20 to 80 K. However, large scale applications of superconductivity for particle accelerators and fusion energy continue to utilize NbTi and Nb_3Sn and thus require liquid helium cryogenic systems.

In the present context, it is not possible to provide a thorough review of the physics and properties of all superconductors. For this, the reader is encouraged to seek out one of several monographs or texts on superconductivity and its applications. The present discussion, therefore, provides only a brief review of the properties of superconductors along with some discussion of their usefulness in applications.

2.5.1 Type I Superconductivity

There are two main types of superconductors with the distinction mainly associated with their electromagnetic properties. Type I superconductors, which comprise most of the pure elemental superconductors, have a sharp transition to the zero resistance state and simultaneously a total screening of magnetic flux within the bulk below T_c, the superconducting transition temperature. Thus, Type I superconductors are often referred to as perfect diamagnetic materials. The normal state in a Type I superconductor can be recovered by the application of an external magnetic field greater than the critical field H_c. Unfortunately, for Type I superconductors and their potential applications, H_c has a rather low value, $\mu_0 H_c \lesssim$ 100 mT, making Type I superconductors unsuitable for magnet and other high field applications. Type II superconductors, which sustain the superconducting state to high fields, are usable for high field applications as discussed in the next section.

Table 2.10 Critical temperature and critical field of Type I superconductors [30]

Material	T_c(K)	$\mu_0 H_0$(mT)
Aluminum	1.2	9.9
Cadmium	0.52	3.0
Gallium	1.1	5.1
Indium	3.4	27.6
Iridium	0.11	1.6
Lead	7.2	80.3
Mercury $\propto$	4.2	41.3
Mercury β	4.0	34.0
Osmium	0.7	6.3
Rhenium	1.7	20.1
Rhodium	0.0003	4.9
Ruthenium	0.5	6.6
Tantalum	4.5	83.0
Thalium	2.4	17.1
Thorium	1.4	16.2
Tin	3.7	30.6
Tungsten	0.016	0.12
Zinc	0.9	5.3
Zirconium	0.8	4.7

The magnetic field-temperature boundary between the superconducting and normal state in a Type I superconductor is given by an empirical relationship between the critical temperature and field,

$$H_c(T) = H_0\left[1 - \left(\frac{T}{T_c}\right)^2\right] \tag{2.30}$$

where H_0 is the critical field at $T = 0$ K. Listed in Table 2.10 are these parameters for known Type I superconductors [30]. Note the range of transition temperatures vary from the highest value of 7.2 K for Pb to 325 μK for Rh. A similar wide variations in the critical field is evident. It is also interesting to note that metals that are normally thought of as good conductors, copper, silver and gold, are not superconductors. This fact is related to the fundamentals of the superconducting state.

A Type I superconductor exposed to an external magnetic field $H < H_c$ will exclude the flux from penetrating into its bulk. This behavior, known as the Meissner effect, is shown schematically in Fig. 2.13. There are essentially two equivalent ways of looking at the Meissner state. The first is to note that because the superconductor has no electrical resistance, persistent screening currents are established on the surface opposing any change of the flux within the bulk. These currents flow in a layer at the surface of thickness $\lambda \approx 50$ nm, known as the London penetration depth. The London penetration depth is one of two fundamental characteristic lengths used to define the behavior of a superconductor. The alternate

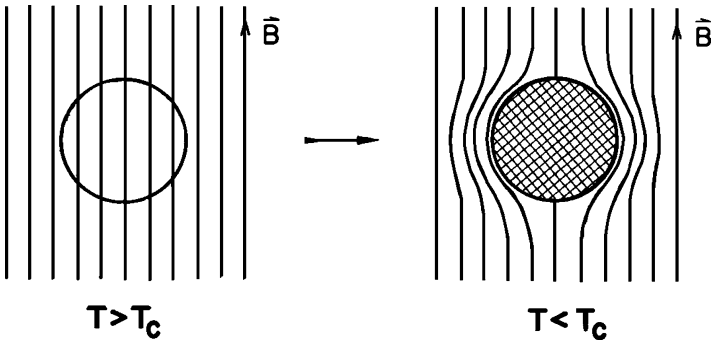

Fig. 2.13 Meissner effect in a superconducting sphere cooled in a constant applied field. Below T_c, $B = 0$ within the superconductor independent of the order of application of magnetic field and low temperature environment

picture is to consider the superconductor as if it were a perfectly diagmagnetic body such that its magnetization always equals the negative of the applied field, $M = -H$. In the superconducting state, these two interpretations lead to equivalent physics. Mainly, describing a superconductor as being a perfect diamagnet has the advantage of always predicting the flux exclusion condition independent of the order of the applied field and immersion in a low-temperature environment.

Superconductivity is brought about by the electrons in the metal forming what are known as Cooper pairs with integer spin and thus obeying Bose – Einstein statistics. This is a complex quantum mechanical phenomenon. However, one can get an appreciation for the properties of Type I superconductors that does not require advanced quantum mechanics by studying the thermodynamics of the superconducting to normal transition. In the normal state, the thermodynamic and transport properties of Type I superconductors are essentially the same as those of other normal metals and are only weakly magnetic ($M \sim 0$). On the other hand, in the superconducting state a metal is perfectly diamagnetic with $M = -H$. In follows that at the transition between the superconducting and normal states, the Gibbs free energies of the two states must be equal. The differential form for Gibbs free energy for a magnetic material is written,

$$dg = -sdT + vdp - \frac{1}{2}\mu_0 H_c^2 \tag{2.31}$$

At the critical temperature, the phase transition occurs at constant temperature and pressure so that $g_n(H_c) = g_s(H_c)$. However, since the normal state is non-magnetic $g_n(H_c) = g_n(0)$ while the superconducting state is diamagnetic, and $g_s(H_c) > g_s(0)$ by the magnetic energy density, $\frac{1}{2}\mu_0 H^2$. Thus, the difference between the Gibbs free energies at zero field may be written as,

$$g_n(0) - g_s(0) = \frac{1}{2}\mu_0 H_c^2 \tag{2.32}$$

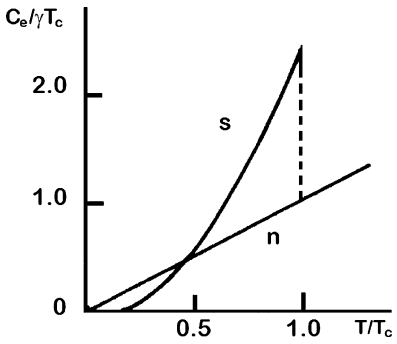

Fig. 2.14 Normalized heat capacity of superconducting and normal state of a Type I superconductor

Combining (2.32) with the empirical relationship for the temperature dependence of the critical field (2.30) yields a relationship for the entropy difference, $S_n - S_s = -\frac{\partial}{\partial T}(g_n - g_s)$ between the two states,

$$S_n - S_s = \frac{2\mu_0 H_0^2}{T_c}\left[1 - \left(\frac{T}{T_c}\right)^2\right]\frac{T}{T_c} \tag{2.33}$$

where $S = \rho s$ refers to the entropy per unit volume of the superconducting material. Note that at T_c, $\Delta S = 0$, which means that the transition is second order and there is no latent heat associated with the superconducting-normal transition at zero applied field. The heat capacity difference, $C_n - C_s = T\frac{\partial}{\partial T}(S_n - S_s)$ at the transition is obtained from the derivative of the entropy,

$$C_n - C_s = \frac{2\mu_0 H_0^2}{T_c}\left[1 - 3\left(\frac{T}{T_c}\right)^2\right]\left(\frac{T}{T_c}\right) \tag{2.34}$$

At T_c, this expression predicts a discontinuous change in the specific heat, $C_n - C_s = -4\mu_0 H_0^2/T_c$ followed by a decrease proportional to T^3 below T_c. Also, recall from Sect. 2.1.2 that the electronic contribution to the specific heat of metals dominates at low temperature, $C_e = \gamma T$. Figure 2.14 displays these dependences. Experiments have confirmed an approximately cubic temperature dependence of the specific heat for T near T_c. However, at lower temperatures, $T < 0.5\ T_c$, an exponential temperature dependence is observed. Such behavior is indicative of an energy gap in the electron density of states and is supporting evidence for the microscopic theory of superconductivity.

The behavior of thermal conductivity of Type I superconductors can be of considerable technical utility. Recall that the thermal conductivity of a metal has two primary contributions due to the transport of electrons and phonons and that it is proportional to the specific heat. For pure metals at low temperatures, the electronic contribution tends to dominate. However, in a superconductor, some of the electrons form Cooper pairs and undergo Bose-Einstein condensation into the ground state, thus being unable to carry thermal energy. As a result, the thermal

conductivity of a pure Type I superconductor is less than that of the normal state for $T < T_c$. In the vicinity of T_c, this dependence is approximately cubic in temperature dropping off exponentially at low temperatures. This behavior is consistent with the temperature dependence to the specific heat, see Fig. 2.14.

As the normal state can be restored by the application of a magnetic field greater than H_c, the thermal conductivity of a pure Type I superconductor at $T < T_c$ but $H > H_c$ should increase relative to that of the superconducting state. In particular, at low temperatures the thermal conductivity should vary linearly with temperature, $k \sim T$, consistent with the free electron model discussed in Sect. 2.3.4. Thus, the thermal conductivity of a strip of Type I superconductor below T_c can be switched by several orders of magnitude by application of an external magnetic field of greater than H_c. This operating principle is useful as a thermal switch in very low temperature refrigeration systems that cool samples to some very low temperature, $T < 1$ K. In this application, once cooled the sample can be thermally isolated by switching off the magnetic field and returning the strip to the superconducting state.

Example 2.4

A superconducting switch, consisting of a strip of tin ($T_c = 3.7$ K) surrounded by a small magnet capable of $H > H_c$, connects the cold plate of a ^{3}He refrigerator ($T = 0.5$ K) to a sample at the same temperature. Calculate the thermal conductivity ratio (k_s/k_n) assuming $k_n = \beta T$ and $k_s = \alpha e^{-(Tc/T)}$ below T_c in the superconducting state.

To find the ratio of the thermal conductivities, it is not necessary to know the absolute values. However at T_c, the thermal conductivities of the two states must be equal: $k_n(T_c) = k_s(T_c)$ or $\beta T_c = \alpha e^{-1}$. This means that $\beta/\alpha = 0.1\ \mathrm{K}^{-1}$. Note that these are not thermal conductivity units, but that is not a problem as again the goal is a dimensionless result. The important boundary condition is that the ratio β/α at T_c be unity. At 0.5 K, the ratio of the thermal conductivities is,

$$\frac{k_n(0.5K)}{k_s(0.5K)} = \frac{\beta T}{\alpha e^{-T_c/T}} = \frac{0.1K^{-1} \times 0.5K}{e^{-7.2}} = 67$$

So the switching ratio of the thermal link is nearly two orders of magnitude.

The critical current I_c is the maximum current that a superconductor can carry in the zero resistance state. This is generally a function of magnetic field. In the case of Type I superconductors, I_c is determined by the magnitude and direction of the magnetic field at the surface of the conductor as compared to H_c (Silsbee's hypothesis). In self field,

$$I_c = 2\pi a H_c \tag{2.35}$$

where a is the radius of the wire. Although H_c is relatively low, Type I superconductors can have large currents. For example, a 1 mm radius lead wire at 4.2 K in its self field can carry in excess of 260 A of resistanceless current. However, since

H_c is so low, Type I superconductors are not suitable for high field magnets. For this, fortunately we have Type II superconductors. As seen in the next section, I_c in Type II superconductors results from an entirely different mechanism having to do with the details of the microstructure.

Before leaving the subject of Type I superconductivity, it is worth mentioning a few aspects of the microscopic theory of superconductivity. The complete theory of superconductivity is based on microscopic interactions between the electrons and phonons within the lattice, leading to correlated behavior of the electrons, known as Cooper pairing. The mathematical treatment of this model is quite complex, requiring a thorough knowledge of advanced quantum mechanics, and is well beyond the scope of this brief survey. Nevertheless, there are some important results of the microscopic theory which are helpful in understanding the general behavior of superconductors.

One major success of the microscopic theory is its ability to predict the superconducting transition temperature of a metal based on knowledge of the electron and phonon energy distributions. The electron–phonon interaction which produces Cooper pairing causes a gap in the density of electron states. This gap is the origin of the exponential specific heat at low temperatures. The width of the gap is directly proportional to the superconducting transition temperature. In the microscopic theory the exact formula is derived for the critical temperature T_c,

$$T_c = 1.14\Theta_D \exp\left(\frac{-1}{UD(\varepsilon_F)}\right) \tag{2.36}$$

where Θ_D is the Debye temperature, and $D(\varepsilon_F)$ is the electron density of states a the Fermi surface. The attractive potential U is due to the electron–phonon interaction which leads to Cooper pairing of the superconducting electrons. Two interesting conclusions follow from (2.35). First, metals with high resistances near room temperature thus possessing large electron–phonon interactions and a high normal state resistivity, will also be more likely to be superconductors. This result, which is approximately borne out by experiment, explains why copper is not a superconductor. Second, metals with even numbers of valence electrons having a smaller $D(\varepsilon_F)$, since they have fewer free electrons are less likely to be superconductors. Empirically, it is found that the transition temperatures of superconductors peak with odd numbers of valence electrons in support of this theoretical conclusion [31, 32]. In its fully developed formalism, the microscopic theory of superconductivity is considered to be one of the major triumphs of theoretical solid-state physics.

2.5.2 Type II Superconductivity

Most theories of superconductivity introduce a second characteristic length, known as the coherence length, ξ. In the microscopic theory, the coherence length is roughly the size of a Cooper pair, while in macroscopic theory it represents the

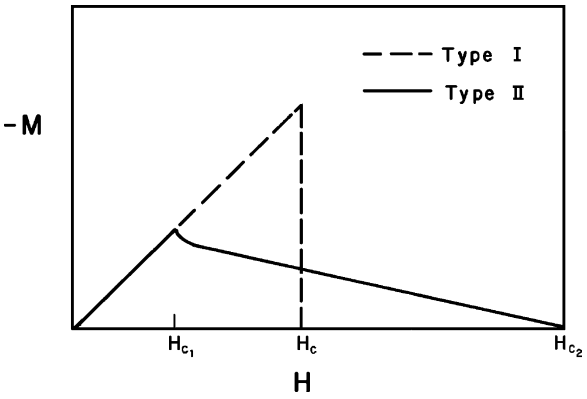

Fig. 2.15 Typical magnetization curves for metal that is either Type I or Type II superconductor. Note that for a Type II superconductor, H_c has only a thermodynamic definition

Table 2.11 Critical temperature and upper critical field of common Type II superconductors [35]

Material	T_c(K)	$\mu_0 H_{c2}$(T)
Nb	9.3	0.29
V	5.4	0.7
NbTi	9.3	13
Nb_3 Sn	18	23
V_3Ga	15	23
Nb_3 Ge	20.5	41

spatial distance over which the superconducting to normal transition occurs. The coherence length is a strong function of the crystal structure and lattice imperfections. Superconductors with large values of $\xi > \lambda$ are Type I, while Type II superconductivity occurs for those materials where $\xi < \lambda$.

The fundamental distinction between Type II and Type I superconductors can be seen by comparing their magnetic behavior. As we discussed above, in a Type I superconductor the magnetic flux is totally excluded provided $H < H_c(T)$. By comparison, in a Type II superconductor penetration of magnetic flux is allowed under certain circumstances. In an ideal Type II superconductor, the magnetic penetration is quantized in units of fluxons, $\phi_0 = h/2e$, and forms a regular triangular array, called a fluxon lattice, based on the magnitude of the external field. In effect, this brings small regions of the superconductor into the normal state. Such behavior, which is clearly a deviation from the perfectly diamagnetic Meissner state, is referred to as the mixed state in Type II superconductivity.

Because of flux penetration, the Type II superconductor in the mixed state is no longer a perfect diamagnet. A typical magnetization curve of a Type II superconductor is shown in Fig. 2.15. Also indicated is a magnetization curve for the same material if it were Type I; however in the case of Type II superconductors H_c is only defined in the thermodynamic sense and does not represent an actual magnetic transition. In Type II superconductors there are two critical fields. The lower critical field H_{c1} represents the transition from the Meissner state to the mixed state, while the upper critical field H_{c2} marks the maximum field for which any superconductivity is present. Listed in Table 2.11 are the metallic Type II superconductors that

were known prior to 1986 [32–34]. These materials are sometimes referred to as low temperature superconductors (LTS) and continue to be the materials of choice for most large superconducting magnet applications. Note that for these materials, although the critical temperature is only slightly higher than that of some Type I superconductors, H_{c2} is often orders of magnitude higher than H_c.

The mixed state in a well annealed Type II superconductor has an equilibrium condition consisting of a uniform fluxon lattice. In such a Type II superconductor, these flux lines are free to move about within the crystal. If the superconductor is subjected simultaneously to an external field and transport current, the flux lines will move under the influence of the Lorentz force, $\boldsymbol{F_L} = \boldsymbol{J} \times \boldsymbol{B}$, causing dissipation. This is an undesirable condition leading to a relatively low value of the critical current I_c. Fortunately, Type II superconductors have been developed that contain imperfections and crystal defects to pin the individual flux lines and thus restrict flux flow. Flux pinning by various forms of lattice imperfections is the dominant mechanism that allows practical superconductors to carry substantial transport currents in magnetic fields approaching H_{c2}. It is an interesting feature of superconductivity that the best properties in Type I superconductors are achieved with high purity, defect free metals while Type II superconductors performance improves by additions of impurities.

For high-field applications there are a limited number of commercially available superconductors. The two materials that are employed most often in magnets are NbTi and Nb_3Sn. NbTi is a binary alloy of approximately equal weight percent of each constituent. It has good mechanical properties, is easily processed in a composite with copper, and has a reasonably high $\mu_0 H_{c2} \approx 15$ T and $T_c \approx 10$ K. As a result, NbTi is the preferred superconductor for all magnetic devices with the exception of those requiring the highest fields, $\mu_0 H \gtrsim 10$ T. The other common practical superconductor, Nb_3Sn, is an intermetallic compound of the general class known as the A-15 s. Its mechanical properties are not as good, being very brittle, but Nb_3Sn has superior high-field characteristics, $\mu_0 H_{c2} \approx 28$ T and $T_c \simeq 18$ K, making it particularly well suited for very high-field magnetic devices. Both of these materials can be made with sufficient flux pinning to achieve high critical current densities. Also, they can be processed into multifilament wire form with copper providing a reliable product that can be cabled and wound into a wide variety of magnet designs.

Figure 2.16 shows schematically how the critical current density, J_c [A/mm^2], varies with magnetic field and temperature for NbTi and Nb_3Sn. The numerical values given in this graph are not state of the art, but rather are shown here for general trends with intrinsic variables. Also shown in the figure are the range of temperatures obtainable by the two lowest-temperature cryogenic fluids, liquid helium and liquid hydrogen. For reasonable current densities in high magnetic fields, it is apparent that low temperature helium provides the only practical coolant for these materials.

The discovery and rapid development of high temperature superconductors has introduced new opportunities for applications. This class of materials are distinct from most LTS because they are non-metals with very poor normal state conductivity. Their mechanical properties are poor and the superconducting properties are

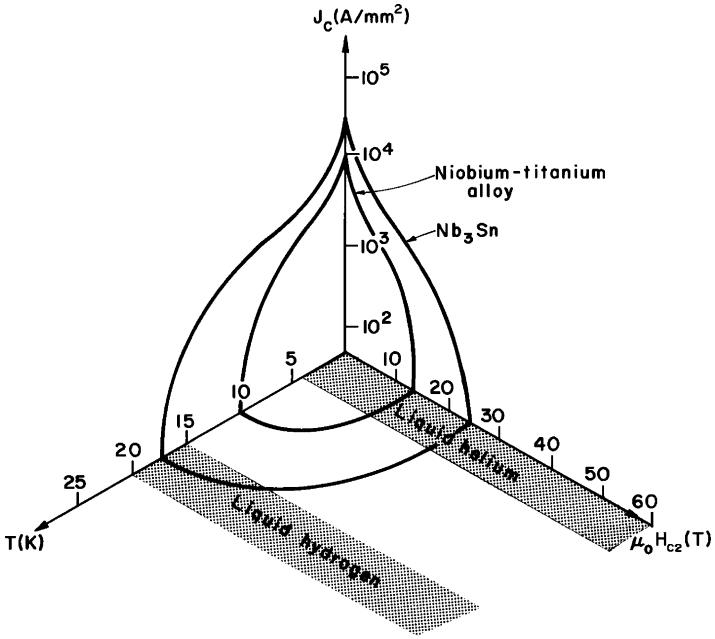

Fig. 2.16 Upper critical field, temperature, and current density for commercial superconducting materials NbTi and Nb_3Sn [35]

Table 2.12 Critical properties of HTS materials. Two values of H_{c2} indicate anisotropic material property [34]

Superconductor	T_c(K)	$\mu_0 H_{c2}$(T)
MgB_2	39	16/2.5
LaSrCuO	40	50
YBCO	90	670/120
$Bi_2Sr_2CaCu_2O_8$	90	280/32
$Bi_2Sr_2Ca_2Cu_3O_{10}$	110	
$TlBaCaCuO_{10}$	110	
$TlBaCaCuO_{10}$	125	~120
$HgBa_2Ca_2Cu_3O_8$	133	~160

more difficult to optimize due to complexities in their reaction heat treatment. Also, in most cases, these superconductors are layered structures with anisotropic properties that depend on their orientation with respect to the applied magnetic field.

Table 2.12 is a list of materials that fall broadly into the class of HTS. Note that all these materials superconducting properties are Type II. In most cases, $\mu_0 H_{c2}$ is only approximately known since its value is so high that it is difficult to measure. These materials are manufactured by different processes than LTS with the procedures being too complex to discuss in the current review. Production of HTS wire suitable for applications also depends on material selection.

Some materials, such as the BSCCO based conductors, are produced in a silver matrix, which provides the needed parallel path for electric current. Other materials such as YBCO can be formed on a variety of substrate materials.

Overall, HTS materials have transition temperatures that are sufficiently high to use other coolants such as liquid neon or nitrogen or by a closed cycle cryocooler. However, since the superconducting properties (J_c, H_{c2}) of these materials all improve with decreasing temperature, some HTS applications are still utilizing helium cooling all be it at somewhat elevated temperatures. Certainly, HTS applications have stimulated the development of small scale cryocoolers, a topic discussed in Chap. 8.

The problems of superconducting materials are of great concern to helium cryogenics. Superconducting materials require helium temperature environments to achieve their properties, but more importantly, the behavior of superconductive devices are governed largely by problems of heat transfer, efficient cooling, and safety. For example, the properties of a superconductor are conducive to carrying electric current provided the material remains below the local critical temperature and field. Thermal equilibrium is not always possible so superconductors must be fabricated in a low-resistance matrix material like copper or aluminum to provide the current-carrying capacity should the superconductor enter the normal state. Proper analysis of this problem requires knowledge of the heat transfer and fluid flow conditions present in the particular magnetic device.

Questions

1. Why does the electrical conductivity of a metal increase while that of a semiconductor decrease with decreasing temperature?
2. Why do alloys generally have lower thermal conductivity than pure metals? What does this say about material selection for structural supports in cryogenic systems?
3. Explain using thermodynamic arguments why the thermal expansion coefficient, α, of a material goes to zero as absolute zero is approached.
4. Why do materials normally get stronger as the temperature decreases?
5. Calculate the ratio σ_y/k for beryllium copper and Teflon at 300, 80 and 4 K. Compare with values in Table 2.8. Comment on their relative usefulness as structural materials.

Problems

1. Calculate the heat content in a two tonne (2,000 kg) iron magnet at 300 K. How much liquid nitrogen is required to cool this magnet to 80 K? How much liquid helium is required to cool this magnet from 80 to 4 K? (Hint: Assume that the internal energy change is entirely absorbed by the liquid resulting is a mass of vapor. Use the Debye model to calculate the change in internal energy, Θ_D(Fe) = 460 K; h_{fg}(He@ 4 K) = 21 kJ/kg; h_{fg} (N_2 @ 80 K = 200 kJ/kg)).
2. Calculate the difference between the constant pressure and constant volume heat capacities of aluminum at 300 K.

3. Derive an expression for the temperature at which the electron and phonon contributions to the heat capacity are equal. Of the elements listed in Tables 2.1 and 2.2, which has the highest value of this temperature?
4. The thermal conductivity of 304 stainless steel varies with temperature as $k(T) = 1.5\ T^{0.4}$ [W/m K]. Calculate the total conduction heat transfer for a 10 mm diameter rod, 100 mm in length. One end of the rod is at 80 K and the other is at 300 K.
5. A Pt resistance thermometer consists of a 1 m long thin wire of pure annealed platnium. Calculate the diameter of the wire based on the requirement that the power dissipation not exceed 0.1 μW at room temperature and the current be less than 10 μA. What is the sensitivity of this sensor, dR/dT?
6. Derive (2.34) starting with the Gibbs free energy change and the empirical form for the critical field of a Type I superconductor,

$$H_c = H_0\left[1 - \left(\frac{T}{T_c}\right)^2\right]$$

   a. *Adiabatic magnetization* is the constant entropy application of the magnetic field that brings the superconductor into the normal state. Derive an expression for the final temperature T_f as a function of H_0, T_c *and* T_i.
   b. Choose a Type I superconductor and calculate the value of $\Delta T_{\max}$, the maximum value for the temperature difference occurring from adiabatic magnetization.

   Hint: You may assume that the normal state specific heat $C_n = \gamma T$ and neglect the phonon heat capacity.
7. Thermal conductivity of copper

   a. Determine the mean free path in a copper sample with a residual resistivity ratio, RRR = 50 for temperatures below 10 K. Use the following values for copper: Fermi velocity $v_F = 1.57 \times 10^6$ m/s and the electron concentration $n = 8.45 \times 10^{28}\ \mathrm{m}^{-3}$.
   b. Estimate the thermal conductivity of the same copper at 2 K.

8. The maximum electrical current that can be carried by a Type I superconductor wire is limited to the current that produces the critical field H_c at the conductor surface (Silsbee's Law).

   a. Derive an expression for the critical current of a cylindrical superconducting wire of radius R as a function of temperature.
   b. How much current can a 1 mm diameter indium wire carry at 1.8 K? [Hint: Use Ampere's Law to determine the magnetic field at the surface of the wire.]

9. A normal metal wire carrying an electrical current will produce heat, raising the temperature of the wire. Estimate the time required for a copper wire carrying a current density of 100 A/mm^2 to heat up from 4.2 to 300 K if it is thermally

insulated from the environment. Assume $C_p = C_v$ and use approximations for both the resistivity and the specific heat as functions of temperature.

10. A sample of wire is made by codrawing a copper tube over an aluminum rod. The aluminum has a cross-sectional area A1 and the copper A2. The wire is stress free at ambient temperature, T = 293 K. Derive a relationship for the stress in either component of the wire as a function of A1, A2, and material properties when the wire is cooled to 4.2 K. For equal cross-sectional areas (A1 = A2), calculate the stress in the copper and compare it with the yield of annealed OFHC copper.
11. A temperature sensor located at 4.2 K requires four Manganin instrument leads to 300 K. The length of the wires is 1 m and the sensor operating current (for two of the leads) is I = 10 μA. Calculate the required wire diameter such that the thermal conduction heat load is equal to the Joule heat (I^2R) when the two leads are energized.
12. Consider a material that has a thermal conductivity varying with temperature as $k = \beta T^2$ and a constant thermal contraction coefficient, α. Derive a relationship for the overall change in length of a rod of initial length L as a function of the temperature difference between the two ends of the rod. Show the result for the special case where the low temperature end is at 0 K. Compare the answer to that for $k =$ constant.
13. Same as Problem 12 except let the thermal conductivity be a linear function of temperature, $k = \beta T$.
14. Calculate the Lorentz ratio ($L = k\rho/T$) for one of the materials in Tables 2.4 and 2.5. Compare to the free electron value, L_0.

References

1. See for example, C. Kittel, *Introduction to Solid State Physics*, 5th ed., Wiley, New York, 1976.
2. See for example, M. W. Zemansky, *Heat and Thermodynamics*, 3rd ed., McGraw-Hill, New York, 1968.
3. CRYOCOMP® is a database code of the state and thermal properties for technical materials.
4. NIST Cryogenic Materials database: http://www.cryogenics.nist.gov/MPropsMAY/material%20properties.htm
5. G. White, *Experimental Techniques in Low Temperature Physics, 3rd Ed.*, Clarendon press, Oxford, 1979.
6. J. W. Ekin, *Experimental Techniques for Low Temperature Measurements*, Oxford University Press, Oxford, 2006.
7. K. Huang, *Statistical Mechanics*, J. Wiley & sons, NY, 1963.
8. M. Nageo, T. Inaguchi, H. Yoshimura, T. Yamada, and M. Iwamoto, Helium Liquefaction by a Gifford-McMahon Cycle Cryocooler, *Adv. Cryog. Engn.* **Vol. 35**, 1251 (1990).
9. R. J. Corruccini and J. J. Gniewek, *Thermal Expansion of Technical Solids at Low Temperatures*, NBS Monograph 29, U.S. Government Printing Office, Washington, DC, 1961.
10. T. H. K. Barron, J. G. Collins, and G. K. White, Thermal Expansion of Solids at Low Temperatures, *Adv. Phys.* **29**, 609 (1980).
11. R. S. Krishnan, R. Srinivasan, and S. Dcvanarayanan, *Thermal Expansion of Crystals*, Pergamon, Oxford, 1979.

12. G. K. White, Metals and Alloys: Expansion and Contraction, *Adv. Cryog. Engn.* **Vol. 30**, 407 (1984).
13. R. L. Powell and F. R. Fickett, *Cryogenic Properties of Copper*, International Copper Research Association, Dec. 1979.
14. R. P. Reed and A. F. Clark, *Materials at Low Temperatures*, American Society of Metals, Metals Park, Ohio, 1983.
15. L. A. Hall, *Survey of Electrical Resistivity Measurements on 16 Pure Metals in the Temperature Range 0-273 K*, NBS Technical Note 365, U.S. Government Printing Office, Washington, DC, 1968.
16. R. A. Matula, Electrical Resistivity of Cu, Au, Pd, and Ag, *J. Phys. Chem. Phys. Ref: Data* **8**, 1147 (1979).
17. G. T. Meaden, *Electrical Resistance of Metals*, Plenum Press, New York, 1965.
18. F. Clark, G. E. Childs, and G. H. Wallace, Electrical Resistivity of Some Engineering Alloys at Low Temperatures, *Cryogenics* **10**, 295 (1970).
19. F. R. Fickett, Magnetoresistivity of Copper and Aluminum at Cryogenic Temperatures, http://lss.fnal.gov/conf/C720919/p539.pdf
20. R. Berman, *Thermal Conduction in Solids*, Clarendon Press, Oxford, 1976.
21. J. G. Hust and L. L. Sparks, *Lorenz Ratios of Technically Important Metals and Alloys*, NBS Technical Note 634, U.S. Government Printing Office, Washington, DC, Feb. 1973.
22. G. K. Batchelor and R. W. O'Brien, Thermal or elecrtrical conduction through granular material, *Proc. Roy. Soc. Lon.* **A335**, 313 (1977).
23. S. W. Van Sciver, M. N. Nellis and J. Pfotenhauer, Thermal and Electrical Contact Conductance Between Metals at Low Temperatures, *Proceedings Space Cryogenics Workshop*, Berlin, Germany (1984).
24. R. E. Peterson and A. C. Anderson, Kapitza Thermal Boundary Resistance, *J. Low Temp. Phys.* **11**, 639 (1973).
25. R. Radebaugh, Thermal Conductance of Indium Solder Joints at Low Temperature, *Rev. Sci. Instrum.* **48**, 93 (1977).
26. *Handbook on Materials for Superconducting Machinery*, Metals and Ceramics Information Center, Battelle, Columbus, Pub. #MCIC-HB-04 (Jan. 1977).
27. R. F. Barron, *Cryogenic Systems*, *2nd Ed.,* Oxford Science, Oxford 1985, Ch. 2.
28. R. de Bruyn Ouboter, Superconductivity: Discoveries during the Early Years of Low Temperature Research at Leiden, *IEEE Trans. on Magnetics* **Vol. Mag-23**, 355 (1987).
29. S. W. Van Sciver and K. R. Marken, *Physics Today* **Vol. 55**, 37 (2002).
30. C. Rose-Innes and E. H. Rhoderick, *Introduction to Superconductivity*, *2nd Ed.,* International Series in Solid State Physics, **Vol. 6**, Pergamon Press, New York, 1978.
31. E. A. Lynton, *Superconductivity*, 3rd Ed., Chapman Hall Ltd. Science Paperbacks, London, 1969.
32. M. N. Wilson, *Superconducting Magnets*, Monographs on Cryogenics, Clarendon Press, Oxford, 1983.
33. Y. Iwasa, *Case Studies in Superconducting Magnets,* Plenum Press, New York, 1994,
34. J. W. Ekin, *Experimental Techniques for Low Temperature Measurements*, Oxford University Press, Oxford, 2006, Appendix A6.6.
35. B. B. Schwartz and S. Foner, Large Scale Applications of Superconductivity, *Physics Today* **30**, 34 (1977).

Further Readings

R. F. Barron, *Cryogenic Systems*, *2nd Ed.,* Oxford Science, Oxford 1985, Ch. 2
R. Berman, *Thermal Conduction in Solids*, Clarendon Press, Oxford, 1976.
J. W. Ekin, *Experimental Techniques for Low Temperature Measurements*, Oxford University Press, Oxford, 2006.
K. Huang, *Statistical Mechanics*, J. Wiley & sons, NY, 1963.

Y. Iwasa, *Case Studies in Superconducting Magnets,* Plenum Press, New York, 1994.
C. Kittel, *Introduction to Solid State Physics*, *5th Ed*., Wiley, New York, 1976.
R. S. Krishnan, R. Srinivasan, and S. Dcvanarayanan, *Thermal Expansion of Crystals*, Pergamon, Oxford, 1979.
E. A. Lynton, *Superconductivity*, *3rd Ed.,* Chapman Hall Ltd. Science Paperbacks, London, 1969.
G. T. Meaden, *Electrical Resistance of Metals*, Plenum Press, New York, 1965.
C. Rose-Innes and E. H. Rhoderick, *Introduction to Superconductivity*, *2nd Ed*., International Series in Solid State Physics, Vol. 6, Pergamon Press, New York, 1978.
M. N. Wilson, *Superconducting Magnets*, Monographs on Cryogenics, Clarendon Press, Oxford, 1983.

Chapter 3
Helium as a Classical Fluid

Of all the cryogenic fluids, helium exhibits behavior that most nearly approximates that of an ideal fluid. This fact is caused mostly by the weak intermolecular potential that helium enjoys. It further manifests itself in the fact that ^{4}He has the lowest critical point of all fluids, $T_c = 5.195$ K, $p_c = 0.227$ MPa and $\rho_c = 69.7$ kg/m^3. As a result of this near ideality, much of the behavior of gaseous and even liquid helium above the superfluid transition can be treated in terms of classical models. This is not to say that quantum effects do not contribute to the behavior. Rather, certain features of helium in this temperature and pressure range are controlled by a combination of physical phenomena, which can be qualitatively if not quantitatively described in terms of classical physics models. Conversely, certain characteristics of helium, most notably that of the liquid state below the superfluid transition and also the solid state, have properties which are so determined by quantum mechanics that classical physics cannot be used in a meaningful way to interpret their behavior. The present chapter focuses on those properties of ^{4}He that are at least semi-classical. The quantum aspects, particularly superfluidity and Bose-Einstein condensation are discussed separately in Chap. 4. This chapter also does not consider the properties of the lighter isotope, ^{3}He, a subject that is covered in Chap. 9. Therefore in the present discussion, we will use helium in a generic sense to mean the abundant isotope, ^{4}He.

3.1 Helium Phase Diagram

As a beginning point to the description of liquid and gaseous helium, it is useful to make reference to the *p-T* phase diagram, Fig. 3.1. In addition to the conventional characteristics such as the critical point and two-phase coexistence, there are several unique features to this phase diagram which should be noted. First, unlike all other substances, the solid state of helium is not obtainable at any temperature unless an external pressure in excess of 2.5 MPa is applied. This characteristic, an artifact of the quantum nature of helium, is caused by the large zero point energy

S.W. Van Sciver, *Helium Cryogenics*, International Cryogenics Monograph Series,
DOI 10.1007/978-1-4419-9979-5_3,

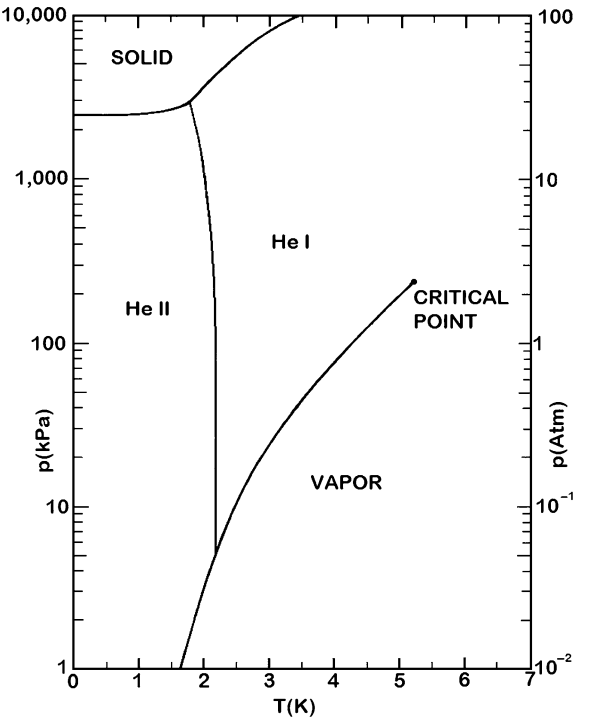

Fig. 3.1 ^{4}He phase diagram

of the helium molecule. Thus, the lowest energy state of helium is that of the liquid, albeit the superfluid state, He II.

Helium is also exceptional in that it has two liquid phases. He I is the normal liquid with characteristics that are typical of classical fluids. In this region, helium acts in many ways as a weakly interacting gas, which is at least in part due to its weak intermolecular interaction and low viscosity. The dynamic viscosity of He I is comparable to that of air at room temperature.

He II, or superfluid helium, has physical features that are truly exceptional. Most notable of these features are the transport properties, with a vanishingly small viscosity and an apparent thermal conductivity many orders of magnitude larger than liquids or even high-conductivity solids. The line that separates the two liquid states is termed the λ-line. This designation was adopted because the specific heat near the transition has the shape of the Greek letter λ. The λ-transition temperature is 2.178 K at saturated vapor pressure and decreases gradually with increasing pressure until it intersects the solid coexistence boundary at 1.763 K, $p = 2.974$ MPa [1].

The phase diagram of helium is also unique in that it lacks a triple point of coexistence between liquid, vapor, and solid, because the solid state can exist only under an external pressure. The intersection of the λ-line with the two phase coexistence regions of liquid and vapor or solid and liquid is not a triple point,

although it occasionally is identified incorrectly as such. As is discussed in the next chapter, the λ-transition is a second-order phase transition, which means it has a discontinuous slope in the temperature dependence of the entropy. There is no latent heat of formation of the He II state and coexistence of He II and He I under equilibrium conditions is not possible.

In the present chapter the properties of helium which are best described in terms of classical models are surveyed. Thus, the subject matter is dominated by the gaseous and normal liquid state, He I. Even with this somewhat arbitrary separation, it is not possible to analyze fully the properties of these "classical" fluids without some reference to the effect of quantum statistics on their behavior. Chapter 4 is reserved for the description of helium as a quantum fluid. Therefore, the bulk of the quantum mechanical analysis of helium is presented there with comparison to the quantum fluid, He II.

3.2 Gaseous Helium

Helium at temperatures substantially above its normal boiling point behaves more like an ideal gas than any other commonly known fluid. This fact is the result of the weak interatomic potential and the spherically symmetric molecular configuration. Of course, at some point gaseous helium must deviate from ideality, otherwise physical phenomena such as the Joule Thomson effect and liquefaction would not occur. However, because of its similarity to an ideal gas, it is often most beneficial to consider properties of gaseous helium in terms of extensions from the ideal gas model.

The first goal of a physical model used to describe helium gas is the development of an understanding of its state properties. From an experimental viewpoint, the most common measurements are those of specific heat, C_p and C_v, and the state properties of pressure, temperature, and specific volume. The latter measurements lead to the equation of state for the gas, which in its complete form can be combined with the thermodynamic principles to determine the relevant state functions including entropy and enthalpy.

The equation of state, which is a functional relationship among p, V, and T, cannot be determined exactly for a particular real gas. However, there exist a number of approximate relationships that also give considerable physical insight into the processes involved. The most notable approximation to the equation of state is known as the virial expansion, which is an expansion involving intermolecular interactions. Furthermore, in developing a model to describe the interactions between helium gas molecules, particularly near the critical point $T_c = 5.2$ K, a concern for quantum mechanical effects is needed. The most common isotope of helium, ^{4}He, obeys Bose-Einstein statistics, which must be taken into account in the complete description of the gas.

3.2.1 Intermolecular Interactions

Any microscopic model for the behavior of helium has as its basis an understanding of the intermolecular potential [2, 3]. This interaction is exactly that which is ignored in the ideal gas model. The intermolecular potential involves the forces between the individual molecules caused by their finite size and mutual attraction. If the helium molecule obeyed classical mechanics and the intermolecular potential were known, then in principle it would be possible to compute the state properties directly. However, in any real sample of gas, there are far too many molecules ($\sim 10^{26}/m^3$) to realistically carry out this calculation. As a result, the normal approach is to use empirical potentials which describe the average molecular interactions. To properly model the problem, these potentials must contain the physics of the molecular interaction, which is composed primarily of two terms: (1) the hard core repulsive interaction and (2) the weaker attractive interaction due to what is called the London-dispersion mechanism.

The hard core repulsive interaction can be understood in rather simple terms. Molecules occupy volume and therefore collide with each other defining what is known as a scattering cross section and a mean free path between collisions. The details of this collision interaction are contained in the steepness of the repulsive potential. The hard core interaction would ultimately be expected to cause deviations from ideal gas behavior because the latter model assumes the molecules are non-interacting point particles. Thus, the hard core repulsion makes its largest correction to the equation of state at high density and temperature.

The attractive term in the molecular interactions is brought on by a mechanism known as the London-dispersion interaction, so termed because it is the same process responsible for light dispersion by molecules. To understand this interaction, it is important to note that a helium molecule is not truly inert. Actually, it is composed of a nucleus containing the positive charge and a "sea" of negative electrical charge surrounding the nucleus. The negative charge has a tendency to oscillate about the nuclear center of the molecule causing a time varying dipole moment. Because of this oscillating dipole, there is a momentary electrostatic potential set up in the vicinity of the molecule which varies as $V_d(r) \approx 1/r^3$. When two molecules are in close proximity and have oscillating dipole moments that are out of phase, there will be net attractive interaction. This interaction scales as the product of the two oscillating dipole moments, $\Phi_a(r) \approx 1/r^6$. Detailed quantum mechanical analysis by London has suggested that the attractive interaction is a sum of terms, the first of which is the dipole contribution. As with the hard core potential, the attractive interaction causes deviations from the ideal gas equation of state. It has the largest effect at low temperatures and high densities, resulting in a tendency for the molecules to exhibit collective behavior which can eventually lead to liquefaction.

Numerous examples of empirical potentials have been proposed to describe the total interaction of inert spherically symmetric molecules such as helium.

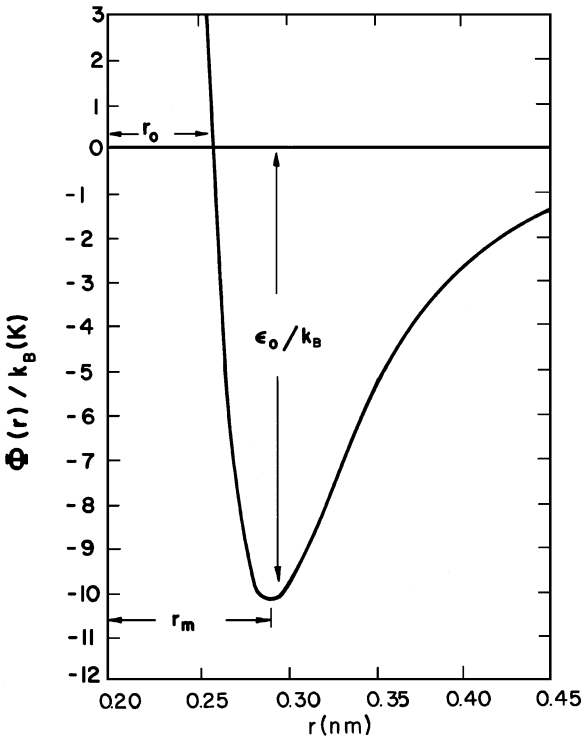

Fig. 3.2 Lennard-Jones 12–6 potential for ^{4}He

Table 3.1 Coefficients of the Lennard-Jones 12–6 potential for common cryogenic fluids [2]

	r_0 (nm)	r_m (nm)	ε_0/k_B
He	0.2556	0.2869	10.22
Ne	0.2789	0.3131	35.7
N_2	0.3681	0.4132	91.5
O_2	0.3433	0.3853	113.0
Ar	0.3418	0.3837	124.0

Probably the most successful, because of its mathematical simplicity and physical basis, is the Lennard-Jones 12–6 potential. This potential has a mathematical form,

$$\Phi_{LJ}(r) = 4\varepsilon_0 \left[\left(\frac{r_0}{r} \right)^{12} - \left(\frac{r_0}{r} \right)^{6} \right] \tag{3.1}$$

that depends on the determination of two parameters: ε_0, which is a measure of the depth of the potential well, and r_0, which is a dimensional scale of the molecular radius. Plotted in Fig. 3.2 is the Lennard-Jones potential for a helium molecule with the quantities ε_0, r_0, and r_m, the radius of the potential minimum, all indicated. Listed in Table 3.1 are these parameters for some common cryogenic fluids as comparison [2].

Other examples of empirical intermolecular potentials that are occasionally used to approximate real gas behavior include the hard sphere potential, square well potential, and the Buckingham exp-6 [4].

3.2.2 Virial Expansion

Suitable selection of the intermolecular potential is insufficient in itself for approximation of the equation of state. It is also necessary to adopt a form for the equation of state which incorporates the preferred form of the intermolecular potential. Such a relationship has numerous forms, but the best for physical interpretations is the so-called virial expansion, which can be written as an expansion in the specific volume v:

$$pv = RT\left(1 + \frac{B}{v} + \frac{C}{v^2} + \frac{D}{v^3} + \ldots\right) \tag{3.2}$$

The quantities B, C, D, and so on are called the second, third, fourth, and higher-order virial coefficients. Note that a special case of the virial expansion is that of the van der Waal equation of state, which will be discussed later.

The physical basis for the virial expansion in the form shown in (3.2) is for each coefficient to describe a particular type of interaction. Thus, the second virial coefficient B should incorporate corrections to the equation of state due to two-body interactions. The third virial coefficient C incorporates corrections due to three-body interactions, and higher-order terms follow the same sequence. The requirement for any theoretical description of the virial coefficients is that it must include the many-body interactions and use a physically realistic potential.

Based on this sequence it should be clear that the second virial coefficient is the largest term in the expansion and therefore makes the largest correction to the ideal gas law. For classical fluids, the second virial coefficient is written,

$$B_{\mathrm{cl}} = -\frac{N}{2}\int_0^{\infty} (e^{\frac{-\Phi(r)}{k_B T}} - 1)4\pi r^2 dr \tag{3.3}$$

where $\Phi(r)$ is the interaction potential assumed to be spherically symmetric and N is the total number of molecules per unit volume. By considering (3.3) it is easy to see that the problem of analytical determination of B becomes quite difficult when complex potentials are employed.

The virial expansion becomes even more difficult to evaluate when considering gaseous helium at relatively low temperatures because of the need to include quantum mechanical effects in the analysis. A complete description of the quantum virial expansion problem is beyond the scope of this book [4]. However, it is instructive to briefly survey the problem to understand better some of the difficulties.

To determine the quantum virial expansion, the equation of state is expanded in terms of a quantity known as the fugacity, $z = e^{-\mu/k_B T}$, where μ is the chemical potential. This is a fairly standard approach in quantum statistical mechanics [4, 5]. The result is an expression for the pressure in terms of this quantity,

$$\frac{p}{k_B T} = \sum_k b_k z^k \tag{3.4}$$

where b_k contains the physics of the problem. These coefficients must be determined by substitution in the time-independent Schrödinger equation,

$$-\frac{h^2}{2m_r}\left[\nabla^2 r\psi + \frac{l(l+1)}{r^2} r\psi\right] + \Phi(r) r\psi = Er\psi \tag{3.5}$$

where $m_r = m_1 m_2/(m_1 + m_2)$ is the reduced mass, l is the angular momentum quantum number, and is the spherically symmetric wave function. The solution to the above problem leads to a set of energy levels, some of which are bound states and some of which are in the continuum. Applying quantum mechanical scattering methods, we calculate the phase shift $\eta_l(q)$, where q is the energy parameter. The phase shift serves the purpose of incorporating interactions into one parameter. The wave function solution to the Schrödinger equation includes the phase shift as part of its argument,

$$\psi \approx \sin(qr - \frac{1}{2}\pi l + \eta_l) \tag{3.6}$$

The virial coefficients are then found by summing over all states, bound and continuum. For ^{4}He this exercise leads to the computed second virial coefficient shown in Fig. 3.3. Also shown in the figure is the second virial coefficient obtained from the classical calculation for comparison. Clearly, the two quantities are different, particularly below the Boyle temperature, defined by the second virial coefficient going to zero; for ^{4}He $T_{Bo} \sim 20$ K. At temperatures below around 10 K, there is about a factor of two difference between the classical and quantum second virial coefficients. Also displayed in Fig. 3.3 are the experimentally determined virial coefficient values, which show close agreement with the calculated quantum coefficient using the Lennard-Jones potential [4].

In addition to virial expansion coefficient values obtained from basic principles, there are also a number of empirical representations of the second virial coefficient that are useful for calculations. A simple general form for the function is described by McCarty [1],

$$B(T) = \sum_i b_i T^{(3-i)/2} \tag{3.7}$$

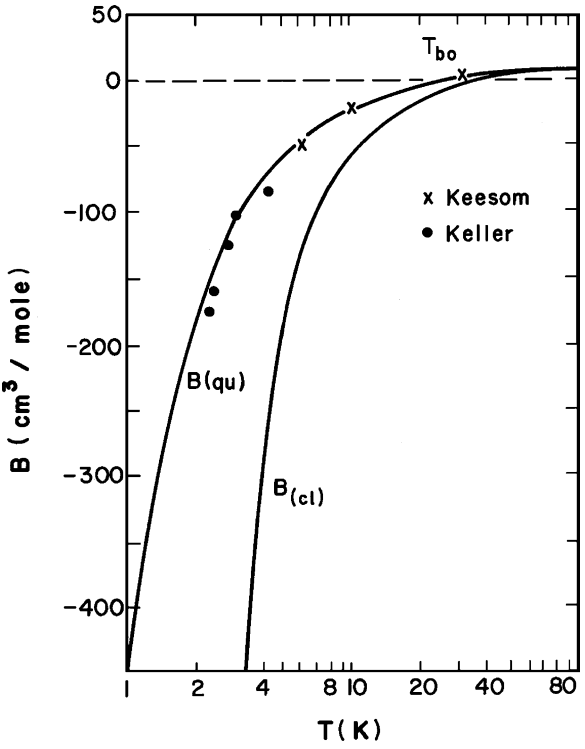

Fig. 3.3 Second virial coefficient for ^{4}He, from Keller[4]

where on the order of nine terms in the expansion are required to fit adequately the temperature dependence over the whole range. Also, a less cumbersome empirical fit suitable below the Boyle temperature has been suggested by Keller [4],

$$B(T) = a - \frac{b}{T} \tag{3.8}$$

where, for ^{4}He, $a = 23.05$ cm^3/mol and $b = 421.77$ cm^3 K/mol.

Example 3.1

Use the empirical expression for the second virial coefficient (3.8) to estimate the Boyle temperature.

The Boyle temperature is approximately that corresponding to $B\ (T_{Bo}) = 0$. From (3.8), this means that $T_{Bo} \sim b/a = 18.3$ K.

Before leaving the subject of the Boyle temperature, it is useful to consider its physical significance in terms of the equation of state. Since T_{Bo} marks the transition between a positive and a negative virial coefficient, it indicates the regions where different parts of the interaction potential dominate. Below T_{Bo}, B is

negative, implying that the pressure is less than would occur for a truly ideal gas. Since the molecules must be attracted to each other to cause this behavior, the London dispersion forces must be the more important in this regime. On the other hand, above T_{Bo}, B is positive, implying the gas pressure is actually greater than that of an ideal gas. To have this effect requires an excess repulsion and therefore the hard core potential must be the more important contribution to the potential in this region. Thus, although the Boyle temperature does not represent a true transition temperature for a particular gas, it does define the range of dominance of the various contributions to the intermolecular interaction.

The third virial coefficient C is more difficult to calculate because it involves three-body interactions. For the classical picture and the hard sphere potential, C can be shown to vary as the square of the molecular volume [4]. Thus, this coefficient is of little importance except at relatively high densities and low temperatures. Efforts to calculate the third and higher virial coefficients for helium have been hampered by the lack of experimental data. Furthermore, the exact form of these coefficients is less important to application than the development of an empirical equation of state suitable for modeling the helium properties over a wide range of temperatures and pressures.

3.2.3 Empirical Equations of State

Development of the theory of quantum virial expansions is helpful for understanding the complexities of gaseous helium at low temperatures. However, for applications, the above format is far too cumbersome to allow rapid calculation of properties. For this reason, empirical equations of state have been developed which make no attempt to fully understand the physical problem, but rather provide a tool for calculation. With a closed-form solution for the equation of state, it is a rather straightforward process to derive the other important thermodynamic properties.

The simplest empirical equation of state takes into account the deviations from ideal behavior in terms of a compressibility factor z. As defined, the compressibility factor may be written

$$z = \frac{pv}{RT} \tag{3.9}$$

which obviously is equal to unity for an ideal gas. In the virial expansion, z is defined as the quantity in parenthesis in (3.2). Historically, the value of z is given empirically in either graphical or tabular forms since it depends on state variables; z for helium are displayed graphically in Appendix A.1.

The most common classical equation of state for a real gas is due to van der Waals,

$$\left(p + \frac{a}{v^2}\right)(v - b) = RT \tag{3.10}$$

Here a and b are constants that depend on the particular gas. Physically, b is related to the strength of the hard core potential so that even at $T = 0$, the fluid occupies a finite volume. a is an effective reduction in pressure due to intermolecular attraction.

The law of corresponding states [2, 6] is a useful tool to characterize a real fluid particularly near its critical point. This law defines a general equation of state as a function of the reduced variables: T/T_c, p/p_c, and v/v_c, that is,

$$\frac{p}{p_c} = \phi(T/T_c, v/v_c) \tag{3.11}$$

where ϕ is an undetermined function that relates these quantities. The van der Waals gas is a special case of (3.11). For the law of corresponding states to apply, several assumptions are needed. First of all, the law ignores quantum effects. Since helium has substantial quantum effects in its real gas behavior it would be expected to deviate from the law of corresponding states. A second assumption has to do with the symmetry of interaction. The law is established on the basis of symmetric molecular potentials. In fact, many molecules have very asymmetric bonding and configuration. A good example of an asymmetric potential is H_2O, but others include CO_2 and organic compounds like CH_4. The law of corresponding states ignores these effects.

The law of corresponding states can be used to determine numerical values for the coefficients in a particular equation of state. In the vicinity of the critical point, all isotherms have an inflection point; see, for example, Fig. 1.2. Thus, it follows that the equation of state must have a zero in its first and second derivative when evaluated at the critical point, i.e.:

$$\left(\frac{\partial p}{\partial v}\right)_{T_c} = \left(\frac{\partial^2 p}{\partial v^2}\right)_{T_c} = 0 \tag{3.12}$$

This represents two equations which must be satisfied by the equation of state. Consider for example the van der Waals equation of state, where there are two coefficients, a and b, that must be determined for a particular gas. Differentiating as in (3.10) these quantities are immediately determined in terms of critical pressure and temperature,

$$a = \frac{27}{64}\frac{R^2 T_c^2}{p_c} \tag{3.13}$$

and

$$b = \frac{RT_c}{8p_c} \tag{3.14}$$

Table 3.2 Critical point coefficients to the van der Waals equation of state for various cryogenic fluids [7]

Fluid	T_c (K)	p_c (MPa)	a (m^6kPa/$kmol^2$)	b (m^3/kmol)	T_{Bo} (K)
He	5.195	0.2275	3.46	0.0237	17.6
H_2	33.19	1.315	24.4	0.0262	112
Ne	44.49	2.678	21.5	0.0173	149
Air	133.0	3.867	133	0.0357	448
N_2	126.2	3.396	137	0.0386	427
Ar	150.7	4.863	136	0.0322	508
O_2	154.6	5.043	138	0.0318	522

Thus, to apply the van der Waals equation of state for a particular gas, one only needs values for the critical pressure and temperature. Listed in Table 3.2 are values of these coefficients appropriate for various gases of interest to cryogenics. These values are calculated using known critical parameters and (3.13) and (3.14).

Finally, one can show by expanding the van der Waal equation of state that the Boyle temperature can be written as,

$$T_{Bo} = \frac{a}{bR} \tag{3.15}$$

which can be used to calculate values for common fluids. Table 3.2 lists the calculated Boyle temperature for the listed fluids. For helium, the value of 17.6 K is close to the value obtained from (3.8), see Example 3.1.

Several more complete empirical equations of state have been developed for gaseous helium [1]. In general, it is not possible to describe adequately the entire *p-v-T* surface using one equation. The forms of the expansions have pressure as a dependent variable:

$$pv = RT\left[1 + \frac{B(T)}{v}\right] + \sum_k \left(\frac{g_k(T)}{v^{k+2}}\right) \tag{3.16}$$

where $g_k(T)$ is a complex summation function over temperature with empirically determined coefficients. By this method, correlations to existing data have been found. Properties derived from these correlations are readily available in tabular form or computer data bases such as REFPROP® [7] and HEPAK®[8]. A sample of these derived properties is reproduced in Appendix 2.

3.3 State Properties of Liquid He I

Helium has such a weak intermolecular interaction that it only liquefies at very low temperatures; the normal boiling point of liquid helium is 4.2 K. In the liquid state it has a relatively low density: the specific gravity of liquid helium at saturated vapor pressure varies between 0.145 and 0.0675 at T_c, making it, next to hydrogen, the

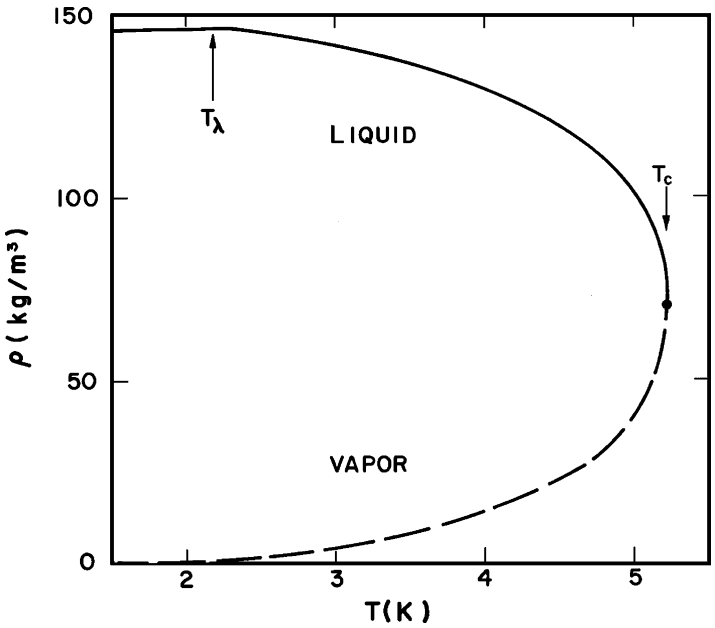

Fig. 3.4 Density of saturated liquid helium

lowest-density condensed fluid. Appendix 2 lists some of the thermodynamic and transport properties of helium as obtained from HEPAK [8]. Provided here is a summary of the properties of liquid helium with emphasis on those characteristics that are unique compared to other fluids.

3.3.1 Density

The saturation density ρ is one of the more important thermodynamic properties of He I because it can be used to derive the equation of state for the liquid. In the He I regime, the liquid density increases continuously from 67.5 kg/m^3 at T_c to 145 kg/m^3 just above T_λ. Plotted in Fig. 3.4 is the saturated density of liquid helium from T_c to below T_λ. Also shown for scale in the graph is the density of the saturated vapor over the same temperature range. A useful quantity to keep in mind is that the saturated liquid is about 7.4 times more dense than its vapor at the normal boiling point, 4.2 K. This point is worth noting as in many cases, the helium vapor mass makes a significant contribution to the total fluid mass in a system. Below T_λ the liquid density is only weakly temperature dependent decreasing slightly before becoming essentially constant for $T \lesssim 2.0$ K. This point will be discussed further in Chap. 4.

The slope of the density profile is a direct measure of the volume expansivity β. Under saturated vapor pressure, this quantity is plotted in Fig. 3.5 from results of

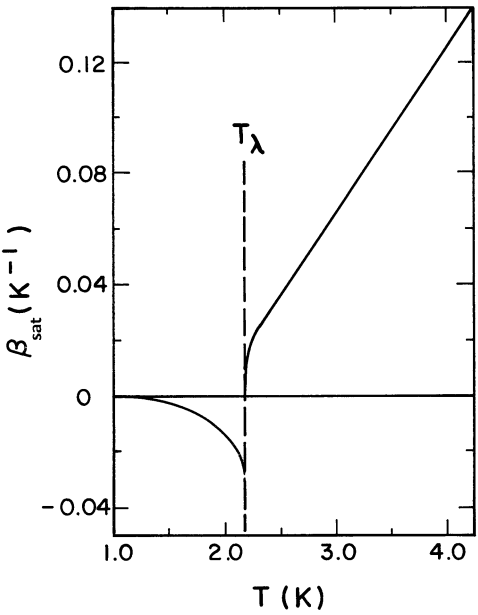

Fig. 3.5 Bulk thermal expansivity of ^{4}He at saturated vapor pressure

Kerr and Taylor [9]. By definition the volume expansivity at saturated vapor pressure is given by,

$$\beta_{\text{sat}} = -\frac{1}{\rho}\left(\frac{\partial \rho}{\partial T}\right)_{\text{sat}} \tag{3.17}$$

where the magnitude and slope of the density along the saturated vapor pressure curve are important. Note that not only does β_{sat} go through zero at T_λ, but it has a discontinuity in slope.

There exists a thermodynamic relationship between the expansion coefficient along the saturated vapor pressure curve, β_{sat}, and the same quantity at constant pressure,

$$\beta_p = \beta_{\text{sat}} + \kappa\left(\frac{\partial p}{\partial T}\right)_{\text{sat}} \tag{3.18}$$

where the bulk isothermal compressibility,

$$\kappa = -\frac{1}{V}\left(\frac{\partial V}{\partial p}\right)_T \tag{3.19}$$

is an additional parameter that must be known to compute β_p. The bulk isothermal compressibility is not strongly temperature dependent except near the critical temperature. Typical values for κ are in the range of 10^{-7} Pa^{-1}. However, the compressibility does have a discontinuity at the λ point which is consistent with the signature of a second-order phase transition. For comparison, the compressibility of water at 20 C is less than 10^{-9} Pa^{-1}.

3.3.2 Thermal Properties

Of the thermodynamic properties of liquid helium, the entropy, specific heat, and latent heat of vaporization have some of the most unique behavior. Shown in Fig. 3.6a–c are these three quantities as determined along the saturated vapor pressure curve. The most pronounced changes in the behavior of the thermal properties occur below T_λ. This region will be discussed in Chap. 4, which is concerned specifically with the properties of He II.

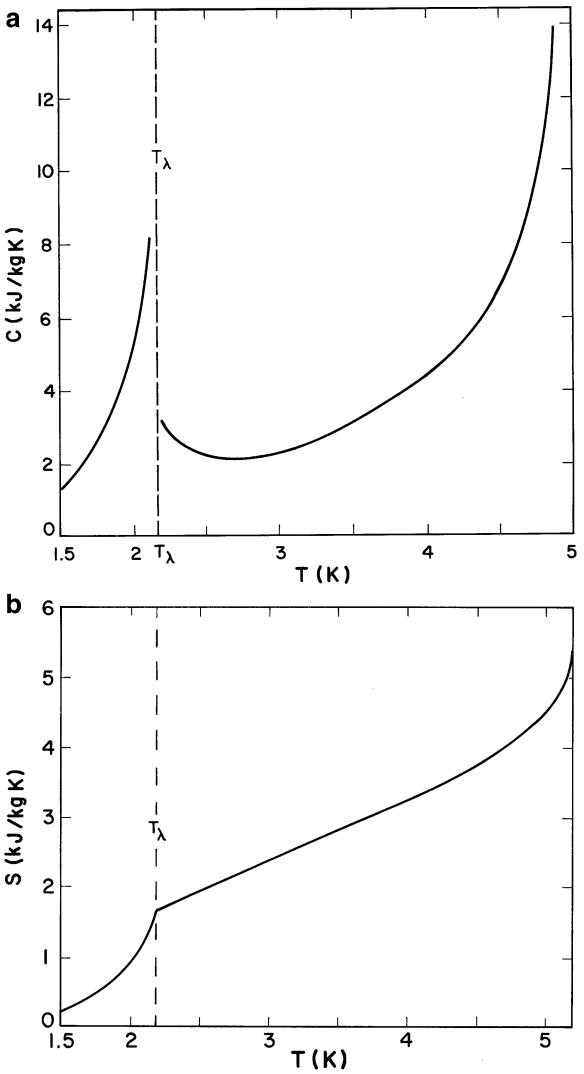

Fig. 3.6 (**a**) Specific heat of liquid helium at saturated vapor pressure. (**b**) Entropy of liquid helium at saturated vapor pressure. (**c**) Latent heat of vaporization of liquid helium

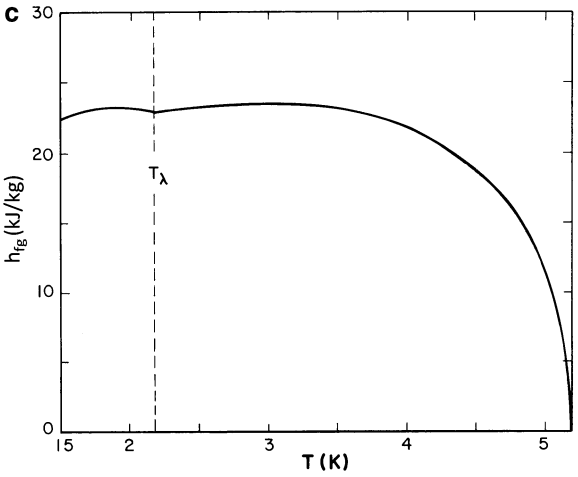

Fig. 3.6 (continued)

The entropy and specific heat above T_λ are not expected to have thermal behavior strongly different from that of a gas. For example, the specific heat of an ideal monatomic gas at constant volume is $C_v = 3/2\text{R}$ and at constant pressure is $C_p = 5/2\text{R}$. An ideal gas of mass 4 would therefore have a $C_v = 3.12$ kJ/kg K and a $C_p = 5.19$ kJ/kg K, respectively. As can be seen in Fig. 3.6a, the specific heat of liquid helium under saturated vapor pressure varies from 2.3 kJ/kg K just above T_λ to 5.2 kJ/kg K at 4.2 K. At temperatures much below T_c, the volume expansivity is a small contribution, making C_{sat} approach that of C_v. However, near T_c the volume expansion makes a substantial contribution, and the saturated values are more similar to constant pressure, $C_{\text{sat}} \approx C_p$. That the specific heat of liquid He I brackets that of an ideal monatomic gas indicates that, in many instances, He I is treatable in terms of modified gas laws. The importance of this statement will become evident in the next section on transport properties.

The latent heat of vaporization h_{fg} of liquid helium is displayed in Fig. 3.6c. This quantity, which is only defined along the saturated vapor pressure curve, is given by the Clausius-Clapeyron equation,

$$\left(\frac{dp}{dT}\right)_{sat} = \frac{h_{fg}}{T(v_g - v_l)} \tag{3.20}$$

where v_g and v_l are the specific volumes of the gas and liquid, respectively.

The heat of vaporization represents the energy required to take a unit mass of helium from the liquid to the vapor state. It is therefore an indirect measure of the strength of the intermolecular bonds associated with the formation of the liquid state. It is possible to compute h_{fg} from intermolecular empirical potentials. This problem is beyond the scope of the present treatment; however, on the experimental side there is a somewhat useful relationship between the heat of vaporization and the normal boiling point of many liquids. Trouton's rule [10] suggests that the ratio of h_{fg} to T_b should be approximately constant,

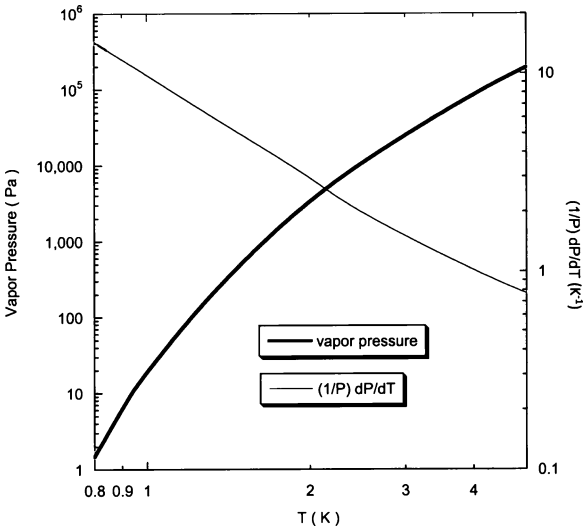

Fig. 3.7 Vapor pressure and its slope for liquid helium

$$\frac{h_{fg}}{T_b} \approx \text{constant} \tag{3.21}$$

where the constant has a value of about 75 J/mol K. This law, which is based primarily on experimental evidence, is obeyed to within 20% for most common liquids. However, it does not do as well for cryogenic liquids. The largest deviation from Trouton's rule occurs for helium where the ratio of $h_{fg}/T_b \approx 20$ J/mol K.

3.3.3 Vapor Pressure

The vapor pressure of any fluid is related to the heat of vaporization through (3.20). Furthermore, the vapor pressure is an important parameter as it is directly related to the liquid temperature and can be used an absolute temperature standard as well as a method of reducing the temperature of a liquid by evacuation of its coexisting vapor. Figure 3.7 is a plot of the vapor pressure and derivative, dp/pdT for liquid helium.

Example 3.2

Use the data in Fig. 3.6 to estimate the heat of vaporization for liquid helium at 1 K

Consider (3.20),

$$\left(\frac{dp}{dT}\right)_{sat} = \frac{h_{fg}}{T(v_g - v_l)} \approx \frac{h_{fg}}{Tv_g}$$

Where we have used the fact the $v_g >> v_l$. Then assuming that the low density helium vapor can be approximated as an ideal gas such that,

$$v_g = \frac{RT}{Mp}$$

In this case, M is the mole weight of helium, 4 kg/kJ and is necessary in the above equation so that v_g is in kg/m^3. Substituting into the vapor pressure derivative equation and rearranging,

$$h_{fg} = \frac{RT^2}{p}\frac{dp}{dT}$$

At 1 K, $\frac{1}{p}\frac{dp}{dT} \sim 10\text{K}^{-1}$. Substituting other values, one obtains $h_{fg} = 83$ J/mole (21 kJ/kg).

3.3.4 Surface Tension

Before leaving the discussion of He I state properties, it is useful to touch briefly on the subject of surface tension. The surface tension has units of energy per area and is associated with the increased energy of the liquid state caused by it having a free surface. Microscopically, the surface tension results from the molecules at the interface being at a higher energy because they have fewer nearest neighbors than those in the bulk. The surface tension, as with the heat of vaporization, goes to zero at T_c where the distinction between the liquid and vapor vanishes.

For liquid helium, the surface tension is quite small again due to its weak intermolecular binding. For classical liquids, the temperature-dependent relationship for σ should take the form,

$$\sigma(T) = \sigma_0\left(1 - \frac{T}{T_c}\right) \tag{3.22}$$

This expression when applied to He I gives a value for $\sigma_o \simeq 0.5308$ mJ/m^2, but does not fit the data well below T_λ. An alternative polynomial fit to σ which includes the He II regime follows the form,

$$\sigma(T) \cong \sigma_0 - \sigma_1 T + \sigma_2 T^2 \tag{3.23}$$

where $\sigma_0 = 0.3534$ mJ/m^2, $\sigma_1 = 1.737 \times 10^{-2}$ mJ/m^{2}K and $\sigma_2 = 2.154 \times 10^{-2}$ mJ/m^{2}K^2. Plotted in Fig. 3.8 is a fit to the surface tension of liquid helium based on data from HEPAK [8]. The classical formulation (3.22) agrees well with the data above the λ-point where quantum effects become important. Below T_λ, the fit described by (3.23) seems to be in better agreement with the data.

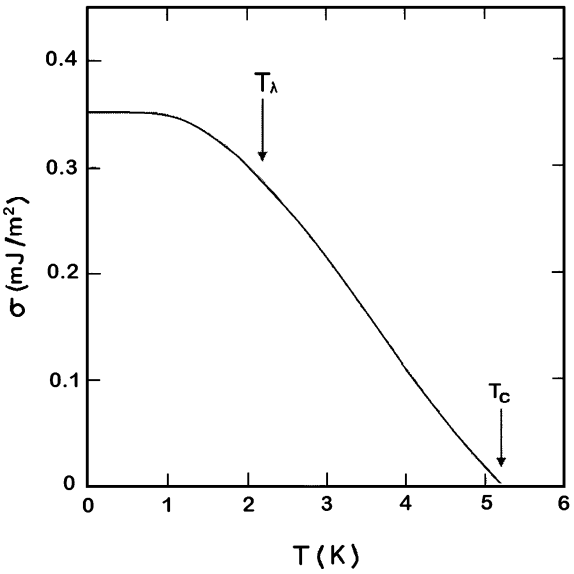

Fig. 3.8 Surface tension of liquid ^{4}He. Data from HEPAK [8]

3.4 Transport Properties of Gaseous and Liquid He I

To derive a model that describes the transport properties of helium, account must be taken of the same effects introduced in the development of the equation of state. More specifically, any complete transport theory must include particle-particle interactions and quantum effects at low temperatures. This approach involves the computation of transport coefficient, similar to virial coefficients in the equation of state, which contain the physics of the interaction. Once these transport coefficients are determined, they can be used to describe the deviation from ideal classical behavior of a fluid such as helium. Several accounts of the theory of the quantum mechanical transport coefficients exist in the literature. Since a fundamental understanding of the derivation of this theory is not particularly necessary for the use of helium transport properties in subsequent chapters, only a cursory review of the principles is included here. For a more complete description of the theory of transport coefficients the reader is encouraged to review the appropriate references [4, 5].

Transport properties such as thermal conductivity and viscosity are set aside from the state properties because they are associated with nonequilibrium phenomena. In fact, these properties are fundamental to the understanding of how a system returns to equilibrium through collision mechanics. Thus, the viscosity and thermal conductivity are applied directly to the interpretation of the behavior of helium under fluid flow and heat transfer conditions.

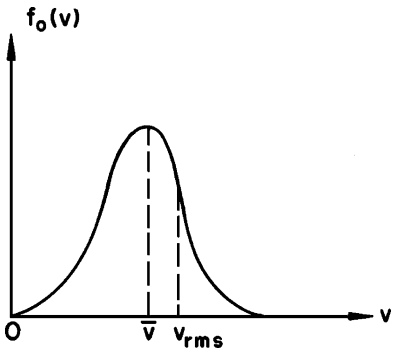

Fig. 3.9 Maxwell-Boltzmann distribution function

3.4.1 Modeling Transport Properties

The beginning point for any model used to describe transport phenomena in a fluid is usually the Maxwell-Boltzmann distribution function, which is the basis of kinetic theory. This function, $f_o(\mathbf{v})$, is a measure of the probability of finding a molecule with velocity $\mathbf{v}$ in a volume at constant temperature T with number density n:

$$f_0(\mathbf{v}) = n\left(\frac{m}{2\pi k_B T}\right)^{3/2} e^{-m(\mathbf{v}-\mathbf{v}_0)^2/k_B T} \tag{3.24}$$

where $\mathbf{v}_o$ is the average velocity of the molecules in the gas. The distribution is peaked at the most probable velocity, $\overline{v} = (2k_B T/m)^{1/2}$ as seen in Fig. 3.9. The root mean square velocity is defined by taking the square root of the integral of this function times $\mathbf{v}^2$ over velocity space, with the result $\mathbf{v}_{\text{rms}} = (3k_B,T/m)^{1/2}$. The Maxwell-Boltzmann distribution function represents the equilibrium velocity profile. Consequently, a good measure of the degree to which a particular system deviates from equilibrium is through the difference between its true distribution and the Maxwell-Boltzmann distribution.

Consider a system containing a fluid which is slightly out of equilibrium. The important quantity to determine for this system is the rate at which it returns to equilibrium through inter-particle collisions. To find this rate, it is first necessary to evaluate the number of collisions that occur between molecules in the system. The number of collisions per unit volume and time at a given position r *i*s defined as

$$Z = \iint \sigma_{\text{tot}} |\overline{\mathbf{v}_1} - \overline{\mathbf{v}_2}| f(r, \mathbf{v}_1, t) f(r, \mathbf{v}_2, t) d^3\mathbf{v}_1 d^3\mathbf{v}_2 \tag{3.25}$$

where a new quantity has been introduced, σ_{tot}, the total scattering cross section, which is an averaged quantity evaluated at the difference in the mean velocities of the two distribution functions.

Before proceeding with the development of the transport coefficients, it is useful to make some rough numerical estimates of quantities defined above. The number of collisions per unit time can be estimated by assuming the scattering cross section

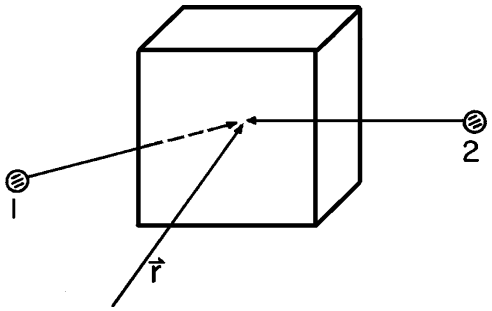

Fig. 3.10 Unit volume in particle space

$\sigma_{\text{tot}} \approx$ constant $\approx 4\pi a^2$, the overlapping cross-sectional area of a two molecule collision. It is then possible to take σ_{tot} out of the integral making it easy to evaluate. In this approximation, the total number of collisions becomes,

$$Z = \left(\frac{8}{\pi}\right)^{1/2} n^2 \sigma_{\text{tot}} \overline{\mathbf{v}} \tag{3.26}$$

Considering helium gas at 4.2 K, 0.1 MPa, just below saturation pressure. For these parameters, the most probable velocity $\overline{v} = (2k_B T/m)^{1/2} = 132\text{m/s}$ and $n = 2.51 \times 10^{27}\text{m}^{-3}$, which is approximately inversely proportional to T at constant p. To estimate the cross section, it is necessary to know the molecular radius. This quantity is not well defined for a quantum mechanical system such as helium at low temperatures. For the present example, the hard core radius defined by the zero of the Lennard-Jones potential is $r_0 = 0.2556$ nm, which gives a value of $\sigma_{\text{tot}} \simeq 80 \times 10^{-20}$ m^2. This value leads to a particle collision rate Z $= 2.73 \times 10^{38}$ m^{-3} s^{-1}.

The number of collisions Z is not the most useful parameter to evaluate for numerical estimate purposes. A more physically meaningful quantity to estimate is the mean free path l between collisions. Consider a unit volume in space position **r** as shown in Fig. 3.10, containing n molecules per unit volume. The total number of collision paths is equal to the total number of collisions divided by two because it requires two molecules to produce a collision. The mean free path can be written in terms of these quantities, such that

$$l = \frac{n}{2Z}\overline{\mathbf{v}} \tag{3.27}$$

As with the example above, again considered helium gas at 4.2 K, 0.1 MPa. For this case, the mean free path works out to be about 0.6 nm, which is only slightly larger than the molecular diameter. The mean scattering time τ is simply related to the mean free path by $\tau = l/\overline{v}$. For helium gas at 4.2 K, $\tau \approx 4.6 \times 10^{-12}$ s. Thus, each helium molecule is undergoing nearly a trillion collisions every second.

To develop expressions for the transport coefficients, it is necessary to introduce non-equilibrium features into the distribution function and then apply these to a

relationship between the dynamic variables, such as mass flux, momentum, and energy. The latter relationship is established in terms of the classical Boltzmann integral differential equation,

$$\frac{\partial f}{\partial t} = -\mathbf{p}\frac{\partial f}{\partial r} + J(ff) \tag{3.28}$$

where f is the actual distribution function of the system, $\mathbf{p}$ is the momentum vector, and $J(ff)$ is a collision term. The collision term introduces some simplicity into the problem because its argument restricts the dynamics of binary collisions.

Following the established correspondence between variables as given by (3.28), the next step is to define a relationship between the actual distribution function and the equilibrium form. One solution to this problem is to write the distribution function as a power series such that

$$f = f_0 + \alpha f_1 + \ldots \tag{3.29}$$

where f_o is the Maxwell-Boltzmann distribution. Inherent in this assumed form is the requirement that the correction terms, αf_1, and so on, be small compared to f_o so the series will converge with a finite number of terms. If only the first term in (3.29) is applied to the relationship between dynamic variables, the result is Euler's equation for ideal fluids. If the first two terms in the expansion are used, the ensuing differential equation is the Navier–Stokes equation. The function f_1 is comprised of the gradients in temperature and velocity.

To determine the transport coefficients and ultimately the transport properties, such as thermal conductivity and viscosity, it is necessary to introduce a set of temperature-dependent integrals $\Omega^{(n,s)}$ that describe the dynamics of the two-particle collisions:

$$\Omega^{(n,s)} = \left(\frac{2\pi k_B T}{m_r}\right)^{1/2} \int_0^\infty \int_0^\infty e^{-\gamma^2} \gamma^{2s+3} (1 - \cos^n \chi) b \, db \, d\gamma \tag{3.30}$$

where b is the impact parameter of the collision and m_r is the reduced mass; $m_r = m_1 m_2/(m_1 + m_2) = m/2$ for identical particles. The other terms contained in the integral include γ, the reduced velocity, and χ the angle of deflection after collision, which is a function of the inter-particle potential and impact parameter b. Obviously, the evaluation of (3.30) is complicated and varies considerably between systems.

3.4.2 Transport Properties

The transport properties of a pure gas such as helium are given in terms of the integrals of the form in (3.30). In particular, the viscosity μ can be determined by

$$\mu = \frac{5}{8}\frac{k_B T}{\Omega^{(2,2)}} \tag{3.31}$$

and the thermal conductivity k as

$$k = \frac{25}{16} \frac{C_v k_B T}{\Omega^{(2,2)}} \tag{3.32}$$

Note that the ratio k/μ is independent of the behavior of $\Omega^{(2,2)}$, having a value equal to $\frac{5}{2} C_v$. At high temperature and low density, this ratio should approach the value of $\frac{15}{4} R = 7.79$ kJ/kg K, consistent with that of an ideal gas.

Before considering how these models apply to the example of helium, it is worthwhile to discuss briefly the changes brought on by introducing quantum mechanics into the treatment. The approach has a similar impact to that of the quantum virial expansion. In particular, the integral expressions introduced in (3.30) now must include the full quantum mechanical scattering process. As before, this requires the development of a phase shift analysis for two-particle scattering. This approach is beyond the scope of the present discussion. Ultimately, the full quantum mechanical treatment can rely on the correspondence principle which states that at high temperature and low density the classical limit should be reached, giving way to agreement with the above described model.

For the specific case of helium in the gaseous or liquid state, the transport properties are reasonably well-established experimental quantities. In Fig. 3.11a, b are plotted the thermal conductivity and viscosity of helium for their applied pressures, 1.0, 0.1, and 0.01 MPa. At low temperatures, the three cases represent supercritical helium, normal helium at atmospheric pressure with associated change of state at 4.2 K, and sub-atmospheric helium with a change of state near 2.5 K. These two orders of magnitude in applied pressure represent the most interesting region for applications involving gaseous or liquid He I.

The first feature of these properties to note is their apparent insensitivity to pressure above about 30 K. Below this temperature, the attractive part of the potential contributes substantially to the interaction. At high temperatures, it is mostly hard core potential which is important. The continuously increasing values for k and μ at high temperatures suggest a power law dependence that varies like T^n for both quantities. In fact, the data above 30 K approximately follow this law with $n \approx 0.6$. Referring to the temperature-dependent integrals (3.30). the leading terms suggest that $\Omega \approx T^{1/2}$, depending on the terms within the integral being weak functions of temperature. Assuming this to be the case, it would be expected that $k \approx \mu \approx T^{1/2}$, which is not far from the experimental result for $T > 30$ K, where C_v is temperature independent.

Apart from the temperature dependence, the magnitude of the transport properties of helium gas need to be compared to theoretical expressions. Considering the ratio of k/μ as a function of temperature above 30 K, we see that this ratio makes a gradual increase from 7.4 to 7.8 kJ/kg K at 300 K. According to theory, $k/\mu = \frac{5}{2} C_v = 7.79$ kJ/kg K for an ideal monatomic gas. Thus, helium at high temperatures is a very good example of near ideality in a real gas. At low temperature, several factors cause a deviation from ideal behavior. The two main ones are the effect of quantum statistics and inter-particle interactions. Both these have increasing importance as the temperature is decreased.

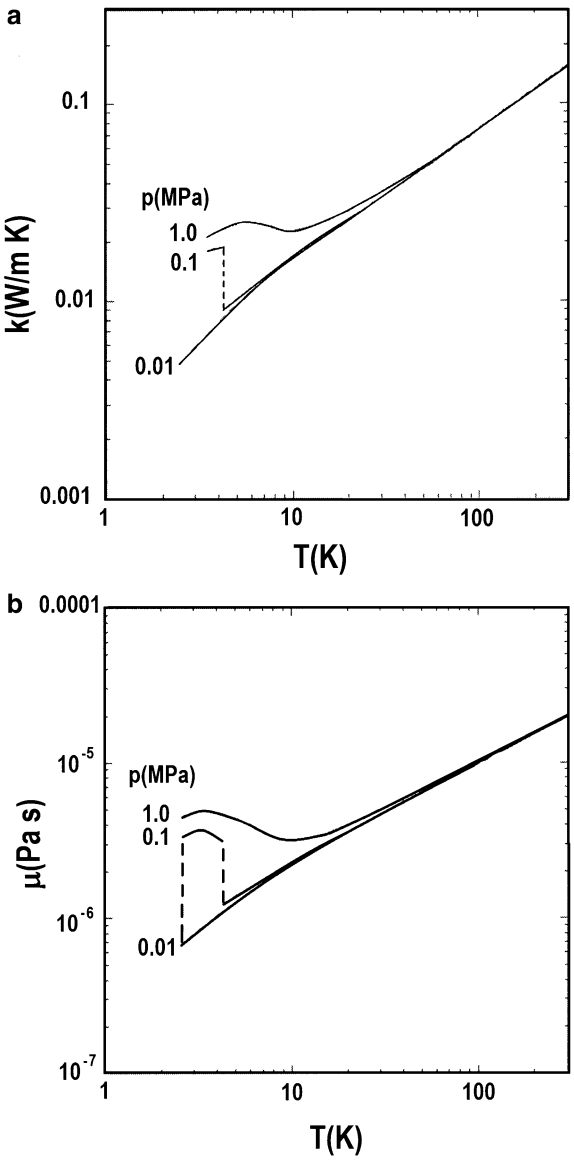

Fig. 3.11 (**a**) Thermal conductivity ^{4}He as functions of T and p. (**b**) Viscosity of ^{4}He as functions of T and p (Data from HEPAK [8])

As can be seen from the above theoretical review of transport properties, first principle calculations of the thermal conductivity and viscosity of a real fluid are very difficult and must be conducted by various expansion techniques. For the purposes of the user of helium gas or liquid, the fundamental approach is beyond interest. Of much greater concern is the behavior of a given fluid, which may be in the liquid or gaseous state, under certain sets of conditions. The approach employed, which will be considered in greater detail in Chaps. 6 and 7, is to develop

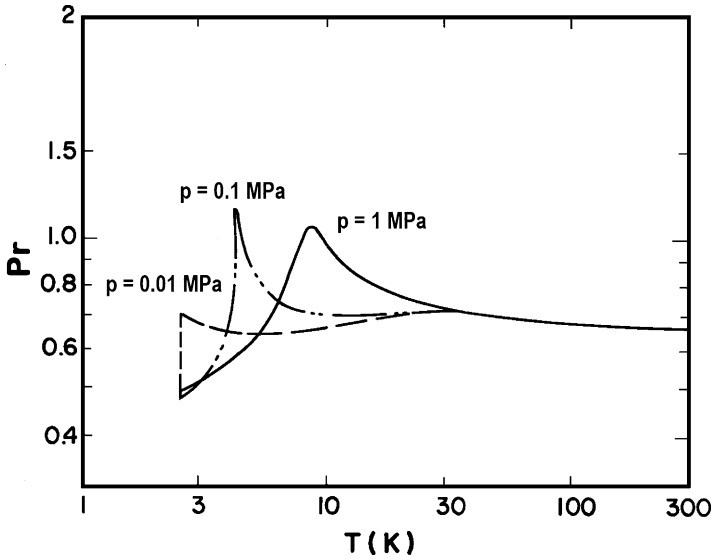

Fig. 3.12 Prandtl number for ^{4}He as a function of T and p

sets of dimensionless numbers. These dimensionless numbers provide a fully general method of analyzing experimental data.

The concept of dimensionless numbers is introduced here because one of them, namely the Prandtl number Pr, is determined by a ratio of the transport properties. Based on dimensional analysis, combining the three properties of viscosity, heat capacity, and thermal conductivity yields the form

$$\mathrm{Pr} = \frac{\mu C_p}{k} \tag{3.33}$$

where the heat capacity is taken at constant pressure. The Prandtl number is a measure of the relative importance of thermal diffusion and mass flow for the transport of heat. For Pr $\approx$ 1, the velocity and temperature profiles are similar under conditions of a small pressure gradient.

For an ideal monatomic gas, the analyses developed in this section can be used to predict the Prandtl number. Inverting the ratio of transport properties a numerical quantity is obtained,

$$\frac{\mu C_v}{k} = \frac{2}{5} \tag{3.34}$$

which is close to the form of the Prandtl number in (3.32) with the exception that the specific heat is measured at constant volume. For an ideal monatomic gas $C_p/C_v = 5/3$ where this ratio sometimes enters computations of gas expansion. The above terms give a theoretical prediction of the Prandtl number for an ideal monatomic gas, Pr $\approx$ 2/3. Plotted in Fig. 3.12 is the Prandtl number for helium

Table 3.3 Experimental value of the Prandtl number for some common liquids under saturated conditions

Liquid	T (K)	Pr
N_2	77	2.20
O_2	90	2.21
H_2	20.4	1.17
H_2O	311	4.52
Hg	750	0.004
He	4.2	1.15

gas and liquid at 1.0, 0.1, and 0.01 MPa. At high temperature the experimental values asymptotically approach 0.67 in agreement with prediction. For comparison, listed in Table 3.3 are the Prandtl numbers for a variety of liquids at both cryogenic and room temperatures. It is important to note that helium exhibits behavior nearest to that of an ideal gas. Liquids that exhibit anomalously large thermal conductivity, such as liquid metals, have correspondingly small Prandtl numbers.

Questions

1. What is the definition of supercritical fluid; two phase and subcooled liquid? Sketch the p-v phase diagram for low temperature helium and show the supercritical, two phase and subcooled liquid regimes.
2. Helium in large quantities is normally transported as a liquid. Explain why.
3. Why does the phase diagram of helium lack a triple point?
4. What is the significance of the Boyle temperature in a real gas? How is it determined?

Problems

1. Gas approximations
   a. Calculate the classical second virial coefficient using the square well potential

$\varphi(r)/k_B$	$=\infty$	$r < 0.25$ nm
	$=-10$ K	$0.25 < r < 0.5$ nm
	$=0$	0.5 nm $< r$

   b. Find the Boyle temperature, T_b.
2. Given a closed container of volume 1 L containing 50 g of helium gas, calculate the following:
   a. The pressure at T = 6 K, assuming that the gas is an ideal gas.
   b. The pressure at T = 6 K, assuming that the gas obeys van der Waal's equation of state.
   c. The pressure at T = 6 K, assuming that the gas obeys the virial equation of state truncated after the second term.

d. The state of the fluid at T = 4.2 K. (Hint: 4.2 K is below T_c and 50 kg/m^3 is greater than ρ_v @ 4.2 K.)

4. Compute the ratio of the surface tension, σ, to the latent heat, h_{fg}, for helium between 2.2 K and T_c. Comment on the behavior.
5. Calculate the mean free path and collision frequency for helium gas at 20 K, 0.1 MPa.
6. Estimate the magnitude of the third virial coefficient for helium at the critical point.

References

1. R. D. McCarty, *Thermophysical Properties of Helium-4 from 2 to 1500 K with Pressures to 1000 Atmospheres,* NBS Technical Note 631, U. S. Government Printing Office, Washington, DC, 1972 and R. D. McCarty, Thermodynamic Properties of Helium-4 from 2 to 1500 K at Pressures to 10^8 Pa, *J. Phys. Chem. Ref. Data* **2**, 923 (1973).
2. J. O. Hirschfelder, C. F. Curtiss, and R. B. Bird, *Molecular Theory of Gases and Liquids,* Wiley, New York, 1954.
3. J. S. Rowlinson, *Liquids and Liquid Mixtures,* 2nd ed., Plenum Press, New York, 1969.
4. W. E. Keller, *Helium-3 and Helium-4,* Plenum Press, New York, 1969.
5. K. Hwang, *Statistical Mechanics,* Wiley, New York, 1963.
6. E. A. Guggenheim, Thermodynamics, North Holland Publishing, Amsterdam (1977).
7. Values obtained from REFPROP® code: http://www.nist.gov/srd/nist23.htm
8. HEPAK database software: http://www.htess.com/hepak.htm
9. E. C. Kerr and R. D. Taylor, The Molar Volume and Expansion Coefficient of Liquid ^{4}He, *Ann. Phys.* **26**, 292 (1964).
10. M. W. Zemansky, *Heat and Thermodynamics,* 5th ed., McGraw-Hill, New York, 1968, p. 368

Further Readings

K. R. Atkins, *Liquid Helium*, Cambridge Univ. Press, Cambridge, England, 1959.
E. A. Guggenheim, Thermodynamics, North Holland Publishing, Amsterdam (1977).
J. O. Hirschfelder, C. F. Curtiss, and R. B. Bird, *Molecular Theory of Gases and Liquids,* Wiley, New York, 1954.
K. Hwang, *Statistical Mechanics,* Wiley, New York, 1963.
R. T. Jacobsen, S. G. Penoncello and E. G. Lemmon, *Thermodynamic Properties of Cryogenic Fluids*, Plenum Press, New York, 1997.
W. H. Keesom, *Helium,* Elsevier, Amsterdam, 1942.
W. E. Keller, *Helium-3 and Helium-4,* Plenum Press, New York, 1969.
C. Kittel, *Elementary Statistical Physics,* Wiley, New York, 1958.
J. S. Rowlinson, *Liquids and Liquid Mixtures,* 2nd ed., Plenum Press, New York, 1969.
A. J. Walton, *Three Phases of Matter,* Clarendon Press, Oxford, 1983.
M. W. Zemansky, *Heat and Thermodynamics,* 5th ed., McGraw-Hill, New York, 1968.

Chapter 4
Classical Helium Fluid Mechanics

In many applications of cryogenics, cooling is best achieved by confining the coolant to a tube or duct and circulating it through the system in a closed loop. In this configuration, the fluid that circulates through the system may be a single phase liquid, single phase gas or a two – phase flow of liquid and vapor. The principal variables in a single phase system are the pressure, temperature and mass flow rate. In two phase flows, additional variables are needed to characterize the state and dynamics. From the engineering point of view, the main quantity of interest is the pressure drop caused by the flowing fluid. In Chap. 5, we will consider the heat transfer issues associated with flowing normal helium.

There are numerous examples where low temperature helium flow is used as a coolant. These include but are not restricted to:

1. The flow of helium in refrigeration piping and heat exchangers. Refrigeration systems that use helium include conventional ^{4}He cycles as well as special devices such as ^{3}He–^{4}He dilution refrigerators for very low temperature research. In the former case, the helium is usually well above the critical temperature and therefore single phase. The major consideration in this application is the appropriate optimization of the trade-off between heat transfer and pressure drop within the flow circuit. In the latter case, the flow may involve passages containing porous media. This is a special case of interest.
2. The flow of liquid helium in transfer piping is also a common application. It occurs whenever liquid is delivered from one storage or distribution system to another. In this case, the flow is nearly adiabatic and heat transfer is not a primary concern. However, since helium transfer usually occurs near the saturated vapor pressure, the process often involves two-phase flow.
3. The use of forced flow helium as a coolant for superconducting magnet systems is also a fairly common application. The general approach here is to force the helium through a duct containing or attached to the composite superconductor. The internal cooling of composite superconductors serves two purposes: to remove steady heating and to thermally stabilize the conductor against electromagnetic disturbances. Thus, this application critically involves both pressure

S.W. Van Sciver, *Helium Cryogenics*, International Cryogenics Monograph Series,
DOI 10.1007/978-1-4419-9979-5_4,

drop and heat transfer to the flowing coolant. An important example of this technology is the Cable in Conduit Conductor (CICC), which consists of many strands of composite superconductor within a metal conduit or jacket. Such conductors are commonly used in high field magnets for fusion.

To understand the details of forced flow helium, it is necessary to be aware of the physical principles associated with heat transfer and fluid flow. These principles are common to a variety of fluid dynamics problems and are based on general engineering science. Since space is limited and the scope of the present discussion quite specialized, only a brief review of this subject is included here. For additional detail, the reader is referred to more extended treatments in books on fluid mechanics.

4.1 Single Phase Internal Flow

Internal flow of classical Newtonian fluids has been studied extensively and is a fairly well understood process. This does not mean that the problems have all been solved because, in general, fluid dynamics is sufficiently complicated to be exactly soluble only in very special cases or by complicated computer codes. Rather, the mode of problem solving is based on a combination of theoretical concepts and empirical evidence leading to semi-empirical correlating functions. This is well established engineering practice.

4.1.1 General Considerations

The general problem to be discussed here concerns internal flow hydrodynamics within a pipe or duct as shown schematically in Fig. 4.1. At any point within the pipe, the state of the fluid is given by its thermodynamic relationship between the local pressure p and temperature T. However, the fluid is not in global equilibrium because it is being transported through the pipe at a mass flow rate, $\dot{m}$. Assuming there are no sinks or sources of fluid, the mass flow rate can be related to the local fluid velocity through the expression

$$\dot{\mathbf{m}} = \rho A \mathbf{v} \tag{4.1}$$

where the density ρ and velocity $\mathbf{v}$ are averaged locally in the direction of flow, and the pipe cross section is given b A.

The fluid is transported through the duct under the influence of externally imposed forces. One such force might be gravity, which is the most important when considering natural convection cooling loops. In most circumstances, the helium within the tube is forced under the influence of an externally imposed pressure head produced by a pump or compressor. These external forces are needed

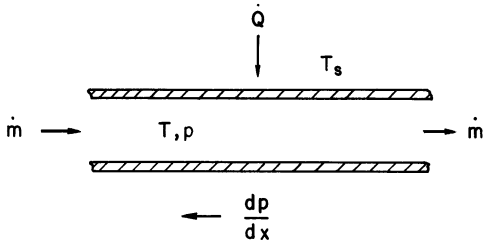

Fig. 4.1 Schematic representation of internal flow

to induce flow since the existence of viscosity results in a pressure drop for any finite mass flow rates. Furthermore, since heat transport is of primary concern in forced flow helium, any heat flow in or out of the system must be determined. This heat transfer rate may result from joule heating within the pipe such as for superconducting cables in the normal state or heat transfer from an adjacent system such as occurs during heat exchanger operation. Heat transfer causes the surface temperatures T_s to be elevated above the local fluid temperature by an amount dependent on the local transfer coefficient.

In general, there are three sets of equations which must be solved to determine the behavior of a Newtonian fluid such as gaseous or liquid helium above T_λ. A complete development of these equations is available in numerous texts on transport phenomena [1, 2]. The first is the continuity equation which is written

$$\frac{\partial \rho}{\partial t} + \nabla \cdot (\rho \mathbf{v}) = 0 \tag{4.2}$$

where $\mathbf{v}$ is a vector velocity and ρ is the local density. The continuity equation is derived from conservation of mass in a fluid element. The second equation is derived from conservation of momentum and is actually a tensor equation. However, for the special case of constant viscosity, the momentum equation reduces to the fairly simple form,

$$\rho \frac{d\mathbf{v}}{dt} = -\nabla \mathbf{p} + \mu \nabla^2 \mathbf{v} + \rho \mathbf{F}_b \tag{4.3}$$

where $\mathbf{F}_b$ is the body force, that is, the force per unit mass of liquid and μ is the fluid viscosity. The total derivative of the velocity is given by

$$\frac{d\mathbf{v}}{dt} = \frac{\partial \mathbf{v}}{\partial t} + \mathbf{v} \cdot \nabla \mathbf{v} \tag{4.4}$$

The combination of (4.2) and (4.3) is generally referred to as the Navier–Stokes equations. The final conservation equation used to describe Newtonian fluids is the energy equation, which simply states that a fluid system must conserve energy. This energy equation may be written

$$\frac{d}{dt}\left(\frac{1}{2}\mathbf{v}^2 + e\right) = -\frac{1}{\rho}\nabla \cdot (\rho \mathbf{v}) + \dot{q} + \mathbf{F}_b \cdot \mathbf{v} \tag{4.5}$$

where e is the specific internal energy and $\dot{q}$ is the specific rate of heat input. The term $\mathbf{F}_b \bullet \mathbf{v}$ is the work done by an external force. It follows that complete solution to problems of Newtonian fluid mechanics requires simultaneous analysis of (4.2), (4.3), and (4.5). With the fluid properties varying with temperature, this process usually requires a numerical approach.

One case, which is treated extensively in elementary fluid mechanics texts, is that of a fluid flowing within a tube or duct. It follows that the velocity can be described by two principal components – u in the direction of the duct axis and v normal to the duct axis and away from the wall. In the present context, it is also assumed that the fluid is in a fully developed steady-state flow pattern and that it is incompressible, that is, $\rho =$ constant. This latter assumption is reasonable for single phase liquid helium and helium gas at low velocity, but it is not suitable for helium gas at high velocities as discussed in the next section.

The standard approach to developing approximate solutions to (4.5) is to invoke what is known as the boundary layer approximation. This approach is based on the following set of requirements for the velocities:

$$u \gg v \quad \text{and} \quad \frac{\partial u}{\partial y} \gg \frac{\partial u}{\partial x}, \frac{\partial v}{\partial y}, \frac{\partial v}{\partial x}$$

In the boundary layer approximation the momentum equation (4.3) reduces to

$$u\frac{\partial u}{\partial x} + v\frac{\partial u}{\partial y} = -\frac{1}{\rho}\frac{\partial p}{\partial x} + \frac{\mu}{\rho}\frac{\partial^2 u}{\partial y^2} \tag{4.6}$$

4.1.2 One Dimensional Internal Flow

One problem that can be solved exactly for these conditions is laminar flow in the fully developed region. Laminar fully developed flow implies that the velocity is parallel to the axis of the duct and must obey the conditions

$$v = 0 \text{ and } \frac{\partial u}{\partial x} = 0 \tag{4.7}$$

The solution to the fluid equations in this regime predicts a parabolic velocity profile proportional to the pressure gradient divided by the viscosity. For a circular cross section channel the solution takes the form

$$u(r) = -\frac{1}{4\mu}\left(\frac{dp}{dx}\right) r_0^2 \left[1 - \left(\frac{r}{r_0}\right)^2\right] \tag{4.8}$$

where r_0 is the radius of the tube. For this special condition, the average velocity can be calculated by integration of (4.8) over the duct cross section,

$$\bar{u} = \frac{r_0^2}{8\mu}\left|\frac{dp}{dx}\right| \tag{4.9}$$

To consider the more general problem of laminar or turbulent flow within a duct, it is useful to define a friction factor f_F given in terms of the relevant quantities[1]

$$f_F \equiv \frac{-(dp/dx)D_h}{2\rho\bar{u}^2} \tag{4.10}$$

where $\bar{u}$ is the average velocity of the fluid along the duct axis. The hydraulic diameter is given in terms of the duct geometry,

$$D_h = \frac{4A}{P} \tag{4.11}$$

for which P is the perimeter of the channel and A the cross-sectional area. This quantity is referred to as the Fanning friction factor, and is literally the ratio of the wall shear stress, $\tau \simeq \mu\, \partial u/\partial y$, divided by the kinetic energy density.

For the case of fully developed laminar flow in a circular duct, the Fanning friction factor has an exact solution,

$$f_F = \frac{16}{\mathrm{Re}_D} \tag{4.12}$$

where $\mathrm{Re}_D = \rho\bar{u}\, D/\mu$. For non-circular cross section ducts, the friction factor is similar to (4.12) although the numerical coefficient is slightly different and the diameter must be replaced by the hydraulic diameter, D_h.

For turbulent flow, which occurs for Reynolds numbers in excess of about 1200, no exact solution exists for the pressure drop. Rather, empirical values such as those displayed in the Moody plot, Fig. 4.2, must be applied. These plots give the friction factor as a function of Reynolds number for different surface roughness conditions. For relatively smooth tubes for Reynolds numbers $1200 < Re_D < 10{,}000$, the Blausius correlation is commonly used,

$$f_F = \frac{0.079}{\mathrm{Re}_D^{\frac{1}{4}}} \tag{4.13}$$

[1] Note that mechanical engineering books define the friction factor as being four times the value given by (4.10).

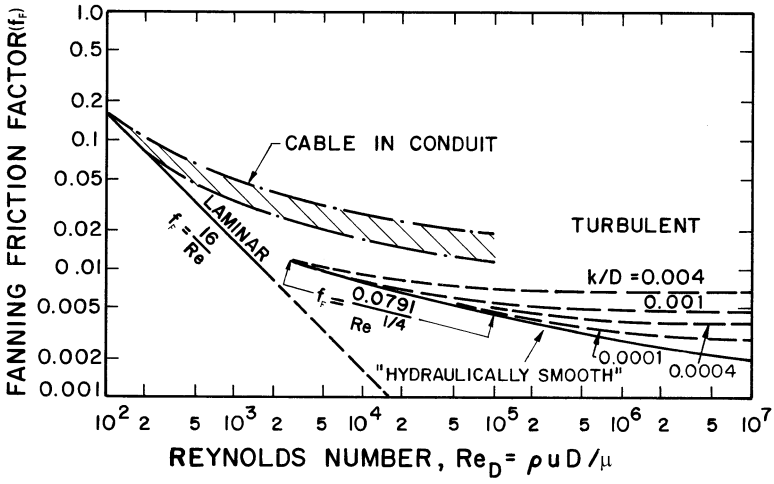

Fig. 4.2 Fanning friction factor for smooth and rough tubing compared to that of cable-in-conduit configuration (From Lue et al. [3])

For higher Reynolds number ($Re_D > 10{,}000$), the von Karman-Nikuradse correlation is popular for smooth tubes,

$$\frac{1}{f_F^{\frac{1}{2}}} = -1.737 \ln\left(\frac{1.25}{\mathrm{Re}_D f_F^{\frac{1}{2}}}\right) \tag{4.14}$$

If the tube is rough with a characteristic dimension k, then the Colebrook correlation adds to (4.14) a surface roughness term,

$$\frac{1}{f_F^{\frac{1}{2}}} = -1.737 \ln\left(\frac{k}{3.7D} + \frac{1.25}{\mathrm{Re}_D f_F^{\frac{1}{2}}}\right) \tag{4.15}$$

For more complex geometries such as cable-in-conduit conductors (CICC), the above correlations are not suitable [3–5]. An approximate curve for the friction factor of CICC is shown in Fig. 4.2. Also, Katheder [5] developed an empirical correlation for the friction factor of these conductors.

$$f_F = \frac{1}{4v^{0.72}}\left(\frac{19.5}{\mathrm{Re}_{D_h}^{0.88}} + 0.051\right) \tag{4.16}$$

where v is the void fraction (area void/total cross sectional area of cable).

Example 4.1

To calculate the pressure drop for liquid helium flow through a smooth tube we need to know the dimensions of the tube and the flow rate. Consider here a tube of length 30 m and diameter 10 mm with a flow of 10 g/s of helium at 4 K, 100 kPa. Under these conditions, helium can be assumed to be incompressible. The relevant properties of helium are: $\rho = 130$ kg/m^3; $\mu = 3.3$ μPa.s.

To calculate the pressure drop, we first need to determine the Reynolds number:

$$\mathrm{Re}_D = \frac{\bar{u}D}{v} = \frac{4\dot{m}}{\pi\mu D} = 3.86 \times 10^5$$

This value of Reynolds number qualifies for the von Karman-Nikuradse correlation of friction factor or it may be obtained from the Moody plot which gives,

$$f_F = 0.0035$$

The overall pressure drop is then obtained by integration of (4.10) over the length of the tube and replacing the average velocity $\bar{u} = 4\dot{m}/\pi\rho D$ to yield,

$$\Delta p = \frac{32}{\pi^2} f_F L \frac{\dot{m}^2}{\rho D^5} = 2.58 \text{ kPa}$$

Note that this pressure drop is small enough ($\Delta p/p \sim 2.5\%$) so the incompressible assumption is valid.
We assume in this example that the fluid is slightly subcooled, entering the tube at 4.0 K, 100 kPa. It will exit at a lower pressure of 97.4 kPa, which corresponds to a saturation temperature of 4.18 K. Therefore the fluid is still subcooled liquid.

Finally, we consider one further point in this example. Any fluid undergoing a pressure drop is exerting friction on the tube. This work is being supplied by the compressor or other prime mover. The friction produces heat that will result in a temperature increase of the fluid. We estimate this as follows,

$$\dot{W}_f = \frac{\dot{m}\Delta p}{\rho} = uA\Delta p$$

which for the example at hand gives about 0.2 W. The friction work goes into heat generation resulting in a temperature increase of the fluid. Since we have assumed that the liquid is subcooled, no boiling occurs until the temperature reaches $T_b(p) = 4.18$ K. For this example, the temperature increase would be only about 5 mK, which is therefore insufficient to result in boiling and the associated two phase flow.

4.2 Supercritical Helium

The discussion in Sect. 4.1 is intended to be a general introduction to the factors affecting forced flow single phase helium cooling systems. The description is kept simple intentionally so as to introduce the important physical quantities such as the friction factor. However, the model presented is not particularly appropriate for low-temperature helium mainly because of the incompressibility assumption. Therefore, it is important to develop a more general fluid mechanics model to treat the case where the helium is in the gaseous state. In developing this description, emphasis is placed on the special case of supercritical helium ($p > 0.23$ MPa) where the fluid is single phase but at low temperature and therefore quite compressible. It is assumed further that the temperature is above T_λ so that the fluid properties are describable by classical hydrodynamics.

4.2.1 Compressible Fluid Mechanics

To model the fluid mechanics of supercritical helium, the Navier–Stokes equations including the effect of finite compressibility are used [6]. Compressibility factors can have profound impact on the observed behavior of supercritical helium. For the steady one-dimensional case discussed in Sect. 4.1, the pressure change in the direction of flow can be derived from (4.2) and (4.3),

$$dp = -\frac{2f_F \rho u^2}{D} dx + u^2 d\rho \tag{4.17}$$

where the first term is identical to that introduced for incompressible fluids while the second term represents the fluid acceleration due to density changes. It is desirable to replace $d\rho$ by a function of the extrinsic variables p and T in order to model the flow in terms of external variables. This can be achieved if the equation of state is known. However, a more general form can be developed through thermodynamic manipulations. Since the density is a function of p and T it can be expanded in terms of these variables:

$$d\rho = \left(\frac{\partial \rho}{\partial p}\right)_T dp + \left(\frac{\partial \rho}{\partial T}\right)_p dT \tag{4.18}$$

According to the thermodynamic definitions the bulk compressibility: $\kappa = \frac{1}{\rho}\left(\frac{\partial \rho}{\partial p}\right)_T$ and the bulk expansivity: $\beta = \frac{1}{\rho}\left(\frac{\partial \rho}{\partial T}\right)_p$. These quantities can be inserted into (4.17) to give the relationship,

$$d\rho = \rho\kappa \, dp - \rho\beta \, dT \tag{4.19}$$

Due to density changes along the flow channel, the velocity of the compressible fluid is not constant. However, in the steady state the mass flow is constant. It is therefore convenient to replace the velocity in (4.17) with the specific mass flow rate $G \equiv \dot{m}/A_{flow} = \rho u$, where A_{flow} is the channel cross section. Substituting this quantity and collecting terms between (4.17) and (4.19), we obtain a coupled relationship between the temperature and pressure variation along the tube:

$$\left(1 - \frac{\kappa G^2}{\rho}\right)\frac{dp}{dx} = -\frac{2f_F}{\rho D}G^2 + \frac{\beta G^2}{\rho}\frac{dT}{dx} \tag{4.20}$$

Note that for small κ and β, this expression simply reduces to the incompressible form given by (4.10).

In addition to the fluid flow equation, we need to consider enthalpy conservation in the fluid when it is subjected to a net heat flux per unit surface area of the tube, q. This is achieved by evaluating the energy equation (4.5). The total heat input per unit area of the tube is related directly to the time rate of change in the stagnation enthalpy (enthalpy + kinetic energy). For a circular cross section with $A_{flow} = \pi D^2/4$, this expression is

$$q = \frac{GD}{4}\frac{\partial}{\partial p}\left(h + \frac{u^2}{2}\right)\frac{dp}{dx} + \frac{GD}{4}\frac{\partial}{\partial T}\left(h + \frac{u^2}{2}\right)\frac{dT}{dx} \tag{4.21}$$

which is simply a one dimensional version of (4.5). Using the definitions of the compressibility and expansivity and noting that the Joule–Thomson coefficient, which governs isenthalpic expansion, is defined by the relationship

$$\mu_j = -\frac{1}{C_p}\left(\frac{\partial h}{\partial p}\right)_T \tag{4.22}$$

we can simplify (4.21) to provide a second coupled relationship between the variation of p and T with position along the tube:

$$q = -\frac{GD}{4}\left(\mu_j C_p + u^2\kappa\right)\frac{dp}{dx} + \frac{GD}{4}\left(C_p - u^2\beta\right)\frac{dT}{dx} \tag{4.23}$$

Given the two relationships for the gradient T and p, it is a straightforward calculation to eliminate variables by simultaneous solution, arriving at separate equations for each gradient; that is,

$$\frac{dp}{dx} = \frac{-2f_F G^2 \rho D + 4qG\beta/\rho D\left(C_p - u^2\beta\right)}{1 - (G^2/\rho)(\kappa + \beta\phi)} \tag{4.24}$$

and

$$\frac{dT}{dx} = \frac{4q/GD\left(C_p - u^2\beta\right) - 2fG^2\phi/\rho D}{1 - (G^2/\rho)(\kappa + \beta\phi)} \tag{4.25a}$$

where an additional parameter has been defined,

$$\phi = \frac{\mu_j C_p + u^2 \kappa}{C_p - u^2 \beta} \tag{4.25b}$$

Needless to say the above expressions (4.23), (4.24), and (4.25) are difficult to apply unless the physical properties have relatively simple behavior. Arp [6] has shown that by approximating the fluid by an ideal gas, with $\kappa \approx 1/p$ and $\beta \approx 1/T$, the above expressions are reduced in complexity. Furthermore, if the velocities are fairly low, $u \lesssim 10$ m/s (4.24) and (4.25) take on more manageable forms:

$$\frac{dp}{dx} = -\frac{2G^2 f_F}{\rho D} + \frac{4qG\beta}{\rho D C_p} \tag{4.26}$$

and

$$\frac{dT}{dx} = \frac{4q}{GDC_p} - \frac{2f_F G^2}{\rho D}\left(\mu_j + u^2 \frac{\kappa}{C_p}\right) \tag{4.27}$$

Note that the first two terms in (4.26) and (4.27) are identical to those for incompressible fluids. It follows that the second term in (4.26) becomes important at low velocities and high heat fluxes while in (4.27) the second term is significant at high velocities and low heat fluxes.

4.2.2 Experimental Confirmation

The above analysis has been tested experimentally by Dean et al. [7] in a 500 m long tube with an $L/D \approx 10^5$ operating in supercritical helium. Two sets of results from their investigation are shown in Figs. 4.3 and 4.4. The two cases show significantly different behavior. The data displayed in Fig. 4.3 represent the regime where the heat flux is large and the flow rate is small. As a result, the temperature profile is monotonically increasing in response to the dominance of the enthalpy flow term, $4q/GDC_p$. At the same time, the pressure profile is linear owing to the considerable impact of the incompressibility term in (4.26).

The second case, shown in Fig. 4.4, is an example of the regime where the heat flux is not large but the mass flow is high. The pressure profile is only slightly nonlinear since it is dominated by the friction-induced pressure drop. In this case, the temperature profile actually has a negative slope owing to the Joule–Thomson expansion effect. This process is well known and is applied in refrigeration systems to achieve cooling. Isenthalpic expansion is discussed more extensively in Chap. 8.

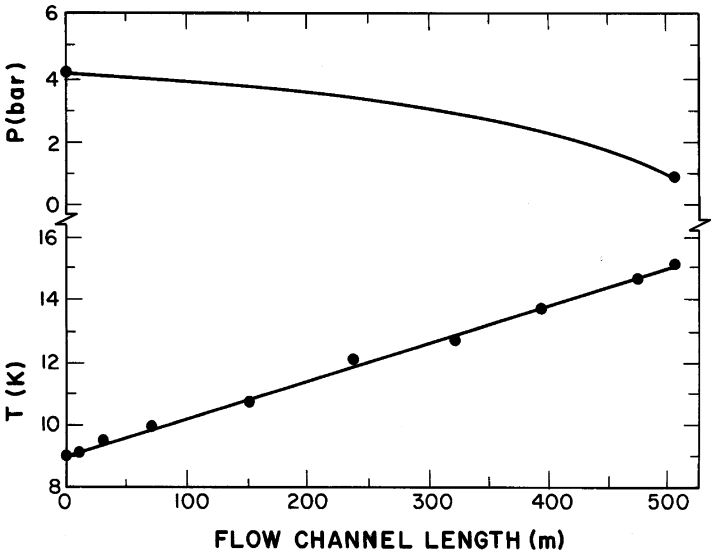

Fig. 4.3 Pressure and temperature profiles with 3.2 bar (0.32 MPa) pressure loss. Computer data $m = 0.928$ g/s, $D = 4.8$ mm, $Q = 0.074$ W/m, $p_{in} = 4.2$ bars (0.42 MPa), $T_{in} = 9.0$ K, $f_F = 0.007$, $Re_D = 1 \times 10^5$. Measured flow = 0.98 g/s. Solid line is computed value (From Dean et al. [7])

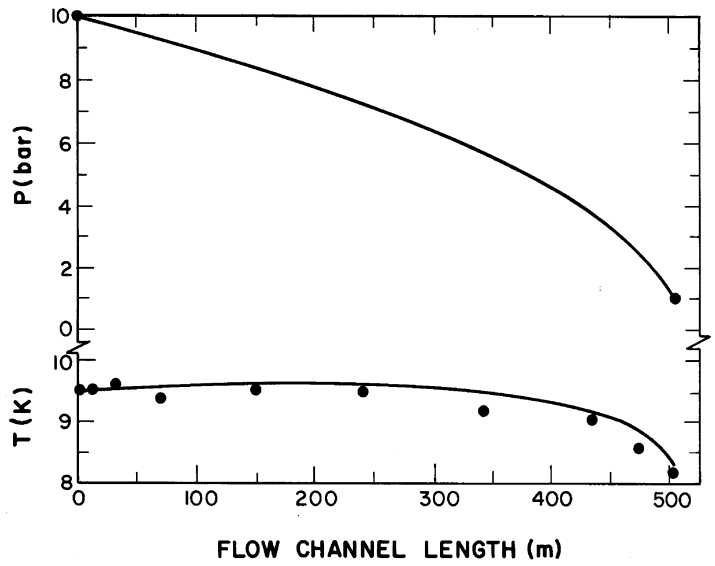

Fig. 4.4 Pressure and temperature profiles with 9 bar (0.9 MPa) pressure loss. Computer data $m = 3.15$ g/s, $D = 4.8$ mm, $Q = 0.062$ W/m, $p_{in} = 10$ bars (1 MPa), and $T_{in} = 9.5$ K, $f_F = 0.005$, $Re_D = 3$–4×10^5. Measured flow = 3.0 g/s. Solid line is computed value (From Dean et al. [7])

An analytical comparison of the above experiments with the compressible fluid theory has been conducted and is shown by the solid curves in Figs. 4.3 and 4.4. One adjustable parameter, the friction factor f_F was used to fit both the pressure drop and temperature profile data possibly due to minor losses in fittings within the loop. Thus in both cases, the friction factor required to fit the data was above that expected for turbulent flow at the Reynolds numbers corresponding to the experimental system.

Supercritical helium represents a fairly good example of a simple, but relatively high density compressible fluid. The hydrodynamic equations appropriate for compressible flow adequately describe the pressure drop and heat transport character. However, the flow characteristics do not represent the entire problem. In particular, it is also of interest to be able to predict the heat transfer coefficient between the tube or duct and the helium stream. The conventional approach to this problem demands the development of engineering correlations appropriate to the particular configuration of interest discussed in Chap. 5.

Example 4.2

Use (4.26) to calculate the pressure gradient at the entrance to the tube in Dean's experiment for the case illustrated in Fig. 4.4. Compare the magnitudes of the friction and acceleration contributions.

One needs to evaluate,

$$\frac{dp}{dx} = -\frac{2G^2 f_F}{\rho D} + \frac{4qG\beta}{\rho D C_p}$$

For the following conditions: $T = 10$ K: $p = 1$ MPa; $\rho = 62$ kg/m^3; $C_p = 7.6$ kJ/kg K; $\beta = 1/\mathrm{T} = 0.1$ K^{-1}. The flow is $\dot{m} = 3$ g/s, the heat flux/length is $\mathrm{Q} = 0.062$ W/m and the tube diameter is $D = 4.8$ mm; $\mathrm{f_F} = 0.005$. These values correspond to a surface heat flux of $q = Q/\pi D = 4.1$ W/m^2 and a mass flux $\mathrm{G} = 4\dot{m}/\pi D^2 = 165$ kg/m^2 s.
The friction contribution to the temperature gradient is:

$$\left.\frac{dp}{dx}\right|_f = -\frac{2G^2 f_F}{\rho D} = -923 \text{ Pa/m}$$

The acceleration contribution is:

$$\left.\frac{dp}{dx}\right| = \frac{4qG\beta}{\rho D C_p} = -119 \text{ Pa/m}$$

Therefore, the acceleration increases the total pressure drop by about 13% over the incompressible case.

4.3 Helium Two-Phase Flow

Whenever liquid helium is allowed to flow at pressures less than the critical pressure, $p_c = 0.23$ MPa, two-phase liquid vapor phenomena can occur. This occurrence often is associated with boiling and heat transfer; however, adiabatic systems can also experience two-phase flow simply as a result of pressure drop and friction loss factors. Two-phase phenomena associated with heat transfer will be discussed in Chap. 5. The present section is concentrated on flow phenomena.

Two-phase internal flow systems are very common and important in helium cryogenic systems. Most often they are encountered in helium transfer systems where the liquid helium is siphoned from one vessel to another through a vacuum insulated line. Obvious factors of concern are the possibilities of excessive pressure drop or flow oscillation, both of which contribute inefficiencies to the helium transfer process. Another common application is for natural circulation cooling loops on thermal shields and magnets. In this case, the two phase nature of the flow can be used to achieve self sustaining flow without a prime mover.

Liquid helium transfer systems as well as other applications have made it essential to be aware of the physical phenomena that commonly occur in flowing subcritical liquid helium. Unfortunately, this subject has not received enough attention from the research community and not a great deal is known. There are several reasons for the incomplete understanding of two phase flowing helium. First, a full understanding of this problem is an awesome task. It is a multi-valued problem dependent on such factors as temperature, pressure, mass flow rate, system configuration, and relationship between the two phases present (liquid and vapor). Consequently, it would take a substantial quantity of empirical data to describe the behavior even in a small number of special cases. Second, two-phase flow in helium systems is very specialized because it is only occasionally used and in very specific configurations. However, recently there has been a greater interest in two phase helium in context of natural circulation loops for superconducting magnet cooling systems [8]. By comparison, two-phase flow in water systems has received a great deal of attention because of numerous engineering applications [9].

4.3.1 Flow Regimes and Transitions

Consider the general character of two-phase flowing liquid and vapor helium. Based on knowledge obtained from experiments with two-phase flows of non-cryogenic fluids, some general statements can be made about the flow characteristics. In conventional fluids, there are approximately seven different flow patterns that can be obtained in a two-phase mixture [10]. These different patterns are shown schematically in Fig. 4.5. The factors that determine which flow pattern is stable for a particular set of conditions include the mass flow rate, densities of each of the

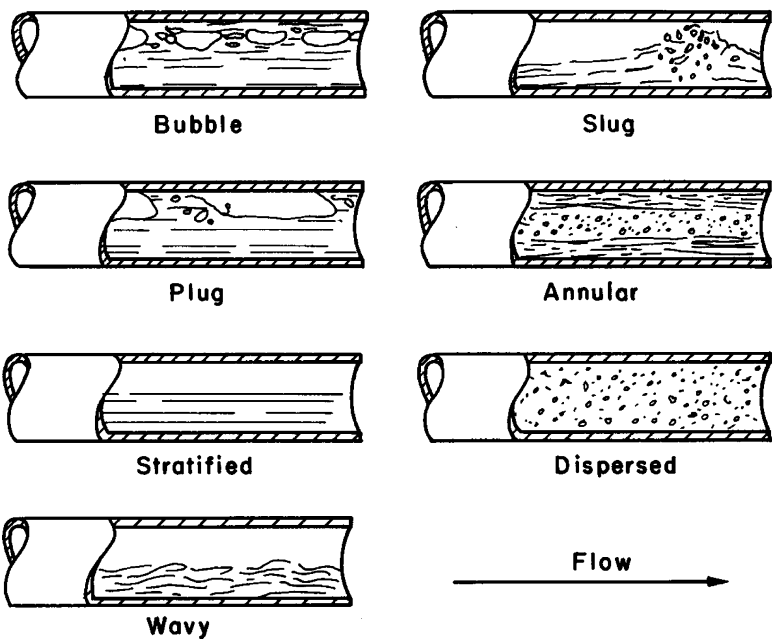

Fig. 4.5 Sketches of flow patterns present in horizontal tubes (From Baker [10])

components, viscosity, heat of vaporization, and liquid surface tension. The qualitative description of each of the flow regimes is as follows:

1. *Bubble flow:* Gas bubbles flow along with the liquid at approximately the same velocity.
2. *Plug flow:* Gas bubbles coalesce to form plugs in the channel. This condition usually occurs for higher mass flow rates and vapor volumes than in bubble flow.
3. *Stratified flow:* Complete separation of liquid and gas occurs owing to density differences. The vapor and liquid occupy unchanging fractions of the cross-sectional area. This flow pattern occurs most commonly in large-diameter channels at low mass flow rate.
4. *Wavy flow:* Similar to stratified flow but due to higher mass flow rate, the interface between liquid and vapor experiences an oscillatory motion.
5. *Slug flow:* The wave amplitude increases until it touches the tube wall resulting in a pattern of vapor slugs separated by totally liquid regions.
6. *Annular flow:* At fairly high vapor fractions and velocities, the flow pattern will overcome the gravitationally induced stratification causing the vapor to flow through the center and the liquid to adhere to the walls. In this flow pattern, the vapor velocity is much greater than that of the liquid.
7. *Dispersed flow:* The liquid film becomes unstable and breaks up into small droplets which are carried along with the vapor stream. This flow regime occurs at the highest mass flow rates.

The above list of flow patterns are at least approximately ordered in terms of increasing flow rate and vapor fraction. Each of these flow patterns is potentially present in liquid–vapor helium systems. Similar behavior is expected to occur in vertically oriented tubes although with slightly different regimes of occurrence. Based on empirical evidence from room temperature fluids, there have been several attempts to correlate two-phase flow into a map which is dependent on system parameters [10, 11]. Unfortunately, due to the limited existence of data on helium systems, very few attempts have been made to compare the behavior of helium with that of other common fluids [12–15].

To make a more qualitative discussion of the subject of two-phase flow, it is necessary to define several physical quantities. The three main definitions pertaining to two-phase flow are:

1. *Void fraction* α: Defined as the ratio of the local vapor volume to the total flow volume. It is normally given in terms of the fraction of cross-sectional area that is vapor, that is,

$$\alpha = \frac{A_v}{A_l + A_v} \tag{4.28}$$

2. *Flow quality* χ: The ratio of vapor mass flow rate to total mass flow of both vapor and liquid:

$$\chi = \frac{\dot{m}_v}{\dot{m}_l + \dot{m}_v} \tag{4.29}$$

By definition, χ is always less than or equal to unity.

3. *Slip ratio S*: Defined as the ratio of the vapor to liquid velocity,

$$S = \frac{u_v}{u_l} \tag{4.30}$$

In two-phase flow the slip ratio is almost always greater than or equal to unity since the less-dense vapor can more easily travel through the duct than can the bulk liquid.

These quantities can be shown to relate to each other through the condition,

$$S = \left(\frac{\chi}{1-\chi}\right)\left(\frac{1-\alpha}{\alpha}\right)\left(\frac{\rho_l}{\rho_v}\right) \tag{4.31}$$

The most important two-phase flow problem for any liquid–gas system is to be able to measure and model the behavior of all three quantities as a function of external parameters.

4.3.2 Pressure Drop Correlations

The pressure drop in two-phase helium systems has been investigated in a number of experiments [13–15]. Across a tube of length L this quantity can be written as a summation of three terms,

$$\Delta p_T = \Delta p_{gr} + \Delta p_a + \Delta p_f \tag{4.32}$$

where Δp_{gr} is the gravitational pressure drop due to change in elevation of the fluid; Δp_a is the acceleration contribution; and Δp_f is that due to friction. . Unlike single-phase incompressible flow, the pressure drop described by (4.32) must take into account the variation in the fluid density along the channel. This contribution is particularly important in flows involving heat transfer.

The gravitational pressure drop for vertically oriented tubes is given by the relationship

$$\Delta p_{gr} = -g \int_0^L \langle \rho \rangle dx \tag{4.33}$$

where the average density $\langle \rho \rangle$ is defined in terms of the void fraction

$$\langle \rho \rangle = \alpha \rho_v + (1 - \alpha)\rho_l \tag{4.34}$$

Therefore, it is necessary to obtain the void fraction before the gravitational pressure drop can be determined. The acceleration contribution to the pressure drop, Δp_a, also has an established form dependent on void fraction and flow quality. It is given by

$$\Delta p_a = G^2 \left(\frac{\chi^2}{\alpha \rho_v} + \frac{(1 - \chi)^2 - 1}{(1 - \alpha)\rho_l} \right) \tag{4.35}$$

where in this case it is necessary to have knowledge of both the void fraction and flow quality. The final pressure drop contribution, Δp_f, in two phase flow is that due to frictional interaction between the tube and wall. This term is expected to be similar in form to that obtained for single phase fluids with the additional complication associated with the two-fluid nature of the problem.

There are several theoretical developments which have been successful at interpreting certain aspects of the pressure drop in two-phase cooling systems. One such approach is known as the Lockhart–Martinelli correlation [16]. The explicit assumptions of this model are as follows:

1. The static pressure drop in the vapor phase is equal to that in the liquid phase for all mass flow rates.

2. The two-phase fluid volume is made up of a linear combination of the vapor and liquid volumes.
3. Friction losses are assumed to dominate, and the effect of momentum change and hydrostatic head are ignored.

The Lockhart–Martinelli correlation for pressure drop introduces several parameters which are functions of measurable quantities. The first of these is the dimensionless two-phase pressure gradient,

$$\phi_l^2 = \frac{(dp/dx)_{TP}}{(dp/dx)_l} \tag{4.36}$$

where the subscript *TP* stands for two-phase. The reference pressure gradient is that of the liquid and corresponds to the traditional incompressible flow equation given by (4.10). The other parameter which is commonly used in relating data to the Lockhart–Martinelli correlation is a ratio of the pressure gradients associated with each phase,

$$\chi_{tt}^2 = \frac{(dp/dx)_v}{(dp/dx)_l} \tag{4.37}$$

where the subscript *tt* refers to both phases being turbulent, a situation that is usually the case for low-temperature helium systems. This parameter can be correlated against the properties of each of the two fluids in the form,

$$\chi_{tt} = \left(\frac{\rho_v}{\rho_l}\right)^p \left(\frac{\mu_l}{\mu_v}\right)^q \left(\frac{1-\chi}{\chi}\right)^r \tag{4.38}$$

where the coefficients take on values that are typically, for example, $p \simeq 0.6$, $q \simeq 0.1$, and $r \simeq 1$. Usually, correlations are indicated by plots of ϕ_l versus χ_{tt} [16].

Several simplified forms to the Lockhart–Martinelli correlation exist in the literature. Levy [17] produced reasonable agreement when correlating experiments to the form

$$\phi_l^2 = \frac{(1-\chi)^{1.75}}{(1-\alpha)^2} \tag{4.39}$$

The above expression is based on a combination of the Lockhart–Martinelli correlation and the relationship for void fraction.

Another rather direct model for pressure drop in two-phase systems that works well for helium systems is referred to as the homogeneous model, which is based on a similar set of assumptions as the Lockhart–Martinelli correlation. The homogeneous model describes a two-fluid system as having the following set of characteristics:

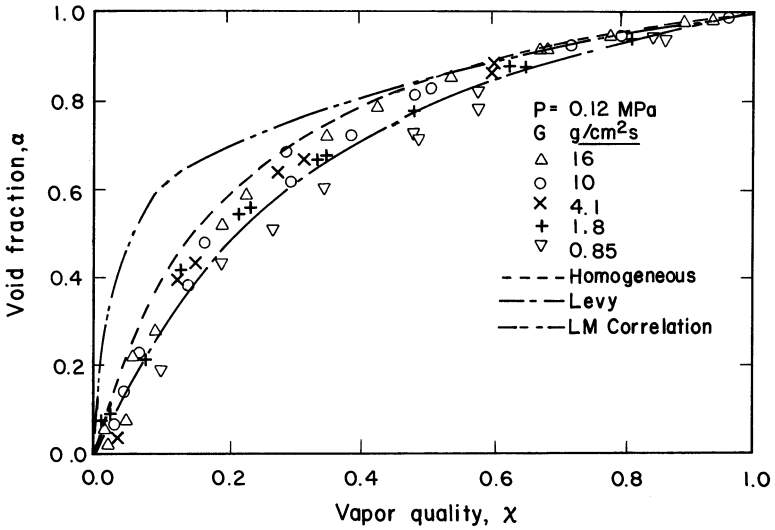

Fig. 4.6 Void fraction for helium flow as a function of vapor quality (From Khalil [13])

1. Equal liquid and vapor velocities ($S = 1$).
2. Thermodynamic equilibrium between phases.
3. Applicability of the single-phase friction factor to the two-phase flow.

Based on these assumptions, the two-phase friction multiplier ϕ_l^2 can be expressed as

$$\phi_l^2 = \left[1 + \chi\left(\frac{\rho_l}{\rho_v} - 1\right)\right]\left[1 + \chi\left(\frac{\mu_l}{\mu_v} - 1\right)\right]^{-n} \tag{4.40}$$

where based on use of the Blausius correlation the coefficient n is taken to be approximately 0.25 in most analyses [18]. The above expression can be related to experimental data if the variation of physical quantities with flow quality is known.

There have been only limited experimental investigations of two-phase pressure drop in liquid helium. Khalil et al. [13] studied two-phase flow in a vertically oriented tube with diameter 6.35 mm and pressures between 0.106 and 0.204 MPa. This work included measurements of the pressure drop Δp, overall mass flow $\dot{m}$, and local average void fraction $\langle\alpha\rangle$. These measurements allowed determination of both void fraction and slip ratio as they depend on vapor quality. The void fraction was compared with the available theoretical developments. Plotted in Fig. 4.6 is the variation of void fraction with vapor quality for different mass flow rates at 0.12 MPa. The theoretical developments do not predict a variation of α with G and no systematic dependence is observed in the data. As can be seen in the figure, the Levy and homogeneous models do a better job of modeling behavior than the Lockhart–Martinelli correlation, which predicts a higher void fraction at low vapor qualities.

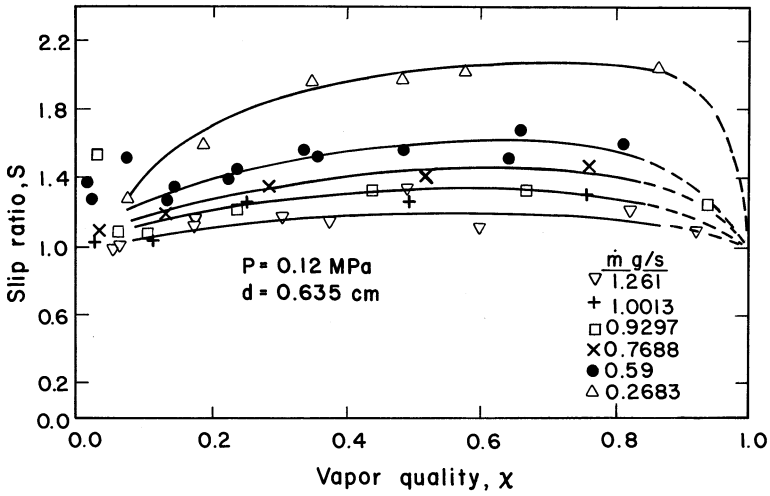

Fig. 4.7 Slip ratio as a function of vapor quality and mass flow rate at 0.12 MPa (From Khalil [13])

Experimental results of the slip ratio variation with vapor quality are shown in Fig. 4.7. The slip ratio is always greater than unity for finite mass flow rates, with the biggest deviation occurring at the highest G.

Other measurements of two-phase pressure drop in helium confirm the analysis based on the homogeneous model. Nakagawa et al. [19] studied the variation of the two-phase friction multiplier (4.40) with vapor quality. This work was carried out on two test loops of diameter 11.4 and 18.4 mm. A summary of these experimental results is shown in Fig. 4.8. As with previous measurements of two-phase flow in helium systems, the authors observed that the homogeneous model was better than the Lockhart–Martinelli correlation for analyzing the data. It is surprising that the homogeneous model, which assumes $S = 1$, adequately describes the pressure drop, particularly in light of the slip ratio measurements displayed in Fig. 4.7. However, it is fortuitous since the homogeneous model is fairly easy to apply.

4.3.3 Natural Circulation Loops

One of the important uses of two phase helium flow in cryogenics is in the operation of a natural circulation loop or thermo-siphon. This device uses the natural behavior of two phase flow in vertical channels to remove heat from a source such as a radiation shield or superconducting magnet. It is therefore a passive cooling device that does not depend on a prime mover to create flow through to the heat load.

Natural circulation loops work on the principle that a heat load on a vertical channel produces a two phase flow that is on average less dense than the liquid phase.

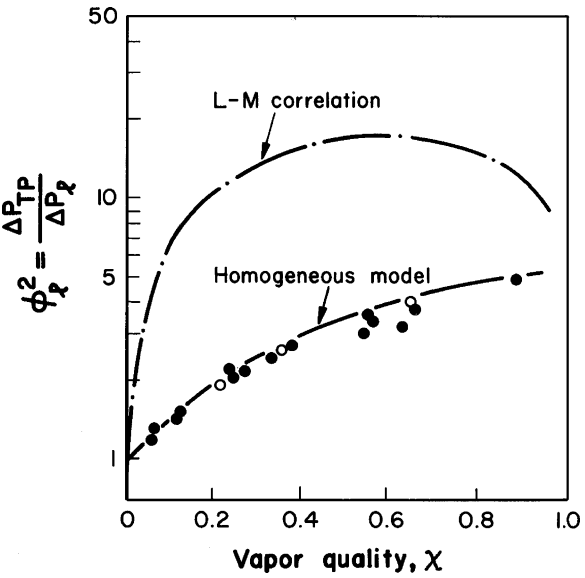

Fig. 4.8 Dimensionless pressure drop in two-phase helium flow (From Nakagawa et al. [19]). The *solid circles* (●) are for the test loop with 11.4 mm ID and the *open circles* (○) are for the test loop with 18.4 mm ID

Thus, there is a gravitational instability lifting the two phase fluid and replacing it with single phase liquid. For example, imagine a U-tube containing a liquid with a free surface at the top such that the liquid is only subcooled by the hydrostatic head (ρgH), Fig. 4.9.

Now if one applies a heat load to one of the vertical legs of the U-tube the liquid will increase in temperature until it reaches saturation after which vapor is formed in the channel. Since the vapor is less dense than the liquid, the average density of the two phase mixture will be less than that on the pure liquid side of the U-tube. This will produce a net driving force for the flow given as,

$$\Delta p_D = \rho_l g H - g \int_0^H \langle \rho(z) \rangle dz \tag{4.41}$$

Under steady operation, the driving force balances against the pressure drop terms that are due to friction and fluid acceleration. The acceleration pressure drop is caused by the decrease of the average density of the fluid as it circulates through the loop. This acceleration may be related to the change in the vapor quality from inlet to outlet.

$$\Delta p_a = G^2 \left(\frac{1}{\rho_v} - \frac{1}{\rho_i} \right) (\chi_{ex} - \chi_{in}) \tag{4.42}$$

At the inlet, $\chi_{in} = 0$ since it is pure liquid. At the outlet, $\chi_{ex} > 0$ but probably less than unity to avoid dry-out of the return line. In (4.42) $G = \dot{m}/A_{flow}$ the

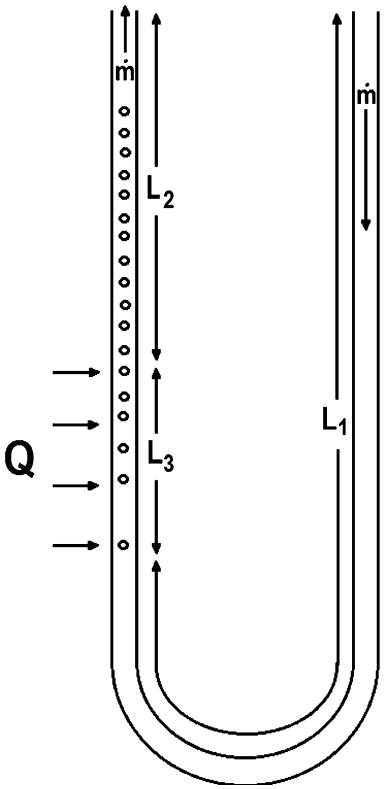

Fig. 4.9 Schematic of a natural circulation loop

mass flux. The other contribution to the pressure drop is due to friction from both the single phase liquid and the two phase flow. On the liquid side, the friction pressure drop is given by the classical expression with the friction factor being a function of Reynolds number. Written in terms of the mass flux, G, this contribution is,

$$\Delta p_l = f \frac{G^2 L_1}{2\rho_l D_h} \tag{4.43}$$

where L_1 is the length of the loop that contains pure liquid. This may include part of the return leg depending on where the heat load is applied and how much subcooling of the liquid is occurring due to the hydrostatic head.

The pressure drop in the two phase portion of the loop can be determined from the analysis presented in Sect. 4.3.2. However, under most circumstances there will be two regimes. The adiabatic portion of the loop, where no heat is applied the void fraction will be a constant value, χ_{ex}. In this region, the friction pressure drop is,

$$\Delta p_{2p}^{A} = f \frac{G^2 L_2}{2\rho_l D_h} \phi_l^2(\chi_{ex}) \tag{4.44}$$

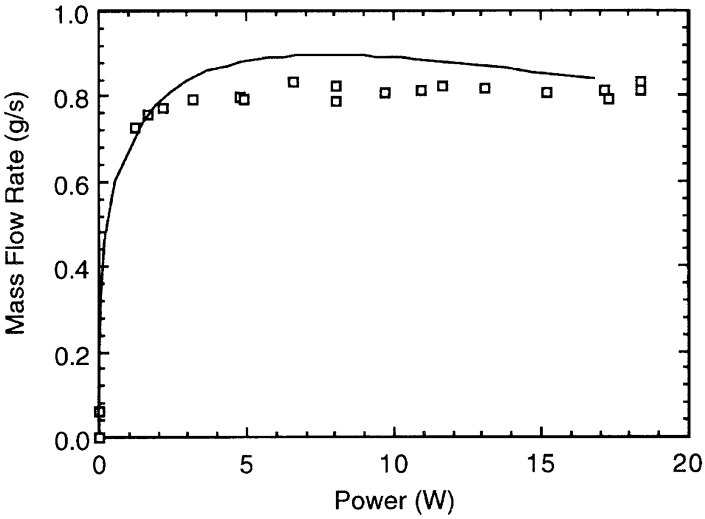

Fig. 4.10 Flow rate through a model natural circulation loop as function of applied heat load (Huang [20])

where ϕ_l^2 is the friction multiplier for the given vapor quality. If all the heat applied to the return line goes into vaporizing the helium, then the vapor mass flow rate and exit quality can be obtained from $\dot{m}_v = \dot{Q}/h_{fg}$ and $\chi_{ex} = \dot{m}_v/\dot{m}$.

In the region of the loop that receives the heat load, the vapor quality changes along the line and that change needs to be considered in calculating the pressure drop. Over the corresponding channel length, L_3, the diabatic pressure drop contribution is,

$$\Delta p_{2p}^{D} = f\frac{G^2 L_3}{2\rho_l D_h}\frac{1}{\chi_{ex}}\int_0^{\chi_{ex}} \phi_l^2(\chi)d\chi \tag{4.45}$$

The variation of quality over the length of the section depends on the details of the heat load. If the heat load is uniformly distributed along the line, then the quality will increase approximately linearly.

To test the above theory, Huang et al. [20] constructed and operated a vertically oriented natural circulation loop that contained a helium mass flow meter. The loop had a vertical height of about 400 mm and tube diameter of 4.6 mm. A steady heat load between zero and 20 W was applied over part of the length of the return line. The results of this test are shown in Fig. 4.10. The solid line is the analysis based on (4.41) through (4.45) applied to the particular conditions of the experiment. Two results are worth noting. First, the analysis appears to agree to within 10% of the experimental data. This is good confirmation of the theory and a suggestion that

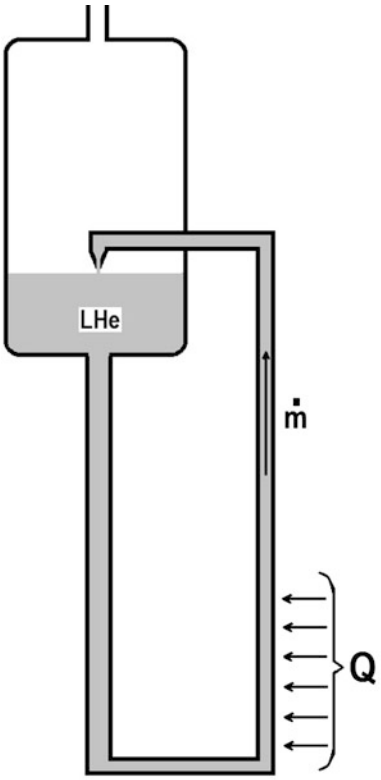

Fig. 4.11 Schematic of a conventional natural circulation loop

two phase thermo-siphon modeling and design are achievable. Second and of greater practical importance is the noted behavior of the mass flow rate with increasing heat load. In this case for heat loads greater that 2 W, the observed mass flow rate is approximately constant. This shows that a natural circulation loop is a very stable device for remote cooling as it can accept a range of heat loads, from cooldown to steady operation without causing hydrodynamic instabilities in the flow.

Figure 4.11 displays a typical configuration of the natural circulation loop in an application. As discussed above, it is important to apply the heat load to the return leg of the loop. In practice, this is done by insulating the supply line from the bottom of the supply vessel to the bottom of the cryogenic system before making contact with the heat load. Once the heat load is in contact with the line, it must have ever increasing elevation avoiding traps until it returns to the supply vessel. One additional feature is to return the two phase flow above the liquid level in the supply vessel to allow it to phase separate, returning the vapor to the refrigerator and allowing the liquid the flow back into the loop. The refrigerator thus only needs to supply enough liquid to the vessel to make up for the liquid boiled away by the heat load.

4.4 Flow Through Porous Media

There are a number of situations in the practice of helium cryogenics where the fluid is made to flow through a porous solid structure. In this context, by porous structure we mean a solid matrix made up of finely meshed sub-elements such as small particles or screens, bonded together into a monolithic component. Typically, the dimensional scale of the pores is much less than that of the containing channel and the fluid dynamics is dominated by the small scale. A few examples of where porous media enter into helium cryogenics are:

- Regenerators and heat exchangers for helium refrigerators: These include the regenerators needed for cryocoolers and heat exchangers for micro-scale recuperative refrigerators.
- Porous insulation for superconducting magnets: An innovative technique for providing active cooling to magnet windings is to support the windings with porous solid insulation that allows some portion of the helium coolant to penetrate the winding.
- Porous plug phase separators for space based liquid helium cooled experiments. In this application, the porous plug provides a back pressure due to the fountain effect in He II to contain the liquid within a container even in zero-g conditions. This topic is discussed further in Chap. 7 on He II heat and mass transfer.

The physical characteristics of porous media are described by a set of dimensions defined as follows:

Pore size: This is the average dimension of the pores within the structure, $\boldsymbol{d_p}$. Most porous media have a distribution of pore sizes due to the complex interconnected nature of the medium. Thus, $\boldsymbol{d_p}$ is some suitable average for flow channel dimension. The pore size is usually measured by microscopic analysis.

Porosity: This is a dimensionless quantity that describes the fraction of the media that is void. The porosity, $\boldsymbol{\alpha}$, is literally defined as the ratio of the void volume to the total volume of the media. Porosity can be measured by a variety of means, although the typical method is by determination of the average density compared to that of the bulk material. The porosity is also given as the actual flow cross sectional area divided by the cross sectional area of the porous media.

Permeability: This is the quantity that characterizes the flow through the media. The permeability, $\boldsymbol{K_D}$, is the physical quantity that relates the pressure drop to the flow rate through the porous medium.

Specific surface area: This is the total particle surface area per unit volume of the medium. $\boldsymbol{S_v}$ is related to the equivalent particle size or pore size when modeling the medium such as consisting of uniform size spherical particles. The specific surface area can be measured by gas adsorption as is discussed in Chap. 10.

Tortuosity: This quantity is theoretically defined as the effective increase in hydraulic path length in a porous medium compared to the linear dimension of the medium. $\omega = \ell/e$ is defined in Fig. 4.12 and is always ≥ 1.

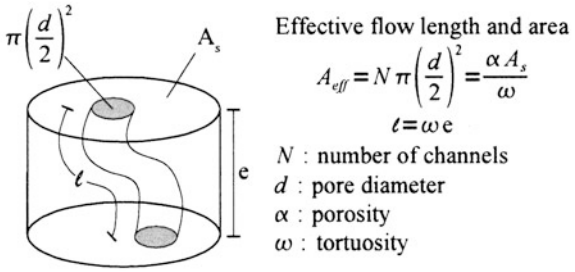

Fig. 4.12 Definition of tortuosity and effective flow area

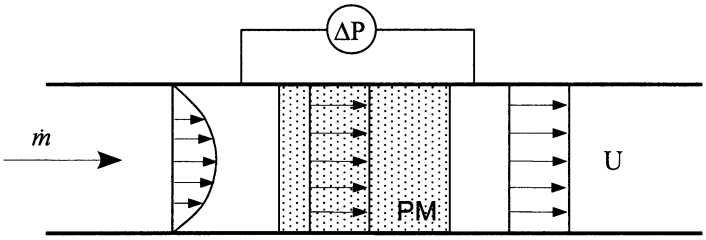

Fig. 4.13 Sample of porous media subjected to a flow

Now consider a sample of porous material (PM) that is placed within a duct, see Fig. 4.13. If the sample is subjected to a one-dimensional flow of a fluid a pressure drop, Δp, is established across the sample. If the flow rate is low, the pressure drop is linearly proportional to the flow rate much like laminar duct flow. This is referred to as the Darcy flow regime and is one method for obtaining the permeability of the medium by measuring,

$$\frac{\Delta p}{L} = \frac{\mu}{K_D} U \tag{4.46}$$

Where U is the velocity averaged over the entire cross section of the sample. This value is considerably different from the velocity of the fluid within the pores which is nominally U/α. If one compares (4.46) to the pressure drop expression for laminar flow, it is easy to show that K_D is proportional to the square of an effective pore diameter, d_p. Equation (4.46) is a scalar relationship that drops the negative sign associated with the pressure gradient through the sample.

As with flow in a one dimensional duct, the laminar flow regime in porous media is limited to occur up to a certain value of the characteristic Reynolds number. However, in porous media there are different Reynolds numbers. For example, one can define a Reynolds number based on the permeability as,

$$\mathrm{Re}_K = \frac{U\sqrt{K}}{\nu} \tag{4.47}$$

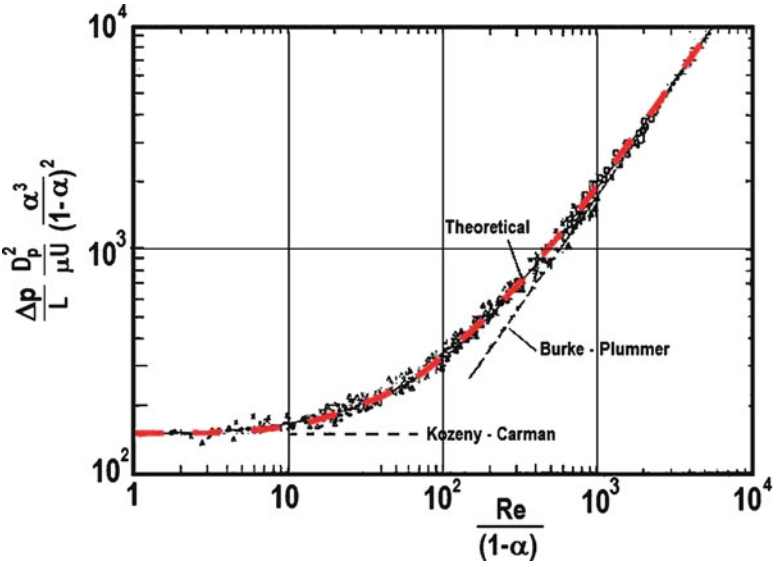

Fig. 4.14 Porous media pressure drop correlation (From Ergun [21])

Using this definition, the laminar regime is limited to flow rates with $\mathrm{Re}_K \leq 1$. For higher Reynolds number, the pressure drop deviates from the linear relationship adding a quadratic contribution that is associated with the form drag around the particles that make up the porous medium. In this regime, the pressure drop is correlated by the relationship,

$$\frac{\Delta p}{L} = \frac{\mu}{K_D} U + b\rho U^2 \tag{4.48}$$

where b is empirically determined.

Ergun [21] confirmed the form of (4.48) by making measurements of the pressure drop across beds of packed spheres. These results are shown in Fig. 4.14. In this case, the Reynolds number is defined in terms of the particle diameter,

$$\mathrm{Re}_{D_p} = \frac{UD_p}{v} \tag{4.49}$$

In this model $D_p \sim 10\sqrt{K}$, indicating the transition Reynolds number for the onset of inertial terms to be $\mathrm{Re}_{D_p} \sim 10$, as seen in Fig. 4.14.

The above discussion is completely general and based on the behavior of classical fluids such as water and air. In the case of normal liquid helium flow through porous media, there are only a limited number of reported measurements. However, overall the behavior of liquid helium flow through porous media is not

substantially different from that of other classical fluids. One potential quantitative variation is in the measured values of the porosity and permeability. Since liquid helium has a very small viscosity and surface tension, it is reasonable to expect the liquid to easily penetrate into the smallest pores in the media. Thus measurements of the permeability and porosity can give higher values with liquid helium than with other fluids, in particular water. This result is at least qualitatively born out by experiment [22].

Helium flow through fine mesh screens is also important technically as many regenerators use this structure rather than packed spheres. Correlations for classical fluid flow through such structures are available in the literature [23, 24]. Again these correlations are mostly based on measurements with classical fluids near room temperature.

By far the most interesting and unique behavior of porous media in helium cryogenics concerns its application as a phase separator in He II storage containers for zero-g applications. We will therefore return to this subject later in that context.

Example 4.3

We need a porous plug pressure drop device for operating as part of a refrigerator. The flow rate is to be 1 g/s of helium supplied at 2 MPa and 6 K. Such a flow might be in part of a recuperative refrigerator with the porous plug acting as a Joule Thomson valve. The outlet pressure is to be 0.3 MPa to avoid two phase flow. We begin by calculating the required permeability assuming that the flow follows Darcy's Law. The assumed physical dimensions are: Diameter of plug = 10 mm; Length of plug = 100 mm.

We first calculate the approach velocity, U,

$$U = \frac{4\dot{m}}{\rho D^2} = 0.11 \text{ m/s}$$

Rearranging Darcy's law for these dimensions and values:

$$K_D = \frac{\mu L U}{\Delta p} = 1.94 \times 10^{-14} \text{ m}^2$$

One can then confirm that Darcy's law is appropriate if the Reynolds number defined as,

$$\text{Re}_K = \frac{\rho U \sqrt{K_D}}{\mu} = 0.5$$

which is less than unity. The flow through the porous media is therefore not affected by inertial terms in the friction factor.

(continued)

Example 4.3 (continued)

What does it mean physically to have a permeability of order 10^{-14} m^2? Returning to the comment above about similarity between laminar duct flow and Darcy's law, one can show that,

$$K_D \approx \frac{D^2}{32}\frac{u_p}{U}$$

Depending on the porosity of the sample, u_p can be larger than U by as much as an order of magnitude. It follows then that $D \sim \sqrt{K_D} \sim 0.1\mu m$. Such a pore size would be obtained in a sample made of particles with diameters no greater than 1 μm.

Questions

1. For adiabatic compressible fluid flow, the pressure will always decrease along the tube, but the temperature can either increase or decrease. Explain how this can occur.
2. Explain how a natural circulation loop works. List the requirements to achieve stable flow.
3. List five applications for porous media in helium cryogenics. Discuss the overall physical characteristics for each case.

Problems

1. Derive the separate equations for the one-dimensional pressure and temperature gradients in a compressible single-phase fluid. Show that for low velocities and nearly ideal gas behavior these expressions reduce to the forms given by (4.26) and (4.27). Determine a relationship for the pressure gradient under the condition where $dT/dx = 0$.
2. Consider single phase liquid helium at 4 K flowing through a 10 mm tube of length 30 m at a mass flow rate of 1 g/s. The mean surface roughness is 10 μm. Calculate the Reynolds number for this flow condition and the overall pressure drop. How much lower would the pressure drop be if the tube were smooth, k = 0?
3. Using the homogeneous model, make a plot of the two-phase friction multiplier ϕ_l^2 as a function of vapor quality χ at 4.5 K and saturation conditions. Use the following dimensions of the tube: L = 5 m; d = 5 mm; mass flow = 1 g/s.
4. Consider the same tube as in problem 2, but in this case it receives a uniform heat flux/length Q/L = 1.25 W/m. (a) Calculate the exit quality of the flow; (b) Calculate the total pressure drop.
5. A 10 mm diameter tube, 10 m in length has a constant flow of 3 g/s of helium. The liquid helium enters as two phase liquid–vapor (χ = 0.4) at 4.5 K and

0.13 MPa. Calculate the pressure drop, Δp, using both the homogeneous model and the Lockhart Martinelli model.

6. Derive a relationship for the permeability of a porous plug made up of n parallel channels of equal diameter, d, per unit area. Use Darcy's law and the laminar flow expression for duct flow.
7. Consider a "cable in conduit conductor" (CICC) consisting of a square cross section tube with inner dimension 10×10 mm^2 and containing 100 round wires of 0.8 mm diameter. The flow rate of single phase liquid helium at 4.2 K is 3 g/s. Calculate the hydraulic diameter and the pressure drop/m of conductor.

References

1. See, for example, B. R. Munson, D. F. Young and T. H. Okiishi, *Fundamentals of Fluid Mechanics 2nd Ed.*,Wiley, New York, 1994.
2. See, for example, R. B. Bird, W. E. Steward, and E. N. Lightfoot, *Transport Phenomena,* Wiley, New York, 1966.
3. J. W. Lue, J. R. Miller, and J. C. Lottin, Pressure Drop Measurement on Forced Flow Cable Conductors, *IEEE Trans. Magnet.* **Mag-15**, 53 (1979).
4. M. A. Daugherty, Y. Huang and S. W. Van Sciver, Pressure Drop Measurements on Supercritical Helium Cooled Cable in Conduit Conductors, *IEEE Trans. on Magnet.* **Mag-25**, 1512 (1989).
5. H. Katheder, Optimum thermo-hydraulic operation regime for cable in conduit superconductors (CICS), *Cryogenics (Supplement)* **Vol. 34,** 595 (1994).
6. This treatment was originally developed by Vincent Arp in: Forced Flow, Single Phase Helium Cooling Systems, *Adv. Cryog. Eng.* **17**, 342 (1972). Although more detailed developments exist today, we retain the present approach for its ease in presentation and understanding.
7. J. W. Dean, W. Stewart, and J. K. Hoffer, Temperature Profiles in a Long Gaseous Helium Cooled Tube, *Adv. Cryog. Eng.* **23**, 250 (1978).
8. J. C. Lottin and F. P. Juster, Liquid helium Thermosiphon for the 4 T CMS magnet, in *Adv. Cryog. Engn.* **Vol. 43**, 1505 (1998).
9. D. S. Scott, Properties of Concurrent Gas-Liquid Flow, *Adv. Chem. Engn.* **Vol. 4**, 199–273, Academic Press, New York, 1963.
10. J. L. Baker, *Flow Regime Transitions at Elevated Pressures in Vertical Two-Phase,* ANL Report 7093, Argonne National Laboratory, Argonne, IL, 1965.
11. P. Griffith and G. B. Wallis, Two Phase Slug Flow, *Trans. ASME* **83**, 307 (1961).
12. H. K. Zust and W. B. Bald, Experimental Observations of Flow Boiling of Liquid Helium I in Vertical Channels, *Cryogenics* **21,** 657 (1981).
13. A. Khalil, Experimental Measurements of Void Fraction in Cryogenic Two-Phase Upward Flow, *Cryogenics* **21**, 411 (1981).
14. H. Haraguchi, S. Kimiya, S. Nakagawa, A. Iwata, M. Yoshiwa, T. Kato, O.Takahashi, E. Tada, and S. Shinamoto, Flow Characteristics of Liquid Helium in a Tube. 1. The Frictional Pressure Drop of Helium Two-Phase Flow, *Proc. Japanese Cryogenic Engineering Conference*, May 16–18, 1983.
15. N. A. Radovcick and R. Moissis, MIT Report No. 7-7673-22. Massachusetts Institute of Technology, Cambridge, MA, 1962.
16. R. W. Lockhart and R. C. Martinelli, Proposed Correlation of Data for Isothermal Two Phase Two Component Flow in Pipes, *Chem. Eng. Prog.* **45,** 39 (1949).
17. S. Levy, Stream Slip-Theoretical Prediction from Momentum Model, *Trans. ASME, J. Heat Transfer* **82**, 113 (1960).

18. R. V. Smith, Fluid Dynamics, in *Cryogenic Fundamentals*, G. G. Haselden (Ed.), Chap. 5, Academic Press, New York, 1971.
19. S. Nakagawa et al., Pressure Drop and Heat Transfer in Helium Two Phase Flow, in *Proceedings of the 10th International Cryogenics Engineering Conference*, IPC Science and Technology Press, London, 1984, pp. 570–573.
20. X. Huang and S. W. Van Sciver, Performance of a Venturi Flowmeter in Two Phase Helium Flow, *Cryogenics* **Vol. 36**, 303 (1996).
21. S. Ergun, Flow through packed columns, *Chemical Engineering Progress* Vol. 48(2), 91 (1952).
22. M. Dalban-Canassy, Counterflow Heat Transfer in He II Contained in Porous Media, PhD Thesis, Florida State University (2009), Ch. 4.
23. J. C. Armour and J. N. Cannon, Flow through Woven Screens, *AIChE Journal* **14 (3),** 415 (1968).
24. W. M. Kays and A. L. London, *Compact Heat Exchangers 3rd Ed.,* McGraw-Hill, 1984.

Further Readings

R. B. Bird, W. E. Steward, and E. N. Lightfoot, *Transport Phenomena,* Wiley, New York, 1966.
B. R. Munson, D. F. Young and T. H. Okiishi, *Fundamentals of Fluid Mechanics 2nd Ed.*,Wiley, New York, 1994.
P. B. Whalley, *Two Phase Flow and Heat Transfer*, Oxford Science, Oxford, 1996.
W. M. Kays and A. L. London, *Compact Heat Exchangers 3rd Ed.,* McGraw-Hill, 1984.
M. Kavainy*, Principles of Heat Transfer in Porous Media*, Springer – Verlag, New York, 1991.

Chapter 5
Classical Helium Heat Transfer

Normal helium (He I) is a simple liquid with state properties that can be described reasonably well by classical models of the type introduced in Chap. 3. However, the dynamics of heat and mass transfer are of particular interest to engineering applications. Heat transfer, which is the subject of the present chapter, is probably the most important single characteristic of cryogenic fluids. The subject has considerable physical basis, and the models used to describe the phenomena are a combination of fundamental physics and engineering correlations. Pool boiling heat transfer is an often studied engineering problem related to cryogenic fluids including liquid helium. Pool boiling is a common term used to describe an experimental configuration consisting of a heater, either a plate or wire, immersed in a large bath of the fluid. Normally, the bath has such an extent that it is possible to assume it to be infinite in size relative to the heater sample. This problem is a classic in heat transfer research; although more complex configurations are needed to model true engineering systems. Heat transfer to forced flow helium is also an important topic as it relates to the design of heat exchangers and superconducting magnets. The fluid dynamics of forced flow helium was covered extensively in Chap. 4. Here we concentrate on the processes of heat exchange. Of course, in the case of forced flow helium the fluid dynamics problem and the heat transfer problem are not completely separable.

There are a number of general characteristics of He I which are worth noting in the context of heat transfer. First of all, it has a rather small thermal conductivity and large specific heat, suggesting that conduction heat transport is of little significance to the overall heat transfer picture. Particularly in the steady state, the heat transport is dominated by convection mechanisms.

The traditional approach to the interpretation of heat transfer is best suited for engineering applications. The general philosophy is to assume that the heat transfer process is too complicated to understand from basic principles. A specific problem requires solution of a complex set of equations which are only treatable in the simplest geometries. Therefore, engineering problems are scaled on the basis of dimensionless variables, which are functions of the properties of the system. It is then possible to construct non-dimensional relationships which when fit to

S.W. Van Sciver, *Helium Cryogenics*, International Cryogenics Monograph Series,
DOI 10.1007/978-1-4419-9979-5_5,

experimental data can be applied universally to other systems. The strength of this approach is in its relative ease of application. These dimensionless relationships have been explored extensively and their forms are available in the literature [1, 2]. Furthermore, the computation of the parameters for a given set of conditions allows straightforward predictions for experimental data. When carried out correctly, the correspondence between experiment and correlations is quite satisfactory. The essential ingredient to this approach is sufficient quantity of experimental data, not only for the particular fluid in question but also for other fluids with widely varying properties. This need must be satisfied to instill reasonable confidence in the particular correlation at hand. Fortunately, for most liquids this kind of ground work has already been laid and the behavior of He I is in satisfactory agreement with the accepted correlations. The quality of the agreement is in part the subject of the present chapter.

For problems of heat transfer, the most important dimensionless quantity to consider is the Nusselt number, Nu. It represents a dimensionless heat transfer coefficient defined by the relationship

$$\mathrm{Nu} = \frac{hL}{k_f} \tag{5.1}$$

where $h = q/(T_s - T_b)$, the heat transfer coefficient of the surface, T_s and T_b are the local surface and bath temperatures, k_f is the thermal conductivity of the fluid, and L is the characteristic length scale in the problem. In pool boiling, L is the dimension of the heater, that is, its diameter or width. In forced flow the length scale is the diameter of the tube or cylinder. As we will see below, the Nusselt number appears in correlations used to describe both free convection and forced convection heat transfer.

In the case of free convection and pool boiling heat transfer the two relevant dimensionless numbers are the Grashof number (Gr) and Prandtl number (Pr). The Grashof number indicates the ratio of buoyancy forces relative to viscous forces; it is represented by the relationship

$$\mathrm{Gr} = \frac{g\beta(T_s - T_b)L^3}{v^2} \tag{5.2}$$

where g is the acceleration of gravity, β is the bulk expansivity, and v is the kinematic viscosity. The Prandtl number, discussed in Chap. 3, is the ratio of the mass to thermal diffusivities of the fluid

$$\mathrm{Pr} = \frac{v}{D_{th}} = \frac{\mu C_p}{k} \tag{5.3}$$

where $D_{th} = k/\rho C_p$. For systems that are dominated by natural convection mechanisms, that is, with negligible forced flow, the Nusselt number is a function of these two numbers,

$$\mathrm{Nu} = \phi(\mathrm{Gr})\ \psi(\mathrm{Pr}) \tag{5.4}$$

where ϕ and ψ are functions that can be determined by the empirical correlation of data.

Most empirical correlations for natural convection are given in terms of the Rayleigh number, which is simply the product of the Grashof and Prandtl numbers,

$$\mathrm{Ra} \equiv \mathrm{Gr}\ \mathrm{Pr} = \frac{g\beta(T_s - T_b)L^3}{D_{th}\nu} \tag{5.5}$$

Simplified correlations can then be written in the form

$$\mathrm{Nu} = C\ \mathrm{Ra}^n \tag{5.6}$$

where C is an empirically determined parameter. The coefficient n is dependent mostly on the geometrical and flow conditions. For a vertically oriented plate in an open bath, $n = \frac{1}{4}$ and $\mathrm{C} = 0.59$ when the flow is laminar while $n = \frac{1}{3}$ and $\mathrm{C} = 0.1$ in the turbulent regime [2]. The type of heat transfer condition that exists in a particular system can be described by the corresponding value of the Rayleigh number. The critical Rayleigh number Ra_c defines the transition between these regimes. For flat plates, the transition between pure conduction and convection occurs for $\mathrm{Ra}_c \approx 10^3$, while the transition between laminar and turbulent convection heat transfer usually occurs for $\mathrm{Ra}_c \approx 10^9$. These concepts assume single-phase heat transfer and consequently are not applicable in heat transfer processes that involve change of phase.

5.1 Regimes of Heat Transfer

To obtain a better physical feeling for pool boiling heat transfer, it is helpful to consider a hypothetical experimental system. Such an experiment, shown in Fig. 5.1, consists of a flat heated plate with some arbitrary orientation exposed to an effectively infinite bath of liquid helium. The experiment consists of heating the plate from inside the insulated region and measuring the temperature difference between the bath and surface, ΔT_s, as it varies with heat flux q. There are a number of variables that affect the results in this experiment. Among these are bath temperature and pressure, surface orientation, physical characteristics of the heated surface including coatings, and frequency of heat flux. The general impact of these variables is described further below.

Given this experimental configuration, a measurement consists of determining a relationship between the heat flux q and ΔT_s. A typical example of such a relationship is shown in Fig. 5.2. There are principally three regimes of heat transfer as indicated in the figure: (1) natural convection, (2) nucleate boiling, and

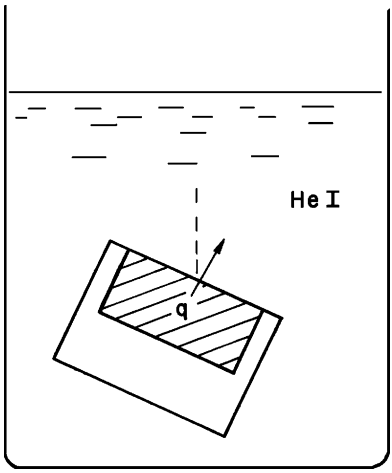

Fig. 5.1 Schematic of pool boiling heat transfer process from a planar surface of arbitrary orientation

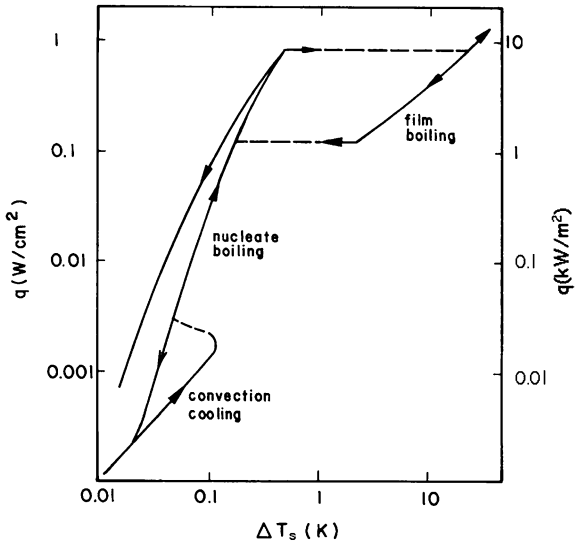

Fig. 5.2 Typical heat transfer relationship for pool boiling liquid

(3) film boiling. Each of these regimes has a characteristically different physical description, a schematic representation of which is shown in Fig. 5.3. At the lowest heat fluxes up to a few W/m^2, heat is transferred by natural convection; see Fig. 5.3a. No phase change is evident. This mechanism is characterized by density-driven convection currents near the heated surface. Surface temperature differences can be determined by the type of correlation given in (5.6). As the heat flux is increased, bubbles of helium vapor begin to form at preferred sites on the surface. These are typically surface imperfections. In the natural convection region, a certain amount of hysteresis in the heat transfer curve results from the activation and deactivation of these nucleation sites.

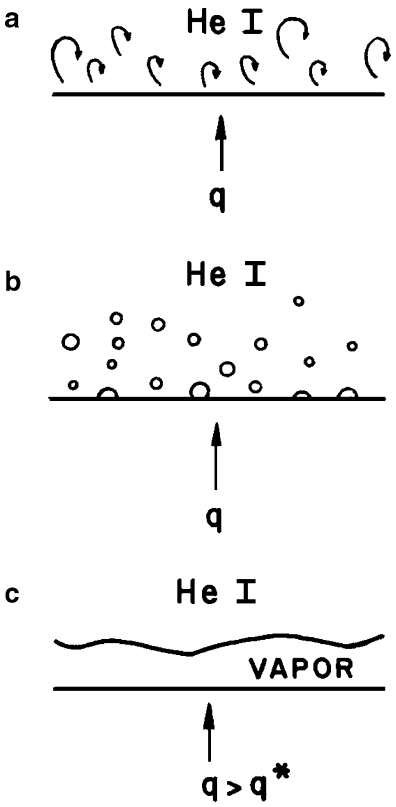

Fig. 5.3 Schematic representation of regimes of heat transfer: (**a**) natural convection, (**b**) nucleate boiling, and (**c**) film boiling

As the heat flux is increased further, the nucleation sites get fully activated, meaning that each site contains one bubble. At this point the surface is referred to as being "educated" since now increasing the heat flux only serves to accelerate the rate of bubble growth and detachment. In the nucleate boiling regime, Fig. 5.3b, there is a layer of superheated liquid adjacent to the heater surface. As a bubble detaches, cold liquid from above rushes down to cool the surface. This bubble growth and detachment causes macroscopic turbulence.

At still higher heat fluxes, the nucleate boiling bubbles get so large and are detaching at such a great rate that they become unstable and coalesce into a continuous vapor film; see Fig. 5.3c. The heat flux at which this occurs is referred to as the peak nucleate boiling heat flux q^*. This regime is called film boiling. The condition is unstable and causes hysteresis in the heat transfer curve, as shown by the upper region in Fig. 5.2. On decreasing the heat flux, it is necessary to go to a value lower than q^* for recovery to the nucleate boiling regime. This recovery value is referred to as the minimum film boiling heat flux q_{mfb} or recovery heat flux q_R. In the film boiling regime, the surface temperature difference is typically an order of magnitude higher than with nucleate boiling. The hysteresis in this regime of heat transfer is associated with the stability of a vapor film below a higher-density liquid.

Numerous factors affect these heat transfer characteristics. For example, the surface condition of the heat transfer sample can affect both the peak heat flux q^* and ΔT_s, in the nucleate boiling regime. It is possible to obtain variations in these quantities by as much as a factor of 2–3 between samples. The mechanism by which surface preparation affects the heat transfer characteristics is believed to be associated with the number of available nucleation sites.

Surface orientation has a profound effect on the heat transfer behavior. Variation of the surface orientation with respect to the gravitational force can cause significant changes in the heat flux and minimum film boiling heat flux. The highest values for both these quantities occur with the surface facing upward, because the buoyancy force aids bubble detachment. This argument supports the observed result that q^* and q_{mfb} are minimum with the surface facing downward.

The thermodynamic state of the liquid helium bath is also an important parameter in the heat transfer process. The bath temperature has a significant effect on various heat transfer parameters, particularly the peak nucleate boiling heat flux q^*. Similarly, the bath pressure affects these values, particularly when considering the subcooled or supercritical state. These variables can be taken into account through the changes in the helium properties with temperature and pressure.

The frequency with which the heat transfer event occurs is also important for both the peak heat flux and temperature difference. At low frequencies up to perhaps 10 Hz, the behavior does not deviate significantly from that of the steady-state process. Heat transfer is controlled largely by convection mechanisms. However, at higher frequencies approaching the kilohertz range there is insufficient time for the bubble nucleation to occur. Consequently, the behavior becomes dominated by simple heat diffusion in the liquid adjacent to the solid. Then temperature differences are caused by two physical mechanisms – the thermal conductivity of the helium and interfacial conductance (Kapitza conductance).

Finally, variations in geometry can have a profound effect on the heat transfer. Many engineering systems consist of channels, tubes, or other complex geometries, which are vastly different from the open infinite bath configuration. Such factors can cause differences in the heat transfer at least in part caused by the limited coolant volume. Some of the physical phenomena that can occur include heat-induced natural circulation and vapor locking in narrow channels. In the following sections, these issues will be discussed in further detail.

5.2 Convective Heat Transfer

At very low heat fluxes in liquid helium, $q \approx 1$ W/m^2, heat is transferred by a combination of conduction and convection. It is described by a heat transfer coefficient $h = q/\Delta T_s$, where h is only weakly dependent on ΔT_s. This regime of heat transfer has only limited technological application in liquid helium because the heat fluxes are quite small. However, the problems of low heat flux heat transfer and of transitions between conduction and convection do have fundamental physical

significance. Certain special cases of heat transfer fall in the general area of exactly soluble classical physics problems.

A good example of such a special interest is the problem of convection onset in a layer of fluid that is heated from below. The main difference between this problem and similar ones concerning pool boiling heat transfer is that the fluid layer is to have a thickness dimension d that enters into the problem in one of the dimensionalized parameters. This problem is referred to as Bénard convection and the instability associated with the transition is called the Rayleigh-Bénard instability. The transition is between conductive heat transfer and steady convection. As the heat flux is increased, the condition where the fluid is at rest carrying heat by conduction is transformed to that where a polygonal convective cell structure occurs. This type of structure has been observed in visual experiments with room temperature fluids. These flows exhibit regularity and structure that have inspired considerable theoretical research into the dynamics of small perturbations in fluids heated from below. Theoretical modeling is achievable because the disturbances are assumed to be sufficiently small that their description, at most, adds linear terms to the fluid equations.

The theoretical description of Bénard convection begins with the continuity equation and the equations for conservation of momentum and energy. The growth or decay of perturbations in the velocity and temperature fields is governed by the following linearized equations [3]:

$$\nabla \cdot \mathbf{v} = 0 \tag{5.7a}$$

$$\frac{\partial \mathbf{v}}{\partial t} = -\frac{1}{\rho_0}\nabla p + v\nabla^2 \mathbf{v} - \mathbf{g}\beta T \tag{5.7b}$$

$$\frac{\partial T}{\partial t} = D\nabla^2 T - w\gamma \tag{5.7c}$$

Solutions to these equations establish the regions of convection growth or decay. The boundary between these regions is defined by a "critical" Rayleigh number which effectively is a nondimensional temperature difference. The most interesting of the three equations is (5.7c) which describes the effect of motion on the temperature gradient. Without the second term, $w\gamma$, the expression is simply the heat diffusion equation. The parameter γ is defined as the undisturbed temperature gradient due only to conduction ($\gamma = q/k$). The physical meaning of the term $w\gamma$ is that of the motion generator. Heat is swept upward while the cold fluid returns. Heat conduction is necessary to generate the initial temperature gradient, but since mass flow is involved, viscosity enters to resist the growth of the perturbation.

The problem of Bénard convection in He I has been studied by a number of workers. Experimental measurements normally consist of determining the variation of the Nusselt number with the normalized Rayleigh number ($\mathrm{Ra}/\mathrm{Ra}_c$). For any fluid, the Nusselt number represents the ratio of the effective thermal conductivity to the actual thermal conductivity obtained without convection. Plotted in Fig. 5.4 is

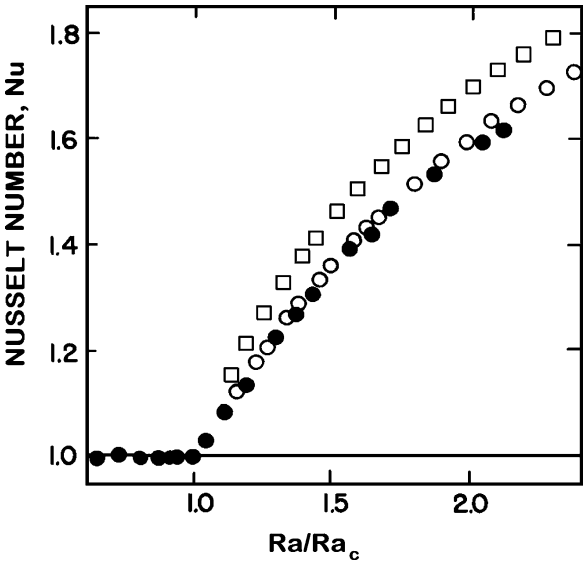

Fig. 5.4 Nusselt number as a function of Ra/Ra_c for Rayleigh-Bénard instability (From Behringer and Ahlers [4])

the normalized Nusselt number for one set of experiments on He I [4]. A number of interesting facts can be gleaned from these data. For example, above Ra_c the Nusselt number increases quite strongly with Ra. This is to be expected because the convection currents improve the heat transport. However, it is worth noting that the behavior of the Nu versus Ra/Ra_c plot appears to be somewhat universal in form. Slight differences in the data displayed in Fig. 5.4 are attributed to geometrical factors in the experiment.

The Rayleigh-Bénard instability is an interesting classical fluids problem. Its connection with helium heat transfer in practical configurations is limited, yet it does give fundamental insight into the fluid flow problem. As the heat flux is increased above about 0.1 W/m^2 bubbles begin to nucleate on the surface and simple convection is no longer the generally applicable solution. This problem is discussed in the next section.

Free convection heat transfer in cold helium gas is a more practically significant process because it can involve large heat fluxes. Helium near the critical point and in the supercritical regime has been studied fairly extensively [5–7]. Near the critical point, the heat transfer is seen to be enhanced considerably. For example, near 0.224 MPa, heat transfer coefficients as high as 100 kW/m^2 K have been observed. Such results correlate with the maxima in the thermodynamic properties near the critical point. Away from the critical point, the results are correlated best as a function of the Rayleigh number as (5.6). A reasonable fit to much of the helium data in this regime can be obtained from the expression [8],

$$Nu = 0.615\ Ra^{0.258} \tag{5.8}$$

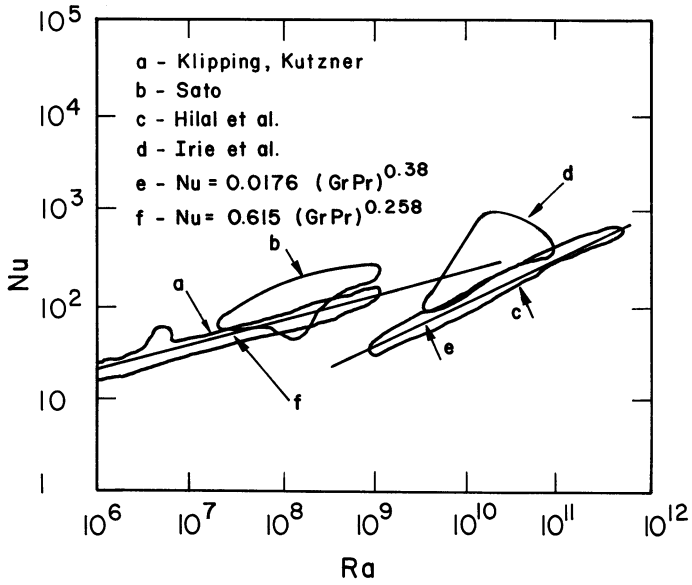

Fig. 5.5 Comparison of data and correlations on free convection heat transfer to supercritical helium (From Hilal [8])

which is close to the form expected for laminar free-convection heat transfer. A compilation of convective heat transfer results for supercritical helium is shown in Fig. 5.5 along with several correlations. There is a characteristic trend to the data; however, the agreement between various experiments is variable.

5.3 Nucleate Boiling Heat Transfer

Above a heat flux of a few W/m^2 in liquid helium the heat transfer surface begins to be covered with a large number of small vapor bubbles. This heat transfer process is quite different from that of natural convection because it is controlled mostly by the hydrodynamics of bubble growth and detachment rather than convection in the liquid.

Two conditions must exist at or near the heat transfer interface before there can be activation of bubble nucleation sites. First, there must be a boundary layer of liquid adjacent to the surface which is in the superheated condition. The thickness of this layer is determined by the thermal conductivity of the liquid, k, and the allowable superheat, $\Delta T_s = T_s - T_b$, where T_s is the maximum superheat temperature and T_b is the bath temperature. The thermal boundary layer thickness can therefore be written

$$\delta \approx \frac{k\ \Delta T_s}{q} \tag{5.9}$$

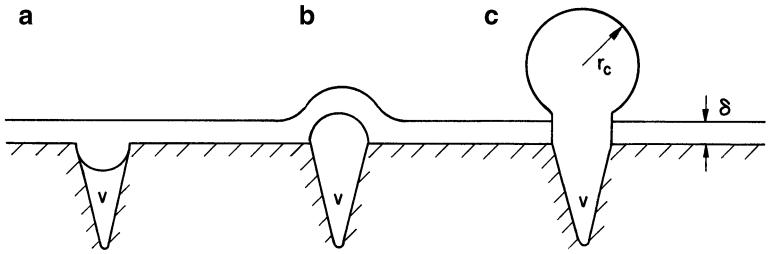

Fig. 5.6 Bubble nucleation on an imperfect surface: (**a**) negative radius of curvature, (**b**) positive radius of curvature, and (**c**) critical radius

Typically, δ is of the order of 1–10 μm for liquid helium near its normal boiling point.

Second, local surface imperfections must exist. These imperfections are necessary to provide preferential regions where bubbles can form. Shown schematically in Fig. 5.6, these imperfections usually are envisioned to be grooves or slots which allow a bubble to form with negative curvature, thus taking advantage of surface tension to stimulate the bubble nucleation. There are two principal reasons why the superheated boundary layer must form near the interface before substantial vapor nucleation can occur. First, the liquid near the interface is subcooled by the hydrostatic head ($\Delta p = \rho g h$) such that the local temperature must increase above ambient before the saturation condition can be attained. Second, and probably more important, in order to have vapor bubbles of positive radius of curvature, the surface tension of the liquid must be overcome.

5.3.1 Nucleation Theory

So far the discussion of nucleate boiling has been quite general and qualitative. However, it is worth considering two specific questions of quantitative nature. These concern the general vapor nucleation problem but are worked out as examples for the case of boiling liquid helium. The first question pertains to the growth of a vapor bubble on a nucleation site or actually anywhere in the bulk fluid. For a given amount of superheat, a bubble will be stable against the surface tension which is trying to collapse it. This problem involves consideration of the stability of a vapor bubble immersed in the bulk liquid – a case similar to that shown schematically in Fig. 5.6c.

The stability of a vapor bubble in the liquid can be evaluated in terms of the Clausius–Clapeyron equation. Considering the change of state between the liquid and vapor, thermodynamic stability requires that the vapor pressure derivative be given by

$$\left.\frac{dp}{dT}\right|_{sat} = \frac{\Delta s}{\Delta v} = \frac{h_{fg}}{T\ \Delta v} \tag{5.10}$$

where h_{fg} is the latent heat of the liquid and $\Delta v = v_g - v_l$ is the difference between the specific volumes of the vapor and liquid. For the interface of the bubble to be stable, it must have a pressure inside, p_v, which exceeds the local saturation pressure, p_s, by an amount related to the surface tension σ. For a spherical bubble, this requirement leads to the expression

$$p_v - p_s = \frac{2\sigma}{r} \tag{5.11}$$

where r is the local bubble radius. Obviously, the smaller the bubble the larger must be the pressure difference.

To get a feel for the order of magnitude of the quantities involved, assume that helium vapor obeys the ideal gas law and that the specific volume of the vapor is much greater than that of the liquid. These assumptions lead to the following approximation:

$$\Delta v \approx v_g \approx \frac{RT}{p} \tag{5.12}$$

Substituting (5.12) into (5.10) leads to a differential relationship

$$\frac{dp}{p} = \frac{h_{fg}}{R}\frac{dT}{T^2} \tag{5.13}$$

This expression must be integrated between saturation (T_s, p_s) and the condition inside the bubble (T_v, p_v) as determined by the stability relationship (5.11). Such a procedure yields a common relationship for the required vapor pressure within a bubble.

$$p_v = p_s e^{h_{fg}\Delta T_s/RT_s^2} \tag{5.14}$$

where a further approximation has been made that the temperature difference, $\Delta T_s = T_v - T_s$, is small compared to T_s.

The present discussion is aimed at determining the minimum radius of a stable vapor bubble in the bulk liquid. Substituting the expression for equilibrium of a vapor bubble (5.11) and allowing the radius to be undetermined, we obtain an expression for the critical radius,

$$r_c = \frac{2\sigma}{p_s}\left(e^{h_{fg}\Delta T_s/RT_s^2} - 1\right)^{-1} \tag{5.15}$$

which subsequently can be solved to determine the approximate value of r_c for any fluid.

Example 5.1

Calculate the critical radius for a vapor bubble in liquid helium at 4.2 K, 100 kPa. Assume that the vapor is superheated by 0.3 K. Estimate the number of helium molecules within the bubble.

Under the assumed conditions, $h_{fg} = 82$ J/mol and $\sigma = 0.15$ mJ/m^2 for a critical temperature difference assume $\Delta T \approx 0.3$ K. Inserting these numerical values into (5.15)

$$r_c = \frac{2\sigma}{p_s}\left(e^{h_{fg}\Delta T_s/RT_s^2} - 1\right)^{-1}$$

yields a critical radius $r_c \approx 16.4$ nm. The volume of the sphere is then,

$$V = \frac{4}{3}\pi r^3 = 1.8 \times 10^{-23}\text{m}^3$$

But the number density of helium molecules at 4.2 K is about 2.6×10^{27}/m^3 so the sphere contains approximately 10^4 atoms. It is reasonable to assume that the bubble containing this many molecules represents a thermodynamic system. Note that the above calculation is limited by the assumptions that $v_g \gg v_l$ and the ideal gas behavior for the vapor phase. These assumptions can lead to considerable inaccuracies in calculations of both the critical radii and the nucleation temperature.

The above calculation contains an assumed value for the superheat required to initiate the nucleation process, ΔT_s. Experimentally determined superheats actually vary by as much as half an order of magnitude. The highest values are obtained for the most ideal surfaces where nucleation is assumed to be homogeneous. These systems give nucleation superheats around 0.35 K at 4.2 K, 0.1 MPa. In fact, homogeneous nucleation superheat has been measured over the entire He I range and shown to agree with the empirical relationship [9]

$$\Delta T_s = 4.322\left(1 - \frac{T_b}{T_c}\right)^{1.534} \tag{5.16}$$

An expression can be derived for the homogeneous nucleation temperature based on a model suggested by Frenkel [10]. The analysis yields the rate of formation of bubbles having the critical radius r_c as defined by (5.11). As a function of the fluid properties, the rate is given by

$$R = n_l\left(\frac{\sigma}{m}\right)^{1/2}\exp\left(-\frac{4\pi}{3}\frac{\sigma\, r_c^2}{k_B T_s}\right) \tag{5.17}$$

where n_l is the number density in the liquid and m is the mass of a helium atom. The critical radius r_c is a function of the superheat ΔT_s, as well as other parameters such as absolute temperature T_s.

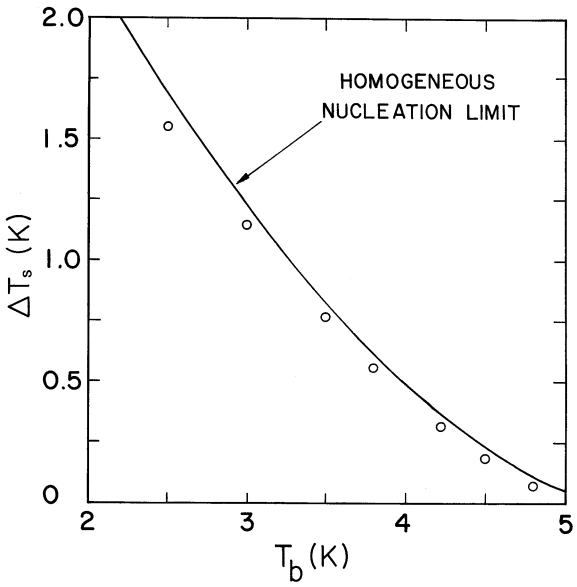

Fig. 5.7 Homogeneous nucleation limit for liquid helium heat transfer (From Flint and Van Cleve [11])

The expression given by (5.17) can be used to calculate the critical radius r_c or preferably the superheat ΔT_s. Such a calculation requires one arbitrary assumption: that of the reaction rate for the onset of nucleation. However, since the critical parameters enter into the exponential, the results are only weakly dependent on the choice of R. Typical values for this quantity are assumed to be 1 $cm^{-3} \cdot s^{-1}$. Furthermore, it is not possible to use the form developed above for the critical radius because the nonideality of the vapor phase plays an important role. Flint and Van Cleve [11] were able to obtain good agreement between experiment and theory if they used the actual behavior of the helium vapor pressure curve. The results of their calculation are shown in Fig. 5.7 along with experimental values for the nucleation superheat. These results were obtained on polished silicon chips oriented vertically in a bath of saturated liquid helium. The critical temperature differences are determined by noting the point where the hysteresis ended in a q versus ΔT curve; see Fig. 5.2. These data indicate a close correspondence between homogeneous nucleation theory and experiment. Typically, nucleation temperatures on real roughened surfaces are lower than those indicated in Fig. 5.7.

5.3.2 Heat Transfer Correlations

Once nucleation has occurred and the bubbles are large enough to be stable against collapse in the bulk fluid, the heat transfer becomes dependent on the hydrodynamics of bubble detachment and growth. To model the nucleate boiling heat transfer in this regime, it is necessary to know a number of quantities including

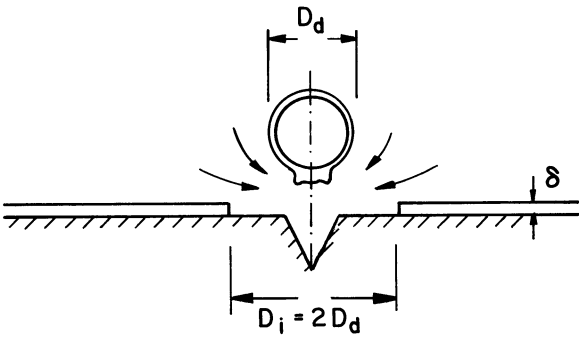

Fig. 5.8 Schematic of departing bubble and area of superheated liquid (From Bald [13])

the rate of bubble growth, frequency of detachment, and something of the hydrodynamics of the two-phase fluid consisting of the liquid in the vicinity of the bubble. A conceptual picture of the hydrodynamics of an individual bubble is beneficial in understanding the heat transfer mechanisms.

In the vicinity of the nucleation site, it was observed by Hsu and Graham [12] that a departing bubble took with it an area of superheated liquid equal to approximately twice the projected area of the bubble. Based on this hypothesis, shown schematically in Fig. 5.8, it is possible to account for the heat removed by one bubble as a sum of two quantities [13]

$$q_b = \frac{4\pi}{3} h_{fg} \rho v \int_A nfr_b^3 \, dA + 2\pi \Delta T_s C_l \rho_l \delta \int_A nfr_b^2 \, dA \tag{5.18}$$

where n is the number of nuclei per unit area of surface and the integrals are over the entire heat transfer surface area. The first quantity on the right-hand side is that due to the latent heat of the helium within the bubble, while the second is the heat required to superheat a new layer of liquid that replenishes the layer taken away with the departing bubble. The difficulties associated with applying (5.18) to real problems are multifold. First, the frequency of detachment f is involved with both terms in (5.18). The heat flux is proportional to f, which is largely an experimental quantity. The quantity is dependent on n, the number of nucleation sites per area, and r_c, the critical size of a departing bubble. The amount of superheat ΔT_s also enters (5.18) in the second term. In principle, this quantity can be determined from (5.17); however, for real surfaces it can vary considerably.

An additional complication enters when attempting to determine the total heat transferred in the nucleate boiling regime. In an actual process, there are two heat transfer terms: one due to bubble hydrodynamics, q_b, and one due to natural convection in the bulk fluid, q_{nc}:

$$q_{nb} = q_b + q_{nc} \tag{5.19}$$

There may be an additional contribution due to the interaction between natural convection and boiling, but it is unclear what form it would take. It is tempting to

neglect the natural convection term, assuming it is small; however, this is not always possible. Except in very special geometries, it is not possible to determine q_{nc} exactly. Therefore, engineering correlations are needed to describe the second term in (5.19). In general, the natural convection heat transfer can be written as a function of the dimensionless Rayleigh number as given by (5.6).

The above analysis has the potential of being able to describe the heat transfer in the nucleate boiling region. However, difficulty arises when determining the variables that enter (5.18) and (5.19). These variables mostly include the functional form of the natural convection, the amount of superheat ΔT_s, the bubble density n, and detachment frequency f. Since this analysis has limited practical usefulness, the preferred approach is to characterize the total heat transfer in terms of an engineering correlation.

The most popular and probably the best correlation used to describe the nucleate boiling regime is due to Kutateladze [14]. It is based on theory and experimental scaling of heat transfer to many different fluids:

$$\frac{h}{k_l}\left(\frac{\sigma}{g\rho_l}\right)^{1/2} = 3.25\times 10^{-4}\left[\frac{qC_{pl}\rho_l}{h_{fg}\rho_v k_l}\left(\frac{\sigma}{g\rho_l}\right)^{1/2}\right]^{0.6} \times\left[g\left(\frac{\rho_l}{\mu_l}\right)^2\left(\frac{\sigma}{g\rho_l}\right)^{3/2}\right]^{0.125}\left(\frac{p}{(\sigma g\rho_l)^{1/2}}\right)^{0.7} \tag{5.20}$$

where g is the acceleration of gravity and h_{fg} is the latent heat of vaporization. Although (5.20) is a complex expression, it does predict a reasonably correct functional dependence for the nucleate boiling heat transfer. Rearranging (5.20) into a more manageable form leads to the relationship

$$q = 1.90\times 10^{-9}\left[g\left(\frac{\rho_l}{\mu_l}\right)^2\chi^3\right]^{0.3125}\left(\frac{p\chi}{\sigma}\right)^{1.75}\left(\frac{\rho_l}{\rho_v}\right)^{1.5} \times\left(\frac{C_{pl}}{h_{fg}}\right)^{1.5}\left(\frac{k_l}{\chi}\right)(T_s - T_b)^{2.5} \tag{5.21a}$$

where

$$\chi = \left(\frac{\sigma}{g\rho_l}\right)^{1/2} \tag{5.21b}$$

and T_s and T_b are the surface and bath temperatures, respectively. The expression given by (5.21) is evaluated more easily. For the case of He I at 4.2 K, 0.1 MPa, the coefficient of proportionality can be calculated to equal 58 kW/m^{2}K^5.

The Kutateladze correlation is in reasonable accord with experimental measurements of heat transfer in He I. However, there is a wide variation in experimental

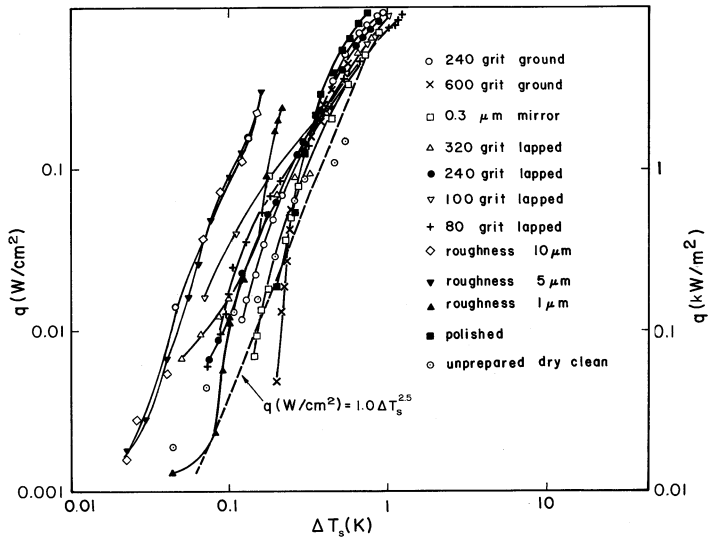

Fig. 5.9 Nucleate boiling heat transfer to He I (Compilation of data and suggested correlation from Schmidt [16])

data owing to the differences in sample preparation and surface material and orientation [15]. It is not too surprising, based on the hydrodynamic arguments above, that different surface preparations would yield much different results.

Figure 5.9 is a compilation of nucleate pool boiling data for flat copper surfaces facing upward and experiencing an increasing heat flux. The data vary over at least half an order of magnitude in ΔT with the smoothest surfaces apparently allowing a larger superheat. The larger superheat seen in smooth surfaces is consistent with the homogeneous nucleation arguments presented at the beginning of this section. Finally, note that an empirical fit used by Schmidt [16] to describe the data is also plotted in Fig. 5.9. This fit, which is quite close to the Kutateladze correlation with the exception of the coefficient of proportionality, is a conservative form useful for engineering applications.

5.3.3 *Maximum Nucleate Boiling Heat Flux*

The qualitative picture applied to the understanding of the maximum heat flux in pool boiling He I is as follows. Imagine a surface populated with a number of nucleation sites. At high heat fluxes, these sites are actively nucleating bubbles that grow to a stable size and detach at a frequency f controlled by buoyancy forces. With increasing heat flux, the number and size of these bubbles grow until a point is reached where they cover a sizable fraction of the heater surface. At this point, the individual bubbles are no longer the lowest-energy condition. They will prefer

to coalesce into a continuous vapor film which will blanket the entire heat transfer surface. This condition usually is referred to as the onset of film boiling. The difficulty is in being able to understand and predict the value of heat flux at which this event occurs, q^*.

To obtain some physical feeling for the occurrence of the maximum heat flux, consider an idealized surface facing upward as in Fig. 5.3b. The vapor bubbles are departing at velocity $\mathbf{v}_v$ while the replenishing liquid moves in the opposite direction at velocity $\mathbf{v}_l$. These velocities are not independent variables because the heat flow is determined by the rate of growth and departure of the vapor bubbles.

The hydrodynamics of this process is described by the Helmholtz instability [17], which pertains to the critical velocity of immiscible fluids moving relative to each other. Assume the liquid and vapor phases represent these two immiscible fluids. Then the boundary separating the two fluids would show an upward-moving vapor and downward-moving liquid. For these two fluids to pass each other undisturbed, the boundary that separates them must remain stable. The stability of this boundary is a function of a number of parameters including the relative velocities and densities of the two fluids. This is believed to be the condition that imposes the peak heat flux limit in classical liquids including He I.

Because of the relative motion of each fluid, there can be a surface wave set up at the interface. The velocity of this wave, c_s, is dependent on a number of factors including the surface tension and properties of the individual phases. The relationship for the surface wave velocity is

$$c_s^2 = \frac{\sigma m}{\rho_l + \rho_v} - \frac{\rho_l \rho_v}{(\rho_l + \rho_v)^2}(\mathbf{v}_v - \mathbf{v}_l)^2 \tag{5.22}$$

where $m = 2\pi/\lambda$ is the wave number of the surface wave. Since (5.22) consists of a difference between two positive quantities, it is possible for c_S^2 to have either a positive or negative value. For $c_S^2 > 0$ the surface wave can exist. If $c_S^2 > 0$ the surface wave velocity is imaginary, implying an instability in the interface. Therefore, the condition for maximum vapor velocity is obtained by equating c_S^2 to zero. Using conservation of mass flow, that is, $\rho_v \mathbf{v}_v + \rho_l \mathbf{v}_l = 0$, a simple expression is obtained:

$$\mathbf{v}_v^* = \left(\frac{\rho_l \sigma m}{\rho_v (\rho_l + \rho_v)} \right)^{1/2} \tag{5.23}$$

If the vapor velocity exceeds the value given by (5.23) there should be an unstable two-phase flow. The result is destruction of the interface between the two phases, which in turn leads to a condition where the vapor film blankets the heat transfer surface. This condition occurs at the maximum heat flux.

Zuber et al. [18] used the above reasoning to predict analytically the maximum heat flux q^*. Assuming that the heat is transported primarily by the vapor velocity and that the latent heat of the liquid that goes into the formation of the bubble is the

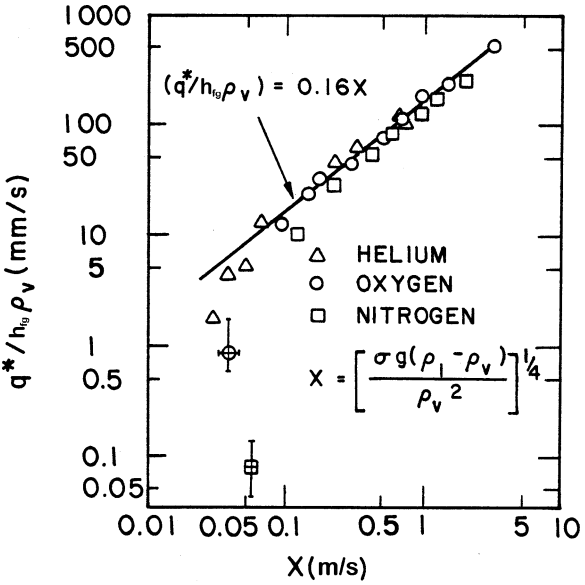

Fig. 5.10 Comparison of peak nucleate boiling heat fluxes with Kutateladze correlation (From Lyon [20])

dominant energy, Zuber and coworkers argued that the maximum heat flux can be written as a product of these quantities, that is,

$$q* = Kh_{fg}\rho_v \left(\frac{\sigma(\rho_l - \rho_v)g}{\rho_v^2}\right)^{1/4} \left(\frac{\rho_l}{\rho_l + \rho_v}\right)^{1/2} \tag{5.24}$$

where K is a numerical factor which in the case under consideration has a value of $\pi/24$. It is possible to derive a similar relationship for q^* from dimensionless group analysis. Based on experimental evidence, a similar relationship has developed acceptance [19, 20] that is,

$$q* = 0.16h_{fg}\rho_v^{1/2}[\sigma g(\rho_l - \rho_v)]^{1/4} \tag{5.25}$$

which is in close agreement with (5.24) with the exception of the last factor. The numerical factor in (5.25) is determined by correlation of numerous experimental results. For a numerical comparison, (5.25) predicts for liquid helium at 4.2 K, 0.1 MPa a value of $q^* = 8.5$ kW/m^2, which is in reasonable agreement with experimental results ranging from 5 kW/m^2 to around 15 kW/m^2. However, to test the relationship represented by (5.25) for a particular fluid, it is necessary to make measurements over a wide range of vapor densities or temperatures. Furthermore, to determine whether the correlation is universally acceptable, measurements of q^* for a variety of fluids are required. These experimental investigations determine the empirical constant of proportionality. Plotted in Fig. 5.10 are normalized measurements of $q^*/h_{fg}\rho_v$ versus the density function given in (5.25) [20]. Reasonable agreement with the correlation is seen for the three cryogenic fluids considered.

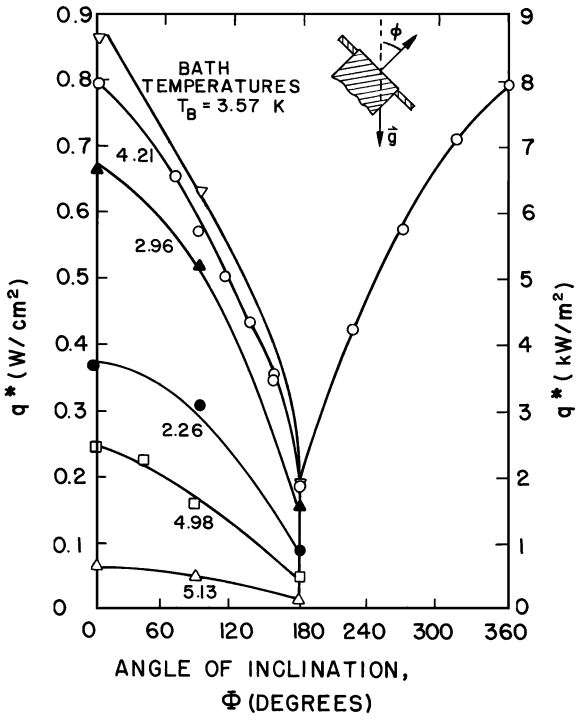

Fig. 5.11 Orientation dependence to the nucleate boiling heat flux (From Lyon [20])

It is worthwhile considering the temperature and orientation dependencies of q^* in comparison to (5.25). At high temperatures, q^* would be expected to decrease because as the critical point is approached there is no phase change associated with boiling and the latent heat vanishes. The theoretical expression indicates that the peak heat flux should go as the latent heat times the fourth root of the density difference. Both quantities vanish at the critical point. At low temperatures the latent heat approaches a constant and the temperature dependence is determined by the square root of the vapor density, which in turn decreases with temperature. Therefore, there should be a maximum in the peak heat flux. Analogous although somewhat less successful arguments can be used to describe the orientation dependence of q^*. Since the peak heat flux is proportional to the square root of the gravitational acceleration g, the buoyancy effects should decrease as the surface is turned from facing upward to facing downward. In fact, based on this simple argument, a surface facing downward should have $q^* = 0$. Experimentally, q^* obtains a minimum value a 180° orientation although its value is considerably greater than zero.

Measurements of the temperature and orientation dependence of q^* have been conducted most comprehensively by Lyon [20]. The orientation dependence of the maximum nucleate boiling heat flux is shown in Fig. 5.11. Note that for these experiments $q^* = 8$ kW/m^2 at 4.2 K which is quite close to the theoretical prediction. Furthermore, for each orientation there is a maximum value in the temperature dependence of q^*. Experimentally, this maximum occurs around 3.6 K. Finally, the

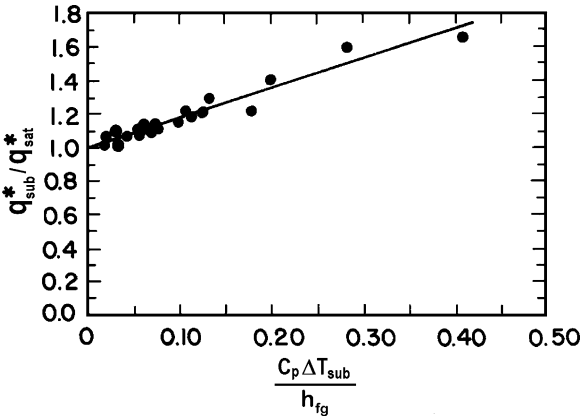

Fig. 5.12 Variation of the peak nucleate boiling heat flux with subcooling (From Ibrahim et al. [21])

orientation dependence is in qualitative agreement with theory. A minimum in q^* does occur at $\theta = 180°$, that is facing downward. However, the value of q^* at $\theta = 180°$ is still quite sizable, being about 25% of q^* for $\theta = 0°$.

The above correlations do not apply when the helium is subcooled to a state substantially off the saturated vapor pressure curve. In this case there can be no coexisting vapor. Some work [21–23] on the effect of subcooling on heat transfer has attempted to treat the peak heat flux correlation in terms of a subcooled temperature difference ΔT_{sub}. The subcooled temperature difference is defined as the difference between the bath temperature T_b and the temperature corresponding to saturation T_{sat}. As heat is applied from the heat transfer surface, the temperature rises. However, in subcooled He I a larger temperature difference is required than in saturated He I. This is due to the need to bring the local environment first to saturation followed by the amount of superheat needed to initiate nucleate boiling. Therefore, the absolute temperature needed to cause boiling at a given pressure should be independent of bath temperature. Such a hypothesis leads to a correlation for the enhancement of peak heat flux q^* with subcooling

$$\frac{q^*_{\text{sub}}}{q^*_{\text{sat}}} = 1 + \frac{aC_p \Delta T_{\text{sub}}}{h_{fg}} \tag{5.26}$$

where a is an empirical parameter found to be close to 1.75. Comparison of experimental results with the correlation given by (5.26) are shown in Fig. 5.12. Agreement is reasonable although the theory has received only limited application.

5.4 Film Boiling

Once the film boiling condition has been established, normally by exceeding q^* under steady-state conditions, a wholly different heat transfer process takes place. In the vicinity of the heat transfer interface the helium takes on a stable two-phase

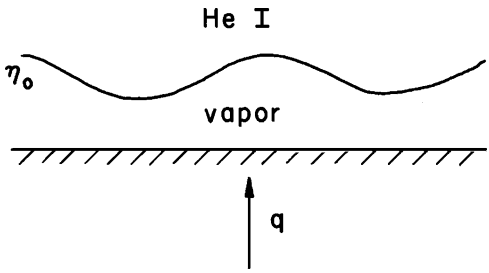

Fig. 5.13 Idealized film boiling heat transfer process

condition with a thin vapor layer blanketing the surface from the He I bath. For a surface facing upward, this condition is gravitationally unstable since the density of the liquid is considerably greater than that of the vapor. Experimentally, it is found that return to the nucleate boiling state requires a decrease in heat flux to q_R or q_{mfb}, which can be substantially less than q^* for most configurations. It follows that there are two principal issues that should be addressed when evaluating the film boiling state. First, given the conditions of film boiling, how is the recovery process explained? In particular, is it possible to predict q_R? This process has to do with the stability of the He I–vapor interface. The second question pertains to the need to correlate the heat transfer coefficient in the film boiling condition. This process normally relies on dimensionless group analysis developed for other liquids.

5.4.1 Minimum Film Boiling Heat Flux

The stability of the vapor film blanketing the heat transfer surface can be evaluated in terms of a hydrodynamic condition referred to as the Taylor instability [17]. This interpretation is a standard approach to treating the interface between two dissimilar fluids. Imagine the condition shown in Fig. 5.13 which is an idealized film boiling heat transfer process. The liquid helium is heavier than the vapor so it would prefer to rewet the surface; however, it is being maintained in the present condition by the high-temperature vapor film. The stability of the liquid-vapor interface is controlled by the behavior of surface wave oscillations. The wave can be assumed to have an amplitude η_0, and a wavelength λ. Surface waves must be damped for the interface to be stable, otherwise the amplitude would grow beyond the vapor film thickness and rewet the surface. It is therefore reasonable to construct a model based on the assumption that the stability of these waves controls the recovery process.

To be more quantitative about the above argument, assume that the stability of a surface wave is assured if the energy associated with surface tension exceeds the combination of the kinetic and potential energies in the wave. Both these terms are related to the amplitude of the surface oscillation η_0, as well as physical parameters

such as densities and surface tension. The kinetic and potential energies can be related as

$$\left.\frac{E}{\tilde{\lambda}}\right|_{KP} = \frac{g(\rho_l + \rho_v)\eta_0^2}{2} \tag{5.27}$$

where $\tilde{\lambda}$ is the wavelength of the surface oscillation and g is the gravitational acceleration. Similarly, the surface term can be written

$$\left.\frac{E}{\tilde{\lambda}}\right|_{\sigma} = \frac{1}{\tilde{\lambda}} \int_0^{\tilde{\lambda}} \Delta p \; \eta \; dx \tag{5.28}$$

where Δp is taken to be the pressure difference and η is a sinusoidal varying wave, that is $\eta = \eta_0 \sin 2\pi x/\tilde{\lambda}$. By integrating over the wavelength of the oscillation and using the approximation that the surface wave oscillation is small compared to $\tilde{\lambda}$, we can evaluate the integral (5.28):

$$\left.\frac{E}{\tilde{\lambda}}\right|_{\sigma} = \frac{4\pi\sigma\eta_0^2}{\tilde{\lambda}^2} \tag{5.29}$$

As already stated, the condition for stability demands that the surface energy exceed the dynamic energy. This leads to a condition on $\tilde{\lambda}$ by demanding that (5.29) not exceed (5.27), that is,

$$\tilde{\lambda} < 2\pi \left(\frac{2\sigma}{g(\rho_l - \rho_v)}\right)^{\frac{1}{2}} \tag{5.30}$$

For liquid helium near 4.2 K, (5.30) is obeyed for wavelengths less than about 2 mm, a dimension that must be comparable to a characteristic distance in the heat transfer problem, for example, the typical bubble dimension.

The minimum film boiling heat flux q_R can be understood by application of the Taylor instability theory to the film boiling heat transfer condition. Lienhard and Wong [24] and Zuber [18] used this analysis, identifying the breakdown of film boiling with the amplitude of the surface wave. The general relationship has one empirical constant and an explicit diameter dependence. For the special case of a flat plane, the correlation is simplified considerably:

$$q_R = 0.16 \; h_{\mathrm{fg}} \rho_v \left(\frac{g\sigma(\rho_l - \rho_v)}{(\rho_l + \rho_v)^2}\right)^{1/4} \tag{5.31}$$

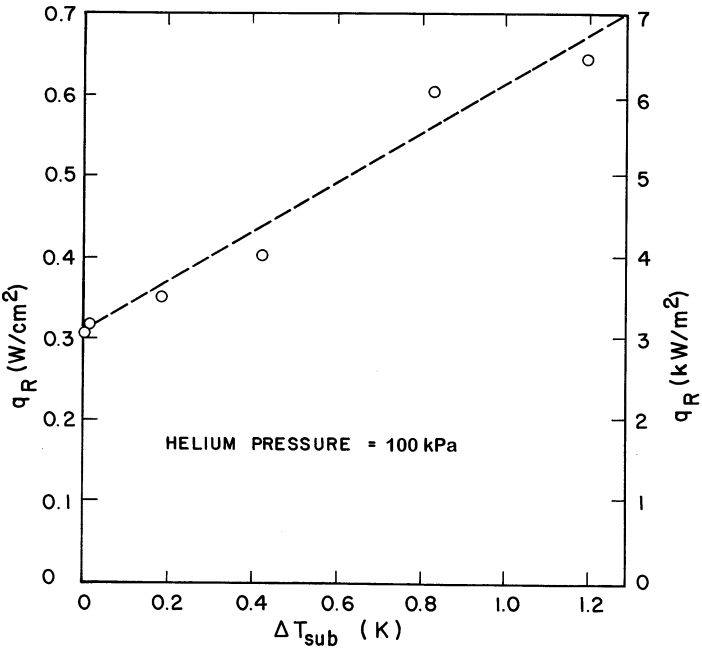

Fig. 5.14 Minimum film boiling heat flux for subcooled He I (from Ibrahim et al. [21])

It is interesting to compare (5.31) with (5.24), which predicts the peak heat flux q^*. Taking a ratio of these two expressions, the only important parameters turn out to be the relative densities of the liquid and vapor,

$$\frac{q_R}{q^*} = \left(\frac{\rho_v}{\rho_l + \rho_v}\right)^{1/2} \tag{5.32}$$

For example, considering liquid helium at 4.2 K, we find that the ratio described by (5.32) has a value of 0.35 at atmospheric pressure. Therefore, assuming $q^* = 8.5$ kW/m^2 as measured by Lyon [21] we find that (5.32) predicts a minimum film boiling heat flux of about 3 kW/m^2 in close agreement with experimental measurements.

The pressure dependence of the recovery heat flux is worth considering in light of the noted behavior of $q^*(p)$. As was observed in the previous section, subcooling increases q^* by about 50% per degree of ΔT_{sub} near atmospheric pressure. The subcooling effect on q_R is greater, as can be seen in Fig. 5.14. Note that q_R increases by about 90% per degree of ΔT_{sub} near atmospheric pressure [18]. The correlating relationships for the minimum film boiling heat flux predict this effect. Subcooling increases the ratio of the vapor to liquid density at saturation, which would result in an increase in q_R/q^*, as observed by experiment.

5.4.2 Heat Transfer Correlations

Once stable film boiling is established, it is of interest to be able to predict the magnitude of the film boiling heat transfer coefficient h_{fb} or the rate of heat flux q_{fb} for a given ΔT. Experimentally, h_{fb} has values that range over more than an order of magnitude between about 0.3 kW/m^2 K and nearly 10 kW/m^2 K, with the latter being achieved for fine wires with diameters of ~10 μm. The film boiling heat transfer also depends on fluid properties, being a function of the vapor and liquid densities, latent heat, and surface tension σ.

A number of semi-empirical correlations exist for prediction of heat transfer on the film boiling condition. The best known and perhaps most accepted of those is due to Breen and Westwater [25]. As in the case of the minimum film boiling heat flux q_R, these authors base their theory on the Taylor instability. They consider the wavelength condition given by (5.30) as the minimum required to release vapor bubbles into the bulk fluid from the boiling film. The correlation depends on the thermal properties of the fluid including specific heat and viscosity in addition to geometrical conditions such as the diameter of the heat transfer sample. The correlation relates the film boiling heat transfer coefficient to these quantities and a number of numerical constants:

$$h_{fb}\left(\frac{\sigma}{g(\rho_l-\rho_v)}\right)^{1/8}\left(\frac{\mu_v(T_s-T_b)}{k_v^3\rho_v(\rho_l-\rho_v)g\lambda'}\right)^{1/4} = 0.37+0.28\left(\frac{\sigma}{gD^2(\rho_l-\rho_v)}\right)^{1/2} \tag{5.33a}$$

where

$$\lambda' = \frac{\left[h_{fg}+0.34C_{p_v}(T_s-T_b)\right]^2}{h_{fg}} \tag{5.33b}$$

and represents an effective latent heat. T_s and T_b are the surface and bath temperatures, respectively. D is the diameter of the heater surface, which for film boiling has an effect on the heat transfer coefficient. For the special case where the heater diameter is greater than a few millimeters, the second term on the right-hand side is small and (5.33) may be approximated by the relationship

$$h_{fb} = 0.37\left(\frac{g(\rho_l-\rho_v)}{\sigma}\right)^{1/8}\left(\frac{k_v^3\rho_v(\rho_l-\rho_v)g\lambda'}{\mu_v(T_s-T_b)}\right)^{1/4} \tag{5.34}$$

Furthermore, in helium for moderate temperature differences, that is $\Delta T \gtrsim 5$ K, the second term in (5.33b) is dominant. Under these conditions, it can be shown easily that film boiling heat transfer $q \approx (T_s-T_b)^{3/4}$.

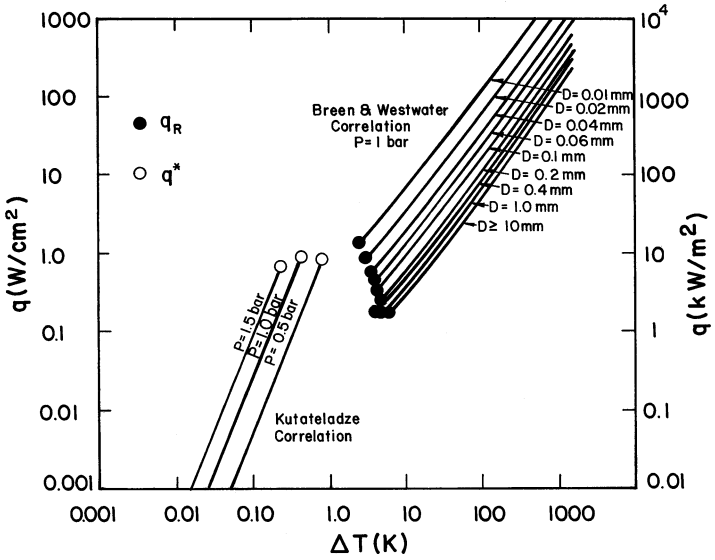

Fig. 5.15 A summary of pool boiling heat transfer correlations for He I

In summary, Fig. 5.15 is a plot of the various predictive relationships for nucleate and film boiling heat transfer [26]. A Comparison between data for nucleate boiling and minimum film boiling has been made already. For the case of film boiling heat transfer, the Breen–Westwater correlation is only moderately successful a predicting experimental data [19]. In general, film boiling heat transfer coefficients measured on fine wires has yielded consistently higher heat transfer coefficients than calculated from the above correlation.

5.5 Surface Effects

For the most part, heat transfer analysis for He I takes little account of the character of the surface. In steady-state heat transfer, the surface is discussed only qualitatively in terms of activated nucleation sites. Heat transfer correlations used to describe nucleate boiling and both critical heat fluxes make no attempt to include the surface character in their treatment. This clearly is a weakness in the theory for there are considerable surface-induced changes in these values. For transient heat transfer, a greater effort is put forth to include the surface physics. As was discussed in Sect. 5.6 Kapitza conductance, which is a solid-state interfacial result, must be included when attempting to understand the transient conduction heat transfer. Since surface characteristics are not generally included in engineering correlations, it is of interest to consider how variations in surface character affect experimental results.

There has not been a great deal of research conducted on surface-dependent heat transfer in He I [27–29]. In the case of steady-state investigations, surface

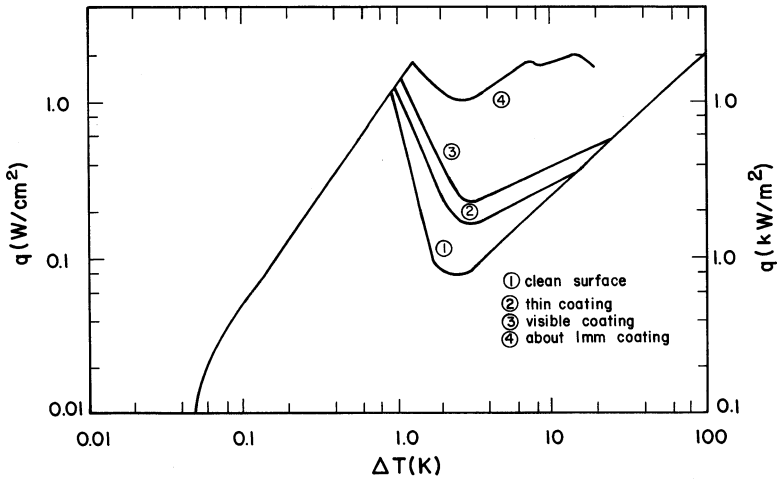

Fig. 5.16 Influence of H_2O coatings on pool boiling heat transfer (From Cummings and Smith [28])

roughness, as measured by the coarseness of the surface abrasive, strongly affects the nucleate boiling regime. This effect can be understood qualitatively by considering arguments of activated nucleation sites. The smoother the surface, the fewer active nucleation sites. Since activated sites induce convection, a polished surface should have a larger surface temperature difference ΔT_s for the same heat flux. This result has been observed by Boissin et al. [27]. Chemical treatment also has shown to affect the nucleate boiling regime [29]. These coatings combined with gross surface roughness have been employed to enhance cooling of composite conductors for large superconducting magnets.

Surface coatings also have been shown to affect the values of peak and recovery heat fluxes, q^* and q_R. The correlations used to describe these events in heat transfer do not include any of the surface characteristics. Cummings and Smith [28] have shown a clear increase in both the peak heat flux q^* and recovery value q_R with increased surface coatings. In their results shown in Fig. 5.16, the coatings were obtained by condensing H_2O crystals on the surface. Similar behavior was observed by Ogata and Nakayama [29] on chemically treated surfaces. These results are not understood in terms of heat transfer models, but they represent interesting and technically significant improvements.

5.6 Channel Heat Transfer

As a very interesting and technically significant special case of pool boiling heat transfer, consider the channel heat transfer problem described schematically in Fig. 5.17. A channel of width w is formed between a heat transfer surface and a

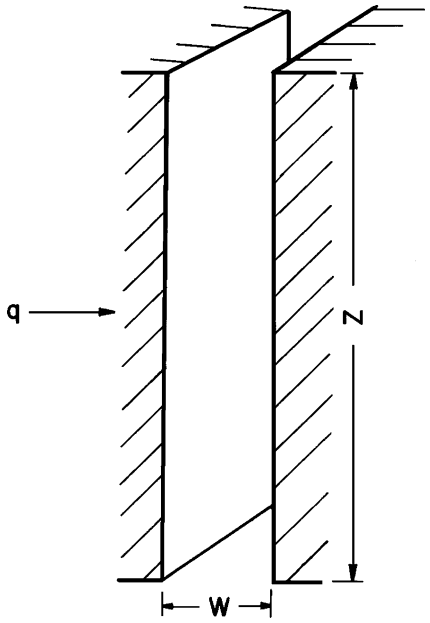

Fig. 5.17 Schematic of a heat transfer channel

second adjacent surface. The channel may be oriented at any angle between vertical and horizontal leading to variations of the heat transfer conditions. This particular problem is significant because it models an open cooling channel in a technical device such as a superconducting magnet. When heat is applied to the surface, the liquid can circulate owing to the thermosiphon effect where bubbles are transported under the influence of buoyancy forces, as discussed in Sect. 4.3.3.

If the channel is heated over its length, then the fluid accumulates vapor and the quality increases. If a low-quality fluid enters a heated tube section from below. Initially, nucleate boiling occurs at the fluid-tube interface. These bubbles are stripped from the wall and produce local bubbly flow. As the fluid continues through the tube more heat is transferred, increasing the vapor quality until slug flow and finally annular flow occur. This sequence of events is illustrated in Fig. 5.18.

Also, as the heat flux from the surface is increased, film boiling may eventually initiate at the top of the channel where the vapor quality is greatest. Because of the induced flow, the peak heat flux at the channel bottom can be quite large. The position dependence of the peak heat flux in one set of experiments is shown in Fig. 5.19. For vertically oriented surfaces in an open bath at 4.2 K, the peak heat flux is usually in the neighborhood of 6 kW/m^2. Therefore, the bottom of the channel has q^* quite close to that observed in an open bath. As the helium is vaporized and transported up the channel, the local peak heat flux is depressed. In the present example, the peak heat flux near the top approaches 3.4 kW/m^2, almost a 50% reduction.

Wilson [31] conducted one study of channel heat transfer in an experiment having variable height and width. The following set of observations were made.

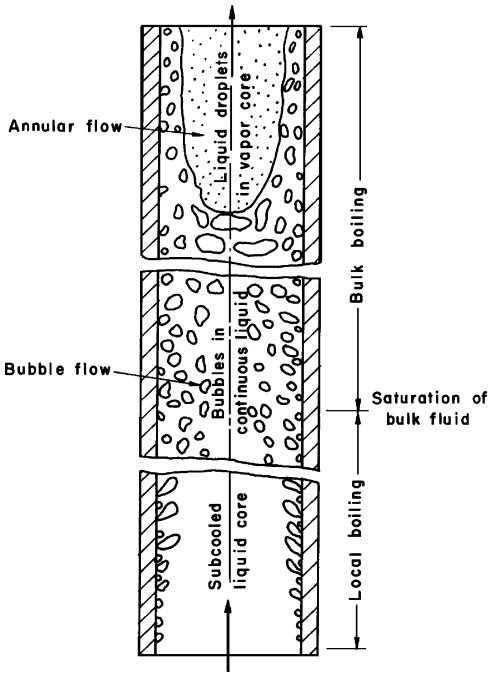

Fig. 5.18 Flow patterns in a vertical heated channel (From Tong [17])

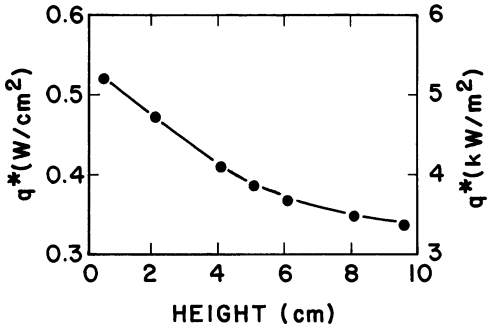

Fig. 5.19 Position dependence of the peak heat flux in a He I cooled channel (Lehangre et al. [30])

First, for small width w, the peak heat flux averaged over the entire surface area was directly proportional to the heat flux in the helium channel and therefore proportional to w. This suggests that the peak heat flux is governed by the bulk fluid flow. Second, for constant w, the peak heat flux was found to be inversely proportional to the square root of the channel height z. Based on the results as they depend on w, this indicates that the bulk heat flow varies as $z^{-1/2}$. Finally, it was found that for $w/z > 0.1$, the channel behaved effectively as an open bath with q^* approaching that of a vertically oriented surface, $q^* \sim 6$ kW/m^2.

Sydoriak and Roberts [32] derived a general relationship for frictionless homogeneous flow of a fluid in a evaporator, which Wilson applied to this channel heat

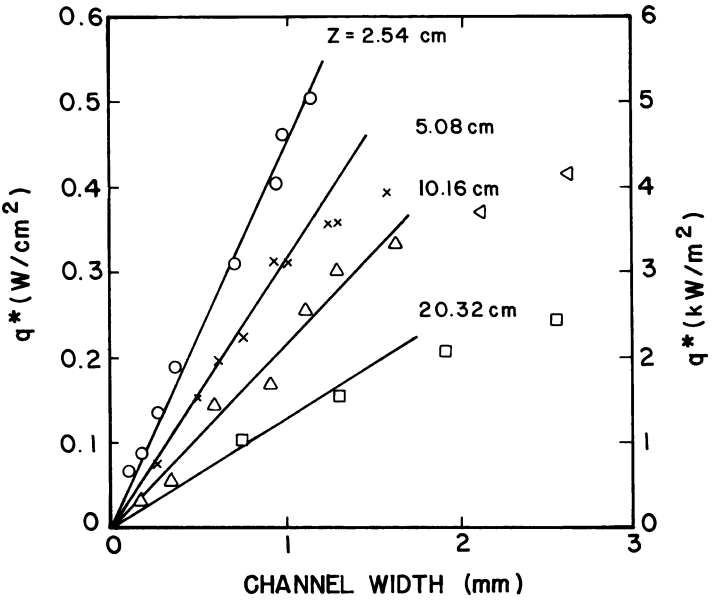

Fig. 5.20 Critical power versus channel width for He I heat transfer (From Wilson [31])

transfer problem. The prediction for the critical power per unit area of heated surface, Q^*/A_s, is given by

$$\frac{Q^*}{A_s} = \frac{w}{\sqrt{z}} \frac{h_{fg}\rho_l}{2} \left[\frac{g\tilde{q}}{\beta - 1} \left(1 - \frac{\ln[1 + \tilde{q}(\beta - 1)]}{\tilde{q}(\beta - 1)} \right) \right]^{1/2} \tag{5.35}$$

where $\beta = \rho_l/\rho_v$ and $\tilde{q}$ is the "critical quality" – the mass ratio of vapor to total (liquid plus vapor) at the channel top when film boiling initiates. This last quantity must be determined empirically although in general it should be a scalable function for different fluids.

A plot of the critical power versus channel width w for different channel lengths z should give a linear plot from which the proportionality function $Q^* z^{1/2}/wA_s$ can be determined. Such a plot is displayed in Fig. 5.20 for four different channel heights. The linear plot obtained yields a critical quality $\tilde{q}$ ranging from 0.33 to 0.26 in the case of the largest channel. Thus, for calculations, (5.35) should be a reasonable approximation for Q^*/A_s assuming a constant value for $\tilde{q} \approx 0.3$.

One difficulty with the above described analysis is that it does not naturally lead into the open bath limit for $w/z > 0.1$. In an effort to develop a more general equation for channel heat transfer, Lehangre et al. [30] suggested a correlation based on a series of experiments of different configuration:

$$\frac{Q^*}{A_s} = \frac{10}{1.7 + 0.125(z/D_h)^{0.88}} \tag{5.36}$$

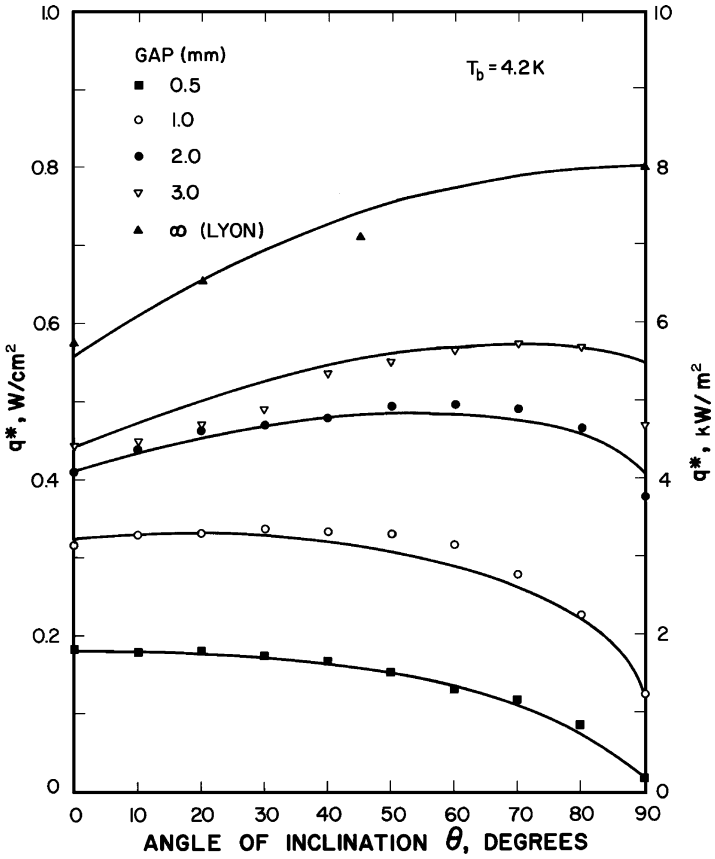

Fig. 5.21 Variation of the peak heat flux with channel orientation and width at 4.2 K. Channel is 127 mm in length [33]

where Q^*/A_s is in kW/m^2. The quantity D_h is the hydraulic diameter which is equal to four times the ratio of the flow cross section to the heated perimeter. Equation (5.36) has the appropriate limit for w/z large; however, for channels other than in the vertical orientation it is not applicable.

Chen and Van Sciver [33] noted that for wide channels the maximum heat flux q^* should correlate with the open bath pool boiling results by Lyon [20] (see Fig. 5.11). The results of these experiments are shown in Fig. 5.21, where the angle θ is measured from the vertical orientation. There are two physical processes that lead to the observed angular dependence of q^*. The first process is nucleate boiling associated with movement of vapor bubbles normal to the heated surface. This effect, which is maximum at an angle of 90°, can be assumed to control the heat transfer process for large w. The other process is associated with the natural circulation of the heated fluid, where the movement is parallel to the heated surface. The natural circulation process is a maximum at $\theta = 0°$ and should

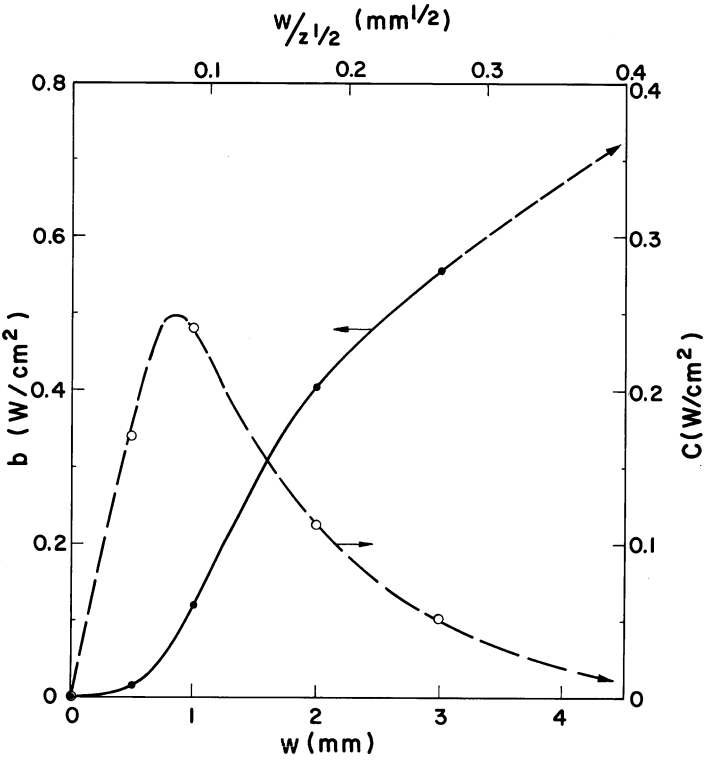

Fig. 5.22 Parameters used to fit the variation of q^* with θ in (5.37)

dominate the heat transfer in the limit of small w. The combination of these two processes is necessary to describe the variation of q^* with θ and w. In particular, one would expect the maximum value of q^* to vary continuously between 0° and 90° as the channel width is increased.

A general correlation used to describe the angle and width dependencies of q^* is of the form

$$q* = b \ \sin\left(\frac{\theta + 90^\circ}{2}\right) + c(\cos\theta)^{1/2} \tag{5.37}$$

where b and c are adjustable parameters, which should be functions of w only. The width dependence of these parameters is shown in Fig. 5.22. The basis for (5.37) is purely empirical evidence. The first term is used to describe the nucleate boiling heat transfer process. The angular dependence is in reasonable agreement with Lyon's pool boiling data. The second term represents the natural circulation process. The $(\cos\theta)^{1/2}$ angular dependence not only fits the experimental data for small w but is consistent with the Wilson's correlation which predicts $q^* \propto g^{1/2}$.

As a final comment on channel heat transfer, the steady-state conditions as described above generally take a considerable time to become established. This is because the natural circulation requires a substantial temperature rise and vapor production before it is fully established. Naturally, the time to reach steady state depends on the magnitude of Q^*/A_s, but for significant heat fluxes, of the order of 1 kW/m^2, this characteristic time can be as much as a second. The existence of a characteristic time for the development of steady-state heat transfer has strong impact on technical applications. Since many systems experience transient heat transfer processes, which are on the millisecond time scale, it is important to appreciate that these heat transfer processes are far from steady state.

5.7 Forced Convection Heat Transfer

The process of heat transfer to forced flow helium is closely tied to the dynamics of the flow states, a topic covered in Sect. 4.1. In the present section, we would like to extend that discussion to include solutions to the energy equation that can be used to treat convective transfer.

5.7.1 General Considerations

The problem of interest involves heat transfer from a surface exposed to flowing liquid helium. If the predominant flow is in the x-direction and the heat transfer is in the direction perpendicular to that of the flow (y-direction), the energy equation may be simplified by using the thermal boundary layer approximation,

$$\frac{\partial T}{\partial y} \gg \frac{\partial T}{\partial x}$$

which is analogous to that assumed for the velocity profile. Assuming for simplicity that the fluid possesses constant properties ρ, C_p, k, and μ, we obtain the corresponding thermal boundary layer equation [2],

$$u\frac{\partial T}{\partial x} + v\frac{\partial T}{\partial y} = \alpha\frac{\partial^2 T}{\partial y^2} + \frac{\mu}{\rho C_p}\left(\frac{\partial u}{\partial y}\right)^2 \tag{5.38}$$

where $\alpha = k/\rho C_p$ is the thermal diffusivity. The first term on the right-hand side of (5.38) represents thermal diffusion. For most fluids of interest in cryogenics, this term is not large and can be neglected.

By suitable normalization, (5.38) can be shown to lead to the definition of the Nusselt number as a general function of Reynolds number and Prandtl number, that is,

$$Nu = \mathrm{f}(\mathrm{Re}_D, \mathrm{Pr}) \tag{5.39}$$

For internal flow, the Nusselt number is defined as:

$$Nu_{D_h} = \frac{hD_h}{k_f} \tag{5.40}$$

where k is a suitably averaged fluid thermal conductivity. In fact, (5.40) is general and not dependent on the boundary layer approximation. Most empirical heat transfer correlations are constructed in a form consistent with (5.39).

5.7.2 Heat Transfer Correlations

Investigations of heat transfer to forced convection helium have shown that traditional engineering correlations are best at describing the data. Results of analysis of the thermal boundary layer indicate that the average Nusselt number should be couched in a form consistent with (5.39). As an aside, be aware that the local heat transfer coefficient can be a considerable function of temperature and therefore varies along the length of the tube. The local heat transfer coefficient is also defined in terms of the local mean fluid temperature,

$$h = \frac{q}{T_s - T_m} \tag{5.41}$$

where T_m is obtained by taking an appropriate average across the channel.

There are numerous single-phase fluid heat transfer correlations for internal flow. Several important factors must be considered when selecting a correlation to apply to a particular system. First, determine whether the fluid is in the laminar or turbulent flow regime. The critical Reynolds number for single-phase internal flow is around 1,200. Second, determine whether the entry region has significant impact on either the hydrodynamics or temperature development. This requirement demands fairly large L/D ratios. Helium has a Prandtl number of the order of unity, so it is expected that these developments will occur almost simultaneously. Finally, once the conditions of flow are established, it is necessary to select among several possible correlations dependent on whether the range of parameters is appropriate for the particular empirical fit.

In fully developed laminar internal flow, there are analytic solutions to the thermal boundary layer equations of the form,

$$Nu_D = \text{constant} \tag{5.42}$$

Where the constant depends on boundary conditions being 4.36 for constant heat flux boundary conditions and 3.66 for constant wall temperature boundary conditions. However, for most helium cryogenic problems, laminar flow almost never occurs. One exception involves flow within porous media a topic discussed below.

For turbulent flows, all engineering correlations are of the form of (5.39) where the average Nusselt number is a function of the fluid Reynolds and Prandtl numbers. In this regime, a number of good correlations exist for single-phase turbulent heat transfer. The Dittos–Boelter expression is perhaps the most common such heat transfer correlation [2],

$$\overline{\mathrm{Nu}} = 0.023 \mathrm{Re}_D^{4/5} \mathrm{Pr}^{2/5} \tag{5.43}$$

where $\overline{\mathrm{Nu}}$ represents the average Nusselt number over the tube length. Correct application of this expression demands consideration of the temperature dependence of the fluid properties. The appropriate properties must be evaluated at the film temperature T_f, defined by

$$T_f = \frac{T_s + T_m}{2} \tag{5.44}$$

which is a simple average between the surface and mean fluid temperatures. The Dittus-Boelter correlation has been used quite effectively for a variety of cryogenic heat transfer problems [34].

In the case of supercritical helium, Giarratano et al. [35] have suggested that a prefactor of 0.022 gives a better fit to their data with a standard deviation of

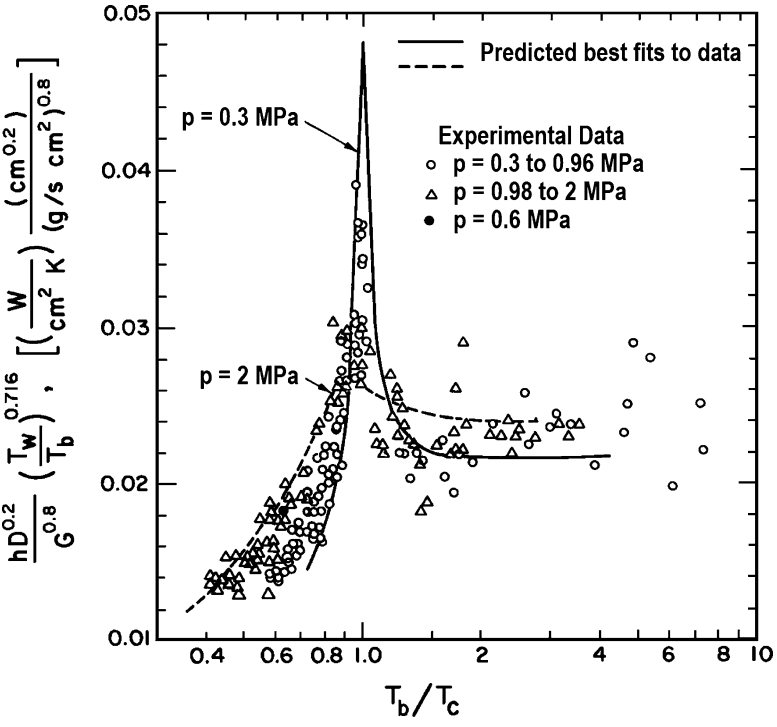

Fig. 5.23 Experimental and predicted heat transfer results for supercritical helium using (5.45) (From Giarratano et al. [35])

14.8% obtained between experimental results and correlation. An improved fit to the experimental data was achieved by use of a slightly modified correlation of the form [13]

$$\mathrm{Nu} = 0.0259\ \mathrm{Re}_D^{4/5}\mathrm{Pr}^{2/5}\left(\frac{T_s}{T_m}\right)^{-0.716} \tag{5.45}$$

where now explicit temperature variation of the properties is taken into account by the last factor. The relationship given by (5.45) correlated to a standard deviation of 8.3% with several sources of experimental data. A normalized form of this comparison is shown in Fig. 5.23, where the heat transfer coefficient is plotted against reduced temperature T_b/T_c, where T_c is the critical temperature.

In general, heat transfer to fully developed forced flow single phase helium can be assumed to have a well-established engineering basis. Since the fluid is single phase, its hydrodynamics can be evaluated in terms of the Navier–Stokes equation of motion including compressibility factors. This problem is quite difficult owing to the variability of physical properties with pressure and temperature. Consequently, its solution requires numerical integration of complicated nonlinear equations. Be aware that this particular problem represents only one special case of forced flow helium. Other problems concerning two-phase flow and transient effects, subjects of subsequent sections in this chapter, are more complex in physical nature.

Example 5.2

Consider a thin walled copper tube of diameter 10 mm carrying liquid helium at 1 g/s and subject to a surface heat flux of 0.1 kW/m^2. The helium enters the tube at 4.2 K and 0.2 MPa. Calculate the tube wall temperature.

At the given temperature and pressure, the properties of helium are: $\rho = 125$ kg/m^3; $\mu = 3 \times 10^{-6}$ Pa s; $k_f = 0.018$ W/m K; Pr = 0.792
For the given flow conditions, the Reynolds number is,

$$\mathrm{Re}_D = \frac{\rho u D}{\mu} = \frac{4\dot{m}}{\pi \mu D} = 42,441$$

Using the Dittus Boelter correlation,

$$\overline{\mathrm{Nu}} = 0.023\,\mathrm{Re}_D^{4/5}\mathrm{Pr}^{2/5} = 105$$

And the heat transfer coefficient,

$$h = \frac{Nu * k_f}{D} = 190\,\mathrm{W/m^2\,K}$$

For a surface heat flux of 1 kW/m^2, this means that the tube surface is 0.526 K above that of the fluid or 4.726 K.

5.7.3 Two Phase Flow Heat Transfer

Two-phase flow in subcritical helium is a complex problem as was discussed in section 4.3; however, the difficulty in understanding the processes involved in two phase flow increases significantly when heat transfer is included. In addition to mass flow rate, vapor quality, and void fraction determining the flow conditions, the effect of heat flux into the fluid also must be considered. In particular, heat transfer can lead to rapid variations of vapor quality along the tube section.

Experimental investigations of two-phase flow heat transfer have been carried out by de La Harpe et al. [36] and Johannes [37]. These studies consist principally of forced flow helium at 4.2 K confined to a tube of a few mm ID with temperature and pressure probes necessary to determine the heat transfer coefficient and critical heat flux for boiling. The latter quantity is strongly geometry dependent and cannot be generalized easily in other systems.

The heat transfer coefficient obtained for two-phase helium is discussed best in terms of classical correlating relationships. The approach is to determine first the Nusselt number corresponding to the Dittus–Boelter equation for the liquid flow only, that is,

$$\mathrm{Nu}_l = 0.023(\mathrm{Re}_l)^{0.8}(\mathrm{Pr}_l)^{0.4}(1-\chi)^{0.8} \tag{5.46}$$

where the last multiplier is to indicate the contribution of only the liquid. Note that $\mathrm{Nu}_l = hD_h/k_l$, where k_l is the liquid thermal conductivity. Measurements of the two-phase heat transfer coefficient have shown that the actual Nusselt number normalized to (5.46) can be correlated to the Lockhart–Martinelli parameter, χ_{tt}, as

$$\frac{Nu_{\exp}}{Nu_l} = A\chi_{tt}^{-n} \tag{5.47}$$

where χ_{tt} is discussed in Chap. 4 and repeated here for convenience,

$$\chi_{tt}^2 = \frac{(dp/dx)_v}{(dp/dx)_l} \tag{4.37}$$

The best fit to the data of Johannes [37] of the form of (5.47) are displayed in Fig. 5.24 for which the appropriate values are $A = 5.40$ and $n = 0.385$. Results of de La Harpe [36] are also displayed as the dashed line in the figure with agreement in form to the data of Johannes, although possessing substantially different values for the coefficient A. Although the above correlation seems appropriate for low to

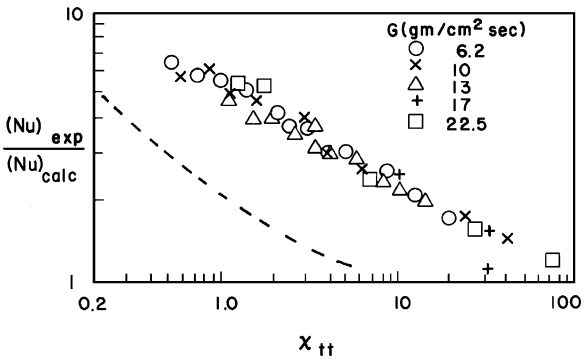

Fig. 5.24 Two-phase heat transfer correlation for helium (From Johannes [37]). The *dashed line* is a comparison to previous measurements of de La Harpe et al. [36]

moderate values of the Lockhart–Martinelli parameter, in the limit of large χ_{tt}, which occurs for small vapor quality, the ratio given by (5.47) must approach unity. Therefore, to be universally applicable the correlation should reflect this fact.

Two-phase heat transfer as with two-phase flow is a complex process which is very difficult to understand fully. If faced with a problem in this area, the best approach is to apply one of the accepted correlations. However, these calculations are only approximate and should be used only as a guide. If greater accuracy is required, experimental modeling is the required approach.

5.8 Transient Heat Transfer

In the previous sections, it was assumed that the heat transfer process had been underway for sufficient time that steady-state conditions existed. The characteristic time required for the steady state to be achieved is equivalent to the time required for convection to become fully established. For nucleate boiling, enough heat must be transferred to vaporize bubbles and allow them to detach. In film boiling the characteristic time is associated with sufficient energy flux to vaporize a layer of helium. This can be represented approximately by

$$\Delta t \approx \frac{\rho h_{fg} \delta}{q} \tag{5.48}$$

where δ is the vapor film thickness. For an order-of-magnitude analysis assume that $\delta \approx 10\ \mu$m. Using the physical quantities for He I at 4.2 K, 0.1 MPa, (5.48) predicts $\Delta t \approx 3/q$ ms, where q is in W/cm^2. For a heat flux of a few W/cm^2, the steady-state conditions are not established until well in excess of a few milliseconds. For times shorter than this value, the heat transfer processes are governed by nonconvective mechanisms such as conduction and radiation.

It is of considerable importance to be able to understand transient heat transfer in liquid helium. Transient heat transfer is fundamental to the analysis of a number of problems including the stability of superconducting magnets. There are several

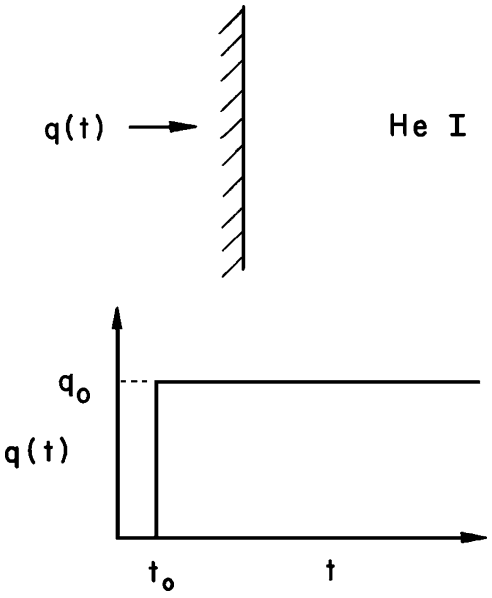

Fig. 5.25 Schematic representation of the transient heat transfer process

aspects to this problem which are worth noting at the beginning. First, for very short times, that is, $\Delta t < 1$ ms, heat transfer processes turn out to be controlled by physical mechanisms similar to those developed for the case of He II, that is, Kapitza conductance. Second, the transition between the region of heat transfer space governed by conduction and that which resembles the steady-state process is important. This transition occurs on time scales consistent with the rough calculation in above. There are several parameters that are associated with transient heat transfer. (1) the peak heat flux $q^*(t)$ or critical energy $\Delta E^* = q^* \Delta t^*$; (2) the interfacial temperature difference ΔT_s; and (3) the effective heat transfer coefficient h. These parameters are governed primarily by the physical properties of helium and the rate of heat transfer.

The various regimes of transient heat transfer can be described best in terms of an idealized experiment, which in fact is not very different from actual experiments performed to investigate the problem. Imagine a solid heat transfer surface as shown in Fig. 5.25, which in this particular case is oriented vertically. Recall that the peak steady-state heat flux for this configuration is in the neighborhood of 6 kW/m^2. In this experimental configuration, a step function heat flux q_0 beginning at t_0 is applied to the sample. With suitable thermometry, which must have a response time faster than a millisecond, the surface temperature is recorded as it varies with time following the initiation of heat transfer.

As an example of the kind of data collected from this type of experiment, measurements by Steward [38] are shown in Fig. 5.26. In this particular case, the heat transfer surface is a thin carbon film which is both heater and thermometer.

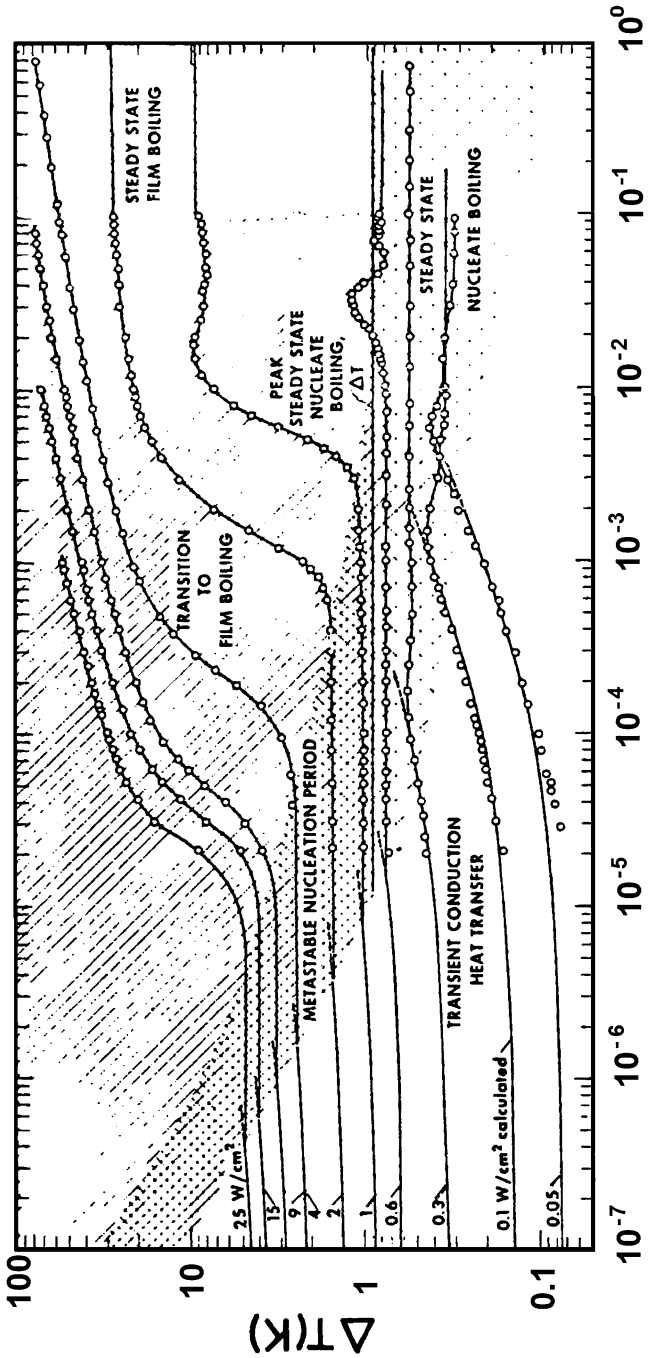

Fig. 5.26 Transient heat transfer to saturated liquid He I from a vertically oriented heater (From Steward [38])

Note that for very short times, the surface temperature rise is not large, although it is an increasing function of heat flux. This short time regime, which is generally much less than 1 ms, is controlled by transient conduction mechanisms. As time progresses, the nucleation of convective mechanisms begins. For low heat fluxes, the heat transfer process eventually transforms to steady-state nucleate boiling. At high heat fluxes, that is, $q > 10$ kW/m^2 (1 W/cm^2), there is a transition to the film boiling state. This latter transition has associated with it an increase in ΔT_s of about an order of magnitude, consistent with the steady-state film boiling heat transfer characteristics. In the steady-state regime, the temperature differences presumably can be described in terms of the correlations introduced in previous sections of this chapter. There are, however, two effects in these data which need further discussion: (1) the size of the heat transfer coefficient in the transient conduction regime and (2) the time associated with the transition to steady-state heat transfer mechanisms.

5.8.1 Surface Temperature Difference

Consider first the problem of the surface temperature difference during transient conduction. Since this mechanism is conduction dominated, it should be possible to understand in terms of diffusion theory. Returning to Fig. 5.25, imagine a steady heat flux through the interface. There are two potential contributors to the associated temperature difference. First, there is a thin fluid layer of thickness δ into which the heat diffuses. The temperature difference across the layer, defined as ΔT_f, should be determined exclusively by heat diffusion in the bulk fluid. Second, there is an interfacial temperature difference that is due to the mismatch of phonon heat transport between the two media. This mechanism, referred to as Kapitza conductance, which will be discussed in Chap. 7. It is a truly interfacial process occurring within a few atomic layers of the solid-helium boundary. The temperature difference due to Kapitza conductance is given the designation ΔT_k.

To evaluate the heat diffusion temperature difference, it is necessary to solve the heat diffusion equation with the proper set of boundary conditions. In one dimension this equation can be written

$$\frac{\partial^2 \Delta T_f}{\partial x^2} = \frac{1}{D}\frac{\partial \Delta T_f}{\partial t} \tag{5.49}$$

given a number of simplifying assumptions. In particular, it is assumed that the thermal diffusivity, $D = k/\rho C$, is a constant independent of temperature or position. Of course, this is not a particularly good assumption for liquid helium, however, it simplifies the model considerably to do so. Furthermore, it is assumed that the solid does not play a major role in the heat diffusion. This approximation has a negligible

effect if the heat transfer surface has small heat capacity. The boundary conditions which are applied to solve (5.49) include

$$\Delta T_f(x,0) = 0 \tag{5.50a}$$

$$\Delta T_f(\infty,t) = 0 \tag{5.50b}$$

and

$$q = -k\frac{\partial \Delta T_f}{\partial x}\bigg|_{x=0} \tag{5.50c}$$

The last condition, being consistent with the constant flux assumption at the interface, is true only if the heat capacity of the heat transfer surface is neglected. The general solution to (5.49) with the above set of boundary conditions leads to

$$\Delta T_f = \frac{q}{k}\left[2\left(\frac{Dt}{\pi}\right)^{1/2}\exp\left(\frac{-x^2}{4\,Dt}\right) - x\ \mathrm{erfc}\left(\frac{x}{2(Dt)^{1/2}}\right)\right] \tag{5.51}$$

where x is the dimension measured into the fluid. At the solid-fluid interface, x = 0, the relationship simplifies considerably to yield

$$\Delta T_f = \frac{2q}{\sqrt{\pi}}\left(\frac{t}{\rho k C}\right)^{1/2} \tag{5.52}$$

For example, consider liquid helium at 4.2 K subjected to a heat flux of 1 W/cm^2 for a time of 10 μs, which is in the transient conduction regime. These conditions lead to a computed value for ΔT_f of about 0.3 K, which is approximately equal to the superheat required to produce homogeneous nucleation computed in Sect. 5.3. It is also worth noting that $\Delta T_f \approx 0.3$ K corresponds to about 1/3 the measured ΔT in Fig. 5.26.

The second mechanism which can lead to an interfacial temperature difference during transient heat transfer is due to Kapitza conductance. The temperature dependence of the Kapitza conductance is understood but the absolute value of the heat transfer coefficient is not predictable. Assuming. that the mechanisms are the same independent of whether the fluid is He I or He II, it is reasonable to write

$$\Delta T_K \simeq \frac{q}{h_K} \tag{5.53a}$$

where $h_K \simeq AT^3$, consistent with experimental measurements of Kapitza conductance. For a copper surface below T_λ, A has been measured to have values around 0.1 W/cm^2·K^4, but with considerable uncertainty. Using this value for $T_b = 4.2$ K in He I, the interfacial temperature difference due to Kapitza conductance should

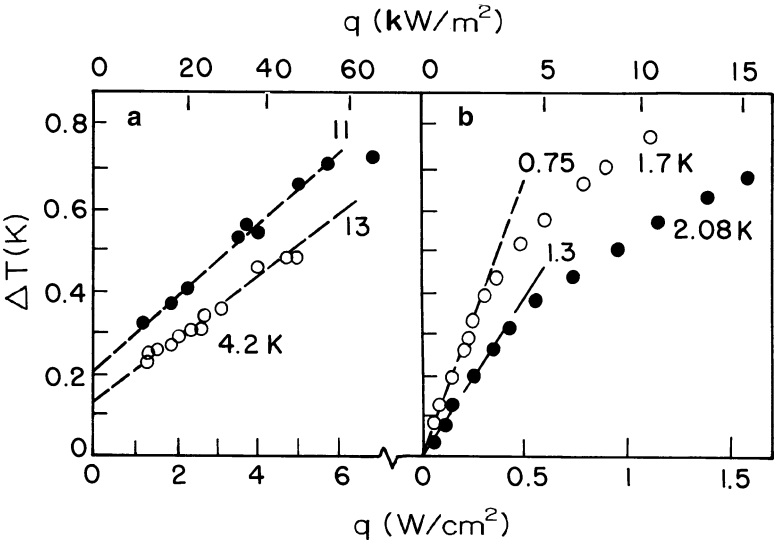

Fig. 5.27 Surface temperature difference for copper samples versus heat flux: (**a**) He I at 4.2 K and (**b**) He II at 1.8 K. Numbers on the straight lines refer to h values in W/cm·K (From Schmidt [39])

vary as $\Delta T_K \approx 0.13\ q$. Therefore, for copper, the Kapitza temperature difference would be the same order as but somewhat smaller than that due to transient conduction except at very short times, $t \lesssim 1\ \mu$s.

On a very short time scale the heat flux dependence of the heat transfer coefficient in He I generally obeys the processes described above. Plotted in Fig. 5.27 is the surface temperature difference for copper samples measured in He I compared to that for He II [39]. On the right-hand side, the figure shows a typical ΔT_s versus q dependence observed for He II. Initially, there is a linear region; however, as the heat flux increases a considerable deviation from linearity occurs because the actual heat transfer varies as $T_s^n - T_b^n$ where $n \approx 3$. A somewhat different effect is observed for the case of He I. Here the dependence of ΔT versus q for high heat fluxes is almost linear, indicating a constant heat transfer coefficient. However, at low heat fluxes the surface temperature does not appear to extrapolate to the origin, indicating some failure in the linear modeling over the regime for which the linear relationship holds. The Kapitza conductance appears to obey the cubic temperature dependence.

In principle, the temperature difference corresponding to a transient heat transfer event can be determined by a series summation of the two contributions described above. It follows that

$$\Delta T_s = \Delta T_K + \Delta T_f \tag{5.53b}$$

where, dependent on the choice of surface materials, one term can dominate the process. For comparison with theory, it should be possible to separate the two quantities in (5.53b) based on their different time dependencies.

5.8.2 Transition to Film Boiling

The other fundamental question related to transient heat transfer concerns the onset of film boiling. For a given heat flux q^*, the time required to reach the film boiling state, Δt^*, is of interest. This quantity establishes the limits to which enhanced heat transfer due to transient conduction can be credited in a heat transfer problem. The problem is understandable by means of a rather simple picture. Given that the transition is associated with the formation of a vapor film, a critical energy is defined as that required to vaporize the helium adjacent to the heat transfer surface and create the film.

A more quantitative model can be developed by assuming that ΔE^* is the energy needed to vaporize a layer of thickness δ, which corresponds to the diffusion length. Employing the transient diffusion model, we note that the diffusion length can be approximated by

$$\delta = \frac{\pi}{2}(Dt)^{1/2} \tag{5.54}$$

where again D is the thermal diffusivity. On a unit area basis, the critical energy is written

$$\Delta E^* = q^* \Delta t^* = \delta h_{fg} \tag{5.55}$$

where h_{fg} is the heat of vaporization of liquid helium at the existing temperature and pressure conditions. Substituting (5.54) into (5.55), we find that the heat flux needed to achieve film boiling is given by

$$q^* = \frac{\pi}{2}\rho h_{fg}\left(\frac{k}{\rho C\ \Delta t^*}\right)^{1/2} \tag{5.56}$$

which for values associated with He I at 4.2 K, 1 bar, simplifies to

$$q^* = 0.07\left(\Delta t^*\right)^{-1/2} \tag{5.57}$$

where q^* is in W/cm^2 and Δt^* is in seconds. Note that this correlating equation does not contain any adjustable parameters. Plotted in Fig. 5.28 are numerous experimentally determined values for q^* along with the simple diffusion model fit given by (5.57). The correspondence is surprisingly good, which supports the basic physical ingredients to the critical energy analysis included in the simple model. A more precise empirical fit has been suggested [39]:

$$q* = 0.127\left(\Delta t^*\right)^{-0.4} \tag{5.58}$$

This form is seen to agree with the data, particularly in the sub-millisecond regime.

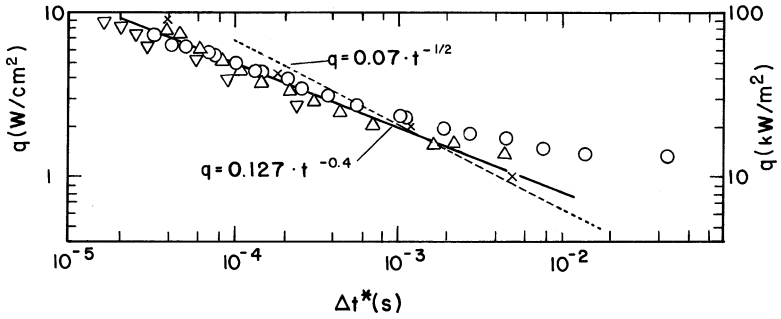

Fig. 5.28 Heat flux versus time for transition to film boiling (As compiled by Schmidt [39])

As a final comment, the transient heat transfer analysis given above is oversimplified. Only two problems have been discussed, the heat transfer coefficient in the conduction regime and the critical energy for the onset of film boiling. In between these two regimes is the transition to film boiling including the dynamics of nucleation and the creation of the vapor film. These are considerably more complex phenomena than can be discussed here. This regime has been analyzed to some extent by Steward [38] by evaluating the orientation and pressure dependence to the type of data displayed in Fig. 5.26. The observations gleaned from this work are more qualitative but suggest that the transition regime is at least in part controlled by conventional heat transfer phenomena. Further work is required to grasp more fully the various aspects of the transient heat transfer problem.

Questions

1. For pool boiling liquids, why is the heat transfer coefficient in nucleate boiling higher than the heat transfer coefficient in free convection?
2. In pool boiling heat transfer, q* depends on surface orientation. Discuss in terms of the bubble formation and detachment picture, why surface orientation should make a difference and what would be the expected trend. $q^* > 0$ in pool boiling heat transfer even for the face down condition, $\Theta = 180$. Why?
3. Discuss the trends in the He I nucleate boiling curve (Fig. 5.9). Is there any correlation with surface roughness? If so, how would this trend be explained in terms of bubble nucleation theory?

Problems

1. Calculate the critical radius of a vapor nucleus in He I at 4.2 and 2.5 K under saturated vapor pressure. Assume a reaction rate of 1 $cm^{-3} \cdot s^{-1}$. Compare this value with the radius determined from (5.15). Estimate the reaction rate consistent with the radius determined from (5.15).

2. Determine the surface temperature at which the maximum in the peak nucleate boiling heat flux q^* in saturated He I occurs. What would be the change in this value if the system we pressurized to $p = 200$ kPa?
3. A vertically oriented, circular cross section channel containing He I at 4.2 K is exposed to a heat flux which varies linearly with height:

$$Q(z) = Q_m\left(\frac{z}{H}\right)$$

where H is the total channel height. Determine as a function *of* Q_m the position where the peak heat flux is first exceeded.
4. The Schmidt model for the transition to film boiling during transient heat transfer, (5.56), implies that the transition occurs when the surface reaches a temperature that is a constant for a given helium bath. Find an expression for the critical surface temperature in the Schmidt model and calculate its value for a saturated He I bath at 4.2 K. Compare your answer with the homogeneous nucleation temperature for the same conditions.
5. Consider film boiling heat transfer from a flat plate in He I. Calculate the plate surface temperature at the minimum film boiling heat flux q_R.
6. A heat exchanger cools supercritical helium at 1 MPa from 6 to 4.5 K. The design consists of a tube immersed in the saturated bath of He I at 4.2 K. Determine the length and diameter of the tube consistent with the following specification: $\dot{m} = 1$ g/s and $\Delta p = 0.01$ MPa . For simplicity assume isothermal conditions on the external surface of the tube.
7. A pool boiling cooled superconducting magnet uses a monolithic conductor 30 mm wide and 3 mm thick. The conductor is cooled on one face by liquid helium in the gap between adjacent turns of 0.5 mm. Calculate the peak heat flux for this conductor in helium at T = 4.6 K, 0.14 MPa, if the wide surface is vertical. How would this result change if the conductor were exposed to an open bath of liquid helium instead of a narrow channel?

References

1. See for example, E. R. G. Eckert and R. M. Drake, *Analysis of Heat and Mass Transfer*, McGraw–Hill, New York, 1972.
2. See for example, F. P. Incropera and D. P. Dewitt, *Fundamentals of Heat Transfer*, Wiley, New York, 1981.
3. J. A. Whitehead, *Survey of Hydrodynamic Instabilities, in Fluctuations, Instabilities and Phase Transitions*, Tormad Riste (Ed.), pp. 153–180, Plenum Press, New York, 1975.
4. R P. Behringer and G. Ahlers, Heat Transport and Temporal Evolution of Fluid Flow Near the Rayleigh-Bénard Instability in Cylindrical Containers, *J. Fluid Mech.* **125**, 219 (1982).
5. F. Irie, G. Kippling, K. Uders, T. Matsushita, U. Ruppert, and M. Takeo, Heat Transfer to Helium in the Near Critical Region, *Adv. Cryog. Eng.* **23**, 326 (1978).
6. M. A. Hilal, R. W. Boom, and M. M. El-Wakil, An Experimental Investigation of Free Convection Heat Transfer in Supercritical Helium, *Int. J. Heat Mass Transfer* **23**, 697 (1980).

7. G. Kippling and K. Kutzner, in *Pure and Applied Cryogenics*, **Vol. 6**, pp. 97–107, Pergamon Press, Oxford, 1967.
8. M. A. Hilal, Analytical Study of Laminar Free Convection Heat Transfer to Supercritical Helium, *Cryogenics* **18**, 545 (1978).
9. D. N. Sinha, J. S. Semura, and L. C. Brodie, Homogeneous Nucleation in 4He: A Corresponding States Analysis, *Phys. Rev.* **A 26**, 1048 (1982).
10. J. Frenkel, *Kinetic Theory of Liquids*, Chap. 7, Dover, New York, 1955.
11. E. Flint and J. Van Cleve, Heat Transport to He I from Polished Silicon Surface, *Adv. Cryog. Eng.* **27**, 283 (1982).
12. Y. Y. Hsu and R. W. Graham, An Analytical and Experimental Study of the Thermal Boundary Layer and the Ebullition Cycle in Nucleate Boiling, *NASA TN D-594* (1961).
13. W. B. Bald, Cryogenic Heat Transfer Research at Oxford, Part I, Nucleate Pool Boiling, *Cryogenics* **13**, 457 (1973).
14. S. S. Kutateladze, *Statistical Science & Technical Publications of Literature on Machinery*, Atomic Energy Commission Translation 3770, Technical Information Services, Oak Ridge, TN (1949), 1952.
15. W. B. Bald and T. V. Wang, The Nucleate Pool Boiling Dilemma, *Cryogenics* **16**, 314 (1976).
16. C. Schmidt, Review of Steady State and Transient Heat Transfer in Pool Boiling Helium I, in *Stability of Superconductors*, pp. 17–32, International Institute of Refrigeration Commission A 1/2, Saclay, France, 1981.
17. L. S. Tong, *Boiling Heat Transfer and Two Phase Flow*, Chap. 2, Wiley, New York, 1965.
18. N. Zuber, M. Tribes, and J. W. Westwater, The Hydrodynamic Crisis in Pool Boiling of Saturated and Subcooled Liquids, in *International Development in Heat Transfer*, Part. II, pp. 230–234, ASME, New York, 1961.
19. R. V. Smith, Review of Heat Transfer to Helium I, *Cryogenics* **9**, 11 (1969).
20. D. N. Lyon, Boiling Heat Transfer and Peak Nucleate Boiling Fluxes in Saturated Liquid Helium Between λ and Critical Temperatures, *Adv. Cryog. Eng.* **10**, 371 (1965).
21. E. Ibrahim, R. W. Boom, and G. E. McIntosh, Heat Transfer to Subcooled Liquid Helium, *Adv. Cryog. Eng.* **23**, 333 (1978).
22. R. Capri, Heat Transfer to Subcooled He I, *Adv. Cryog. Eng.* **29**, 281 (1984).
23. Yu. Kirichenko, K. V. Rusanov, and E. G. Tyurina, Heat Transfer in Subcooled Liquid Cryogens, *Cryogenics* **23**, 209 (1983).
24. J. H. Lienhard and P. T. Y. Wong, The Dominant Unstable Wavelength and Minimum Heat Flux During Film Boiling on a Horizontal Cylinder, *J. Hear Transfer* **86**, 220 (1964).
25. B. P. Breen and J. W. Westwater, Effects of Diameter of Horizontal Tubes on Film Boiling Heat Transfer, *Chem. Eng. Prog.* **58**, 67 (1962).
26. E. G. Brentari, P. J. Giarratano, and R. V. Smith, Boiling Heat Transfer for Oxygen, Nitrogen, Hydrogen, and Helium, *NBS Technical Note 317*, U.S. Government Printing Office, Washington, DC, Sept. 20, 1965.
27. J. C. Boissin, J. J. Thibault, J. Roussel, and E. Faddi, Boiling Heat Transfer and Peak Nucleate Boiling Flux in Liquid Helium, *Adv. Cryog. Eng.* **13**, 607 (1967).
28. R. D. Cummings and J. L. Smith, Boiling Heat Transfer to Liquid Helium, Liquid Helium Technology, *Proceedings of the International Institute of Refrigeration*, Commission 1, Boulder, CO, Pergamon Press, Oxford, 1966, pp. 85–96.
29. H. Ogata and W. Nakayama, Boiling Heat Transfer to Helium from Machined and Chemically Treated Copper Surfaces, *Adv. Cryog. Eng.* **27**, 309 (1982).
30. Lehangre, J. C. Boissin, C. Johannes, and A. de La Harpe, Critical Nucleate Boiling of Liquid Helium in Narrow Tubes and Annuli, *Proceedings of the 2nd International Cryogenics Engineering Conference*, p. 274, Hiffe Science and Technology, Brighton, 1968.
31. M. N. Wilson, Heat Transfer to Boiling Liquid Helium in Narrow Vertical Channels, Liquid Helium Technology, *Proceedings of the International Institute of Refrigeration*, Commission 1, Boulder, CO, Pergamon Press, Oxford, 1966, pp. 109–114.

32. R. G. Sydoriak and T. R. Roberts, Study of Boiling in Short Narrow Channels and Its Application to Design of Magnets Cooled by Liquid $H_2$and N_2, *J. Appl. Phys*. **28**, 143 (1956).
33. Z. Chen and S. W. Van Sciver, Channel Heat Transfer in He I–Steady State Orientation Dependence, *Adv. Cryog. Eng*. **31**, (1986).
34. R. F. Barron, *Cryogenic Heat Transfer*, Taylor Francis, Philadelphia, 1999.
35. P. Giarratano, V. D. Arp, and R. V. Smith, Forced Convection Heat Transfer to Supercritical Helium, *Cryogenics* **11**, 385 (1971).
36. A. de La Harpe, S. Lehongre, J- Mollard, and C. Johannes, Boiling Heat Transfer and Pressure Drop of Liquid Helium I Under Forced Circulation in a Helically Coiled Tube, *Adv. Cryog. Eng*. **14**, 170 (1963).
37. C. Johannes, Studies of Forced Convection Heat Transfer to Helium I, *Adv. Cryog. Eng*. **17**, 352 (1972).
38. W. G. Steward, Transient Helium Heat Transfer Phase I–Static Coolant, *Int. J. Heat Mass Transfer* **21**, 863 (1978).
39. C. Schmidt, Transient Heat Transfer and Recovery Behavior of Superconductors, *IEEE Trans. Magnet*. **Mag-17**, 738 (1981).

Further Readings

R. F. Barron, *Cryogenic Heat Transfer*, Taylor Francis, Philadelphia, 1999.
A. Bejan, *Convection Heat Transfer,* Wiley, New York, 1984.
E. R. G. Eckert and R. M. Drake, *Analysis of Heat and Mass Transfer*, McGraw–Hill, New York, 1972.
J. Frenkel, *Kinetic Theory of Liquids*, Chap. 7, Dover, New York, 1955.
W. Frost, *Heat Transfer at Low Temperatures,* Plenum Press, New York, 1975.
F. P. Incropera and D. P. Dewitt, *Fundamentals of Heat Transfer*, Wiley, New York, 1981.
L. S. Tong, *Boiling Heat Transfer and Two Phase Flow*, Wiley, New York, 1965.
P. B. Whalley, *Two Phase Flow and Heat Transfer*, Oxford Science, Oxford, 1996

Chapter 6
Helium as a Quantum Fluid

Some of the quantum mechanical aspects of gaseous and liquid helium have been introduced in Chap. 3 to explain deviations from the traditional classical fluid behavior. In particular, it was shown that the equation of state and transport properties must be modeled in terms of quantum mechanical scattering theory rather than relying on fully classical treatments. These are not the most dramatic quantum features of helium. In fact, liquid helium below $T_\lambda = 2.177$ K at saturated vapor pressure behaves in such a way that its physical properties can be understood only by using a fully quantum mechanical model with a sizable fraction of the particles in the "condensed" ground state. This condensed state is envisioned to have a number of unique characteristics including zero entropy and viscosity.

In advance of discussing the quantum features of helium, it is worthwhile to ask two related questions: (1) What makes helium behave as a quantum fluid and (2) why don't other fluids possess similar characteristics? To answer these questions, it is helpful to consider the most obvious quantum mechanical characteristic of liquid helium. This characteristic is not the existence of superfluidity, but rather the fact that helium does not solidify even at absolute zero unless subjected to a sizable external pressure ($p \approx 2.5$ MPa)! The explanation for this phenomenon can only be satisfying if one includes the quantum mechanical interpretation of matter. In this interpretation the position of a helium molecule cannot be defined absolutely but rather is limited by the spread of its wave function. Furthermore, the Heisenberg Uncertainty Principle describes the extent to which the position x of a molecule and its momentum P can be defined simultaneously:

$$\Delta P \Delta x \approx \hbar \tag{6.1}$$

where $\hbar = h/2\pi$ and $h =$ Planck's constant $= 6.63 \times 10^{-34}$ J·s. Among other things, the Heisenberg uncertainty principle can be used to estimate the zero point energy of molecules.

An elementary application of the Heisenberg Uncertainty Principle can suggest why the liquid is apparently the lowest energy state of helium at absolute zero. The argument goes as follows. For the solid state to exist it must possess some

S.W. Van Sciver, *Helium Cryogenics*, International Cryogenics Monograph Series,
DOI 10.1007/978-1-4419-9979-5_6,

degree of long-range order. To have this long-range order, the lattice structure must be periodic with fixed positions for the helium molecules. The extent to which this localization is required is somewhat ill-defined, but for the sake of the present discussion assume that the position of a given molecule must be defined to within 10% of the inter-atomic spacing in the lattice. For the case of solid helium the inter-atomic spacing is of the order of two atomic radii or 0.5 nm. Therefore, we will require that the position of a molecule must be defined *vis a' vis* (6.1) to within $\pm$ 0.05 nm. Uncertainty in the helium molecule position leads to an uncertainty in the momentum, which is related to the zero point energy. The momentum uncertainty is directly related to the kinetic energy uncertainty, $\Delta E \approx (\Delta P)^2/2\ m$, which may be defined as the zero point energy. Therefore,

$$\frac{\Delta E}{k_B} \approx \frac{\hbar^2}{2mk_B(\Delta x)^2} \tag{6.2}$$

For the case of the common helium isotopes ^{4}He, with a $\Delta x \approx 0.05$ nm, the zero point energy in temperature units turns out to be $\Delta E/k_B \approx 24$ K. This energy is considerably larger than the attractive potential energy well depth for helium, $\phi/k_B \approx 10$ K, see Fig. 3.2. Therefore, based on this simple argument helium would not be expected to solidify.

For comparison consider the case for hydrogen solidification. Since hydrogen is a diatomic molecule with a total mass half that of helium, its zero point energy should be about twice that of helium or $\Delta E/k_B \approx 50$ K. However, since it is a diatomic molecule, hydrogen has a much stronger intermolecular potential, $\phi/k_B \approx 100$ K, brought on by the non-spherical molecular symmetry. As a result of this stronger potential, hydrogen is observed to solidify with a triple point occurring around 14 K.

Thus, helium is the only molecule that can exist in the liquid state at absolute zero. It is therefore an ideal system to study as a quantum fluid. Since the common isotope of helium is ^{4}He, the molecule has integer spin and obeys Bose-Einstein statistics. A fundamental premise of this statistical model is to allow a large fraction of the population to be in the ground state, thereby affecting the physical behavior. It is worth noting that the other stable isotope of helium, ^{3}He, obeys Fermi-Dirac statistics because of the odd number of neutrons and would be expected to behave very differently from ^{4}He. In particular, Fermi-Dirac statistics denies the existence of a highly populated ground state by the Pauli exclusion principle. As can be seen in a more detailed discussion of ^{3}He in Chap. 9, the lighter helium isotope has physical properties that are quite different from those of ^{4}He although it too does not easily solidify due to its large zero point energy.

In the present chapter, the concept of quantum fluids is introduced with helium as the example. Where possible, the bridge between experimental evidence and theory is described. The discussion focuses on the physical understanding of liquid helium including its transport properties. In Chap. 7, the bulk heat and mass transport of He II will be discussed more from an applications viewpoint.

6.1 Ideal Quantum Gases

A system of non-interacting particles obeying quantum statistics is considered to be an ideal quantum gas. There are a number of physical systems in nature that display quantum gas behavior. Common examples include the behavior of electrons and phonons in solids. Also, low density gas molecules at low temperatures can show quantum mechanical behavior as we discussed in Chap. 3. Of most recent interest are gases made up of Rb or H atoms that undergo Bose-Einstein condensation.

Helium is also a good example of a quantum gas; however, its gaseous state does not exist at sufficiently low temperature or high density to show pronounced quantum effects. Liquid helium below T_λ, He II see Fig. 3.1, shows a number of unique quantum features although it can hardly be considered a non-interacting fluid. However, understanding the behavior of an ideal quantum gas in the same temperature and density regime as that of He II can be a helpful tool in interpreting the some of the behavior of the liquid. To appreciate more fully the physics of quantum gases, particularly helium, the present section develops a theoretical description of an ideal Bose gas. A number of physical properties are calculated including entropy, specific heat, and phase transition thermodynamics. Several of these features are remarkably similar to those of liquid He II.

The theory of an ideal quantum gas begins with the correct statistical picture. For details on how to go about this development, the reader is referred to one of numerous monographs on statistical mechanics [1, 2]. Since it is beneficial for appreciation of different statistical systems, the general concepts of quantum statistical mechanics as they apply to the helium problem are surveyed here.

Consider an ideal quantum gas consisting of N non-interacting point particles where N is a large number on the order of 10^{23}. We define the Hamiltonian H for this system:

$$H = \sum_{i=1}^{N} \frac{P_i^2}{2m} \tag{6.3}$$

where P is the momentum of the ith particle and m is the particle mass. The Hamiltonian is the kinetic energy operator for the wave equation that describes the group of particles that make up the gas. In this case, it is independent of particle position. In its present form (6.3) is cumbersome since it is a sum over all N particles. To simplify the analysis it is necessary to introduce a complete set of eigenfunctions to the Hamiltonian which are also eigenfunctions of the particular statistical picture. These eigenfunctions must obey Bose statistics and are therefore symmetric under the interchange of particles. By contrast, the eigenfunctions of a Fermi system are anti-symmetric under particle interchange.

For the ideal non-interacting system, energy eigenvalues are defined according to single-particle energy levels. It is possible to divide these single-particle levels into groups containing g_i, levels, with an assigned average energy ε_i. The occupation number of the ith cell is then given by n_i where this value is

assumed to be small compared to g_i. It follows that the total particle number N and total energy E are sums over these levels,

$$N = \sum_i n_i \tag{6.4a}$$

and

$$E = \sum_i n_i \varepsilon_i \tag{6.4b}$$

The difference between statistical pictures becomes evident through the allowable population density of each level within a given cell. For the Bose system any number of particles may occupy a given state. In the Fermi system the occupation number of a given state is restricted to being either 0 or 1.

The classical limit of either statistical picture must lead to the Boltzmann statistical distribution. The correspondence principle is a formal statement of this limit. For quantum gases, it is required that both Fermi and Bose gases obey Boltzmann statistics in the limit of high temperature. As with a Bose gas, the Boltzmann gas does not restrict the occupation number of a particular level. However, the state that results from the interchange of particles is considered to be new for the Boltzmann gas but is indistinguishable for the Bose gas.

For each statistical picture presented above, there is a distribution function that describes the probability that a particle occupies a particular energy level. Since the number of particles in a given state is large, the difference between the actual and the most probable distribution functions is insignificant. The distribution function for each of the statistical pictures can be written in terms of the energy of the ith level:

$$n_i = \frac{1}{z^{-1} e^{\beta \varepsilon_i} + \gamma} \tag{6.5}$$

where the particular statistical pictures determine the value of γ. For Bose-Einstein statistics $\gamma = -1$, for Fermi-Dirac $\gamma = +1$, and for Boltzmann $\gamma = 0$. In the above equations z is referred to as the fugacity and is explicitly written $z = e^{\beta \mu}$, where μ is the chemical potential and $\beta = 1/k_B T$. Given the above expressions and description it is possible to solve for the properties of any particular system once the eigenvalues and boundary conditions are known.

Consider an ideal quantum gas confined to a cubical volume of linear dimension L. Since the particles are non-interacting, the potential energy can be neglected. The problem then reduces to solving the time-independent Schrodinger equation,

$$-\frac{\hbar^2}{2m} \nabla^2 \psi_n = \varepsilon_n \psi_n \tag{6.6}$$

where ψ_n are eigenfunctions of the system. Application of proper boundary conditions including continuity of the wave function and its derivative leads to a set of eigenvalues,

$$\varepsilon_n = \frac{h^2 n^2}{2mL^2} \tag{6.7}$$

where the momentum is also quantized such that $P = n(h/L) = n(\delta P)$. The quantity $\delta P = h/L$ can be considered to be the dimensions of the momentum space lattice.

The ideal gas problem deals with such a large number of particles that the discreteness of the momentum lattice becomes unimportant. It is therefore possible to make what is termed the continuum approximation which is equivalent to making the lattice dimension go to zero, $\delta P \rightarrow 0$. The approximation replaces the summation by an integral over momentum space. The total particle number may then be written

$$N = \sum_i n_i \simeq \frac{V}{h^3} \int n \, d^3P \tag{6.8}$$

As is discussed below, care must be exercised when making this continuum approximation for the Bose system. Because of the potentially large number of particles in the zero momentum state, the discreteness of the lattice must be maintained for this state.

The integral in (6.8) is written explicitly by including the distribution function in the equation for the particle number density:

$$\frac{N}{V} = \frac{2\pi}{h^3} (2m)^{3/2} \int_0^\infty \frac{\varepsilon^{1/2} d\varepsilon}{z^{-1} e^{\beta\varepsilon} + \gamma} \tag{6.9}$$

Often the density of energy states $D(\varepsilon)$ in the particular statistical picture is defined in terms of the proportionality factor in (6.9) such that

$$D(\varepsilon) = \frac{2\pi V}{h^3} (2m)^{3/2} \varepsilon^{1/2} \tag{6.10}$$

A similar expression was introduced in Chap. 2 as part of the description of electron and phonon gas models in solids.

As an example, consider the statistical expression for the particle density (6.9) for a Boltzmann gas. For this special case, (6.9) can be simplified because $\gamma = 0$:

$$\frac{N}{V} = \frac{2\pi (2m)^{3/2}}{h^3} z \int_0^\infty \varepsilon^{1/2} e^{-\beta\varepsilon} d\varepsilon = \frac{1}{\lambda_T^3} z \tag{6.11}$$

where $\lambda_T = (h^2/2\pi m k_B T)^{1/2}$ is referred to as the thermal de Broglie wavelength. At the very least, (6.11) explicitly defines the fugacity z as a function of temperature

and density. This quantity is used in the computation of the total energy, entropy, or other thermodynamic quantities of the Boltzmann gas.

The thermal de Broglie wavelength is a characteristic quantity that determines when quantum mechanics becomes an important factor in the behavior of a system. In the wave nature of matter, this quantity is the characteristic wavelength. Therefore, an estimate can be made for the temperature at which quantum effects become important by allowing λ_T to be of the order of the particle size. For the helium molecule, the thermal de Broglie wavelength is,

$$\lambda_T(^4\mathrm{He}) \approx \frac{0.87\mathrm{nm}}{T^{1/2}} \tag{6.12}$$

Equating λ_T with the particle diameter in liquid helium ($d \simeq 2r_m \simeq 0.51$ nm), we find that the temperature at which quantum effects should become important is around 2.9 K. Although this temperature is rather close to the superfluid transition in liquid helium, $T_\lambda = 2.177$ K, it should not be construed as a prediction of this effect. The thermal de Broglie wavelength being comparable to atomic dimensions makes no prediction of Bose-Einstein condensation or the superfluid transition in He II. Rather, it indicates approximately where to expect to observe the onset of pronounced quantum effects. Because of its smaller mass, ^{3}He would have a slightly higher temperature onset of quantum phenomena based on the above argument, see Chap. 9.

6.1.1 Density of an Ideal Bose Gas

Now consider a Bose gas contained in a volume V. In a similar fashion to the above discussion, an expression can be written for the number density subject to Bose-Einstein statistics:

$$\frac{N}{V} = \left(\frac{1}{\lambda_T}\right)^3 \frac{2}{\sqrt{\pi}} \int_0^\infty \frac{x^{1/2}dx}{z^{-1}e^x - 1} + \frac{1}{V}\left(\frac{z}{1-z}\right) \tag{6.13}$$

Here it has been necessary to separate off the population of the zero momentum state because of an anomaly that results when the discrete sum is taken to the integral form. The second term in (6.13) is therefore introduced to take care of the discontinuity when $z \to 1$. The above expression is a complete representation of the number density of an ideal Bose gas. It has the proper high-temperature limit when $e^{\beta(\varepsilon-\mu)} \gg 1$, which leads to the exact Boltzmann form of (6.11).

The integral contained in the first term of (6.13) is a general function,

$$g_{3/2}(z) = \frac{2}{\sqrt{\pi}} \int_0^\infty \frac{x^{1/2}dx}{z^{-1}e^x - 1} \tag{6.14}$$

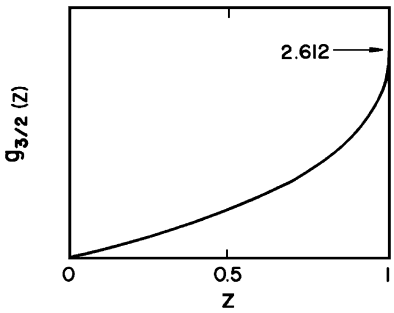

Fig. 6.1 Riemann zeta function for $n = 3/2$

that is a specific example of a Riemann zeta function. This function actually is defined as a summation

$$g_n(z) = \sum_{l=1}^{\infty} \frac{z^l}{l^n} \tag{6.15}$$

where it is only bounded for values of $0 \leq z \leq 1$. The Riemann zeta function has been studied extensively and is tabulated in the literature [2]. For the special case in (6.14), Fig. 6.1 shows the form of this function. It is relatively well behaved, monotonically increasing from zero to $g_{3/2}(1) = 2.612$.

Returning to the expression for the number density of a Bose gas, (6.13), the first term on the right-hand side represents the number of particles in the non-condensed state. The second term is the density of particles in the ground state, N_0/V. Rearranging (6.13) to give an explicit expression for this quantity,

$$\frac{N_0}{V} = \frac{N}{V} - \frac{1}{\lambda_T^3} g_{3/2}(z) \tag{6.16}$$

In the above form, it is apparent that for the population of the zero momentum state to be finite, the right-hand side must be greater than zero. This requirement predicts a transition in a Bose gas. The transition temperature T_c is defined as the highest temperature that can sustain nonzero N_0/V, i.e. for $g_{3/2}(1)$. Substituting this value and rearranging to make an expression for T_c, we obtain

$$T_c = \frac{h^2}{2\pi m k_B} \left(\frac{1}{\mathbf{v}_c g_{3/2}(1)} \right)^{2/3} \tag{6.17}$$

where $v_c = (V/N)_{Tc}$ is the critical specific volume. Note that the population of the zero momentum state is a continuous function and not until the system is at absolute zero do all the particles occupy this state. By combining (6.16) and (6.17)

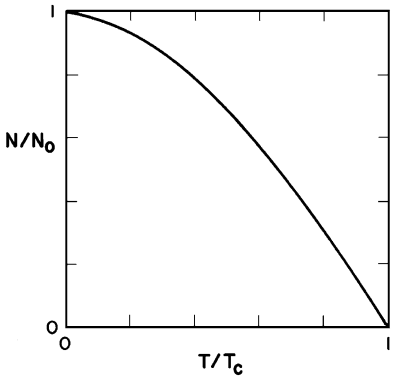

Fig. 6.2 Fraction of particles in the ground state as a function of reduced temperature for an ideal Bose gas

it is easy to show that the ground state population is a temperature-dependent quantity normalized only by the critical temperature:

$$\frac{N_0}{N} = 1 - \left(\frac{T}{T_c}\right)^{3/2} \quad \text{for} \quad T \leq T_c \tag{6.18a}$$

$$= 0 \qquad\qquad \text{for} \quad T > T_c \tag{6.18b}$$

This result is shown graphically in Fig. 6.2. Note that although the actual value for N_0 varies continuously through the transition, there is a discontinuity in dN_0/dT at T_c.

6.1.2 *Internal Energy of an Ideal Bose Gas*

The internal energy E of an ideal Bose gas can be computed similarly. In terms of the discrete system, the expression for E is given in (6.4b) as a sum over the product $n_i\varepsilon_i$ for each of the particle states. This form is converted by means of the continuum approximation to an integral over the density of states function $D(\varepsilon)$:

$$E = \frac{2\pi}{h^3}(2m)^{3/2}V\int_0^\infty \frac{e^{3/2}d\varepsilon}{z^{-1}e^{\beta\varepsilon} - 1} \tag{6.19}$$

Note that in this case there is no longer a problem with the continuum approximation because although the population of the $p = 0$ state may be finite the energy per particle in that state is identically zero, by definition.

Because the internal energy has a different form dependent on whether it is below or above T_c, it is useful to evaluate its behavior as a function of temperature. Substituting the quantities introduced as part of the density expression into (6.19), the internal energy may be written

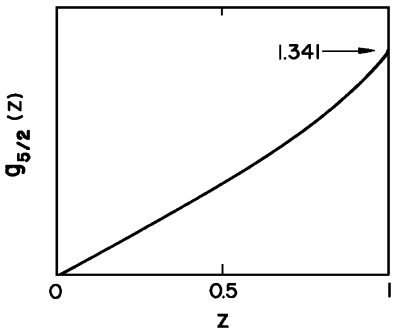

Fig. 6.3 Riemann zeta function for $n = \frac{5}{2}$

$$\frac{E}{N} = \frac{3}{2}\left(\frac{1}{\lambda_T}\right)^3 v k_B T g_{5/2}(1) \quad \text{for} \quad T \leq T_c \tag{6.20a}$$

$$= \frac{3}{2}\left(\frac{1}{\lambda_T}\right)^3 v k_B T g_{5/2}(z) \quad \text{for} \quad T > T_c \tag{6.20b}$$

where $g_{5/2}(z)$ is the same Riemann zeta function defined in (6.15). In integral form,

$$g_{5/2}(z) = \frac{4}{3\sqrt{\pi}} \int_0^\infty \frac{x^{3/2} dx}{z^{-1} e^x - 1} \tag{6.21}$$

As with $g_{3/2}(z)$, the above quantity is a smoothly varying function from 0 to its maximum value of 1.341 at $z \to 1$ (Fig. 6.3).

At this point, it is instructive to check the correspondence principle as it applies to the high-temperature limit of a Bose gas. Referring to the discrete form of the Riemann zeta function (6.15), we see that at high temperatures $g_n(z) \approx z + \cdots$ for all n. Substituting only the leading term into the equations for the density and internal energy of a Bose gas, we obtain the classical limiting form $E/N = \frac{3}{2} k_B T$, which is consistent with the principle of equipartition of energy, i.e. $\frac{1}{2} k_B T$ for each degree of freedom. Therefore, the theory as developed to this point has the proper high-temperature limit.

6.1.3 *Specific Heat of an Ideal Bose Gas*

The constant volume specific heat C_v is related simply to the internal energy through its temperature derivative, $C_v = (dE/dT)_v$. Therefore, taking derivatives of (6.20) with respect to temperature yields

$$\frac{C_v}{N k_B} = \frac{15}{4} g_{5/2}(1) \frac{v}{\lambda_T^3} \quad \text{for} \quad T \leq T_c \tag{6.22a}$$

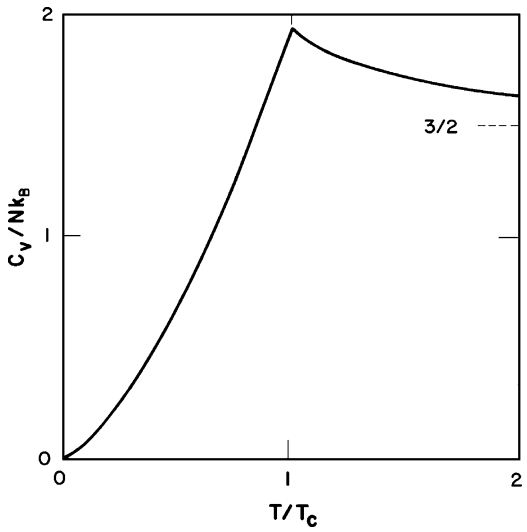

Fig. 6.4 Specific heat constant volume of an ideal Bose gas

$$\frac{C_v}{Nk_B} = \frac{15}{4} g_{5/2}(z) \frac{v}{\lambda_T^3} - \frac{9}{4} \frac{g_{3/2}(z)}{g_{1/2}(z)} \quad \text{for} \quad T > T_c \tag{6.22b}$$

The shape of the constant volume specific heat is shown graphically in Fig. 6.4. There are three notable features in the form of the specific heat of an ideal Bose gas. First, at high temperatures $T \gg T_c$, $g_n(z) \rightarrow z \approx \lambda_T^3/v$, which asymptotes to the classical result that $C_v = 3/2Nk_B$. This is to be expected based on similar arguments about the behavior of the internal energy. Second, below T_c the Riemann zeta function takes on a constant value and the specific heat is determined by the temperature dependence of the thermal de Broglie wavelength. Therefore below T_c, C_v goes to zero as $T^{3/2}$. It is possible to think of this behavior in a different way. Since the ground state has no energy of excitation, C_v is only a measure of the fraction of molecules in the excited states. Since this fraction decreases as $T^{3/2}$, it follows directly that the specific heat should have a similar dependence. The third aspect to the ideal Bose gas specific heat is that of its transition. The form as developed above does not predict a discontinuity in value of C_v but does show a cusp characteristic of a discontinuity of slope. A similar set of calculations for the constant pressure heat capacity C_p yields results that are not altogether different. As expected at high temperatures, the form of C_p/Nk_B approaches $\frac{5}{2}$, the classical limit. However, at the transition the value of C_p shows a discontinuity consistent in form to the behavior of a first-order phase transition.

6.1.4 Vapor Pressure of an Ideal Bose Gas

The discontinuity in specific heat is analogous to that of a first-order phase transition. Another question to ask might be: What is the behavior of the pressure over the same range of temperature? If there is a first-order phase transition, two

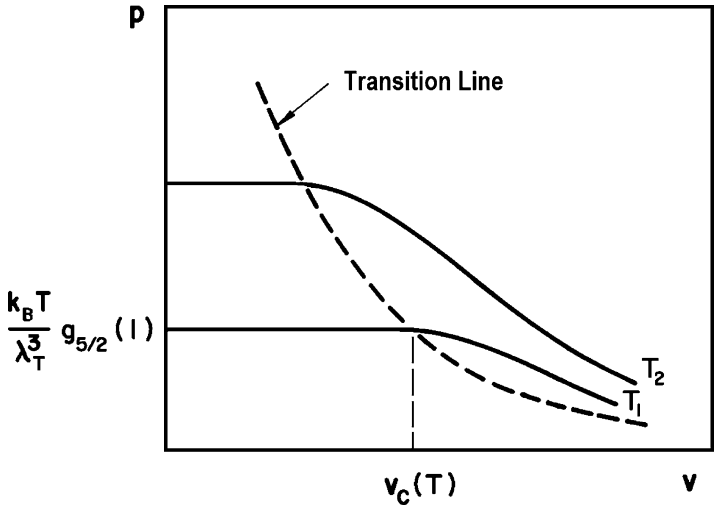

Fig. 6.5 Vapor pressure isotherms of an ideal Bose gas

phases should coexist although the phases would be of different character to classical liquid–gas coexistence. In the case of an ideal Bose gas the two phases would be the normal vapor and the vapor that is in the BE condensed state.

To develop an expression for the equilibrium pressure for a Bose gas, it is best to use the fact that the pressure-volume product is simply related to the internal energy for all ideal gases through the expression

$$pv = \frac{2}{3}\frac{E}{N} \tag{6.23}$$

It then follows that the equilibrium pressure can be written

$$\frac{p}{k_B T} = \frac{1}{\lambda_T^3} g_{5/2}(1) \quad \text{for} \quad v \leq \mathbf{v}_c \tag{6.24a}$$

$$= \frac{1}{\lambda_T^3} g_{5/2}(z) \quad \text{for} \quad v \geq \mathbf{v}_c \tag{6.24b}$$

where v_c is the critical specific volume. Note that according to (6.24a) the pressure of an ideal Bose gas is zero at absolute zero. A more subtle fact to consider is that the pressure for $v < v_c$ (6.24a) is independent of the actual volume. This fact can be seen in Fig. 6.5, which is a p-v diagram for an ideal Bose gas. The region below the transition line at T_c has a horizontal vapor pressure curve indicative of a two-phase region. Two-phase coexistence normally implies the transition is first order; however, a useful way of checking this fact is to compute the latent heat of transformation.

6.1.5 Latent Heat of an Ideal Bose Gas

If the phase transition associated with condensation in the ideal Bose gas is first order, then it should have a latent heat. The latent heat h_{fg} of transformation is defined in by the Clausius-Clapeyron equation,

$$\left(\frac{dp}{dT}\right)_{T_c} = \frac{h_{fg}}{T\Delta v} \tag{6.25}$$

where the vapor pressure derivative is taken at the transition temperature and Δv represents the specific volume difference between the two phases. Since the condensed phase can be assumed to occupy zero volume, the volume change is the specific volume at the critical temperature,

$$\Delta v = \mathbf{v}_c = \frac{\lambda_T^3}{g_{3/2}(1)} \tag{6.26}$$

Taking the derivative of the vapor pressure as given by (6.24a), the expression for the Clausius-Clapeyron equation becomes

$$\left(\frac{dp}{dT}\right)_{T_c} = \frac{1}{T_c \mathbf{v}_c}\left[\frac{5}{2}k_B T \frac{g_{5/2}(1)}{g_{3/2}(1)}\right] \tag{6.27}$$

where the quantity in brackets is the latent heat of transformation, $h_{fg} = 1.284 k_B\, T$, on a per molecule basis. On an absolute scale, this energy is quite large, being comparable to the internal energy of an ideal classical monatomic gas at the same temperature.

The theory of an ideal Bose gas is instructive to consider because it shows how quantum mechanics affects the behavior of an ideal non-interacting gas. In nature, ^{4}He exists as a liquid at low temperatures and as one might expect its behavior is not that close to that of an ideal gas. Liquid ^{4}He is known to undergo a phase transition to superfluid state, referred to as He II, at a temperature $T_\lambda = 2.177$ K under saturated vapor pressure. Substituting the specific volume of liquid ^{4}He in the equation for T_c, (6.17), we can predict that an ideal Bose gas would have a transition at 3.14 K. Although T_c and T_λ are fairly close in value, the correspondence should not necessarily be taken as indicating that T_λ marks the beginning of Bose-Einstein condensation in liquid ^{4}He. This is because there are several dissimilarities between the behavior of an ideal Bose gas and liquid ^{4}He. First the transition in between He I and He II is known to be second order with a discontinuity in slope of the entropy. The specific heat has a logarithmic infinity in value at T_λ. Consequently, the Bose-Einstein interpretation of the λ-transition appears to be an oversimplification in that the order of the two transitions is not the same. The other noted difference occurs in the low-temperature properties. Below T_c the Bose gas has a specific heat that goes

as $T^{3/2}$ which is related to the changing population of the ground state. This is markedly different as we will see from the behavior of liquid He II, which has a specific heat that goes as T^n where n varies from 3 at low temperatures, T<1 K, to around 6 near T_λ. Further, in He II the temperature dependence to the specific heat is due to the characteristics of the excitation spectrum in the fluid rather than the changing population density in of the ground state.

Although there are several noted differences between the behavior of an ideal Bose gas and that of liquid ^{4}He, there is little doubt that the transition between He I and He II is affected by Bose-Einstein quantum statistics. He II has a number of unique properties that make it very different from conventional fluids. As will be seen in subsequent sections, many of these properties can be interpreted in terms of physical models that rely heavily on the existence of a condensed phase. The physics of this condensed phase is clearly more complex than that of the condensed ideal Bose gas. This is due, at least in part, to the fact that the excitation spectrum and interactions of the He II system are more complex than assumed in the ideal Bose gas.

6.2 Liquid He II Properties

When considering theoretical descriptions of He II, it is necessary to extend the models beyond that of the ideal gas. Two major features to the theory must be included: (1) a description of the excitation spectrum which is relevant to the state properties and (2) a fluid mechanics model that can be used to describe the transport properties. The first component of the theory, although having relatively little engineering application, is most effective at interpreting such physical properties as specific heat and entropy. The latter model emphasizes understanding of the transport properties such as viscosity and thermal conductivity. Both models are useful for understanding the unique properties of He II.

To provide a better basis for the theoretical description, we begin with survey of the properties of He II. In performing this survey, the emphasis is placed on those properties that are particularly important for the applications. For a further description of other He II properties, the reader should consult one of several references on the physics of liquid helium.

As has already been discussed in the introduction to Chap. 3, liquid helium can exist in either of two phases. Liquid helium above T_λ is referred to as normal helium or He I, and has properties similar to other monatomic liquids. Superfluid helium as it is commonly called, or He II, is the equilibrium state below T_λ and has a number of outstanding features particularly associated with its transport properties. The λ-line separates these two liquid states as shown in Fig. 3.1, the phase diagram of helium. The λ-line stretches between the liquid–vapor phase transition at low pressure and the solid–liquid phase boundary at high pressure ($p \approx 3$ MPa). The actual values of the pressure, temperature, and density of liquid helium at the λ-transition are listed in Table 6.1 [3]. The transition between these

Table 6.1 λ-transition as a function of temperature, pressure, and density [3]

T(K)	p(MPa)	ρ(kg/m^3)
1.767	3.015	179.8
1.80	2.827	178.4
1.85	2.528	176.1
1.90	2.211	173.5
1.95	1.876	170.5
2.00	1.52	167.1
2.05	1.141	163.0
2.10	0.733	158.0
2.15	0.282	151.3
2.177	0.005	146.2

two states of the liquid is associated with a change in slope of the entropy. Thus, the λ-transition is second-order as defined by Ehrenfest and has no latent heat of transformation. The physical significance of a second-order phase transition here is that the two phases cannot coexist in equilibrium. This fact has limited practical significance because near the λ-transition thermal relaxation times are long and small deviations from equilibrium are achieved easily in actual experimental systems.

It is the goal of the present section to survey the properties of He II which are of greatest technical significance. These properties can be categorized into two principal types: (1) state properties: specifically the density, entropy and specific heat and (2) transport properties: viscosity and heat conductivity. As will become evident, this is a natural separation of the properties in light of the theoretical description of He II.

6.2.1 State Properties of He II

The state properties that are particularly useful for practical applications are those of specific heat, entropy, and density. The former two are also quite important for further understanding of the He II excitation spectrum. Consider the specific heat, shown graphically in Fig. 6.6 on a log-log plot. In presenting the specific heat in this form, several interesting features can be seen in addition to the λ-transition. At very low temperatures, $T \lesssim 0.6$ K, the specific heat obeys a cubic dependence as,

$$C = (20.4 \pm 0.4)T^3 \,\mathrm{J/kg\,K} \tag{6.28}$$

where C refers to the specific heat at saturated vapor pressure. In this temperature regime, the differences between C, C_p, and C_v are insignificant. The physical

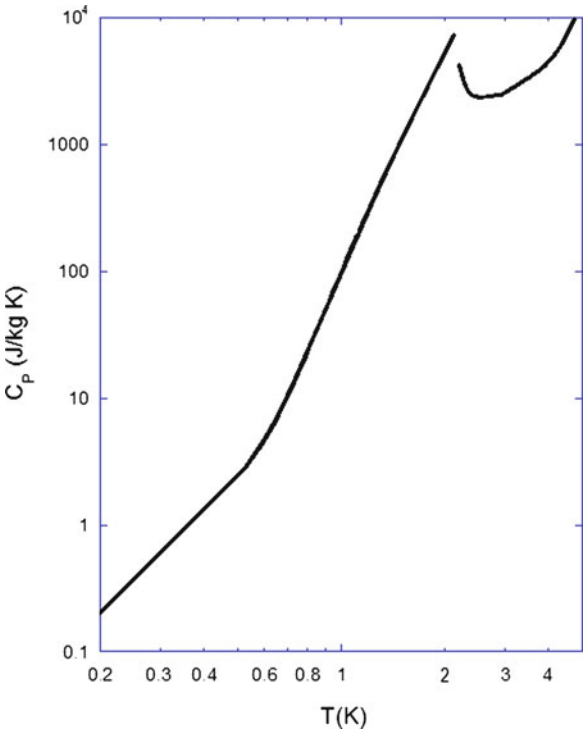

Fig. 6.6 Specific heat of liquid helium under saturated vapor pressure

explanation for this dependence is presented in the next section; however, at this point it is worth recalling that the low-temperature specific heat of a phonon gas is also proportional to T^3. This effect is important supportive evidence for the Landau theory of He II, which is based on an excitation spectrum dominated by longitudinal phonons for $T \leq 0.6$ K.

At higher temperatures, the apparent power law to the specific heat increases by about a factor of two. Historically, the region has been divided into two segments where the temperature dependence goes as

$$C = 108\, T^{6.7}\ \mathrm{J/kg\,K} \qquad \text{for} \quad 0.6 < T < 1.1\ \mathrm{K} \tag{6.29a}$$

$$= 117 T^{5.6}\ \mathrm{J/kg\,K} \qquad \text{for} \quad 1.1 \leq T \leq 2.17\ \mathrm{K} \tag{6.29b}$$

In the Landau theory a new excitation termed the "roton" is introduced to explain the behavior of the heat capacity in this region, which is clearly unique to liquid helium.

The entropy of liquid helium is shown in Fig. 6.7 also on a log-log scale. At the λ-transition, the discontinuity of slope can be seen quite clearly, indicating a second-order phase transition. Based on the general theory of phase transitions introduced by Ehrenfest, a first-order phase transition has associated with it both a

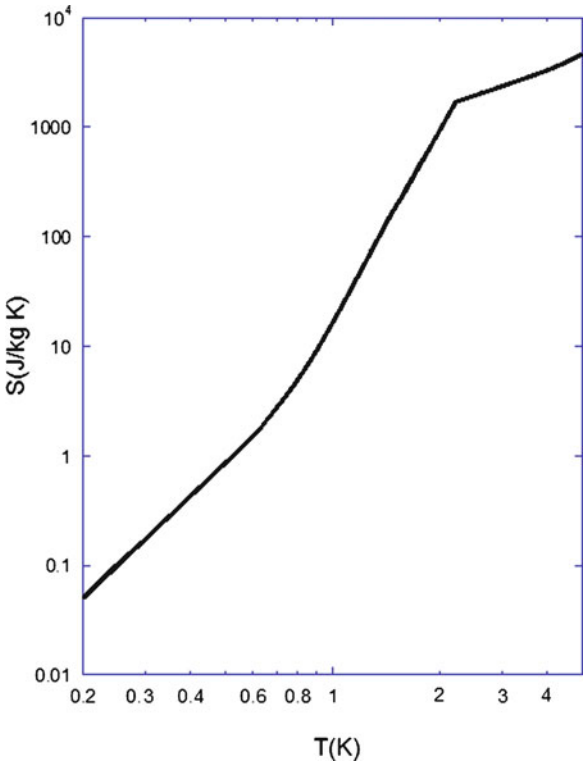

Fig. 6.7 Entropy of liquid helium under saturated vapor pressure

change in entropy and molar volume. These quantities are related through the Clausius-Clapeyron equation,

$$\left(\frac{dp}{dT}\right)_{T_c} = \frac{\Delta s}{\Delta v} \tag{6.30}$$

where the changes in s and v occur at the transition. The above expression follows directly from the continuity of the Gibbs potential at the transition. A second-order phase transition must have both continuity of Gibbs potential and entropy. Therefore, the analogous expression to (6.30) becomes,

$$\left(\frac{d^2p}{dT^2}\right)_{T_c} = \frac{\Delta C_p}{Tv\Delta\beta} = \frac{\Delta\beta}{\Delta\kappa} \tag{6.31}$$

where β is the bulk expansivity and κ the bulk isothermal compressibility. It follows that for a second-order phase transition C_p, β, and κ are discontinuous. As discussed in Chap. 3, these effects are observed in the properties of liquid helium near the λ-transition.

Finally, the density of He II as shown in Fig. 6.8 displays some interesting characteristics. At saturated vapor pressure, the density goes through a broad

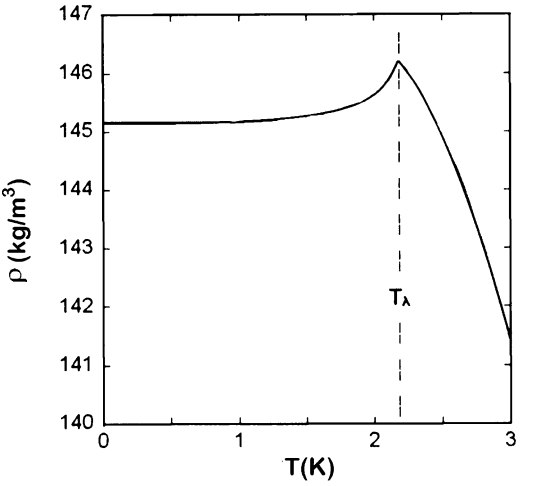

Fig. 6.8 Density of liquid helium under saturated vapor pressure

maximumwith a discontinuity in slope at 6 mK above the λ-transition. Below that temperature, He II has a negative thermal expansion coefficient. The density of He II under saturated vapor pressure approaches a near constant value of 145.3 kg/m^3 which is 0.55% less dense than at its maximum but is 16% more dense than He I at its normal boiling point, 4.2 K, 0.1 MPa where $\rho = 125$ kg/m^3. Thus, the bulk expansivity of He II is near zero, which is required by the third law of thermodynamics as the temperature approaches absolute zero.

The existence of a negative thermal expansion coefficient leaves open some interesting potential applications. One possibility that has been investigated to some degree is that of performing isentropic compression of the fluid to produce cooling. Consider, as an example, the effectiveness of isentropic compressive cooling of He II initially at 2.100 K and saturated vapor pressure. Isentropic compression is achieved by reversibly applying pressure to a piston while the system is isolated from the environment. For numerical calculations take the final pressure to be $p_f = 2$ MPa. The statement of isentropic compression equates the specific entropies:

$$s(T_f,\ 2\ \text{MPa}) = s(2.1\ \text{K, SVP}) \tag{6.32}$$

As a result of this compression, the final temperature should be 1.932 K, which represents a 0.168 K reduction in temperature.

6.2.2 Transport Properties of He II

The behavior of He II when subjected to a mass or heat flow clearly demonstrates the unique character of the fluid since the observed effects are totally different from that which would be expected based on classical fluid mechanics. In considering

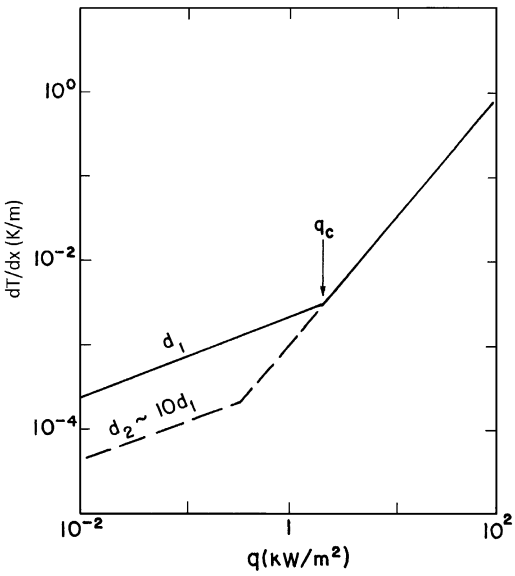

Fig. 6.9 Temperature gradient in a He II filled channel as a function of heat flux density q. The critical heat flux q_c, represents a transition between laminar and turbulent flow. Note $d_1 \sim 1$ mm if $T \simeq 1.9\ K$

He II under mass flow conditions, the most obvious property to evaluate is the form of the viscosity. Surprisingly however, for He II this property depends on the way it is measured. One can measure the apparent viscosity of He II by essentially two different methods: (1) by measuring the pressure drop in laminar flow through capillaries and (2) by measuring damping of a rotating disk immersed in the liquid. At the outset, it should be noted that both methods yield essentially the same results for ordinary liquids including He I.

To measure the viscosity of He II flowing through a capillary, a pressure gradient must be established and a mass flow measured. Since the viscosity to be measured is extremely small, ~1 μPa or 1/1000th that of water, the capillary must have a very small diameter ($d \sim$ μm) to ensure that the flow is laminar. For this case, experimental evidence shows that almost independent of channel dimension the viscosity becomes immeasurably small just below the λ-transition. This result is contrary to that obtained using a rotating viscometer. Here the measurement consists of a change in moment of inertia of a disk rotated in the fluid. For He II, the viscosity measured by a rotating viscometer obeys a more conventional form, actually increasing with decreasing temperature. Thus, an important test of any theory of He II is that it must be able to describe these very different mass transport results.

The heat transport character of He II is also quite unique. In general, the apparent thermal conductivity of He II is extremely large, being at least several orders of magnitude greater than other liquids or even high-conductivity metals. Furthermore, the heat conductivity cannot simply be described as a property like the bulk thermal conductivity. This behavior can be seen most clearly by reference to a specific experimental measurement. For a channel containing He II and subjected to an axial heat current, the temperature gradient displays two regimes, shown schematically in Fig. 6.9. For low heat fluxes up to a critical value q_c, the helium

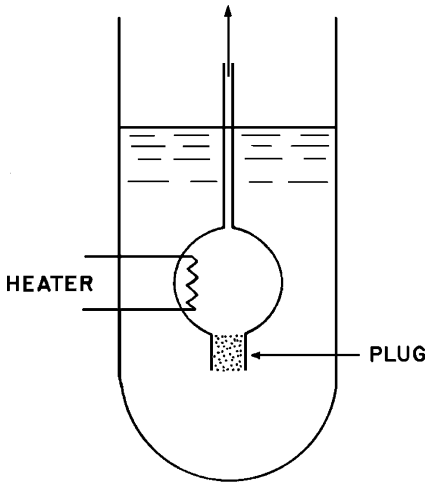

Fig. 6.10 Experiment to demonstrate the fountain effect

obeys a heat transport relationship with the temperature gradient being directly proportional to heat flux. However, unlike the bulk thermal conductivity, the proportionality constant in this regime has a very strong diameter dependence, with the helium getting less conductive as the diameter decreases. Additionally, in this heat flow regime a corresponding pressure difference is set up across the channel with the value being proportional to the temperature difference such that,

$$\Delta p = \rho s \Delta T \tag{6.33}$$

where the proportionality factor is the product of density ρ and specific entropy s. This relationship between pressure and temperature gradients, known as London's equation, gives rise to the so-called fountain effect which causes He II to flow through very small channels driven by a temperature difference.

Above the critical heat flux q_c, He II enters another heat transport regime where the temperature gradient becomes roughly proportional to the cube of the heat flux and independent of channel dimensions. For reasons that will become apparent later in this chapter, this regime is generally associated with the onset of a unique kind of turbulence in the He II. It should also be noted that the transition point between the two heat flow regimes in He II is diameter dependent.

6.2.3 Fountain Effect

In addition to the above described heat flow behavior, there are other unique features in the transport properties of He II. One, commonly referred to as the fountain effect, results from the noted relationship between the pressure and temperature difference in He II, London's equation (6.33). This effect can have quite spectacular results. Consider, for example, the idealized experiment shown in Fig. 6.10. A vessel containing He II is placed in a bath also of He II initially at the

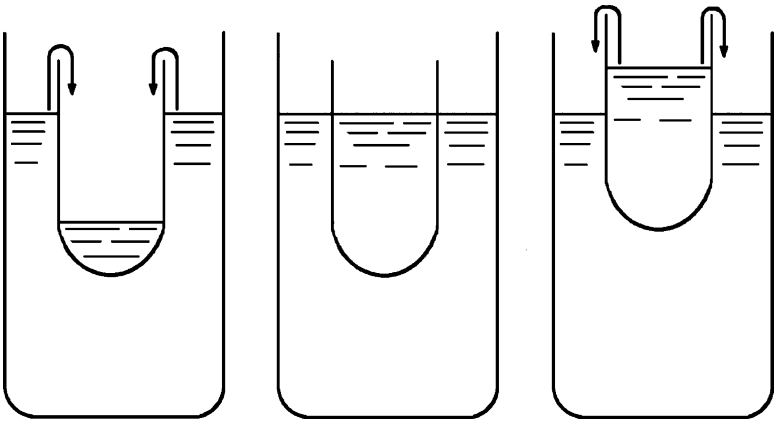

Fig. 6.11 Schematic of a film flow experiment

same temperature. A porous material forms a semi-permeable separation between the two vessels and the inner vessel is instrumented with a heater. In equilibrium, all temperatures and pressures are equal. However, if heat is applied to the inner vessel, its temperature rises. As a consequence of the unique properties of He II described by (6.33), the pressure rises in the inner vessel and the helium level will increase until it squirts out the top channel forming a fountain from which the effect gets its name. Although this effect is quite fantastic, we will see shortly that it is based on sound physical principles in the theory of He II.

Related to the fountain effect is the existence of what is known as helium film flow. It is a known physical phenomenon that liquids at saturation will form multilayer films adsorbed on surfaces in the vicinity of the bulk liquid. What is unique about He II is that this saturated film, which is typically less than a micrometer thick, is mobile. Mobility of the He II film permits the liquid to flow under the influence of the fountain pressure. Again consider an idealized experiment. Assume a bath of He II contains a separate, smaller vessel with an open top above the bath surface; see Fig. 6.11. As the inner vessel is lowered into the liquid a pressure difference is established due to hydrostatic head, $\Delta p = \rho g \ \Delta h$. But all surfaces are coated with helium film, so that the fluid can flow between the two reservoirs driven by the pressure difference. The flow rate depends on the details of the experimental conditions; however, it is generally fast enough to see the inner level increase. If the inner vessel is lifted out of the helium bath, the hydrostatic pressure difference works in the opposite direction, causing the liquid to flow out of the vessel.

The existence of helium film flow was first observed by H. Kamerlingh Onnes in 1922; however, he interpreted it in terms of an evaporation and condensation mechanism. In 1937, Rollin and Simon were able to show that the mobility of the helium film is based on the theory of He II. As a result, this film flow process is sometimes referred to as the Rollin film. Considerable research has been conducted to expand the understanding of He II film flow. Factors that affect the thickness of

the film include height above the helium bath, substrate material, and temperature. Empirical relationships have been suggested which relate the film thickness d with the height H above the helium bath:

$$d = \frac{K}{H^n} \tag{6.34}$$

where H is the film height in cm, $K \simeq 3 \times 10^{-6}$ cm^{n+1} and n is between 0.3 and 0.45. For numerical values, note that the film at about 1 cm above the liquid is approximately 30 nm (300 Å) thick, which corresponds to around 80 atomic layers. Mobility of He II films has been demonstrated down to thickness of a few atomic layers, see Sect. 10.2.

The practical significance of the Rollin film is that in addition to mass flow through the film there can also be heat flow. The existence of heat flow through the mobile He II film can affect strongly the system performance. One particular example is the pumping work required to maintain He II at constant temperature. If the helium is contained in a vessel with an opening for pumping at the top, the film will climb the walls of the container. Heat will be conducted between the point on the container, which may be as high as T_λ, and the bath. If the opening to the container is large, this heat flow can cause a sizable load on the bath. The best method to reduce this heat inflow is to restrict the free surface of helium on which the pump is working. This will reduce proportionally the helium film flow. This topic is discussed further in Chaps. 8 and 9.

6.3 Excitations in He II

Until the 1930s, the unique properties of He II had little fundamental theoretical understanding. London was the first to point out the close correspondence between the behavior of a Bose gas and He II [4]. This observation resolved only part of the problem because the gas models do not adequately describe the transport properties. Furthermore as discussed above, the state properties of He II are quite different from those predicted by the Bose gas model, both in terms of the order of the transition and the low-temperature specific heat.

The first attempt to develop a more complete theory of He II was introduced by Tisza [5]. Tisza suggested that liquid He II may be thought to consist of two interpenetrating fluids, a concept which is similar to a model developed by Gorter and Cashmir to qualitatively describe the behavior of superconductors [6]. Although the two-fluid model was chronologically the first theory to advance significantly the understanding of He II, it did not satisfactorily address the behavior of the state properties. The Landau theory [7] of excitations in He II both explains the physics of properties such as the specific heat and entropy as well as providing a more fundamental understanding of the two fluid nature of He II. The latter topic is addressed in the next section.

Landau approached the problem of He II by introducing an excitation spectrum that might consist of a number of different modes. The spectrum is semi-empirical in that it is adjusted to predict experimental data in a consistent manner. Two types of excitation were introduced as part of the model, each having different regions of significance. First, like all liquids, He II is envisioned to possess longitudinal phonon excitations; transverse phonons can exist only in the solid state. These longitudinal phonons are characterized by a velocity c_l, such that its energy spectrum can be written,

$$\varepsilon = c_l P \tag{6.35}$$

where P is the momentum of the phonon given explicitly by $P = hk$ with k being the wave number.

The other excitation mechanism unique to He II is referred to as the "roton". The name "roton" originally was attached to this mechanism because of the feeling that it may represent some form of quantized circulation. However, this suggestion is of no practical significance. It is most important to note that the rotons bring about a higher wave-number excitations in the He II spectrum. These are characterized by a minimum in the spectrum and has the general form

$$\varepsilon = \Delta + \frac{(P - P_0)^2}{2\mu} \tag{6.36}$$

where Δ is the minimum energy to excite one roton and P_0 and μ are empirically determined quantities. Based on experimental data, numerical values for these parameters are [8]:

$$\frac{\Delta}{k_B} = 8.65 \text{ K}$$

$$\frac{P_0}{\hbar} = 0.191 \text{ nm}^{-1}$$

$$\mu = 0.16 m_4$$

where m_4 is the atomic mass of a helium atom. Combining the two excitation mechanisms into one continuous spectrum results in the dispersion curve, shown in Fig. 6.12. The regions described by the two types of excitation are highlighted on the curve. Note that Δ in particular is temperature dependent.

The test of the theory is in its ability to predict experimental data. It is relatively easy to calculate the specific heat for the phonon part of the spectrum. Using the Debye model for longitudinal phonons, the specific heat at low temperatures may be written as,

$$C_{ph} = \frac{2\pi^2 k_B^4}{15\rho\hbar^3 c_l^3} T^3 \tag{6.37}$$

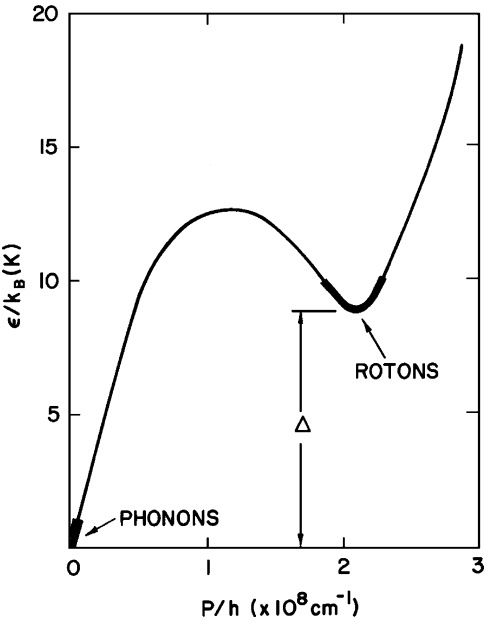

Fig. 6.12 Dispersion curve indicating the elementary excitations of the Landau theory

which can be evaluated for the properties of He II to give, $C_{ph} = 20.7T^3$ J/kg K. This value is an extremely good prediction of experimental results given by the empirical correlation in (6.28).

A further check for the existence of phonon excitations in He II is in the behavior of the thermal conductivity at low temperatures. For $T \lesssim 0.6$ K, the normal fluid density is nearly zero so the heat cannot be transported by the internal convection mechanism, which was briefly discussed in the introduction to this chapter and is covered in more detail in the next section. Rather in this temperature regime, the thermal conductivity of He II behaves like that of a dielectric solid at low temperatures where,

$$k_{ph} = \frac{1}{3}\rho C_{ph} v_1 l \tag{6.38}$$

The velocity v_1 is the speed of first sound (longitudinal phonons) in liquid helium ~240 m/s and l is the mean free path for the phonons. The phonon mean free path at low temperatures is often dominated by boundary scattering so that $l \sim d$, the tube diameter [8]. For a tube of 1 mm diameter, (6.38) predicts k ~50 W/m K at 0.5 K with a temperature dependence of T^3.

The roton excitations in He II dominate the physical behavior for high temperatures, $T \gtrsim 1$ K. As with phonons, rotons are collective excitations in the liquid. Since the roton region of the dispersion curve is at high temperatures, the physical processes obey Boltzmann statistics. Applying Landau's dispersion relationship to the He II, one can derive expressions for the thermodynamic

properties. As expected, these expressions are exponential in the roton energy gap Δ. In particular, the entropy may be written,

$$s_r = \frac{2(k_B\mu)^{1/2}P_0^2\Delta}{(2\pi)^{3/2}\rho\hbar^3T^{1/2}}\left(1+\frac{3k_BT}{2\Delta}\right)e^{-\Delta/k_BT} \tag{6.39}$$

and the specific heat contribution,

$$C_r = \frac{2\mu^{1/2}P_0^2\Delta^2}{(2\pi)^{3/2}\rho\hbar^3k_B^{1/2}T^{3/2}}\left[1+\frac{k_BT}{\Delta}+\frac{3}{4}\left(\frac{k_BT}{\Delta}\right)^2\right]e^{-\Delta/k_BT} \tag{6.40}$$

All of which are functions of k_BT/Δ. It is important to note that all expressions have an exponential cutoff at low temperatures, indicating a relatively small roton contribution for T <1 K. Also, although indicated as a constant in (6.39) and (6.40), Δ decreases somewhat as T approaches T_λ.

The theoretical expression for the roton contribution to the specific heat (6.40) does not obviously agree with the empirical expression (6.29) where $C \approx T^{5.6}$. Since the specific heat is dominated by rotons only between 1.1 and 2.1 K, the distinction between the power law and an exponential form is not large, see problem 8. Nonetheless, it should be noted that the variation of specific heat near T_λ is one method to measure energy gap associated with the roton minimum, Δ, indicating a fairly close correspondence with (6.40). The empirical expression (6.29) is used mostly for calculations of an engineering and applied nature.

6.4 Two-Fluid Model

Although the theory of excitations in He II advanced by Landau and others has considerable physical basis, it is not very useful for describing the transport properties. The two fluid model, which was originally suggested by Tisza and later refined by Landau, treats He II as if it were made up of two fully miscible fluid components and takes the state properties of entropy and specific heat as given quantities. This two-fluid model is then a description of the fluid mechanics of He II, which is particularly successful at describing heat and mass transport.

The two-fluid model envisions the He II to be comprised of two interpenetrating fluid components: normal fluid, which contains the excitations in the liquid, and the superfluid. At this point it is worth making a comment about nomenclature. Often in generic terms, He II is referred to as "superfluid" because this was the word used to describe its behavior before the existence of the two-fluid model. Subsequent to the introduction of the two-fluid model, it has been more correct to refer to liquid helium below T_λ as He II and the component in the two-fluid model as superfluid. This convention, which assumes some knowledge of the physics of He II, will be used throughout this book.

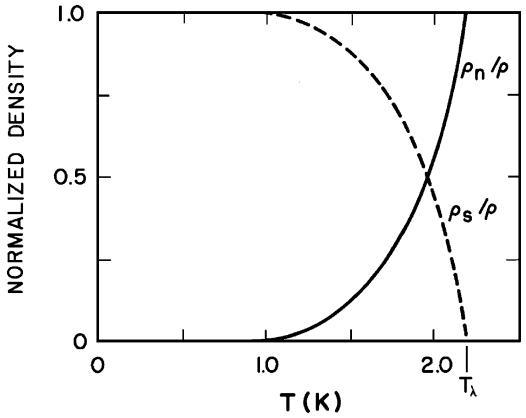

Fig. 6.13 Ratio of normal and superfluid densities in He II

The normal fluid component to the He II is assumed to behave as an ordinary liquid. It is described by having a density ρ_n, viscosity μ_n, and specific entropy s_n. On the contrary, the superfluid component has density ρ_s, no viscosity ($\mu_s = 0$), and no entropy ($s_s = 0$). The properties of the fluid must be comprised of a linear combination of the two components. Thus, the density is a sum of the two component densities,

$$\rho = \rho_s + \rho_n \tag{6.41}$$

Since the superfluid has no entropy, it follows that the He II entropy can be written in terms of the normal fluid component alone:

$$\rho s = \rho_n s_n \tag{6.42}$$

As was discussed in the previous section, the entropy of He II is strongly temperature dependent, going approximately as $T^{5.6}$ between 1.1 K and T_λ. For the two-fluid model, it is assumed that $s_n = s_\lambda$, the entropy at the λ-point, and that all the temperature dependence in (6.42) enters through the variation of the normal fluid density. It is therefore possible to write

$$\frac{\rho_n}{\rho} = \left(\frac{T}{T_\lambda}\right)^{5.6} \quad \text{for} \quad T \leq T_\lambda \tag{6.43}$$

as the temperature dependence of the normal fluid density. The ratios of normal and superfluid densities to that of the bulk liquid are shown in Fig. 6.13. Recall that for He II the density has a rather weak temperature dependence so these curves closely correspond to the total density profile for each component. Due to this strong temperature dependence, the superfluid component composes about 99% of He II at 1 K.

Concerning the viscosity, the model assumes that $\mu_s = 0$ and the dissipative interaction is due only to the normal fluid. This assumption corresponds to the

physical fact that the superfluid experiences no resistance to flow and therefore no turbulence. The superfluid can flow through a channel without viscous drag along the boundaries. In other words, the velocity of the fluid will be the same at the center of the channel as near the sides. The equivalent mathematical expression for this statement is to say that the superfluid velocity can have no curl:

$$\nabla \times \mathbf{v_s} = 0 \tag{6.44}$$

This description of the superfluid viscous interaction is only partially correct. Above a certain critical velocity $\mathbf{v}_c$, the superfluid does transition to a turbulent state but by itself remains an invicid fluid consistent with (6.44).

6.4.1 Equations of Motion

As described by the two-fluid model, He II can be thought to consist of two separate interpenetrating fluids. This picture should not be taken too literally. It is only a model and the existence of superfluid and normal fluid components is a hypothesis. Nonetheless, the existence of this model allows equations of motion to be written that describe the behavior of the fluid.

In particular, the momentum density $\mathbf{j}$ of He II can be written as a sum of the momentum density components,

$$\mathbf{j} = \rho_s \mathbf{v}_s + \rho_n \mathbf{v}_n \tag{6.45}$$

where $\mathbf{v}_s$ and $\mathbf{v}_n$ are the superfluid and normal fluid velocities. An interesting and important special case of (6.45) is when there is no net mass flow and $\mathbf{j} = 0$. Thus, the bulk He II is static although the superfluid and normal fluid components can flow in opposite directions consistent with the requirement that,

$$\rho_s \mathbf{v}_s = -\rho_n \mathbf{v}_n \tag{6.46}$$

This expression leads to the notion of "internal convection" or "counterflow" where the two fluids can flow and carry entropy in He II without experiencing macroscopic mass flow.

In addition to the expressions for density (6.41) and momentum (6.45), the two-fluid model relies heavily on conventional fluid mechanics which is used to describe the behavior of each component. The continuity equation describes the rate of change of the density in a given volume of space, that is,

$$\nabla \cdot \mathbf{j} = -\frac{\partial \rho}{\partial t} \tag{6.47}$$

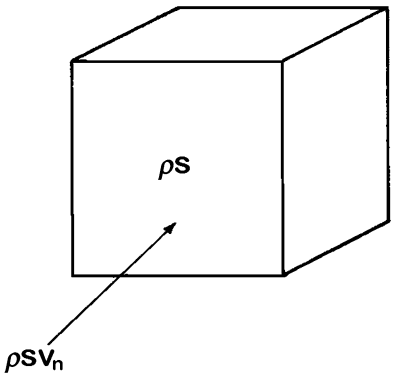

Fig. 6.14 Schematic volume containing He II

where each component of He II must obey this relationship. Euler's equation describes the acceleration of an ideal fluid. An ideal fluid supports no shear stress even in motion and has negligible viscosity. As a consequence, the only force acting on the fluid is that due to its pressure gradients:

$$\frac{\partial \mathbf{v}}{\partial t} + \mathbf{v} \cdot \nabla \mathbf{v} = -\frac{1}{\rho} \nabla p \tag{6.48}$$

The above expression is analogous to Newton's second law applied to fluids; stated simply, it defines the rate of acceleration of a fluid subjected to a force per unit volume ∇p.

For the development of the two-fluid model we start by reducing (6.48) to a linear expression. Since the second term on the left-hand side goes as $\mathbf{v}^2$ for small velocities, it is neglected and assuming an incompressible fluid leads to

$$\frac{\partial \mathbf{j}}{\partial t} \simeq -\nabla p \tag{6.49}$$

The suitability of Euler's equation to describe the behavior of the superfluid component should appear obvious. By definition the superfluid does not support shear flow or have a viscous interaction. However, for the normal fluid there is an important viscous term that enters a number of physical processes including heat transport. In the description of these processes, more complex fluid mechanics are required in the form of the Navier–Stokes equation applied to the normal fluid.

Finally, we need to develop an expression for the behavior of the entropy flow of He II. Since fluids described by Euler's equation experience no dissipative interaction, all processes are reversible. Reversibility of fluid flow processes implies that entropy must be conserved. It is therefore possible to write an expression for entropy conservation which is analogous to mass conservation in the continuity equation. Consider a volume containing helium with density ρ and specific entropy s; (see Fig. 6.14). Here the entropy per unit volume is $\rho s = \rho_n s_n = \rho_n s_\lambda$

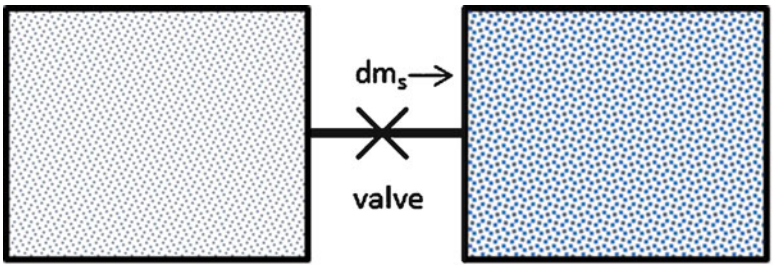

Fig. 6.15 Isentropic process involving He II

since the normal fluid is the only component with nonzero entropy. Furthermore, the rate of flow of entropy into the volume is determined by the flow of the normal fluid at velocity v_n. This process can be treated by an expression that relates the entropy content to the entropy flow:

$$\frac{\partial}{\partial t}(\rho s) = -\nabla \cdot (\rho s \mathbf{v}_n) \tag{6.50}$$

This expression is analogous to the continuity equation for mass conservation.

The first step in development of the equations of motion for He II is to consider the superfluid component. To do this, it is helpful to imagine an idealized experiment. Assume there exists a volume containing a number of helium atoms with a total mass m. A conceptual picture of this system is shown in Fig. 6.15. The volume is connected to another volume containing helium but there is a special valve between these two volumes, which only allows the superfluid component to flow. In practice, such a valve can be made by packing fine powder into the tube which clamps the normal fluid by viscous interaction but allows the superfluid to flow.

The thermodynamic function that is useful in describing the change in the internal energy of the system associated with a change in mass dm is the Gibbs potential per unit mass, g. Assuming the system is open only to the addition of superfluid, we can write the differential form of the first and second laws of thermodynamics as

$$dE = T\ ds - p\ dv + g dm \tag{6.51}$$

Two initial assumptions can be used to simplify the (6.51). First, for a constant volume process, $dv = 0$, so that the second term is eliminated. More importantly, the entropy is constant, $ds = 0$, since the fluid that is being added to the box is only superfluid with all particles in the ground state. Therefore, the change in internal energy is proportional to the change in mass, that is,

$$dE = g dm \tag{6.52}$$

It is sometimes more helpful to think of this process in terms of a thermodynamic driving force that is the gradient of the potential. The acceleration of the superfluid is equal to the negative of the thermodynamic driving force:

$$\frac{d\mathbf{v}_s}{dt} = -\nabla g \tag{6.53}$$

This expression can be written in terms of common thermodynamic quantities by using the differential form of the specific Gibbs potential,

$$dg = -s\ dT + v\ dp \tag{6.54}$$

and since this is a total differential, (6.53) can be inserted to provide an equation of motion for the superfluid component:

$$\frac{\partial \mathbf{v}_s}{\partial t} = s\nabla T - \frac{1}{\rho}\nabla p \tag{6.55}$$

Note that between (6.53) and (6.55) the velocity derivative has been changed from a total to partial derivative. This approximation, which is good to terms of order $\mathbf{v}^2$, is useful in placing the equation in its well known form. The above expression, (6.55), is of fundamental importance to understanding the behavior of He II. Although its existence seems to be based on an idealized example, it is extremely effective at predicting numerous physical aspects of He II including the fountain effect and sound propagation both of which are discussed next.

6.4.2 Thermomechanical Effect

The thermomechanical effect, or fountain effect as it is more commonly known, is predictable from the equation of motion for the superfluid component in the two-fluid model. As has already been discussed in the properties section of this chapter, there exists a relationship between temperature difference and pressure difference in He II known as London's equation, (6.33). Furthermore, the proportionality factor is the volumetric entropy ρs. To see how this relationship originates, consider the experimental setup shown in Fig. 6.16. Two containers each filled with He II are connected together through a superfluid filter or fine capillary having a diameter $<1\ \mu$m. The capillary allows superfluid component to flow from one container to the other while the normal fluid is clamped by the viscous interaction to the walls of the capillary.

In steady state, the two containers have equal Gibbs potentials, and, furthermore, the fluid will not be accelerating; that is $\partial \mathbf{v}_s/\partial t = 0$. It follows that by

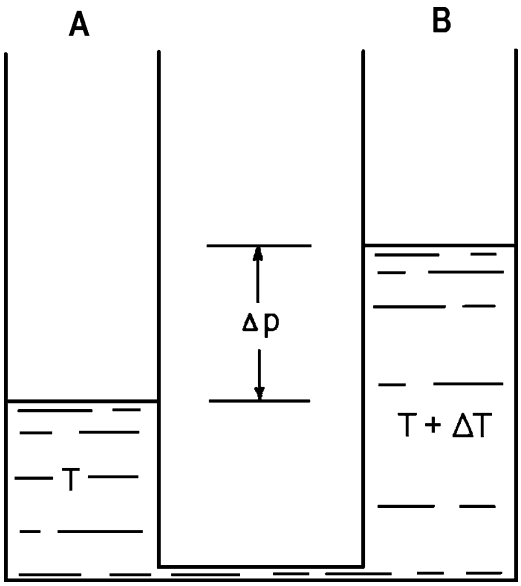

Fig. 6.16 Thermomechanical effect: He II reservoirs connected by a narrow capillary maintain level difference due to temperature difference, $\Delta p = \rho s \Delta T$

setting the left-hand side of (6.54) to zero, the fountain pressure relationship is derived:

$$\frac{dp}{dT} = \rho s \tag{6.56}$$

If, as in Fig. 6.16, the temperature on either side of the capillary is not equal, there will be a flow of helium under the influence of the induced pressure difference. This process will continue until the hydrostatic head ($\rho g\ \Delta h$) equals the fountain pressure ($\rho s\ \Delta T$). It is worth noting the order of magnitude of this effect. At 1.8 K, $dp/dT = 80$ Pa/mK or about 5% of the vapor pressure per millikelvin. Thus, a 1 mK temperature difference between the two sides in Fig. 6.16 will, cause a 80 Pa pressure difference which corresponds to about a 60 mm helium liquid level difference.

A corollary to the thermomechanical effect is something called the mechanocaloric effect, which relates the heat flow brought on by physically forcing the helium from one side to the other. Consider the system as described above in equilibrium where initially $T_A = T_B$ and the two heights are the same. Now imagine that a movable, insulating piston on the left-hand side pushes the helium down and through the capillary; see Fig. 6.17. Since only the superfluid can pass through the capillary, the effect of the flow will be to reduce the entropy per unit volume on the right, B, and increase it on the left, A. In other words, the temperature on the right

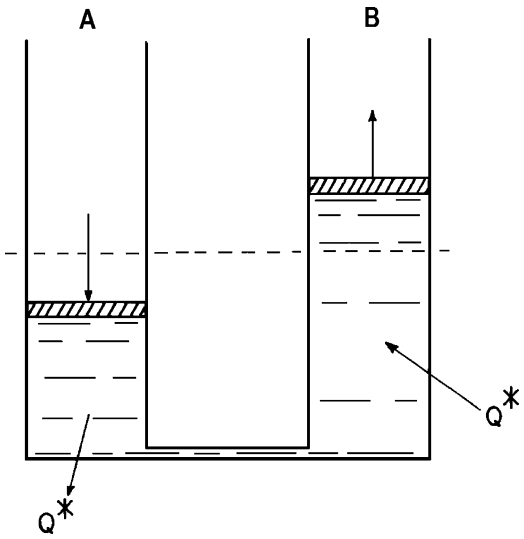

Fig. 6.17 Mechanocaloric effect: He II forced to flow between reservoirs connected by a narrow capillary. Excess heat content Q* is transferred to the surroundings from A and received from surroundings to B

will go down and on the left it will go up. The effect is similar to heating the fluid on the left and cooling it on the right. The equivalent heat that it transferred is,

$$Q^* = \rho s T \Delta V \tag{6.57}$$

where ΔV is the volume of helium flowing between these two vessels.

To bring this system back to equilibrium the amount of heat Q^* must be transferred between the two vessels through some other means than through the capillary. One method would be if these two vessels were immersed in a constant temperature bath of He II. In that case, the higher temperature side would liberate heat into the bath and the low temperature side would absorb the same quantity of heat. However since the process is isentropic, the final state would be identical to the initial condition.

As a final comment, the above thought experiment is definitely idealized. It requires two frictionless, insulating pistons. This is because if the helium is in contact with its vapor, heat will also be transferred through the vapor phase by evaporation and condensation processes. The lower-entropy fluid on the right will absorb heat from the vapor by condensation while the higher-entropy fluid on the left will reduce its temperature by evaporating some of the liquid into the vapor phase.

6.4.3 Sound Propagation

One of the most interesting characteristics of He II is ability to transmit more than one type of sound wave. In addition to ordinary or first sound, which is a density variation brought on by local pressure gradients, there is a mechanism called second

sound, which is propagation of thermal waves as a result of fluctuations in the local entropy. The existence of second sound is predicted by the two-fluid model.

To begin, we consider briefly the origin of ordinary first sound. Sinusoidal wave propagation can be obtained analytically by combining the continuity equation (6.47) with Euler's equation for an ideal fluid with linear response (6.48). The result is a wave equation that associates pressure and density:

$$\nabla^2 p = \frac{\partial^2 \rho}{\partial t^2} \tag{6.58}$$

This differential equation has the standard solution of a sine wave varying function. The wave packet has a characteristic speed c_1 given by,

$$c_1^2 = \left(\frac{\partial p}{\partial \rho}\right)_s = \frac{\gamma}{\rho \kappa} \tag{6.59}$$

where the partial differentiation is taken at constant entropy and γ is the ratio of the specific heats, C_p/C_v. The speed of first sound in liquid helium is of the order 200 m/s.

Second sound is the result of entropy fluctuation rather than density fluctuations as in ordinary sound. Beginning with the entropy conservation equation (6.50) and the equation of motion for the superfluid component (6.55) the pressure gradient may be rewritten as

$$-\nabla p = \rho\left(\frac{\partial \mathbf{v}_s}{\partial t} - s\nabla T\right) \tag{6.60}$$

The time rate of change of the momentum is equal to the negative of the pressure gradient. Taking the derivative of (6.45) and dropping all except linear terms in velocity, we obtain

$$\frac{\partial \mathbf{j}}{\partial t} = -\nabla p \simeq \rho_s \frac{\partial \mathbf{v}_s}{\partial t} + \rho_n \frac{\partial \mathbf{v}_n}{\partial t} \tag{6.61}$$

which combined with (6.60) results in an expression for the difference in the acceleration of the two fluid components:

$$\frac{\partial \mathbf{v}_n}{\partial t} - \frac{\partial \mathbf{v}_s}{\partial t} = -\frac{\rho}{\rho_n} s\nabla T \tag{6.62}$$

The above expression can be used to illustrate some important physical facts. In non-dissipative He II, a temperature gradient produces a relative acceleration of the two fluid components. Because the relative densities of the two fluid components are related to the entropy, a temperature gradient implies a variation in ρ_s/ρ_n.

To make (6.62) approach more closely a wave equation, one can take the divergence of each side and then replace the superfluid velocity with the continuity equation. The results are simpler if it is assumed that the total density is constant, $\partial\rho/\partial t \approx 0$. A relationship is then obtained for the normal fluid velocity in terms of the second derivative of the temperature,

$$\frac{\rho_n}{\rho_s}\frac{\partial}{\partial t}(\rho\nabla\cdot\mathbf{v}_n) = -\rho s\nabla^2 T \tag{6.63}$$

The left-hand side may be written in terms of the fluid entropy by the conservation of entropy equation, (6.50). This result is reduced to a fairly simple form if the entropy does not vary significantly with time and position; that is,

$$\frac{\partial^2 s}{\partial t^2} = \frac{s^2\rho_s}{\rho_n}\nabla^2 T \tag{6.64}$$

which is referred to as the linearized second sound equation. It predicts a sine wave varying function propagating with speed c_2 given by

$$c_2^2 = \frac{s^2\rho_s}{\rho_n}\left(\frac{\partial T}{\partial s}\right)_\rho \simeq \frac{\rho_s}{\rho_n}\frac{Ts^2}{C_v} \tag{6.65}$$

The expression for the speed of second sound turns out to be quite accurate and is even used as a method of measuring the entropy of He II [9]. Typical values for c_2 are around 20 m/s between 1 and 2 K.

It is worth noting at this juncture the different methods available for measurement of second sound. As might be expected, these methods have analogues in the measurement of first sound, except that a travelling temperature wave is detected with a thermometer rather than a travelling pressure wave being detected with a pressure transducer. There are principally two methods of measuring the velocity of second sound. The most obvious is the time-of-flight method shown schematically in Fig. 6.18a. A heater is located some distance away from the source providing a pulse that travels the length of the channel. The pulse is detected at some time later, $t = L/c_2$. This method, although effective, is cumbersome since the channel must be fairly long to have good resolution, but in that case there can be attenuation of the pulse due to other considerations to be discussed below. Consequently, the time-of-flight method is not the most convenient for measuring c_2.

Second sound may also be measured by a resonance method. In this case, a channel is constructed with a closed end, as in Fig. 6.18b. Within the channel there is a heater that can be driven at variable frequency. Also installed in the channel is a movable thermometer located between the heater and closed end of the tube. The principle, which was originally employed by Peshkov [10] to determine c_2, is to drive the heater at a resonant frequency of the channel, $\nu = n\,c_2/2L$, where n is an integer. The temperature sensor is then moved along the tube, detecting the

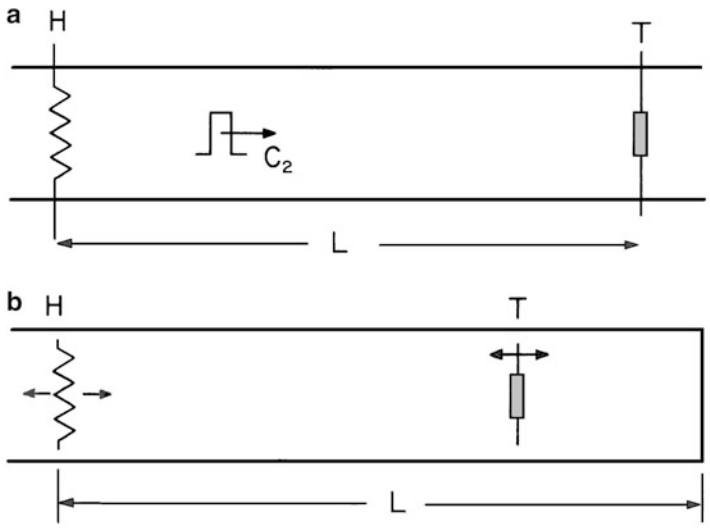

Fig. 6.18 Measurements of the velocity of second sound: (**a**) time-of-flight method and (**b**) resonance method

resultant standing wave. Besides simplicity, there are other advantages of this resonant method for detecting second sound. In such a device, one can continuously monitor the amplitude of the second sound wave. As we will discuss below, the amplitude of the second sound wave is attenuated by turbulence in a fairly well understood manner. Therefore, a continuously operating second sound resonator can be used as a local detector of turbulence in He II.

Another method for detecting second sound is based on the associated oscillating relative motion of the two fluid components [11]. A thin metallic foil containing sub-micron diameter holes and immersed in He II can deflect a time variation of ρ_s/ρ_n. This occurs because the normal fluid is unable to flow through the holes and thus will exert a pressure on the foil, while the superfluid component will flow through the sub-micron holes. Such a devise can be driven at a desired frequency to produce a traveling wave of second sound. Similarly, the device can detect the arrival of the second sound as a deflection of a detector foil of the same material. One advantage of using such a second sound detector is that it does not generate as much entropy as the heater-thermometer system.

Second sound has been measured extensively everywhere from T_λ to near absolute zero and as a function of pressure. Values for c_2 at near saturated vapor pressure are compared to c_1 in Fig. 6.19. Note that c_2 is approximately constant (~20 m/s) over the range 1–2 K. At lower temperatures the second sound speed increases rapidly as $T \rightarrow 0$ K. Theory predicts that the limiting low-temperature value of second sound speed is $c_1/\sqrt{3} \simeq 137$ m/s, although it is difficult to measure below 1 K due to the very low normal fluid density.

In summary, the important factors controlling first sound and second sound are listed in Table 6.2. For He II and the two-fluid model, first sound requires that the

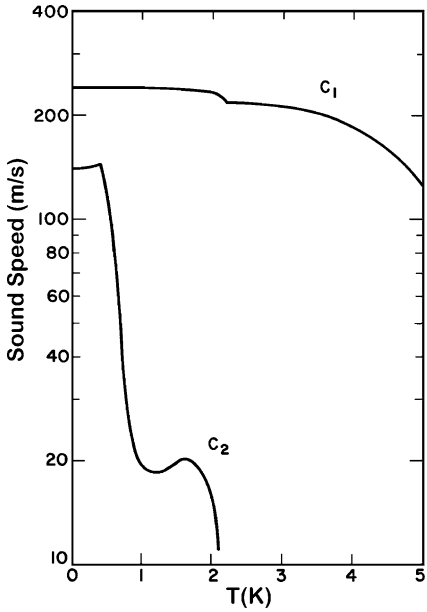

Fig. 6.19 Speeds of sound in liquid helium

Table 6.2 Comparison of sound propagation in He II

	First sound	Second sound
Driving force	δp	δT
Propagator	$\delta\rho$	δs
Density (ρ)	Wavelike	~ constant ($\rho_n \mathbf{v}_n \approx -\rho_s \mathbf{v}_s$)
Temperature (T)	~ constant ($\mathbf{v}_s \approx \mathbf{v}_n$)	Wavelike
Speed	$c_1 = \left(\frac{\gamma}{\rho\kappa}\right)^{1/2} \approx 240$ m/s	$c_2 = \left(\frac{\rho_s}{\rho_n}\frac{Ts^2}{C_v}\right)^{1/2} \approx 20$ m/s
Relationship	$\nabla^2 p = \frac{\partial^2 \rho}{\partial t^2}$	$\nabla^2 T = \frac{\rho_n}{s^2\rho_s}\frac{\partial^2 s}{\partial t^2}$

two component velocities be in the same direction, while second sound is associated with a counterflow having $\mathbf{v}_s$ in the opposite sense to $\mathbf{v}_n$. The existence of second sound in He II can be used as a diagnostic tool since it is attenuated by forces of interaction between the two fluid components. Thus, the variation of the second sound amplitude can give information about the local state of the helium.

6.4.4 Viscous Flow

Until now we have not fully considered the impact of viscosity in the two-fluid model for He II. In the prediction of second sound the viscosity of each component is assumed to be negligible, allowing the use of a linearized form of Euler's equation. On the other hand, in analyzing the thermomolecular fountain effect,

the normal component has been given sufficient viscosity that it cannot flow at all through a capillary with $d < 1$ μm. In actual fact, neither of these assumptions are correct since the normal fluid has a measurable viscosity which is of the order of 1 μPa-s in the regime of interest. The present section examines how the introduction of the normal viscosity μ_n into the two-fluid model aids in the prediction of several important physical phenomena.

To begin, a viscous term is introduced into the linearized Euler's equation (6.49), resulting in an expression for the rate of change of the momentum that includes dissipation,

$$\frac{\partial \mathbf{j}}{\partial t} = -\nabla p + \mu \nabla^2 v \tag{6.66}$$

where the viscosity μ enters along with the second-order derivative of the velocity. Note that the superfluid viscosity is zero in the two-fluid model and that the momentum can be written as a sum of the two components, $\mathbf{j} = \rho_s \mathbf{v}_s + \rho_n \mathbf{v}_n$ (6.45). Combining these facts and keeping only terms which are linear we can rewrite (6.66) a

$$\rho_s \frac{\partial \mathbf{v}_s}{\partial t} + \rho_n \frac{\partial \mathbf{v}_n}{\partial t} = -\nabla p + \mu_n \nabla^2 \mathbf{v}_n \tag{6.67}$$

where the left-hand side is simplified by the assumption that ρ_s and ρ_n are weak functions of time. Recall that a relationship for the time derivative of the superfluid component has already been derived (6.55). Combining that relationship with (6.67) gives the two linearized equations that describe the flow of He II including the normal fluid viscosity,

$$\rho_s \frac{\partial \mathbf{v}_s}{\partial t} = \rho_s s \nabla T - \frac{\rho_s}{\rho} \nabla p \tag{6.68}$$

and

$$\rho_n \frac{\partial \mathbf{v}_n}{\partial t} = -\rho_s s \nabla T - \frac{\rho_n}{\rho} \nabla p + \mu_n \nabla^2 \mathbf{v}_n \tag{6.69}$$

The above expression (6.69) is generally referred to as the Navier–Stokes equation for the normal fluid component. It is of interest here to determine how well these equations predict the transport properties of He II.

As mentioned in Sect. 6.2.2, there are two principal methods for measuring the viscosity of a fluid: Poiseuille type flow through a capillary and the damping of an oscillating disk. For the case of ordinary liquids, these two methods yield essentially identical results. However, in the case of He II, very different results are obtained which can be understood only in terms of the two-fluid model.

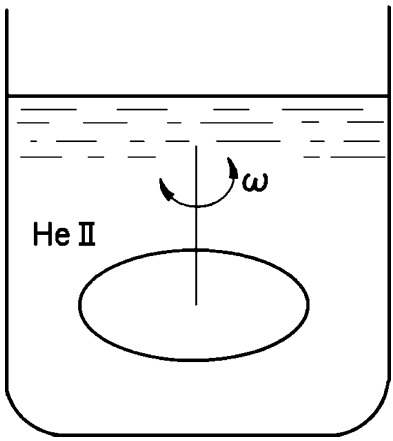

Fig. 6.20 Oscillating disk for viscosity measurement

Let us first consider Poiseuille flow. If two vessels containing He II at different temperatures are connected together through a capillary of very small diameter, we have previously stated that the apparent viscosity of the helium is extremely small if not zero. Some measurements have indicated that $\mu \lesssim 10^{-12}$ Pa-s, which is about six orders of magnitude less than the viscosity of He I. A further surprising feature of these measurements is the relationship between mass flow or fluid velocity and pressure difference. To first order, the mass flow is independent of Δp. These results can also be interpreted in terms of the two-fluid model. In the channel, the normal fluid interacts strongly with the boundaries and is therefore locked in place. The superfluid component has zero viscosity and thus can flow through the channel without losses. The fluid in motion is the superfluid component and the apparent viscosity should be extremely small. This result is consistent of course with the fountain effect, requiring that the pressure difference be proportional to temperature difference. If the above description were complete, the superfluid component would be expected to accelerate indefinitely. However, this does not occur and the superfluid appears to transport itself at constant velocity nearly independent of the pressure difference. This velocity is termed the critical velocity $\mathbf{v}_c$ and also as we will see impacts the behavior of the heat transport. Briefly, above the critical velocity the superfluid becomes turbulent, which brings about new interactive mechanisms between the two fluid components.

The alternative method of measuring the viscosity of He II is to oscillate a disk in the liquid and measure the damping; see Fig. 6.20. Since the damping of the oscillation is a function of moment of inertia and drag with the fluid, the oscillatory mass is related closely to the viscosity of the liquid. The results of this measurement are substantially different from the Poiseuille experiment discussed above. In fact, what is observed is more traditional behavior for the viscosity; see Fig. 6.21. Below the λ-point the measured viscosity decreases, forming a broad minimum of a nearly constant value around 1.4 μPa-s between 2.0 and 1.5 K. Below this temperature the viscosity increases almost exponentially with decreasing temperature. It is of primary interest to interpret these results in terms of the two fluid model. Unlike Poiseuille flow, the oscillating disk technique forces the normal fluid to

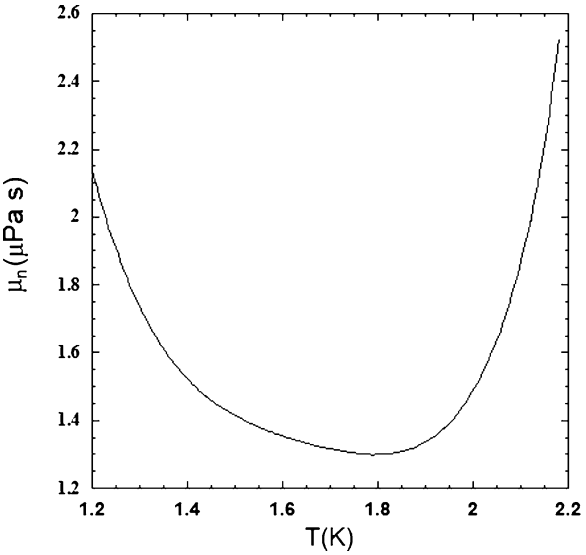

Fig. 6.21 Viscosity of He II as measured by oscillating disk

flow against its own viscous drag forces. Since the normal fluid interacts strongly with the boundaries, the oscillating disk directly measures its viscosity. Therefore, the results plotted in Fig. 6.21 actually represent the behavior of the normal fluid viscosity μ_n.

One of the landmark experiments involving rotating He II was performed by E. Andronikashvili [12]. This work is of great significance for it clearly supports the concept of the two fluid model and agrees very well with other measurements of He II properties. The basic idea of the experiment is shown in Fig. 6.22. It employs a rotating viscometer; however, unlike the measurement described above, this device is fitted with a large number of narrowly spaced parallel plates. The plate spacings were chosen so that they were less than the viscous penetration length, $d < (2\mu_n/\rho\omega)^{1/2}$. This condition requires all the viscous fluid to rotate with the plates. The two fluid model demands that the only fluid in motion would be the normal fluid and thus the moment of inertia would be proportional to ρ_n. Thus the Andronikashvili experiment directly measures the normal fluid density. The results of this experiment are shown in Fig. 6.23, which is a plot of ρ_n/ρ versus temperature. Also indicated in the graph are values of ρ_n/ρ measured by second sound (6.65). The agreement between the two experimental findings is remarkable and adds considerable support to the physical basis of the two fluid model.

6.4.5 Heat Transport

The behavior of He II subjected to a heat flow can be interpreted similarly in terms of the two-fluid model. Consider two reservoirs containing He II and connected by a channel of diameter d. At this point it is important to require that d be small, of the

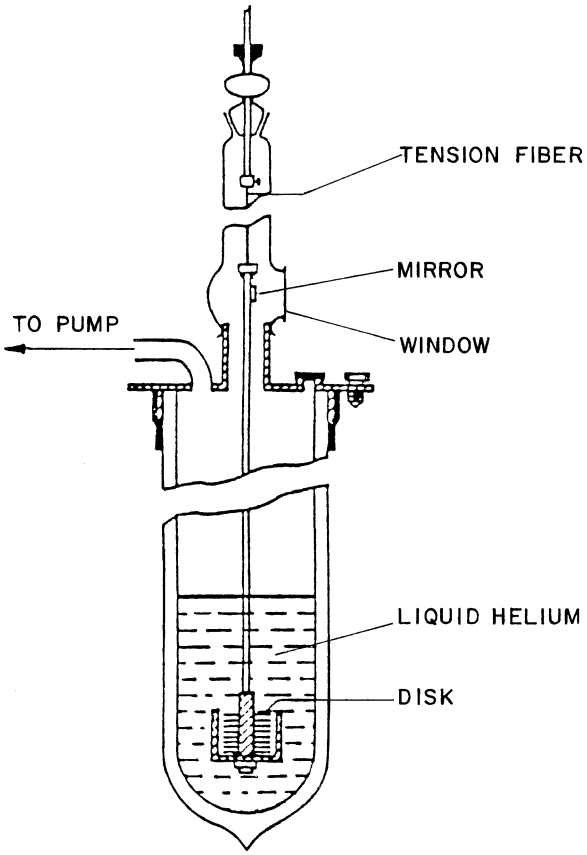

Fig. 6.22 Schematic diagram of Andronikashvili experiment [12]

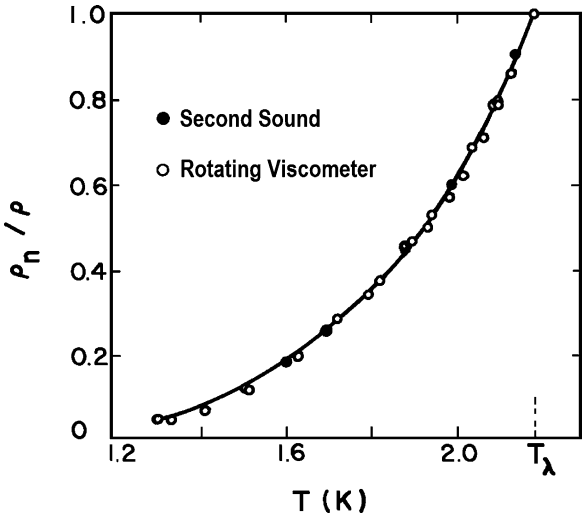

Fig. 6.23 ρ_n/ρ as a function of temperature compared with experimental results of Andronikashvili: ●, from second sound measurements and ○, from rotating viscometer

order 10 μm or less; however, the actual physical limitations are defined more clearly in the next section. If heat Q is applied to one reservoir, the temperature will rise and heat will be conducted through the connecting channel to the other reservoir. As long as the helium obeys ideal two-fluid hydrodynamics, the relationship between the temperature difference and pressure difference is established from London's equation, $\Delta p = \rho s \Delta T$.

To solve the heat flow problem in the steady state, the two fluid equations are combined, noting that $\partial \mathbf{v}_s/\partial t = \partial \mathbf{v}_n/\partial t = 0$, to yield

$$\nabla p = \mu_n \nabla^2 \mathbf{v}_n \tag{6.70}$$

which is known as the Poiseuille equation. It is interesting to note that (6.70) indicates a nonzero normal fluid velocity no matter how small the channel diameter. Thus, the assumptions that lead to the fountain effect are oversimplified.

Given a one dimensional channel of constant diameter d, (6.70) can be simplified to relate the normal fluid velocity along the channel axis v_n to the pressure and temperature gradients:

$$\frac{dp}{dx} = \rho s \frac{dT}{dx} = -\frac{\beta \mu_n \mathbf{v}_n}{d^2} \tag{6.71}$$

where x is the distance along the channel and β is a numerical constant determined by the geometrical conditions. Note that $\beta = 12$ for parallel plates or large aspect ratio rectangular cross sections and $\beta = 32$ for circular tubes.

Recall that in He II heat can only be carried by the normal fluid component. Thus, for the case where the net mass flow is zero, $v = 0$, the heat flux density q is directly proportional to v_n:

$$q = \rho s T \mathbf{v}_n \tag{6.72}$$

Subsequently, (6.72) will be shown to have a more general form when considering nonzero net mass flow. Eliminating v_n from the Poiseuille equation, (6.71), we obtain a heat conductivity equation that should describe the behavior of the ideal He II:

$$q = -\frac{d^2 (\rho s)^2 T}{\beta \mu_n} \frac{dT}{dx} \tag{6.73}$$

Note that this expression has a form similar to pure conduction although the function of proportionality, which is like an effective thermal conductivity k_{eff}, varies as the square of the diameter. Consider as an example heat flow in a 10 μm diameter circular tube containing He II at 1.9 K. By inserting the appropriate physical properties for He II, we can calculate an effective thermal conductivity of 49 kW/mK. This quantity increases strongly with temperature dominated by the dependence of $(\rho s)^2\, T \approx T^{12}$. Thus, although k_{eff} is around 100 times greater than that of high-purity copper at 1.9 K it is only about 25 W/mK at 1 K.

If (6.73) were the only expression determining the heat transport in He II, it would be possible to increase the effective thermal conductivity indefinitely by simply increasing the diameter, since $k_{\text{eff}} \sim d^2$. However, there is a physical limitation resulting from the existence of a critical velocity in the superfluid component. This critical velocity is the same one that limits the rate of helium flow through a channel under Poiseuille flow. It marks the transition to turbulent states in He II. This turbulence can occur in both the normal fluid and superfluid components, and as we will see has significant impact on both heat and mass transport behavior of He II.

Example 6.1

A 5 mm diameter circular cross section capillary contains He II at 1.8 K. For a heat flux q = 1 kW/m^2, calculate the temperature gradient and pressure gradient assuming the flow is ideal.
Inverting (6.72) solving for the magnitude of the temperature gradient,

$$\frac{dT}{dx} = \frac{32\mu_n}{d^2(\rho s)^2 T} q$$

Substituting numerical values for the various properties, gives a value of dT/dx = 0.15 K/m. Then the pressure gradient is obtained from London's equation, $dp/dx = \rho s dT/dx = 12.2$ kPa/m .

6.5 Vortices and Turbulence in He II

As outlined in the previous section, He II has a number of unique physical properties, the most notable being its transport properties. However, the two fluid model developed so far is incomplete because it contains no upper limit for the special heat and mass flow processes. Such behavior is not observed experimentally. Rather what is seen is a limiting critical velocity $\mathbf{v}_c$ above which the He II begins to exhibit viscous-like flow and nonideal heat transport. The subject of the present section is to convey the significance of this critical velocity and how it affects the unique properties of He II. In particular, we will show the origin of a new dissipative mechanism that controls heat transport in large systems.

6.5.1 Helium II in Rotation

In considering the flow of He II in the two-fluid model, an assumption was made that the superfluid component has zero viscosity, that is $\mu_s = 0$. This assumption leads to the requirement that superfluid velocity cannot have a gradient

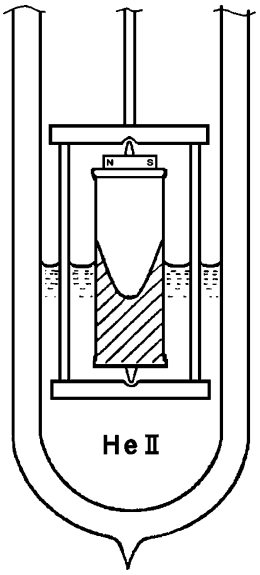

Fig. 6.24 Simple rotating bucket as used by Osborne [13]

perpendicular to the flow direction, that is $\nabla \times \mathbf{v}_s = 0$. An interesting contradiction occurs when this condition is applied to He II in rotation.

Consider a vessel containing He II rotating with an angular frequency ω. For the case in discussion, the temperature of the fluid will be taken to be below 1 K so there is hardly any normal fluid present and $\rho_s \simeq \rho$. Also to simplify the description, it will be assumed that the fluid is incompressible allowing $\rho \simeq$ constant and $d\rho/dt = 0$. It follows from the continuity equation that $\nabla \cdot \mathbf{j} = 0$, and since the normal fluid density is essentially zero,

$$\nabla \cdot \mathbf{v}_s = 0 \tag{6.74}$$

or the divergence of the superfluid velocity must vanish also. Combining (6.74) with $\nabla \times \mathbf{v}_s = 0$ requires that the superfluid obey Laplace's equation, with the curl-free relationship for the superfluid velocity,

$$\nabla^2 \mathbf{v}_s = 0 \tag{6.75}$$

which for a simple rotating vessel like in Fig. 6.24 has only one solution: that the He II must be at rest with $\mathbf{v}_s = 0$.

It is a straightforward argument to show that $\mathbf{v}_s = 0$ for any fluid that obeys Laplace's equation. Introducing the concept of circulation, we define

$$C = \oint \mathbf{v}_s \cdot dl \tag{6.76}$$

where the integral is taken around any simple path in the fluid. The circulation is a measure of the rotation of the fluid. Stokes' law can be applied to (6.76), yielding

$$\oint \mathbf{v}_s \cdot dl = \int_s \nabla \times \mathbf{v}_s \cdot ds \tag{6.77}$$

where $d\mathbf{s}$ is the integral over the surface enclosed by C. But for the superfluid, $\nabla \times \mathbf{v}_s = 0$, which can be satisfied only by

$$\oint \mathbf{v}_s \cdot dl = 0 \tag{6.78}$$

a condition that requires $\mathbf{v}_s = 0$.

The above conclusion is in contradiction to experiment. In 1950, Osborne [13] reported an experiment that measured the rotation of a single bucket of He II as shown in Fig. 6.24. The remarkable result is that he found under all conditions that the helium rotated with a parabolic meniscus as with a classical fluid. Furthermore, if all the helium rotated, the vertical height z of the meniscus should be given by the simple relationship

$$z = \frac{\omega^2}{2g} r^2 \tag{6.79}$$

where g is the acceleration of gravity, ω is the rotation frequency and r is the radial coordinate. Note that if only the normal fluid component rotated there would be a ratio ρ_n/ρ multiplying the right-hand side of (6.79). Osborne's experiments were in general agreement with (6.79), which leads to the conclusion that He II behaves as an ordinary liquid when rotating in a simple bucket.

The explanation for the apparent contradiction between experiment and theory of He II lies in the method by which turbulence is introduced into the liquid. The qualitative picture of He II above its critical velocity imagines the existence of an array of vortex lines brought on by the rotation of the fluid. Each vortex line contains a unit of angular momentum and can be used to explain numerous physical phenomena associated with He II. London first postulated the existence of vortex lines, but their actual observation did not occur until nearly 30 years later.

The vortex line array exists as follows. Rotating He II contains vortex cores shown in Fig. 6.25. The array is similar to the fluxoid array in a Type II superconductor. Each vortex core contains a unit of circulation. The behavior of this array is governed by quantum mechanics to the extent that each unit of circulation is determined by the quantization rule,

$$\oint \mathbf{P} \cdot d\mathbf{q} = nh \tag{6.80}$$

where $\mathbf{P} = m\mathbf{v}$ is the momentum and $d\mathbf{q} = d\mathbf{l}$. It is apparent that the circulation C is quantized based on (6.80) which may be rewritten as

$$\oint \mathbf{v}_s \cdot d\mathbf{l} = n \frac{h}{m} \tag{6.81}$$

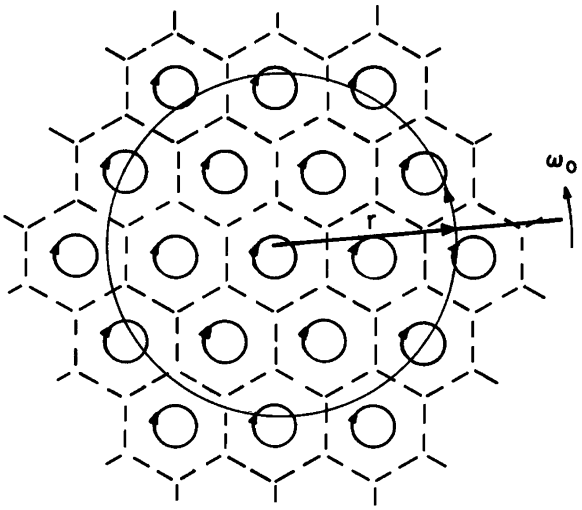

Fig. 6.25 Idealized vortex array in rotating He II

where h/m is a unit of circulation. For a regular array, each vortex core contains one unit of circulation equal to h/m.

The existence of a regular array of vortex lines is helpful in resolving the apparent contradiction between experiment and the two-fluid model. In particular, if the array is as shown in Fig. 6.25, the circulation cancels locally because each vortex borders another and the line separating the two has zero velocity. Therefore, taking an arbitrary path containing numerous vortices, we find that the net circulation within this path is zero. However, at the boundary of the container, the circulation does not cancel, leaving a net value around this path consistent with the entire fluid in rotation. Thus, the contradiction can be resolved by assuming the existence of a vortex array.

The density of vortex lines depends on the angular frequency. To compute this density n_0, begin by determining the total circulation of a path of radius r in the rotating He II. For the case with the rotation at constant angular frequency ω_0, integration of (6.76) yields

$$C = 2\pi r^2 \omega_0 \tag{6.82}$$

Because this path contains a total number of vortex lines $N = n_0(\pi r^2)$, the total circulation is $N(h/m)$ or

$$C = n_0 \frac{h}{m} \pi r^2 \tag{6.83}$$

Equating (6.82) and (6.83), we can calculate density of vortex lines that depends only on the angular frequency:

$$n_0 = \frac{2\omega_0 m}{h} \cong 20\omega_0 \quad \text{per mm}^2 \tag{6.84}$$

where ω_0, is in rad/s. For a reasonable angular frequency of perhaps 1 rad/s, (6.84) indicates a sizable vortex line density. It should therefore be possible to observe vortex lines in rotating helium if they could somehow be made visible.

Visual observation of vortex lines in rotating helium was first achieved by Williams and Packard in 1974 [14]. In their experiment, the vortex lines were made visible by trapping electrons in the vortex core. It is an established characteristic to the behavior of electrons in liquid helium that they will form small voids or bubbles on the order of a few nanometers in diameter. These electron bubbles are attracted to the vortex core as a result of the Bernoulli potential, caused by the electron bubbles' tendency to reduce its surface energy. In the vortex line visualization experiment, electrons emanating from a β-decay of a radioactive source were trapped on the vortices in a rotating bucket of liquid He II. The electrons subsequently were accelerated through an electrostatic potential, striking a phosphorus screen with the existence of a vortex line being recorded as a flash of light. One aspect to these measurements, which was not predicted, was the mobility of the vortex lines. A vortex appeared to be created and destroyed at the boundaries of the rotating bucket. Also, the vortices moved throughout the fluid at a rate which made it necessary to add some ^{3}He to the rotating bucket to produce viscous damping. Figure 6.26 are images of the vortex line array seen by Williams and Packard [14].

More recently, Bewley et al. [15] performed a new series of vortex line visualization experiments in rotating He II using a different method. In these experiments the lines were decorated with micron scale solid hydrogen particles, illuminated with laser light and digitally recorded with a CCD camera. In this case, the vortex lines were observed from the side, as seen in Fig. 6.27, as an array of parallel lines with hydrogen particles approximately equally spaced along them. These experiments were performed near T_λ presumably with sufficient normal fluid present to dampen the vortex line motion.

The observations accrued from both these experiments on visualization of vortex lines overall appear consistent with the description of the turbulent state. The number of vortex lines were seen to be proportional to angular frequency ω_0, as predicted by (6.84) and the spacing between lines was approximately equal to $(h/2\omega_0 m)^{1/2}$, both consistent with theory. As can be seen in these results, the turbulent superfluid component in He II has unique characteristics.

6.5.2 *Critical Velocities*

At this point it may appear that there is a contradiction in the description of experiments which involve rotating He II. Recall the Andronikashvili experiment which consisted of rotating closely spaced disks in liquid helium. In that work only the normal fluid component rotated with the device. This result appears to be in contradiction with the rotating bucket experiments of Osborne where the entire helium fluid is seen to be in motion. A distinction between these two observations can be made in terms of the magnitude of rotation velocity. To put the entire bucket of helium in rotation it is necessary to exceed a critical velocity to establish an

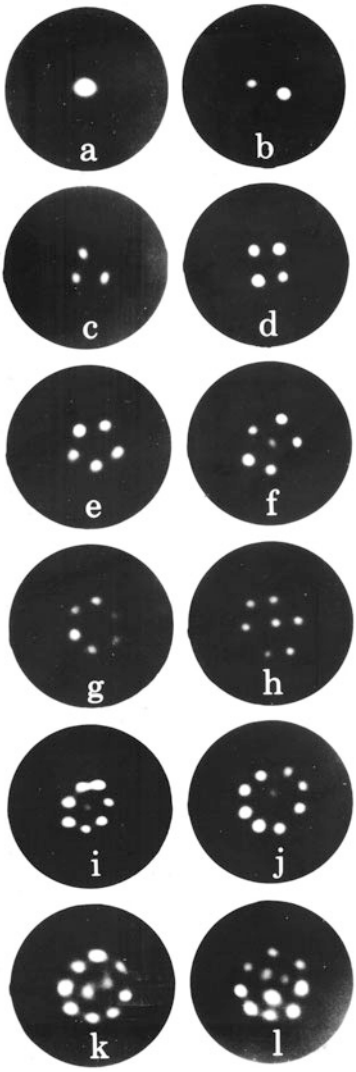

Fig. 6.26 Photographic reproduction of vortex line array in rotating He II (from Yarmchuk and Packard [14]): (**a**) through (l) indicate increasing angular frequency

interaction between the normal and superfluid components. This critical velocity is also of prime importance in the development of a complete picture of the heat transport of He II.

The critical velocities of the two components in He II have different origins. For the superfluid, the critical velocity $\mathbf{v}_{sc}$ is that which is necessary to create quantized vortex lines, which are in the form of a random tangle characterized by a line density per unit volume, L. The normal fluid component on the other hand can be thought of as having a critical velocity $\mathbf{v}_{nc}$ associated with the transition from ordinary laminar to turbulent flow. The normal fluid critical velocity can be considered in terms of classical hydrodynamic principles such as exceeding a critical Reynolds number. Finally, with the two-fluid model there exists the

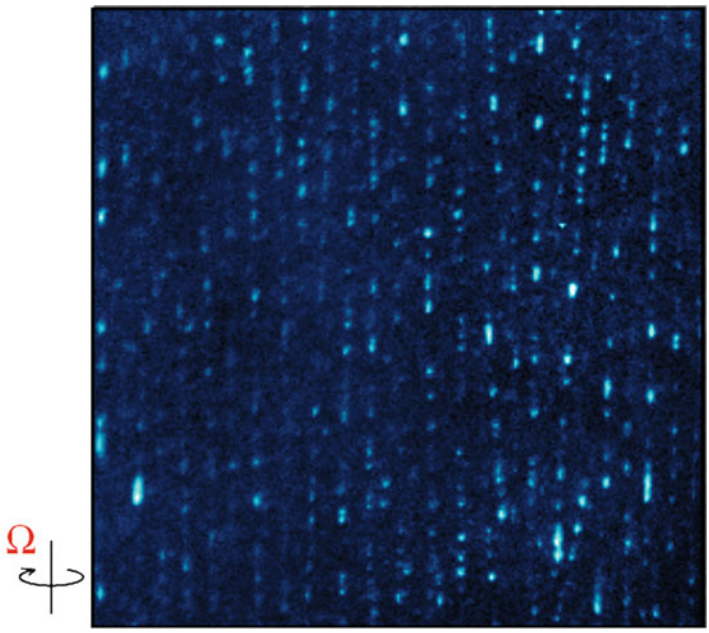

Fig. 6.27 Micron size solid hydrogen particles attached to superfluid vortex lines produced by rotation at a frequency $\Omega = 0.3$ Hz. Measurements were made slightly below T_λ. (From Bewley et al. [15])

possibility of a critical velocity associated with the relative motion of the two components, $|\mathbf{v}_n – \mathbf{v}_s|_c$. It should be emphasized that all three of these critical velocities may impact the behavior of mass and heat flow in He II.

First, consider the superfluid critical velocity $\mathbf{v}_{sc}$. Recall that the superfluid velocity is more or less independent of pressure difference for flow within a channel. The equation of motion for the superfluid component predicts an acceleration of this component under the influence of a pressure gradient, ∇p. Clearly, the acceleration cannot go on indefinitely; the superfluid has some limiting or critical velocity above which frictional forces may contribute. It is possible to understand the concept of a superfluid critical velocity by invoking the following semi-classical argument.

Imagine that the He II is confined to flow in a channel of dimension d. At very small velocities, the flow will be laminar. However, with increasing $\mathbf{v}_s$, there comes a point where the ideal laminar flow breaks down and turbulence is created. Thus, the critical velocity is that which is necessary to create turbulence or vortices in the channel. In He II the behavior of vortices is controlled to a large extent by quantum mechanics where a vortex contains one quantum of circulation. One might then ask, what is the characteristic size of a vortex? Employing the Heisenberg uncertainty principle, $\Delta p \, \Delta x \approx h$, the position of a helium molecule in rotation around the vortex must be defined to within some fraction of the radius.

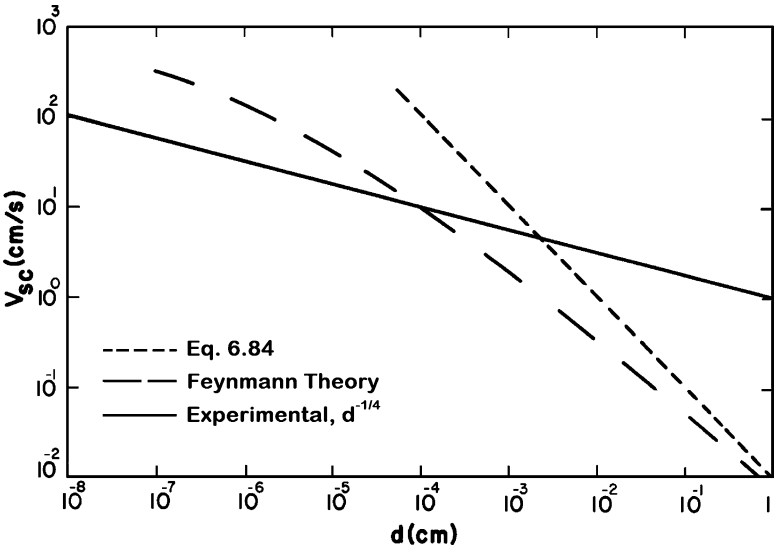

Fig. 6.28 Superfluid critical velocity: — experimental $d^{1/4}$ law; – – – Feynmann theory; - - - Eq. (6.85)

Furthermore, the vortex must fit within the channel which has a characteristic dimension d. For the sake of discussion, we choose $\Delta x \approx d/10$ for the vortex to exist. This numerical assumption leads to an equation for $\mathbf{v}_{sc}$:

$$\mathbf{v}_{sc} \approx \frac{10h}{md} \approx \frac{10^{-4}}{d} \text{ m/s} \tag{6.85}$$

where m is the mass of the helium molecule. Clearly, the above picture is oversimplified. A more detailed theoretical development due to Feynmann [16] however, results in a similar expression for $\mathbf{v}_{sc}$:

$$\mathbf{v}_{sc} = \frac{h}{\pi md}\left(\ln\frac{4d}{a_0} - K'\right) \tag{6.86}$$

where a_0 is the size of a vortex core ($a_0 \sim 1$ nm) and K' is a numerical constant. It is interesting to note that although the Feynmann equation (6.86) has a stronger theoretical basis than (6.85) it still is dominated by an inverse diameter dependence.

Although the above theoretical arguments seem reasonable, the superfluid critical velocity is an empirically determined quantity. Plotted in Fig. 6.28 are different theoretical expressions for $\mathbf{v}_{sc}$ as well as an empirical fit to existing data in the literature. The experimental data appears to roughly follow a $d^{-1/4}$ law,

$$\mathbf{v}_{sc} \simeq d^{-1/4} \text{in cm/s} \tag{6.87}$$

based on results in small diameter channels, with d in cm. It should be noted that the measurement of critical velocity in the superfluid component is sometimes

disturbed by the existence of a similar transition in the normal fluid. Consequently, some discrepancy between theory and experiment may be attributed to experimental variations.

In addition to superfluid turbulence it is possible to have turbulence in the normal fluid component of He II. This effect can be described in terms of more conventional fluid dynamic models. It is generally assumed that the nonzero normal fluid viscosity ($\mu_n \sim 1$ Pa s) that causes a transition from laminar to turbulent flow in the normal fluid component. In this picture, there exists a critical velocity $\mathbf{v}_{nc}$ that describes the unstable transition from laminar to turbulent flow. In classical fluids this transition is defined in terms of a critical Reynolds number Re_c, which is a dimensionless quantity made up of the ratio between inertial and viscous forces. For most classical fluids, the critical Reynolds number for flow in a tube occurs near

$$\mathrm{Re}_c = \frac{\rho \mathbf{v}_c d}{\mu} \approx 1200 \tag{6.88}$$

For He II, the appropriate critical Reynolds number should be made up of the normal fluid velocity and viscosity,

$$\mathrm{Re}(\mathbf{v}_{nc}) = \frac{\rho \mathbf{v}_{nc} d}{\mu_n} \tag{6.89}$$

Note that this expression contains the total density of He II and not just that of the normal fluid component. Equation (6.89) predicts a fairly strong temperature dependence of the normal fluid critical velocity. At low temperatures, $T < 1.5$ K, the temperature dependence of $\mathbf{v}_{nc}$ is dominated by the normal fluid viscosity μ_n which goes as T^{-5}.

Example 6.2

Consider a 1 mm diameter channel filled with He II at 1.8 K and estimate the critical velocities with the corresponding heat flux in thermal counterflow.

As a consequence, the helium is made to flow by the introduction of a heat flux q. Since the superfluid component can carry no entropy, the normal fluid velocity $\mathbf{v}_n$ is determined entirely by the heat transport expression, (6.72). The critical heat flux for the introduction of normal fluid turbulence can then be given by the combination of (6.72) and (6.88) such that

$$q_{nc} = sT \frac{\mu_n}{d} \mathrm{Re}(\mathbf{v}_{nc})$$

which for 1.8 K a tube diameter of 1 mm, and a critical Reynolds number $Re_c \sim 1{,}200$ yields $q_{nc} \simeq 1.50$ kW/m^2.

(continued)

Example 6.2 (continued)

The value of the critical heat flux necessary to induce turbulence in the superfluid component is determined by rearrangement of (6.72). Keeping in mind that zero net mass flow implies $\rho_s \mathbf{v}_s = -\rho_n \mathbf{v}_n$, we calculate the critical heat flux for the onset of superfluid turbulence as

$$q_{sc} = \frac{\rho_s \rho}{\rho_n} sT\mathbf{v}_{sc}$$

For the empirically determined values for $\mathbf{v}_{sc}$, (6.86) gives $q_{sc} \simeq 3.6$ kW/m^2 at 1.8 K. Of course, these numbers vary considerably with diameter and fluid temperature.

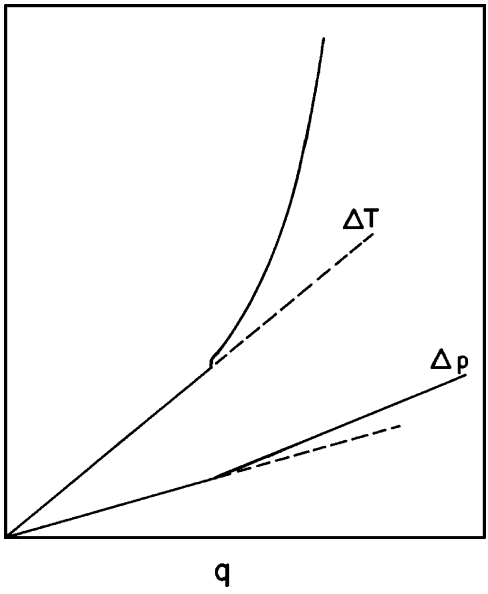

Fig. 6.29 Typical behavior of the temperature and pressure difference across a channel as a function of heat flux in counterflow He II. Note the transition at q_c

The practical significance of both critical velocities is in their signaling transitions in the behavior of $\mathbf{v}_s$ and $\mathbf{v}_n$. In particular, the onset of turbulence is expected to affect both the heat transport and fluid flow. Above these critical velocities, additional interactive terms must be included in the fluid flow equation which describes the temperature and pressure gradients. The two contributions of greatest importance are the turbulent pressure gradient and what is known as the mutual friction interaction that determines the temperature gradient. Typical behavior of the pressure and temperature difference across a channel is shown in Fig. 6.29.

The first issue to consider when introducing turbulence into the problem is how its existence affects the pressure gradient measured within the fluid in counterflow. As already noted, in the Poiseuille regime, the pressure gradient along a capillary is proportional to the normal fluid velocity which in turn is proportional to the heat

flux. This relationship is no longer accurate above the critical velocity of the normal fluid, $\mathbf{v}_{nc}$, where turbulence contributes to the behavior of the fluid.

One way to look at the pressure gradient due to the flow of the normal fluid is in terms of classical fluid mechanics. In the turbulent regime, the normal fluid friction factor is greater than that in the laminar regime due to the thinning of the boundary layer. If we assume that the Blausius correlation for the friction factor $f = 0.079/Re^{1/4}$ applies for the turbulent normal fluid component, then the pressure gradient is,

$$\frac{dp}{dx} = -\frac{0.158\mu_n^{1/4}\rho^{3/4}}{d^{5/4}} v_n^{7/4} \tag{6.90}$$

which in turn can be written in terms of the heat flux by substitution of $q = \rho s T \mathbf{v}_n$ (6.49). This relationship predicts a non-linear pressure dependence in counterflow above the critical heat flux, a result that has been shown to be accurate of small diameter channels ($d \lesssim 100$ μm) as is shown qualitatively in Fig. 6.29. However, as is discussed below, this picture is not entirely complete since the interaction between the normal and superfluid components eventually dominates the behavior.

6.5.3 Mutual Friction

Referring to Fig. 6.29, one can see that the transition in the temperature difference in turbulent He II is more pronounced. The new interaction that brings about this change is hypothesized to be the result of a viscous-like drag between the normal fluid component containing the excitations and the turbulent superfluid component with vortices. The existence of this force was first introduced to help explain heat transport data by Gorter and Mellink [17]. It has since been given a physical basis by several experimental and theoretical studies.

The basic idea of the mutual friction interaction is as follows. In turbulent He II there are two fluid components, a normal fluid containing excitations and the superfluid component with associated quantized vortices. For the present argument's sake, these two components will be assumed to be travelling in opposite directions in thermal counterflow. The vortex will be taken to be travelling at $\mathbf{v}_L$, vortex line velocity, which is of the order of $\mathbf{v}_s$. A schematic representation of this situation is shown in Fig. 6.30.

The force per unit length on vortex is dependent on the relative velocities of $\mathbf{v}_L$ and $\mathbf{v}_n$ as well as the densities of each. Theoretical justification for the exact form of this quantity is beyond the scope of the present discussion. However, using dimensional analysis alone, one would expected that the force per unit length of the vortex would be of the form,

$$\mathbf{f} = \frac{\rho_s \rho_n}{\rho^2} \mu_n |\mathbf{v}_n - \mathbf{v}_s| \tag{6.91}$$

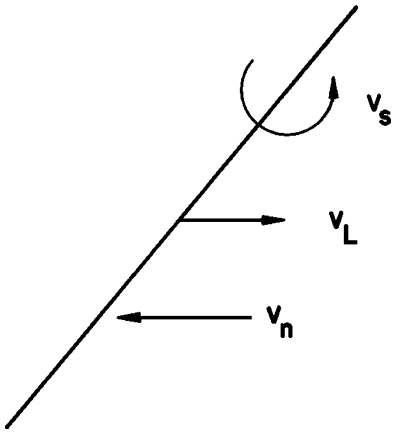

Fig. 6.30 Schematic of the normal fluid and superfluid vortex interaction

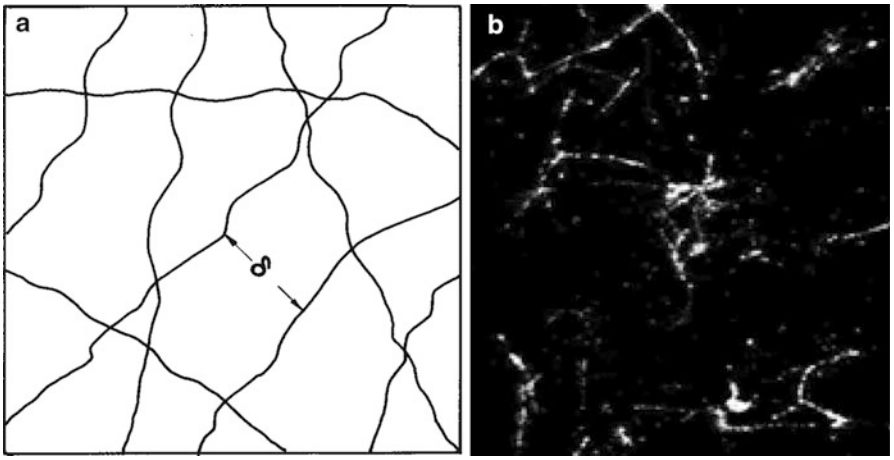

Fig. 6.31 (**a**) Schematic representation of a vortex array with $\delta \sim L^{-1/2}$ being the average vortex line spacing; (**b**) photo of vortex lines decorated with micron scale solid hydrogen particles [18]

where μ_n is the only possibility relevant viscosity. It is assumed that **f** is proportional to the product of ρ_s and ρ_n, so that the interaction would be a maximum where these two quantities are approximately equal. Other arguments can be made to justify **f** going as $|\mathbf{v}_n - \mathbf{v}_s|$, which are based on classical turbulent interactive mechanisms.

To determine the total interaction per unit volume of He II, we consider the macroscopic picture of the turbulent state. As envisioned, the He II consists of a tangled mass of vortex lines schematically shown in Fig. 6.31a and displayed visually by decorating the lines with solid hydrogen particles in Fig. 6.31b. Unlike the picture of rotating He II with a regular matrix of vortex lines, heat-induced vortex lines form an isotropic mass which is assumed to be spatially non-varying. This assumption is not generally true but it simplifies the physical explanation. The vortex array is described by two quantities: L, the vortex line length per unit volume

of fluid, and δ, the mean spacing between vortex lines. For a given set of conditions, the vortex line length has one stable value. In the model first proposed by Vinen [19], the steady-state length is seen as a balance between the rate of generation of vortex lines and the rate of decay. Therefore, in steady state,

$$\left.\frac{dL}{dt}\right|_{\text{gen}} = \left.\frac{dL}{dt}\right|_{\text{decay}} \tag{6.92}$$

and the line length takes on the constant value L_0. The total force per unit volume of He II is the product of the line force $\mathbf{f}$ and the line length L_0.

Vinen used dimensional arguments to show the variation of the vortex line length with velocity. For the two quantities defined in (6.92), the fundamental dependencies may be written

$$\left.\frac{dL}{dt}\right|_{\text{gen}} = \frac{\chi_1 B \rho_n}{2\rho} \mathbf{v}_{ns} L^{3/2} \tag{6.93}$$

where $\mathbf{v}_{ns} = |\mathbf{v}_n - \mathbf{v}_s|$ is the relative velocity of the normal and superfluid components and χ_1 and B are parameters describing the interaction between normal fluid and a vortex. The decay of the vortex lines also has a simple functional form,

$$\left.\frac{dL}{dt}\right|_{\text{decay}} = -\frac{\chi_2 h}{2\pi m} L^2 \tag{6.94}$$

where χ_2 is of order unity and a function of temperature. Equating (6.93) and (6.94) in the appropriate form, we obtain the steady-state vortex line length, to within numerical constants, as

$$L_0 = a(T)\left(\frac{\rho_n}{\rho}\mathbf{v}_{ns}\right)^2 \tag{6.95}$$

where $a(T)$, which is of order 10^{13} s^2/m^4 at 1.8 K, is a temperature dependent coefficient that can be estimated from theory or measured experimentally [20]. Note that (6.95) indicates that $L_0 \sim |\mathbf{v}_n - \mathbf{v}_s|^2$. In thermal counterflow, $\rho_n v_n = -\rho_s v_s$ and $q = \rho s T v_n$, which can be substituted into (6.95) to predict the equilibrium vortex line density,

$$L_0 = a(T)\left(\frac{\rho_n}{\rho_s}\right)^2 \left(\frac{q}{\rho s T \mathbf{v}_n}\right)^2 \tag{6.96}$$

At a heat flux of 10 kW/m^2, (6.96) estimates $L_0 \sim 10^{10}$/m^2, which corresponds to a vortex line spacing ~10 μm. It is worth pointing out that this distance is 3–4 orders of magnitude larger than the vortex core size.

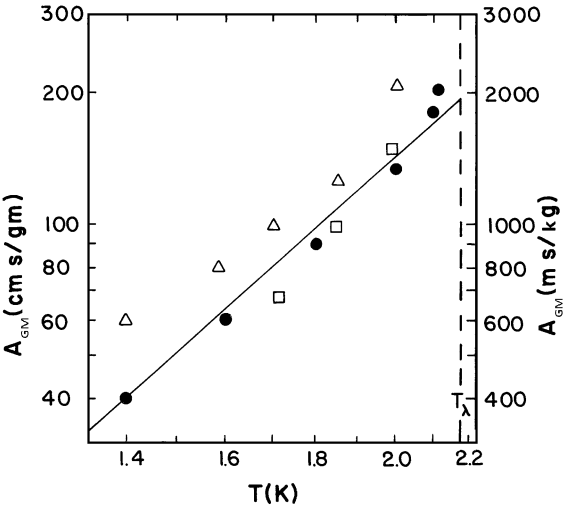

Fig. 6.32 Gorter-Mellink mutual friction parameter (Data are from Refs. [22–25])

Using the above form for the vortex line length and force per unit length, we can write the total mutual friction force per unit volume of He II. The treatment developed originally by Vinen and extended by Schwarz [21] includes a small velocity offset $\mathbf{v}_0$, such that the final equation has the form

$$\mathbf{F}_{ns} = L_0\mathbf{f} = A_{GM}\rho_n\rho_s(\mathbf{v}_n - \mathbf{v}_s - \mathbf{v}_0)^2(\mathbf{v}_n - \mathbf{v}_s) \tag{6.97}$$

where A_{GM} is termed the Gorter-Mellink mutual friction coefficient. According to the model presented above, $A_{GM} \approx \rho_n^2/\rho^3$, but because the physical quantities χ_1 and χ_2 are undetermined, the coefficient must be evaluated empirically.

There have been a wide variety of measurements of the Gorter-Mellink parameter with typical values displayed in Fig. 6.32. The theory presented by Vinen also predicts a temperature and pressure dependence which should be dominated by the square of the normal fluid density ρ_n. The quantity ρ_n^2/ρ^3 has a strong temperature dependence going roughly as $(T/T_\lambda)^{13}$, while the experimentally determined value for A_{GM} exhibits a much weaker temperature dependence, that is $A_{GM} \approx T^3$.

The pressure dependence of the Gorter-Mellink coefficient is less well established. Some work has shown that the variation of the heat conductivity of turbulent He II with pressure can be interpreted only by a pressure dependence of A_{GM}. Since this quantity varies as ρ_n^2/ρ^3, its pressure variation is not a large effect except near the λ-transition. For example, at $T = 2.0$ K, the ratio between ρ_n^2/ρ^3 at 0.25 MPa and saturated vapor pressure is 1.17. This should be compared to the experimental ratio of $A_{GM}(0.25)/A_{GM}(0)$ of 1.19 ± 0.05 at 2 K. Such a comparison, although within experimental error, does not established fully the pressure dependence of A_{GM}.

Given the existence of this additional interactive mechanism between the two components in He II, the two-fluid hydrodynamic equations can be modified to

include these terms. The result of this modification are equations for each of the two fluids:

$$\rho_n \frac{\partial \mathbf{v}_n}{\partial \mathrm{t}} = -\frac{\rho_n}{\rho}\nabla p - \rho_s s \nabla T + \mu_n \nabla^2 \mathbf{v}_n + A_{GM}\rho_n \rho_s |\mathbf{v}_n - \mathbf{v}_s|^3 \tag{6.98}$$

$$\rho_s \frac{\partial \mathbf{v}_\mathrm{s}}{\partial \mathrm{t}} = -\frac{\rho_s}{\rho}\nabla p + \rho_s s \nabla T - A_{GM}\rho_n \rho_s |\mathbf{v}_n - \mathbf{v}_s|^3 \tag{6.99}$$

which are similar to (6.56) and (6.70) except that they add the terms due to mutual friction. The expressions as given above are somewhat simplified over those used by Vinen and others. In particular, (6.98) and (6.99) lack any explicit indication of either critical velocity, $\mathbf{v}_{sc}$ or $\mathbf{v}_{nc}$. Critical velocity can be taken into account by introduction of a small velocity offset $\mathbf{v}_0$, as shown in (6.97). However, since this correction is quite small, it is neglected in the present treatment of turbulent He II.

6.5.4 Steady-State Heat Transport

Consider the problem of steady-state heat transport, $d\mathbf{v}_s/dt = d\mathbf{v}_n/dt = 0$, in a one dimensional channel containing He II. This problem, which has already been discussed for the non-turbulent case, can be solved analytically to give an expression for the temperature gradient in terms of the velocities of each component:

$$\frac{dT}{dx} = -\frac{\beta \mu_n \mathrm{v}_n}{\rho s d^2} - \frac{A_{GM}\rho_n}{s}|\mathrm{v}_n - \mathrm{v}_s|^3 \tag{6.100}$$

where β is defined previously. Note that (6.100) is a scalar equation established with the understanding that dT/dx is negative in the direction of v_n. If there is no net mass flow, that is, counterflow is the only important transport mechanism, then $\rho_s \mathbf{v}_s = -\rho_n \mathbf{v}_n$ and the temperature gradient may be written to depend only on the heat flux:

$$\frac{dT}{dx} = -\frac{\beta \mu_n q}{d^2 (\rho s)^2 T} - \frac{A_{GM}\rho_n}{\rho_s^3 s^4 T^3} q^3 \tag{6.101}$$

where use has been made use of $q = \rho s T \mathrm{v}_n$. Note that the first term in (6.101) is the same as developed to describe the viscous flow of non-turbulent He II. The second term describes the mutual friction contribution. Because it lacks diameter dependence and goes as the cube of the heat flux, the second term dominates the temperature gradient at high heat fluxes and large diameter channels, that is, $d \gtrsim 1$ mm. For example, at 1.9 K, a 1 mm diameter circular cross-section channel will have the largest contribution to the temperature gradient from the mutual

friction for heat fluxes in excess in 100 W/m^2. For many practical applications, larger heat fluxes are of interest indicating that under these circumstances the first term can be ignored in the description of heat transport in He II.

There is a fundamental assumption that enters into the description of He II heat transport as given by (6.100). The concept of critical velocity has been introduced to separate the regions of turbulent and non-turbulent heat transport. However, simply adding the laminar and turbulent terms to describe heat transport in He II assumes that the transition between these two regions is continuous. This is not what is observed experimentally.

The actual situation concerning the heat flux dependence of the temperature and pressure gradients in counterflowing turbulent and non-turbulent He II is more complex. At very low heat fluxes, much less than that necessary to create turbulence, the laminar expression suitably describes the heat transport and the temperature and pressure gradients are proportional to q. Similarly, at very high heat fluxes, the turbulent expression does an adequate job of explaining experimental data. However, the behavior in the transition region is more variable. Around q_c, there is often hysteresis in the relationships between ΔT or Δp and q. Sometimes the turbulent character is suppressed beyond q_c, because of the need to nucleate vortices. Once the turbulent state exists, the vortices do not dissipate easily, persisting below q_c. Hysteresis is common in the temperature gradient behavior and sometimes two transitions are observed [20, 26]. Similar character is seen often in the pressure gradient near q_c. At this point it is not clear whether a simple addition of terms as in (6.100) is correct. Far enough away from q_c either the laminar or turbulent expression dominates so that the details of the transition region are of small consequence. This is often the case in practical applications of He II.

6.5.5 *Forced Convection Heat Transport*

Up to now, the heat transport has been assumed to occur in static He II; that is pure thermal counterflow with zero net momentum ($\mathbf{j} = 0$). This is an important assumption leading to the derivation of the heat flow equations. It is of interest, however, to consider the effect of net mass flow when the entire fluid is driven by a pressure gradient, resulting in a total fluid velocity $\mathbf{v}$. Pressure-gradient-induced flow in He II is really only possible if the thermo-mechanical effect is small because the normal fluid velocity can be affected significantly by viscous drag. For small-diameter channels where the thermo-mechanical effect is considerable, mass flow is controlled essentially by the superfluid velocity. As this situation leads to considerable complication, it will not be discussed here. Rather, the other heat transport regime will be considered, which is demonstrated by the mutual friction term. There are numerous examples in the literature where $\mathbf{v}_s$ and $\mathbf{v}_n$ are independently controlled variables.

Neglecting the laminar term in the temperature gradient expression (6.100) and assuming one dimensional flow, we obtain a simplified expression that does not depend on net mass flow:

$$\frac{dT}{dx} = -\frac{A_{GM}\rho_n}{s}|\mathbf{v}_n - \mathbf{v}_s|^3 \tag{6.102}$$

Now since momentum conservation must be obeyed in the two-fluid model (6.46), a more general relationship for q as a function of velocity is:

$$q = \rho s T(\mathbf{v}_n - \mathbf{v}) \tag{6.103}$$

which reduces to the previous form when $\mathbf{v} = 0$. This relationship can be derived in general by applying conservation of momentum and energy to the He II in a moving reference frame. It can also be shown to be the correct assumption when solving the problem of forced flow with no net heat flux, that is, $q = 0$.

Substitution of (6.102) into (6.101) leads to the somewhat surprising result that the temperature gradient in forced flow He II is independent of velocity; that is for all velocities,

$$\frac{dT}{dx} = -\frac{A_{GM}\rho_n}{\rho_s^3 s^4 T^3} q^3 \tag{6.104}$$

which is identical to the mutual friction term in (6.101). It should be emphasized that this derivation has not included the potentially important term associated with the net enthalpy transport of the flowing helium, $\rho C v \Delta T$. Because enthalpy transport is actually more relevant to the practical heat transfer character of forced flow He II, this subject is considered further in the next chapter. It is the purpose of the present discussion to principally identify the invariance of (6.104) with fluid velocity.

6.5.6 *Attenuation of Second Sound*

An alternative method to study the turbulent state of He II is to measure the attenuation of second sound. The principle is based on the fact that relative motion of the two fluid components in second sound can be affected by the mutual friction interaction. In the turbulent regime, the solution of the time-varying wave propagation equation (6.65) is modified. It can be shown by using (6.98) and (6.99) that second sound obeys the expression

$$\frac{\partial^2 T}{\partial t^2} = c_2^2 \nabla^2 T + \frac{A_{GM}\rho q^2}{\rho_s^2 s^2 T^2}\frac{\partial T}{\partial t} \tag{6.105}$$

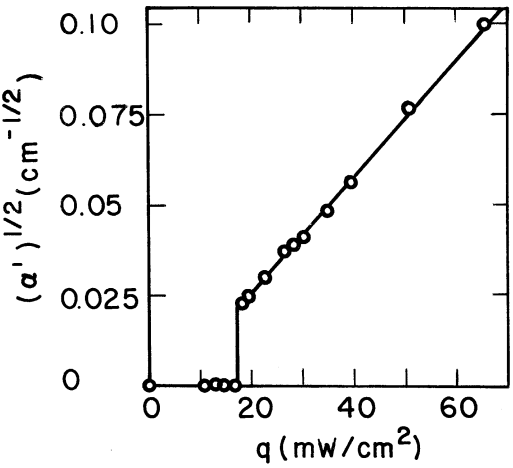

Fig. 6.33 Measurements of the attenuation of second sound in He II (From Vinen [27])

where the second term on the right-hand side causes the attenuation and is additional to the normal linearized second sound equation. The rate at which this attenuation takes place leads to an exponential process with a coefficient

$$\alpha = \frac{A_{GM}\rho q^2}{2\rho_s^2 s^2 T^2 c_2} \tag{6.106}$$

The Gorter-Mellink coefficient A_{GM} enters explicitly in (6.106), allowing its value to be determined directly by measurement of α.

Experimentally, the amplitude of a traveling wave is proportional to $e^{-\alpha x}$. In thermal counterflow, the quantity α is found generally to consist of two terms,

$$\alpha = \alpha_0 + \alpha'(q) \tag{6.107}$$

where the first term is more or less independent of heat currents and the second term is the result of the mutual friction interaction. The second term in (6.107) is seen to vary as the square of the heat flux q, such that

$$\alpha' = C(q - q_0)^2 \tag{6.108}$$

where the proportionally factor, C, is a function of temperature and pressure. Measurements by Vinen [27] which show the q^2 dependence to α are displayed in Fig. 6.33. Quite apparent in these measurements is the onset of attenuation at the critical velocity. Below q_c, there is no heat-flux-dependent attenuation. Also, note the approximate magnitude of $q_0 \approx 5$ mW/cm^2 by extrapolation of the attenuation coefficient to $\alpha' = 0$. This value is in close agreement with the critical heat flux q, estimated from Fig. 6.28.

The second sound attenuation method is a powerful probe of the mutual friction interaction. It represents an effectively independent method for determining the mutual friction coefficient A_{GM}. This point was exploited by Vinen who made a

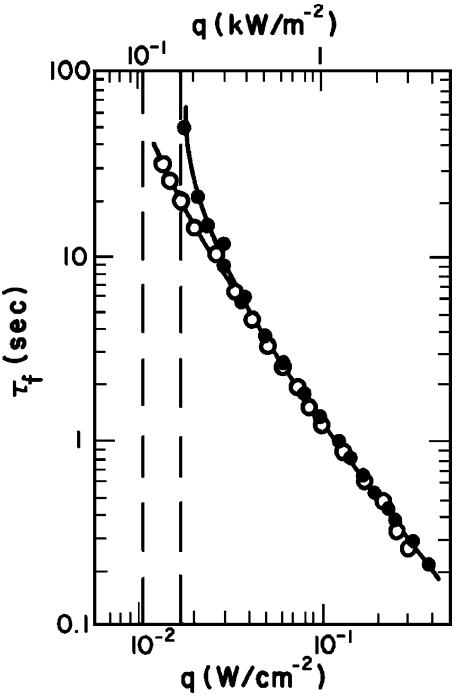

Fig. 6.34 Characteristic time for buildup of turbulence in He II at 1.41 K. The symbols represent different channel configurations (From Vinen [27])

simultaneous measurement of A_{GM} by both methods on the same channel. The results of these measurements strongly demonstrate that the two methods are for all practical purposes equivalent. However, the possibility of geometrical factors affecting A is somewhat less well established.

6.5.7 *Development of Turbulence*

In the preceding development, it has been assumed generally that the He II is either in the non-turbulent state, obeying isentropic laminar flow models, or in the turbulent state with the additional mutual friction interaction. Here we consider the rate at which the turbulent state is created when the fluid is initially in the ideal vortex-free condition. This problem has received extensive experimental investigation. The general approach is to measure the time rate of change of the second sound attenuation after a steady heat flux is applied that is $q > q_c$. The general character of the results indicates a characteristic time for the development of the fully turbulent state. This characteristic time τ_f has been shown to be both heat flux and temperature dependent. Typical results for an experiment by Vinen are shown in Fig. 6.34. An empirical fit to these data indicate that the time constant has the simple form,

$$\tau = aq^{-3/2} \tag{6.109}$$

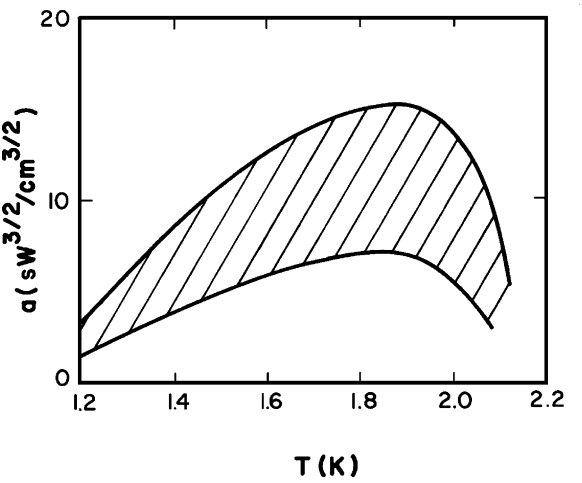

Fig. 6.35 Coefficient of the turbulence buildup expression for different channels (From Chase [28])

where a is a temperature and geometry-dependent quantity. Chase [28] has measured this coefficient for a number of channel configurations ranging from open ducts to complex geometries. Figure 6.35 displays the empirically determined coefficients a. The variation is between a factor of 3 and 5. It should be noted that this quantity is not always reproducible and will be shorter if the helium is not allowed to reach equilibrium without turbulence before a measurement. Full recovery to the non-turbulent state can take on the order of hundreds of seconds.

6.5.8 Second Sound Shock

The above discussion of transient phenomena assumes that the turbulence develops in a globally uniform, homogeneous fashion. However, highly transient thermal counter flow does not allow the development in a uniform way because there is a propagation velocity for the turbulent front. This propagation velocity is related to the velocity of second sound just as the ordinary sound velocity determines the propagation of pressure waves.

One can think about this process in terms of a small, short duration, $\Delta t \sim 1$ ms, rectangular heat pulse applied at the end of a channel containing initially quiescent He II. If the amplitude of the pulse is low, $\Delta T \sim 1$ mK, it will propagate at the second sound velocity. There may be some attenuation due to residual turbulence, but generally speaking most of the energy will travel at c_2.

If the amplitude of the pulse is significantly increased to $\Delta T \sim 100$ mK, several changes to the propagating pulse are observed [29, 30]. One is that the shape of the pulse changes being no longer rectangular due to an amplitude dependence of the second sound velocity. This effect can lead to either a forward or backward sloping pulse.

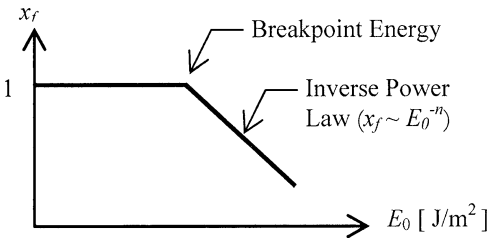

Fig. 6.36 Schematic of the behavior of the energy transport fraction (6.110) as a function of applied pulse energy

However, of greater interest is the apparent limit to the allowable energy content in the pulse. As the amplitude of the heat pulse that generates the second sound is increased, the temperature change ΔT also increases up to a limit after which it tends to plateau. Since the duration of the pulse is approximately constant, the temperature plateau means that there is limit to the amount of energy that can be carried by the second sound pulse. Experiments have shown this limit, sometimes referred to as the breakpoint energy, to be of order 100 kJ/m^2 [31, 32]. An alternate way to present this result is in terms of the energy transport fraction,

$$x_f = \frac{\Delta E_p}{\Delta E_0} \approx \frac{\int \rho C dT_p}{q \Delta t_H} \tag{6.110}$$

where ΔE_p is the energy carries by the heat pulse and ΔE_0 is the energy supplied to the pulse by the heater. The behavior of the energy fraction is shown qualitatively in Fig. 6.36. Below the breakpoint energy, the energy transport fraction is close to unity. Above that value, the transport fraction decreases as E_0^{-n}, where n ~1.

The physical interpretation of this result is suggest that the intense second sound pulse produces such a large thermal gradient and counterflow relative velocity that intense turbulence is generated, probably on the back side of the front. This turbulence in turn produces strong attenuation of second sound by mutual friction. This will in turn mean that the heat transport is now more of a diffusive process. This diffusive process is what controls transient heat transport in turbulent He II. Since this topic is of significant technical interest, it will be discussed further in the next chapter along with the other more applied characteristics to heat and mass transport in He II.

Questions

1. List and briefly discuss the properties of liquid helium below T_λ that make it a superfluid?
2. How does the Two Fluid Model for He II differ from models for mixtures of two classical fluids?
3. Can He II be modeled as an ideal Bose gas? If not, what properties of He II are different from those of the Bose gas?
4. Why does He II remain in the liquid state at very low temperatures?

Problems

1. Make a plot of the temperature and pressure gradients versus heat flux in a 50 μm diameter tube containing He II at 1.8 K. Consider both the normal fluid viscous and mutual friction interactions. Indicate the location of and the importance of critical velocities.
2. Starting with the equation for the vapor pressure of an ideal Bose gas (6.24a), cast it in the form of the virial expansion as discussed in Chap. 3. Placed in this form, the second term represents the ideal quantum gas correction which appears as part of the second virial coefficient. Compare the value of this correction to the difference between the classical and quantum second virial coefficients at 4 K (see Fig. 3.3).
3. Calculate the latent heat per mole of an ideal Bose gas at 2 and 4 K, Compare these values with the latent heat of liquid helium at the same temperatures.
4. Using the empirical relationships for the entropy, specific heat, and normal and superfluid densities, derive an expression for the temperature dependence of the second sound velocity c_2. Plot your result and compare it to Fig. 6.19.
5. Calculate the angular frequency at which one vortex could exist in a 1 cm diameter tube containing He II and spinning about its longitudinal axis. One method to prevent vortex formation in rotating He II is to subdivide the helium pool into many cells, perhaps with a honeycomb structure or porous medium. Calculate the cell radius necessary to prevent the formation of vortices in a bucket rotating at an angular frequency of $\omega = 1$ rad/s.
6. Consider a rectangular cross section chamber containing He II. Second sound can be generated and detected across the 10 mm width of the chamber, while a steady-state heat can be applied perpendicularly down the length of the chamber. Assume that the helium bath temperature is 1.8 K.
   (a) Calculate the second sound velocity and the frequency of the lowest harmonic standing wave which could be set up within the chamber;
   (b) If the standing wave has an amplitude of 5 mK at the generator, what will be the amplitude at the detector if a 10 kW/m^2 steady-stare heat flux is applied perpendicular to the second sound standing wave.
7. Consider a small capillary tube of length 10 mm and diameter 2 μm connecting two reservoirs of He II. One reservoir is maintained at 1.8 K. The other reservoir is heated to some temperature higher than 1.8 K but not greater than T_λ. Calculate the temperature difference, ΔT, and pressure difference, Δp, between the two reservoirs as a function heat flow, Q. Hint: You may assume that the flow is laminar, but you will need to consider the temperature dependent properties of He II.
8. Make a graphical comparison between the roton contribution to the specific heat, (6.40), and the empirical form for the specific heat (6.29) between 1.1 and 2.1 K.

References

1. L. D. Landau and E. M. Lifshitz, *Statistical Physics*, Addison-Wesley, Reading, MA, 1969.
2. K. Huang, *Statistical Mechanics*, Wiley, New York, 1963.
3. Data from HEPAK®.
4. F. London, *Superfluids*, Vol. II, Dover Publications, New York, 1954.
5. L. Tisza, The λ-Transition Explained. *Nature*, **Vol. 141**, p 913 (1938).
6. C. J. Gorter and H. Cashmir, *Physica* **1**, 305 (1934) or see F. London, Superfluids Vol. 1, Dover, NY, 1960, pp. 15–19.
7. L. Landau, Theory of the Superfluidity of Helium II. *Phys. Rev*., **Vol. 60, No. 4**, 356 (1941).
8. J. Wilks, *Liquid and Solid Helium*, Clarendon Press, Oxford, 1967.
9. J. Maynard, Determination of the Thermodynamics of He II from Second Sound Data, *Phys. Rev*. **B14**, 3868 (1976).
10. V. Peshkov, Determination of the Velocity of Propagation of the Second Sound in He II, *J. Phys. (USSR)* **10,** 389 (1946).
11. R. J. Donnelly, The Two-Fluid Theory and Second Sound in Liquid Helium, *Phys. Today* **Vol. 62,** 34 (2009).
12. E. L. Andronikashvili, *Zh. Eksp. Theor. Fiz*. **16,** 780 (1946); **18**, 424 (1948).
13. D. V. Osborne, The Rotation of Liquid Helium II, *Proc. Phys. Soc*. **A63**, 909 (1950).
14. G. A. Williams and R. E. Packard, Photographs of Quantized Vortex Lines in Rotating He II, *Phys. Rev. Lett*. **33**, 280 (1974); E. A. Yarmchuk and R. E. Packard, Photographic Studies of Quantized Vortex Lines, *J. Low Temp. Phys*. **46,** 479 (1982).
15. G. P. Bewley, D. P. Lathrop, K. Sreenivasan, Superfluid Helium: Visualization of quantized vortices, *Nature* **441**, 558 (2006).
16. R. P. Feynmann, Application of Quantum Mechanics to Liquid Helium, in *Progress in Low Temperature Physics*, C. J. Gorter (Ed.), Vol. I, p. 17, North Holland Publishing, Amsterdam, 1955.
17. C. J. Gorter and J. H. Mellink, On the Irreversible Processes in Liquid Helium II, *Physica* **XV**, 285 (1949).
18. T. Chagovets and S. W. Van Sciver, A Study of Thermal Counterflow using PTV, *Phys. Fluids*, **Vol. 23**, 107102 (2011).
19. W. F. Vinen, Theory of the Mutual Friction, *Proc. R. Soc. (London)* **A242**, 493 (1957).
20. J. T. Tough, Superfluid Turbulence, in *Progress in Low Temperature Physics*, D. F. Brewer (Ed.), Vol. VIII, Chap. 3, North Holland Publishing, Amsterdam, 1982.
21. K. W. Schwarz, Turbulence in Superfluid Helium: Steady Homogeneous Counterflow, *Phys. Rev*. **18**, 245 (1978).
22. V. Arp, Heat Transport through Helium II, *Cryogenics* **10,** 96 (1970).
23. W. F. Vinen, Experiments on Steady Heat Currents, *Proc. R. Soc. London* **A240**, 114 (1957).
24. S. W. Van Sciver, Kapitza Conductance of Aluminum and Heat Transport Through Subcooled He II, *Cryogenics* **18**, 521 (1978).
25. D. F. Brewer and D. O. Edwards, Heat Conduction by Liquid Helium II in Capillary Tubes. III. Mutual Friction, *Philos. Mag*. **7**, 721 (1962).
26. W. F. Vinen, Critical Heat Currents in Wide Channels, *Proc. R. Soc. London* **A243**, 400 (1957).
27. W. F. Vinen, Experiments on Transient Effects, *Proc. R. Soc. London* **A240**, 128 (1957).
28. C. E. Chase, Thermal Conduction in Liquid Helium II. I. Temperature Dependence Effects of Channel Geometry, *Phys. Rev*. **127**, 361 (1962); Thermal Conduction in Liquid Helium II. *Phys. Rev*. **131,** 1898 (1963).
29. T. N. Turner, Using Second Sound Shock Waves to Probe the Intrinsic Critical Velocity of Liquid Helium II, *Phys. Fluids* **Vol. 26**, 3227 (1983).
30. J. R. Torczynski, On the Interaction of Second Sound Shock Waves and Vorticity in Superfluid Helium, *Phys. Fluids* **Vol. 27**, 2636 (1984).

31. T. Shimazaki, M. Murakami, and T. Iida Second Sound Wave Heat Transfer, Thermal Boundary Layer Formation and Boiling: Highly Transient Heat Transport Phenomena in He II, *Cryogenics* **Vol. 35**, 645 (1995).
32. D. K. Hilton and S. W. Van Sciver, Direct Measurements of Quantum Turbulence Induced by Second Sound Shock Pulses in Helium II, *J. Low Temp. Phys.* **Vol. 141**, 501 (2005).

Further Readings

K. R. Atkins, *Liquid Helium*, Cambridge University Press, Cambridge, 1959.
T. Guenault, *Basic Superfluids*, Taylor Francis, London, 2003.
K. Huang, *Statistical Mechanics*, Wiley, New York, 1963.
W. E. Keller, *Helium-3 and Helium-4*, Plenum Press, New York, 1969.
L. D. Landau and E. M. Lifshitz, *Statistical Physics*, Addison-Wesley, Reading, MA, 1969.
F. London, *Superfluids*, Vol. II, Dover Publications, New York, 1954.
S.J. Putterman, *Superfluid Hydrodynamics*, Elsvier, Amsterdam, 1974.
D. R. Tilley and J. Tilley, *Superfluidity and Superconductivity*, Adan Hilger, Boston, 1986.
J. Wilks, *Liquid and Solid Helium*, Clarendon Press, Oxford, 1967.

Chapter 7
He II Heat and Mass Transfer

Chapter 6 emphasized the physics of He II including heat transport in the laminar flow and the turbulent mutual friction regimes. These mechanisms are fundamental to the behavior of He II, although that discussion mostly described idealized behavior. In the present chapter we will build on the fundamental understanding of He II to treat practical heat and mass transfer problems that may occur in He II systems. In doing so, the concepts already developed must be extended into regimes that are more usable in engineering calculations. To be more specific, the emphasis of Chap. 6 has been to understand the interactive mechanisms and the two fluid nature of He II. Thus, of principal concern is the behavior of the transport properties including mainly the normal fluid viscosity μ_n and the turbulent state with the associated mutual friction parameter A_{GM}. Of interest now is to use these concepts in understanding such phenomena as the maximum heat flux, q^*, the maximum energy deposition, ΔE^*, and the corresponding temperature difference, which can be either within the fluid or across a solid-fluid interface. The goal of the present chapter is to establish a connection between the engineering parameters q^*, ΔE^*, and ΔT and the physical properties of the fluid and solid-fluid boundaries. In establishing this connection there are a number of subjects of practical interest which must be addressed. These include steady-state heat transport, transient heat transport, forced flow pressure drop and heat transport, surface Kapitza boundary conductance, and film boiling. Some of these phenomena are also important in pool boiling He I heat transfer, which is the subject of Chap. 5.

Before delving into these individual subjects, it is worth describing, in a general way, the surface heat transfer character of liquid He II. This character in actuality is quite similar qualitatively to that of He I or other conventional fluids, although as we will see the numerical values and physical explanations are considerably different. Figure 7.1 shows a typical steady-state heat transfer curve for a metal surface at the end of a duct containing He II, see Fig. 7.2. As is discussed below, the duct also may contain a temperature difference ($T_m - T_b$). Figure 7.1 is intended only to display the regions of heat transfer. As is demonstrated in what follows, actual numerical values of these regimes are strongly dependent on geometry, temperature, pressure, and surface conditions. That the heat transfer surface is

S.W. Van Sciver, *Helium Cryogenics*, International Cryogenics Monograph Series,
DOI 10.1007/978-1-4419-9979-5_7,

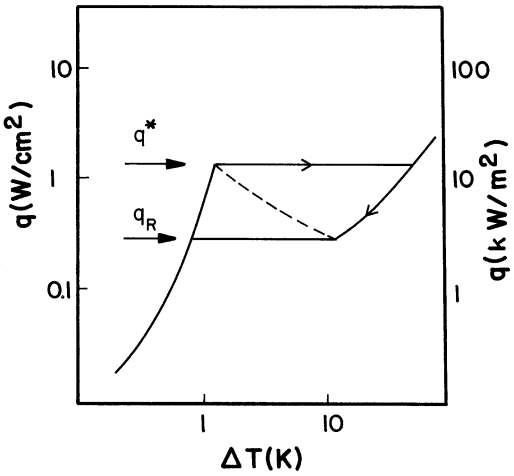

Fig. 7.1 A typical steady-state beat transfer curve for a metal surface at the end of a duct containing He II

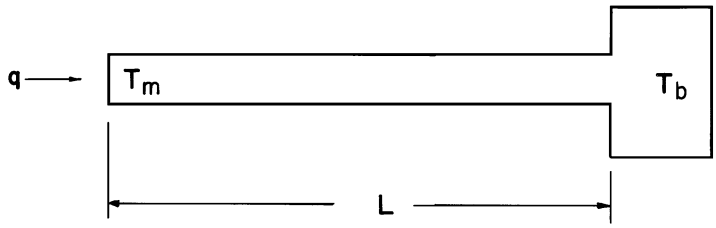

Fig. 7.2 Schematic of a horizontal duct of length L containing He II

located at the end of a channel rather than in an open bath is also important in determining critical values. As we will see, the very high effective thermal conductivity of He II results in a thermal boundary layer that can take on the dimensions of the duct, thus controlling much of the heat transfer process.

For small q up *to* q^*, the surface temperature difference, ΔT_s, is governed by interfacial phenomena having more to do with the character of the solid than that of the liquid helium. This is called the Kapitza regime. In this regime, there is no surface boiling, rather the temperature difference is a result of thermal impedance between the two dissimilar materials, the metal or insulating solid and liquid He II. Also, the maximum heat flux q^* is strongly geometry and helium state dependent and is characterized by the point where the helium adjacent to the interface exceeds the local boiling point. The maximum heat flux is also time dependent, achieving very high values for short-duration heat pulses. Once this maximum is exceeded, the heat transfer transitions to a film boiling process where a film consisting of either He I, vapor, or both blankets the surface. Finally, in some configurations there is

observed a hysteresis in the heat transfer curve exemplified by the requirement to reduce q below q^* in order to return to the Kapitza regime. This process is reasonably well understood in He I and other classical fluids, being described by a hydrodynamic instability which leads to an engineering correlation. However, in He II the problem is more complex and has received less attention, owing to the experimental difficulty of achieving steady state and strong variations with configuration. It is the physical understanding of this heat transfer curve that is the goal of the present chapter. The description is based heavily on the physics of heat transport in He II contained in Chap. 6.

7.1 Steady-State He II Heat Transport in Wide Channels

The first question to ask is: What are the limitations to heat transport in a channel containing He II? Since the heat transport equations for He II have already been developed, it should be straightforward to apply this theory to determine practical heat transfer limitations. In doing so, it is assumed that the heat transport equations can be applied over finite temperature differences simply by taking into consideration the temperature dependence of the fluid properties. Note that He II cannot exist above the λ-transition, 2.177 K at SVP, which at least establishes liquid temperature boundaries to the heat transfer problem. For a channel of finite length L, as shown in Fig. 7.2, subjected to a constant heat flux q, there is a temperature difference established across its length, that is $\Delta T_{He\ II} = T_m - T_b$. In general, this temperature difference occurs because of two loss mechanisms discussed in Chap. 6: (1) the normal fluid viscous interactions with the channel walls and (2) the mutual friction between the two fluid components. We therefore consider here two classes of problems. The first concerns the heat and mass transfer in large systems such as occur in superconducting magnets and particle accelerators. In this case, the channel diameters and heat fluxes are sufficiently large to allow the mutual friction term to dominate the heat flow process. Thus, for this class of problems, the normal fluid viscous contribution to the temperature and pressure gradient can be neglected. The second class of problems which we will discuss subsequently involve heat and mass transfer through very small diameter capillaries or porous media. This heat transfer regime is mostly of interest in space applications and small scale cooling channels such as occur in some high current density magnets. In this latter case, at low heat fluxes, the flow is ideal and the pressure and temperature gradients obey London's equation with viscous flow dominating the normal fluid. At moderate to high heat fluxes, both laminar and turbulent contributions must be included in the analysis. Problems in this regime are the most complex to analyze.

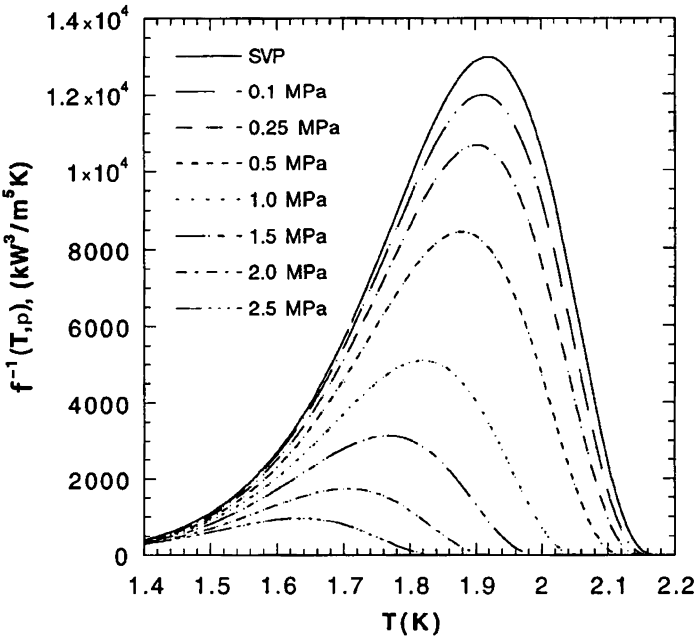

Fig. 7.3 Heat conductivity function for turbulent He II

7.1.1 He II Heat Conductivity Function

For wide channels, the normal fluid viscous term can generally be neglected so that the He II temperature gradient equation (6.101) may be simplified in one dimension as,

$$\frac{dT}{dx} = -f(T, p)q^m \tag{7.1}$$

where we define $f(T, p) = A_{GM}\rho_n/(\rho_s s^4 T^3)$ with A_{GM} being the mutual friction parameter and ρ_n and ρ_s are the normal and superfluid densities, respectively. According to theory $m \sim 3$; however, experimentally m has been shown to vary from about 3 to nearly 4 as the temperature approaches T_λ [1, 2]. A good mean value for practical calculations is to set $m = 3.4$, which is consistent with experiment over the temperature range from 1.7 K to T_λ [3–5]. The physics behind (7.1) is discussed extensively in Sect. 6.5. The quantity $f^{-1}(T, p)$ behaves much like a thermal conductivity in that it is a fluid property that controls the temperature gradient in the presence of a heat flux. It is therefore of interest to understand the variation of $f^{-1}(T, p)$ with state variables. Plotted in Fig. 7.3 is this function as it depends on temperature and pressure between 1.4 K and T_λ and $p =$ SVP and 2.5 MPa for the case where $m = 3$. Note that the temperature dependence is quite strong with a maximum occurring around $T \approx 1.9$ K at SVP. The pressure dependence is weaker.

In the data presented in Fig. 7.3, Vinen's [1] values for the Gorter-Mellink parameter have been used. Furthermore, it has been assumed that $A_{GM} \sim \rho\rho_n^2/\rho^3$ which is based on theory [6]. Then based on an empirical fit to the Gorter-Mellink parameter, it is possible to write an analytic expression for the heat conductivity function,

$$f^{-1}(T,p) = g(T_\lambda)\left[t^{5.7}(1-t^{5.7})\right]^3 \tag{7.2}$$

where $g(T_\lambda) = \rho^2 s_\lambda^4 T_\lambda^3/A_\lambda$, $t = T/T_\lambda$, $S_\lambda = 1559$ J/kg·K, and $A_\lambda = A_{GM}(T_\lambda) \simeq 1450$ m·s/kg. Note the maximum in (7.2) occurs at t = 0.885, which is 1.929 K at SVP. The values presented in Fig. 7.3 are good to about ±10% at saturated vapor pressure and have been compared to experiment up to about 0.7 MPa. Numerical values for $f^{-1}(T, p)$ are listed in Appendix A.3.

Recently, Sato et al. [7–10] performed extensive measurements of the average heat conductivity in turbulent He II over a wider range of temperatures and pressures up to 1.5 MPa. This work confirmed that the best fit to the heat conductivity function follows a power law $m = 3.4 \pm 0.1$. This extensive set of data was then used by Sato to develop an improved correlation for the turbulent heat conductivity function. The form of this correlation is similar to (7.1) where $m = 3.4$ and the heat conductivity function is written as a product of two terms,

$$f^{-1}(T,p) = h(t)g_{peak}(p) \tag{7.3}$$

where the reduced temperature $t = T/T_\lambda$ and $h(t,p)$ and $g_{peak}(p)$ are empirical functions. The normalized empirical function $h(t, p)$ is shown in Fig. 7.4 indicating a high quality correlation. This function has a peak at $t_{peak} = 0.882$.

Sato fit this quantity to a polynomial function,

$$h(t) = 1 + \left(t - t_{peak}\right)^2 \sum_{n=0}^{9} \{a_n(t-1)^n\} \tag{7.4}$$

where the polynomial coefficients are given in Table 7.1

The pressure dependent function was also fit to a polynomial as,

$$g_{peak}(p) = \exp\left(a + bp + cp^2\right) \tag{7.5}$$

where the coefficients (a, b and c) and the fit are shown in Fig. 7.5. This correlation is clearly an improvement over (7.2) and Fig. 7.3 and is recommended for more accurate numerical calculations. However, for approximate calculations particularly when they involve analytic solution, it is often more convenient to use the simplified form and keep the value of $m = 3$.

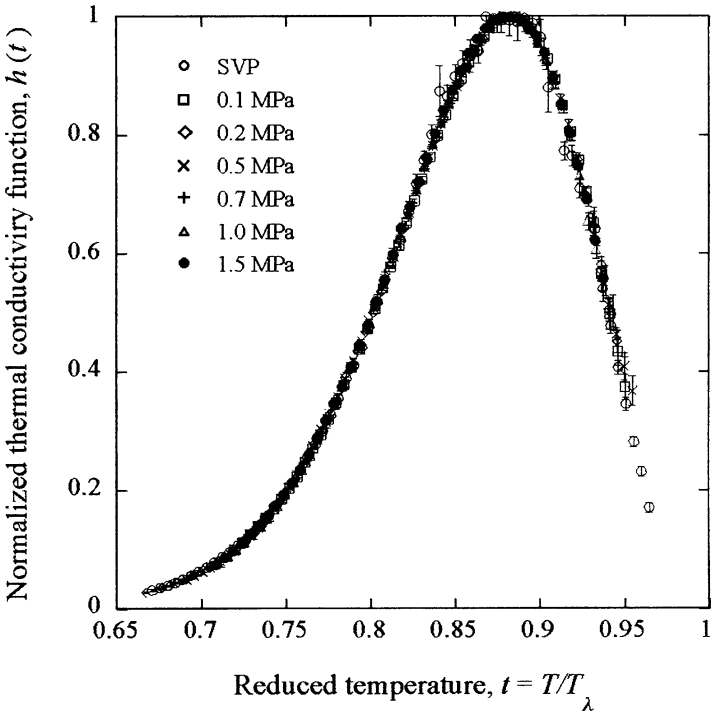

Fig. 7.4 Normalized thermal conductivity function at various pressures (Sato [6])

Table 7.1 Polynomial coefficients for (7.4) (Sato [6])

$a_0 = -71.818$	$a_1 = 1.2172617 \times 10^3$
$a_2 = -1.4992321 \times 10^4$	$a_3 = -3.9491398 \times 10^5$
$a_4 = -2.9716249 \times 10^6$	$a_5 = -1.2716045 \times 10^7$
$a_6 = -3.8519949 \times 10^7$	$a_7 = -8.6644230 \times 10^7$
$a_8 = -1.2501488 \times 10^8$	$a_9 = -8.1273591 \times 10^7$

7.1.2 Peak Heat Flux in Wide Channels

We now consider the limits to steady state heat transport in a finite-length channel. For a given steady heat flux, it is possible to determine the corresponding ΔT by integration of (7.1) (or the more refined Sato correlation, 7.3) for specified boundary conditions, e.g. T_b = constant. The maximum heat flux q^* is then established according to the maximum allowable temperature difference the channel, which for a given bath temperature T_b is $\Delta T_m \sim (T_\lambda - T_b)$. It follows that for a channel of length L

$$q^* = \left(\frac{1}{L} \int_{T_b}^{T_\lambda} \frac{dT}{f(T,p)} \right)^{1/m} \tag{7.6}$$

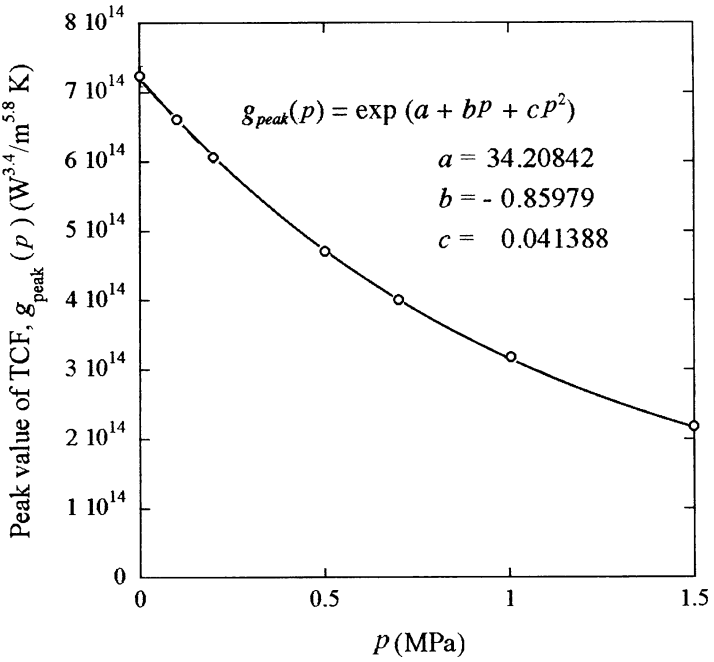

Fig. 7.5 Pressure dependence of the peak value of the thermal conductivity function (Sato [6])

This integral is mostly a function of T_b and only weakly dependent on other factors such as pressure. The integrated heat conductivity function is then defined as,

$$q^* L^{1/m} \equiv Z(T_b) = \left(\int_{T_b}^{T_\lambda} \frac{dT}{f(T,p)} \right)^{1/m} \tag{7.7}$$

which should be independent of channel length. Plotted in Fig. 7.6 are experimentally determined peak heat fluxes q^* for different channel lengths varying everywhere from 0.1 to 3 m. Two different correlations of the data are displayed: $Z'(T_b)$ for $m = 3$ and $Z(T_b)$ the other for $m = 3.4$. In either case, the agreement between data and correlation is acceptable.

By a similar analysis it is possible to determine the pressure dependence of the maximum heat flux q^*. Integration of the corresponding heat conductivity function $f^{-1}(T, p)$ predicts a decreasing maximum heat flux with elevated pressure. By analytic integration of (7.2), a prediction can be made for the behavior of q^* with pressure. The results of this analysis for four bath temperatures are displayed in Fig. 7.7. Also displayed are experimentally observed [4, 12] maximum heat fluxes for short channels up to 0.3 MPa. The agreement is again reasonable for the available data. As discussed above, an improved correlation can be obtained by using $m = 3.4$ and the Sato form for the heat conductivity function.

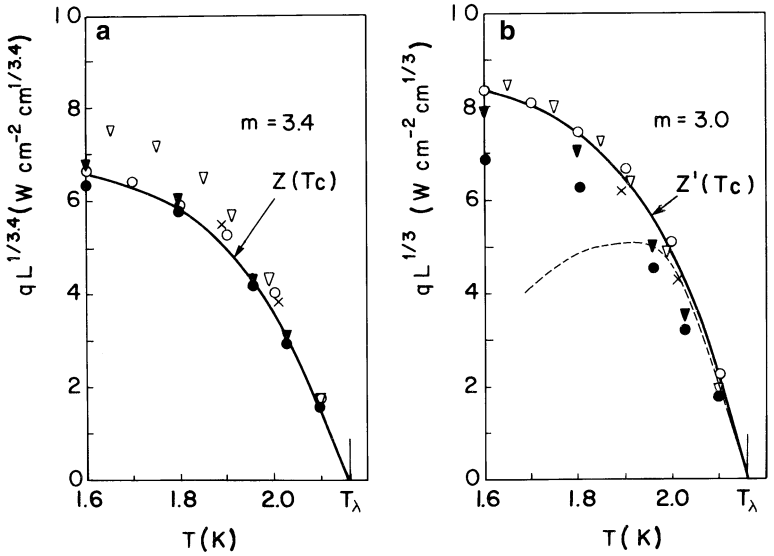

Fig. 7.6 Generalized steady-state limiting heat flux in He II (as compiled by Seyfert [11]). (**a**) is for the case where $m = 3.4$; (**b**) for the case with $m = 3$. The *dashed line* in (**b**) corresponds to near saturation boiling for a hydrostatic head of 0.1 m

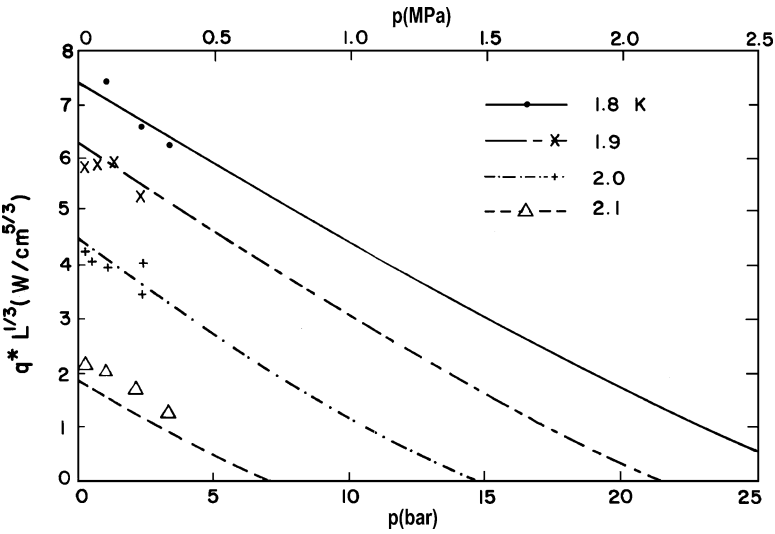

Fig. 7.7 Maximum heat flux in a He II-containing channel as a function of pressure (Data from Refs. [4] and [12])

It should be kept in mind that the form and physical explanation for heat transport in He II place no fundamental limit to the maximum steady state value for q^*. Everything depends on the allowable temperature difference. For example, with $T_b = 1.8$ K and $m = 3$, Fig. 7.4 predicts a product $q^*L^{1/3} = 7.4$ W/cm$^{5/3}$. Therefore, for a channel of length 10 μm, this analysis would predict a q^* in excess of 70 W/cm^2 (700 kW/m^2) truly a remarkable heat flux for liquid helium temperatures.

Example 7.1

Consider a 1 m long, 1 cm^2 cross section channel (see Fig. 7.2) containing He II at 2 K but pressurized to 0.5 MPa. Calculate the maximum heat flux in the He II channel.

To calculate the maximum heat flux, one needs to integrate the function. We use the simplified correlation with $m = 3$.

$$q^*L^{1/3} \equiv Z(T_b) = \left(\int_{T_b}^{T_\lambda} \frac{dT}{f(T,p)} \right)^{1/3}$$

Between 2 K and T_λ (p = 0.5 MPa). Since the channel is pressurized to 0.5 MPa, however, the appropriate form for $f^{1}(T,p)$ must be used, see Fig. 7.3. Fortunately, this integration has already been performed in Fig. 7.7. At 2 K and 0.5 MPa, $q^*L^{1/3} = 3$ W/cm$^{5/3}$. Thus, the a 1 m long, 1 cm^2 cross section channel, Q* = 0.65 W.

7.1.3 Peak Heat Flux in Saturated He II

In the discussion above, it has been assumed arbitrarily that the peak heat flux q^* is determined by the condition where the helium adjacent to the heater surface reaches the λ-point. This limit is not always met particularly in He II near its saturated vapor pressure for reasons having to do with the helium temperature distribution and the phase diagram, displayed in Fig. 7.8. We begin with the assumption that due to the high effective thermal conductivity of He II, the helium within the heat transfer region obeys equilibrium thermodynamics. This assumption allows the state of the helium everywhere in an experiment or engineering system to be described by a point on the equilibrium phase diagram.

Now consider a simple example, that of the heat transfer process occurring at the bottom of a vertical channel containing saturated liquid helium at 1.8 K, 1.6 kPa (12.5 torr). The heat transfer process is occurring at a certain depth, h, below the liquid-vapor interface; see Fig. 7.9. Thus, without any heat being applied, the state of the helium at the bottom of the channel can be described by location ① on the phase diagram in Fig. 7.8. The pressure applied at the heat transfer surface is therefore $p = p_0 + \rho gh$, where h is the hydrostatic head of the liquid helium. If heat

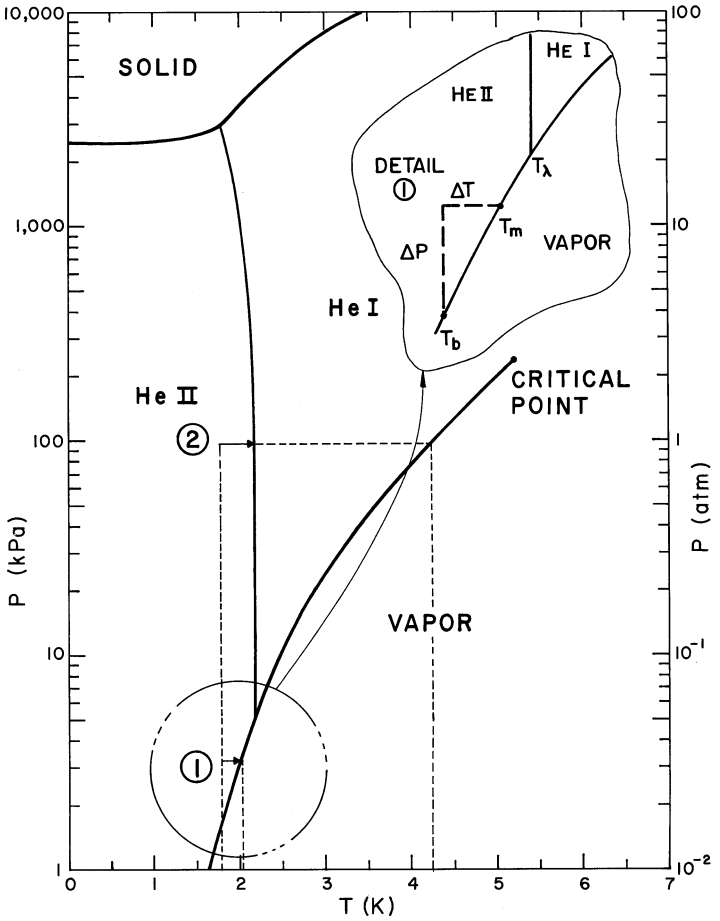

Fig. 7.8 Phase diagram of helium showing condition ① of near saturation and condition ② of subcooled helium to p = 100 kPa

is applied to induce heat transfer in the system, there will be a local temperature excursion ΔT that is determined by heat flow mechanisms as discussed above. The local temperature increases but the pressure is fixed, unless the experimental configuration is small enough for the thermomolecular effect to make a significant contribution. Neglecting this complication for the time being, as an increasing heat flux is applied, the temperature at the bottom of the channel will increase following a horizontal line as shown in the inset of Fig. 7.8 until at a certain heat flux it meets the liquid-vapor interface at which point boiling commences.

The value of the maximum temperature excursion is determined by the slope of the vapor pressure curve such that for finite ΔT,

$$\Delta T_m = \int_{p_0}^{p_0+pgh} \left(\frac{dT}{dp}\right) dp \tag{7.8}$$

Fig. 7.9 Vertical channel containing in near saturated He II

The slope of the pressure curve, $(dT/dp)_{sat}$ can be obtained from helium property tables or database codes. However, it is also known from thermodynamics through the Clausius-Clapeyron equation,

$$\left.\frac{dp}{dT}\right|_{sat} = \frac{h_{fg}}{T\Delta v} \approx \frac{h_{fg}}{Tv_g} \tag{7.9}$$

which can be further simplified by assuming the helium vapor to be an ideal gas, that is $v_g = RT/p$. This results in an approximate form for the allowable temperature increase,

$$\Delta T_m \simeq \frac{RT^2}{h_{fg}} \ln\left(1 + \frac{\rho g h}{p_0}\right) \tag{7.10}$$

This expression is suitable for $\Delta T_m \ll T_b$. For larger values of ΔT it is better to evaluate the saturation temperature at the pressure corresponding to the given hydrostatic head.

Under saturation conditions, this means that the maximum ΔT_m the He II can sustain may be less than that in pressurized liquid where $T_m = T_\lambda$. How does this impact the maximum heat flux? Returning to (7.6) and replacing T_λ with T_m, we note that the peak heat flux, q^* will be suppressed relative to the results shown in Fig. 7.6 with the amount of suppression dependent on h, the hydrostatic head. Considering the example above and let $h = 0.1$ m, we can recalculate the quantity $q^*L^{1/3}$ for is case. The result as a function of bath temperature is shown by the dashed line in Fig. 7.6b. Note that the magnitude of the suppression is small near T_λ, but becomes significant at lower temperatures since in that case, the maximum temperature, T_m is well below T_λ.

It is worth noting that the pressure corresponding to the λ-point is $p_\lambda = 4.97$ kPa (37 torr), which is equivalent to a column of helium about 3.55 m high. This fact is important because if a saturated vapor pressure He II system with vertical dimension larger than several meters is constructed, it would experience a heat transfer limitation determined by T_λ rather than the saturation line.

Example 7.2

Consider a 0.1 m long vertical channel (see Fig. 7.9) containing He II boiling at 1.638 kPa corresponding to a saturated vapor pressure at 1.8 K. Thus, the liquid free surface is at 1.8 K. If a heat flux is applied to the bottom of the channel, the temperature at that point will increase until it reaches local saturation at which point local boiling will occur. Calculate the maximum temperature of the He II at the bottom of the channel.

Since the liquid level is not very large, we can use the approximate expression for ΔT_m (7.10),

$$\Delta T_m \cong \frac{RT^2}{h_{fg}} \ln\left(1 + \frac{\rho g h}{p_0}\right)$$

Substituting values, $h = 0.1$ m, $h_{fg} = 23$ kJ/kg, the resulting $\Delta T_m = 0.025$ K and $T_m = 1.825$ K. As indicated, this is an approximate result. The more accurate result would be obtained by calculating the saturation temperature, T_s, corresponding to the pressure $p = p_0 + \rho gh = 1{,}638$ Pa + 145 kg/m^3 × 9.8 m/s^2 × 0.1 m = 1,780 Pa. Then referring to a data base code, one obtains T_s (p = 1780 Pa) = 1.824 K. These values are very close, since the head is not large. The result would not be as good if the level were significantly larger.

Alternatively, it is possible to create a subcooled liquid condition whereby the pressure at the heat transfer surface is higher than that due to the hydrostatic head. This condition can occur, for example, in a closed volume He II region cooled by a saturated bath heat exchanger. In this case, the pressure on the closed volume can take on any value between saturation and the solid line at 2.5 MPa. The subcooled He II state is shown on the phase diagram, Fig. 7.8, by position ②. Here it is assumed that the applied pressure is 100 kPa. A similar argument to that presented above applies when determining the temperature excursion; however, in the subcooled case the maximum temperature is governed by the λ-transition (at $p = 100$ kPa, $T_\lambda = 2.168$ K). In this case, the limit on maximum temperature relatively well fixed and only weakly dependent on applied pressure.

The conditions that exist once the maximum heat flux is exceeded are of great importance to understanding the heat transfer in this regime, a topic which is discussed more extensively in Sect. 7.6. Generally, there are two cases that can

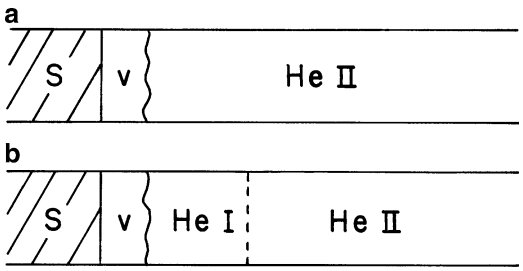

Fig. 7.10 Schematic of boiling in He II: (**a**) saturation condition and (**b**) subcooled condition

occur, each of which is associated with one of the two conditions indicated on the phase diagram in Fig. 7.8. For the saturation case, which applies to position ①, q^* corresponds to the helium adjacent to the interface achieving saturation conditions. A schematic representation of the resulting physical condition for $q > q^*$ is shown in Fig. 7.10a. Displayed is a solid heat transfer surface blanketed by a vapor film which in turn is bounded by the He II at local saturation temperatures. This phase boundary is defined clearly because the He II-vapor transition is first order.

The alternative film boiling heat transfer situation occurs whenever q^* is exceeded under subcooled conditions, such as ② in Fig. 7.8. For this case the phase transition is between He II and normal liquid He I. Since, with rare exception, the maximum heat flux in He I is substantially less than that in He II, exceeding q^* under subcooled conditions invariably results in a double transition, first creating a film of liquid He I followed by boiling of the He I to form a vapor film. This triple-phase phenomenon brings all three helium states in close proximity to the heat transfer interface. A schematic representation of this process is shown in Fig. 7.10b. Through the He II–He I interface, shown as a dotted line in the figure, the density ρ and temperature T should be continuous. Visualization experiments of boiling in saturated and subcooled He II have observed the interfaces between the vapor-He I and the He I-He II phases [13]. This result is shown in Fig. 7.11. Being able to observe the He I – He II phase boundary is particularly significant since the physical properties of helium should be continuous through the phase transition.

7.1.4 He II Heat Transfer in Cylindrical Geometries

Besides the simple linear geometry represented by a one-dimensional tube with constantheat flux, there has been considerable work carried out on cylindrical geometries consisting of a heated cylinder or wire immersed in a large bath of He II [14–16]. It is easy to show, by assuming that the Gorter-Mellink equations

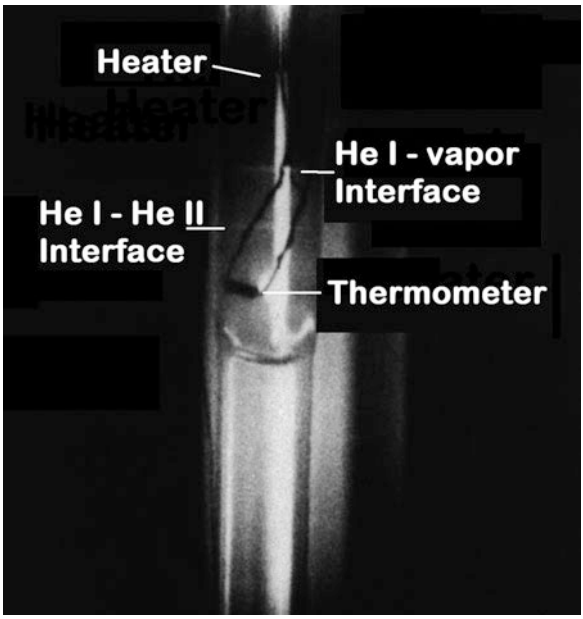

Fig. 7.11 Subcooled He II boiling showing the He I-vapor and He II – He I phase boundaries [13]

apply in cylindrical geometry, that the steady-state heat transport equation can be written as

$$\frac{dT}{dr} = -f(T)q_0^m\left(\frac{r_0}{r}\right)^m \tag{7.11}$$

where q_0 is the heat flux per unit area of the heated cylinder of radius r_0. The difference in (7.11) occurs because the heat flux decreases as the radius increases. Comparison of (7.11) with experiment has given reasonable agreement, with essentially the same heat conductivity function as applies in linear geometries [17, 18]. In a similar fashion to that applied to (7.3), integration of (7.11) leads to the maximum heat flux,

$$q_0^* = \left(\frac{m-1}{r_0}\int_{T_b}^{T_\lambda}\frac{dt}{f(T)}\right)^{1/m} \tag{7.12}$$

The important observation to make about (7.12) is that the peak heat flux q_0^* has as its scaling length r_0 rather than L as in the linear system. This means that, provided the radius of the container is much larger than that of the heater, the boundary conditions far from the heater should not affect q^* significantly. This is certainly contrary to the behavior in linear geometries.

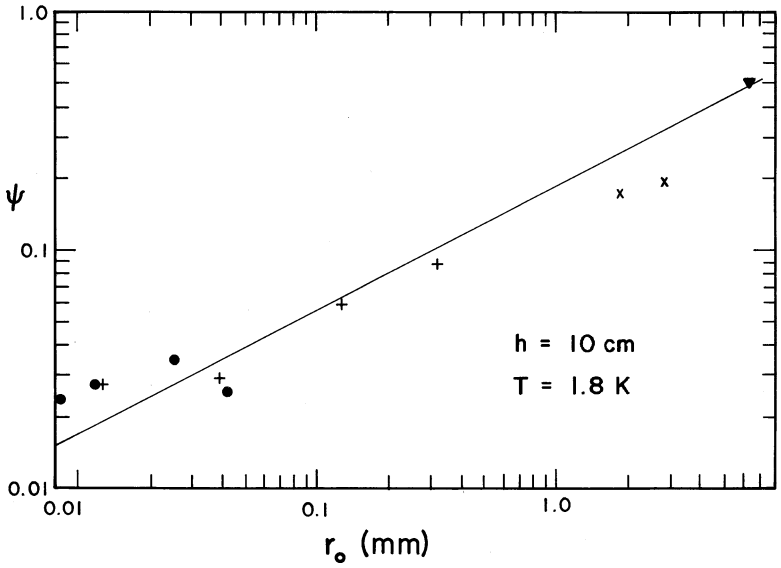

Fig. 7.12 Empirical correlating function for heat transfer in cylindrical geometries [17, 18]

Unlike the linear one-dimensional system, there have been fewer attempts to correlate the peak heat transport in cylindrical geometries with that of (7.12). This is due in part to the lack of reliable data, which are more difficult to obtain in cylindrical geometries. In one experiment, data were fit for small temperature differences $\Delta T \approx 10$ mK in the range of $T_b = 1.8$ K [17, 18]. It was found that the expression given by (7.11) is not entirely suitable to correlate the experimental values of q_0^* without introducing a radius-dependent quantity Ψ defined by

$$q_0^* = \left(\frac{2\Psi}{r_0} \int_{T_b}^{T'} \frac{dT}{f(T)} \right)^{1/3} \tag{7.13}$$

where $T' \simeq T_b + 0.01$ K. Ψ was found empirically to depend on radius, being roughly proportional to $r_0^{1/2}$. The results of this correlation are shown in Fig. 7.12. Note that Ψ is always less than 1, indicating that the peak heat flux is always less than that predicted by the idealized theory. This fact is somewhat surprising because the temperature gradients appear to be given accurately by (7.11).

7.1.5 Static Bath He II Heat Exchangers

He II heat exchangers are indispensable components for superconducting magnets and other systems cooled with pressurized He II. However, because of the unusual properties of He II, specifically the high effective heat conductivity and strong

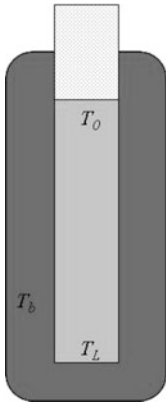

Fig. 7.13 Schematic of a simple static He II heat exchanger

temperature dependent heat capacity, conventional heat exchanger design methods, such as effectiveness or NTU, are not suitable. In this section, we discuss the design of He II heat exchangers based on the available transport equations.

There have been a number of He II heat exchangers designed and developed for applications. The most common of these is the static bath type system, shown schematically in Fig. 7.13. The principal component of this system is a saturated He II reservoir of active length L and cross section A in thermal contact through its surface to a surrounding pressurized He II reservoir. Any heat generated in the pressurized He II reservoir must be transferred through the solid wall to the saturated bath where it is removed by evaporation of the liquid. For this type of system, there are three design criteria:

1. The surface area of the heat exchanger must be large enough to transfer the heat with minimal ΔT between the two reservoirs. Normally, the surface heat transfer process is controlled by the Kapitza conductance of the heat exchanger material and possibly thermal conduction through the solid wall. These quantities combine into an overall heat transfer coefficient, U. It is important to make the heat exchanger of copper or other high conductivity material to avoid a significant conduction thermal resistance.
2. Boiling in the bulk liquid within the heat exchanger should be avoided. This means that the liquid should be subcooled by the hydrostatic head enough to avoid surface boiling which could degrade performance.
3. There must be sufficient He II cross section in the saturated bath to transport the heat by counterflow with a small temperature gradient.

The beginning point for the analysis of a static He II heat exchanger is the steady state He II heat equation with surface heat transfer,

$$\frac{d}{dx}\left(f(T)^{-1}\frac{\partial T}{\partial x}\right)^{\frac{1}{3}} - \frac{PU}{A}(T - T_b) = 0 \tag{7.14}$$

where $f(T)^{-1}$ is the He II heat conductivity function appropriate for fully developed turbulent conditions and T is the temperature of He II within the heat exchanger. U is the overall heat transfer coefficient between the two reservoirs. Equation (7.14) can be simplified by making the following change of variables:

$$\Theta = \frac{T_b - T}{T_b - T_0} \tag{7.15a}$$

and

$$m_{HeII} = \left[\frac{PU(T_b - T_0)^{2/3}}{f^{-\frac{1}{3}}A}\right]^{\frac{3}{4}} \tag{7.15b}$$

With the constant properties assumption the following dimensionless equation results,

$$\frac{d}{dx}\left(\frac{d\Theta}{dx}\right)^{1/3} - m_{HeII}^{\frac{4}{3}}\Theta = 0 \tag{7.15c}$$

Equation (7.15a) is analogous to the classical fin equation in conduction heat transfer except for the non-linear thermal conduction feature of the He II. However, the solution to (7.15a) is similar and can be preformed semi-analytically depending on boundary conditions [19]. Just as in the case of the fin equation, the boundary condition at the end of the heat exchanger determines the exact form of the solution.

If we define the origin at the surface of the He II, the boundary condition at $x = 0$ is $\Theta = 1$ by definition. The fluid temperature increases away from the free surface. The boundary condition at the bottom of the heat exchanger ($x = 1$) can have difference cases:

1. Convection heat transfer: $\left(f^{-1}\frac{d\Theta}{dx}\right)^{\frac{1}{3}} = U\Theta_L(T_b - T_0)^{\frac{2}{3}}$
2. Adiabatic: $\left(\frac{d\Theta}{dx}\right)_L^{\frac{1}{3}} = 0$
3. Prescribed temperature: $\Theta(x = L) = \Theta_L$
4. Infinite length: $\Theta(x = L) \xrightarrow{L=\infty} 0$

and $m_{HeII}L$ is dimensionless fin length. Each case has a slightly different form for the solution. Typically, in a good design $m_{HeII}L \sim 1$; however, it can take on any value. If $m_{HeII}L >> 1$, then the heat transfer process is only weakly affected by the boundary condition at $x = L$ and the infinite length solution is a good approximation for all cases.

To calculate the total heat transfer through the heat exchanger, one integrates (7.15c) one time to obtain the temperature gradient, $d\Theta/dx$. This quantity is then evaluated at x = 0 such that,

$$Q = -A\left(f^{-1}\frac{dT}{dx}\right)_{x=0}^{\frac{1}{3}} \tag{7.16}$$

Table 7.2 Coefficients of (7.17) for different boundary conditions: $\beta = AU^3(T_b - T_0)^2/2Pf^{-1}$ (From Ref. [19])

Boundary condition	γ	Θ_L^2
Convection heat transfer	$\Theta_L^2 - \beta\Theta_L^2$	$\frac{1}{2\beta} - \left[\frac{1}{4\beta^2} - \frac{1-(Q/M_{Hell})^4}{\beta}\right]^{1/2}$
Adiabatic	Θ_L^2	$1 - (Q/M_{Hell})^4$
Prescribed temperature	†	†
Infinite length	0	0

†Value is determined by implicit solution

The result of this calculation is an expression for the total heat transfer,

$$Q = M_{HeII}(1-\gamma)^{\frac{1}{4}} \tag{7.17}$$

Where $M_{HeII} = 1.19A[m_{HeII} f^{-1}(T_b - T_0)]^{1/3}$ which is analogous to the total heat transfer expression obtained from the fin equation. The dimensionless quantity γ is a function of the particular boundary conditions imposed at $x = L$. The corresponding form for γ is listed in Table 7.2. Note that if $\gamma << 1$, the total heat transfer is only a weak function of the boundary conditions at $x = L$ and the infinite length heat exchanger is a good approximation with $Q = M_{HeII}$.

The temperature profile along the heat exchanger can be further calculated by integrating (7.15c) a second time. This solution depends on the choice of boundary condition at $x = L$. The resulting general solution for the temperature profile is obtained by solving the integral,

$$\int_{\Theta_L}^{1} \frac{d\Theta}{\left(\Theta^2 - \gamma\right)^{\frac{3}{4}}} = 1.68 m_{HeII} x \tag{7.18}$$

For all boundary conditions except the infinite heat exchanger, the solution of (7.18) requires numerical methods. For the special case of the infinite channel, $\gamma = 0$ and $Q_L = 0$, which leads to the closed form solution,

$$\Theta(x) = \left[\frac{1}{0.84 m_{HeII} x + 1}\right]^2 \tag{7.19}$$

One can compare the numerical solution for fixed boundary conditions at $x = L$ to that of the infinite channel. The results for adiabatic solution are shown in Fig. 7.14.

The performance of a He II heat exchanger can also be treated in a fashion similar to that of ordinary fins. Using the conventional expression for the effectiveness of a fin, we obtain

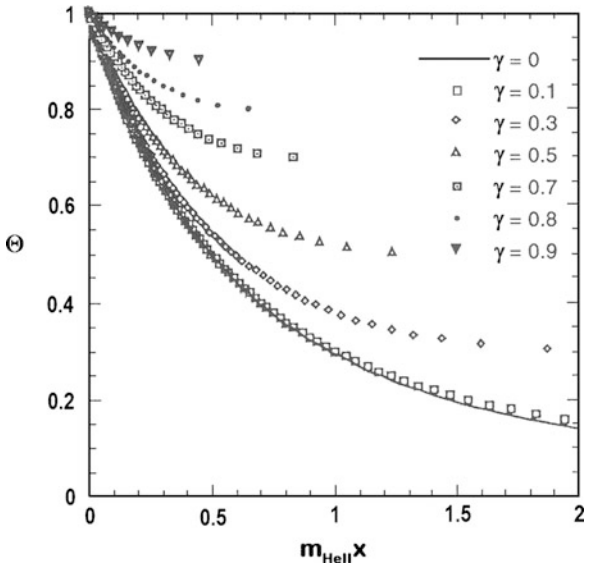

Fig. 7.14 Dimensionless temperature profile along a He II heat exchanger. The data points are obtained by numerical solution of (7.15) for adiabatic boundary conditions with different values of γ. Also shown by the solid line is the analytic solution for $\gamma = 0$ (7.19)

$$\varepsilon_f = \frac{Q_{actual}}{UA(T_b - T_0)} = \left[\frac{2Pf^{-1}(1-\gamma)}{U^3A(T_b - T_0)^2}\right]^{\frac{1}{4}} \tag{7.20}$$

Note that for typical values, $f^{-1} = 10{,}000\ \mathrm{kW^3/m^5\ K}$, $U = 2\ \mathrm{kW/m^2\ K}$ and $(T_b - T_0) = 50$ mK we obtain $\varepsilon_f \sim 30\ (P/A)^{1/4}$ in SI units. Therefore, for all reasonable geometries, $\varepsilon_f >> 1$. For short heat exchangers with $\Theta_L \sim 1$, ε_f is simply equal to the ratio of the actual surface area to the base area. For long heat exchangers, where $\Theta_L << 1$, the effectiveness is still generally much greater than unity because of the high effective thermal conductivity of the He II.

In a similar fashion, the fin efficiency can be defined as,

$$\eta_f = \frac{Q}{UA_{fin}(T_b - T_0)} = \varepsilon_f \left(\frac{A}{A_{fin}}\right) \tag{7.21}$$

This quantity is almost always of order unity unless $\Theta_L << 1$. Typically, $\eta_f \sim 1$ unless $m_{HeII}L > 1$.

Before leaving the subject of He II heat exchangers, it is important to comment on one of the other limitations to the performance of static saturated bath heat exchangers. This is related to item 2 above in the list of design considerations. For a heat exchanger to perform well, the heat transfer process should be only governed by Kapitza conductance at the heat exchange surface. However, if boiling occurs

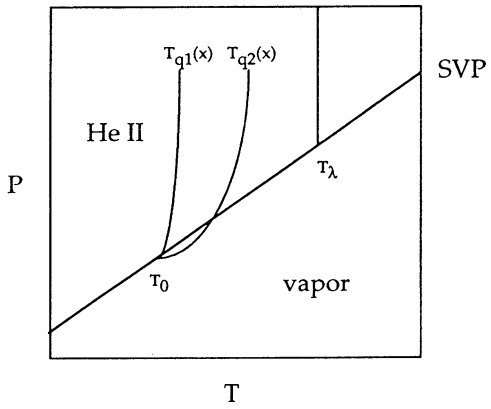

Fig. 7.15 Localized region of the He II phase diagram illustrating the boiling condition that can occur in a static, saturated bath heat exchanger

within the heat exchanger, it is possible that the performance will be degraded. To avoid bulk boiling in the bath, we therefore need to ensure that nowhere the heat exchanger does the He II reach saturation conditions. Such conditions can occur at various points within the heat exchanger due to the non-linear temperature profile and varying heat flux within the He II column.

Figure 7.15 illustrates this situation. The free surface of the heat exchanger is assumed to be fixed at T_0, while below that point the liquid is subcooled by the hydrostatic head (ρgh). With no heat load, the temperature in the heat exchanger is uniform at T_0. However, with a heat load, the temperature below the surface increases due to the Gorter-Mellink heat transfer. The temperature profile is steepest at the surface of the liquid due to the accumulation of heat flux ($q(x)$) along the channel. Two representative temperature profiles are shown in the figure. Boiling will occur if the predicted temperature profile crosses the saturation line, see $T_{q2}(x)$. In this case, the slope of the temperature profile at the surface is steeper than the slope of the saturated vapor curve allowing the bulk liquid to boil locally. If the heat flux is increases, the boiling region will expand within the heat exchanger.

The critical condition for boiling can be made more quantitative by equating the slope of the temperature profile at the free surface ($x = 0$) to the slope of the saturated vapor pressure line,

$$\left.\frac{dT}{dx}\right|_{x=0} = \rho_l g \left.\frac{dT}{dp}\right|_{svp} \tag{7.22}$$

As before, the slope of the saturated vapor pressure line is given by the Clausius-Clapeyron equation as,

$$\left.\frac{dp}{dT}\right|_{svp} = \frac{h_{fg}}{T\Delta v} \approx \frac{h_{fg}p}{RT^2} \tag{7.23}$$

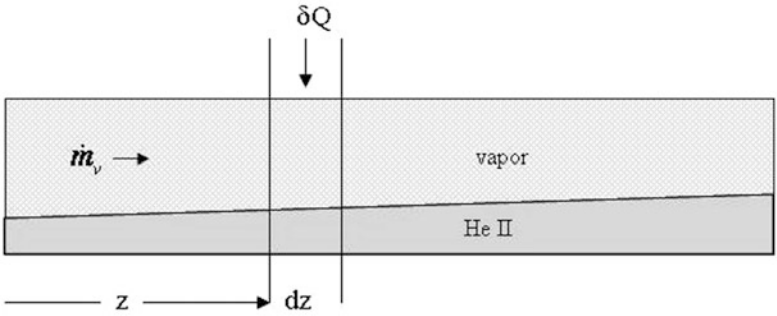

Fig. 7.16 Schematic of He II-vapor two phase flow system

where the last approximate form results from assuming the saturated helium vapor obeys the ideal gas law. Substituting the form for the counterflow heat transport in the He II (7.1) and assuming for simplicity that $m = 3$, the following expression occurs,

$$q_{\max} = \left(\frac{\rho_l g R T^2 f^{-1}}{h_{fg} p_0} \right)^{\frac{1}{3}} \tag{7.24}$$

This expression has a peak near 1.87 K at $q_{max} = 14$ kW/m^2. It decreases from the peak dominated by the temperature dependence of the heat conductivity function, $f^{-1}(T, p)$.

7.1.6 He II Two Phase Heat Transfer and Flow

In recent years, applications have emerged that use of He II in a horizontal tube in co-existence with its saturated vapor. The first of these involves the use of a near horizontal He II – vapor heat exchanger to cool subcooled He II for the LHC accelerator magnets [20]. The other recent application involves the use of horizontal two phase He II – vapor lines in large RF cavity accelerators [21]. Proper design of these systems depends on a thorough picture of the relevant helium hydrodynamics.

We begin by considering a long, horizontal tube that is partially filled with near static He II, see Fig. 7.16. In such a system, there are three basic heat transfer mechanisms: (1) Gorter-Mellink counterflow in the bulk liquid; (2) forced convection mass transport in the vapor phase; and (3) mass exchange by evaporation or condensation between the two phases. The addition of the mass transfer between the two phases makes the heat transfer process in two-phase He II far more complex problem than that of single-phase He II.

We first discuss the semi-analytic solution to this problem for which several simplifying assumptions required. First, the liquid within the tube is assumed to be in a stratified flow condition with a near horizontal interface between the liquid and vapor. This is a reasonable assumption based on experiments. Next, thermal gradients normal to the axis of the tube are assumed to be negligible so that the problem becomes that of two coupled one-dimensional systems. Finally, the liquid is assumed to be in local thermodynamic equilibrium with its vapor so that $T_L(z) = T_v(z)$, where z is the axial dimension coordinate. The goal is to construct a model to predict the behavior of the temperature profile, $T(z)$, liquid level or void fraction ($\alpha = A_v/A$), and liquid, vapor mass flow rates, $\dot{m}_l, \dot{m}_v$ and total heat transfer, Q.

For most cases of interest the liquid is nearly static so that the pressure drop along the tube is determined primarily by friction in the vapor phase, which is given by the expression,

$$\frac{dp}{dz} = -\frac{2f_F}{\rho_v D_H}\left(\frac{\dot{m}_v}{\alpha A}\right)^2 \tag{7.25}$$

where f_F is the Fanning friction factor, α is the void fraction and A is the total cross section of the tube. In (7.25), $\dot{m}_v$ and α will in general be functions of z so that dp/dz is not a constant. In a stratified flow system, α is directly related to the liquid level.

At any point along the channel, the total heat flux is a combination of two terms: the flux of vapor due to evaporation and the counterflow heat flux through the He II. These two terms sum directly,

$$Q(z) = \dot{m}_v h_{fg} - (1-\alpha)A\left(f^{-1}\frac{dT}{dz}\right)^{\frac{1}{3}} \tag{7.26}$$

where the first term on the right is the heat carried by convection of the vapor and the second is the liquid counterflow heat transport. h_{fg} is the heat of vaporization. In (7.26) there are three unknowns: $\dot{m}_v$, α and dT/dz.

Since the He II and vapor are in thermodynamic equilibrium, it follows that the pressure gradient may be written in terms of the derivative along the saturation line of He II and the local temperature gradient,

$$\frac{dp}{dz} = \left.\frac{dp}{dT}\right|_{svp}\frac{dT}{dz} \approx \frac{\rho_v h_{fg}}{T}\frac{dT}{dz} \tag{7.27}$$

where use has been made of the Clausius-Clapeyron equation, $dp/dT)_{svp} = \Delta s/\Delta v \approx \rho_v h_{fg}/T$ for an ideal gas which approximates low density helium vapor. Combining (7.25) and (7.27), we obtain a relation for the temperature gradient in terms of the vapor mass flux,

$$\frac{dT}{dz} = \frac{-2f_D T}{\rho_v^2 h_{fg} D_H}\left(\frac{\dot{m}_v}{\alpha A}\right)^2 \tag{7.28}$$

which is again a relationship between three unknowns dT/dz, $\dot{m}_v$ and α.

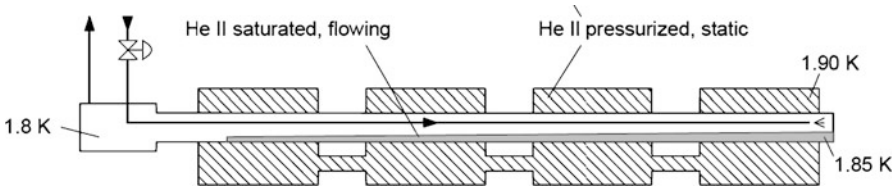

Fig. 7.17 Configuration of the He II bayonet heat exchanger [24]

The third relationship between the unknowns in the problem is obtained by considering the He II to be essentially static, $v_l \approx 0$ and using the hydrostatic head condition on the pressure. In this case with the saturation condition, we can state that the pressure at the bottom of the channel is a sum of the saturation pressure plus the hydrostatic head, $p_0 = p_s(T) + \rho g y$ where y is the liquid level. Taking p_0 to be a constant and differentiating, it follows that the pressure gradient is directly proportional to the void fraction gradient or slope in the liquid/vapor interface,

$$\frac{dp}{dz} = -\rho_l g \frac{dy}{dz} \tag{7.29}$$

Again making use of the chain rule and Clausius-Clapeyron equation for an ideal gas, we obtain a relationship between the temperature and void fraction gradient,

$$\frac{dy}{dz} = -\frac{\rho_v h_{fg}}{\rho_l g T} \frac{dT}{dz} \tag{7.30}$$

Equation (7.30) suggests that a large temperature gradient will result in a large slope of the liquid/vapor interface as indicated in Fig. 7.16.

The above expressions has an analytic solution for a rectangular cross section channel with a constant heat flux [22], which simplifies the problem of relating the liquid level (y) to the void fraction, α. The results of the analysis were successfully compared to experiment. An important outcome of the analysis was to show that for typical geometries of horizontal He II heat exchangers, the heat transported by the coexisting vapor is roughly ten times as efficient as that carried by counterflow. Thus, the benefits of horizontal two phase He II cooling systems are evident. Numerical studies of near horizontal two phase He II-vapor systems has been performed in the context of RF cavity accelerator development [23]. The goal of this work was to be able to model the temperatures, flow rates and liquid levels in existing cryogenic facilities. Such a modeling effort has been sufficiently successful to add credence to the belief that similar two phase He II systems can be designed and successfully operated.

An important application of a near horizontal He II – vapor system is the so called bayonet heat exchanger developed for the LHC, shown schematically in Fig. 7.17 [24]. This unique design uses a corrugated tube partially filled with He II to extract the heat loads from the accelerator magnets. The two phase liquid from

the refrigerator is expanded into the far end of the heat exchanger with the vapor returning above the stratified liquid. The heat exchanger works by a similar principle as discussed above, but in this case the heat flux is determined by the heat exchange through the wall of the tube into the saturated two phase flow.

The heat transfer rate is determined by the overall heat transfer coefficient of the heat exchanger, which is equal to the series thermal resistance of the two surface heat transfer coefficients and the thermal resistance of the corrugated tube. Since the saturated bath side of the heat exchanger is only partially filled with liquid, the wetted surface area is not well defined. However, experiments have shown that a combination of He II film flow and liquid droplet entrainment in the vapor provides a very effective heat exchange process even for high void fraction [25].

A simplified analysis [24] of the bayonet heat exchanger is based on similar assumptions as were discussed above in two phase He II flow modeling. In the case of the heat exchanger, the following assumptions are made. First, the void fraction is sufficiently high that the pressure drop is determined entirely by the vapor flow rate,

$$\frac{dp}{dz} = -\frac{2f_D}{\rho_v D_H}\left(\frac{\dot{m}_v}{A}\right)^2 \tag{7.31}$$

Second, that the total heat transfer, $Q = qL$, determines the overall change in the vapor mass flow rate,

$$Q = qL = h_{fg}(\dot{m}_{out} - \dot{m}_{in}) \tag{7.32}$$

where $q = UP(T_o - T_i)$, the heat removed per unit length of the heat exchanger. Third, the vapor quality, $\chi = \dot{m}_v/\dot{m}_{out}$ at the outlet is assumed to be unity, pure vapor flow and $\chi_0 = \dot{m}_{in}/\dot{m}_{out}$. For these conditions, (7.31) can be integrated over the length of the heat exchanger assuming a circular cross section tube of diameter D, to yield the total pressure drop,

$$\Delta p = \frac{32f_D}{3\pi^2}\frac{q^2}{\rho_v h_{fg}^2}\frac{L^3}{D^5}\left(\frac{1-\chi_0^3}{(1-\chi_0)^3}\right) \tag{7.33}$$

This equation establishes the minimum diameter that meets the pressure drop requirements. In addition, a criterion is suggested on the maximum vapor velocity of 5 m/s to ensure that the flow is stratified. This leads to,

$$A \geq \frac{qL}{h_{fg}\rho_v v_{\max}}\frac{1}{1-\chi_0} \tag{7.34}$$

Depending on boundary conditions, the two criteria based on (7.33) and (7.34) yield similar constraints on the heat exchanger design. For example, a 100 m long bayonet heat exchanger with a 1 W/m heat load would need to have diameter of

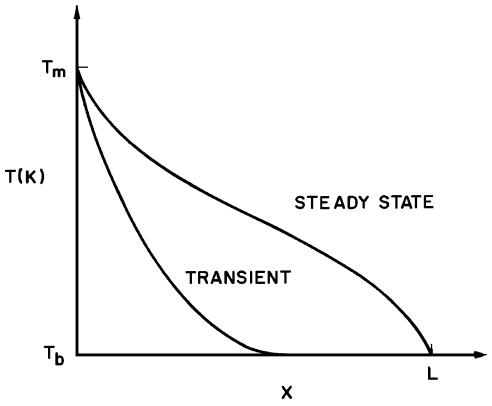

Fig. 7.18 Schematic temperature distributions in He II under steady-state and transient conditions

about 50 mm for a ΔT of 50 mK. This is to be compared to 180 mm diameter tube that would be required to carry the same heat load over the same temperature difference in pure thermal counterflow in bulk He II.

7.2 Transient Heat Transport in Wide Channels

A thorough understanding of the time evolution of the temperature distribution in He II is of the utmost importance to fully describe the heat transfer process. Up until this point, the assumption has been made that the heat transfer is steady-state and can be interpreted by using equilibrium thermodynamic models and the helium phase diagram. This assumption is certainly an oversimplification because there are a number of time-dependent phenomena that affect the heat transport properties of He II. To determine the relative significance of transient phenomena in a heat transfer problem, the following questions must be asked: At what point in time does a system exposed to some change in the heat flux reach steady state? What are the physical processes that control this time development? To answer these questions it is necessary to take account of the energy scales associated with heat transport in He II.

We begin by considering a one-dimensional channel of length L cooled by a constant temperature bath at one end, see Fig. 7.2. Initially, the temperature of this system is uniform at T_b. However, if a heat flux is applied at the end away from the bath, a temperature distribution will evolve until eventually a steady-state condition is achieved with the temperature at the heated end being $T_m > T_b$. Typical transient and steady-state temperature distributions are shown schematically in Fig. 7.18.

There are a number of energy inputs required to achieve the steady-state temperature distribution in He II. The first of these we may associate with the acceleration of the two fluid components, normal and superfluid, to v_n and v_s, respectively. Since the fluids are initially at rest, it is necessary to apply sufficient kinetic energy for steady-state counterflow to be established. For typical heat

fluxes, the normal fluid and superfluid velocities are of the order of a few tens of mm/s. This value leads to a kinetic energy density of considerably less than 1 J/m^3, which we will see is very small on the scale of interest.

Since the He II is initially in the non-turbulent state, a second energy flux which must be applied to the system is that necessary to create the turbulence. This process has been described physically in Chap. 6 with an expression for the time required to create turbulence in a channel being,

$$\tau = aq^{-3/2} \tag{6.109}$$

The coefficient a is a temperature-dependent function of the order of 10^5 W$^{3/2}$·s/m^3. Equation (6.109) has no length dependence, presumably because the growth of turbulence travels at the velocity of second sound and therefore would be essentially uniform in a short channel at moderate heat flux. Rearranging (6.109) we can determine the energy required to produce turbulence as,

$$q\tau = aq^{-1/2} \tag{7.35}$$

which for heat fluxes in the range of a few tens of kW/m^2 gives an estimated value of about 1 kJ/m^2. For a channel having a length of the order of 1 m, the energy density associated with the creation of turbulence works out to be $q\tau \approx 1$ kJ/m^3.

Also of concern is the energy carried by the second sound pulse itself. This mechanism is probably most important at the highest values of heat flux. Second sound shock was discussed in Chap. 6 and it was shown that depending on conditions, an energy as large as 100 J/m^2 can propagate along a channel in advance of the turbulent front. For very short times, this can be the dominant mechanism for heat transfer and as was mentioned above is probably the mechanism for turbulence propagation. Still this is not a large amount of energy compared to the heat content of the He II itself.

The final principal energy input required to create the steady-state temperature distribution in Fig. 7.18 is that of the enthalpy content of the He II itself. The heat capacity of liquid helium is very large, particularly near the λ-transition where on a volumetric basis it is of the order of 1 MJ/m^3 K. Therefore to establish the steady-state temperature distribution sufficient heat must be applied to increase the fluid temperature from that of the bath to its local steady-state value $T(x)$. In practical systems this increase is of the order of 0.1 K. The required energy density needed to achieve a given temperature distribution can be written

$$\varepsilon_C = \frac{\rho}{A_0 L}\int_0^L dx \int_{T_b}^{T(x)} C_p(T)dT \tag{7.36}$$

which is of the order of 100 kJ/m^3. Furthermore, as the length of the channel increases the dominance of this term increases, particularly for long channels with $L \gtrsim 1$ m. Because the enthalpy profile dominates the transient heat input, other

energies associated with this problem rarely are considered. Therefore, it is assumed that at least for engineering systems experiencing moderate heat fluxes ($q \sim 10$ kW/m^2), the transient temperature distribution is controlled by heat transport and enthalpy considerations. As a result, a diffusion like model has been shown to describe the problem effectively.

7.2.1 He II Diffusion Equation

For background, we consider the time dependent heat transport in a conductive solid. This process is described by a well-known diffusion equation, which in one dimension is,

$$\frac{\partial T}{\partial t} = D_{th} \frac{\partial^2 T}{\partial x^2} \tag{7.37}$$

where $D_{th} = k/\rho C$ is the thermal diffusivity having units of m^2/s. The form of (7.37) has the inherent assumption of constant properties, k, ρ, and C. Otherwise, the equation is somewhat more complex. Equation (7.37) has been solved for a wide variety of boundary conditions with non-dimensional results applicable to many of the problems. However, without going through a specific solution for a particular set of conditions, some physical discussion of its implications can be made. In particular, it is possible to construct a characteristic time, called the diffusion time τ_D, which is obtained by non-dimensionalizing (7.37) and has the form

$$\tau_D = \frac{L^2}{D_{th}} \tag{7.38}$$

where the length L is the total length of the conduction path. For the case of the one-dimensional rod heated at one end, L is the overall length. The diffusion time is a measure of the thermal relaxation of the system. In most diffusion problems, the solution is scaled in terms of the dimensionless Fourier number,

$$Fo = \frac{t}{\tau_D} \tag{7.39}$$

Since the conduction is dominated by exponential terms, τ_D is not the actual relaxation time but is proportional to the time required to reach the steady state. For $Fo >> 1$, the problem is essentially in steady state, while for $Fo \lesssim 1$, the full diffusion equation must be considered.

To achieve a high rate of heat diffusion it is necessary to have a high thermal diffusivity. Solids possessing the largest values of D_{th} are high-conductivity metals at low temperatures, where not only if k large, but the specific heat C is small.

For example, high-purity copper near 4 K has $\rho C \approx 1$ kJ/m^3 and a thermal conductivity $k \approx 1$ kW/m K which gives $D_{th} \approx 1$ m^2/s. For high-purity metals at low temperatures the diffusion time constant, assuming a characteristic length $L \approx 1$ m, is of the order of seconds.

Although He II clearly does not obey the simple diffusion equation (7.37), it is useful nonetheless for physical understanding to make some order-of-magnitude comparisons. Since turbulent He II in one dimension obeys the nonlinear heat flow equation given by (7.1), it is possible to define an effective thermal conductivity, albeit dependent on heat flux,

$$k_{\text{eff}} = \frac{1}{f(T,p)q^2} \tag{7.40}$$

As can be seen in Fig. 7.3, the quantity, $f^{-1}(T, p)$ typically has a value around 10,000 kW^3/m^5 K near 1.8 K and saturated pressure. Therefore, for a heat flux $q = 10$ kW/m^2, the effective thermal conductivity is of order 100 kW/m K, which is about two orders of magnitude larger than for high-purity metals at low temperatures. Of course, the heat flux dependence of k_{eff} works against the transport of large heat fluxes. At 100 kW/m^2, k_{eff}, is reduced by two orders of magnitude to around 1 kW/m K, which is comparable to that of copper in the same temperature range.

The effective thermal diffusivity of He II, D_{eff}, can also be defined according to the analogy with solid conduction. Around 1.9 K, $\rho C \approx 0.5$ MJ/m^3 K, which gives a value for $D_{\text{eff}} \approx 0.2$ m^2/s. For a characteristic length of 1 m, this effective thermal diffusivity leads to a characteristic time constant $\tau_D \approx 5$ s. Furthermore, since the diffusion time goes as the square of the characteristic dimension, larger systems have time constants that can be very long compared to other time constants in the problem.

To properly treat transient heat transfer problems in He II; however, it is necessary to use a general heat diffusion equation. The derivation of the equation is analogous to that of the ordinary diffusion equation although the thermal conduction relationship must be replaced with the nonlinear Gorter-Mellink expression (7.1). The result may be written in the form of a one-dimensional heat diffusion-like equation,

$$\rho C_p \frac{\partial T}{\partial t} = \frac{\partial}{\partial x}\left(\frac{1}{f(T)}\frac{\partial T}{\partial x}\right)^{1/3} \tag{7.41}$$

where again we assume for simplicity that $m = 3$ in the counterflow heat conduction term. This expression has a very similar appearance to the ordinary diffusion equation, with the one exception that it involves an unusual power of the temperature gradient. Because of the nonlinear character of (7.41), it is apparent that extraordinary efforts are needed to solve this equation. There are in fact several methods available to treat this equation, here we will only consider approximate analytic solutions. Numerical solution of the He II energy equation will be discussed in a subsequent section.

We begin by casting (7.41) into a dimensionless form by introducing the variables,

$$\Theta^* = \frac{T - T_b}{T_\lambda - T_b} \tag{7.42a}$$

and

$$x^* = \frac{x}{L} \tag{7.42b}$$

$$\tau \equiv \frac{t}{f^{1/3}\rho C(T_\lambda - T_b)^{2/3}L^{4/3}} \tag{7.42c}$$

Which then reduces (7.41) to dimensionless form as,

$$\frac{\partial \Theta^*}{\partial \tau} = \frac{\partial}{\partial x^*}\left[\left(\frac{\partial \Theta^*}{\partial x^*}\right)^{1/3}\right] \tag{7.43}$$

By analogy to (7.37) one can interpret the quantity $D_{HeII} = 1/f^{1/3}\rho C(T_\lambda - T_b)^{2/3}$ like a thermal diffusivity for He II with the characteristic diffusion time being proportional to $L^{4/3}$. This is a notable difference from classical heat diffusion. In that case, doubling the characteristic length increases the thermal relaxation time by a factor of four, while in He II the increase is by a factor of $2^{4/3} = 2.52$.

7.2.2 *Analytic Solution Methods*

One solution method for the nonlinear heat transport equation (7.43) employs a technique known as similarity solutions [26–28]. This approach makes use of changes of variables which reduce the nonlinear partial differential equation (7.43) to a nonlinear ordinary differential equation that is inherently easier to solve. Then making the approximation that the heat conductivity function and specific heat are constant over the range of interest (7.43) can be integrated to obtain the solution. Note that the constant properties assumption is only a good approximation for $\Theta^* << 1$.

The similarity solution method uses what are termed stretching transformations which leave the partial differential equation unchanged. The solution of (7.43) is then determined by choice of boundary conditions. We considered here two problems of interest. The first problem concerns the application of a constant heat flux q at $x = 0$, which is referred to as the clamped flux problem. It leads to boundary conditions of the form

$$\left.\frac{\partial \Theta^*}{\partial x^*}\right|_{x=0} = -\frac{q^3 f L}{T_\lambda - T_b} \quad \text{for all } t \tag{7.44a}$$

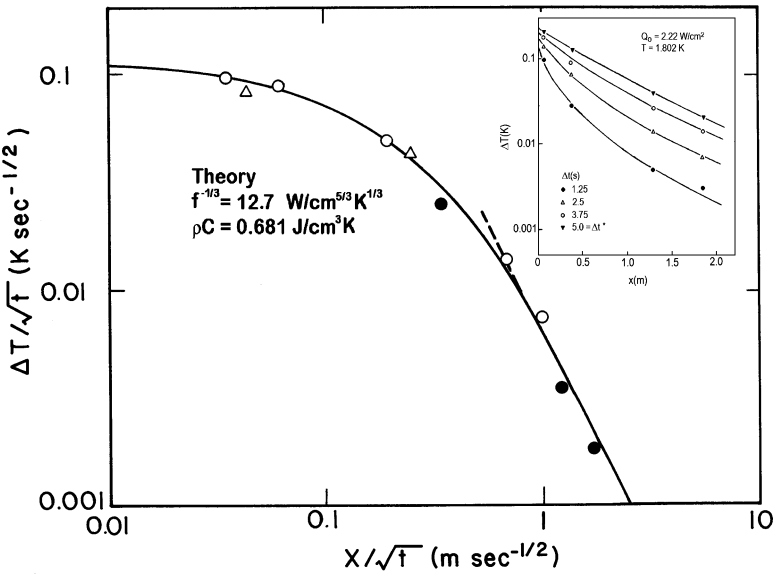

Fig. 7.19 Calculated normalized temperature profile for clamped flux in He II at $T_b = 1.8$ K and $q = 22$ kW/m^2 model by Dresner [26] compared to experimental data (inset) [29]

and

$$\Theta^*(x, 0) = 0 \tag{7.44b}$$

$$\Theta^*(\infty, \tau) = 0 \tag{7.44c}$$

The first of these conditions originates from the requirement that the heat flux q obey the nonlinear heat conductivity equation at $x = 0$.

It can be shown that the general solution for the temperature distribution should take a functional form [26],

$$\Theta/\tau^{1/2} = y(x/\tau^{1/2}) \tag{7.45}$$

Therefore, a plot of experimental data in this form should provide a universal curve representing the function y. Displayed in Fig. 7.19 are interpolated results from the long one-dimensional channel described earlier. The data do in fact follow a universal curve. In addition, the magnitude of the general solution can be determined to have a simple form when evaluated at $x = 0$, that is

$$\left.\frac{\Delta T}{t^{1/2}}\right|_{x=0} = a^2 q^2 \left(\frac{f}{\rho C}\right)^{1/2} \tag{7.46}$$

where a is a proportionality constant of order unity. At large values of x, the result approaches an asymptotic dependence such that

$$\left.\frac{\Delta T}{t^{1/2}}\right| = \left(\frac{4\sqrt{3}}{9}\right)\left(\frac{1}{\rho C}\right)^{3/2}\left(\frac{1}{f}\right)^{1/2}\frac{t}{x^2} \tag{7.47}$$

This expression is exemplified by the linear region on a log-log plot for large $x/\tau^{1/2}$.

The above analysis is also able to predict the critical energy flux ΔE^* beyond which the heat transfer enters film boiling. For the clamped flux problem, this quantity has been measured experimentally by detecting the time to film boiling, Δt^*, for a given heat flux. A relationship that fits the experimental data has the simple form

$$\Delta t^* = \kappa q^{-4} \tag{7.48}$$

where κ is a temperature-dependent function [29]. The same relationship also follows from the above theoretical analysis, and κ is predicted to take the form

$$\kappa = \frac{\rho c(T_\lambda - T_b)^2}{f a^4} \tag{7.49}$$

where a is the same numerical coefficient as given in (7.46). By inserting average values for the heat conductivity function and the volumetric specific heat into (7.49), the predicted coefficient κ agrees with experiment to within about 20%.

The other problem of interest in one-dimensional transient heat transfer is the determination of the temperature profile resulting from a given energy deposition. This pulsed-source problem, which can also be solved by the similarity solution method, must obey the boundary conditions

$$\int_{-\infty}^{\infty} \rho C(T - T_b)dx = \Delta E \quad \text{for all time} \tag{7.50a}$$

$$\Theta(x, 0) = 0 \tag{7.50b}$$

$$\Theta(\infty, \tau) = 0 \tag{7.50c}$$

where $\Delta E = q\Delta t$ is the total thermal energy applied per unit channel area. Again using the similarity solution method, it can be shown that the pulsed-source problem has a general solution of the form [27],

$$\Theta\tau^{3/2} = y'(x/\tau^{3/2}) \tag{7.51}$$

where y' is another undetermined function. As in the clamped flux problem, (7.51) is a powerful result because it indicates the form in which to plot data. Plotted in terms of these variables, the experimental data should follow a universal curve.

By substitution of (7.51) into (7.43), a solution to the temperature distribution can be obtained with the simplifying assumption of constant properties. The resulting equation takes the form

$$\Delta T\ t^{3/2} = \frac{4}{3\sqrt{3}} \Delta E \left(\frac{f}{\rho C}\right)^{1/2} \left(\frac{1}{Z^4 + b^4}\right)^{1/2} \tag{7.52a}$$

where

$$Z = x\Delta E(\rho C f)^{1/2} t^{-3/2} \tag{7.52b}$$

and

$$b = \frac{2\left[\Gamma\left(\frac{1}{4}\right)\right]^2}{3\sqrt{3}\pi} = 2.855 \tag{7.52c}$$

That this solution fits the original heat conductivity equation can be verified by the reader.

Experimental verification of the above analysis is displayed in Fig. 7.20. The inset shows the time variation of the temperature distribution after a discrete energy pulse is applied. These data, plotted in the form suggested by the similarity solution, map out the universal curve given by (7.52a). The universal curve plotted in the figure has as its necessary input average values for the heat conductivity function and heat capacity, but when ΔT is small, these properties do not vary substantially over the range of interest. The agreement between experiment and theory is entirely adequate for engineering applications.

7.2.3 *Numerical Solution of the He II Diffusion Equation*

The above analytical treatment is useful for providing a physical description of the problem as well as developing scaling relationships to correlate data. However, a complete solution including the temperature dependence of the physical parameters is only possible by numerical methods. The usual approach is to apply finite difference methods. Here the exact differentials in T, x, and t are replaced by finite differences with an appropriate choice of mesh size. These in turn lead to a set of simultaneous equations for the temperature at the nodes in the mesh. Solutions of this type have been carried out for two different boundary conditions [30]. In both cases the clamped heat flux condition at $x = 0$ is assumed. However, different

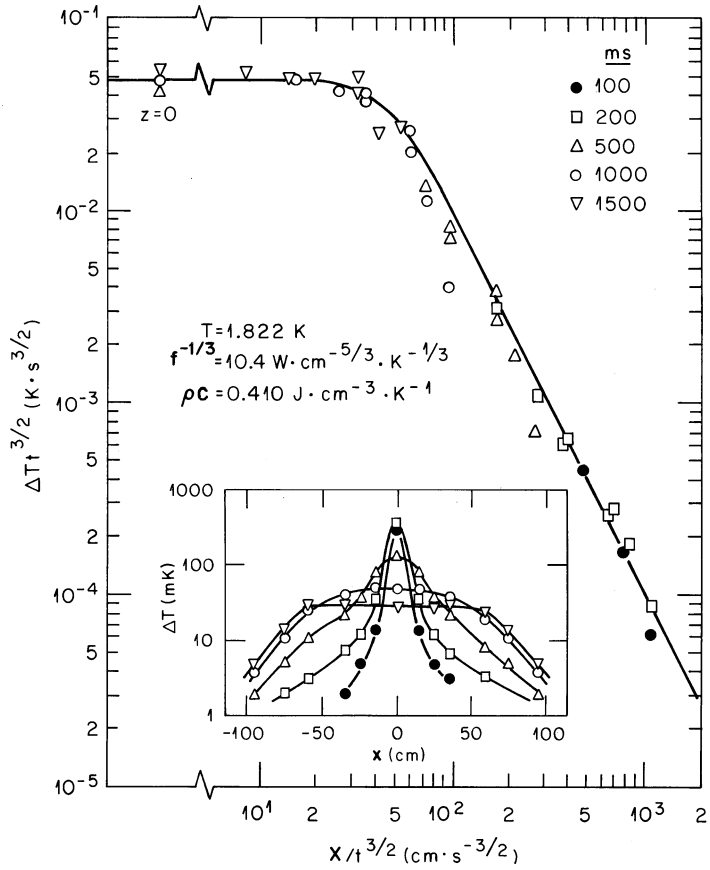

Fig. 7.20 Normalized temperature distribution for the helium channel subjected to a pulsed heat source (From Dresner [27])

boundary conditions are applied at $x = L$ where the channel contacts the reservoir. These conditions have two forms,

$$\left.\frac{d\Theta}{dx}\right|_{x=L} = 0 \quad \text{adiabatic end} \tag{7.53a}$$

and

$$\Theta|_{x=L} = 0 \quad \text{isothermal end} \tag{7.53b}$$

Particularly for the first case, it is useful to scale the data in terms of a ratio of energies ($\Delta E^*/\Delta E_0$), where these quantities are defined individually as

$$\Delta E^* = q\ \Delta t^* \tag{7.54}$$

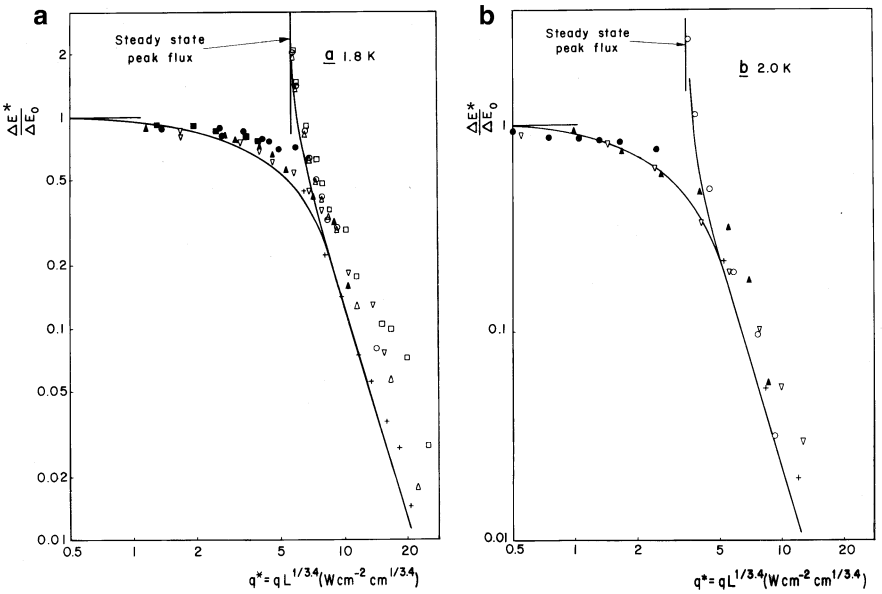

Fig. 7.21 Maximum energy flux for a step-function heat pulse. Steady-state peak heat flux represents the open-channel solution. $\Delta E^*/\Delta E_0 \leq 1$ is the closed-channel solution: (**a**) 1.8 K and (**b**) 2.0 K (as compiled by Seyfert et al. [30])

and

$$\Delta E_0 = L\int_{T_b}^{T_\lambda} \rho C_p \, dT \tag{7.55}$$

Therefore, (7.55) represents the energy applied through the heat transfer surface which is necessary to reach film boiling at Δt^*. The other energy, ΔE_0, represents the total enthalpy available within the constant cross section channel of length L. Obviously, for the adiabatic end condition, the ratio $\Delta E^*/\Delta E_0 \leq 1$. For short, high-energy heat pulses such that the heat diffusion length is much shorter than the total channel length L, the solution is independent of choice of boundary condition established at $x = L$.

Plotted in Fig. 7.21 are the numerical solutions to the one-dimensional heat transfer problem for two different bath temperatures, 1.8 and 2.0 K. In either case the ratio of energy is plotted versus the scaling parameter $qL^{1/m}$, where in this case $m = 3.4$ by selection of the authors [30]. The data give comparable agreement for $m = 3$. Note that for values of $qL^{1/.34}$ in excess of 10 at 1.8 K and 5 at 2.0 K, there is no significant difference between the two boundary conditions at $x = L$. The steady-state limit corresponds to the results presented in Sect. 7.1.2.

In conclusion, a general comment is in order concerning transient heat transfer in He II. As noted above the time constant to establish the steady state can be quite

large, particularly in long one-dimensional system. Although this fact may be surprising considering the extremely high effective thermal conductivity of He II, it is due to the large heat capacity of He II resulting in a finite thermal diffusivity. Therefore, care should be exercised when applying steady-state heat transfer models. It is best first to estimate the thermal diffusion time to determine whether the system is actually in the steady state. For transient problems, the heat diffusion model is generally suitable. Unfortunately, it is not known whether there are limits of this model, and extrapolation beyond the regions where experimental data exist should be avoided.

7.3 Forced Convection Heat Transport in Wide Channels

We now extend the topic of turbulent He II heat transport to include the effect of forced convection or net flow velocity. This subject is a somewhat more general heat transport problem than has been considered so far because it includes an additional variable, the net flow velocity, v. Forced convection was introduced in Chap. 6 as part of the two-fluid model applied to He II heat transport.

A general configuration for a forced flow heat transfer problem is shown in Fig. 7.22. A channel of constant cross section and length L connects two reservoirs at temperatures T_1 and T_2. A steady state or transient heat q flux is applied in this case at one end of the channel and the temperature gradient within the fluid is established. Breakdown of heat transfer occurs at a peak heat flux, q^*, which depends on a number of factors including the fluid velocity. In fact, this configuration is not easily obtainable because a temperature difference normally corresponds to a pressure difference under saturation conditions. However at least in principle, it is possible to create the appropriate conditions with a frictionless piston that forces the liquid from volume 1 to volume 2 at velocity v. Alternatively, one could establish these conditions by forcing He II to flow through a channel of length $2L$ with both ends in thermal contact with a reservoir at temperature T_2.

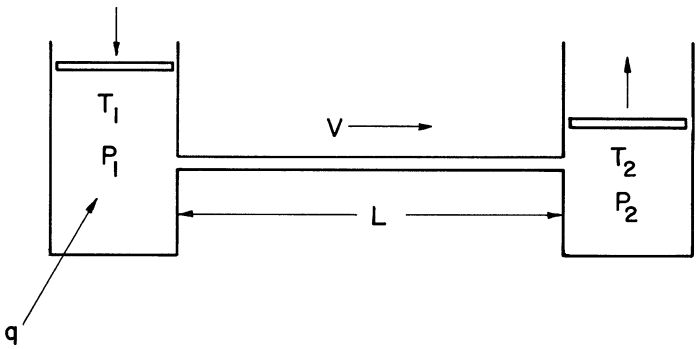

Fig. 7.22 Schematic representation of configuration required to obtain forced flow He II

7.3.1 He II Energy Equation

We begin by developing the heat balance equation that describes the forced flow He II system [31]. In developing this equation, two fundamental assumptions are made about the physical behavior of He II**.** These assumptions are not proved here but are justified by the analysis of experimental data.

The first assumption is that the heat flow by internal convection mechanisms is not affected by the net velocity of the fluid. This point has been discussed as part of the two-fluid model in Chap. 6. As an aside, it is possible to understand physically the invariance to velocity by analogy to an ordinary heat conduction mechanism. In the latter case, heat transported by conduction in a moving medium is no different from that of the medium at rest provided $v \ll c$, the speed of sound. Furthermore, by making the normal set of simplifications to reduce the problem to one-dimensional heat flow in turbulent He II**,** the nonlinear heat conductivity equation can be used to describe the heat conducted by internal convection,

$$q_{ic} = -\left(f(T,p)^{-1}\frac{dT}{dx}\right)^{1/3} \tag{7.56}$$

where $f^{-1}(T,p)$ is the same temperature-dependent heat conductivity function. The power law dependence of (7.56) has been assumed to be 1/3 although the analysis follows essentially the same procedure if a different coefficient is assumed.

The second assumption is that the heat carried by ordinary convection mechanisms can be described by the flow of enthalpy between two points in the system,

$$q_{fc} = \rho \mathbf{v}\ \Delta h \tag{7.57}$$

where $dh = h_1 - h_2$ represents the specific enthalpy difference between temperatures T_1 and T_2. For simplicity (7.57) assumes the fluid density to be constant, which is a reasonably good approximation for He II.

The above two assumptions lead to an equation that is appropriate for analyzing the temperature profile in forced flow He II. This is achieved by combining differential forms of (7.56) and (7.57) and equating them to the time rate of change of the local enthalpy. The resultant equation is similar to the time-dependent heat equation for static He II except that it contains the extra convection term. In one dimension this expression takes the form,

$$\rho\frac{\partial h}{\partial t} - \frac{\partial}{\partial x}\left[\left(\frac{1}{f}\frac{\partial T}{\partial x}\right)^{1/3}\right] + \rho\mathbf{v}\frac{\partial h}{\partial x} = q_0 \tag{7.58}$$

where the temperature and pressure dependence of the heat conductivity function is implied. This equation is sometimes referred to as the He II energy equation.

Given the boundary conditions for a channel containing He II, it is a straightforward problem to integrate (7.58) and thus determine the temperature profile as a function of flow velocity and time. Unfortunately, a general solution to (7.58) requires numerical methods because the equation is nonlinear and the functions such as h and f have rather strong temperature dependencies.

7.3.2 Steady State Heat Transport: Analytic Solution

A good approximate solution to the steady-state problem, $\partial h/\partial t = 0$, can be obtained by assuming constant properties, f and C_p, and neglecting pressure drop effects such that $dh = C_p\, dT$. This approximation leads to an exactly soluble one dimensional differential equation. Making the following change of variables,

$$\Theta^* = \frac{T - T_2}{T_1 - T_2} \tag{7.59a}$$

$$x^* = \frac{x}{L} \tag{7.59b}$$

and defining the dimensionless variable,

$$K_v = \rho C_p \mathbf{v} (fL)^{1/3} (T_1 - T_2)^{2/3} \tag{7.59c}$$

an exactly soluble form of the Bernoulli equation results,

$$-\frac{d}{dx^*}\left[\left(\frac{d\Theta^*}{dx^*}\right)^{1/3}\right] + K_v \frac{d\Theta^*}{dx^*} = 0 \tag{7.60}$$

where $q_0 = 0$ has been assumed. Equation (7.60) coupled with the appropriate boundary conditions can determine the steady-state temperature profile in a one-dimensional channel.

Before proceeding to the solution, the physical interpretation of the dimensionless number K_v deserves some comment. As it represents the ratio of the heat carried by forced convection, $\rho C_p v \Delta T$, to that carried by counterflow, $(f^1 \Delta T/L)^{1/3}$, K_v is analogous to the classical Peclet number, $Pe = \rho C_p v L/k$, that is the ratio of forced convection to thermal conduction in classical liquids. Therefore, $K_v \sim 1$ marks the boundary between thermal counterflow dominated heat transfer and forced convection dominated heat transfer in He II.

The results of integrating (7.60) for a channel of length $2L$ with its center at T_1 and ends fixed at T_2 are displayed in Fig. 7.23. The left-hand side of the figure can be interpreted as the case where the velocity of flow is in the opposite direction to the heat flow by counterflow while the right-hand side refers to these quantities working in parallel. Note that the limitations of to the accuracy of this solution are

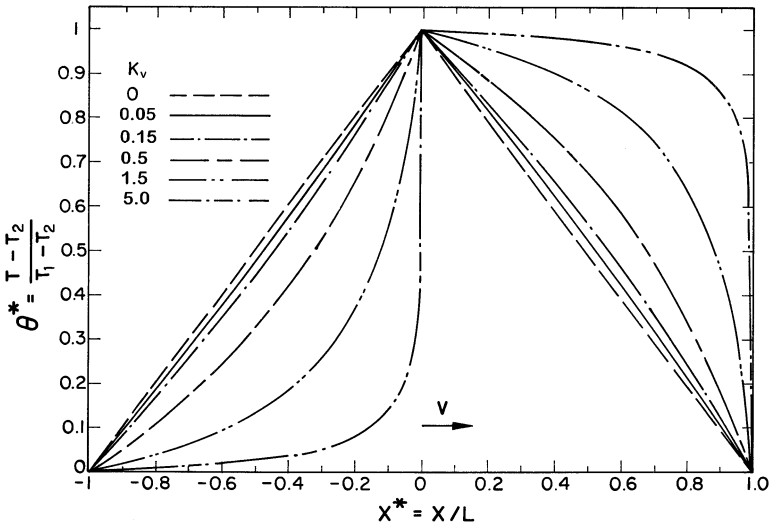

Fig. 7.23 Normalized temperature distribution in forced flow He II with fixed temperature boundary conditions $K_v = \rho C_p \mathbf{v}(fL)^{1/3}(T_1 - T_2)^{2/3}$

primarily in terms of the temperature dependence of the heat capacity C_p and heat conductivity function $f^{-1}(T,p)$. The solution should be quite good for small $\Delta T = T_1 - T_2$ such that $\Delta T/T \ll 1$. The impact of this approximation is seen in the zero velocity profile ($K_v = 0$) which is linear, while in fact for large ΔT the profile has considerable curvature. Also note that the nonzero velocity profiles for positive and negative K_v are symmetric about the line corresponding to $K_v = 0$.

There have been several reports of measured temperature profiles within forced flow He II which have been compared to numerical analyses based on the theory described above [32–34]. In general, these measurements have shown temperature profiles analogous to those displayed in Fig. 7.23. In those cases, (7.60) was solved numerically and compared to experimental data with good agreement.

Given the solution to the temperature profile it is straightforward to determine the total heat transport, $q = q_{fc} + q_{ic}$, by integration of (7.60). This result can be normalized to the form

$$\frac{q}{q_0} = -\left(\frac{d\Theta^*}{dx^*}\right)^{1/3} + K_v\Theta^* \tag{7.61}$$

where K_v is defined above and

$$q_0 \equiv \left(\frac{T_1 - T_2}{fL}\right)^{1/3} \tag{7.62}$$

which represents the heat carried by the internal convection mechanisms for He II having zero velocity ($K_v = 0$). The results of this calculation are shown by the solid

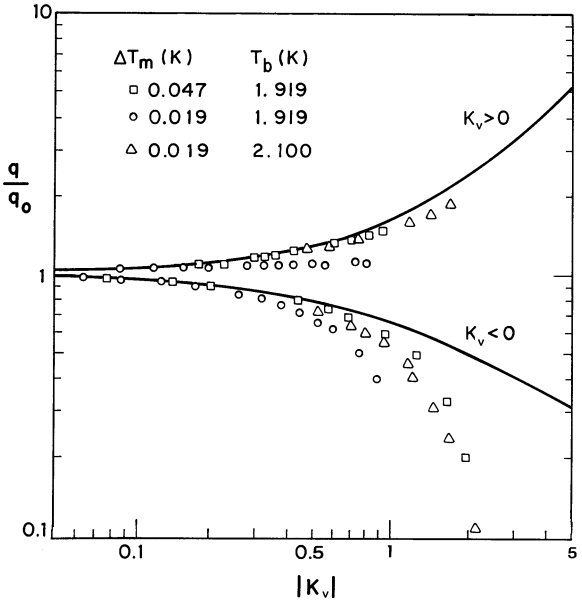

Fig. 7.24 Normalized peak heat flux for forced flow He II with $K_v = \rho C_p \mathbf{v}(fL)^{1/3} (T_1 - T_2)^{2/3}$ (Data from Jones and Johnson [34])

curves in Fig. 7.24. The data points are from an experiment by Johnson and Jones [34]. Although there is considerable enhancement of heat transport in the direction of flow even for small K_v, values of K_v greater than unity are required before the total heat transport is enhanced significantly in a midpoint heated channel of length $2L$. This result occurs because forced flow suppresses the total heat transport when the velocity and heat flux are anti-parallel.

7.3.3 Pressure Drop in Turbulent He II

The above solution to the steady state He II energy equation neglected any effect due to the pressure drop along the channel thus allowing the simplification, $dh = C_p\, dT$. However, in forced flow He II, there can be a significant pressure drop associated with flow. The pressure drop in fully turbulent He II has been measured for a variety of channel geometries with the most notable feature of these measurements being the similarity of friction factor to that for classical fluids. In other words, the pressure drop may be correlated with the expression,

$$\Delta p = 2 f_F \rho v^2 \left(\frac{L}{D}\right) \tag{7.63}$$

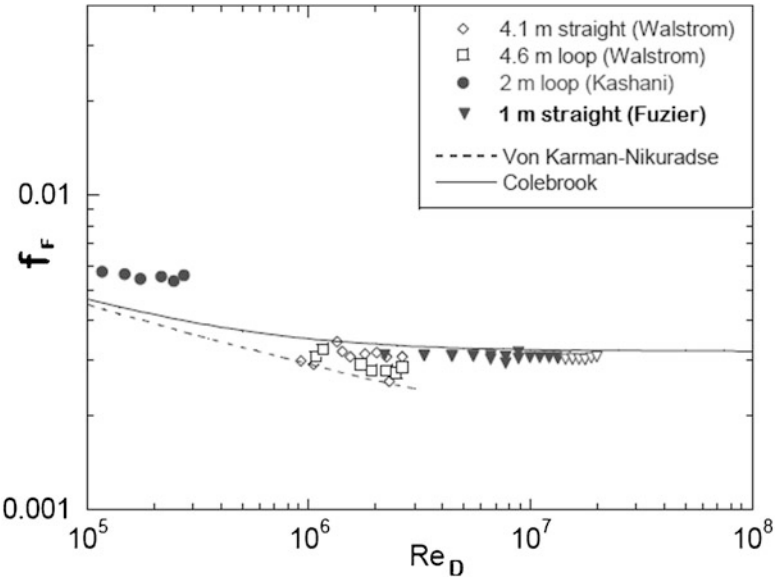

Fig. 7.25 Friction factor for He II forced flow compared to classical correlations (Fuzier [35])

where the Fanning friction factor, f_F, is similar to that observed for classical fluids. For example, for a smooth tube, the friction factors for He II in the Reynolds number regime $\mathrm{Re}_D > 2 \times 10^4$ appear to be fairly well described by the von Karman-Nikuradse correlation,

$$\frac{1}{f_F^{\frac{1}{2}}} = -1.737 \ln\left(\frac{1.25}{\mathrm{Re}_D f_F^{\frac{1}{2}}}\right) \tag{7.64}$$

where the Reynolds number is defined by $\mathrm{Re}_D = \rho v D/\mu_n$. At high Reynolds number, the tube surface roughness begins to play a role in the observed friction factor tending to an almost constant value. In this regime, the Colebrook correlation is preferred,

$$\frac{1}{f_F^{\frac{1}{2}}} = -1.737 \ln\left(\frac{k}{3.7D} + \frac{1.25}{\mathrm{Re}_D f_F^{\frac{1}{2}}}\right) \tag{7.65}$$

Note that both these correlations were discussed in Chap. 4 in the context of pressure drop in classical helium flow. For non circular cross section channels, present evidence suggests that the friction factor may also be correlated by classical correlations based on the Reynolds number.

Figure 7.25 shows measurements of the turbulent friction factor for He II compared to the classical correlations above [35]. Similar results have been obtained for other geometries [36–39]. One can easily see that the agreement is reasonable.

This result can be understood in terms of the two fluid model. In relatively high Reynolds number flows, both fluid components can be assumed to be fully turbulent with the superfluid component containing a very high vortex line density that interacts with the normal fluid component. In this case, the two fluids are strongly coupled together in motion. On the other hand in the viscous boundary layer, the normal fluid velocity profile is what controls the wall friction. Thus, the friction factor should scale with the classical Reynolds number with the relevant density and velocity being that of the total fluid while the viscosity scale is that of the normal fluid component, μ_n.

The above development for the most part assumes that the helium flow is fully developed and turbulent. This allows both the use of the turbulent pressure drop correlations and the turbulent heat transport relation. More complex phenomena can occur particularly in flow systems consisting of narrow channels in laminar flow, which can lead to fountain effect driven flows. We return to this topic in a later section.

7.3.4 He II Joule Thomson Effect

Walstrom considered the problem of steady state forced flow He II with pressure drop [40]. In this case, the enthalpy gradient must include the pressure terms,

$$\frac{\partial h}{\partial x} = \left(\frac{\partial h}{\partial T}\right)_p \left[\frac{\partial T}{\partial x} - \left(\frac{\partial T}{\partial p}\right)_h \left(\frac{\partial p}{\partial x}\right)\right] = C_p \left(\frac{\partial T}{\partial x} - \mu_j \frac{\partial p}{\partial x}\right) \tag{7.66}$$

where $\mu_j = \frac{\beta T - 1}{\rho C_p}$ is the Joule Thomson coefficient with β being the bulk expansivity. For He II, β is relatively small and negative ($\beta \sim -0.01$ K^{-1}) so that μ_j is negative and dominated by the incompressible term. In addition, since the pressure gradient may be large in this case, it is no longer possible to neglect that contribution to the He II two fluid equations (6.98) and (6.99). If one further makes the assumption that the pressure gradient can be replaced by $\Delta p/L$ and replace μ_j by $-1/\rho C_p$, then the full energy equation results,

$$\rho C_p \frac{\partial T}{\partial t} - \frac{\partial}{\partial x}\left[\frac{1}{f}\left(\frac{1}{\rho s}\frac{\Delta p}{L} + \frac{\partial T}{\partial x}\right)\right]^{\frac{1}{3}} + \rho v C_p \frac{\partial T}{\partial x} - v\frac{\Delta p}{L} = q_0 \tag{7.67}$$

The full solution to this equation requires numerical methods.

Before discussing the solution to (7.67), it is instructive to gauge the relative importance of the pressure and temperature gradient terms. Obviously, if the pressure drop is small, then (7.67) reduces to (7.58). On the other hand, if the pressure drop approaches $\Delta p \sim \rho C_p \Delta T$, then its impact must be considered. A typical value for $\rho C_p \sim 1$ MJ/m^3 K and $\Delta T \sim 0.1$ K. Therefore, as long as $\Delta p << 100$ kPa (1 atm)

the impact on the temperature profile will be small. For high velocity flows or very long channels, this condition is not met and one must use the full energy equation.

In steady state He II flow, the above expression predicts a monatonically increasing temperature profile along the channel. Walstrom solved the steady state problem analytically by making the following substitutions,

$$T_0 = \frac{1}{\rho C_p}\left(\frac{q_0 L}{v} + \Delta p\right) \tag{7.68a}$$

$$x^* = \frac{x}{L} \tag{7.68b}$$

$$\tau = \frac{T}{T_0} \tag{7.68c}$$

$$\beta = fL\left(\rho v C_p\right)^3 T_0^2 \tag{7.68d}$$

and

$$c = \frac{C_p/s}{(1 + q_0 L/v\Delta p)} \tag{7.68e}$$

Note that according to the empirical fit to the heat capacity of He II (6.29b), the numerator in (7.68e) can be approximated by a constant, $C_p/s \approx 5.6$.

Consider the case where $q_0 = 0$, such that the resulting temperature gradient is entirely due to friction. In classical non-conductive fluids, this condition results in a continuous temperature increase with the slope of the temperature profile is directly proportional to the Joule-Thomson coefficient, μ_j. Figure 7.26 shows the calculated temperature profile for fixed temperature boundary conditions.

7.3.5 *Transient Heat Transport in Forced Flow He II: Numerical Solution*

There have been a number of efforts at modeling transient heat transport in forced flow He II [41–44]. In the present context, there is insufficient space to discuss the methods in detail and the reader is encouraged to consult the original references for more information. Here we summarize the methods used by Fuzier to model this problem [44].

The principal challenge to the numerical solution of (7.67) is the non-linear nature of the partial differential equation. In particular, the fractional power to the

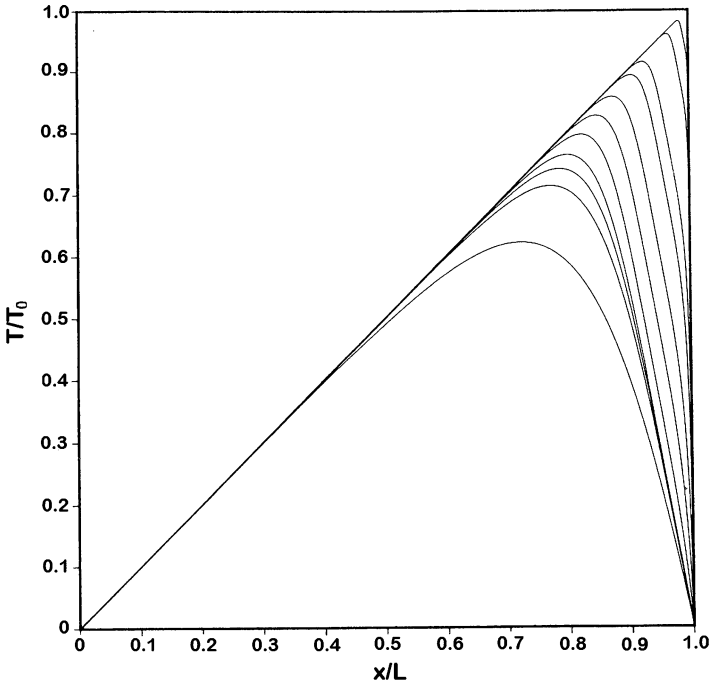

Fig. 7.26 Dimensionless temperature profile due to the Joule Thomson effect in He II forced flow with constant temperature boundary conditions. In this case, $q_0 = 0$ and $T_0 = \Delta p/\rho C_p$ (From Walstrom [40])

heat conductivity function must be handled with care to avoid numerical instabilities. Fuzier used a semi-implicit finite difference scheme to discretize the energy equation:

$$\rho C_i^n \frac{T_i^{n+1} - T_i^n}{\Delta t} - \frac{1}{\Delta x}\left[\frac{1}{f_{i+1/2}^n{}^{\frac{1}{3}} \left| \frac{\Delta P}{\rho s_{i+1/2}^n L} + \frac{T_{i+1}^n - T_i^n}{\Delta x} \right|^{\frac{2}{3}}} \left(\frac{\Delta P}{\rho s_{i+1/2}^n L} + \frac{T_{i+1}^{n+1} - T_i^{n+1}}{\Delta x} \right) \right.$$
$$\left. - \frac{1}{f_{i-1/2}^n{}^{\frac{1}{3}} \left| \frac{\Delta P}{\rho s_{i-1/2}^n L} + \frac{T_i^n - T_{i-1}^n}{\Delta x} \right|^{\frac{2}{3}}} \left(\frac{\Delta P}{\rho s_{i-1/2}^n L} + \frac{T_i^{n+1} - T_{i-1}^{n+1}}{\Delta x} \right) \right]$$
$$+ \rho v C_i^n \frac{T_{i+1}^{n+1} - T_{i-1}^{n+1}}{2\Delta x} = Q_0 + v\frac{\Delta P}{L} \tag{7.69}$$

where X_i^n represents the value of X at the node i after n time intervals. This scheme is first order accurate in time and second order accurate in space. This model was used to compare to transient heat transfer measurements on a 0.86 m long, 10 mm ID channel at fluid velocities up to 20 m/s. A uniform grid consisting of 8,000 nodal

points was used to represent the length of the test section. Time steps of order 10 μs were typically used for the solution. The initial condition before the generation of the pulse corresponds to the steady-state, linearly increasing temperature profile in the test section due to the Joule-Thomson effect.

A heat pulse that is deposited locally in a channel containing forced flow He II will produce a temperature rise that propagates along the channel at approximately the net flow velocity, v. As the thermal pulse moves along the channel, it will experience an overall increase in its background temperature due to the Joule Thomson effect. For example, at a velocity of 10 m/s and T = 1.7 K, forced flow He II increases its temperature at about 30 mK/m of channel length. In addition, the pulse temperature profile will broaden due to diffusion in the He II. The time scale for this process is similar to that discussed in Sect. 7.2, but is not generally dependent on the fluid velocity.

As an example, Fig. 7.27 displays two cases of transient heat transfer experimental results compared to the numerical model. Both are for the same base temperature, $T_b = 1.7$ K and the same heat pulse, 99 kW/m^2 for 20 ms. The only difference is the fluid velocity which is 2 m/s in Fig. 7.26a and 16 m/s in Fig. 7.26b. It is quite apparent that the He II energy equation does a good job of modeling the shape and propagation of the heat pulse. One should note that this level of agreement is not always achieved. In particular, at intermediate velocities (4 m/s $< v <$ 14 m/s), the model deviates from the experimental results. At present, this observation appears to be the result of the formulation of the solution. In the case where there is significant pressure drop, the heat flux in the He II is given by,

$$q = -\left[\frac{1}{f}\left(\frac{1}{\rho s}\frac{\Delta p}{L} + \frac{\partial T}{\partial x}\right)\right]^{\frac{1}{3}} \tag{7.70}$$

The problem occurs when the pressure drop and temperature gradient are of roughly equal magnitude and opposite sign, which can occur in regions on the trailing edge of the pulse. This is a physically unrealistic aspect of the model.

7.4 Heat and Mass Transfer in Porous Media

7.4.1 Steady Laminar Heat Transport in He II

The problem of He II heat and mass flow through porous media is significantly different from flow in wide channels. In particular, much of the porous media fluid dynamics is in the laminar regime and the transition to turbulence. Further, the geometry of porous media is not well characterized as one has with a one-dimensional channel and involves multidimensional flow. Thus, we need to consider issues of how to model the geometry of the porous media. These issues are similar to those appropriate for classical fluids in porous media, a subject introduced in Sect. 4.4.

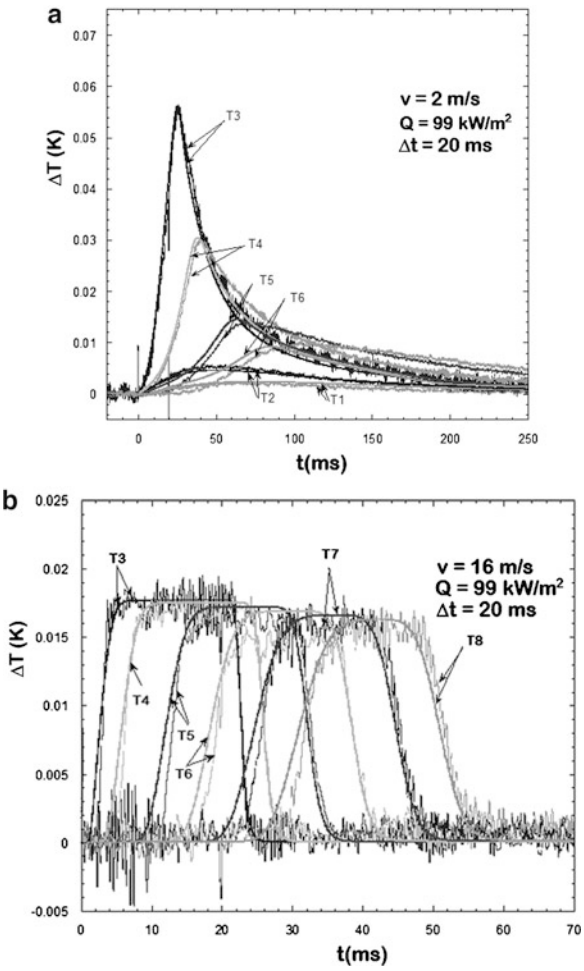

Fig. 7.27 Experimental and numerical time evolution of the temperature profile at various locations in a 0.86 m long, 10 mm ID channel. The smooth lines correspond to the numerical model. A 20 m long, rectangular heat pulse of power density 99 kW/m^2 was generated at t = 0. T_b = 1.7 K. The flow velocity: (**a**) 2 m/s, (**b**) 16 m/s [44]

As was discussed in Chap. 6, laminar flow conditions occur in He II whenever the fluid velocity is below the critical velocity. These conditions can occur even in static He II, since heat transport causes a relative velocity of the two fluid components. In He II there are two relevant critical velocities: $\mathbf{v}_{sc}$ which is associated with the onset of turbulence in the superfluid component and $\mathbf{v}_{nc}$ for the normal fluid component. $\mathbf{v}_{sc}$ depends strongly on the method by which it is measured. To remind the reader from Chap. 6, most experimental data are correlated to the empirical relationship,

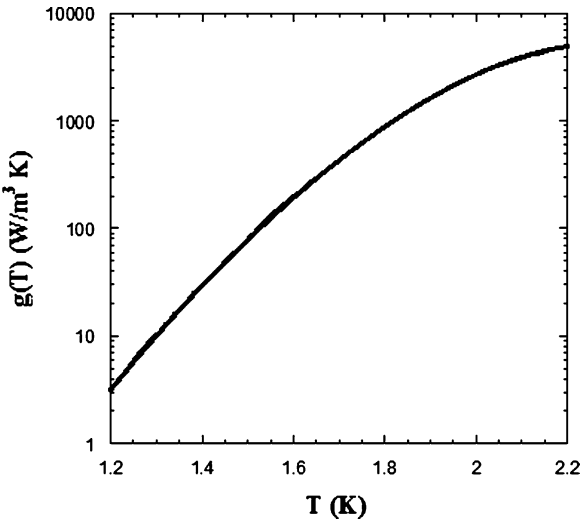

Fig. 7.28 Proportionality function in the He II laminar flow equation

$$\mathbf{v}_{sc} \simeq d^{-1/4} \quad \text{in cgs units} \tag{6.86}$$

where d is the characteristic diameter of the channel. On the other hand, the normal fluid critical velocity is interpreted in terms of classical turbulent onset such that,

$$\mathbf{v}_{nc} \approx \frac{\mu_n \mathrm{Re}_c}{\rho d} \tag{6.88}$$

where the critical Reynolds number is $Re_c \approx 1{,}200$. Note that this relationship involves the normal fluid viscosity but the total density.

Laminar heat flow in He II, which occurs for low normal fluid velocities in narrow channels, the heat conductivity equation may be written in a form similar to Fourier's law although the function of proportionality varies as the square of the diameter,

$$q = -\frac{(\rho s d)^2 T}{\beta \eta_n} \frac{dT}{dx} = -g(T) \frac{d^2}{\beta} \frac{dT}{dx} \tag{7.71}$$

where $g(T) = (\rho s)^2 T/\mu_n$. β is a numerical coefficient that depends on channel geometry; $\beta = 12$ for parallel plates and $\beta = 32$ for circular tubes. The laminar flow heat conductivity function, $g(T)$, increases strongly with temperature dominated by the dependence of $(\rho s)^2 T \sim T^{12}$. Figure 7.28 displays $g(T)$ between 1.2 K and T_λ. Appendix A.3 gives numerical values for this coefficient at saturated vapor pressure.

In the laminar flow regime, due to the isentropic nature of the system, the pressure drop due to flow is related to the temperature gradient through London's Equation,

$$\frac{dp}{dx} = \rho s \frac{dT}{dx} \tag{7.72}$$

The Fountain Effect, a unique feature of He II, can be understood in terms of this expression. Specifically, in ideal superflow, a temperature gradient induces a pressure gradient, which in practice can lead to net mass flow of the fluid.

In the laminar flow regime, the heat flow induced pressure gradient is related to the temperature gradient through London's equation. The result is given by,

$$q = -\frac{\rho s d^2 T}{\beta \mu_n} \frac{dp}{dx} = -g(T) \frac{d^2}{\rho s \beta} \frac{dp}{dx} \tag{7.73}$$

where β is the same geometrical factor as in (7.71). This relationship can be easily integrated over finite lengths and temperature difference to give practical results.

7.4.2 He II Heat and Mass Transfer Through Porous Media

In porous media, the geometry is not as well defined and the characteristic dimension, d, is more difficult to know. In laminar (Darcy) flow, the pressure gradient is related to the permeability K_D of the medium,

$$\frac{dp}{dx} = -\frac{\mu}{K_D} U \tag{7.74}$$

where U is the average approach velocity. K_D is proportional to the square of the pore diameter times the porosity, α. For a typical pore diameter $d_p = 1$ μm and porosity of 10%, that means the $K_D \sim 10^{-13}$ m^2. By analogy in the case of He II flow through porous media, one can write the laminar flow equation as,

$$\frac{dp}{dx} = -\omega \frac{\mu_n}{K_{Dn}} U_n \tag{7.75}$$

where U_n is the normal fluid velocity averaged over the sample cross section. This equation also contains the tortuosity factor, ω, to account for the increase in effective path length compared to the overall thickness of the sample. By definition, $U_n = \alpha v_n$, where v_n is the normal fluid velocity in the pores. In pure counterflow, $q = \rho s T v_n$, so one can substitute for the normal fluid velocity,

$$\frac{dp}{dx} = -\omega \frac{\mu_n}{K_{Dn}} \left(\frac{\bar{q}}{\rho s T} \right) \tag{7.76}$$

where as written $\bar{q}$ is the heat flux averaged over the sample area, $\bar{q} = \alpha q$.

In the laminar regime, He II obeys London's equation (7.72), so the temperature gradient may simply be written,

$$\frac{dT}{dx} = -\omega \frac{\mu_n}{K_{Dn}} \left(\frac{\bar{q}}{(\rho s)^2 T} \right) \tag{7.77}$$

which can be rearranged to,

$$\bar{q} = -g(T) \frac{K_{Dn}}{\omega} \frac{dT}{dx} = -\frac{g(T)}{\rho s} \frac{K_{Dn}}{\omega} \frac{dp}{dx} \tag{7.78}$$

where K_{Dn} is the permeability for the normal fluid and $g(T)$ is the temperature dependent function in Fig. 7.27.

Equation (7.78) can be used to measure the permeability of a porous medium by recording either the pressure or temperature difference across a sample subjected to a heat flux [45, 46]. Note that the the value of K_{Dn}/ω may be different from the permeability measured by other methods due to the unique properties of He II. Baudouy et al. [47] even found K_{Dn} to be temperature dependent.

Above the critical velocity, the flow through the porous media is no longer ideal and mutual friction begins to contribute to the temperature gradient. In that case, the temperature gradient through the material should be described by a modified version of (7.1),

$$\frac{dT}{dx} = -f(T,p)q^3$$

which becomes,

$$\frac{dT}{dx} = -\omega f(T,p) \left(\frac{\bar{q}}{\alpha} \right)^3 \tag{7.79}$$

where x is the dimension measured through the sample.

Equations (7.77) and (7.79) probably oversimplify the difficulty in calculating the temperature gradient in He II counterflow through porous media. The quantities, K_{Dn}, α and ω are at best approximately known and depend on the method of measurement. In the turbulent regime, the situation is even more complex due to the non-linear heat equation (7.1). In the porous medium, the channel cross section can vary significantly through out the material. Since the temperature gradient is proportional to q^3, regions that constrict the flow will have an even larger effect on the temperature difference. In fact, there is not much known about the behavior of the Gorter-Mellink equation in regions of high gradient. Thus, this is a topic worthy of continued study.

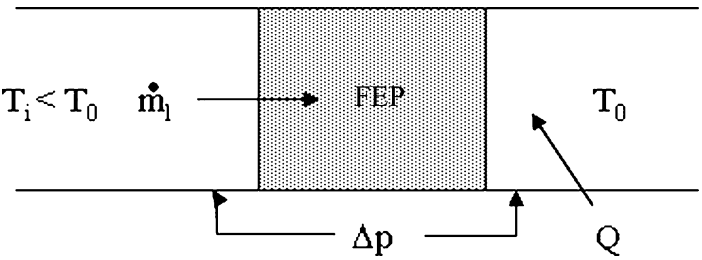

Fig. 7.29 Schematic of a Fountain effect pump

7.4.3 He II Fountain Pumps

Fountain Effect Pumps (FEPs), shown schematically in Fig. 7.29, are unique to He II. Essentially, this type of pump uses the Fountain Effect to force He II to flow through a porous plug. A heater at the outlet of the pump provides the chemical potential difference to drive the fluid flow. Such a device, which has been developed and demonstrated for space based applications, usually consists of a sintered ceramic disk or plug with a heater located on the downstream side. Typical pore size of the material is of order 0.1 μm.

An ideal fountain pump obeys the London Equation and produces a pressure head corresponding to the temperature difference produced by a heater downstream of the flow. If one integrates the London equation (7.72) along lines of constant chemical potential the corresponding static pressure head is given in Fig. 7.30. Thus, for an ideal fountain pump, the maximum pressure head is about 50 kPa for a bath at 1.8 K. Higher pump heads can be accomplished by running several pumps in series. However, the pump head decreases significantly with increasing mass flow rate.

For an ideal fountain pump, the corresponding mass flow rate is given by the relationship,

$$Q = \dot{m} S_o T_o \tag{7.80}$$

where the subscript o applies to the conditions at the pump outlet. This relationship suggests that the pump flow rate can be increased by simply adding more heat downstream, but there are limitations [49]. In a FEP, the addition of heat increases the temperature of the helium on the upstream side of the pump due to the removal of the superfluid component. This heat must be extracted by a He II refrigeration system to maintain low temperature at the pump inlet. Another important limit is the onset of turbulence above the superfluid critical velocity. To avoid this limit the design a fountain pump must have sufficient cross sectional area to ensure that the velocity within the pores does not exceed v_c, typically about 100 mm/s for porous media.

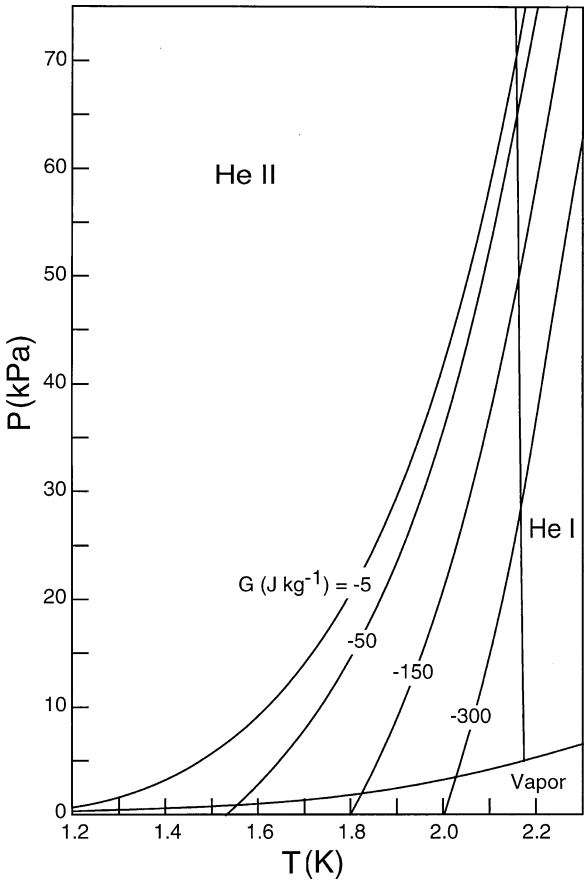

Fig. 7.30 He II phase diagram showing lines of constant chemical potential [48]

For a porosity of 30%, this velocity corresponds to an approach velocity of about 30 mm/s. Equation (7.80) can be rearranged in terms of the inlet conditions to yield,

$$\dot{m} = \frac{\dot{Q}}{(1 + C_p/s)\Delta p/\rho + s_i T_i} \tag{7.81}$$

where s_i is the entropy at the inlet to the fountain pump and Δp is the hydraulic pressure head.

Another limitation to the application of FEP is the overall low thermodynamic efficiency. For an ideal FEP, the ideal thermodynamic efficiency is given as,

$$\eta = \frac{\Delta p}{\rho q} = \frac{1}{1 + C_p/s} \cong \frac{1}{6.6} = 15\% \tag{7.82}$$

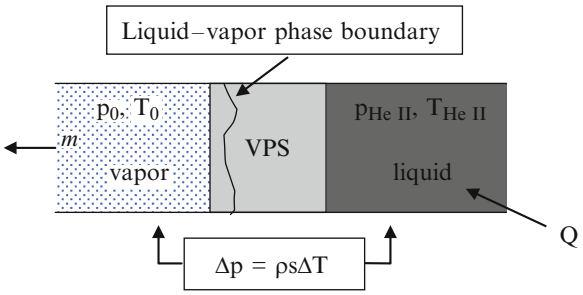

Fig. 7.31 Schematic of a vapor phase separator

However, this is an upper limit and real pumps have even lower performance. This efficiency should be compared to typical mechanical pump efficiencies which is of order 50%. Therefore, the main advantage of a fountain pump is in its ease of application. The pump consists of a heater and porous plug. There are no moving parts.

The design of practical FEPs goes beyond the above discussion. To maintain ideal flow conditions in the pump corresponding to an approach velocity below a few 10s mm/s, the pump surface area is frequently much larger than the pipe cross section in the attached flow circuit. If these conditions are exceeded, pump performance will degrade; however, the FEP will continue to pump the helium until the inlet temperature exceeds T_λ.

7.4.4 He II Vapor: Liquid Phase Separators

Another unique application for porous media is with He II- vapor phase separators (VPS) that have been developed for containment of He II in space applications. A VPS consists of a porous plug, frequently made from sintered stainless steel powder, which extracts the heat from a He II reservoir by allowing evaporation at the surface of the plug. In this application, the characteristic pore size is larger than for the FEP, because it is required to have some flow of the normal fluid component to ensure operation. A schematic of a VPS is shown in Fig. 7.31.

A He II-vapor phase separator provides a pressure difference across it given by the London equation (7.72). In use, the upstream side of the phase separator is wetted with He II while the downstream side is pumped to low pressure, lower than the saturated vapor pressure of the liquid. The phase separator works in the following way. Heat generated in the He II reservoir is carried through the porous plug by thermal counterflow to the liquid-vapor interface, which preferably occurs within the body of the plug. The heat is then removed by evaporation of the liquid at low pressure. The associated temperature difference across the plug provides the fountain pressure to hold the liquid within the He II reservoir. The total vapor mass flow is determined by this rate of heat generation, $\dot{m} = Q/h_{fg}$. To supply the vapor,

liquid must flow through the plug to the liquid-vapor interface. The heat flow in the liquid is also given by,

$$Q = \alpha A \rho s T (v_n - v) \tag{7.83}$$

where A is the plug cross section and α is the void fraction. Setting the two forms of the heat flow equal to each other and substituting $v = \dot{m}/\rho\alpha A$ one obtains an expression for the pressure drop as a function of v_n. Then assuming purely laminar flow in the phase separator, $v < v_c$, the critical velocity, the mass flow rate can then be written as,

$$\dot{m} = \frac{\rho K_{Dn}}{\beta \eta_n} \left(\frac{sT}{sT + h_{fg}} \right) \frac{\Delta p}{L} \tag{7.84}$$

where K_{Dn} is defined in (7.75). This relationship appears to fit experimental data for small mass flow rates. If the velocity within the plug exceeds v_c, turbulence in the superfluid degrades the performance and the mass flow increases more slowly with Δp.

The design of a porous plug phase separator is dependent on first knowing the mass flow needed to extract the heat load to the He II reservoir. The pressure drop across the plug is determined by the desired operating temperature of that reservoir. The physical dimensions and pore size of the porous plug follow by analysis of (7.84). Most phase separators developed for space applications consist of a sintered stainless steel structure with a typical pore size is between 1 and 10 μm [50, 51].

7.5 Kapitza Conductance

A very different problem of heat transfer in He II relates to that which occurs at an interface between a solid and the liquid. This process is in contrast to heat transport in the bulk fluid, which has been the subject so far. Surface heat transfer is more controlled by the interfacial character, including the properties of the solid state, rather than that of the bulk He II. In general, there are two regimes of surface heat transfer in He II as exemplified by the two positive slope portions of the heat transfer curve; see Fig. 7.1. At low ΔT, no boiling occurs and the heat transfer is controlled by a phenomenon called Kapitza conductance. At high ΔT and for heat fluxes greater than q^*, the surface is blanketed by a film of He I or vapor or both. In this region, the heat transfer is determined primarily by the character of the vapor film. The present section concerns itself with the first problem, that of heat transfer directly from the solid surface into the liquid He II or Kapitza conductance. Section 7.6 overviews the subject of film boiling heat transfer.

Thermal boundary conductance occurring at the interface between a solid and liquid He II was first studied by Kapitza [52] in 1941 during an experiment on the flow of heat around a copper block immersed in the liquid. Within the liquid helium

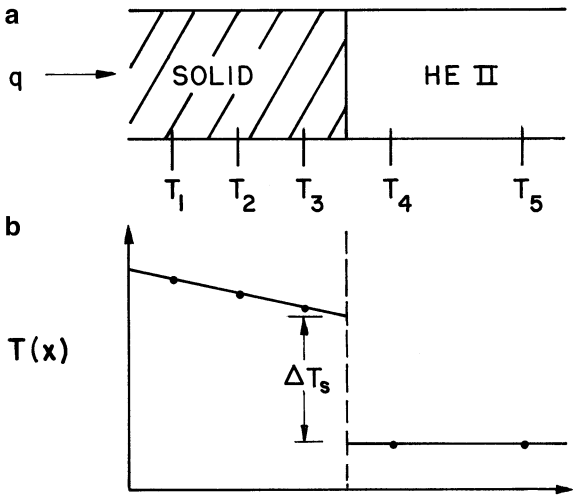

Fig. 7.32 Schematic of Kapitza conductance experiment: (**a**) temperature sensors located in the vicinity of a solid-He II interface and (**b**) temperature profile

the temperature gradients were seen to be negligible; however, a sizable temperature difference did occur between the copper block and the He II. This discovery spawned a considerable quantity of fundamental and applied research some of which is discussed in the present section. However, Kapitza conductance is also of great technical interest because it often results in the largest temperature differences in a He II heat transfer problem. For an order of magnitude comparison, a heat flux of 1 kW/m^2 can lead to a temperature difference of about 0.1 K across an interface due to this effect. Within turbulent He II the same heat flux would require about 1,000 m of one-dimensional channel to produce an equivalent temperature difference!

The general term Kapitza conductance has taken on much broader connotation over the years since its discovery. In particular, it now refers to the interfacial thermal boundary conductance which occurs between any two dissimilar materials where electronic transport does not contribute. Thus, Kapitza conductance occurs at the interface between a metal and water at room temperature. However, since the effect is strongly temperature dependent it makes a negligible contribution to the heat transfer coefficient except at low temperatures. For example, Kapitza conductance does contribute to the heat transfer process between a metal and He I at high heat flux, as is discussed in Chap. 5, but in general is neglected in classical fluid heat transfer because the thermal boundary layer dominates the process.

The measurement of Kapitza conductance is achieved by a method shown schematically in Fig. 7.32a. A solid of some finite thermal conductivity is in intimate contact with He II in a one-dimensional configuration. The temperature at various points within the solid and He II are measured as they vary with applied heat flux q. In the steady state, a temperature profile is obtained as shown schematically in Fig. 7.32b. The profile can be extrapolated to the He II-solid

interface to determine the surface temperature difference ΔT_s. By this method, the bulk properties of the two media can be eliminated from the measured temperature differences.

Kapitza conductance usually is given an empirical definition; ideally defined in the limit where q and ΔT_s are vanishingly small,

$$h_{K_0} = \lim_{\Delta T_s \to 0} \frac{q}{\Delta T_s} \tag{7.85}$$

where the 0 subscript refers to the limit as $\Delta T_s \to 0$. This quantity has a fairly strong temperature dependence going as T^n with n varying anywhere between 2 and 4. A more general definition of Kapitza conductance simply relates it to finite values of q and ΔT_s:

$$h_K = \frac{q}{\Delta T_s} \tag{7.86}$$

Because of its nonlinear nature, definition (7.86) is of more practical interest to engineering applications.

There are a number of applications for He II where knowledge of the Kapitza conductance is of substantial importance. In refrigeration involving He II, its value strongly impacts the proper design of components, particularly heat exchangers. Because of the strong temperature dependence, the importance of Kapitza conductance to heat transfer problems increases with decreasing temperature. In very-low-temperature dilution refrigeration the Kapitza conductance becomes the dominating heat transfer process. Knowledge of the Kapitza conductance of materials at higher temperatures, $T > 1$ K, is also important. Here the desire is to cool large devices such as superconducting magnets or space instruments. For proper design of these devices, it is necessary to have a good knowledge for the effective heat transfer coefficient.

Although Kapitza conductance is an experimentally defined quantity, there has been considerable theoretical work aimed at understanding this complex phenomenon. Therefore, before discussing the empirical behavior of h_K any further, a review of the physical theories used to explain its behavior is presented.

7.5.1 Phonon Radiation Limit

The first theory to successfully characterize the qualitative features of Kapitza conductance is referred to simply as the phonon radiation limit [53, 54]. The model is an overestimate of the true Kapitza conductance because it includes too many energy transport mechanisms. However, the theory does show the proper temperature dependence of h_K.

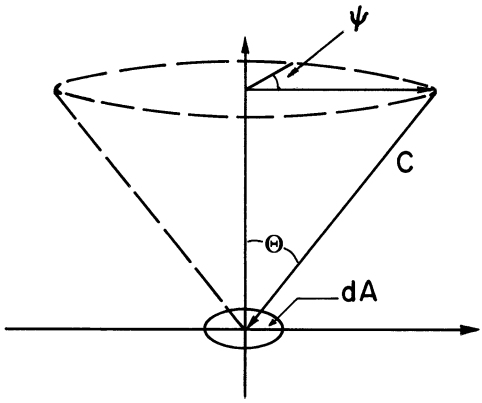

Fig. 7.33 Hemispherical region surrounding an elemental surface area for phonon heat transfer

A body above absolute zero contains thermal energy, which in the case of insulators is in the form of a phonon spectrum while for conductors it may be due partially to the electrons. Phonons are quantized lattice vibrations and are analogous to photons, which of course are quantized electromagnetic radiation. Ignoring for the moment any effect electrons may have on these concepts, it is reasonably straightforward to identify the phonon energy spectrum for a particular solid (see Chap. 2). Since the Kapitza conductance is mainly of interest at low temperatures, it is not a bad approximation to use the Debye theory to describe this energy spectrum. In the Debye model, the internal energy may be written as a temperature-dependent quantity,

$$E_{\text{ph}} = aT^4 \tag{7.87}$$

where $a = \frac{3}{5}\pi^4 (N/V)\, k_B/\Theta_D^3$ and $T \ll \Theta_D$, the Debye temperature. For most solids, the Debye temperature is in the range of several hundred Kelvin, making this approximation quite reasonable for the Kapitza conductance at helium temperatures.

To quantify the problem of phonon radiation between two media, assume there is a unit interfacial area dA on which phonons are incident at velocity c. A schematic of the hemispherical region surrounding this elemental area is shown in Fig. 7.33. The angle of incidence of the phonon is given in spherical coordinates by θ and Ψ, but only the perpendicular component of the incident phonon transmits the energy. More detailed theory discussed later includes the coupling of transverse phonons at the interface, but for simplicity the present treatment will neglect this effect. The perpendicular component of the velocity can be writtenin terms of the angle θ such that

$$c_\perp = c \cos\theta \tag{7.88}$$

The heat flux into the area dA is the then product of the energy density and perpendicular velocity component such that $dq = c_\perp E_{ph}$. It follows that the net heat

flux per unit area is obtained by integration of dq over the hemisphere in θ and Ψ. This procedure yields

$$q = \frac{1}{4\pi}\int_0^{2\pi} cE_{\text{ph}} \sin\theta \cos\theta d\theta = \frac{1}{4} cE_{\text{ph}} \tag{7.89}$$

In the Debye approximation, the speed of sound in a solid is given as

$$c = \frac{k_B \Theta_D}{\hbar}\left(\frac{6\pi^2 N}{V}\right)^{-1/3} \tag{7.90}$$

where for solids c is of the order of 3 km/s while for He II the speed of sound never exceeds 240 m/s. Substituting (7.90) and (7.87) into (7.89), we obtain an equation for the total heat flux carried by phonon radiation:

$$q = \sigma T^4 \tag{7.91a}$$

and

$$\sigma = \frac{\pi^4}{10\hbar}\left(\frac{k_B}{\Theta_D}\right)^2\left(\frac{3N}{4\pi V}\right)^{2/3} \tag{7.91b}$$

The reader who is familiar with radiation heat transfer should recognize this form to be analogous to the heat transported by photon radiation. Note that (7.91b) includes the variable material properties through the molar volume (N/V) and Debye temperature. The quantity σ can vary considerably between materials, which according to the theory leads to a quite different heat transfer coefficients. For example, since σ is inversely proportional to c^2, it follows that the ratio of heat fluxes by phonon radiation should differ by a factor of 100 between He II and solids at low temperatures. This is one of the major weaknesses of the phonon radiation theory in that it only considers the thermal character of the solid.

Now consider the radiation of phonons between two different media, between which there exists an interface. For the sake of discussion, assume there is no appreciable temperature gradient occurring in either bulk material and that the flow of heat from one side to the other produces an interfacial temperature difference ΔT_s. In order for this interface to be defined as a boundary between two bulk media, it must be confined to a thickness that is small compared to the characteristic phonon wavelength, $\lambda_D = hc/k_B\Theta_D$. For solids $\lambda_D \approx 100$ μm, which is large compared to most interfacial dimensions.

The net heat flux through the interface is actually a difference between two values, the radiant energy incident on the high-temperature side, $q(T + \Delta T)$, minus that incident from the low-temperature side, $q(T)$,

$$q_{\text{net}} = q(T + \Delta T) - q(T) \tag{7.92}$$

Assuming that both these quantities can be described in terms of the phonon heat flux expression (7.91a) and also that the coefficient σ is the same in either media, it follows that the net heat flux is a difference between the phonon radiation expressions of the two media:

$$q_{\text{net}} = \sigma(T + \Delta T)^4 - \sigma(T)^4 \tag{7.93a}$$

which can be expanded to

$$q_{net} = 4\sigma T^3 \Delta T \left[1 + \frac{3}{2}\frac{\Delta T}{T} + \left(\frac{\Delta T}{T}\right)^2 + \frac{1}{4}\left(\frac{\Delta T}{T}\right)^3\right] \tag{7.93b}$$

In the limit of small ΔT, (7.93b) gives an explicit definition for the phonon radiation limit Kapitza conductance in terms of σ:

$$h_K^p = 4\sigma T^3 \tag{7.94}$$

where the superscript p refers to the phonon radiation limit. The assumption that σ is independent of media clearly is not accurate, particularly when dealing with interfaces between solids and He II. However, it is argued that the smaller value of σ (that of the solid) controls the heat transfer because the net heat flux q_{net} must be in the direction from high to low temperature. As a reference point, the phonon radiation limit applied to copper ($\Theta_D = 343$ K, $N/V = 0.86 \times 10^{23}$ cm^{-3}) predicts a Kapitza conductance of

$$h_K^p = 4.4T^3 \text{ kW/m}^2 \cdot \text{K} \tag{7.95}$$

or 30 kW/m^2 K at 1.9 K. We now compare the Kapitza conductance predicted by the phonon radiation limit with experiment values.

Listed in Table 7.3 are calculated values from the phonon radiation limit and the highest values obtained experimentally for typical metals and nonmetals. It is important to note that the experimental values for the same material vary considerably, in some cases by as much as an order of magnitude. However, since the phonon radiation limit should represent an overestimate of h_K, it is most appropriate to compare it to the highest measured values. The first result gleaned from this comparison is that the phonon radiation calculation always gives values for h_K that are higher than experiment, sometimes by as much as an order of magnitude. This fact is consistent with the understanding that the phonon radiation limit overestimates h_K. Second, although it is not apparent from the tabular data, the general temperature dependence of h_K predicted by the phonon radiation limit is borne out. Recall that experiment yielded a form for $h_K \approx T^n$ with $2 < n < 4$. Finally, as with the phonon radiation limit, there is a measurable dependence of h_K on the value of Θ_D for the particular solid. This fact can be seen most clearly in Fig. 7.31, which is

Table 7.3 Comparison of highest experimental values for the Kapitza conductance with the phonon radiation limit (Compiled by Snyder [54])

Solid	Θ_D (K)	h_K^P (1.9 K) (kW/m^2·K)	h_K (1.9 K) (kW/m^2·K)
Hg	72	440	30
Pb	100	190	32
In	111	171	11
Au	162	155	8.8
Ag	226	55	6
Sn	195	54	12.5
Cu	343	30	7.5
Ni	440	19	4.0
W	405	18	2.5
KCI	230	22	6.9
SiO_2 (quartz)	290	19	5.7
Si	636	6.4	4.2
LiF	750	5.1	4.5
$A1_2O_3$	1,000	1.5	1.6

a log plot of h_K versus Θ_D^{-1}. The linear interpolation indicates there is a coloration of the form

$$h_K \propto \Theta_D^{-n} \tag{7.96}$$

where the phonon radiation limit predicts $n = 2$ and experiment, as shown in Fig. 7.34, yields values of $n \approx 1$.

There are a number of problems with the phonon radiation limit, particularly when it applies to solid–He II interfaces. It is clearly a crude approximation to a complex problem and is limited by the numerous factors incorrectly accounted for in the theory. These factors include:

1. A failure to distinguish adequately between the different media on either side of the interface. The Debye temperatures that enter the problems are associated with the solid media. Any correction to the theory should include the characteristics of both media.
2. An assumed coupling between both longitudinal and transverse phonon modes. This is particularly a problem for He II where transverse phonons cannot be sustained.
3. Reflections at boundaries are not considered, implying a perfect transmission coefficient. This assumption clearly overestimates the heat transport. A finite reflection coefficient at the interface would be expected, particularly for solid–He II interfaces where the phonon spectra are so different.
4. Crystal structure at the interface is ignored. This is potentially an important factor owing to the solid having long-range order while the liquid is not periodic.
5. Phonons are assumed to be the only heat transport mechanism. However, some experiments have shown that electrons in metals play a significant role in the heat transfer at the interface.

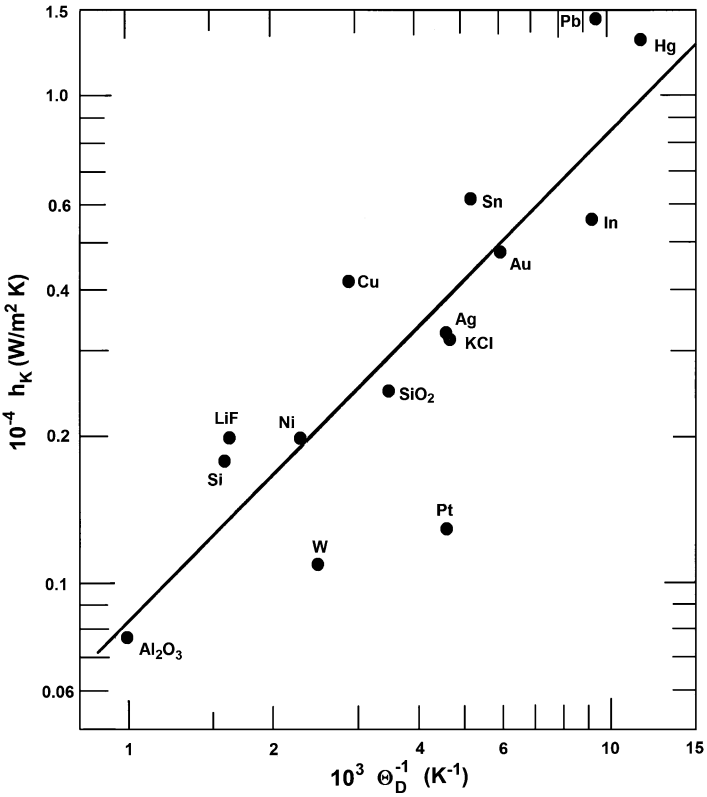

Fig. 7.34 Kapitza conductance at 1.5 K —largest values observed for each solid (Compiled by Challis [55])

6. The existence of interfacial films or impurities is not considered. Layers of adsorbed impurities can have substantial effect on the heat transfer from practical surfaces. However, even for clean surfaces the detailed character of the helium adjacent to the interface must be considered.

The above factors are part of improved theories of Kapitza conductances. The first such improvement was due to Khalatnikov in 1952 [56]. It basically addresses the first three objections to the phonon radiation limit as listed above.

7.5.2 Acoustic Mismatch Theory

The first real advance in the theory of Kapitza conductance was made by the development of the acoustic mismatch theory of Khalatnikov [56]. This theory is based on an analogy with classical acoustics or boundary scattering in optics.

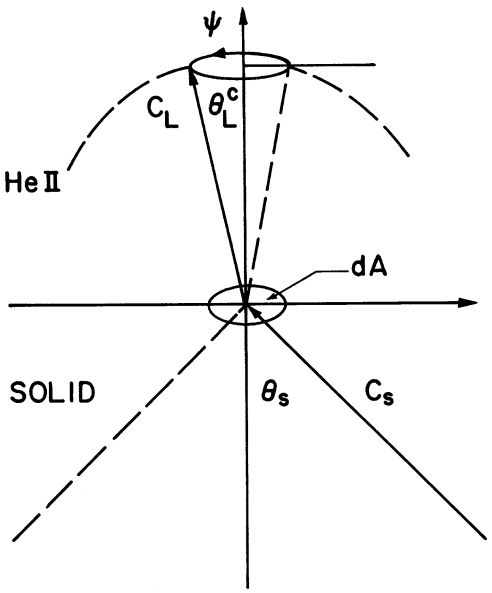

Fig. 7.35 Schematic of interface between solid and He II

In some ways the theory is similar to the phonon radiation limit except that it includes a very important additional mechanism; that of the finite reflection coefficient at the boundary between the two media. The basic approach involves the derivation of the phonon transmission coefficient using conservation of momentum and energy at the boundary. Because the acoustic mismatch theory explicitly accounts for the difference between the two media, it is expected to be a better description for the solid–He II case where the speed of sound differs by an order of magnitude on either side of the interface.

Consider an interfacial region between two media, for example, a solid and He II. This example is of current interest so it will be emphasized throughout the following discussion. The liquid is able to transmit only longitudinal phonons. A schematic of the interface is shown in Fig. 7.35. By analogy with optics, these regions can be thought of as a low-refractive-index solid adjacent to a high-refractive-index liquid. Because of the difference in refractive index, a phonon that is incident on the boundary from the liquid side would be reflected off the interface unless its angle of incidence is less than a critical value, θ_L^c. Within this angle the transmitted phonons are diffracted to an angle θ_s, on the solid side. The locus of maximum angles θ_L^c forms a cone of transmission which is determined solely by the speed of sound ratio in the two media:

$$\theta_L^c = \arcsin\left(\frac{c_L}{c_s}\right) \tag{7.97}$$

For interfaces between metals and He II, the ratio c_L/c_s is about 0.1, which corresponds to a critical angle of about 6°. The acoustic mismatch theory assumes

that phonons strike the interface between the two media at an angle θ_s, but only those that are scattered into an angle less than θ_L^c can be transmitted. All other phonons are reflected internally.

The above argument can be extended to describe the phonon heat transport across an interface. The total heat transport is determined by integration over the cone of transmission, much as was accomplished above for phonon radiation although now only angles less than θ_L^c are allowed:

$$q = \frac{1}{4\pi}\int_0^{2\pi} d\Psi \int_0^{\theta_L^c} c_L E_{\text{ph}} \sin\theta\cos\theta d\theta = \frac{1}{4} c_s E_{\text{ph}} \left(\frac{c_L}{c_s}\right)^3 \tag{7.98}$$

Note that (7.98) is similar in form to the phonon radiation limit result except that it is modified by the ratio $(c_L/c_s)^3$, which for solid–He II interfaces is of the order of 10^{-3}.

The above expression theoretically predicts the heat transport carried by phonons that are refracted into the angle θ_L^c. However, not all phonons that fall within this cone are actually transmitted, because there is a finite transmission coefficient for phonons incident on the boundary. This transmission coefficient t is given in terms of the acoustic impedance Z of each medium:

$$t = \frac{4Z_L Z_s}{(Z_L + Z_s)^2} \tag{7.99}$$

where $Z_L = \rho_L c_L$ and $Z_s = \rho_s c_s$. For the case concerning the solid–He II interface it is apparent that $Z_s \gg Z_L$ and (7.99) can be simplified such that

$$t = 4\frac{Z_L}{Z_s} = 4\frac{\rho_L c_L}{\rho_s c_s} \tag{7.100}$$

As an example, consider the interface between He II and copper. In this case $Z_s \approx 10^3 Z_L$, which corresponds to a transmission coefficient of approximately 0.5%.

Combining the equations for the heat flux (7.98) and the transmission coefficient (7.100), we find that an expression for the transmitted heat flux is

$$q_t = q \times t = \left(\frac{\rho_L c_L^4}{\rho_s c_s^4}\right) c_s E_{\text{ph}} \tag{7.101}$$

which is similar to the phonon radiation limit except for the extra term in the parentheses.

An additional aspect to the acoustic mismatch theory concerns the fact that the fluid can sustain only longitudinal phonons. Instead of the expression for the energy density used in the phonon radiation limit, in the acoustic mismatch theory the expression must include only longitudinal phonons. Thus, the corresponding form for the energy density is

$$E_{\text{ph}}^{L} = \frac{4\pi^5 k_B^4 T^4}{15\hbar^3 c_L^3} \tag{7.102}$$

Combining the energy density equation for longitudinal phonons (7.102) with the transmitted heat flux, we obtain q_t given by (7.101), a temperature-dependent expression for the transmitted heat flux:

$$q_t = \frac{4\pi^5 k_B^4 \rho_L c_L}{15\hbar^3 \rho_s c_s^3} T^4 \tag{7.103}$$

As with the phonon radiation limit it is possible to replace the prefactor in (7.103) by σ.

The net heat flux across the interface is obtained by subtracting the incident flux on either boundary. By suitably redefining σ it is possible to use (7.93) and (7.94) to predict the Kapitza conductance in the acoustic mismatch theory. For a small interfacial temperature difference, the result is

$$h_K^A = \frac{16\pi^5 k_B^4 \rho_L c_L}{15\hbar^3 \rho_s c_s^3} T^3 \tag{7.104}$$

where the superscript A refers to the acoustic mismatch theory. Note that the expression for the Kapitza conductance derived from the acoustic mismatch theory is determined by the properties of both media, a dependence left out of the phonon radiation limit. A more rigorous calculation in the acoustic mismatch theory replaces the sound speed in the solid, c_s, by its transverse component, c_t.

It is more convenient to have an expression for the Kapitza conductance in terms of the Debye temperature and other properties of the media. By replacing the transverse speed of sound c_t by its expression in terms of the Debye temperature Θ_D, a simplified expression is obtained:

$$h_K^A = \left(\frac{6\pi^4}{5}\right) \frac{RF\rho_L c_L T^3}{M\Theta_D^3} \tag{7.105}$$

where $R = 8.31$ J/mol K is the universal gas constant and M is the molecular weight. The multiplicative factor F, which is a function of the ratio c_t/c, is included, but for most solids, F is of the order of unity and so is not a particularly important factor in (7.105). For helium properties at saturation pressure and assuming $F = 1.6$, we can simplify to a useful form,

$$h_K^A = 5.5 \times 10^7 \left(\frac{T^3}{M\Theta_D^3}\right) \quad \left(\text{kW/m}^2 \cdot \text{K}\right) \tag{7.106}$$

where M is in units of g/mol. As is the case with the phonon radiation limit, the acoustic mismatch theory predicts a variation of h_K^A with the Debye temperature as $h_K^A \approx \Theta_D^{-3}$. This dependence is similar to that of the phonon radiation limit, $h_K^P \approx \Theta_D^{-2}$. However, both theoretical approaches overestimate the experimentally determined Debye temperature variation, $h_K \approx \Theta_D^{-n}$ where $n \approx 1$.

7.5.3 Small Heat Flux Kapitza Conductance ($\Delta T \ll T$)

Now consider the relationship between the above theoretical treatments and actual experimental data. Plotted in Fig. 7.35 are model calculations and experimental data for the Kapitza conductance of a He II-copper interface at temperatures above 1.3 K. As can be seen in the figure, the phonon radiation limit forms an upper bound to experimental data consistent with the model excluding boundary scattering effects. Similarly, the Khalatnikov acoustic mismatch theory predicts a Kapitza conductance about 200 times smaller than the phonon radiation limit. Insertion of numerical values for copper into (7.106) results in the expression for the Kapitza conductance,

$$h_K^A = 0.021T^3 \text{ kW/m}^2 \cdot \text{K} \tag{7.107}$$

The experimental data displayed in Fig. 7.35 show basically the same temperature dependence with some variations. The best fit to these data indicate h_K proportional to T^n with n ranging between 2 and 4. Perhaps more surprisingly from the experimental viewpoint is that the magnitude of h_K at a given temperature varies by at least an order of magnitude among samples. Part of this variation can be attributed to surface morphology. The upper shaded region in the figure is for copper surfaces that are cleaned carefully either chemically or mechanically and perhaps recrystallized at room temperature to reduce surface strain. On the other hand, lower values are generally obtained for dirty surfaces, indicated by the lower shaded region, for which less effort was made to maintain surface cleanliness. Based on the available experimental data, approximate forms for the Kapitza conductance in this temperature range are suggested:

$$h_K \simeq 0.9T^3 \text{ kW/m}^2 \cdot \text{K for clean surface} \tag{7.108}$$

$$\simeq 0.4T^3 \text{ kW/m}^2 \cdot \text{K for dirty surface} \tag{7.109}$$

with potentially as much as a factor of two variation in value.

It can be seen from Fig. 7.36 that although the theoretical treatments bracket the experimental data, neither does a particularly good job of predicting the results. Nevertheless, the physical interpretation contained in the acoustic mismatch theory generally is believed to be correct. In fact, the theory does a much better job of interpreting the magnitude of h_K in the very-low-temperature regime, $T < 0.3$ K [57].

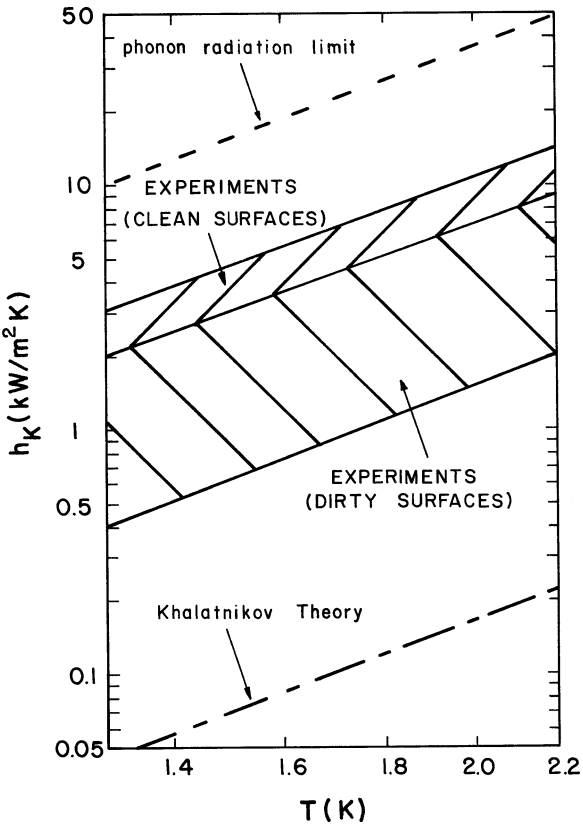

Fig. 7.36 Experimental values for the Kapitza conductance of copper between 1.3 K and T_λ (Compiled by Snyder [54])

Therefore, the problem with the theory appears to be that it does not include additional thermal coupling mechanisms which can make a large contribution, particularly at relatively high temperatures, $T > 1$ K.

A number of improvements to the acoustic mismatch theory have attempted to bring the calculations in closer agreement with experiment. One such improvement adds to the model a high-density helium layer at the interface between the solid and bulk liquid [57–60]. The existence of this layer has been demonstrated in helium adsorption studies, see Sect. 10.2. It occurs because the helium molecules are bound tightly to the surface by van der Waal interactions. Since the interfacial region consists of several components—the solid, perhaps two high-density atomic layers of solid helium, and then the liquid – it is possible to have boundary scattering occur at each of these interfaces. Finite phonon transmission and reflection coefficients can be assumed to occur at each boundary. Defining the phonon absorption coefficient v as the fraction of incident phonons that are absorbed, we can make this an adjustable parameter and fit the data to the best choice of $0 < v < 1$. This approach allows for a good fit to experimental data above 0.5 K [54].

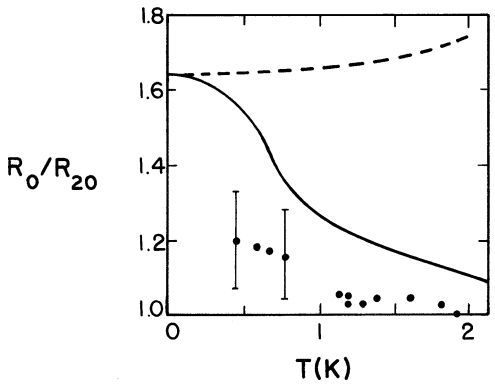

Fig. 7.37 The ratio of the Kapitza resistance under saturated vapor pressure and under a pressure of 2 MPa (R_0/R_{20}): •, experimental points; - - -, Khalatnikov theory; ——, dense-layer theory (From Wilks [61])

There are several additional features to the Kapitza conductance which are worth noting, partly because they prove the existence of additional physical processes but also because they relate to problems of applied interest. The first feature to consider is the dependence of the Kapitza conductance on externally applied pressure. Plotted in Fig. 7.37 are the ratio of the measured Kapitza resistance ($1/h_K$) at 2 MPa to that at saturated vapor pressure [58, 62]. Also displayed in the figure are two theoretical treatments, the Khalatnikov theory and the same theory modified to include the dense helium layer without finite reflection coefficients. Note first that the experimentally determined ratio is not much different from unity, particularly in the range of technical interest, above 1 K. The unmodified Khalatnikov theory on the contrary predicts a sizable effect for all temperatures, mostly due to the variation of the fluid properties with pressure. For the modified theory a smaller ratio is predicted, particularly at high temperatures, although it is still above the experimental results. Because the pressure dependence of the Kapitza conductance is not a large effect, it is generally not considered in practical calculations.

A second factor that leads to variations in h_K is the application of a magnetic field. This is an important physical observation for it indicates that there must be other heat transport mechanisms contributing at the interface. In particular, since electrons in the solid are affected by a magnetic field, there must be a coupling between electrons in the metal and phonons in the helium adding to the heat transport. Two types of experiment have been performed to investigate this effect. The first has shown a larger Kapitza conductance for a Type I superconductor for fields above B_C. For lead the ratio h_K (normal)/h_K (superconductor) has been shown to vary between 1.3 and 3 for different samples. This observation is probably the most direct evidence of some type of electron-phonon coupling at the interface. For normal metals such as copper, there have been fewer investigations of the effect of magnetic field on Kapitza conductance. Some reports have indicated h_K for normal metals increases by about 10% in a 1 T magnetic field. However, there is insufficient data available to predict this effect to higher magnetic fields.

Beyond the above two experimental features, there is evidence that the Kapitza conductance is affected strongly by the application of interfacial coatings to the solid, either in the form of applied materials or adsorbed gases. Generally, coatings decrease the apparent Kapitza conductance because they tend to the insulating materials with low thermal conductivities. The effect of a few monolayers of adsorbed gas has not been investigated thoroughly, although it has little importance for practical applications where the surfaces are not kept very clean.

7.5.4 Large Heat Flux Kapitza Conductance ($\Delta T \approx T$)

Up until this point, the theory and experiments associated with the Kapitza conductance for small ΔT have been emphasized. However, in applications of He II large heat fluxes can occur, which in turn result in large temperature differences across the interface such that $\Delta T \approx T$. Because of this occurrence, it is desirable to develop a method of handling the heat transfer process for finite ΔT. Returning to the simplest theories, either phonon radiation limit or acoustic mismatch for finite ΔT, the heat flux through the interface may be written as a sum of terms involving the ratio ($\Delta T/T$), (7.93). It follows that the Kapitza conductance for finite ΔT is larger than h_K, by the magnitude of this expansion,

$$h_K(\Delta T) = h_{K_0}\left[1 + \frac{3}{2}\frac{\Delta T}{T} + \left(\frac{\Delta T}{T}\right)^2 + \frac{1}{4}\left(\frac{\Delta T}{T}\right)^3\right] \tag{7.110}$$

where for $\Delta T/T \approx 0.5$, the bracketed quantity is approximately equal to 2. Note that the expansion given by (7.110) makes the initial assumption of an explicit T^3 dependence of h_{K0} consistent with theory. However, experimental measurements vary considerably from this exact form, obeying power laws varying between T^2 and T^4. Some additional characteristic to the Kapitza conductance may also be expected to occur when the surface temperature exceeds T_λ.

There have been several attempts [62–67] to correlate the Kapitza conductance for finite ΔT with the form of (7.110). These have not been entirely successful largely because of the deviation between the theory and experimental temperature dependence of this effect. An alternative correlation suggested [65] for practical applications is:

$$q_s = \alpha\left(T_s^n - T_b^n\right) \tag{7.111}$$

where a and n are adjustable parameters. Note that if one equation is able to fit the experimental data for one sample over the whole temperature difference range, then it should be possible to expand (7.111) consistent with the low heat flux temperature dependence. Similar to the behavior of the experimental data for small ΔT, the high ΔT Kapitza conductance also varies considerably with sample. Plotted in Fig. 7.38

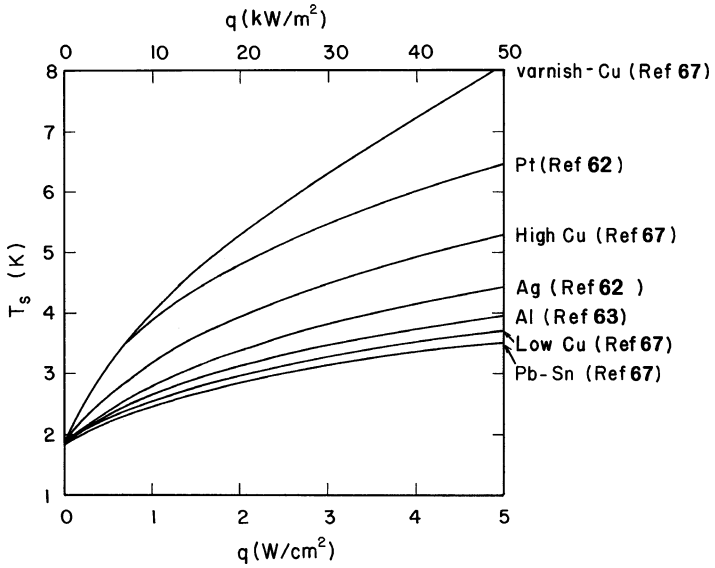

Fig. 7.38 Surface temperature versus heat flux for large ΔT Kapitza conductance

Table 7.4 High heat flux Kapitza conductance fitting parameters for metals at 1.8 K

Metal	Surface condition	T_s at 10 kW/m^2	α (kW/m^2·K^n)	n	References
Cu	As received	3.1	0.486	2.8	
	Brushed and baked	2.85	to		
	Annealed	2.95	0.2	3.8	[65]
	Polished	2.67	0.455	3.45	[67]
	Oxidized in air for 1 month	2.68	0.46	3.46	[67]
	Oxidized in air at 200°C for 40 min	2.46	0.52	3.7	[67]
	50-50 PbSn solder coated	2.43	0.76	3.4	[67]
	Varnish coated	4.0	0.735	2.05	[67]
Pt	Machined	3.9	0.19	3.0	[62]
Ag	Polished	2.8	0.6	3.0	[62]
Al	Polished	2.66	0.49	3.4	[63]

are measurements of T_s as it depends on q_s for different materials. A range of results for copper are shown which indicate the variation with surface preparation. Listed in Table 7.4 is a summary of published data for Kapitza conductance of pure metals at high ΔT. Displayed are the surface preparation, surface temperature at a heat flux $q = 10$ kW/m^2, and the best-fit functional form to these data. Note that most of the fits give values of $n = 3 \pm 0.5$, which is systematically lower than the theoretical value of $n = 4$. Also, the best fit to the coefficient in (7.111) is for $\alpha \simeq 0.05$ W/cm^2·K^{n+1} but with substantial variation. Finally, it is interesting to note that the variation in Kapitza conductances at large ΔT is not nearly as great as is obtained in the limit $\Delta T \to 0$, where an order-of-magnitude deviation in h_k is seen.

Example 7.3

Calculate the temperature of an "as received" copper surface when subjected to a heat flux of 5 kW/m^2 at 2.1 K using both the small ΔT approximation and the empirical correlation for large ΔT.

For small ΔT, the Kapitza conductance of as received (dirty) copper is given by the expression (7.109),

$$k_K = 0.4T^3 \text{ kW/m}^2 \text{ K} = 3.7 \text{ kW/m}^2 \text{ K}$$

$$T_s = T_b + q/h_K = 2.1 + 1.35 = 3.45 \text{ K}$$

For large ΔT, the empirical correlation is given by,
$q_s = a\left(T_s^n - T_b^n\right)$ where for "as received" samples $a = 0.486$ kW/m^2 K^n and $n = 2.8$.
Solving for T_s,

$$T_s = \left(\frac{q}{a} + T_b^n\right)^{\frac{1}{n}} = 2.82 \text{ K}$$

Note that this is about a factor of two difference in ΔT, being 1.35 K in the small ΔT approximation and 0.72 K in the large flux correlation.

In classical fluid heat transfer, the heat transfer coefficient usually increases with fluid velocity or Reynolds number, see Chap. 5. This is because the net flow velocity thins the boundary layer at the heater surface and induces convection. It is therefore reasonable to ask whether non-boiling heat transfer in He II can similarly be enhanced by flow. There have been several experimental investigations on this topic [68, 69].

At first glance, one would not expect enhancement to heat transfer in the Kapitza regime as long as the fluid remains below T_λ. This is because the heat exchange is controlled by phonon transport and that there is no significant thermal boundary layer contribution the heat transfer coefficient. Experiments have generally supported this position, however, the situation is not so simple when the helium locally transitions to He I by exceeding T_λ. In that case, since the fluid near the heater is either He I or vapor, the helium flow can significantly improve the process. Furthermore for local heat transfer within a tube, the action of the fluid flow will also tend to sweep the hot helium away from the heated region which will allow a more rapid recovery to the non-boiling state once the heat flux is reduced. This effect is in addition to the overall enhancement to the He II heat transport that can occur for relatively high fluid velocities, see Sect. 7.3.

7.6 Film Boiling Heat Transfer

Until now the existence of boiling phenomena in He II has been mentioned only as the condition reached when the critical heat flux q^* is exceeded. However, there are a number of complicated heat transfer processes that can occur above q^* that deserve more discussion. This regime of heat transfer is of significant technical importance for its occurrence can lead to catastrophic events in cryogenic systems where good heat transfer must be maintained continuously. Unfortunately, boiling heat transfer in He II is one of the least understood process in He II heat transfer.

In He II above the peak heat flux, the fluid in the region of heat transfer can contain several phases in coexistence. Consequently, the physical interpretation of the heat transfer processes is more difficult than in single-phase He II. For heat fluxes above q^* there occurs a discontinuous jump in the surface temperature. This transition marks the formation of a film of helium vapor, liquid He I, or both blanketing the heat transfer surface. These general characteristics of the transition to film boiling are best couched in the context of the surface heat transfer curve such as Fig. 7.1. In the film boiling state, the heat transfer is much less effective because of the low thermal conductivity vapor film insulating the surface from the bulk He II. Typical values for the film boiling heat transfer coefficient $h_{fb} = q/\Delta T_s$ are 10–100 times smaller than the Kapitza conductance coefficient. However, these values are strongly dependent of a number of physical parameters including heater configuration, bath temperature, pressure, and saturated versus subcooled liquid state. An additional feature in the heat transfer curve, also commonly observed in He I, is the occurrence of a recovery heat flux q_R that is less than q^*. The existence of $q_R < q^*$ causes hysteresis in the heat transfer curve, see Fig. 7.1. However, unlike pool boiling He I, this hysteresis is not observed universally in all He II heat transfer experiments.

There are three possible film boiling conditions that can exist in He II above q^*. To establish which condition is expected for a given set of externally imposed factors, it is necessary to consider the helium state in the vicinity of the heat transfer surface. The first condition corresponds to the local pressure at the heated surface being less than the saturation pressure at the λ-point, that is $p_\lambda = 5.04$ kPa. This is referred to as the saturation boiling condition. It is achieved by having a local temperature excursion above T_{sat}, the saturation temperature at the local pressure. The resulting boiling state is a coexistence of two phases; saturated vapor and He II.

The second condition occurs when the local pressure at the heat transfer surface is large enough to exceed p_λ at the heat transfer surface. A consequence of exceeding q^* is the production of a film of low-thermal-conductivity He I which covers the surface. If the heat flux q is not greater than the corresponding critical heat flux in He I for that configuration, the heat transfer process will be stable, allowing nucleate boiling to occur in the He I film and heat conduction in He II. Note that the boundary between the He II and He I is not clearly defined in this case because the phase transition from He I to He II is second order, allowing only a continuous density profile. It is important to be aware that, because q^* in He II is under most circumstances much higher than that in He I, the limiting of this process to two phases usually only occurs for temperatures near T_λ.

The third boiling condition occurs at the solid-helium interface when q^* is exceeded in subcooled He II for temperatures well below T_λ, that is $T_b < 2.1$ K. In this regime, the critical heat flux is greater than that in He I and the He I film becomes unstable and enters film boiling. The result is a triple-phase process consisting of vapor film blanketing the surface, a very thin He I film, and bulk He II. As with the second condition, the He I-He II boundary is not sharply defined. It is apparent that this third film boiling condition, although occurring commonly in engineering systems employing subcooled He II, is the most complex to understand because of the existence of multiphase processes.

There exists one additional type of boiling in He II which does not fall in any of the three above categories. This type of boiling occurs in the bulk fluid rather than at the interface. It can be achieved only in special configurations where the surface heat flux does not exceed q^* but the channel heat flux surpasses the local boiling condition. For example, this condition was discussed in the context of the design of static He II heat exchangers, Sect. 7.1.4. As a result, He I and vapor are nucleated in the bulk and the heat transport properties of the fluid are modified. This process is analogous to bulk boiling in ordinary fluids.

The fundamental description of the film boiling heat transfer clearly requires a more complex theoretical description than considered so far. Furthermore, it appears that there is no broadly applicable theory capable of handling the multiphase boiling processes. As a result, most research on this problem is of the category of engineering correlations combined with empirical evidence. Since the understanding of the process relies heavily on suitable experimental data, a review of measurements of film boiling heat transfer coefficients is presented first. Subsequently, a comparison is made between the available theories and experimental results. Finally, a description is included of some of the less understood heat transfer phenomena such as recovery from the film boiling state and time-dependent effects.

7.6.1 Film Boiling Heat Transfer Experiments

The film boiling heat transfer process depends strongly on several factors. The first of these has to do with the configuration of the heater. Experiments to date have mainly focused on two heater configurations, flat surfaces and round wires. In the case of the flat surfaces, some are placed at the end of a He II duct while others are in an open bath. Round wire heat transfer experiments are almost all done within an open bath. Recall that the onset of film boiling is determined by the integrated thermal gradient in the He II, thus in a one-dimensional linear geometry the duct length and cross section are important factors affecting q^*. On the other hand, in a cylindrical geometry, as discussed in Sect. 7.1.4, the thermal boundary layer is restricted to occur within a few radii of the heater. Thus, the heat transfer from cylinders can be studied in a large bath without loss of generality.

The experimental measurements of the film boiling heat transfer coefficient for various heater configurations have been extensive; however, they have also been rather restrictive in regime of investigation. The most obvious restriction is

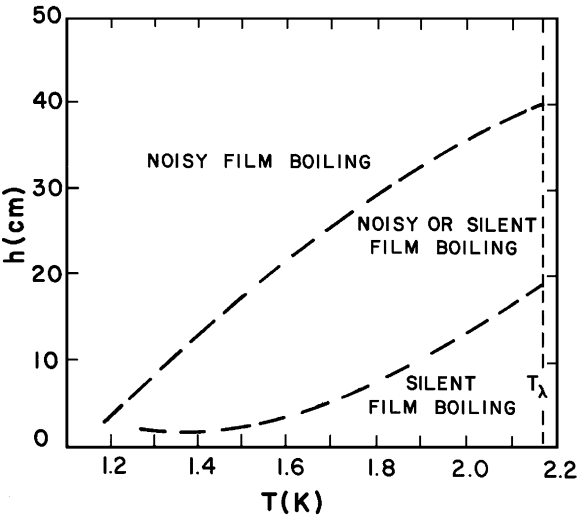

Fig. 7.39 Regimes of noisy and silent boiling from wire heaters in saturated He II (From Leonard [70])

associated with the total allowable heat transfer, which is a system limitation. Therefore, film boiling heat transfer surfaces are usually much less than 1 cm^2 in area, which places rather strict constraints on the sample. Historically, most experiments have been carried out in near saturated He II, leading to a boiling state consisting of vapor-He II coexistence. More recently, more measurements have been performed in subcooled He II primarily due to the interest in its application in large superconducting magnet systems. Thus, the second important factor impacting the film boiling heat transfer process is the state of the He II bath; mainly its temperature and pressure.

In near saturation He II, there exist two different regimes of film boiling heat transfer. These are referred to as "noisy" and "silent" boiling. Noisy boiling is apparent by the existence of audible sound emanating from the heat transfer region. Silent boiling, on the other hand, is film boiling without this audible sound. Frequencies observed in noisy boiling can vary anywhere from a few Hz to tens of kHz. The frequency is generally a function of heat flux although in no well-established pattern. The regions of noisy and silent boiling are seen to depend on bath temperature and depth of immersion.

Plotted in Fig. 7.39 is a map of these two regimes based on one set of data on wire heaters [70]. This map should not be construed as universally applicable. It appears from these results that noisy boiling occurs for larger immersion depths and lower temperatures. The occurrence of noisy or silent boiling also has a significant effect on the heat transfer coefficient h_{fb}. In regimes of overlap where either noisy or silent boiling is seen to occur, it is usually the case that a slightly higher heat transfer coefficient is measured during silent boiling. This effect, which appears systematic in published experiments, is nonetheless only of the order of 10–20% in the majority of reported results [71–75].

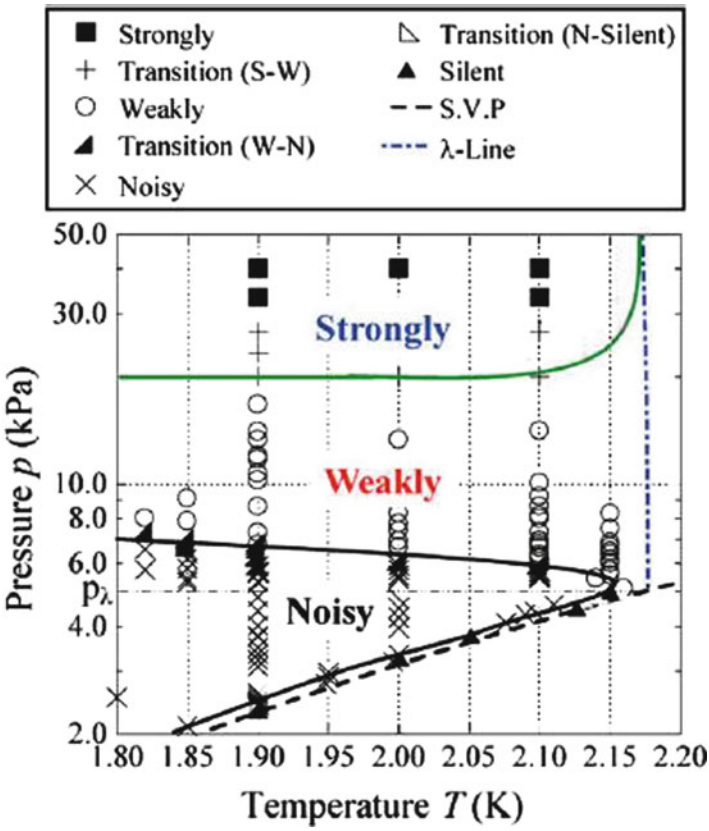

Fig. 7.40 Regimes of noisy and silent boiling from wire heaters in saturated He II. q = 10 W/cm^2 (From Nozawa et al. [76])

Recent experiments performed in saturated and subcooled He II have revealed the existence of four film boiling regimes in He II [76]. These are the two saturated boiling states, noisy and silent boiling and two new subcooled boiling states: strongly and weakly subcooled boiling. A map showing the regime of existence for these four states for a flate heater is given in Fig. 7.40. Note that the strongly and weakly subcooled boiling states only exist at pressures above p_λ.

The existence of the four film boiling states have been confirmed by a variety of measurement techniques including pressure and temperature fluctuations as well as visualization. In particular, Takada et al. [77] performed a series of visualization studies on film boiling on a 50 μm diameter round wire. This work revealed clear differences in the hydrodynamics of boiling as can be seen in Fig. 7.41. Of note is the periodic nature of the film boundary for silent and subcooled boiling states while the noisy boiling is more stochastic. These results can also be used to obtain an average vapor film thickness that can be correlated with the heat transfer coefficient.

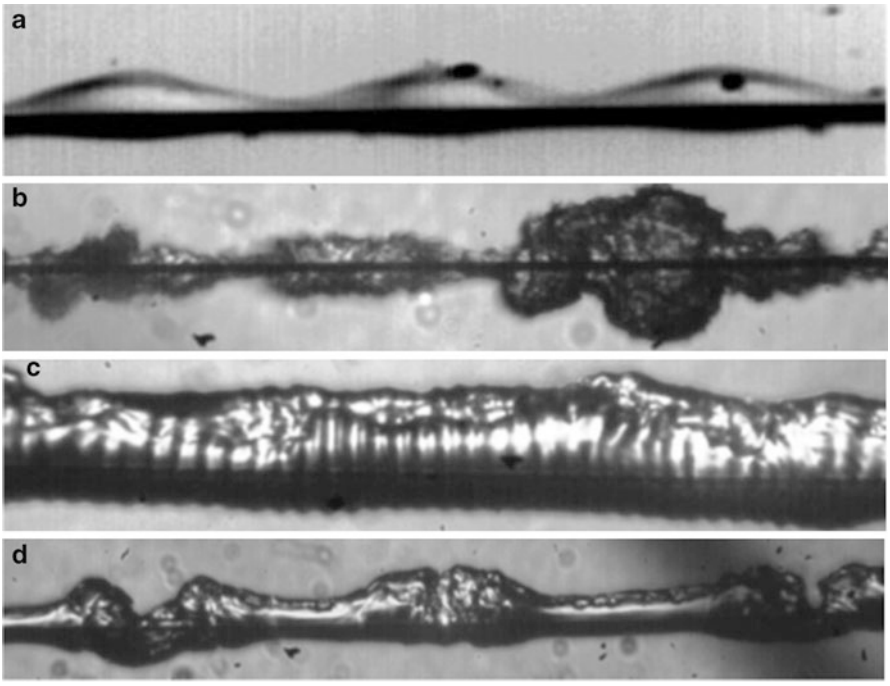

Fig. 7.41 Visualization of four boiling states in He II heat transfer from a round wire: (**a**) silent boiling at 2 K under saturated vapor pressure, q = 19.3 kW/m^2; (**b**) noisy boiling at 2.1 K and 5.3 kPa, q = 373 kW/m^2; (**c**) weakly subcooled boiling at 2.1 K and 16 kPa, q = 601 kW/m^2; (**d**) strongly subcooled boiling at 2.1 K and 100 kPa, q = 396 kW/m^2 (From Takada et al. [77])

We now consider the film boiling heat transfer coefficient. Table 7.5 lists some typical values for h_{fb} under different conditions and for different configurations. There is a notable wide range of values of h_{fb} depending on surface temperature, fluid pressure and heater configuration. However, a few trends are immediately evident from the data in Table 7.5. First, h_{fb} is generally largest for small diameter wires such that there occurs approximately a factor of two increase in value with an order-of-magnitude decrease in heater diameter, d_H. As is discussed below, this behavior can be interpreted in terms of a fairly simple vapor film conduction model. In addition to the diameter dependence, h_{fb} for cylindrical heaters as well as for flat plates is also a function of depth of immersion in the saturated helium or externally applied pressure. Any theoretical effort to model the film boiling heat transfer coefficient therefore must consider these issues.

As mentioned above, the film boiling heat transfer coefficient is seen to depend on diameter in a significant way. Plotted in Fig. 7.42 is typical behavior of h_{fb} for fixed bath temperature and a specific hydrostatic head [72]. The general tendency is for h_{fb} to increase with decreasing diameter. Also, plotted in Fig. 7.43 are typical heat transfer coefficients for heated wires as a function of hydrostatic head h and

Table 7.5 Typical film boiling heat transfer coefficients

Sample	T_b (K)	T_s (K)	Δp (kPa)[a]	h (kW/m^2·K)	References
Wire ($d = 25$ μm)	1.8	150	0.56	2.2	[79]
Wire ($d = 50$ μm)	2.1	80	100	3.6	[77]
	2.1	50	10	6.2	"
Wire ($d = 76$ μm)	1.8	150	0.42	1.1	[79]
Wire ($d = 200$ μm)	2.05	150	0.14	0.66	[74]
Cylinder ($d = 1.45$ mm)	1.78	80	0.06	0.22	[75]
Cylinder ($d = 14.6$ mm)	1.88	40	0.10	0.2	[73]
	2.14	40	0.10	0.2	"
Flat plate					
Flat rectangular plate	1.8	75	0.14	0.22	[72]
(39 mm × 11 mm)	1.8	75	0.28	0.3	"
	1.8	75	0.84	0.55	"
Flat surface ($d = 13.7$ mm)	2.01	40	0.13	0.69	[4]
	2.01	25	0.237	0.98	"

[a]1 kPa = 7.5 torr = 703 mm He II

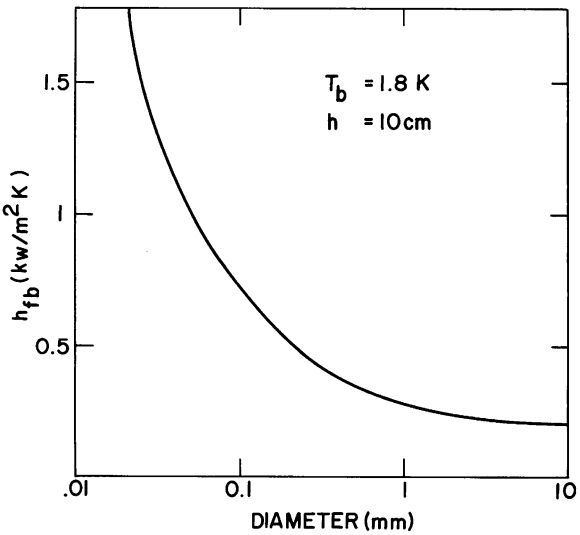

Fig. 7.42 Film boiling heat transfer coefficients as a function of heater diameter for constant hydrostatic head ($h = 10$ cm)

surface temperature, T_s. In general, the heat transfer coefficient increases with helium head and decreases with surface temperature. At small depths, the relationship is roughly linear with h [72].

The situation that occurs in subcooled He II, where the boiling is associated with multiphase phenomena, is generally more complex. In addition, there have been fewer experiments performed under these conditions so data are less prevalent.

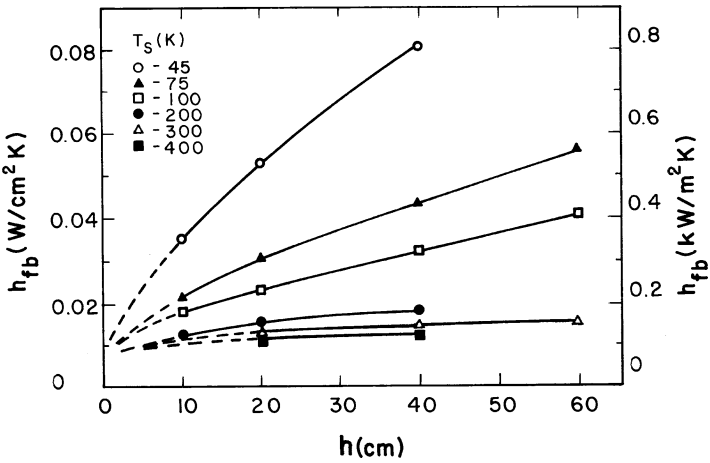

Fig. 7.43 Film boiling heat transfer coefficients versus immersion depth (From Betts and Leonard [72])

However, in general it is observed that the film boiling heat transfer coefficient is higher in the subcooled condition compared to that at saturation. Furthermore, higher pressures on subcooled He II tend to increase h_{fb}. This latter effect may be caused by the increased thermal conductivity of the helium vapor film for higher pressures. Few investigations of the dependence of h_{fb} on heater diameter have been reported for subcooled He II.

7.6.2 *Theoretical Models for Film Boiling Heat Transfer*

A simple model can be constructed to show the origin of the diameter dependence to the film boiling heat transfer. The model is based on an assumption that heat is transported through the vapor film by thermal conduction only. The conceptual picture therefore would represent a stable vapor film of constant thickness δ surrounding the heat transfer surface. Consider a cylindrical heater of radius r as shown in Fig. 7.43. An estimate of the vapor film thickness δ can be obtained from the relationship

$$\delta = \frac{\overline{k}}{h_{fb}} \tag{7.112}$$

where the mean thermal conductivity $\bar{k}$ is taken over the temperature range between the bath T_b and surface T_s. As an example, in Table 7.5 the heat transfer coefficient for a 76 mm diameter wire is about 1.1 kW/m^2 K, obtained for a surface temperature of 150 K. The average thermal conductivity of helium gas in this temperature

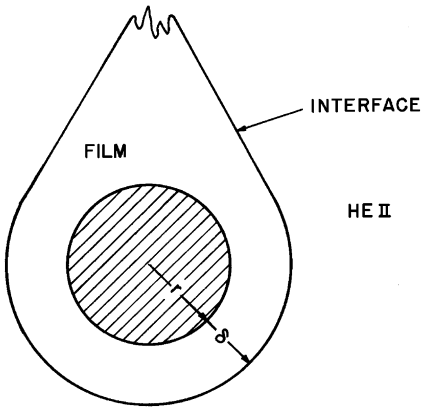

Fig. 7.44 Schematic of cylindrical beater surrounded by a vapor film

range is $\bar{k} \approx 0.06$ W/m K, which corresponds to $\delta \sim 50$ μm. This thickness is fairly large compared to typical heater wire diameter. Also, note that the mean free path in the vapor is of the order of 1 μm, which is much shorter than the film thickness so this thermal conduction model could provide a reasonable approximation.

The simple heat conduction model can be used to interpret the diameter dependence of h_{fb} shown in Fig. 7.42. Making one further assumption that the vapor film thickness does not vary appreciably with heater radius, a relationship can be derived for the ratio of heat transfer coefficients by simply integrating the conduction heat transfer through the film (Fig. 7.44):

$$\left.\frac{h(r)}{h_0}\right|_{fb} = \frac{\delta/r}{\ln(1+\delta/r)} \tag{7.113}$$

where h_0 refers to the film boiling heat transfer coefficients obtained for flat plates. Thus, as the radius of the heater decreases the film boiling heat transfer coefficient is expected to increase purely as a result of radial heat conduction. Generally, such a result is borne out by experiment, see Fig. 7.42.

An alternative model suggested by Takada et al. [77] is based on the steady state heat transport equation in cylindrical coordinates (7.13). The basis of the model is to assume that the heat flux through the surface of the vapor film is equal to the heat conducted through the bulk He II. The stable thickness of the vapor film is then set by the condition that the heat flux in the He II is q^*. Therefore, as the heat generated in the wire increases, the outer radius of the vapor film must increase to limit the heat flux. The thicker film would have a lower average thermal conduction, which would translate to a lower overall heat transfer coefficient. Such a trend can be seen in Fig. 7.43 as the average heat transfer coefficient decreases with increasing heater temperature.

A more detailed theoretical attempt to correlate film boiling heat transfer is due to Rivers and McFadden [78]. This work treats film boiling heat transfer in saturated He II in terms of a boundary layer model. The equations that describe

the problem are conservation of mass, momentum, and energy for two-dimensional, steady-state heat transfer. In rectangular coordinates these equations may be written

$$\frac{\partial u}{\partial x}+\frac{\partial v}{\partial y}=0 \tag{7.114}$$

$$u\frac{\partial u}{\partial x}+v\frac{\partial v}{\partial y}=\frac{1}{\rho_f}F_b+\frac{\mu_f}{\rho_f}\frac{\partial^2 u}{\partial x^2} \tag{7.115}$$

and

$$u\frac{\partial T}{\partial x}+v\frac{\partial T}{\partial y}=\frac{k_f}{\rho_f C_{pf}}\frac{\partial^2 T}{\partial x^2} \tag{7.116}$$

where the body force F_b represents the buoyancy of the vapor film. The solution of this set of equations has been accomplished by assuming fourth-order polynomials for the temperature and velocity profiled and matching boundary conditions at the wall and the vapor–He II interface. The result is a dimensionless form to the Nusselt number,

$$\text{Nu Gr}^{-1/4}=f(Q_b,\text{Gr},H_i,\text{Pr}) \tag{7.117}$$

where the Prandtl number for the film is

$$\text{Pr}=\frac{\mu_f C_{pf}}{k_f} \tag{7.118}$$

and the Grashof number,

$$\text{Gr}=\frac{g\,D^3\rho_f\left(\rho_b-\rho_f\right)}{\mu_f^2} \tag{7.119}$$

describes the heat transfer process. To determine the exact form of (7.117) for a given problem it is necessary to apply numerical integration. The end product of this analysis is a solution for the Nusselt number and steady-state film thickness as a function of the interfacial heat flux. Two regimes become evident in this result. The transition between these two regimes occurs at a value of $Q_b\,\text{Gr}^{-1/4}\approx 1$, where Q_b is the dimensionless interfacial heat flux,

$$Q_b=\frac{Dq_b}{k_f\Delta T_f} \tag{7.120}$$

For values of $Q_b\ \mathrm{Gr}^{-1/4} < 1$, the heat transfer is dominated by convection. In this regime, the heat transfer coefficient is a function of the integral enthalpy which can be normalized to the form

$$H_i = \frac{\Delta h_i}{C_{pf}\Delta T_f} \tag{7.121}$$

For values of $Q_b\ \mathrm{Gr}^{-1/4} > 1$, the heat transfer is via conduction mechanisms. Comparison between experiment and the theory described above is only partially successful.

An alternative approach to the theory of film boiling heat transfer has been suggested by Labuntzov and Ametistov [79]. This theory is based on the idea that film boiling is a nonequilibrium process involving heat and mass transfer at the vapor–He II interface. Thus, it is essential to account for the processes of vaporization and condensation. These processes have been investigated theoretically in detail; the following relationships for the dimensionless fluxes of mass, momentum, and heat have been obtained:

$$\Delta\tilde{p} - 2\sqrt{\pi}\frac{1-0.4\beta}{\beta}\tilde{j} = 0.44\tilde{q} \tag{7.122a}$$

where

$$\Delta\tilde{p} = \frac{p'' - p_s}{p_s} \tag{7.122b}$$

$$\bar{q} = \frac{q}{p_s(2R'T_i)^{1/2}} \tag{7.122c}$$

$$\tilde{j} = \frac{j}{\rho_s(2R'T_i)^{1/2}} \tag{7.122d}$$

In the above equations R' is the gas constant for helium ($R' = R/M = 2{,}079$ J/kg • K), T_i is the temperature of the liquid helium at the interface, β is the condensation coefficient, ρ_s and p_s are the equilibrium density and pressure corresponding to T_i, and p'' is the vapor pressure corresponding to the helium vapor film at the interface. The derivation of (7.122a) is beyond the scope of the present treatment although it is obtained analytically from the Boltzmann kinetic equation [80]. Equation (7.122a) can be applied to the solution of interface mass and heat transfer for ordinary liquids as well as He II. However, for ordinary liquids heat transfer is controlled by convective processes in the bulk. For He II these convective processes are enhanced by two-fluid internal convection which dominates the heat transfer in most cases. The form of (7.122a) is approximate since it is assumed that $\Delta\tilde{P} \ll 1, \tilde{j} \ll 1$. If this is not the case, it is necessary to use the full nonlinear solutions.

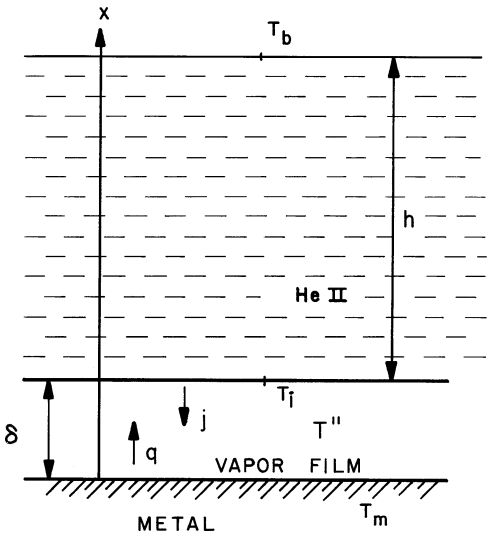

Fig. 7.45 Heat mass transfer process in film boiling He II

Now consider the existence of a film boiling state as shown schematically in Fig. 7.45. In the steady state the vapor film is of constant thickness δ, and consequently $j = 0$. There is no net mass flow across the He II–vapor interface. Under these conditions, (7.122a) can be simplified to

$$\Delta\tilde{p} = 0.44\tilde{q} \tag{7.123}$$

or for a given hydrostatic head

$$q = 2.27\rho gh(2RT_i)^{1/2} \tag{7.124}$$

The physical meaning of (7.124) is that it represents the heat flux necessary to establish a stable vapor film in He II. Note that this is a considerably different interpretation for the critical heat flux than that based on the peak temperature difference within the bulk fluid. Thus, there is some contradiction between the results of Sect. 7.1 and (7.124). There are several possible resolutions for this contradiction.

The first explanation is to imagine conceptually that the film boiling state can be obtained spontaneously anytime the condition described by (7.124) is satisfied. However, this argument is contradictory to experiment, particularly for critical heat fluxes in one-dimensional channels. On the other hand, there is some disagreement between experiment and the He II peak heat flux predicted by turbulent heat transport in cylindrical geometries. It is possible that the condition described by (7.124) is a clue to this discrepancy; however, this point has yet to be analyzed.

As an alternate explanation [80], it is to suggest that the film boiling state once established obeys the kinetic relationship derived above. This idea is not contradictory to the peak heat flux being the point where the helium temperature near the

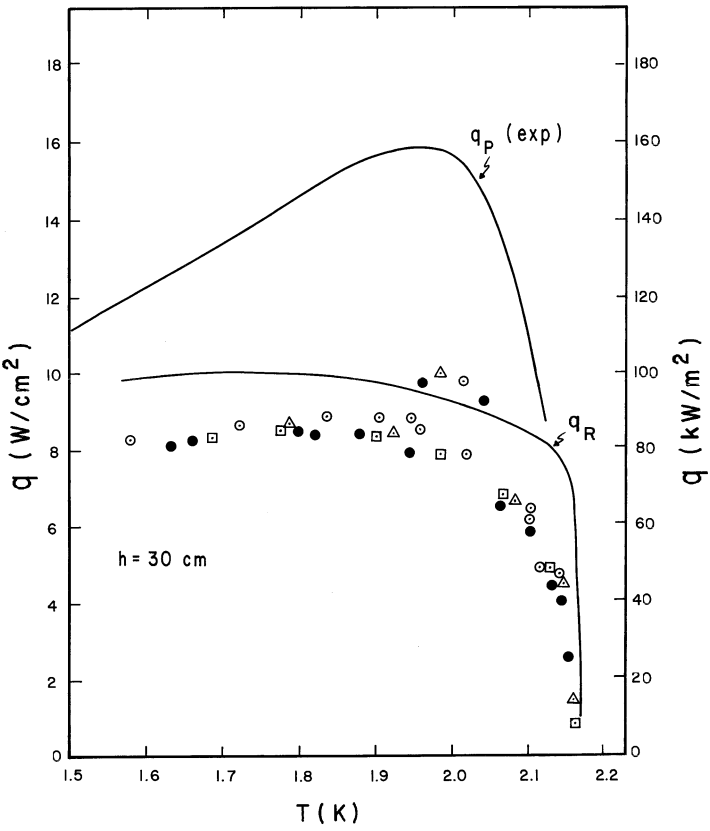

Fig. 7.46 Comparison of calculations using the kinetic theory with experimental results (From Kryukov and Van Sciver [81])

interface reaches T_{sat} or T_λ. However, once this film is established it will remain stable against collapse until the heat flux falls below the value given by (7.124), provided it is less than the applied heat flux. Thought of in this manner, the molecular kinetic theory provides a mechanism of interpreting the minimum film boiling heat flux in He II, that is q_R.

The connection between these two alternate concepts for recovery from film boiling has been investigated analytically for heated cylinders in saturated He II. The comparison of this model with experiment has been carried out for the few configurations where minimum film boiling heat flux data are available [81]. The best agreement occurs with data acquired on small-diameter wires. Plotted in Fig. 7.46 are the experimentally measured peak and minimum film boiling heat fluxes versus temperature for a cylindrical wire of diameter 76.2 μm [82]. The theoretical plot for q_R is also shown to provide quite close agreement with experiment. Unfortunately, the correspondence between theory and experiment for other

configurations of larger dimension is not nearly as close. Consequently, there is still considerable disagreement as to the correct mechanism needed to describe the film boiling state in He II.

An alternate approach for the recovery from the film boiling state has been suggested by experiments that have shown a correlation between the minimum film boiling heat flux and the film boiling heat transfer coefficient. For a specific configuration consisting of a flat plate at the end of a duct, the value of q_R was shown to increase monotonically with h_{fb}. This condition was observed to prevail in both saturated and subcooled He II. Furthermore, the ratio q_R/h_{fb} was found to take on an essentially constant value of about 23 K, suggesting the existence of a critical temperature difference for recovery from film boiling. This critical temperature difference should be related in some fundamental way to the collapse of the vapor film.

7.6.3 Transient Film Boiling Heat Transfer

Typically, the heat transfer process to He II is transient in nature with associated time dependent phenomena. This occurs when film boiling is caused by a rapid transient disturbance such as might happen when a superconducting magnet quenches or a He II cryostat has a loss of vacuum accident. Understanding the heat transfer in this regime is helpful with the design and safe operation of large scale He II systems.

We consider the case where film boiling has been established by exceeding the critical heat flux followed by a reduction of the heat flux to some lower value. If the heat flux is reduced below the minimum film boiling flux q_R, recovery to the nonboiling state should begin. This dynamic process is governed by transient heat transfer within the system.

We first consider the time dependent recovery from the film boiling state. It is assumed that at time $t = 0$ the film boiling state is initiated and that a steady heat rate Q is applied for a time Δt_f. Since Q is greater than the peak heat flux, the temperature of the surface will increase dependent on the mass and heat capacity of the heated section. For long times, this process would lead to a steady temperature based on the balance between the heat rate and film boiling heat transfer. After Δt_f, the heat generation ceases ($Q = 0$) and the recovery process begins. Empirically, the recovery process is found to take a length of time Δt_R which is a function of Δt_f before the vapor film collapses [83]. It is assumed further that the controlling mechanism for recovery is the enthalpy stored within the heated sample and the film boiling heat transfer coefficient is a constant, h. The fluid simply acts as a constant temperature bath. Using the Debye approximation to the specific heat, we can show that the above assumptions lead to a correlation between Δt_f and Δt_R which can be written explicitly as

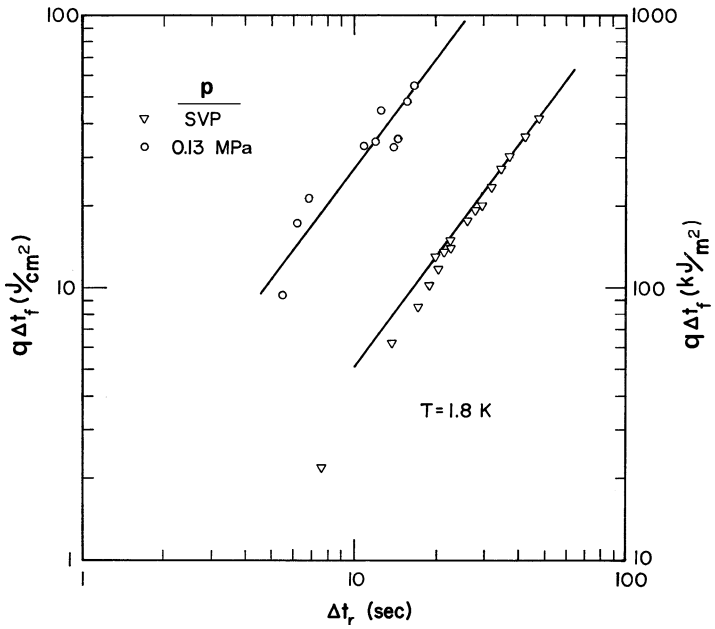

Fig. 7.47 Correlation between the energy applied to a film boiling heat transfer sample and the time to recovery

$$Q\Delta t_f = 0.176\Theta_D \left(\frac{M}{mR}\right)^{1/3} (hA\Delta t_R)^{4/3} \left(1 + \frac{4}{5}\alpha + \frac{4}{6}\alpha^2 + \ldots\right) \tag{7.125}$$

where $\alpha = hT_m/Q \leq 1$ with T_m being the maximum temperature of the heat transfer surface. The total mass of the heat transfer sample is m and its cooled surface has area A. The properties of the heat transfer sample enter through its molecular weight M and Debye temperature Θ_D.

The correlation suggested by (7.125) has shown reasonable agreement with experiment. By allowing the heat transfer coefficient h to be a constant adjustable parameter, one can fit experimental data for the relationship between Δt_f and Δt_R. This fit is shown in Fig. 7.47. By establishing the correlation based on only the leading term in (7.125), the best-fit heat transfer coefficients are $h = 0.18$ kW/m^2 K at SVP and $h = 0.62$ kW/m^2 K at 0.13 MPa. It is interesting to note that these values of h are roughly 60% of typical steady-state film boiling heat transfer coefficients for flat plates.

The other problem of interest is to the understand transient recovery in subcooled He II. This problem has more to do with the time-dependent heat transport in the bulk fluid than film boiling heat transfer. Rather than correlating the time to recovery based on the thermal capacity of the heater, the approach here is to determine the maximum steady-state heat flux which allows recovery after an intense short-duration heat pulse is applied to a heat transfer sample. The short-duration heat pulse is assumed to be larger than the maximum energy flux to locally

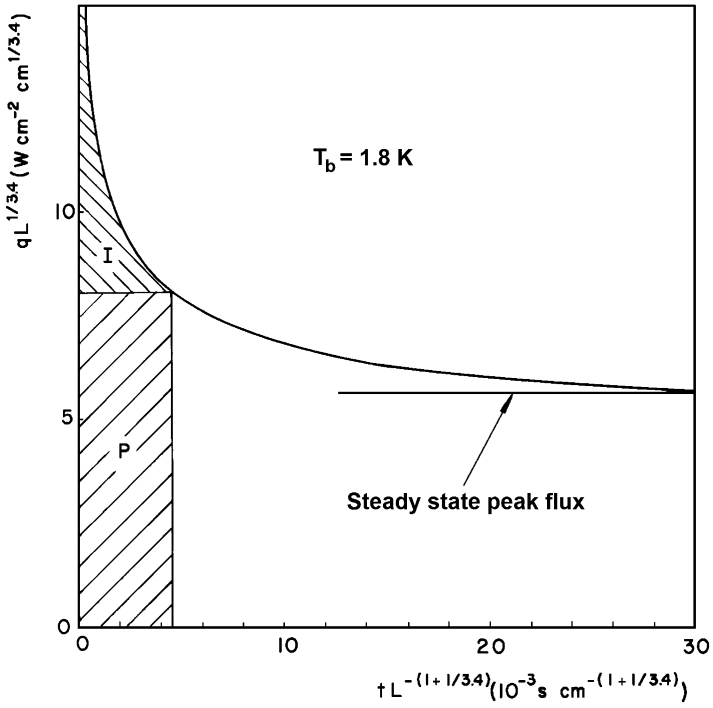

Fig. 7.48 Schematic description of the transient recovery process in He II with post-heating (From Seyfert [30])

bring the He II to T_λ and thus break down heat transfer. Consequently, the heat transfer at the solid-helium interface breaks down and further heat is stored in the solid or in the helium adjacent to the heater. After the heat pulse, the excess heat can be transferred through the He II by the established transient heat transfer mechanisms. Now if the steady-state heat flux is not too large, the combination of it with the remaining excess energy being released from the heat transfer sample will not exceed the maximum transient energy flux in the He II. The result is a temporary recovery to the non-boiling state. Recovery is temporary only if the steady-state heat flux is larger than the maximum steady-state heat flux in He II for that particular configuration.

The above set of conditions are illustrated graphically in Fig. 7.48, which is a normalized transient heat transfer plot for He II at 1.8 K. The solid curve represents the maximum heat flux that can be applied for a given time before breakdown of He II heat transfer occurs. This condition is established according to Sect. 7.2. Now consider a short-duration, high-level heat pulse applied to the heat transfer sample. Since this energy is larger than that transferable by the He II, the excess is stored in the heat transfer sample. The total energy contained in the pulse is shown by region I in the figure. Subsequent to the pulse, the heat flux is dropped to a lower level q_p which is still above the maximum steady-state meat flux q^*. However, temporary recovery will occur because the transient heat transfer mechanism can continue.

Thus, the sum of the two areas I and P determines the length of time before unrecoverable thermal breakdown occurs. This model has been compared successfully to transient heat transfer experiments in He II [60]. The problem is of significant practical interest to superconducting magnet technology.

Example 7.4

For the rectangular flat plate film boiling heat transfer data at T = 1.8 K and Δp = 0.14 kPa in Table 7.5, estimate the thickness of the vapor film assuming that heat is carried only by gaseous conduction. Compare the calculated thickness to the mean free path in the vapor.

In this case, the average thermal conductivity can be approximated by$k_{He}(40)$K = 0.4W/m K. The approximate thickness of the film is then,

$$t = \bar{k}/h_{fb} = 0.4 \text{ W/m K}/220 \text{ W/m}^2 \text{ K} = 2 \text{ mm}$$

The mean free path is calculated by
The mean free path is calculated by,

$$l \approx \frac{1}{n\sigma} \sim \frac{k_B T}{\pi d^2 p} = \frac{1.38 \times 10^{-23} J/K \times 40K}{\pi\left(2.56 \times 10^{-10} m\right)^2 \times 1600 Pa} = 1.67 \ \ \mu\text{m}$$

Questions

1. Heat transfer from a solid surface to a bath of He II does not have a nucleate boiling regime. Why?
2. One method to increase the heat transfer coefficient in the Kapitza regime would be to roughen the surface, thereby increasing the effective area. What are the practical limits to this approach? [Two points to keep in mind are that the surface material has a finite thermal conductivity and the phonon coupling is over a certain range.]
3. Assume that you wish to design a He II heat exchanger that consists of a U-tube immersed in a pressurized He II reservoir. The upper ends of the tube empty into a saturated bath of He II maintained at a constant 1.7 K. For these conditions, draw a sketch of the temperature profile along the U-tube from one end to the other.
4. For Question 3 above, suppose that you wanted to enhance the performance of the heat exchanger. Would there be a benefit to putting a pump in the line to force the He II through the U-tube. List the design constraints on selecting the parameters for the circulation system.

Problems

1. Consider a sphere of radius r_0 in a large bath of He II. Derive an expression for the steady-state temperature gradient as a function of radial coordinate r.

Determine the peak heat flux as it depends on bath temperature. Assume that mutual friction is the only important interaction and the ambient pressure is 0.1 MPa. [Hint: This problem is analogous to that of heat transfer in cylindrical geometries discussed in Sect. 7.1.4.]

2. Estimate the maximum surface heat flux q_0 for a cylindrical wire of diameter 1 mm in He II at 1.8 K, 0.1 MPa. What would be the effect of increasing the external pressure to 1 MPa?
3. Show that the transient heat transfer solution given by (7.52) for the fixed energy deposition obeys the heat conductivity equation for He II.
4. Estimate the Kapitza conductance at 1.9 K of aluminum for small ΔT, by each of the following methods:

   a. Phonon radiation limit.
   b. Acoustic mismatch theory.
   c. Experimental results listed in Table 7.3.

5. Show that the variation of the film boiling heat transfer coefficient with heater radius may be written in the form given by (7.113). For the data listed in Table 7.5 from Ref. [79] (d = 25 and 76 μm), estimate the film thickness δ and the limiting heat transfer coefficient h_0 for large radii.
6. A metallic copper heater is located at the bottom of a 50 cm long vertical channel containing He II at 1.9 K. Assume the pressure at the top of the channel is saturation and that heat flow is governed by mutual friction.

   a. Find the peak heat flux q^*. [Note: Although (7.10) is valid for this case, it is more accurate to use tabulated vapor pressure of helium].
   b. Estimate the heater surface temperature just below q^*.

7. Consider a 2 m long, 5 mm ID smooth tube which contains 1.8 K He II flowing at a mass flow rate of 20 gm/s. Calculate the total pressure drop across the tube assuming the flow is fully developed and turbulent. Estimate the total temperature rise in the He II flow due to the Joule Thomson effect. [Hint: you may use the simplified form for the JT coefficient of an incompressible liquid].
8. Derive (7.84) for the mass flow through an ideal vapor – He II phase separator.

References

1. W. F. Vinen, Mutual Friction in a Heat Current in Liquid Helium II. I. Experiments on Steady State Heat Currents, *Proc. R. Soc. London* **A240**, 114 (1957).
2. V. Arp, Heat Transport through Helium II, *Cryogenics* **10**, 96 (1970).
3. C. E. Chase, Thermal Conduction in Liquid Helium II I: Temperature Dependence, *Phys. Rev.* **Vol. 127**, 361 (1962).
4. S. W. Van Sciver, Kapitza Conductance of Aluminum and Heat Transport through Sub-cooled He II, *Cryogenics* **18**, 521 (1978).
5. G. Bon Mardion, et al, Steady State Heat Transport in Superfluid Helium at 1 Bar, *Proc. 20th Intern. Cryog. Engn. Conf.*, IPC Technology Press, London (1978) pp. 214–222.

6. W. F. Vinen, Mutual Friction in a Heat Current in Liquid Helium II. III. Theory of Mutual Friction, *Proc. R. Soc. London* **A242**, 493 (1957).
7. A. Sato, et al, Normalized Representation for Steady State Heat Transport in a Channel Containing He II Covering Pressure Range up to 1.5 MPa, *Proc. 7th Intern. Cryog. Engn. Conf.*, Beijing, China (2004) pp. 849–52.
8. A. Sato, et al, Steady State Heat Transport in a Channel Containing He II at High Pressures up to 1.5 MPa, *Adv. Cryog. Engn.* **Vol. 49**, 999 (2004).
9. A. Sato, et al, Temperature Dependence of the Gorter-Mellink Exponent *m* Measured in a Channel Containing He II, *Adv. Cryog. Engn.* **Vol. 51A**, 387 (2006).
10. M. Maeda, et al, Heat Transport Near the Lambda Line in a Channel Containing He II, *Adv. Cryog. Engn.* **Vol. 51A**, 379 (2006).
11. P. Seyfert, Practical Results on Heat Transfer to Superfluid Helium, in *Stability of Superconductors*, pp. 53–62, International Institute of Refrigeration Commission A 1/2, Saclay, France, 1981.
12. C. Linnet and T. H. K. Frederking, Thermal Conditions at the Gorter-Mellink Counterflow Limit between 0.01 and 3 Bar, *J. Low Temp. Phys.* **Vol. 21**, 447 (1975).
13. S. R. Breon and S. W. Van Sciver, Boiling in Subcooled and Saturated He II, Advances in Cryogenic Engineering **31**, 465 (1986) and Boiling Phenomena in Pressurized He II Confined to a Channel, *Cryogenics* **26**, 682 (1986).
14. A. C. Leonard and M. A. Clermont, Correlation of the Vaporization Onset Heat Flux for Cylinders in Saturated Liquid Helium II, in *Proc. 4th Intern. Cryog. Engn. Conf.*, IPC Science and Technology Press, London, 1972, pp. 301–306.
15. J. S. Goodlang and R. K. Irey, Nonboiling and Film Boiling Heat Transfer to a Saturated Bath of Liquid Helium, *Adv. Cryog. Eng.* **14**, 159 (1969).
16. T. H. K. Frederking and R. L. Haben, Maximum Low Temperature Dissipation Rates of Single Horizontal Cylinders in Liquid Helium II, *Cryogenics* **8**, 32 (1968).
17. S. W. Van Sciver and R. L. Lee, Heat Transfer to He II in Cylindrical Geometries, *Adv. Cryog. Eng.* **25**, 363 (1980).
18. S. W. Van Sciver and R. L. Lee, Heat Transfer from Circular Cylinders in He II, in *Cryogenic Processes and Equipment in Energy Systems*, ASME Publication No. H00164, 1981, pp. 147–154.
19. S.W. Van Sciver, Heat Transfer through Extended Surfaces Containing He II, *ASME Journal of Heat Transfer* **Vol. 121**, 142 (1999).
20. A. Bezaguet, J. Casas-Cubillos, P. Lebrun, M. Marquet, L. Tavian, and R. van Weelderen, The superfluid helium model cryoloop for the CERN Large Hadron Collider, *Adv. Cryog. Engr.* **Vol. 39**, 649 (1994).
21. G. Horlitz, T. Peterson and D. Trines, A 2 Kelvin Helium II Distributed Cooling System for the 2x250 Gev e + e- Linear Collider TESLA, *Cryogenics* **Vol. 34** (Supplement), 131 (1994).
22. S. W. Van Sciver, Heat and Mass Transfer Processes in Two Phase He II/Vapor, *Cryogenics* **Vol. 39**, 1039 (1999).
23. Y. Xiang, B. Peterson, S. Wolff, S. W. Van Sciver , and J. G. Weisend II, Numerical Study of Two-Phase Helium II Stratified Channel Flow with Inclination, *IEEE Trans. On Applied Superconductivity* **Vol. 10**, 1530 (2000) and Y. Xiang, N. N. Filina, S. W. Van Sciver, J. G. Weisend II and S. Wolff, Numerical Study of Two-Phase He II Stratified Channel Flow, *Adv. Cryog. Engn.* **Vol. 45B**, 1001 (2000).
24. Ph. Lebrun, L. Serio, L. Tavian and R. van Weelderen, Cooling Strings of Superconducting Devices Below 2 K: the Helium II Bayonet Heat Exchanger, *Adv. Cryog. Engn.* **Vol. 43A,** 419 (1998).
25. B. Rousset, L. Grimaud, A. Gauthier, Stratified Two-Phase Superfluid Helium Flow: I*Cryogenics* **Vol. 37**, 733 (1997) and L. Grimaud, A. Gauthier, B. Rousset, J. M. Delhaye, Stratified Two-Phase Superfluid Helium Flow: II, *Cryogenics* **Vol. 37**, 739 (1997).
26. L. Dresner, Transient Heat Transfer in Superfluid Helium, *Adv. Cryog. Eng.* **27**, 411 (1982).

27. L. Dresner, Transient Heat Transfer in Superfluid Helium-Part II, *Adv. Cryog. Eng.* **29**, 323 (1984).
28. L. Dresner, *Similarity Solution of Non-Linear Partial Differential Equations*, Pitman Publishing, Boston, MA, 1983.
29. S. W. Van Sciver, Transient Heat Transport in He II, *Cryogenics* **19**, 385 (1979).
30. P. Seyfert, J. Lafferranderie, and G. Claudet, Time Dependent Heat Transport in Subcooled Superfluid Helium, *Cryogenics* **22**, 401 (1982).
31. S. W. Van Sciver, Heat Transport in Forced Flow He II: Analytic Solution, *Adv. Cryog. Eng.* **29**, 315 (1984).
32. R. Srinvasan and A. Hofmann, Investigations on Cooling with Forced Flow of He II, *Cryogenics* **25**, 641 (1985).
33. A. Kashani and S. W. Van Sciver, Steady State Forced Convection Heat Transfer in He II, *Adv. Cryog.* Eng. **31**, (1986).
34. W. W. Johnson and M. C. Jones, Measurements of Axial Heat Transport in Helium II with Forced Convection, *Adv. Cryog. Eng.* **23**, 363 (1978).
35. S. Fuzier and S. W. Van Sciver, Steady-State Pressure Drop and Heat Transfer in He II Forced Flow at High Reynolds Number, *Cryogenics* **41**, 453 (2001) and S. Fuzier, S. Maier and S. W. Van Sciver, Pressure Drop in Forced Flow He II at High Reynolds Numbers, in *Proc. 19th Intern. Cryog. Engn. Conf.*, Grenoble, France July, 15, 2002, pp. 755–8.
36. P.L. Walstrom, J.G. Weisend II, J.R. Maddocks, and S.W. Van Sciver, Turbulent Flow Pressure Drop in Various He II Transfer System Components, *Cryogenics* **Vol. 28**, 101 (1988).
37. M.A. Daughterty and S.W. Van Sciver, Pressure Drop Measurements on Cable-in-Conduit Conductors of Various Geometries, *IEEE Trans. on Magnetics* **27**, 2108 (1991).
38. A. Hofmann, A. Khalil and H.P. Kramer, Operational Characteristics of Loops, *Adv. Cryog. Engn.* **33**, 471 (1988).
39. B. Rousset, G. Claudet, A. Gauthier, P. Seyfert, P. Lebrun , M. Marquet , R. Van Weelderen and J. Duchateau, Operation of a Forced Flow Superfluid Helium Test Facility and First Results, *Cryogenics (Supplement)* **Vol. 3,** 134 (1992).
40. P. L. Walstrom, Joule-Thomson Effect and Internal Convection Heat Transfer in Turbulent He II Flow, *Cryogenics* **Vol. 28**, 151 (1988).
41. A. Kashani, S.W. Van Sciver, and J.C. Strikwerda, Numerical Solution of Forced Convection Heat Transfer in He II, *J. Num Heat Transfer*, *Part A*, **Vol. 16**, 213 (1989).
42. L. Bottura and C. Rosso, Finite Element Simulation of Steady-State and Transient Forced Convection in Superfluid Helium, *Intern. J. Numerical Methods in Fluids*, **Vol. 30**, 1091 (1999).
43. Rousset B., Claudet G., Gauthier A., Seyfert P., Martinez A., Lebrun P., Marquet M. and Van Weelderen R., Pressure Drop and Transient Heat Transport in Forced Flow Single Phase Helium II at High Reynolds Numbers, *Cryogenics (Supplement)* **Vol. 34**, 317 (1994).
44. S. Fuzier and S. W. Van Sciver, Experimental Measurements and Modeling of Transient Heat Transfer in Forced Flow He II at High Velocities, *Cryogenics* **Vol. 48**, 130 (2008).
45. R. Maekawa and B. Baudouy, Heat Transfer through Porous Media in the Counterflow Regime, *Adv. Cryog. Engn.* **Vol. 41**, 983 (2004).
46. M. Dalban-Canassy and S. W. Van Sciver, Steady Counterflow He II Heat Transfer Through Porous Media , *Adv. Cryog. Engn.* **Vol. 55**, 1327 (2010).
47. B. Baudouy, et al, Heat Transfer through Porous Media in Static Superfluid Helium, *Adv. Cryog. Engn.* **Vol. 51**, 409 (2006).
48. B. Maytal, J. A. Nissen and S. W. Van Sciver, Iso-chemical Trajectories in the P-T Plane for He II, *Cryogenics* **Vol. 30**, 730 (1990).
49. P. Kittel, Losses in Fountain Effect Pumps, in *Proc. 11th Intern. Cryog. Engn. Conf.*, Butterworth, UK (1986) pp. 317–322.
50. A.R. Urbach, J. Vorreiter and P. Mason, Design of a Superfluid Helium Dewar for the IRAS Telescope, in *Proc. 7th Intern. Cryog. Engn. Conf.*, IPC Science and Technology Press, UK (1978) pp. 126–133.

51. D. Petrac and P. V. Mason, Evaluation of Porous-Plug Liquid Separators for Space Helium Systems, in *Proc. 7th Intern. Cryog. Engn. Conf.*, IPC Science and Technology Press, UK (1978) pp. 120–5.
52. P. L. Kapitza, The Study of Heat Transfer on Helium II, *J. Phys. (USSR)* **4**, 181 (1941).
53. T. H. K. Frederking, Thermal Transport Phenomena at Liquid Helium II Temperatures, *Adv. Cryog. Heat Transfer* **64**, 21 (1968).
54. N. S. Snyder, Heat Transport through Helium II: Kapitza Conductance, *Cryogenics* **Vol. 10**, 89 (1970).
55. L. J. Challis, Experimental Evidence for a Dependence of the Kapitza Conductance on the Debye Temperature of a Solid, *Phys. Lett.* **26A**, 105 (1968).
56. M. Khalatnikov, *Introduction to the Theory of Superfluidity*, Chap. 111, W. A. Benjamin, New York, 1965.
57. R. E. Peterson and A. C. Anderson, The Kapitza Thermal Boundary Resistance, *J. Low Temp. Phys.* **11**, 639 (1973).
58. L. J. Challis, K. Dransfeld, and J. Wilks, Heat Transfer Between Solids and Liquid Helium II, *Proc. R. Soc. London* **A260**, 31 (1961).
59. D. Cheeke and H. Ettinger, Macroscopic Calculation of the Kapitza Resistance Between Solids and Liquid ^{4}He, *Phys. Rev. Lett.* **37**, 1625 (1976).
60. P. H. E. Meijer and J. S. R. Pert, New Kapitza Heat Transfer Model for Liquid ^{4}He, *Phys. Rev. B* **22**, 195 (1980).
61. J. Wilks, *The Properties of Liquid and Solid Helium*, Chap. 14, Clarendon Press, Oxford, 1967.
62. B. W. Clement and T. H. K. Frederking, Thermal Boundary Resistance and Related Peak Flux During Supercritical Heat Transport from a Horizontal Surface Through a Short Tube to a Saturated Bath of Liquid Helium II, *Liquid Helium Technology, Proceedings of the International Institute of Refrigeration*, Commission I, Boulder, CO, Pergamon Press, Oxford, 1966, pp. 49–59 (see also Ref. 29).
63. K. Mittag, Kapitza Conductance and Thermal Conductivity of Copper, Niobium, and Aluminum in the Range from 1.3 to 2.1 K, *Cryogenics* **13**, 94 (1973).
64. S. W. Van Sciver, Kapitza Conductance of Aluminum and Heat Transport from a Flat Surface through a Large Diameter Tube to Saturated He II, *Adv. Cryog. Eng.* **23**, 340 (1977).
65. G. Claudet and P. Seyfert, Bath Cooling with Subcooled Superfluid Helium, *Adv. Cryog. Eng.* **27**, 441 (1981).
66. S. W. Van Sciver, Developments in He II Heat Transfer and Applications to Superconducting Magnets, *Adv. Cryog. Eng.* **27**, 375 (1981).
67. A. Kashani and S. W. Van Sciver, Kapitza Conductance of Technical Copper with Several Different Surface Preparations, *Cryogenics* **25**, 238 (1985).
68. H. P. Kramer, Heat Transfer to Forced Flow Helium II, in *Proc. 12th Intern. Cryog. Engn. Conf.*, Southampton, UK, Butterworth, UK, 1988, pp. 299–304.
69. J. G. Weisend II and S. W. Van Sciver, Surface Heat Transfer Measurements in Forced Flow He II, in *Superfluid Helium Heat Transfer*, ASME HTD-Vol. 134 ed. J. P. Kelly and W. J Schneider, 1990, pp 1–7.
70. A. C. Leonard, Helium I Noise Film Boiling and Silent Film Boiling Heat Transfer Coefficient Values, in *Proc. 3rd Intern. Cryog. Engn. Conf.*, pp. 109–114, ILIFFE Science and Tech. Publications, Guilderford, Surrey, U.K., 1970.
71. R. K. Irey, Heat Transport in Liquid Helium II, in *Heat Transfer at Low Temperatures*, W. Frost (Ed.), Plenum Press, New York, 1975.
72. K. R. Betts and A. C. Leonard, Free Convection Film Boiling from a Flat, Horizontal Surface in Saturated He II, *Adv. Cryog. Eng.* **21**, 282 (1975).
73. J. S. Goodling and R. K. Irey, Non-Boiling and Film Boiling Heat Transfer to a Saturated Bath of Liquid Helium, *Adv. Cryog. Eng.* **14**, 159 (1969).
74. R. C. Steed and R. K. Irey, Correlation of the Depth Effect on Film Boiling Heat Transfer in Liquid Helium I, *Adv. Cryog. Eng.* **15**, 299 (1970).

75. R. M. Holdredge and P. W. McFadden, Boiling Heat Transfer from Cylinders in Super-fluid Liquid Helium II Bath, *Adv. Cryog. Eng*. **11**, 507 (1966).
76. M. Nozawa, N. Kimura, M. Murakami and S. Takada, Thermo-fluid Dynamics of Several Film Boiling Modes in He II in the Pressure Range between Atmospheric Pressure and Saturated Vapor Pressure, *Cryogenics* **Vol. 49**, 583 (209).
77. S. Takada, M. Murakami, and N. Kimura, Heat Transfer Characteristics of Four Film Boiling Modes Around a Horizontal Cylindrical Heater in He II, *Adv. Cryog. Engn.* Vol. 55A, 1355 (2010).
78. W. J. Rivers and P. W. McFadden, Film-Free Convection in Helium II, *Trans. ASME, J. Heat Transfer*, **88C**, 343 (1966).
79. D. A. Labuntzov and Ye. V. Ametistov, Analysis of Helium II Film Boiling, *Cryogenics* **19**, 401 (1979).
80. P. L. Bhatnager, E. P. Gross, and M. Krook, A Model for Collision Processes in Gases. I. Small-Amplitude Processes in Charged and Neutral One-Component Systems, *Phys. Rev*. **94**, 511 (1954).
81. A. P. Kryukov and S. W. Van Sciver, Calculation of the Recovery Heat Flux from Film Boiling in Superfluid Helium, *Cryogenics* **21**, 525 (1981).
82. G. D. Lemieux and A. C. Leonard, Maximum and Minimum Heat Flux in Helium II for a 76.2 μm Diameter Horizontal Wire at Depths of Immersion Up to 70 cm, *Adv. Cryog. Eng*. **13**, 624 (1968).
83. S. W. Van Sciver, Correlation of Time Dependent Recovery from Film Boiling Heat Transfer in He II, *Cryogenics* **21**, 529 (1981).

Further Readings

F. P. Incropera and D. P. Dewitt, *Fundamentals of Heat Transfer*, Wiley, New York, 1981.
G. E. Myers, *Analytical Methods in Conduction Heat Transfer*, McGraw-Hill, New York, 1971.
S. W. Van Sciver, He II (Superfluid Helium), Chapter 10 in *Handbook of Cryogenic Engineering*, ed. J. G. Weisend II, Taylor & Francis, Washington, DC (1998), pp. 445–483.
J. Wilks, *The Properties of Liquid and Solid Helium*, Chap. 14, Clarendon Press, Oxford, 1967.

Chapter 8
Liquefaction and Refrigeration Systems

Although the emphasis of this book is on the development of a physical understanding of helium as a cryogenic fluid, the discussion would be incomplete without at least an overview of the various methods of obtaining low-temperature helium. Such methods are based solidly in engineering thermodynamics and rely primarily on a combination of processes that make up a thermodynamic cycle. A thermodynamic cycle consists of a closed circuit where the working fluid, for example helium, is compressed, expanded, and heat exchanged in such a way as to achieve cooling. The most thermodynamically ideal cycle is the Carnot cycle which consists of a combination of isothermal and isentropic processes. However, the Carnot cycle is difficult, if not impossible, to achieve in a practical system. Real refrigeration and liquefaction systems are made up of similar processes and are usually compared in their performance to that of the ideal Carnot cycle. These issues form the content of the present chapter.

Here we will only consider cycles that use working fluids in their processes. The topic of refrigeration using magnetic materials is discussed in Chap. 10. In most gas refrigeration cycles, the cooling is achieved by an expansion process from high to low pressure. There are mainly two types of gas expansion that we will consider. *Isentropic expansion* is that where the fluid does work and expands slowly and reversibly such that its entropy is constant ($\Delta S = 0$). This is the best method of expansion because there is no entropy generation and it therefore produces the largest temperature change for a given pressure change. The other common gas expansion process is *isenthalpic expansion,* where the fluid undergoes a pressure change without heat transfer ($\Delta Q = 0$) but no work is done and the process is irreversible. Isenthalpic expansion is common in practical refrigeration systems for its ease of use. However, it is of lower thermodynamic efficiency because it is an irreversible process resulting in an increase of entropy ($\Delta S > 0$).

A further distinction between different refrigeration cycles has to do with whether the cycle involves steady flows or oscillatory flows. In the former case, the flow that initiates at the high pressure point at the exit of the compressor passes continuously through a closed circuit consisting of heat exchangers and expansion devices extracting the heat load and ultimately returning to the compressor inlet.

S.W. Van Sciver, *Helium Cryogenics*, International Cryogenics Monograph Series,
DOI 10.1007/978-1-4419-9979-5_8,

Such cycles are referred to as *recuperative*. The other class of refrigeration cycles involves oscillatory flows that intermittently expand and compress the gas exchanging heat with a thermal reservoir or regenerator. In these cycles a unit of fluid moves back and forth between regions of high and low pressure and temperature exchanging heat with a regenerator. These cycles are therefore referred to as *regenerative*.

The present chapter begins with an ideal liquefaction process as a point of comparison. A number of practical recuperative cycles commonly used for cryogenics are then discussed. A comparison between liquefaction and refrigeration is given including some aspects of component non-ideality. This discussion is then followed by an introduction to regenerative refrigeration cycles and their practical embodiment in modern cryogenic refrigerators.

8.1 Ideal Liquefaction

The thermodynamic limitations of the liquefaction process can be demonstrated best by consideration of an ideal system, that is, a cycle that performs at Carnot efficiency and consequently consists of reversible isothermal and isentropic processes. The purpose of this cycle is to cool a fluid from ambient to its normal boiling point and then condense it into liquid.

We will first consider a Carnot refrigerator producing cooling to a low-temperature reservoir. Furthermore, unlike the discussion in the previous section, we assume that the refrigerator consists of a large number of cycles each producing an incremental temperature decrease of the working fluid. This process can be thought to occur physically by a large number of reservoirs operating at intermediate temperatures T_i as in Fig. 8.1. The total cycle is then the sum over all these cycles, the continuous version of which becomes an integral between T_H and T_C.

Therefore, an ideal Carnot refrigerator achieves a certain amount of cooling at T_C by performing a continuous process [1]. The work done to carry out this process can be approximated by an integral expression,

$$w = -\int_{T_H}^{T_C} \frac{dQ}{T}(T_H - T) \tag{8.1}$$

where each increment of refrigeration operates between T_H and T. To produce liquefaction in a liquid–gas system, there are two contributions to the work that must be included:

1. w_g is the work required to cool a unit mass of gas from ambient temperature to its boiling point T_{bp}.
2. w_l is the work required to convert a unit mass of gas at T_{bp} to a unit mass of liquid.

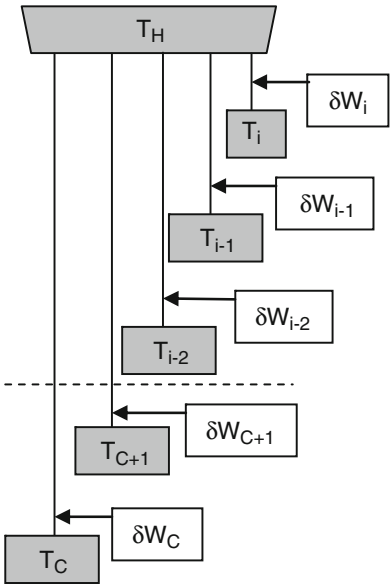

Fig. 8.1 A series of infinitesimal Carnot refrigerators

The second term, which is the liquefaction work, always operates between T_{bp} and T_H. For this term $dQ = T\Delta s = h_{fg}$, the latent heat per unit mass of liquefied gas. The integral in (8.1) then collapses to its value at the low temperature end T_{bp}, yielding the second contribution to the work,

$$w_l = h_{fg}\left(\frac{T_H}{T_{bp}} - 1\right) \tag{8.2}$$

It is quite apparent in (8.2) that the term in brackets simply represents the coefficient of performance of a Carnot refrigerator operating between T_{bp} and T_H.

The total work w_T to liquefy a unit mass of gas is simply a sum of the above two terms. Rearranging w_T in a form that is easier to evaluate, we obtain

$$w_T = T_H\left(\int_{T_{bp}}^{T_H}\frac{C_p}{T}dT + \frac{h_{fg}}{T_{bp}}\right) - \left(\int_{T_{bp}}^{T_H} C_p dT + h_{fg}\right) \tag{8.3}$$

Cast in this way, the total work can be seen to consist of two quantities. The first represents the entropy difference between the gas at room temperature and the liquid at T_{bp}. The second term is the heat or enthalpy difference between the gas at room temperature and the liquid at T_{bp}. Note that this quantity enters as a negative because it is thermodynamically recoverable.

The above definitions can be placed on clearer footing by consideration of a T-S diagram for a real fluid. An idealized example of such a diagram is shown in Fig. 8.2. Achievement of liquefaction as described above can be identified on this

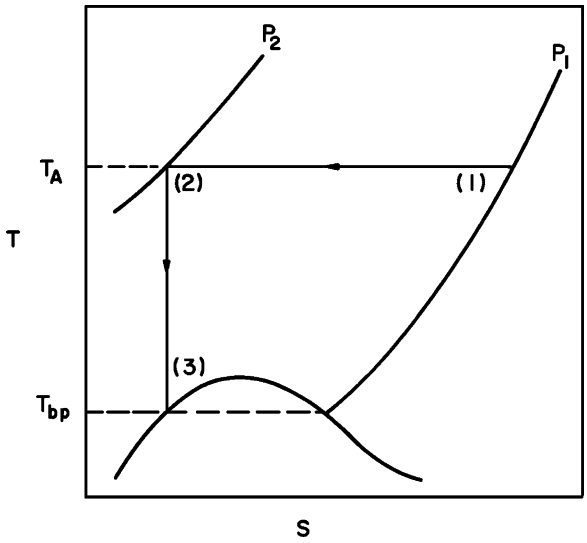

Fig. 8.2 *T-S* diagram showing ideal liquefaction process 1 → 3

diagram by the path 1-2-3. Here, step 1–2 is an isothermal process followed by step 2–3 which is an isentropic expansion of the fluid to the normal boiling point T_{bp}.

In practical terms, the flow circuit used to achieve this process is shown in Fig. 8.3. Here there are two principal components. An isothermal compressor brings the fluid to high pressure, p_2, at which point the entropy is the same as the liquid at the normal boiling point. The isentropic expansion engine then reduces the fluid temperature until it is converted to a liquid. The total work per unit mass of fluid (8.3) is therefore given by the difference in the state functions evaluated at the end points of the ideal liquefaction path,

$$w_t = T_H(s_1 - s_3) - (h_1 - h_3) \tag{8.4}$$

Typically, for real fluids, these quantities are tabulated, permitting the above calculation to be performed trivially. However, for the case concerning helium, which is nearly an ideal gas, these functions can also be calculated with reasonable accuracy from (8.3). It is instructive to perform this calculation as an example to appreciate better the numerical values associated with the liquefaction process.

The two contributions to the liquefaction work of helium are the enthalpy and entropy terms. The enthalpy term is

$$\Delta h = \int_{T_{bp}}^{T_H} C_p dT + h_{fg}. \tag{8.5}$$

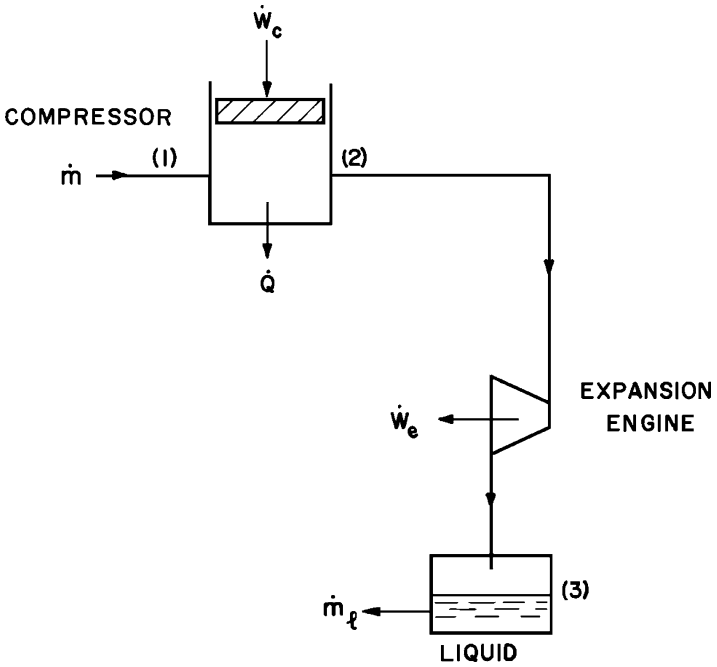

Fig. 8.3 Flow circuit for ideal expansion liquefier

Since helium is a good approximation to an ideal monatomic gas, we substitute a constant value for the heat capacity, $C_p \simeq \frac{5}{2}R = 20.8$ J/mol K. The latent heat of helium is tabulated and is a temperature-dependent quantity but at its normal boiling point of 4.2 K, $h_{fg} = 84$ J/mol. Combining these two contributions in (8.5) the result is

$$\Delta h = 20.8\,J/mol\,K(300 - 4.2)\,K + 84\,J/mol = 6237J/mol$$

where the high temperature is set arbitrarily to 300 K. Note that helium has a very small latent heat compared to other common fluids, a fact due to weak intermolecular binding which is discussed further in Chap. 3; thus, the vast majority of the work to liquefy helium goes into cooling the gas to the liquefaction temperature. This is not necessarily the case for liquefaction of other cryogenic fluids.

The entropy contribution to the liquefaction of helium can be calculated similarly,

$$\Delta s = \int_{T_{bp}}^{T_H} \frac{C_p}{T} dT + \frac{h_{fg}}{T_{bp}} \tag{8.6}$$

which for helium, as a nearly ideal gas, can also be evaluated directly between ambient temperature and the normal boiling point as,

Table 8.1 Ideal liquefaction work of cryogenic fluids

Fluid	T_{bp} (K)	W_T (kJ/kg)	W_T (kW h/L)
O_2	90	634	0.202
Ar	87	476	0.188
Air	80	722	0.176
N_2	77	761	0.171
H_2	20.4	11,890	0.231
He	4.2	6,850	0.236

$$\Delta s \simeq 20.8 \frac{J}{molK} \ln\left(\frac{300}{4.2}\right) + \frac{84}{4.2} \frac{J}{molK} = 109\ J/molK$$

Here it is useful to note that the latent heat contribution is significant, representing about 20% of the entropy difference term. Combining the enthalpy and entropy terms, we calculate that the ideal work to liquefy a unit of helium as 26,463 J/mol or 6615 kJ/kg. At saturated vapor pressure densities this work per unit volume of liquid is 0.236 kW h/L. Thus, it appears that for an ideal liquefier the cost of liquefaction in terms of electricity is not a major factor. It should be emphasized, however, that real liquefiers of helium are far from ideal, typically operating at between 2% and 25% Carnot efficiency, see Sect. 8.8.

As has already been indicated, the above calculation was performed to demonstrate the importance of different terms in the liquefaction process. A simpler and more accurate procedure uses tabulated values for entropy and enthalpy; then calculates the work trivially by means of (8.4). T-S-H diagrams that give these values for helium in graphical form are given in Appendix A.5. Also, there are tabulated data available in the literature [2] and in database programs [3, 4]. To use the *T-S-H* diagrams directly to calculate ideal liquefaction work, points (1) and (3) of the liquefaction path must be located. Point (1) represents helium at a temperature and pressure of 300 K and 0.1 MPa. At this point the entropy and enthalpy are [3],

$$s_1 = 31.6 kJ/kg\ K \quad \text{and} \quad h_1 = 1574 kJ/kg$$

At point (3), the saturated liquid state at 4.2 K and 0.1 MPa,

$$s_3 = 3.55 kJ/kg\ K \quad \text{and} \quad h_3 = 9.9 kJ/kg$$

Insertion of these values into (8.4) yields $w_T = 6850$ kJ/kg, quite close to that calculated using the ideal gas law above. This result is in part a demonstration of the near ideality of helium gas.

In summary and for comparison, Table 8.1 lists most of the common cryogenic fluids including helium with their ideal work to liquefy a unit mass and volume. In each case, these values are obtained from the tabulated state properties of the respective fluids. It is interesting to note that all these fluids have w_T within 20% of 0.2 kW h/L, a quantity that has no fundamental significance but is useful to keep in mind for calculation purposes.

8.2 First Law of Steady Flows

In advance of discussing the more practical aspects of helium liquefaction and cooling, it is necessary to introduce the important concept known as the first law of steady flows. This concept is useful because actual liquefaction processes occur in the steady flow conditions through a cycle and not strictly at thermodynamic equilibrium.

The first law of steady flows can be understood best by reference to Fig. 8.4. Here a unit volume of helium is considered where the symbols are identified as follows:

- Rate of heat removed from unit volume, $\dot{Q}$
- Rate of work done on the fluid in volume, $\dot{W}$
- Mass flow rate, $\dot{m}$
- Specific enthalpy of the fluid, h
- Specific entropy of the fluid, s

For simplicity we neglect changes in the potential and kinetic energies. For helium these terms are generally quite small and their inclusion would serve only to complicate the derivations at hand. Now although the unit of fluid is in motion, it still represents a thermodynamic system. One can understand this statement by transforming into the frame of reference of the moving fluid. In the frame moving at a velocity, $u = \dot{m}/\rho A$, a unit mass of fluid moves throughout the cycle undergoing various thermodynamic processes which can be calculated as if it were in thermodynamic equilibrium. Of course, one additional requirement is that the fluid velocity be low compared to the sound speed to avoid compressibility effects.

It is reassuring to note that introduction of the above concept does not significantly modify the thermodynamic relationship already introduced for the work necessary to liquefy a unit mass of fluid (8.4). The only variation is to redefine the work on a unit mass flow basissuch that (8.4) is rewritten in the form,

$$\frac{\dot{W}}{\dot{m}} = T_H \Delta s - \Delta h \tag{8.7}$$

where the entropy and enthalpy differences are per unit mass.

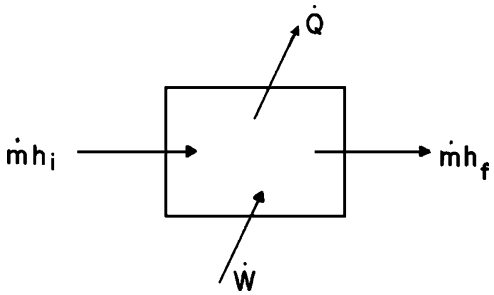

Fig. 8.4 Unit volume illustrating the first law of steady flows

To understand better the discussion of practical refrigeration systems, it is helpful to define several quantities related to continuous flow refrigeration:

- Work per unit mass compressed, $\dot{W}/\dot{m}$.
- Work per unit mass liquefied, $\dot{W}/\dot{m}_l$.
- Fraction of mass flow liquefied or yield, $y = \dot{m}_l/\dot{m}$.

An optimized practical design endeavors to minimize $\dot{W}/\dot{m}_l$, and maximize the yield y. In addition, there are several terms useful in the identification of the thermodynamic efficiency of a particular refrigeration cycle. It follows from (1.6) that the coefficient of performance (COP) in a flow system is the ratio of the heat removed at low temperature to the work at high temperature:

$$\mathrm{COP} = \frac{\dot{Q}_c}{\dot{W}} \tag{8.8}$$

Obviously, for a Carnot cycle, $\mathrm{COP} = T_C/(T_H - T_C)$. As a measure of the deviation from Carnot efficiency, a quantity referred to as the figure of merit (FOM) is defined as the ratio of the ideal Carnot work $\left(\dot{W}_i\right)$ and actual rate of work done $\left(\dot{W}\right)$ such that

$$\mathrm{FOM} = \frac{\dot{W}_i}{\dot{W}} \tag{8.9}$$

Proper design will attempt to maximize FOM as much as is reasonable. Typically, the highest efficiency helium refrigerators have FOM $\approx$ 25%.

8.3 Isenthalpic Expansion

Up until now refrigeration or liquefaction has been considered only in terms of the ideal processes involved. Furthermore, the methods by which this refrigeration occurs have not been thoroughly identified. In an effort to approach more realistic refrigeration systems, the present section considers one of the most common refrigeration/liquefaction processes, that of isenthalpic expansion also known as the Joule–Thomson effect. As will become evident, this process is most useful in refrigeration systems involving higher boiling point cryogens (e.g. LN_2, LO_2). Its use in helium liquefaction is mainly in the final expansion stage of a more complex cycle.

8.3.1 Joule–Thomson Effect

The Joule–Thomson effect was one of the first methods used in liquefaction of cryogenic fluids. The method consists of performing an isenthalpic expansion of the

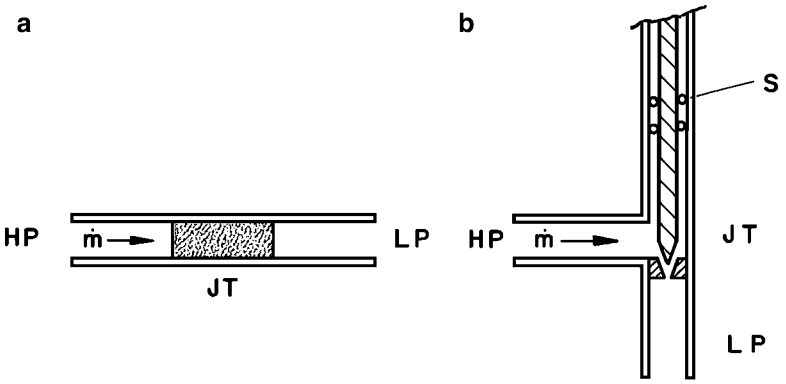

Fig. 8.5 Two types of Joule–Thomson valve: (**a**) porous plug and (**b**) controllable needle valve

fluid through a valve or other flow constriction capable of sustaining a relatively large pressure drop. By definition there is no work done by the fluid but the process can be made to be adiabatic by insulating the constriction; it is still irreversible. In practice, there are several methods by which the Joule–Thomson effect is achieved. A simple and direct method is to place a porous plug within an insulated channel such that the pressure drop through the media is about right for the desired flow conditions. This concept, illustrated in Fig. 8.5a, can be nearly isenthalpic because the channel is insulated, giving adiabatic conditions ($\dot{Q} = 0$). However, porous plugs are not adjustable so care must be exercised in choosing the proper flow resistance for the desired operating conditions. An alternative to the porous plug J-T valve is to use an adjustable needle valve that restricts the pressure drop to occur over a small region (Fig. 8.5b). For the needle valve, thermodynamic ideality is not strictly achieved because the system is not totally insulated due at least to the conducted heat load down the valve stem. However, this inefficiency must be weighted against the adjustability and ease of operation that accompany the JT valve.

In either case, the J-T valve has one purpose and that is to allow isenthalpic expansion of the fluid. Isenthalpic expansion means that the specific enthalpy of the fluid entering the valve must equal that of the exiting fluid, which is at lower pressure. It follows that differential cooling can only be achieved if the constant enthalpy curve in p-T space has a positive slope. This requirement can be explained in more common terms by introduction of what is called the Joule–Thomson coefficient μ_j, which is simply the slope of a constant enthalpy curve in p-T space:

$$\mu_j \equiv \left(\frac{\partial T}{\partial p}\right)_h \tag{8.10}$$

To achieve cooling by the Joule–Thomson effect, this quantity must be positive. However, for real gases, μ_j can be either positive or negative depending on the state of the fluid. Note that the Joule–Thomson coefficient was previously introduced in

the discussion of real gas behavior in Chap. 3 and to explain the temperature profile in forced flow compressible helium in Chap 4.

The form of μ_j as given in (8.10) is not particularly useful for understanding the physical processes involved; however, it can be cast in more meaningful context by some standard thermodynamic manipulations. Using a theorem of partial differentiation, we can rewrite the Joule–Thomson coefficient as

$$\mu_j = -\left(\frac{\partial T}{\partial h}\right)_p \left(\frac{\partial h}{\partial p}\right)_T \tag{8.11}$$

The enthalpy h is a state function that can be expanded in terms of p and T such that

$$dh = \left(\frac{\partial h}{\partial T}\right)_p dT + \left(\frac{\partial h}{\partial p}\right)_T dp \tag{8.12}$$

But the enthalpy also has a familiar differential form,

$$dh = T\ ds + v\ dp \tag{8.13}$$

The first term on the right-hand side of (8.13) can be rearranged by use of a $T\ ds$ equation for single phase fluids,

$$T\ ds = C_p dT - T\left(\frac{\partial v}{\partial T}\right)_p dp \tag{8.14}$$

where the constant pressure specific heat is,

$$C_p = T\left(\frac{\partial s}{\partial T}\right)_p \tag{8.15}$$

and the second term was modified by the use of the Maxwell relation,

$$\left(\frac{\partial v}{\partial T}\right)_p = -\left(\frac{\partial s}{\partial p}\right)_T \tag{8.16}$$

Equating common terms in (8.12), (8.13), and (8.14), we can do a straightforward calculation to produce the relationship for μ_j, in terms of useful thermodynamic functions:

$$\mu_j = \frac{1}{C_p}\left[T\left(\frac{\partial v}{\partial T}\right)_p - v\right] \tag{8.17}$$

Based on (8.17), the only additional information required to complete the form for μ_j are the equation of state and the constant pressure specific heat C_p. In actual fact, the most important issue is to determine the locus of points in p-T space below which the Joule–Thomson coefficient is positive. The curve that describes these points is referred to as the inversion curve and is defined by the location where $\mu_j = 0$.

The inversion curve can be derived for any gas with an established equation of state. The most simple of equations of state is that for an ideal gas, $pv = RT$, for which the Joule–Thomson coefficient is always zero as can be seen by substitution into (8.17). Therefore, there would be no cooling (or warming) of an ideal gas that undergoes isenthalpic expansion. This is a clear statement that the Joule–Thomson effect is a second-order process brought on by non-ideality of gases.

To understand physically how μ_j can be nonzero, we return to the original thermodynamic relationship (8.11) and note that the specific enthalpy may be written

$$h = e + pv \tag{8.18}$$

where e is the specific internal energy of the fluid. Substituting (8.18) into (8.11), one obtains a different relationship for μ_j,

$$\mu_j = -\frac{1}{C_p}\left[\left(\frac{\partial e}{\partial p}\right)_T + \left(\frac{\partial (pv)}{\partial p}\right)_T\right] \tag{8.19}$$

The first term within the parentheses, $(\partial e/\partial p)_T$, represents the deviation from ideal gas behavior of Joule's law; since $e = C_v T$. For an ideal gas this term is zero, but for real gases where there are interactive potentials between molecules, $(\partial e/\partial p)_T$ is always negative. It is easy to understand why this is true. Consider a volume containing a unit mass of gas at constant temperature. If the volume is reduced, a result of increasing the external pressure, the average intermolecular spacing decreases. Joule's law is derived by assuming all the energy within the gas is in the form of random kinetic energy of the molecules. However, as the real gas is compressed, some of this kinetic energy is converted to potential energy, thus decreasing the internal energy of the system and making $(\partial e/\partial p)_T < 0$.

The second term in (8.19) can be either positive or negative. In simple terms, it measures the deviation from Boyle's law, which states that $pv = f(T)$ only, a behavior obviously obeyed by an ideal gas. This term can be understood best by taking limiting values. At high temperature and high pressure, the molecules in the gas are brought close together but have large kinetic energies so that they are mostly affected by the repulsive term in the potential. The temperature must be high so the effect of the attractive term in the potential is negligible. This effect was discussed in Chap. 3 and manifests itself in a compressibility factor, $Z > 1$. Therefore, since the repulsive interaction makes the gas less compressible than an ideal gas,

$$\left(\frac{\partial (pv)}{\partial p}\right)_T > 0$$

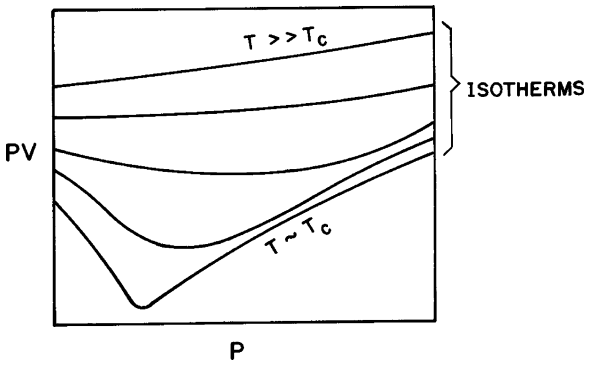

Fig. 8.6 Variation of pv as a function of absolute pressure for a real gas (From Barron [5]).

The behavior of this term at relatively low pressures and temperatures is considerably different. Specifically, this region is more strongly affected by the attractive term of the potential. This term tends to make the gas effectively more compressible because the fluid is approaching the condensation temperature and

$$\left(\frac{\partial(pv)}{\partial p}\right)_T < 0$$

The behavior of both contributions to the pv term in (8.19) are summarized in Fig. 8.6.

8.3.2 Joule–Thomson Coefficient of Real Gases

The thermodynamic properties of a real gas are described best in terms of an empirical equation of state. In Chap. 3, several equations of state appropriate for helium gas have been introduced. Here the Joule–Thomson coefficient is evaluated using one of these classical equations of state.

The most common classical equation of state is that of a van der Waals gas, see Sect. 3.2.3. As stated previously, this equation of state is given by the expression

$$\left(p + \frac{a}{v^2}\right)(v - b) = RT \tag{8.20}$$

Here a and b are constants listed in Table 3.2 that depend on the particular gas being approximated. For helium the values of these two constants are $a = 3.46$ m^6 kPa/kmol^2 and $b = 0.0237$ m^3/kmol. For the van der Waals equation of state the form of μ_j can be computed by differentiation and rearrangement of (8.20). Specifically, the volume derivative can be shown to be

$$\left(\frac{\partial v}{\partial T}\right)_p = \frac{R}{RT/(v-b) - (2a/v^3)(v-b)} \tag{8.21}$$

Substituting into (8.15) yields the equation for the Joule–Thomson coefficient,

$$\mu_j = \frac{1}{C_p}\left[\frac{(2a/RT)(1-b/v)^2 - b}{1-(2a/vRT)(1-b/v)^2}\right] \tag{8.22}$$

The above equation can be used to compute values of μ_j for a van der Waals gas as a function of temperature and specific volume, albeit a tedious process, see problem 8.3. As has been mentioned above, one point of interest is the location of the inversion temperature, below which the Joule–Thomson effect produces cooling. Since the inversion temperature T_{inv} is defined at $\mu_j = 0$, its form for a van der Waals gas can be determined by setting the numerator of (8.22) to zero. This gives,

$$T_{\text{inv}} = \frac{2a}{bR}\left(1 - \frac{b}{v}\right)^2 \tag{8.23}$$

which appears to be a relatively simple solution except for the fact that v is coupled to T through the equation of state. In p-T space the inversion curve of a van der Waals gas is a polynomial function.

A useful value to compute from the inversion curve is that of the maximum inversion temperatures T^m_{inv}. This value can be easily calculated from (8.23) by taking the low-density limit, i.e. taking $p \to 0$ or $v \to \infty$. For a van der Waals gas the solution for T^m_{inv} is in terms of the constants a and b:

$$T^m_{\text{inv}} = \frac{2a}{Rb} \tag{8.24}$$

Substituting the values for helium into (8.24) yields the value of $T^m_{\text{inv}} = 35.2$ K. Plotted in Fig. 8.7 is the actual inversion curve for helium [6]. Because of the small slope to the high-temperature isenthalps, it is difficult to determine accurately T^m_{inv}; however, for helium $T^m_{\text{inv}} \approx 45$ K, a quantity reasonably close to that determined by the van der Waals gas model.

There is practical significance to the fact that the helium inversion curve lies below 45 K. To achieve cooling by isenthalpic expansion requires that the helium entering the Joule–Thomson valve be at a temperature substantially below this value. Hydrogen and neon are the only fluids with normal boiling points below 45 K, hydrogen being the most abundant of the two. Consequently, in the early development of helium liquefaction capability it was necessary first to liquefy hydrogen and then to use the hydrogen bath to precool the incoming helium flow. Subsequently, other methods were developed to allow liquefaction without LH_2

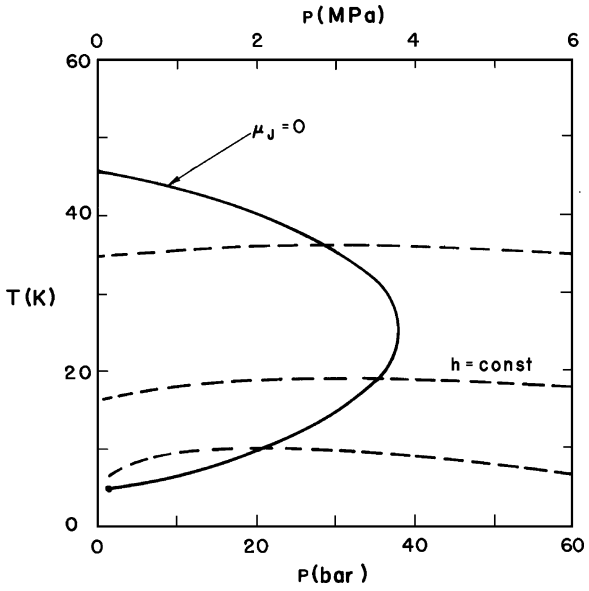

Fig. 8.7 Inversion curve for helium

precooling. However, it still remains a challenge to precool the helium to below the inversion curve so that the Joule–Thomson effect can be used.

Recall from Chap. 3 that the Law of Corresponding States and the van der Waals equation of state indicate that the two coefficients, a and b are given in terms of critical properties as,

$$a = \frac{27}{64}\frac{R^2 T_c^2}{p_c} \tag{8.25}$$

and

$$b = \frac{RT_c}{8p_c} \tag{8.26}$$

Since the Joule–Thomson coefficient is a function of the equation of state, the Law of Corresponding States should also give the inversion curve as universal function in terms of the reduced quantities, $\tau = T/T_c$ and $\pi = p/p_c$. For a van der Waals gas, the ratio of the maximum inversion temperature given by (8.24) to the critical temperature has a constant value of 6.75. Furthermore, the entire curve can be shown to obey a reduced form displayed in Fig. 8.8 [6]. This graph can be used to determine an approximate inversion curve for most common gases. However, it should be pointed out that the van der Waals equation of state is only one approximation to a real gas and others equations exist that give comparable shape to the inversion curve, see for example problem 8.1. Listed in Table 8.2 are the critical

Table 8.2 Critical point coefficients to the van der Waals equation of state and maximum inversion temperature for various cryogenic fluids

Fluid	T_c (K)	p_c (MPa)	a (m^6 kPa/$kmol^2$)	b (m^3/kmol)	T^m_{inv} (K)	T^m_{inv}/T_c
He	5.2	0.227	3.46	0.0237	45	8.3
H_2	33.2	1.315	24.4	0.0262	202	6.1
Ne	44.5	2.678	21.5	0.0173	260	5.9
$\mathbf{N_2}$	126.2	3.396	137	0.0386	623	4.9
O_2	154.6	5.043	138	0.0318	761	4.9

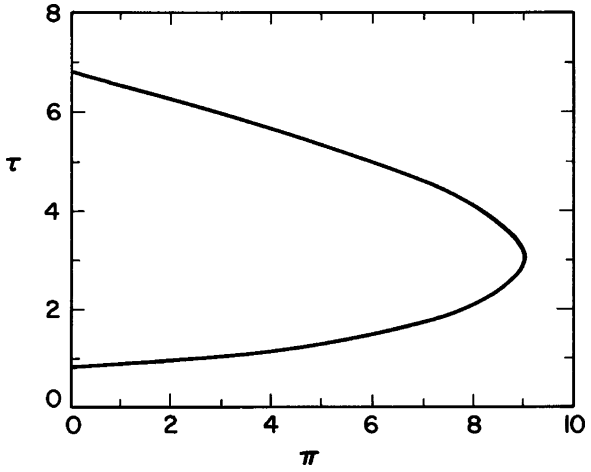

Fig. 8.8 Inversion curve for a van der Waals gas in terms of reduced pressure ($\pi = p/p_c$) and temperature ($\tau = T/T_c$) [6]

temperatures and maximum inversion temperatures for some cryogenic fluids. The reduced inversion temperature is approximately constant, with an increase for the case of helium where quantum effects would be expected to be largest.

Isenthalpic expansion for cooling of cryogenic fluids has advantages and disadvantages. What makes the method so useful is its ease of application. No moving parts are required and the J-T value is a relatively small, inexpensive component. A further advantage is that there is no major problem with expanding into the region of two-phase liquid vapor coexistence. Thus, the common application of a J-T value is at the final stage of a helium liquefaction system where the liquid actually is produced. However, as discussed above it is not possible to achieve helium liquefaction with only the Joule–Thomson effect unless the incoming fluid is somehow cooled to below 40 K. Thus, additional methods must be combined with the J-T expansion stage to achieve liquefaction. These methods, which are discussed below, may include precooling with another cryogenic fluid (like liquid hydrogen at 20 K) or adiabatic expansion of the incoming fluid requiring it to do work. The latter method has definite advantages as it uses the same working fluid and can be more efficient. This topic will be discussed further in Sect. 8.5.

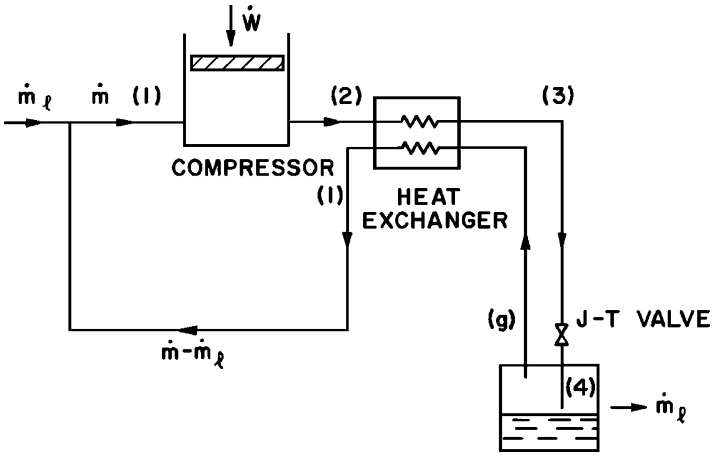

Fig. 8.9 Schematic diagram of Joule–Thomson liquefier

8.3.3 Joule–Thomson Liquefier

The simplest practical method to achieve liquefaction of helium is by direct application of the Joule–Thomson effect. However as was discussed above, it is necessary to begin this process inside the inversion curve, which for helium implies an initial temperature below about 40 K. This requirement will be overlooked for the time being. Future discussion will indicate how to bring the fluid below the inversion temperature initially. The Joule–Thomson liquefier is sometimes referred to as a simple Linde–Hampson system. This system provides a simple inexpensive method for liquefaction of a gas whose inversion temperature is above ambient, i.e. all gases except neon, hydrogen and helium. This method is also the basis for a wide range of small scale cryocoolers operating at intermediate temperatures (T ~ 100 K).

The principal components of the Joule–Thomson liquefier are shown in Fig. 8.9. In addition to the compressor stage, the system requires two components: a heat exchanger and a Joule–Thomson value. The heat exchanger, schematically shown in Fig. 8.9, is actually a rather complex component to design. A good heat exchanger has a number of desirable traits, all of which require careful attention to detail:

1. Maximum surface area for heat transfer.
2. Minimum resistance to fluid flow (Δp small).
3. Minimum mass (for cooldown).

Of the three characteristics listed, 1 and 2 are at least moderately counteractive, and therefore good design involves trade-offs between these two characteristics. It is necessary to be familiar with heat transfer and fluid flow characteristics of helium before discussing heat exchanger design. Chapters 4 and 5 consider these topics for helium in some detail. For the present discussion, it will be assumed that the heat exchanger is an ideal component, meaning that there is only heat transfer between the

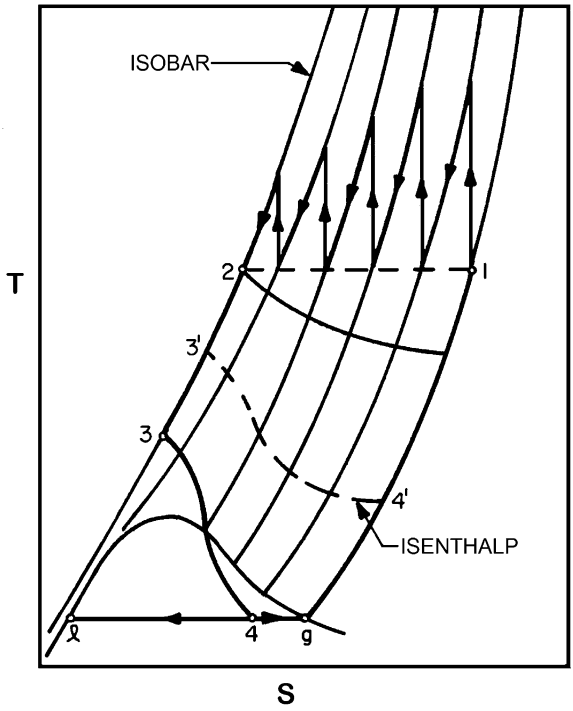

Fig. 8.10 *T-S* diagram showing isenthalpic expansion processes

high and low pressure gas flows, otherwise the system is adiabatic, $\dot{Q} = 0$. Furthermore, friction pressure drop across the heat exchanger will be neglected. It should be noted that the above assumptions can be substantially different from isothermal conditions, where the temperatures of the two gas streams are the same. This distinction will be clearer as examples are considered. In the thermodynamic language of cryogenic systems, heat exchangers are assumed to conserve enthalpy flow.

The other major component in the simple liquefier shown in Fig. 8.9 is the Joule–Thomson valve. As described in the previous section, the J-T valve performs an isenthalpic expansion of the high-pressure stream. Provided the inlet temperature is well below the inversion curve, the J-T expansion can produce a two-phase mixture of liquid and vapor helium. The yield of this expansion stage is determined by an enthalpy balance between the incoming high-pressure stream and the two coexisting phases at ambient pressure.

Another way of looking at the yield of a Joule–Thomson refrigerator is by reference to a *T-S* diagram; see Fig. 8.10. Here the points on the flow chart in Fig. 8.9 are indicated. The compressor stage involves step (1)–(2). A truly isothermal compression would follow a horizontal line on the *T-S* diagram; however, this is not realistic. Also shown in the figure is the path of a five-stage real compression process that consists of a series of isentropic compressions followed by an isobaric heat transfer to the reservoir. The reasons for this multistage process are discussed later.

The compression stage is followed by an isobaric heat exchange process that brings the gas from (2) to (3), reducing its temperature and entropy. The cooling used to bring the gas from (2) to (3) is transferred from the return low-pressure stream through the heat exchanger where the exiting gas is brought back to ambient conditions. Point (3) represents the inlet to the J-T valve. Step (3)–(4) is then an isenthalpic expansion into the two-phase coexistence region. In principle, it is easy to determine the liquefaction yield y by balancing the enthalpy of the high pressure fluid at the valve inlet to that of a mixture of the low pressure liquid plus vapor at the outlet. The fraction of gas which is not liquefied follows the isobaric return stage (g) to (1), where its enthalpy is used to cool the incoming fluid through the heat exchanger. Finally, since the return gas has a smaller mass flow by the amount liquefied, in advance of recompression there is a make-up flow added to the stream to maintain $\dot{m}$ constant.

The above description is a qualitative indication of the type of analysis that is necessary in the design of a Joule–Thomson liquefier. To make a more quantitative determination of the liquefaction fraction or yield of this system, it is necessary to invoke the first law of steady flows. For simplicity, we assume no work or external heat is applied to the system and that the heat exchanger conserves enthalpy. With this set of assumptions, the analysis requires writing down enthalpy conservation for the combination of the heat exchanger, Joule–Thomson valve, and liquid yield, that is,

$$\dot{m}h_2 = (\dot{m} - \dot{m}_l)h_l + \dot{m}_l h_l \tag{8.27}$$

where $\dot{m}_l$ is the liquid mass flow rate and h_l is the specific enthalpy of the liquid. Defining the yield or fraction liquefied as $y = \dot{m}_l/\dot{m}$, we can rearrange (8.27) to give an expression for this value as,

$$y = \frac{h_1 - h_2}{h_1 - h_l} \tag{8.28}$$

It is apparent from (8.28) that the working fluid must be below the inversion curve for the fluid to cool through the J-T valve. Unless the specific enthalpy of the high-pressure stream, h_2, is less than that of the low-pressure side, h_1, the quantity described by the right-hand side of (8.28) will always be negative, indicating that no liquid yield is possible. Note that the yield is only a function of the fluid properties and the compression ratio p_2/p_1. For a given fluid and initial temperature, the pressure is the only quantity that may be varied in the optimization process. This is a standard procedure for determining the best operating conditions of a particular system.

The maximum yield for the simple Joule–Thomson refrigerator occurs when h_2 in (8.28) is a minimum. This is a result of h_1 and h_l being fixed by boundary conditions. The minimum in h_2 is found by taking its derivative with respect to pressure and setting it equal to zero:

$$\left(\frac{\partial h_2}{\partial p}\right)_T = 0 \tag{8.29}$$

Referring to the definition of the Joule–Thomson coefficient, (8.10), we note that the above derivative can be written in terms of μ_j:

$$\left(\frac{\partial h}{\partial p}\right)_T = -\mu_j C_p \tag{8.30}$$

Therefore, the best place to begin an isenthalpic expansion is on the inversion curve, i.e. where $\mu_j = 0$.

Example 8.1

Calculate the yield for a simple Joule–Thomson system operating such that points (1) and (2) are fixed at 20 K.

Although this seems like an unphysical system, in principle it could be achieved by precooling the helium with a liquid hydrogen bath. The first question to ask is: What is the best operating pressure for p_2? The answer of course is derived by reference to the inversion curve, Fig. 8.7. Here at 20 K, the pressure corresponding to the inversion curve is about 3.8 MPa, a not unreasonable value for a helium compressor. Given the initial temperature and pressure, it is a straightforward process to determine the yield by substituting the tabulated values for the specific enthalpies into (8.28):

$$h_1(20\text{ K},\ 0.1\text{ MPa}) = 118.6 kJ/kg$$

$$h_2(20\,\text{K}, 3.8\text{ MPa}) = 108.0 kJ/kg$$

$$h_l(4.2\,\text{K}, 0.1\text{ MPa}) = 9.9 kJ/kg$$

The result of that calculation gives $y = 0.098$.

The yield of the liquefaction system is not the only factor to be considered when evaluating the quality of design. In particular, it is important to have a thermodynamically efficient process to minimize the work required. For an idealized system, such as the one considered here, it is possible to evaluate the work required to produce a unit mass of liquid and compare this value with the thermodynamically ideal process described earlier. To perform this calculation, we again assume that the various thermodynamic processes in the cycle are ideal. The work required for liquefaction is entirely that of the compressor which operates at constant temperature. The first law of steady flows, when applied to the compressor in the Joule–Thomson refrigerator, gives an expression for the compressor work

$$\frac{\dot{W}_c}{\dot{m}} = T(s_1 - s_2) - (h_1 - h_2) \tag{8.31}$$

where $\dot{m}$ is the total mass flow. To cast (8.31) in a form that is better compared with an ideal system, substitute the definition of yield,

$$y = \frac{\dot{m}_l}{\dot{m}} = \frac{h_1 - h_2}{h_1 - h_l}.$$

A general expression for the work per unit mass liquefied by this process is then

$$\frac{\dot{W}_c}{\dot{m}_l} = \left(\frac{h_1 - h_l}{h_1 - h_2}\right)[T(s_1 - s_2) - (h_1 - h_2)] \tag{8.32}$$

Rather than work out the value for (8.32) given a particular system, it may be more instructive to compare it with the ideal liquefaction system given by

$$\frac{\dot{W}_i}{\dot{m}_l} = T(s_1 - s_l) - (h_1 - h_l) \tag{8.33}$$

Then for the Joule–Thomson liquefier, the ratio of these two quantities, (8.32) and (8.33), gives the figure of merit,

$$FOM = \left(\frac{h_1 - h_2}{h_1 - h_l}\right)\left(\frac{T(s_1 - s_l) - (h_1 - h_l)}{T(s_1 - s_2) - (h_1 - h_2)}\right) \tag{8.34}$$

Example 8.2

Considered the above helium Joule–Thomson liquefier (Example 8.1) and calculate the figure of merit (FOM).

Since the system is initially at 20 K, with the high-pressure side at 3.8 MPa, the entropy of each state is known:

$$s_1(0.1\ \text{MPa}, 20\ \text{K}) = 17.52 kJ/kgK$$

$$s_2(3.8\ \text{MPa}, 20\ \text{K}) = 9.35 kJ/kgK$$

$$s_3(0.1\ \text{MPa}, 4.2\ \text{K}) = 3.55 kJ/kgK$$

Using these values gives a figure of merit of FOM = 11.4%. It should be noted that this value only takes into consideration the liquefaction between 20 and 4.2 K. To consider the overall efficiency of the liquefaction process, it would be necessary to include the stage operating between 300 K and 20 K. The above proviso makes the calculation of the work per unit mass liquefied from $(\dot{W}_c/\dot{m}_l)$ (8.32) incomplete as well.

A number of factors can contribute to inefficiencies in the system, tending to reduce the FOM below what is calculated for an ideal system. With respect to the compression stage, it must be borne in mind that a truly isothermal compressor is not realizable. Real compressors actually operate in a two-step process, the first being a near adiabatic compression followed by heat exchange with an isothermal

reservoir. This process, which is sometimes referred to as polytropic, is shown schematically in step (1)–(2) of Fig. 8.10. The isothermal compression is approximated by a multistage two-step process. The necessity to provide a multistage process occurs because the adiabatic compression causes rather large temperature increases in the gas that can cause damage to the equipment. Furthermore, a multistage process more closely approaches an isothermal process, as can be seen in the *T*-*S* diagram, and consequently is more thermodynamically efficient.

The problem of temperature rise in the adiabatic compression stage is demonstrated most dramatically by reference to an example. Assume it were desirable to achieve a single-stage compression of helium between 0.1 and 1.0 MPa at 300 K. This would consist of an adiabatic compression stage followed by an isothermal heat exchange. We can find out the result of this process by equating the entropy before and after compression,

$$s_1(300\ \text{K},\ 0.1\ \text{MPa}) = s_2(T_2,\ 1\ \text{MPa})$$

which determines the maximum temperature T_2. The result gives a rather high temperature at the end of compression, $T_2 \approx 750$ K. This condition can cause a number of undesirable effects including physical damage to the compressor and its lubricants. For efficiency as well as hardware limitations, it is therefore desirable to carry out multistage compression.

The above discussion assumes that the liquefaction system already has achieved the steady state and consequently all temperatures (1) through (4) are constant. In practice, the cooldown process is of equal concern particularly for dynamic cooling devices. The partial cooldown of a simple Joule–Thomson liquefier may be represented on the *T*-*S* diagram by the cycle (1)–(2)–(3′)–(4′). During this intermediate stage of operation, there would be no liquefaction and the mass flow would be constant throughout. The net effect of continuing the cooldown would be to reduce gradually (3′)–(3) and (4′) into the two-phase region to (4). Naturally, the rate at which the cooldown takes place depends on the thermal capacity of the system, mainly the heat exchangers. This fact points out the desirability of minimizing the mass of the refrigeration components, which is trait 3 of the characteristics of good refrigerator and heat exchanger design.

During the cooldown process, the fluid entering the JT expansion valve may temporarily have a temperature and pressure corresponding to a point outside the inversion curve. This would seem to imply a negative JT coefficient and thus no cooling. However, it is important to note that it is the integrated value of the JT coefficient over a finite pressure drop that determines whether cooling is achieved through a cycle. This point has been studied for many different fluids and conditions by Maytal [7].

8.3.4 Cascade JT Liquefier

The use of the intermediate-temperature fluids in the liquefaction of low-temperature liquids has been an established technique since the beginning of cryogenics. In fact the

concept was used by Pictet in the first liquefaction of O_2. The cascade liquefaction system, which is a special case of this concept, consists of a series of closed-cycle systems each using the change of state from liquid to gas to achieve cooling. Thus, a true cascade system employs working fluids with overlapping two-phase coexistence regions. The cascade system can have high thermodynamic efficiency but it is generally cumbersome because of the number of stages required. Furthermore, it is not possible to have a true cascade liquefier that produces liquid helium or even liquid hydrogen and neon because the critical points of these fluids are below the triple point of the next higher-temperature liquid. However, some aspects of the cascade system can be applied in the liquefaction of helium. Precooling of the gas in a liquefier consisting of heat exchangers, expansion engines, and a Joule–Thomson valve, cannot be considered a true cascade system, but the benefits are similar [8].

Figure 8.11 displays a hybrid JT-cascade system for liquefaction of helium. The flow diagram is for a helium liquefier using this method combined with a simple Joule–Thomson liquefier. The system consists of several circuits, each containing a different working fluid. All circuits, except the helium liquefier, operate in a closed-cycle mode, where the liquid reservoir simply provides the refrigeration for the next lower stage. Since this system uses the Joule–Thomson effect, it is only necessary for the working fluid to be below its inversion temperature before cooling can occur. Consequently, each working fluid can have a wider temperature span than with a conventional cascade system. The working fluids must have inversion temperatures above the boiling point of the next-higher working fluid in the system. In the case displayed in Fig. 8.11, the helium is precooled by a closed-cycle hydrogen liquefier. In turn, since the inversion temperature of hydrogen is 202 K, it can be precooled by liquid nitrogen or a similar boiling fluid with $T_{bp} < 202$ K. In this circuit it is possible to produce the liquid necessary to precool the hydrogen circuit with a simple nitrogen cycle, since T_{inv} of nitrogen is above room temperature. In principle, the above described hybrid JT-cascade system could be expected to produce liquid helium, although probably with low thermodynamic efficiency because of the compounding effect of numerous Joule–Thomson liquefiers, all of which operate at rather low figures of merit.

8.3.5 He II JT Liquefier

Production of the low-temperature phase of liquid helium, He II, is an area of special interest. Unlike normal helium liquefiers, these systems are not mass produced, but with the developments around such projects as the Large Hadron Collider, there is now considerable experience with large scale He II liquefaction and refrigeration [9, 10].

In most cases, He II liquefaction systems exist as an addendum to a normal helium closed-cycle refrigeration. Thus, the starting point for the low-temperature ($T \approx 1.8$ K) stage is often an isothermal bath of liquid helium near atmospheric pressure and about 4.2 K. This approach is not essential because it is equally

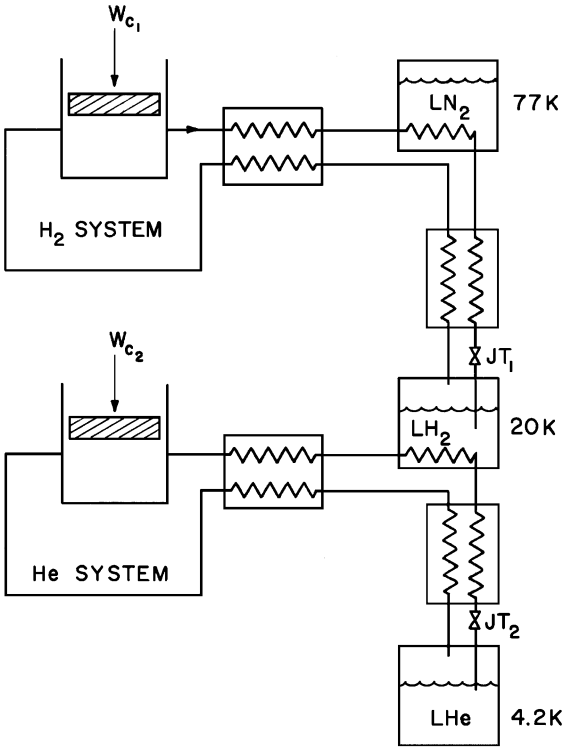

Fig. 8.11 Flow diagram for a hybrid cascade system for liquefaction of helium [8]

possible to expand directly to corresponding low pressures ($p < 5$ kPa). However, the existence of a normal helium bath allows its use in other parts of the system or to intercept heat leaks at higher temperature with improved thermodynamic efficiency.

A schematic of a He II liquefaction system using this concept is shown in Fig. 8.12. A second J-T valve operates between the normal helium bath and the low-temperature heat exchanger dropping the saturation pressure to $p \approx 1.6$ kPa corresponding to $T_b = 1.8$ K. The return flow of helium vapor is then available to precool the incoming fluid. This heat exchanger may be of an unconventional design because the low-density vapor has considerably different heat transfer and fluid flow characteristics [11].

Above the heat exchanger a compressor returns the flow to complete the circuit. The simplest approach, suitable for relatively small systems ($Q_c < 100$ W), is to recompress the helium vapor at ambient temperature with a conventional high-capacity vacuum pump operating between 1.6 and 100 kPa. Since the vacuum pump output is near atmospheric pressure it can then feed into the return line of the liquefier compressor. The disadvantage of this approach is that the vapor density is

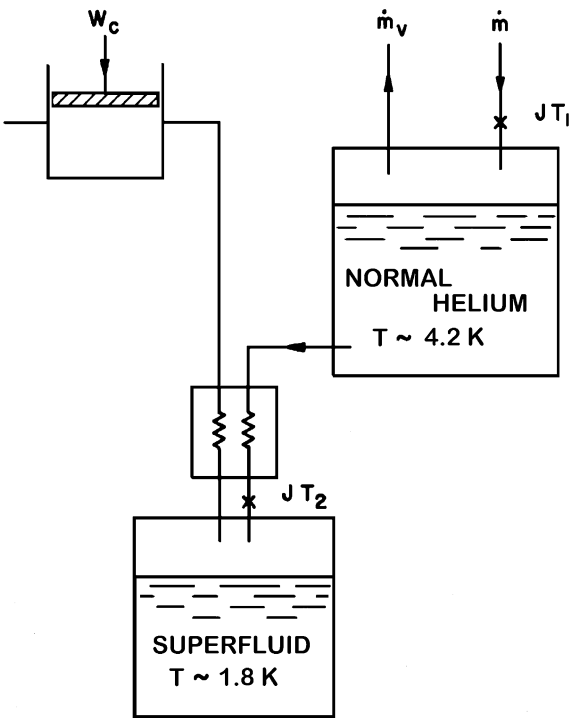

Fig. 8.12 Schematic of He II liquefaction/refrigeration system

too low to allow good heat exchange with incoming fluids, which works against the thermodynamic efficiency of the cycle.

An alternative method that is in use with large He II liquefier/refrigeration systems involves the use of cold compressors [12]. This method seems to contradict thermodynamic principle by performing work on a fluid at low temperature. However, the main advantage of improved heat transfer with the higher density gas is more important than the added compressor work. Such cold compressors typically have compression ratios (p_{out}/p_{in}) of about 10 requiring that there be multiple units in series to bring the gas pressure above ambient.

As a quantitative example of this technology, consider an isenthalpic expansion of helium from 0.1 MPa, 4.2 K to 1.6 kPa corresponding to the saturated vapor pressure at 1.8 K. A low-temperature helium *T*-*S* diagram is shown in Fig. 8.13. The expansion follows along path (1)–(2). Determination of the yield for the process is analogous to the methods applied above in conventional J-T helium liquefaction. By equating the enthalpies before and after expansion, we obtain an expression for the yield,

$$y = \frac{h_v - h_1}{h_v - h_l} \tag{8.35}$$

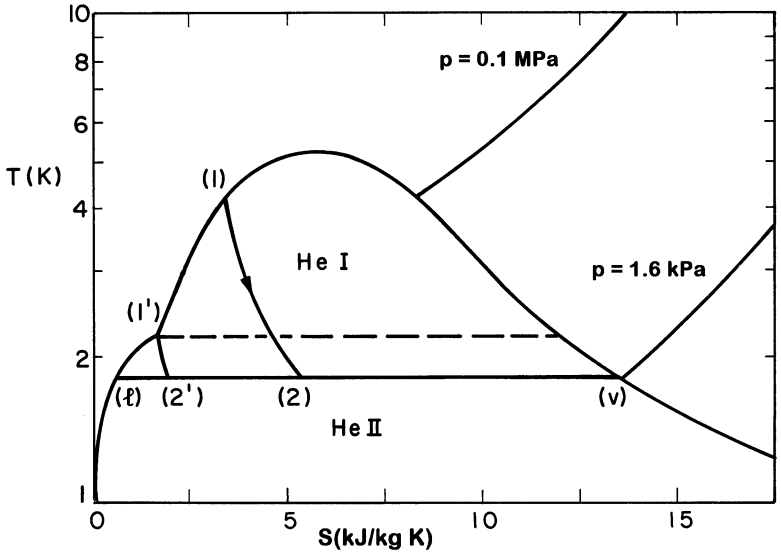

Fig. 8.13 Low temperature T-S diagram for helium showing both He I and He II regions and isenthalpic expansion to 1.8 K

where the subscripts apply to the various locations on the *T-S* diagram. For the process under consideration, the yield $y = 62\%$. Although this yield is fairly high it can be improved considerably by precooling the incoming fluid with the return vapor flow. For example if one is able to subcool the inlet to the J-T valve to 2.2 K, just above the λ-temperature, the isenthalpic expansion will follow path $(1')$–$(2')$ with a corresponding yield $y = 89\%$. See problem 8.8.

Before leaving the current subject, it is worth mentioning one potentially unique feature of a He II liquefaction/refrigeration system. As was discussed in Chap. 6, the saturated He II film attached to the surfaces above the liquid level in a bath can flow and carry heat as a result of a pressure or temperature difference. This film is known as the Rollin film. A potential technical problem occurs if the Rollin film reaches regions of higher than bath temperature and in turn conducts heat back into the bath. Also, the saturated film will have a higher vapor pressure than that of the bulk allowing preferential evaporation.

This problem is of greatest concern in small He II baths such as in laboratory size systems designed to reach as low temperature as possible. Since the film thickness is a function of the height above the liquid, small systems have a greater propensity for this problem. It probably has a negligible influence on large He II refrigeration systems such as for example are part of the LHC.

8.4 Isentropic Expansion

A thermodynamically more efficient method to achieve cooling of a liquid–gas system is to make the fluid do expansion work. If done carefully, this kind of expansion can be nearly adiabatic and reversible, thereby approaching an isentropic process, $\Delta s = 0$. Since the Carnot cycle is comprised of isothermal and isentropic stages, it is clear that the expansion by the performance of work is a very good method to produce cooling.

To determine the effectiveness of an expansion process for the production of cooling it is useful to define a parameter similar to the Joule–Thomson coefficient. This parameter, referred to as the isentropic expansion coefficient, μ_s, is equal to the slope of the constant entropy line in p-T space:

$$\mu_s = \left(\frac{\partial T}{\partial p}\right)_s \tag{8.36}$$

As before, this quantity may be expressed in terms of other common thermodynamic variables. By using an identity of partial differential equations and a Maxwell relation, the expression for μ_s becomes

$$\mu_s = \frac{T}{C_p}\left(\frac{\partial v}{\partial T}\right)_p \tag{8.37}$$

where use has been made of the definition for the constant pressure specific heat, $C_p = T\left(\frac{\partial s}{\partial T}\right)_p$. Comparison of (8.37) with (8.17) produces a simple relationship between the Joule–Thomson coefficient μ_j and the isentropic expansion coefficient μ_s:

$$\mu_j = \mu_s - \frac{v}{C_p} \tag{8.38}$$

Recall that for an ideal gas, $\mu_j = 0$, so in that case $\mu_s = v/C_p$. This latter expression clearly shows that isentropic expansion always produces a temperature drop since v/C_p is always a positive quantity. Thus, the isentropic process is not dependent on real gas behavior to achieve cooling.

Normally, one is interested in the change of the temperature caused by a finite pressure drop. For an ideal gas, where $pv = RT$, one can easily show by integration of (8.37) that the temperature ratio resulting from a given isentropic expansion pressure ratio is,

$$\ln\left(\frac{T_i}{T_f}\right) = \frac{R}{C_p}\ln\left(\frac{p_i}{p_f}\right). \tag{8.39}$$

For helium, which is nearly an ideal gas above 30 K, $R/C_p \sim 2/5$. For a pressure ratio of 10, the corresponding temperature ratio should be about 2.5; i.e. adiabatic expansion of helium gas from 1 MPa and 300 K to 0.1 MPa should result in final gas temperature of about 120 K.

For a real gas, μ_s and thus the temperature drop can be either greater or less than the value computed above. In particular, for the case of a van der Waals gas, applying the equation of state (8.20)–(8.37) yields an expression for μ_s,

$$\mu_s = \frac{v}{C_p}\left[\frac{1 - b/v}{1 - (2a/vRT)(1 - b/v)^2}\right] \tag{8.40}$$

where consistent with the initial statement, the quantity in brackets can be either greater or less than unity. However, unless the density and temperature are close to the critical point, this value does not deviate markedly from that of an ideal gas.

8.4.1 Claude Liquefier

The present section summarizes how to employ isentropic expansion by the performance of work as part of a helium liquefaction or refrigeration system. Since the maximum inversion temperature for helium is about 40 K, allowing the gas to performance work is an essential feature of a modern helium liquefier. Without this procedure, it would only be possible to liquefy helium by using the Linde-Hampson cycle with precooling the gas using either liquid hydrogen ($T \approx 20$ K) or liquid neon ($T \approx 27$ K). Fortunately, by diverting some of the high-pressure gas flow stream through an expansion engine, near-isentropic processes can instead be used to precool the helium stream to below T_{inv}.

It is most instructive to deal with this subject by way of a specific system. The Claude cycle as it was first developed provides a good working example. A flow scheme for the Claude liquefaction system is shown in Fig. 8.14. The system consists of a compressor, three heat exchangers with an expansion engine operating on the second, and a Joule–Thomson valve for the final expansion stage. The purpose of the expansion circuit is to divert a fraction of the incoming high-pressure gas stream through an engine performing work as the gas expands to the low-pressure side. Modern liquefiers and refrigerators are more complex than the Claude cycle but use similar combinations of expansion processes.

Two coupled expansion circuits, such as the Claude cycle provides, have several advantages over the simple Linde-Hampson cycle. First, such a cycle has the potential of being more efficient because part of the process stream is undergoing isentropic expansion with inherently higher thermodynamic efficiency. Second, in principle the overall efficiency of the cycle can be improved by taking advantage of

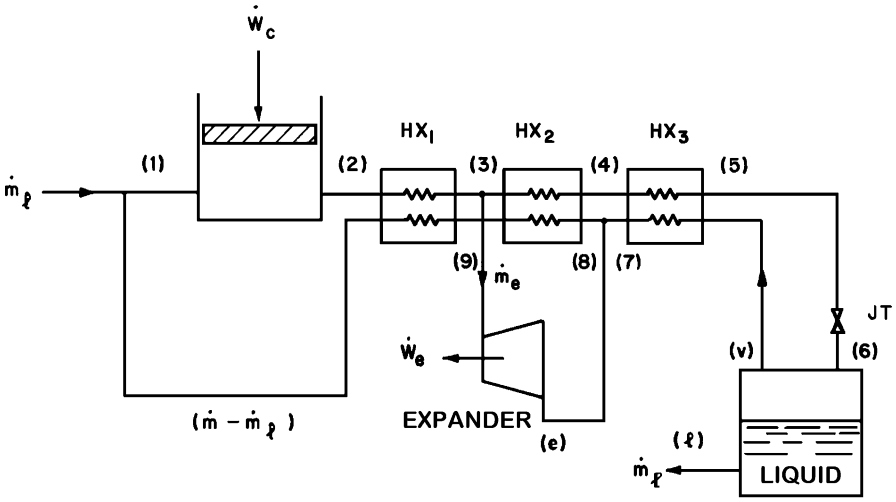

Fig. 8.14 Flow scheme for Claude liquefaction system

the work produced by the expansion circuit, an option that makes sense particularly for large systems. Finally, since there are now two or more coupled flow circuits, the main cooling circuit and that through the expander, it is possible to vary the fraction of the flow that is diverted in order to optimize the performance.

The Claude cycle is displayed on a *T*-*S* diagram in Fig. 8.15. Note that the points as indicated on the flow chart are also shown in Fig. 8.14. Point (3) is particularly interesting because it indicates the position where the two circuits separate. The isentropic expansion reduces the temperature to point (e). The higher-pressure stream continues until point (5) where the J-T valve produces an isenthalpic expansion into the two-phase region. Thus, in the Claude system there are two free parameters to select, the high-pressure value, p_2, and the fraction of gas through the expansion engine circuit, $\dot{m}_e/\dot{m} = x$. To see how these parameters enter the calculations of yield and net work, it is necessary to consider the thermodynamics of both processes.

Applying the first law of steady flows to the entire system and assuming that the expander work is recoverable; the energy balance through the main circuit then yields,

$$-\frac{\dot{W}_e}{\dot{m}} = (1-y)h_1 + yh_l - h_2 \tag{8.41}$$

where as before $y = \dot{m}_l/\dot{m}$. The expander work $\dot{W}_e$ enters (8.41) in the negative sense because the gas is doing work against an external load. In addition to the above expression, one can obtain a separate independent equation by applying the first law on the expansion circuit,

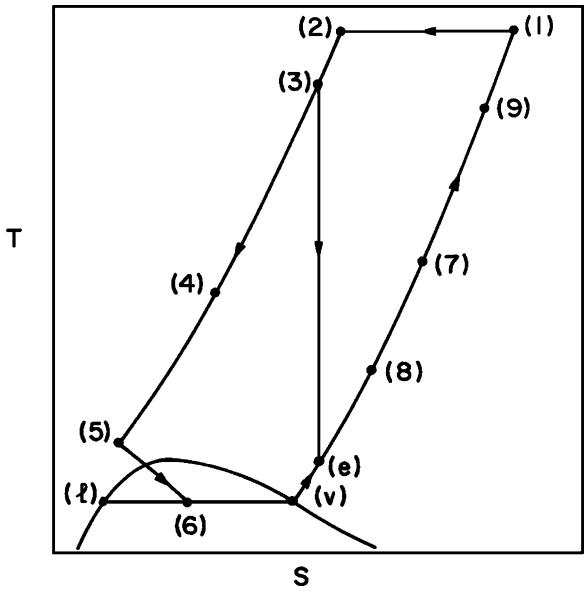

Fig. 8.15 *T-S* diagram for operating Claude system

$$-\frac{\dot{W}_e}{\dot{m}} = x(h_e - h_3) \tag{8.42}$$

where the fraction of flow through the expansion circuit, $x = \dot{m}_e/\dot{m}$, is an adjustable parameter. The above two equations allow the determination of the net yield y and the thermodynamic efficiency or *FOM* of the Claude cycle.

The yield is independent of whether the expander work is used in the thermodynamic cycle. An expression for y can be established by simply equating (8.41) and (8.42) which gives

$$y = \left(\frac{h_1 - h_2}{h_1 - h_l}\right) + x\left(\frac{h_3 - h_e}{h_1 - h_l}\right) \tag{8.43}$$

Note that the first term in (8.43) is identical to the yield of the simple Joule–Thomson liquefier. As has already been discussed, this quantity is only positive when $T < T_{\text{inv}}$. However, the second term is always positive and so it is possible, based on suitable choices of x and p_2, to have a positive yield at temperatures above the inversion curve. Two cautionary steps must be exercised when evaluating the yield from (8.43). First, conservation of mass is not a component of this analysis. Based only on (8.43), it appears that to maximize the yield x

should take on its maximum value; however, conservation of mass flow requires that $y + x \leq 1$. Furthermore, it is unreasonable to set $y + x = 1$ because this would allow no mass flow on the low-pressure side of the last heat exchanger, a physically undesirable situation since the heat exchanged is cooled by this return flow.

Optimizing the Claude cycle requires fixing the mass flow fraction x at its optimum value. However, determination of the optimum conditions can only be achieved by analyzing the complete cycle on a component basis. This is done by balancing the enthalpy flow through the heat exchangers, taking into consideration inefficiencies, to obtain temperatures at each node in the cycle, see Fig. 8.14. As these equations are coupled, they must be solved simultaneously to obtain the best choice for flow through the expansion circuit for maximizing yield.

The second step that must be taken when evaluating the yield of a system that includes an expander is to establish the absolute value of the enthalpy at either the inlet or outlet of the engine. Since the pressure drop is given, the absolute values of h_e or h_3 must be known to establish $h_3 - h_e$. This quantity should be maximized to achieve maximum yield. Obviously, h_e and/or h_3 are not free parameters and are established by absolute temperatures at (3) and (e). As can be seen in Fig. 8.14, T_3 is always less than T_2. However, the value of T_3 cannot be established without resorting to the more complex analysis of heat transfer and fluid flow for a particular system, which is beyond the scope of the present discussion. The examples presented below are based on assumptions for these values. A particular set of assumptions can be checked for consistency against thermodynamic laws, such as an efficiency value greater than that of a Carnot cycle, but these are only approximate calculations to show the overall framework of the analysis.

In addition to the yield of the Claude system, one can also determine the net work involved in liquefying a unit mass of fluid. Assuming that the net work is equal to the difference between the compressor work and expander work $(\dot{W} = \dot{W}_c - \dot{W}_e)$, we obtain

$$\frac{\dot{W}}{\dot{m}} = [T(s_1 - s_2) - (h_1 - h_2)] - x(h_3 - h_e) \tag{8.44}$$

The first term in (8.44) is identical to that of the Joule–Thomson refrigerator, while the second term is the net gain achieved by using the expander work. As with the yield, to minimize the net work the second term should be optimized. Clearly, the net work for the Claude system must be greater than the ideal expansion system allowing the assumptions applied to (8.44) to be checked for correctness.

To evaluate the practical aspects of the above discussion, consider the use of the Claude cycle for liquefaction of helium. Here for the sake of clarity, we assume that all processes are thermodynamically ideal, that is the expansion engine operates isentropically, $\Delta s = 0$ and the J-T valve provides isenthalpic expansion. The Claude cycle is as described above and displayed schematically in Fig. 8.14. The first parameter that must be selected is the value of the compressor output pressure, p_2.

Two practical considerations enter here. First, whether the hardware can withstand the pressure difference particularly in terms of compressor and expander pressure drop. Second, since the last step of the process is through a J-T valve, it probably makes little sense to have p_2 above the maximum inversion pressure. With these factors under consideration, a realistic value to choose in this example is $p_2 =$ 2.0 MPa. Therefore, the thermodynamic states at three points on the cycle are established:

1. Low-pressure return side:

$$p_1 = 0.1\,MPa$$

$$T_1 = 300\,K$$

$$s_1 = 31.6\,kJ/kg\,K$$

$$h_1 = 1574\,kJ/kg$$

2. High-pressure inlet side:

$$p_2 = 2\,MPa$$

$$T_2 = 300\,K$$

$$s_2 = 25.4\,kJ/kg\,K$$

$$h_2 = 1580\,kJ/kg$$

(l) Saturated liquid state:

$$p_3 = 0.1\,MPa$$

$$T_3 = 4.2\,K$$

$$s_3 = 3.5\,kJ/kg\,K$$

$$h_3 = 9.9\,kJ/kg$$

As has been stated above, there are two values to select in determining the yield and net work, namely, x and T_3. Based on (8.43), a desirable choice is a maximum value for x; however, mass conservation sets an upper limit for $y = 1 - x$. For the present

discussion we therefore somewhat arbitrarily assume $x = 0.33$ and $T_3 = 200$ K. These assumptions establish the thermodynamic state at point (3):

3. Inlet to expansion engine:

$$p_3 = 2MPa$$

$$T_3 = 200\,K$$

$$s_3 = 23.3kJ/kg\ K$$

$$h_3 = 1060kJ/kg$$

The expansion engine performs an isentropic expansion on the gas, defining the thermodynamic state of the exiting gas ($s_e = s_3$):

(e) Exit from expansion engine:

$$p_e = 0.1MPa$$

$$T_e = 60.6\,K$$

$$s_e = 23.3kJ/kg\ K$$

$$h_e = 326kJ/kg$$

With the above four thermodynamic states and the value of x fixed, it is a straightforward computation to determine y by substitution of numerical values into (8.43). This calculation results in a yield of $y = 0.15$. Note that once T_3 is selected, the yield is directly proportional to x. For this set of parameters $x + y = 0.48$, which seems reasonable but possibly not optimum.

It is also an easy calculation to determine the net work for the Claude system and to compare this value with a thermodynamically ideal system. Since (8.44) is written on a per unit mass compressed basis (W/m), we can simply divide it by the yield from (8.43) to get the work per unit mass liquefied, which is more directly comparable with an ideal system. For the example above, the net work per unit mass of liquid can be determined as:

$$\frac{\dot{W}}{\dot{m}_l} = \frac{1}{y}\left(\frac{\dot{W}}{\dot{m}}\right) = 10,834kJ/kg$$

This value has little physical significance by itself but does when compared with the thermodynamically ideal case ($\dot{W}_i/\dot{m}$):

$$\frac{\dot{W}_i}{\dot{m}_l} = T(s_1 - s_l) - (h_1 - h_l) = 6866\,kJ/kg$$

The ratio of these two values gives the figure of merit for this particular Claude system:

$$\text{FOM} = \frac{\dot{W}_i}{\dot{W}} = 64\%$$

Determination of the figure of merit represents a thermodynamic check on the correctness of the above assumptions. If the *FOM* computed above worked out to be greater than unity, it would be in violation of the second law of thermodynamics. Nothing in the analysis so far prevents this from happening. Clearly, a complete calculation, which must be done numerically, has built into it a check to prevent this unphysical condition from occurring. The above example indicates the advantages of performance of work on an ideal liquefaction system. Although the Claude system is very simple in its introduction of this concept, it accrues advantages. In fact, modern refrigerators and liquefiers of helium use cycles employing the same basic principles. As the systems evolve into complexity, the ability to evaluate their performance analytically diminishes, leading to an increased number of numerical assumptions.

8.4.2 Collins Helium Liquefaction System

In the 1940s the Collins helium liquefier evolved out of an effort to produce a commercial system using expansion engines to precool several heat exchangers [13]. Today, the Collins cycle is the basis of virtually all large scale helium liquefiers. The Collins system is actually quite similar to the Claude system except that the former uses between two and five expansion engines rather than just one. A schematic diagram of a two-engine Collins system is shown in Fig. 8.16. In designing the Collins system, there are a greater number of degrees of freedom over that of the Claude system. Depending on the number of expansion circuits, i, there are an equal number of expansion circuit mass flows to select, $\dot{m}_{ei}$. Furthermore, the temperature at the inlet to each expansion engine must be determined to compute the yield. Once these quantities are known it is a straightforward computation to determine the yield for the Collins system,

$$y = \frac{h_1 - h_2}{h_1 - h_l} + x_1 \frac{\Delta h_{e1}}{h_1 - h_l} + x_2 \frac{\Delta h_{e2}}{h_2 - h_l} + \ldots \tag{8.45}$$

where Δh_{ei} is the enthalpy change through the ith expansion engine and x_i is the mass flow ratio through the ith circuit. Conservation of mass requires that $y + \Sigma_i x_i \leq 1$.

The first Collins liquefiers were developed with two expansion engines. Typical working temperature ranges for the expanders are from 60 to 30 K and 15 to 8 K, respectively. During steady-state operation the approximate values for the expander mass flow fractions are $x_1 = 0.30$ and $x_2 = 0.55$ at 1.5 MPa. Insertion of these

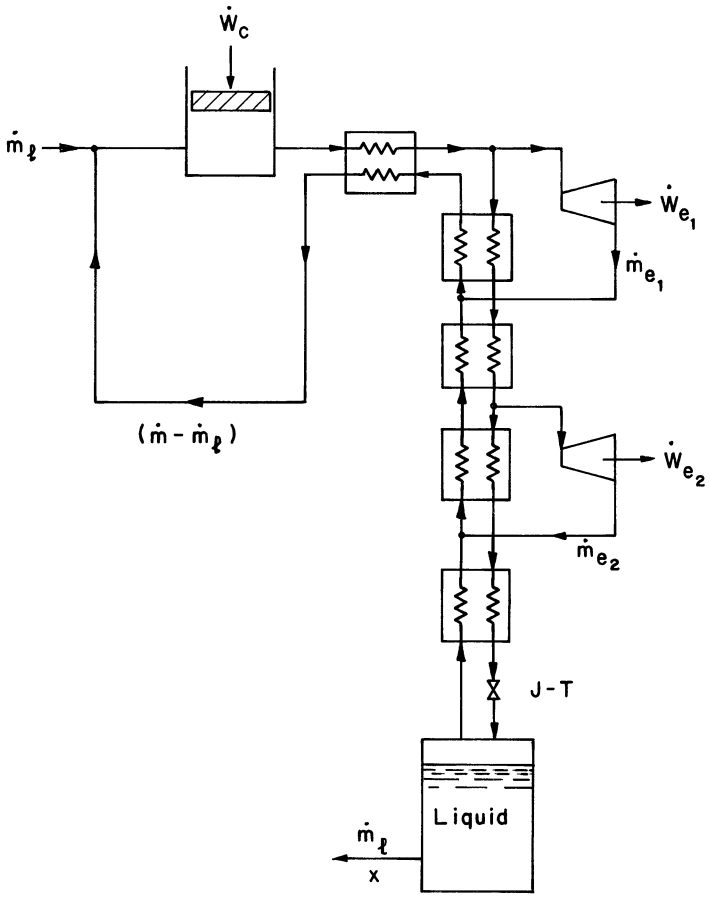

Fig. 8.16 Schematic diagram of Collins liquefaction system

numerical values into (8.45) leads to a yield of only 3.6%. However, it has been demonstrated that the liquid yield could be improved by a factor of 2–3 by using a liquid nitrogen precooler above the first heat exchanger. Precooling with liquid nitrogen is a fairly common approach for moderate size systems. In addition to improving the liquid yield, the liquid nitrogen can also be used to cool adsorption beds for extracting impurities from the helium stream.

8.5 Closed–Cycle Refrigeration

Until this point, the discussion has concentrated on systems whose primary purpose it is to liquefy helium. Thus, the principal questions that have been asked are: What is the yield of a particular liquefaction cycle and what is the work per unit mass

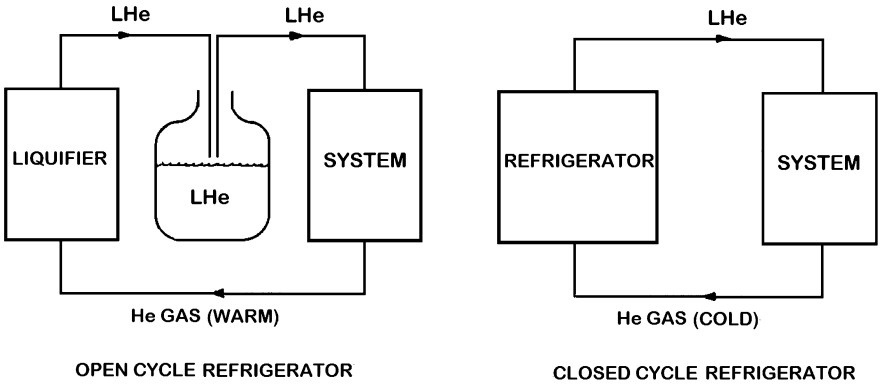

Fig. 8.17 Two different approaches to cooling a system with liquid helium

liquefied? In either case these questions relate only to the production of liquid helium. It is assumed that the helium is used to cool some device. However, there are many cases where it is more appropriate to integrate the helium supply with the application whether it is to supply liquid or extract heat at low temperature. In practice, many large systems have, as part of their standard operation, a closed-cycle refrigerator to provide continuous cooling at low temperature, $\dot{Q}_c$. This approach is desirable because it can achieve a higher thermodynamic efficiency and dedicated operation with the closed-cycle nature reducing the probability of helium vapor losses and contamination. The further advantage of a closed-cycle refrigerator in terms of thermodynamic efficiency can be seen most clearly by a single but instructive example.

Consider two different methods of cooling a system to liquid helium temperatures. One method is shown schematically in Fig. 8.17a. Here the cooling of the device is achieved in two stages. First, helium is liquefied and stored in a container. Subsequently, or possibly simultaneously, helium is transferred from the storage container to the system to be cooled. Heat generated in the system Q_c and absorbed at low temperatures is removed by the latent heat of the liquid helium. In this case, the enthalpy of the evaporated helium is lost because the heat is being generated at low temperatures and the cold gas escapes to be recovered and re-liquefied later. Certainly, if Q_c were the result of conduction from the external environment, the situation would be considerably different. In that case, the vapor can cool the structure continuously, thereby reducing the total heat absorbed by the liquid helium. Liquid helium has a relatively small latent heat, $h_{fg} \sim 21$ kJ/kg at 4.2 K. This value is equivalent to 0.73 W h/L at saturated vapor pressure densities. A useful quantity to keep in mind is that 3/4 W dissipated in liquid helium for 1 h will boil away 1 liquid liter. The work required to produce a unit mass of liquid in an ideal Carnot cycle has been computed above to be 6,866 kJ/kg. The coefficient of performance (COP) is defined in terms of the number of watts that must be dissipated at 300 K to produce 1 W of cooling at low temperatures. For the above open-cycle system, the $COP = h_{fg}/\dot{W}_i = 1/326 = 0.0031$.

Table 8.3 Power requirements for various ideal refrigeration modes

Fluid	T(K)	Closed-cycle refrigeration ($W_{300\ K}/W_{4.2\ K}$)	Open-cycle refrigeration ($W_{300\ K}/W_{4.2\ K}$)	Ideal liquefaction (W·h/L)
He	4.2	70.4	326.0	236
H_2	20.4	13.7	31.7	278
Ne	27.1	10.1	15.5	447
N_2	77.4	2.88	3.87	173
Ar	87.3	2.44	2.95	185
O_2	90.2	2.33	2.89	195

Now compare the above computation with a closed-cycle refrigerator, such as shown schematically in Fig. 8.17b. Closed cycle means that the helium gas is recovered cold through the refrigeration system. This approach allows the enthalpy of the gas to be returned through the cycle to precool the incoming high-pressure stream by means of one or more heat exchangers. The efficiency of such a device is inherently much higher. If the system were based on an ideal Carnot refrigerator, the *COP* would be given in terms of the absolute temperatures T_C and T_H that is, $COP = T_C/(T_H - T_C) = 1/70.4 = 0.0142$, about a factor of 4.6 higher than the open-cycle system. Real systems that perform at less than Carnot efficiency have a similar ratio of efficiency for closed versus open-cycle operation.

Listed in Table 8.3 are values for power requirements of open and closed-cycle refrigeration assuming ideal thermodynamic efficiencies. Comparison of the second and third columns indicates that helium accrues the greatest thermodynamic advantage by operating as a closed cycle. This is because the latent heat of liquid helium is small compared to the enthalpy of the gas between 300 K and T_{bp}. The ratio of columns 2 and 3 decreases as the boiling point of the liquids increase. For the high-temperature cryogenic fluids such as O_2 and N_2, the latent heat is larger than the enthalpy of the gas between T_b and 300 K. The last column in Table 8.3 indicates the minimum power requirements to liquefy a liter assuming an ideal process. This quantity is computed by using (8.33) and dividing by the density of the liquid at saturated vapor pressure.

As is the case for liquefaction systems, real low temperature refrigerators operating on a particular cycle achieve a fraction of ideal thermodynamic efficiency. That fraction is called the figure of merit (*FOM*). Thus, real refrigerators have a similar makeup to real liquefiers. However, there exists a clear distinction between refrigerators and liquefiers in that the refrigerator is to provide cooling while the liquefier is to condense fluid. For liquid–gas refrigeration systems there are primarily two methods of extracting the low-temperature heat load. With *isothermal refrigeration* the heat load is absorbed by a constant temperature liquid reservoir producing saturated vapor that returns through the cycle. This approach is nearly identical to liquefaction with the heat load being taken by the phase change. Alternatively, the heat load may be absorbed over a range of temperatures not determined by the boiling point of specified liquids. Such systems are not designed to produce liquid

but rather are specified in terms of the low temperature refrigeration performance that depends on the temperature, $Q_c(T)$. These systems include the regenerative cryocoolers that operate on a different class of cycle than do the recuperative cycles discussed so far. In this section, we begin with a discussion of isothermal refrigeration system design. We next present the topic of *isobaric refrigeration* based on recuperative cycles but where liquid is not produced and the gaseous enthalpy is used to absorb the heat load. Finally, we discuss the entire subject of *regenerative* cycle design, which is based on a totally different approach to low temperature refrigeration.

8.5.1 Isothermal Refrigeration

There is not a large difference between the system configuration for an isothermal refrigerator and that of a liquefier. In fact, the only distinction is that heat $\dot{Q}_c$ is applied to an evaporator bath rather than liquid being extracted. Consequently, unlike a liquefier that requires makeup gas, the mass flow $\dot{m}$ in the isothermal refrigerator is the same throughout the cycle. This distinction will result is slightly different performance of heat exchangers, since the mass flow rate is now equal on both sides. Beyond that one issue, the optimization of the cycle is identical to that of a liquefier.

An example of an isothermal refrigerator based on the Claude cycle is displayed in Fig. 8.18. Note the similarity between that figure and Fig. 8.14. Applying the first law of thermodynamics to the isothermal Claude cycle, the rate of heat extraction at low temperatures may be written

$$\frac{\dot{Q}_C}{\dot{m}} = (h_1 - h_2) + x(h_3 - h_e) \tag{8.46}$$

which is related to the yield equation for the liquefaction cycle. In fact, it is generally true for isothermal refrigeration that

$$y = \frac{\dot{Q}_C}{\dot{m}(h_1 - h_l)} \tag{8.47}$$

a quantity that is equal to the ratio of actual refrigeration to ideal refrigeration. However, one should be careful in application of (8.46) and (8.47). Since the mass flow is now conserved throughput the cycle, the condition applied to the return side heat exchangers is somewhat different. This affects the low-temperature end of the refrigerator and allows more latitude in the selection of mass flow through the various parallel circuits. It should result in slightly higher yield than in a pure liquefier and overall better performance.

Apart from this one fact, isothermal refrigeration is related directly to the liquefaction process. Thus, the optimization procedure follows a set of criteria similar to those outlined in Sect. 8.3.1.

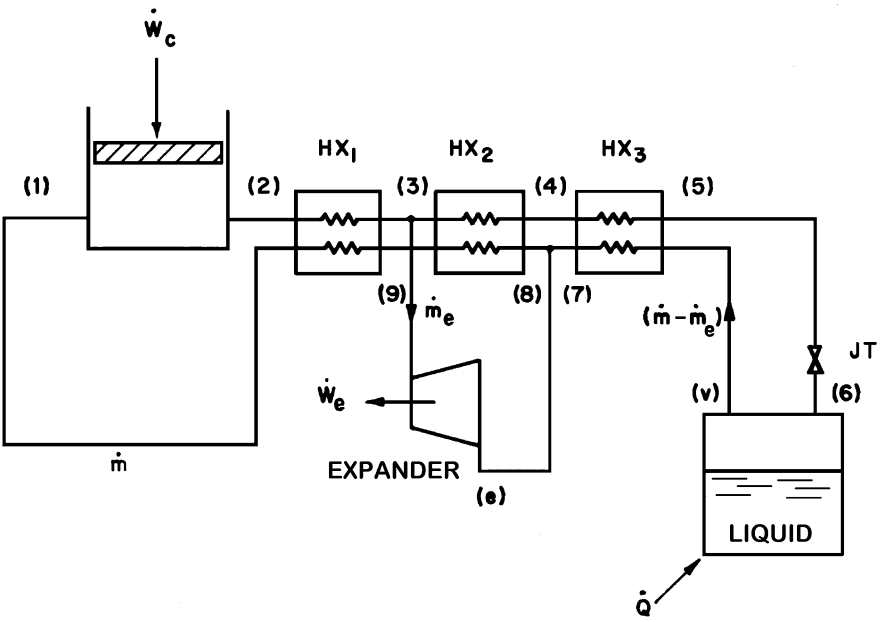

Fig. 8.18 Schematic of isothermal refrigerator based on Claude cycle

8.5.2 Isobaric Refrigeration

If refrigeration is needed at temperatures outside the liquid regime, then one approach is to use an isobaric gas cycle refrigerator. Here the heat load is absorbed in the vapor enthalpy at low temperatures producing a specific temperature increase. There are several reasons why this mode of operation is useful as a type of refrigeration. For one, it permits the operating temperature of the low end to be a free parameter adjustable within design constraints and not restricted to the boiling point of the cryogenic fluid. For helium, isobaric refrigerators are particularly useful for systems operating above $T_c = 5.2$ K. Avoiding the two-phase coexistence region permits the refrigerator to be constructed without a Joule–Thomson expansion stage. This approach may permit higher thermodynamic efficiency.

A common cold gas isobaric refrigeration cycle is also known as the Reverse Brayton cycle. This cycle is shown in Fig. 8.19 and its *T*-*S* diagram in Fig. 8.20. Actually, the cycle shown in the *T*-*S* diagram is not strictly a Brayton cycle because the compression shown is isothermal. The system uses the expansion engine to provide cooling to a low-temperature heat sink. The amount of heat absorbed at low temperature is equal to the enthalpy change of the gas as it passes through the low-temperature heat sink. This quantity may be written

$$\frac{\dot{Q}_C}{\dot{m}} = h_5 - h_4 \tag{8.48}$$

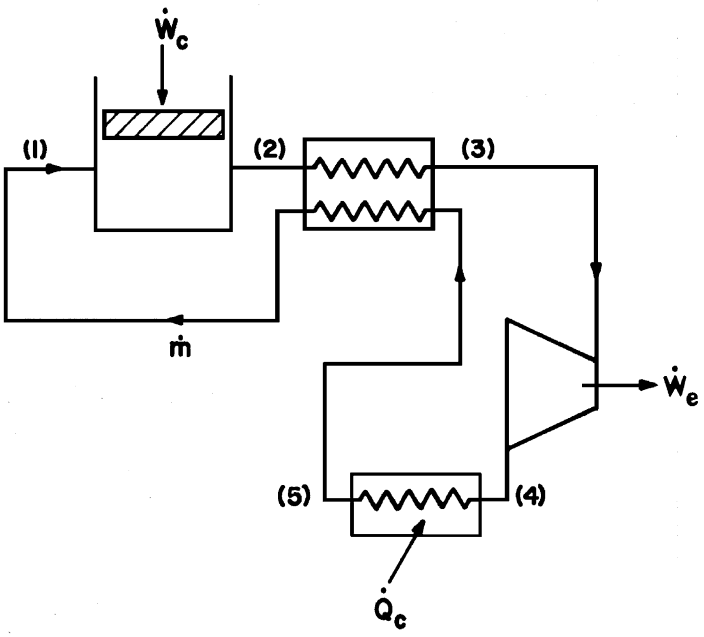

Fig. 8.19 Schematic of isobaric (Reverse *Brayton cycle*) refrigerator

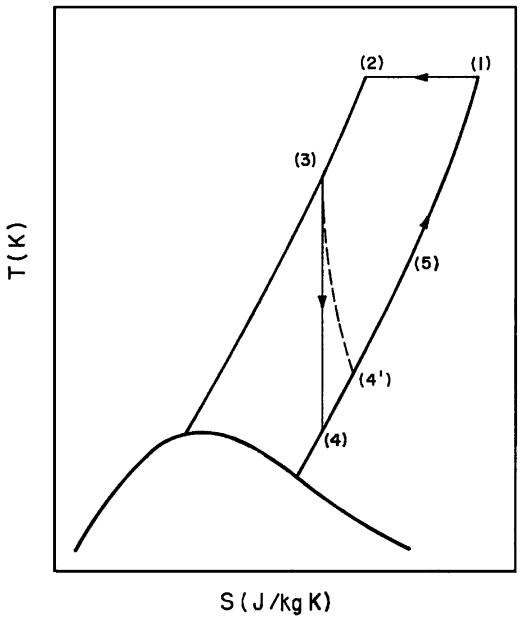

Fig. 8.20 *T-S* diagram of isobaric (Reverse *Brayton cycle*) refrigerator

The various locations on the flow chart are also indicated on the *T*-*S* diagram. Note that (5) is at a temperature that is comparable to (3), the inlet to the expansion engine.

As has been the case for the liquefier design, the isobaric refrigerator is not determined fully by thermodynamic considerations. Applying the first law of steady flows to the entire cycle gives an alternate expression for the refrigeration,

$$\frac{\dot{Q}_C}{\dot{m}} = (h_1 - h_2) + (h_3 - h_4) \tag{8.49}$$

where the first term is the isenthalpic contribution is only positive provided $T < T_{\text{inv}}$. The second term in (8.49) is the cooling produced by the isentropic expansion engine and is always positive. For the presently considered cycle, (8.48) and (8.49) do not determine fully the refrigeration power. However, if one additional constraint is established such as the desired exit temperature to the load heat exchanger, there is enough information to determine the performance.

Example 8.3

Calculate the cooling power per unit mass flow rate for a Reverse Brayton cycle that is to provide refrigeration at 100 K. Assume that the compressor outlet pressure is 2 MPa.

The refrigerator should operate such that the maximum temperature at the exit of the low temperature heat exchanger not to exceed 100 K. Therefore, in addition to (8.48) and (8.49), it is known that $T_5 = 100$ K. Furthermore, let us establish the usual set of starting conditions: at low pressure (l),

$$p_1 = 0.1\ MPa$$

$$T_1 = 300\ K$$

$$s_1 = 31.6 kJ/kgK$$

$$h_1 = 1574 kJ/kg$$

at high pressure (2),

$$p_2 = 2MPa$$

$$T_2 = 300\ K$$

$$s_2 = 25.2 kJ/kgK$$

$$h_2 = 1580 kJ/kg$$

and exiting the low-temperature heat exchanger (5),

$$p_5 = 0.1\ MPa$$

$$T_5 = 100\ K$$

$$s_5 = 25.7\ kJ/kg\ \cdot K$$

$$h_5 = 534\ kJ/kg$$

Combining (8.48) and (8.49), an expression for conservation of enthalpy through the first heat exchanger is obtained:

$$h_3 = h_2 - h_1 + h_5 = 540\ kJ/kg$$

it then follows that state (3) is established:

$$p_3 = 2MPa$$

$$T_3 = 100K$$

$$s_3 = 19.5kJ/kgK$$

$$h_3 = 540kJ/kg$$

Finally, h_4 and T_4 are fixed by isentropic expansion:

$$p_4 = 0.1MPa$$

$$T_4 = 30K$$

$$s_4 = 19.5kJ/kgK$$

$$h_4 = 170kJ/kg$$

Now returning to either (8.48) or (8.49) we obtain the cooling power of the refrigerator:

$$\frac{\dot{Q}_C}{\dot{m}} = 364\,kJ/kg$$

(continued)

Example 8.3 (continued)

To determine the efficiency of this cycle it is useful to compare the value of $\dot{Q}_c$ with the total work done. This exercise establishes the coefficient of performance. The net work is computed by assuming the expansion engine work can be utilized:

$$\frac{\dot{W}}{\dot{m}} = T_2(s_1 - s_2) - (h_1 - h_2) - (h_3 - h_4) = 1496\,kJ/kg$$

These values are based on a specific example, however, it is still useful to compare the coefficients of performance to that of an ideal cycle. For the above example,

$$\text{COP} = \frac{\dot{Q}_C}{\dot{m}} = 0.243$$

While for an isothermal Carnot refrigerator operating between 100 K and 300 K the coefficient of performance is,

$$\text{COP} = \frac{T_C}{T_H - T_C} = 0.50$$

That the above designed refrigerator operates at a figure of merit less than 50% is due largely to the isobaric operation. Because the system must cool the gaseous helium to 30 K and then heat it isobarically to 100 K, its efficiency would be lower when compared to an isothermal system operating continuously at 100 K.

8.6 Regenerative Referigeration Cycles

Regenerative refrigeration cycles are distinguishable from recuperative cycles as they involve cyclic processes that do work to extract heat from the cold point in the cycle with the low temperature being stored in a refrigerator component known as the *regenerator*. A regenerator is much like a recuperative heat exchanger with the principal difference being that the former needs to have a large volumetric heat capacity to store as much thermal energy as possible as the fluid streams alternately flow through the matrix. During the cyclic process, a significant amount of heat is alternately stored in, and released by, the regenerator, a feature that is different from recuperative cycles where heat is continually transferred from one fluid stream through the solid heat exchanger to the other fluid stream, while the solid components remain at a steady state temperature. In general, cryogenic refrigerators based on regenerative cycles are suitable for lower cooling power applications compared to the larger recuperative cycle machines.

There are several regenerative refrigeration cycles of interest in helium cryogenics. To cover this subject completely, however, would require far more space than is

allocated here. Therefore, the present discussion is limited to presentation of the Stirling cycle and the Gifford McMahon (GM) cycle, both of which are in common and widespread use today in cryogenics. In addition, these two cycles have been the main venue for development of what are commonly known as pulse tube cryocoolers. The primary distinction between the conventional regenerative cryocoolers and the pulse tube cryocoolers exists in the method used to produce the necessary phase shift between the flow and pressure oscillations, and the optimum value of that phase shift. In their conventional embodiment, the Stirling and GM cycles control the motion of a *displacer* to move the refrigerated fluid through the regenerator. The timing of the displacer motion with respect to the production of low and high pressures determines the phase shift for the Stirling and GM cryocoolers. In the more modern pulse tube refrigerators the necessary phase shift is achieved without the use of any cold moving parts, such as a displacer. Instead, one of various room temperature mechanisms can be used to optimize the phase shift. The lack of any cold moving parts and the associated long-term reliability explain the attractiveness of pulse tube refrigerators. A complete description of pulse tube refrigeration cycles is beyond the scope of the present discussion, however a few of its salient features are provided below.

8.6.1 Stirling Cycle

The Stirling cycle refrigerator evolved from the heat engine cycle invented by Robert Stirling in 1827 [1]. Operated in reverse, the Stirling engine produces cooling. The Phillips Company was the first to commercially produce refrigerators that operated on this cycle. The Stirling cycle may be approximated as consisting of two isothermal and two isochoric (constant volume) processes. A schematic representation of the cycle is shown in Fig. 8.21. Refrigeration is achieved by isothermal expansion of the working fluid. There are three main components shown: regenerator (R), compressor/expander, and displacer (D). The displacer works in concert with the compressor during the compression, expansion, and shuttle processes to move the alternately high- and low-pressure working fluid through the regenerator.

The four stages displayed in Fig. 8.21 outline a procedure whereby these components produce cooling. Once the process has achieved the steady state it can be described in terms of *p*-*V* and *T*-*S* diagrams as in Fig. 8.22. However it is important to keep in mind that the fluid does not flow continuously around the cycle as in a recuperative refrigerator.

The cycle is described as follows. At (1) a unit of helium is compressed but resides in the upper compression chamber at high temperature since the displacer is at its lowest position. From (1) to (2), the displacer is moved to its upper position forcing the fluid through the regenerator into the expansion chamber. This process takes place at constant volume. Since the expansion end of the regenerator is colder than the helium the pressure of the gas decreases to (2). Step (2)–(3) is an isothermal expansion of the fluid in the lower chamber achieved by moving the displacer upward with the compressor. This process extracts heat from the regenerator at T_c. Between (3) and (4) the displacer is returned to its lowest position, forcing the cold

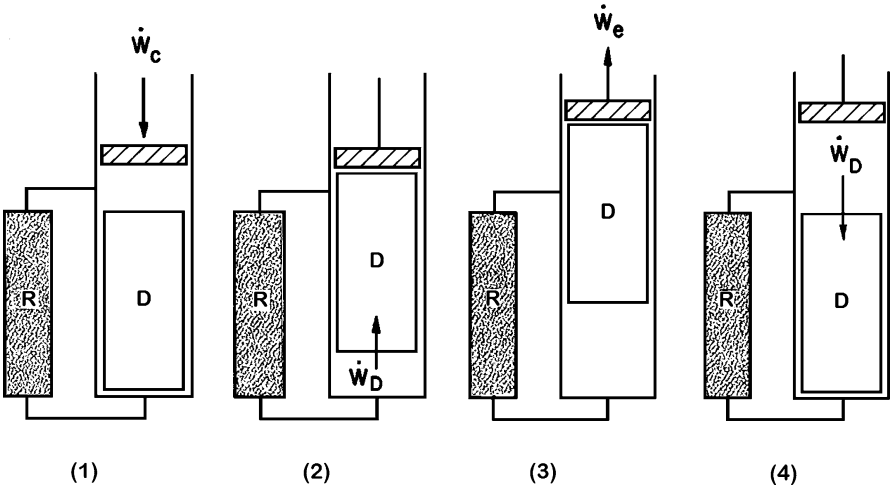

Fig. 8.21 *Stirling cycle* refrigerator

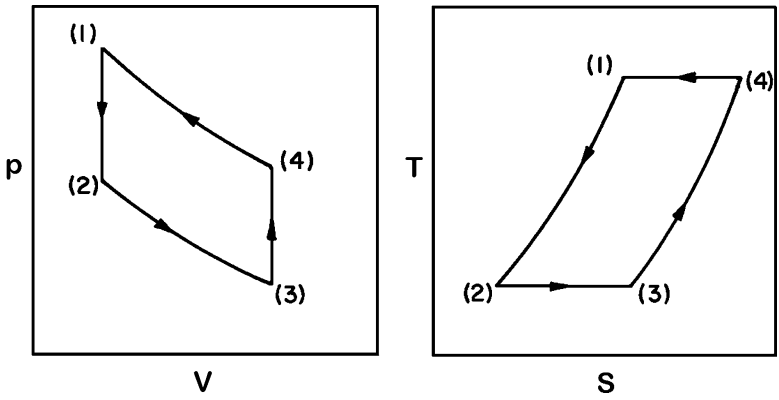

Fig. 8.22 *p-V* and *T-S* diagrams for *Stirling cycle*

fluid back through the regenerator to the compression chamber. Heat is extracted from the regenerator since the gas is now colder and the working fluid is then recompressed to (1) isothermally. Because of the periodic nature of the cycle, cooling is not continuous. However, if the regenerator has sufficient heat capacity, temperature fluctuations at the low end can be minimized.

The regenerator is a component not present in most recuperative refrigeration cycles. It performs a similar function to the counterflow heat exchanger in a recuperative refrigerator with a few exceptions. A properly designed regenerator should have the following characteristics:

1. Minimum flow resistance.
2. Minimum longitudinal heat conductance.

3. Large surface area for maximum heat transfer between the fluid and the solid matrix.
4. Large volumetric heat capacity of the solid matrix.
5. Minimum void volume.

The characteristics of regenerators appear similar to those of good recuperative heat exchangers, with the exception of the large heat capacity. This requirement is particularly difficult in the application of the Stirling cycle to helium liquefaction or refrigeration because, as discussed in Chap. 2, most solid materials have rather low specific heats at liquid helium temperatures. As a result, metals with low Debye temperature (Θ_D) like lead or tin are often used in the lower end of a regenerator. However, even these metals become unusable for regenerators below about 10 K. To achieve refrigeration below 10 K, recuperative refrigerators use special materials with specific heat anomalies that are associated with magnetic ordering phase transitions. These materials are discussed further in Sect. 2.1.3.

For an ideal Stirling cycle, the total refrigeration resulting from the isothermal expansion of a gas from p_2 to p_3 is given by the relationship

$$\frac{Q_c}{m} = \frac{R}{M} T_c \ln \frac{p_2}{p_3} \tag{8.50}$$

where T_c is the expansion temperature, M is the molar mass of the working fluid (4 kg/kmol for helium). Ideally, the cooling rate would be linearly proportional to the cycle frequency. However, in actual applications frictional losses and other non-idealities increase with frequency, providing optimum performance parameters for practical refrigerators.

Example 8.4

Calculate the performance of a Stirling cycle refrigerator is to operate between 100 and 300 K with an inlet pressure of 0.1 MPa and compressor output at 2 MPa. This can be compared to the Reverse Brayton cycle refrigerator discussed above.

Since these temperatures and pressures are far above the critical point for helium, it is fair to approximate the helium gas as an ideal gas for the present calculations. Since steps (1)–(2) and (3)–(4) are isochoric, we can use the ideal gas law to calculate p_2 and p_4,

$$\begin{aligned} p_1 &= 2 \text{ MPa}; p_2 = p_1(T_2/T_1) = 0.67 \text{ MPa}; \; p_3 = 0.1 \text{ MPa}; \\ p_4 &= p_3(T_4/T_3) = 0.3 \text{ MPa} \end{aligned}$$

Then the isothermal heat removal rate at low temperature is,

$$\frac{Q_c}{m} = \frac{R}{M} T_c \ln \frac{p_2}{p_3} = 2.08 \text{ kJ/kg K} \times 100 \text{ K} \times \ln(0.67/0.1) = 395 \text{ kJ/kg}$$

(continued)

Example 8.4 (continued)

And the heat rejected into the high temperature reservoir is,

$$\frac{Q_h}{m} = \frac{R}{M} T_h \ln \frac{p_4}{p_1} = 2.08 \text{ kJ/kg K} \times 300 \text{ K} \times \ln(0.33/2) = -1184 \text{ kJ/kg}$$

Thus, the coefficient of performance for this cycle is,

$$COP = \frac{Q_c}{Q_h - Q_c} = \frac{395}{1184 - 395} = 0.5 = \frac{T_c}{T_h - T_c}$$

Note that this is the same *COP* as for a Carnot cycle. Although the Stirling cycle has theoretically the same *COP* as the Carnot cycle, there is an important difference. Since the Stirling cycle has two isochoric processes, heat is stored (or recovered) at constant volume during those stages of the cycle. Thus, the Stirling cycle moves more heat for the same cooling power, which can result in further inefficiencies in its practical application. On the other hand, as a Stirling cycle refrigerator does not require such high compression ratios as Carnot it provides a more practical approach for applications.

There are a number of factors that lead to less than ideal behavior in a Stirling cycle refrigerator. One area of critical importance is in the regenerator design. It is desirable to have the regenerator effectiveness be as high as possible meaning large surface area and small flow passages, but this may not be possible in practice. Real regenerators contain a non-zero void volume that traps gas during the cycle. The gas in the void volume does not provide any cooling during expansion and reduces the overall system efficiency. Also, the regenerators contribute to the overall pressure drop of the cycle and axial conduction can lead to entropy generation.

8.6.2 Gifford McMahon Cycle

The Gifford–McMahon cycle was originally proposed in the early 1960s as a regenerative cycle that could potentially reach the helium temperature range [14, 15]. The GM cycle is similar to the Stirling cycle except that the oscillatory flow is achieved by cycling valves that select where the flow distributes in the cycle, see Fig. 8.23.

The GM cycle description is shown in Fig. 8.24. At the beginning of the first stage of the cycle, the displacer is at its lowest position with the outlet (return) valve closed. The inlet (high pressure) valve is opened to allow high pressure helium gas to fill the regenerator and space above the displacer at room temperature. Then, with the inlet valve still open, the displacer is moved to its upper position. The high pressure gas passes through the regenerator and is cooled isobarically by the matrix. Cold gas then fills the space below the displacer. Next, with the displacer at its

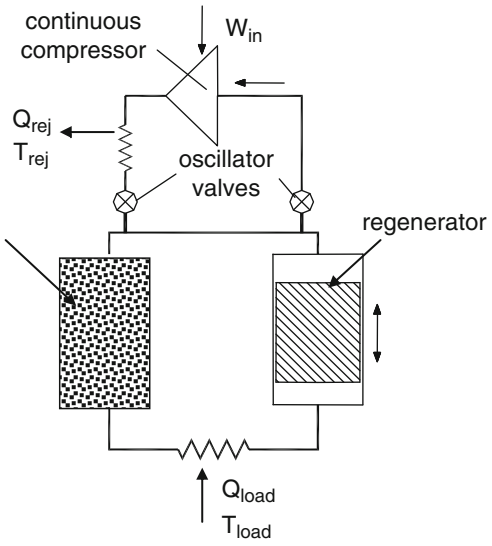

Fig. 8.23 Gifford–McMahon cycle

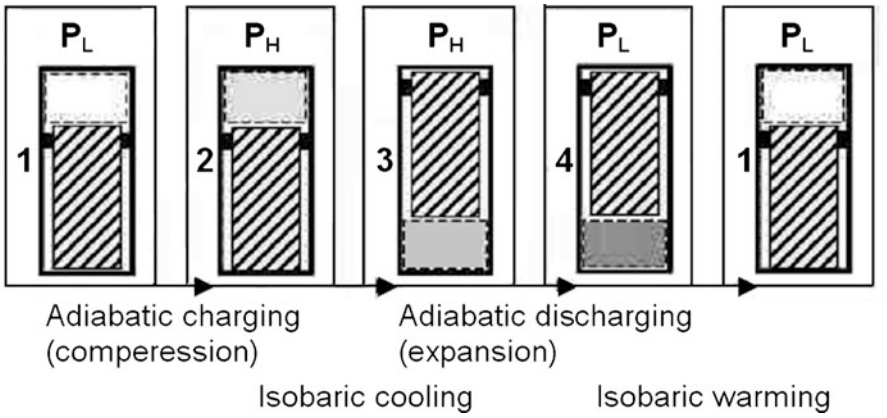

Fig. 8.24 Cycle description for the GM refrigerator

upper position, the inlet valve is closed and the outlet valve is opened. The gas in the regenerator and cold space below the displacer undergoes expansion, which produces the refrigeration. Finally, with the outlet valve still open, the displacer moves back to the lowest position. The low pressure cold gas is warmed isobarically by the matrix refilling the space above the displacer at room temperature completing the cycle.

Thermodynamically, the GM cycle is slightly more complex than the Stirling cycle. The cooling and warming processes are isobaric while the compression and expansion processes are isothermal. However, neither the compression nor expansion processes involve a constant mass since there is flow into and out of the system through the valves. The significant pressure drop occurring at the valves reduces the

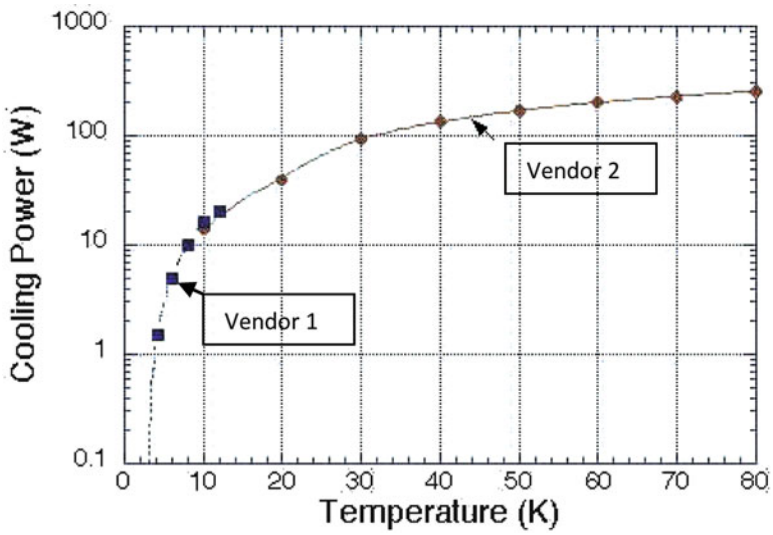

Fig. 8.25 Typical cooling capacity of commercial Gifford McMahon cryocoolers

overall thermodynamic efficiency of the GM cycle compared with that of the Stirling cycle.

Figure 8.25 displays typical cooling characteristics of large commercial single stage GM cryocoolers. Performance is usually quoted in terms of cooling power at 80 K (for which these machines are in the range of 300 W). Note that the cooling power drops by about an order of magnitude at 10 K. Better low temperature ($T < 10$ K) performance can be obtained with a two stage machine, but usually with reduced cooling power at higher temperatures. Such machines require about 7 kW of compressor power therefore operating at about 10% of Carnot efficiency.

8.6.3 Pulse Tube Cryocoolers

Pulse tube cryocoolers come in a variety of configurations and space does not permit a complete explanation of all aspects of pulse tube technology [16]. Here we consider two variations of the design. Both are based on the orifice pulse tube with the distinction being in the compressor configuration. Figure 8.26 shows these two configurations. For the Stirling type pulse tube cryocooler, the cycle frequency is established by the compressor frequency, which is typically of order 100 Hz. On the other hand, the GM cycle based pulse tube has a cycle frequency set by the cycling of the valves and is generally of lower frequency, a few Hz.

As with the conventional Stirling and GM cycles, the pulse tube contains a regenerator through which the cold and hot fluid is periodically cycled. The thermal gradient in the regenerator is established in steady state with the low temperature end in direct contact with the cold end of the pulse tube. However, a pulse tube does

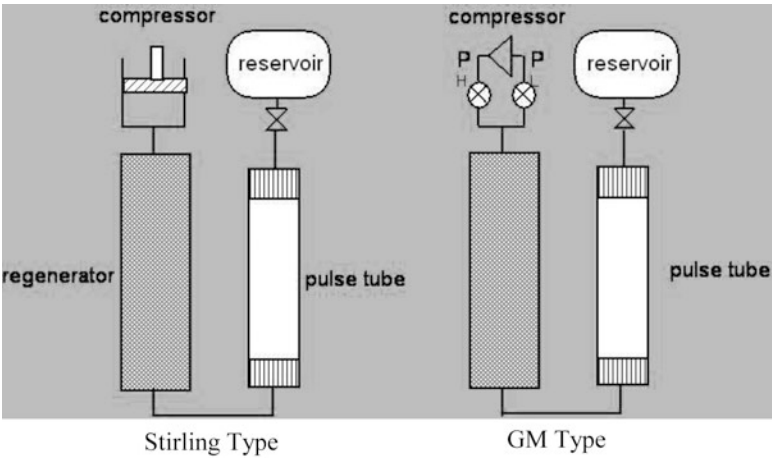

Fig. 8.26 Comparison of Stirling type and GM type pulse tube cryocoolers [16]

not have a displacer. Rather the pulse tube component, that is simply a tube with heat exchangers at either end, produces a net amount of cooling over the cycle by a work transfer of energy from the cold to warm end. The work transfer can be envisioned to occur through the action of a 'squishy' gas piston in the open pulse tube volume. In such a conceptualization, the gas piston is comprised of the gas that never travels far enough during any part of the cycle to leave the pulse tube at either end. During the compression portion of the cycle the gas at the cold end pushes on the gas piston moving it toward the warm end, while during the expansion portion of the cycle, the gas piston pushes back on the cold end gas. Since the pressure is higher during the first part of this cycle, and lower during the latter, a net flow of work occurs from the cold to the warm end.

Optimized cooling with a pulse tube requires a proper phase shift between the pressure and flow oscillations. A variety of phase-shifting mechanisms have been developed to accomplish this objective.

Currently, there are a number of pulse tube cryocoolers that can achieve cooling powers in excess of 1 W at 4.2 K. Examples of their application include small capacity liquefiers and conduction cooling of low temperature superconducting magnets as well as helium temperature electronic systems.

8.6.4 Hybrid Helium Liquefiers

Although the regenerative refrigeration cycles are not primarily used for liquefaction, systems are being developed based on combining a two-stage pulse tube cooler with other cycles to produce small scale liquid helium plants. In this case, the cryocooler is used in place of an expansion engine to reduce the helium temperature to a low enough temperature so that isenthalpic expansion can produce liquid. Such a hybrid system

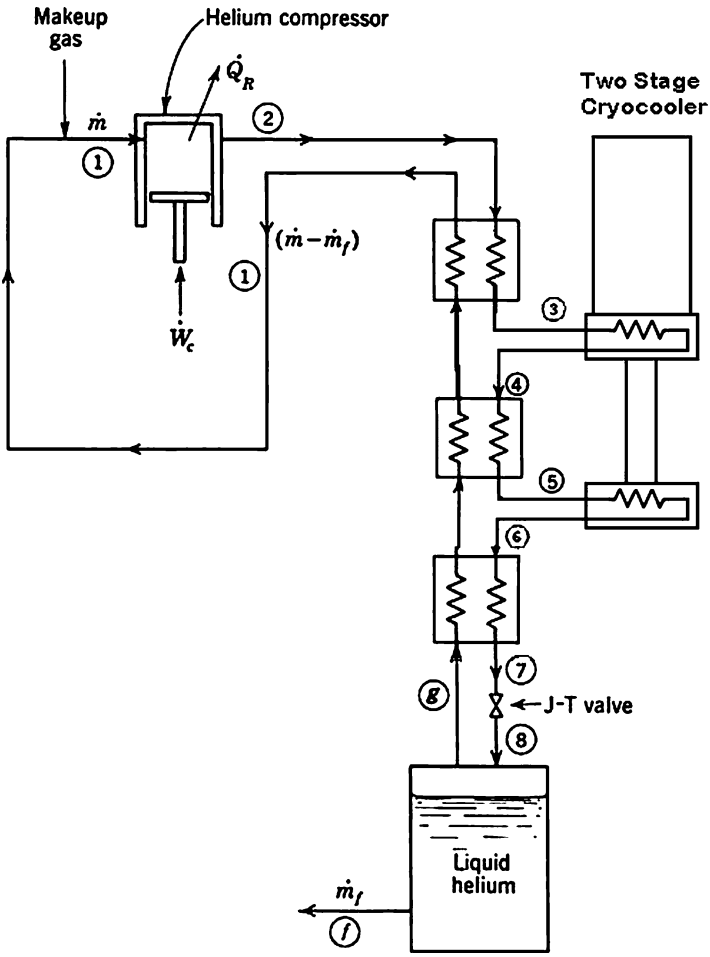

Fig. 8.27 Helium liquefier based on a two stage cryocooler precooling the Linde-Hampson cycle

based on a modified Linde Hampson cycle is shown in Fig. 8.27. In this case, the incoming helium stream is cooled by passing through three heat exchangers. Between the first and second heat exchanger, the high pressure stream passes through a heat exchanger attached to the first stage of the cryocooler. The flow then passes through another heat exchanger before heat exchanging with the second stage of the cryocooler. After the final heat exchanger, the flow expands through a JT valve. The temperature of the helium stream at the inlet to the JT valve will depend on the mass flow rate and the cooling power of the cryocooler.

A typical modern cryocooler may have a first stage cooling power of 50 W at 50 K and second stage power of 10 W at 10 K. This is generally a small capacity compared to recuperative refrigerators and thus limits the liquefaction rate for such systems to of order 1 liquid liter/h.

8.7 Nonideal Refrigeration Components

Practical refrigeration components are not capable of operating ideally or reversibly. Heat exchangers must always transfer heat across a finite temperature difference and expanders always allow some heat transfer between the working fluid and the device. Compressors are not fully isothermal as discussed above. The net effect of irreversible operation is to increase the work required per unit of refrigeration produced. The optimum operating parameters (e.g., pressure ratio, inlet temperatures, and mass flow fractions for expanders) for a particular cycle are critically dependent on the degree of reversibility in each component in the system.

The degree of reversibility of a component is usually expressed as a ratio of actual performance to the ideal performance obtained by a reversible process. The performance parameter of interest for an isentropic compressor or expander is the change in enthalpy experienced by the fluid. The efficiency, η, is defined as the actual change in enthalpy divided by the maximum enthalpy change for a reversible process:

$$\eta = \frac{\Delta h_{\text{actual}}}{\Delta h_{\text{reversible}}} \tag{8.51}$$

For example, the efficiency of the expander in the cycle depicted in Fig. 8.20 can be expressed as

$$n_e = \frac{h_3 - h_{4'}}{h_3 - h_4} \tag{8.52}$$

where $h_3 - h_4$ is the enthalpy change produced by an isentropic expansion. Typical expansion efficiencies are in the range of 70% for state-of-the-art machinery.

The thermal effectiveness is a similar measure of performance for heat exchangers. According to the first law of thermodynamics for a flowing system, enthalpy must be conserved in a heat exchanger. The second law requires that the outlet temperature cannot be lower than the inlet temperature at the cold end of a counterflow heat exchanger. At the hot end, the outlet temperature cannot be higher than the inlet temperature. Using the points shown in Figs. 8.19 and 8.20, these three constraints can be expressed as

$$\dot{m}_i(h_2 - h_3) = \dot{m}_o(h_1 - h_5) \tag{8.53a}$$

$$T_5 \leq T_3 \tag{8.53b}$$

and

$$T_1 \leq T_2 \tag{8.53c}$$

where $\dot{m}_i$ and $\dot{m}_o$ are the inlet and outlet mass flow rates. The maximum possible enthalpy transferable is always the lesser of the enthalpy difference on the two sides of the heat exchanger. The largest possible enthalpy difference occurs when the fluid is at the maximum temperature occurring within the heat exchanger at one end and at the minimum temperature at the other end. Note that a difference in mass flow rates between the two heat exchanger legs can produce a large difference in the maximum enthalpy change possible in each of the two legs. The thermal effectiveness of the heat exchanger is defined as the ratio of the actual enthalpy change in a leg of the heat exchanger divided by the maximum possible enthalpy change,

$$\frac{\Delta h_{\text{actual}}}{\Delta h_{\max}} \tag{8.54}$$

As an example, consider the heat exchanger in the cycle depicted in Fig. 8.20. For the high-pressure leg of the heat exchanger, the maximum possible enthalpy drop would occur if the fluid entered at temperature T_2 and left at temperature T_5. Therefore, the maximum possible enthalpy differences in the two legs of the heat exchanger are

$$\Delta h_{\max 2-3} = h(p_2, T_2) - h(p_3, T_5) \tag{8.55a}$$

and

$$\Delta h_{\max 5-6} = h(p_1, T_2) - h(p_5, T_5) \tag{8.55b}$$

The maximum possible enthalpy change for either fluid stream is the lesser of these two quantities. The thermal effectiveness can be written in terms of the actual enthalpy change by inserting (8.54) into (8.55). The thermal effectiveness for heat exchangers used in refrigeration systems typically ranges around 90%. Heat exchangers with larger thermal effectiveness are large and expensive and must be made with care to minimize the pressure drop.

8.8 Refrigeration Technology

When designing and constructing a helium cryogenic system for a particular application, it is necessary to keep in mind a number of factors that are influenced by economics and operational methods. Included among these are:

1. *Duty cycle*: Is the system to be operated on a short-term basis or is it part of a dedicated, closed cycle system?
2. *Owning and operating cost*: A system may be costly to operate because of large running costs including power, labor, or materials.
3. *Overall size of the system.*

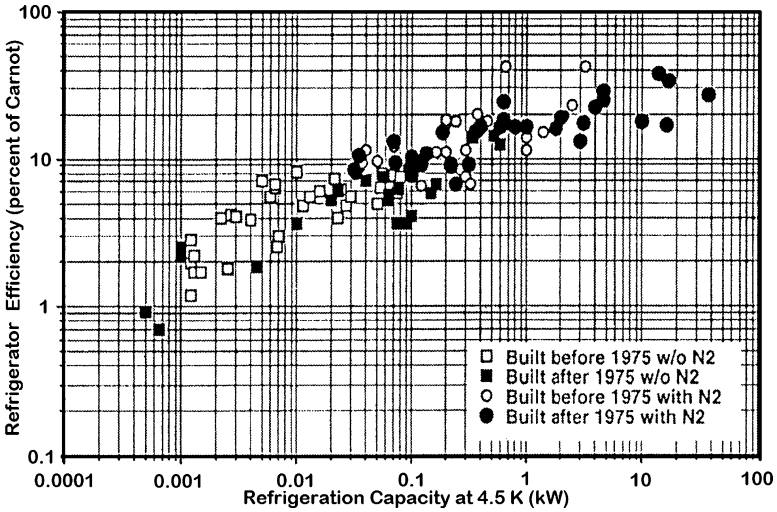

Fig. 8.28 Efficiency of cryogenic refrigeration systems (From Strobridge [17] and revised by Burns and Green [19])

Within the context of the above factors there are several choices that can be exercised when providing the helium coolant to a system. One of four methods is appropriate for cooling the system to liquid helium temperatures.

1. Purchase liquid helium and vent the helium vapor that evolves.
2. Purchase helium gas, liquefy it on a batch basis, and vent the vapor.
3. Purchase helium gas, liquefy it on a batch basis, and recover the evolved vapor which is then re-liquefied.
4. Purchase helium gas and a closed-cycle refrigerator. Run the system on a continuous basis, recovering the gas cold.

Of the above four methods, the first is suitable only for small systems with low duty cycles. Because helium is a rare and expensive commodity, this approach should be limited in use. More typically, a combination of the second and third methods is used in small research laboratories, where the percentage of helium recovery depends on the care with which the system is operated. The last method, although most efficient, is actually only suitable for systems that have the cryogenics as an integral part. Clearly, economics is the major factor that determines the cooling method best suited for a particular application.

Actual refrigeration systems operate far from the ideal efficiency. This fact occurs because practical cycles deviate from Carnot and the system components operate at less than ideal efficiency. Some of the non-idealities of components have been described above; however, those components that have the greatest tendency for nonideal performance are the moving parts, including compressors and expansion engines.

The usual way of displaying actual refrigerator efficiencies is to display them as a fraction of Carnot efficiency, $T_C/(T_H - T_C)$. Plotted in Fig. 8.28 are actual

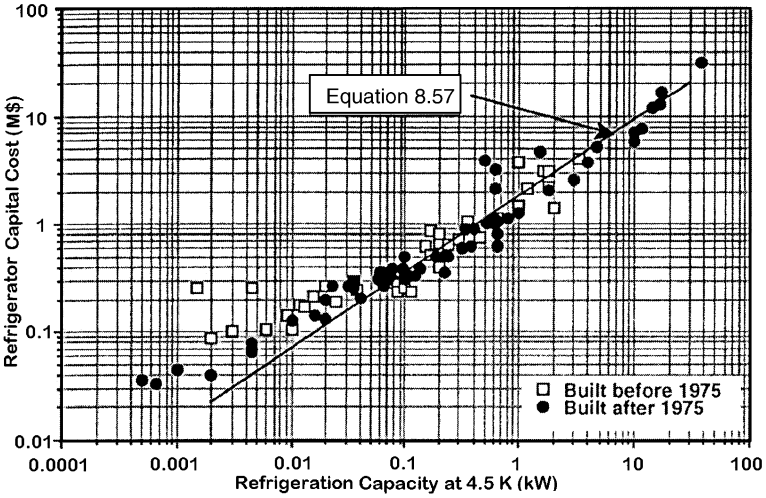

Fig. 8.29 Cost of low-temperature refrigerators and liquefiers as a function of 4.5 K capacity (From Burns and Green [19])

efficiencies (as a % of Carnot) of various cryogenic systems versus their 4.5 K refrigeration capacity [18, 19]. This graph is revised from the original survey by Strobridge [18]. It is significant to note that the most important factor in the efficiency is the 4.5 K capacity of the machine. The reasons for the increase in efficiency with size are twofold. For larger refrigerators, there is more to be gained by making the system more efficient. The total power saved can be a significant cost item and worth pursuing. Also, larger systems can justify more stages of refrigeration and expansion, thus allowing the cycle to be tuned closer to ideal conditions. An actual refrigeration system is made up of a number of individual components.

The cost of refrigeration components has been surveyed by a number of authors. Plotted in Fig. 8.29 are costs as summarized by Burns and Green [18]. Plotted is the capital cost in M$US versus that refrigeration capacity at 4.5 K based on the most recent study. The graph suggests a relationship for the cost of refrigeration of the form

$$C = \sigma P^n \tag{8.56}$$

where σ is an empirical coefficient and n is an exponent less than unity. For C to be the cost in millions of dollars and P be the 4.5 K cooling power in kilowatts, in 1997 Burns and Green found $\sigma = 6000$ and $n = 0.7$ to be the best-fit parameters. This relationship appears to fit all the data to within a factor of two. Furthermore, as standard units become available, the empirical relationship suggested by Fig. 8.29 has an exponent closer to unity. This fact is the result of certain fixed costs such as engineering and design that enter in the development of a new system. The nonlinearity of capital cost coupled with the costs of operation and maintenance

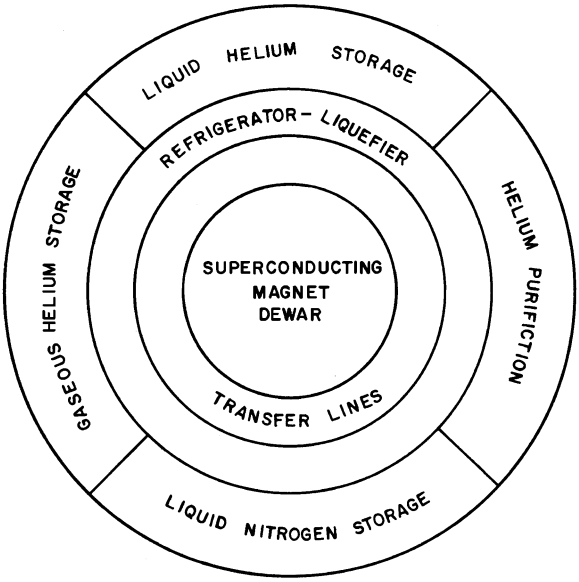

Fig. 8.30 Components making up a cryogenic system (From Robinson [21])

are factors which must be considered when determining which cooling scheme is appropriate for a particular system.

A schematic representation [20] of the way these components fit together in the system is shown in Fig. 8.30. Besides the helium refrigerator or liquefier, there must be storage of gaseous and liquid helium and nitrogen. Furthermore, in the helium system, there must be some form of purifier to recycle the gas. Finally, there must be a system of vacuum insulated transfer lines to take the fluids from storage or liquefier to the system.

8.9 Summary

The foregoing chapter presents a survey of the principles of refrigeration and liquefaction applied to helium. Greater detail can be considered particularly with respect to real systems and components. However, as the goal of this book is the emphasis of basic principles rather than hardware, no further discussion of this subject is given here. For the reader who is particularly interested in this subject, several of the references listed at the end this chapter will provide greater detail.

Questions

1. What is the primary difference between a cryogenic refrigerator and a liquefier? How does that difference affect design of the flow circuit?

2. Why does it take more energy to cool something from room temperature to 4 K, than it does to warm the same thing from 4 K to room temperature?
3. What feature on a T-S diagram identifies the optimum discharge pressure for a simple Linde-Hampson liquefier or refrigerator?
4. A cascade helium liquefier based on a Linde-Hampson cycle requires pre-cooling with LH_2 and LN_2. Why is this? Discuss the thermodynamic efficiency of such a cycle compared to that of a simple Claude cycle, which may not require pre-cooling.
5. Most practical refrigeration cycles have a Figure of Merit less than that of the Carnot cycle. Why?
6. List as many sources as you can of inefficiency in a real refrigerator based on a Claude cycle.
7. Discuss the difference between closed and open cycle isothermal refrigeration. What are the principal advantages to closed cycle systems?
8. Discuss the design of a heat exchanger versus that of a regenerator. What is the function of each? What are the primary differences?
9. Compare the thermodynamic efficiency of a Stirling cycle to that of a Gifford-McMahon cycle. Why is one more efficient than the other?

Problems

1. An alternate equation of state for real gases is described by the relationship

$$pv = \frac{RT}{(1 - b/4v)^4} - \frac{a}{v}$$

   (a) Using the universal behavior of gases near the critical point, determine the coefficients a and b as functions of critical parameters. Evaluate a and b for helium.
   (b) Derive a relationship for the inversion temperature T_{inv} and calculate its reduced maximum value (T^m_{inv}/T_c).
   (c) Derive an expression for the Joule–Thomson coefficient μ_j and determine its value for helium at the critical point.

2. (a) Calculate the ideal liquefaction work for helium that is initially at liquid nitrogen temperature, 77 K.
   (b) Determine the minimum quantity of liquid nitrogen required to precool a unit mass of helium gas from 300 to 77 K. ($h_{fg} = 198$ kJ/kg for LN_2).
   (c) Compare the total work required for the liquid nitrogen precooling method to that of an ideal liquefier.

3. Calculate the temperature corresponding to the maximum inversion pressure for a van der Waals gas. Determine the corresponding temperature and pressure for helium gas.

4. Derive the following relationship for the entropy change for a van der Waals gas:

$$s_2 - s_1 = C_p \ln\left(\frac{T_2}{T_1}\right) + R \ln\left(\frac{v_2 - b}{v_1 - b}\right)$$

Begin from a total differential of the entropy. Find the relationship between temperatures and specific volumes for an isentropic change in state.

5. A particular piston compressor can achieve a maximum pressure ratio of $p_2/p_1 = 100$ by either isentropic or isothermal compression of a gas. The compressor is to be used in one of two processes within a refrigeration cycle: (1) isentropic compression followed by isochoric cooling of the gas in the cylinder, or (2) isothermal compression. Calculate the entropy change, heat removed from the gas, and the maximum gas temperature for each process. Assume an ideal gas that begins at $p = 0.1$ MPa, $T = 300$ K and ends up at $T = 300$ K. Given that the pressure ratio and that the maximum operating temperature will always be limited for real compressors, which process should be used in the refrigeration cycle?
6. The Collins helium liquefaction system uses five heat exchangers and two expanders, one cooling heat exchanger #2 and one cooling heat exchanger #4. Draw the refrigeration cycle for this system showing the locations of all components. Label the various stages of cooling on a helium *T*-*S* diagram. Assume the following:

$$p_1 = 0.1 \text{ MPa} x_1 = 0.25 T_{e1} = 70 \text{ K}$$

$$p_2 = 2 \text{ MPa} \quad x_2 = 0.5 \quad T_{e1} = 10 \text{ K}$$

$$T_H = 300 \text{ K}$$

Calculate the yield, compressor work, and figure of merit for an ideal liquefier.

7. Consider the ideal isothermal helium refrigerator based on the Claude cycle with the first heat exchanger fixed by liquid nitrogen precooling at 77 K.
   (a) Calculate the cooling per unit mass flow. Determine an optimum based on varying m_e.
   (b) Estimate the liquid nitrogen consumption.
   (c) Determine the effective FOM for the entire system. Assume that $T_1 = T_2 = 300$ K and $p_1 = 0.1$ MPa; $p_2 = 3$ MPa.
8. For the simple He II refrigerator shown schematically in Fig. 8.12, assume the inlet temperature to JT_2 is at 2.2 K, 0.1 MPa and the system is in steady-state operation.
   (a) Calculate the refrigeration capacity per unit mass flow.
   (b) Estimate the temperature of the vapor which is exiting the heat exchanger on the return side.

9. A Stirling refrigerator is used to cool an infrared sensor. The working fluid is helium gas which may be treated as ideal. 1f the pressure and temperature at point 1 (see Fig. 8.16) are 0.5 MPa and 100 K, the volume ratio (V_3/V_2) is 10 and p_2 is 0.1 MPa, Find:

   (a) The pressure, temperature, and volume at points l through 4.
   (b) The temperature of the regenerator after steps 1 and 2 if it consists of 0.1 kg of copper and has an initial temperature of 100 K.
   (c) Repeat part b if the regenerator consists of 0.1 kg of lead.
   (d) On the basis of thermodynamics alone, which of the above materials is preferable for use in the regenerator?
   (e) Find the coefficient of performance (COP).

10. An isobaric refrigerator is to be designed with an inlet temperature $T_1 = T_2 =$ 300 K and an inlet pressure $p_1 = 0.1$ MPa to provide cooling at temperatures at or below 18.5 K. Assume the refrigerator is too small to use the work produced by the expander.

    (a) For a heat exchanger effectiveness and an expander efficiency of unity, calculate the compressor work per unit of cooling produced $(\dot{W}/\dot{Q}_c)$ for isothermal compressor outlet pressures of 0.5, 1, 2, 4, and 10 MPa. Plot $\dot{W}/\dot{Q}_c$ as a function of the compression ratio p_2/p_1 and fit the curve with an equation.
    (b) Redo the calculation in part a assuming a heat exchanger effectiveness of 0.95 and expander efficiency of 0.7.

11. Starting with the relationship for the entropy of an ideal gas,

$$s = C_p \ln T - R \ln p + s_0$$

    estimate the pressure necessary to reduce the entropy of 300 K helium gas to that of the liquid phase at 4.2 K, 0.1 MPa. Use the ideal gas equation of state to estimate the inter-molecular spacing. Is this physically possible?
12. Use the typical cooling capacity for a GM cryocooler (Fig. 8.25) to calculate the time needed to cool a 10 kg mass of copper from 80–10 K. Assume that the copper and cryocooler are thermally insulated from the environment so that the only heat to remove is the internal energy of the copper mass. Redo the calculation for the case where the mass has a steady heat generation of 10 W.
13. A counterflow heat exchanger is to be used to cool high pressure ($p_h = 2$ MPa) helium gas at 20 K and a mass flow rate of 1 kg/s. The low pressure return stream is at 0.1 MPa and enters the heat exchanger at 5 K.

    (a) Assuming the heat exchanger is 100% effective, what are the outlet fluid stream temperatures?
    (b) Calculate the same quantities for $\varepsilon = 90\%$. For this case, calculate the log-mean temperature difference and the required UA.
    (c) Make a sketch of the temperature profile along the heat exchanger for both cases.

References

1. M. W. Zemansky, *Heat and Thermodynamics*, 5th ed.. McGraw-Hill, New York, 1968.
2. R. D. McCarty, *Thermophysical Properties of Helium-4 from 2 to 1.500 K* with *Pressures to 1000 Atmospheres*, NBS Technical Note 631, U.S. Government Printing Office, Washington, DC, 1972.
3. HEPAK® is a data base software available through Cryodata.
4. REFPROP® is a data base software available through the National Institute for Standards and Technology.
5. R. F. Barron, *Cryogenic Systems*, 2nd ed, Oxford Science Press, 1985.
6. F. E. Hoare, L. C. Jackson, and N. Kurti, *Experimental Cryophysics*, Butterworth, London, 1961.
7. B. Z. Maytal and A Shavit, On the Integral Joule Thomson Effect, *Cryogenics*. **Vol. 34**, 19 (1994).
8. J. M. Geist and P. K. Lashmet, Compact Joule Thomson Refrigerator Systems 15 – 60 K, *Adv. Cryog. Engn.* **Vol. 6**, 73 (1961).
9. G. Claudet, A. Lacaze, P. Roubeau, and J. Verdier, The Design and Operation of a Refrigerator System Using Superfluid Helium, in *Proc. 5th Intern. Cryog. Engn Conf.*, Butterworth, Surrey, U.K., 1974, pp. 265–267.
10. S. Claudet, et al., Specification of Eight 2400 W @ 1.8 K Refrigeration Units for the LHC, in *Proc. 18th Intern. Cryog. Engn. Conf.*, Mumbai, India 2000, Narosa Publishing, New Delhi, 2000, pp. 207–210.
11. S. J. Welton, et al, Design, Development and Testing of the JT Refrigerators for the 45-T Hybrid Magnet, *Adv. Cryog. Engn* **Vol. 41**, 1283 (1996).
12. G. Claudet, and R. Aymar, Tore Supra and He II Cooling of Large High Field Magnets, *Adv. Cryog. Engn.* **Vol. 35**, 55 (1990).
13. S. C. Collins, Helium Refrigerator and Liquefier, *Adv. Cryog. Engn* **Vol. 11**, 11 (1966).
14. G. Walker, *Cryocoolers, Part 1: Fundamentals*, Plenum Press, New York, 1983.
15. H. O. McMahon, and W. E. Gifford, A New Low-Temperature Gas Expansion Cycle, *Adv. Cryog. Engn.* **Vol. 5**, Plenum Press, NY, 1960, pp. 354–367.
16. R. Radebaugh, A Review of Pulse Tube Refrigeration, *Adv. Cryog. Engn.* **Vol. 35**, 1191 (1990).
17. W. E. Gifford and R. C Longsworth, Pulse Tube Refrigeration Progress", *Adv. Cryog. Engn* **Vol. 10**, 69 (1965).
18. T. R. Strobridge, *Cryogenic Refrigerators—An Updated Survey*, NBS Technical Note 655, U.S. Government Printing Office, Washington, DC, 1974.
19. R.A. Burns and M.A. Green, An Update on Estimating the Cost of Cryogenic Refrigeration, *Adv. Cryog. Engn.* **Vol. 43,** 1661 (1998).
20. C. Trepp, "Problems of Large Scale Refrigeration", in *Low Temperatures and Electric Power*, pp. 31–41, Pergamon Press, New York, 1970.
21. G. Y. Robinson, "Economics of Cryogenic Systems for Superconducting Magnets", *Adv. Cryog. Engn.* **Vol. 25**, 341 (1981).

Further Readings

R. F. Barron, *Cryogenic Systems*, 2nd ed, Oxford Science Press, 1985.
F. E. Hoare, L. C. Jackson, and N. Kurti, *Experimental Cryophysics*, Butterworth, London, 1961.
R. B. Scott, Cryogenic engineering, Met-Chem Research, 1959 (1988).
K. Timmerhaus and T. Flynn, *Cryogenic Process Engineering*, Plenum Press, New York, 1989.
M. W. Zemansky, *Heat and Thermodynamics*, 5th ed. McGraw-Hill, New York, 1968.

Chapter 9
^{3}He and Refrigeration Below 1 K

By far, the most abundant naturally occurring isotope of helium is ^{4}He. However, there exists one other stable isotope, ^{3}He, which is only about 0.1 ppm of natural helium but can be obtained readily as a byproduct of nuclear reactions. The physical behavior of low-temperature ^{3}He is fundamentally quite different from that of the common isotope and ^{3}He has application in a number of areas in cryogenics; most notable of these is the role it plays in the achievement of temperatures below 1 K. This temperature range is primarily of interest in the studies of basic physical phenomena.

Interest in performing experiments with ^{3}He was not raised significantly until the mid 1940s, when it was determined that ^{3}He was a by-product of the Li^6 neutron capture reaction,

$$^6\mathrm{Li} + n \rightarrow {}^3\mathrm{H} + \alpha$$
$$\hookrightarrow {}^3\mathrm{He} + \beta$$

$$\tau = 12.5 \text{ year}$$

and therefore could be isolated in quantities sufficient for low-temperature experimentation. ^{6}Li is relatively abundant, occurring as 7.5% of natural lithium, and the tritium β-decay reaction has a half-life of 12.5 year. Consequently, the wide availability of neutrons in experimental fission reactors has made ^{3}He available to numerous researchers in low-temperature physics. Although the gas is a relatively expensive commodity, costing more than $ 100 to $1000US per STP liter, it is still orders of magnitude less costly than it would be to separate ^{3}He from natural helium. In recent years, the cost of ^{3}He has escalated significantly as a result of increased demand mostly as a detector of neutrons [1]. This development has put heavy financial and access burdens on low temperature physicists working in the sub-Kelvin temperature range.

S.W. Van Sciver, *Helium Cryogenics*, International Cryogenics Monograph Series,
DOI 10.1007/978-1-4419-9979-5_9,

9.1 Properties of Pure ^{3}He

Some properties of liquid ^{3}He are listed in Table 9.1. Note that the critical point is below the normal boiling point of ^{4}He. This should not be surprising given the lighter molecule. In fact, when ^{3}He was first discovered and separated there was some doubt about whether it would liquefy at all due to the very high zero point energy. Today ^{3}He is used in a number of low temperature experimental systems and usually condensed by heat exchange with a boiling pot of boiling ^{4}He (He II) at $T \approx 1$ K.

The relatively low binding energy of ^{3}He also causes the vapor pressure to be significantly higher than that of the common isotope. This fact is important for distillation of ^{3}He–^{4}He mixtures as well as reducing the pumping speed required for very low temperature ($T < 1$ K) refrigerators. One other important feature of ^{3}He is that is possesses a nonzero magnetic moment due to the unpaired nuclear spin. The magnetic moment is responsible for a large spin entropy which contributes a major fraction of the fluid entropy over much of its temperature range. For example, the ratio of specific heats of ^{3}He and ^{4}He at 1 K is about 40, a ratio that increases with decreasing temperature.

^{3}He is observed to experience a superfluid transition at about 2.6 mK, about three orders of magnitude in temperature below the λ-point of ^{4}He. This ratio should also not be surprising owing to the wholly different statistical character of the two fluids, see Table 9.2. ^{4}He has integral nuclear spin and obeys Bose–Einstein statistics. ^{3}He, on the other hand, has half-integer spin and a nuclear magnetic moment, and thus obeys Fermi–Dirac statistics, similar to that of electrons. These two statistical models predict very different physical behavior. Consider for example, the condensation mechanisms associated with superfluid transitions in ^{3}He and ^{4}He. The superfluid transition from ^{4}He is described approximately by Bose–Einstein (BE)

Table 9.1 Some properties of liquid ^{3}He [2]

Normal boiling point (K)	3.191
Critical constants	
T_c (K)	3.324
p_c (MPa)	0.115
ρ_c (kg/m^3)	41.3
Density at 0 K (kg/m^3)	82.3
Compressibility at 0 K (mm^3/J)	361
Heat of vaporization at 0 K (J/mol)	20.56
Surface tension at 0 K (mJ/m^2)	0.16
Velocity of sound at 0 K (m/s)	183
Thermal conductivity at 3.2 K (W/mK)	0.020
Viscosity at 3.2 K (μPa s)	1.9
Magnetic moment (nuclear magnetons)	−2.127
Vapor pressure at 1.7 K (kPa)	10.9
Specific heat at 1.0 K(J/mol · K)	4.222
Superfluid transition (mK)	2.6

Table 9.2 Statistical comparison of Helium isotopes

	^{4}He	^{3}He
Nuclear spin	Integer	Half integer
Statistics	Bose–Einstein	Fermi–Dirac
Magnetic moment	None	–2.127 μ_B
Condensation	BE type	BCS type

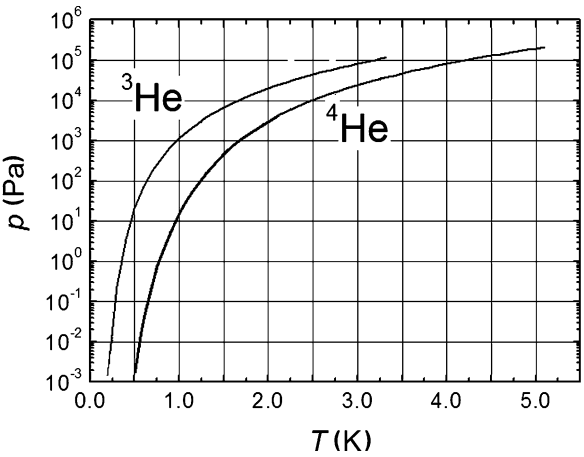

Fig 9.1 Vapor pressure of ^{3}He and ^{4}He (From Huang [3])

condensation. In the case of ^{3}He, the condensation is more analogous to that occurring in a superconductor which requires pairing of the Fermi particles to create the Bose condensate.

The vapor pressure of ^{3}He is greater than that of ^{4}He, allowing a lower temperature to be achieved by simply pumping on the liquid. A graphical comparison of the vapor pressure as a function of temperature for the two isotopes is shown in Fig. 9.1. Note that the pressure is on a semi-log scale in this graph and that the ^{3}He vapor pressure is between one and two orders of magnitude greater than that of ^{4}He for the same bath temperature. Therefore, it is much more efficient to operate a pumped ^{3}He refrigerator. However, since ^{3}He is a very expensive commodity, it is generally only available in gaseous form. Therefore, the design a ^{3}He evaporative refrigerator must include a boiling ^{4}He pot to provide the heat sink to condense the circulating ^{3}He. This pot also offers a thermal barrier and heat sink to minimize the conductive and radiative heat loading on the ^{3}He stage.

The practical embodiment of such a system is shown schematically in Fig 9.2. The incoming ^{3}He is condensed to liquid by thermal contact with the boiling ^{4}He bath. The operating temperature of this bath is normally in the 1–1.3 K range depending on the overall heat loading and ultimate pressure of the pump or cold compressor (0.1–1 torr). A separate pump loop circulates the ^{3}He at a pressure of 0.1 torr achieving temperatures in the range of 0.4 K. Unfortunately, even though

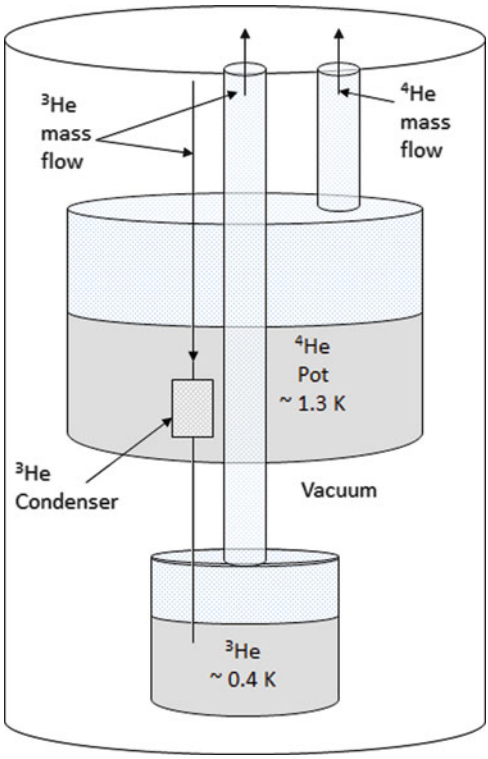

Fig 9.2 Schematic of ^{3}He refrigerator

this is significantly below the temperature achievable using ^{4}He, it still is not low enough for many low temperature experiments of interest. Fortunately, there is another refrigeration method that uses the characteristics of ^{3}He-^{4}He mixtures to achieve steady temperatures in a millikelvin range.

9.2 ^{3}He–^{4}He Mixtures and Dilution Refrigeration

We now consider the behavior of mixtures of ^{3}He and ^{4}He. Before doing so, we should keep in mind that the only difference between these two isotopes is that ^{3}He has one fewer neutron in the nucleus. This means that the two isotopes obey different statistical models, which clearly manifests itself in divergent behavior of the two fluids. Otherwise, they are chemically identical. One should keep in mind the significant difference between the behavior of mixtures of ^{3}He and ^{4}He versus mixtures of soluble classical fluids like liquid O_2 and N_2.

^{3}He and ^{4}He mixtures are technically important for they allow improved methods of cooling at very low temperatures. How this works can be understood by reference to the equilibrium phase diagram of the ^{3}He–^{4}He mixture system is shown in Fig. 9.3. The first thing to note in this diagram is that the λ-point, which marks the

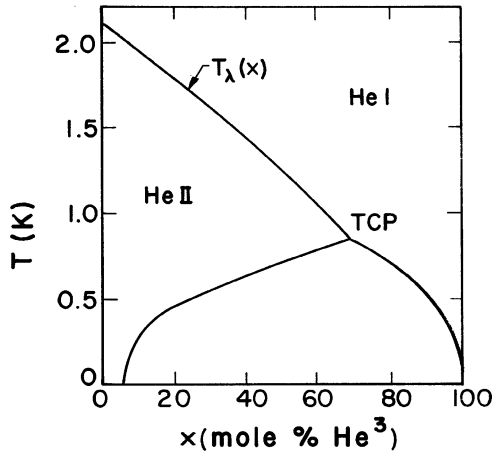

Fig. 9.3 Phase diagram of ^{3}He–^{4}He mixtures

phase transition between He I and He II, is depressed by the addition of ^{3}He. In fact, this transition disappears at 66.9% ^{3}He where it terminates at the tri-critical point (TCP). Significant for refrigeration is the existence of a phase-separation region below this point. ^{3}He–^{4}He mixtures are the only systems that experience a separation of phases due to isotopic mass differences!

In the temperature-concentration plane, the TCP occurs at $T = 0.872$ K and $x = 66.9\%$. The TCP is physically quite interesting because it represents the intersection of three phase boundaries, one being a second-order phase transition, the λ-line. Another feature apparent in Fig. 9.3 is the finite solubility of ^{3}He in the ^{4}He-rich phase. At absolute zero the phase boundary intersects the concentration axis at $x = 6.4\%$. This effect is contrary to classical physical arguments which would require a two-phase region in equilibrium at absolute zero to be completely separated to achieve minimum entropy. However, this is not a classical system. The occurrence of finite solubility of ^{3}He in ^{4}He even at absolute zero is the result of the quantum statistical character of the system. More important technically is that this feature allows dilution refrigerators to operate achieving near absolute zero temperature.

The existence of a finite solubility allows heat to be removed from the system by transferring ^{3}He from the pure component to the dilute component and thereby extracting the entropy of mixing, which is finite even at absolute zero. In a two-phase system, the entropy of mixing can be written

$$\Delta s = \frac{R}{M}[x \ln x + (1-x)\ln(1-x)] \tag{9.1}$$

where M, the molecular weight of ^{3}He, is equal to 3 kg/kmol. For ^{3}He–^{4}He mixtures at $T \simeq 50$ mK, $x = 0.064$ and thus $\Delta s = 0.66$ kJ/kg K. At any finite temperature, a very sizable amount of heat can be removed by this mechanism. The process forms the basis for dilution refrigeration. The principles of which are described here only briefly. The reader who is interested in further detail should consult one of various books on low temperature physics [2, 4].

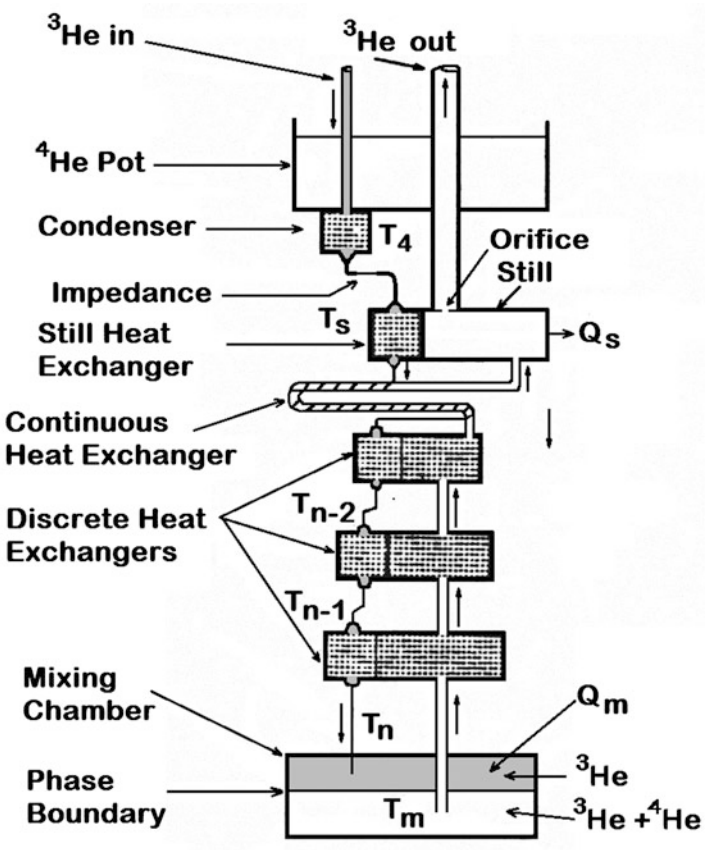

Fig. 9.4 Principal parts of a continuously operating dilution refrigerator [2]

The principal components of a continuously operating dilution refrigerator are shown in Fig. 9.4. The system consists of a closed-loop circulation system in which ^{3}He is usually the circulating component. Refrigeration is obtained by locating the phase boundary between the two fluid components in the mixing chamber at the lower end of the system. Then by circulating the ^{3}He, the entropy of mixing is removed from this region. The rate of cooling, independent of nonideal loss mechanisms, is

$$Q = \frac{\dot{m}}{M} T \Delta s = \frac{\dot{m}}{M} RT[x \ln x + (1 - x) \ln(1 - x)] \tag{9.2}$$

Based on (9.2) a mass flow rate of 0.3 mg/s is required to obtain a cooling power of 10 μW at 50 mK, a reasonable value for a moderate-size dilution refrigeration system. The state-of-the-art in this technology is continuous cooling in the range of a few millikelvin.

In addition to the mixing chamber, there are several other important components to the dilution refrigerator. The ^{4}He pot, which operates around 1.2 K, condenses the circulating ^{3}He similarly as in a conventional ^{3}He refrigerator and provides a low-temperature heat sink for heat leaks into the system. Usually a combination of concentric counterflow and discrete heat exchangers are used in dilution refrigerators. The latter type are more effective at obtaining the lowest temperatures. The still is the point in the cooling circuit where the ^{3}He is preferentially evaporated to produce the circulation. Due to its high value, the low pressure ^{3}He gas is circulated through a special vacuum pump to prevent loss of product and then returned to the refrigerator by condensation with the ^{4}He pot. Typically, the still operates around 0.5 K where the ^{3}He vapor pressure is high enough to obtain sizable mass flow easily. Often a special ^{4}He film flow inhibitor or orifice is installed in the still pumping line so that the superfluid film will not creep up and cause significant ^{4}He evaporation. Circulation of ^{4}He can result in degradation of the performance of a ^{3}He–^{4}He dilution refrigerator.

Dilution refrigerators are the best method of obtaining continuous cooling a temperatures below 0.4 K and modern systems now reach below 10 mK. Also, recently developed are dilution refrigerators that operate with cryocoolers to replace the liquid ^{4}He bath [5]. Other options include adiabatic demagnetization can be employed to reach the millikelvin regime using paramagnetic salts as working elements. This topic is discussed in Sect. 10.3. It is also possible to reach the micro-kelvin regime using adiabatic demagnetization of nuclear spins. However, in both these cases, it is generally not possible to obtain continuous cooling.

9.3 Statistical Models for Pure ^{3}He

We now delve briefly into the physics of ^{3}He to provide a better understanding of the unique features of this fluid. By analogy to the treatment of pure ^{4}He in Chap. 6, it is appropriate to discuss the physical models for ^{3}He in terms of deviations from the ideal quantum gas model. In this case, we consider quantum statistical mechanics applied to particles obeying Fermi–Dirac statistics. This problem is basically similar to the free-electron model in metals with the relative temperature range and densities being the main differences.

As is the case for the ideal Bose gas model, the properties of an ideal Fermi gas are established in terms of a summation over discrete energy levels. The properties of an ideal quantum gas can be obtained by taking these discrete levels in the density of states to be infinitesimal and converting the summation to an integral. The resulting expression for the number density can be written

$$\frac{N}{V} = \frac{2\pi}{h^3}(2m)^{3/2}\int_0^\infty \frac{\varepsilon^{1/2}d\varepsilon}{z^{-1}e^{\beta\varepsilon}+1} \tag{9.3}$$

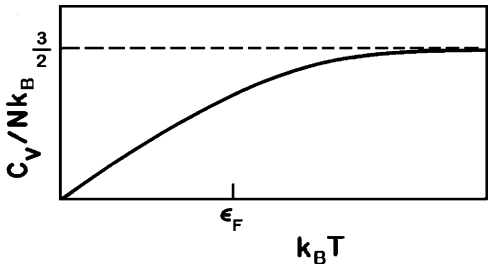

Fig. 9.5 Specific heat of an ideal Fermi gas [5]

where, as in the case of the Bose gas, $z = e^{\beta\mu}$ is the fugacity, μ the chemical potential and $\beta = 1/k_BT$. Equation (9.3) is an application of (6.9) for the special case of a system of particles obeying Fermi–Dirac statistics. Note that an important corollary to Fermi statistics is that the system of particles must obey the Pauli exclusion and therefore can have energy level occupation numbers of 0 or 1. This fact is important because there is no need to be concerned with substantial occupation numbers in the ground state as is the case in Bose statistics. By further analogy with the discussion in Chap. 6, the energy density of a set of Fermi particles is

$$\frac{E}{V} = \frac{2\pi}{h^3}(2m)^{3/2}\int_0^\infty \frac{\varepsilon^{1/2}d\varepsilon}{z^{-1}e^{\beta\varepsilon}+1} \tag{9.4}$$

which can be used in consort with (9.3) to derive the properties of the gas. Note that for a set of Fermi particles having spin s, the energy levels have a $(2s + 1)$ degeneracy, which is only removed by splitting the levels in a magnetic held. At $T = 0$, all levels are occupied up to the Fermi energy which is defined by the expression

$$\varepsilon_F = \frac{\hbar^2}{2m}\left(\frac{6\pi^2}{(2s+1)}\frac{N}{V}\right)^{2/3} = k_BT_F \tag{9.5}$$

Introducing numerical values appropriate to ^{3}He with spin $\frac{1}{2}$, the Fermi temperature T_F is computed to be 4.9 K. Therefore, considerable effects of degeneracy in ^{3}He are expected at low temperatures. For a finite temperature, a fraction of the particles are excited above the Fermi energy, the result of which is a smearing of the distribution function ε_F.

The specific heat of an ideal Fermi gas is obtained from the derivative of the internal energy per particle:

$$\frac{C_v}{Nk_B} = \frac{1}{Nk_B}\left(\frac{\partial E}{\partial T}\right)_v \tag{9.6}$$

The result of this calculation [5] is plotted in Fig. 9.5 for a range of energies including ε_F. Note that at high temperatures, $k_BT > \varepsilon_F$; the specific heat asymptotically

approaches the Boltzmann limit of $C_v = 3/2Nk_B$. At low temperatures, $k_B T \ll \varepsilon_F$; the behavior of a degenerate Fermi gas is evident with a linear temperature dependence of the specific heat,

$$\frac{C_v}{Nk_B} \simeq \frac{\pi^2}{2}\frac{T}{T_F} \tag{9.7}$$

which is the same result obtained for the free-electron model in Chap. 2.

The behavior of liquid ^{3}He is different from that of an ideal Fermi gas. This is primarily the result of the sizable interparticle interactions which occur in the fluid. Landau's theory of Fermi liquids is a fairly straightforward approach to this problem [5–7]. This theory, which is primarily a modification to the ideal quantum gas model, calls for introducing an effective mass m^*, which in turn modifies the relationship for the physical properties of the Fermi liquid. The effective mass should then be calculable and compared with experimental results for ^{3}He.

Considering the behavior of the specific heat at low temperatures, the Landau theory predicts that

$$\frac{C_v}{Nk_B} = \frac{m^*}{m}\left(\frac{C_v}{Nk_B}\right)_{\text{ideal}} \simeq \frac{\pi^2}{2}\left(\frac{T}{T_F^*}\right) \tag{9.8}$$

where in this case the modified Fermi temperature is given by the expression

$$T_F^* = \left(\frac{m}{m*}\right)T_F \tag{9.9}$$

By comparing (9.8) with experiment it is possible to determine the effective mass appropriate to ^{3}He. For example, plotted in Fig. 9.6 is the specific heat of liquid ^{3}He compared to that of an ideal Fermi gas of liquid density, $T_F = 4.9$ K. Clearly, the ideal gas model is a poor representation of the experimental data. A better fit to the low-temperature specific heat is obtained with a choice of effective mass about twice that of the ^{3}He nucleus, which indicates the Fermi temperature appropriate to the Landau model is closer to 2.5 K.

The transport properties of ^{3}He can also be understood in terms of Fermi liquid theory. The theoretical development of this problem stems from a solution to the semi-classical Boltzmann equation. In this model the viscous and thermal interactions are associated with the scattering of quasiparticles at the Fermi surface. For an isotropic fluid, the relationship for the viscosity may be written in the general form for $T < T_f$

$$\mu \approx \frac{A}{T^2} \tag{9.10}$$

where A is a function of the effective mass. At low temperatures, $T \lesssim 0.1$ K, the viscosity of ^{3}He has been shown to be consistent with the inverse square relationship

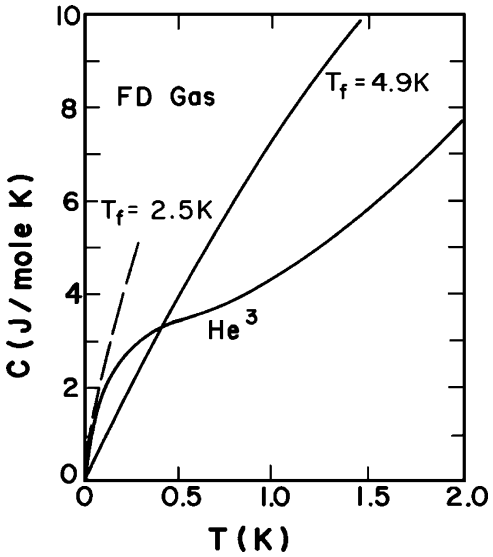

Fig. 9.6 Specific heat of liquid ^{3}He compared to curves for ideal Fermi gas [8]

in (9.10) with $A = 0.38 \pm 0.06\ \mu Pa\ s\ K^2$. This means that the viscosity of ^{3}He is about 100 mPa s at 3 mK, a value close to that of light machine oil.

The thermal conductivity according to Fermi liquid theory should go as,

$$k \approx \frac{B}{T} \tag{9.11}$$

The inverse temperature dependence of the thermal conductivity comes from the fact that a degenerate Fermi liquid has C_v proportional to T which when coupled with the form of the viscosity yields $k \approx T^{-1}$. Experimental results generally support this conclusion although only at very low temperatures, $T < 20$ mK, where C_v is linear with temperature with $B \sim 0.4$ mW/m [9]. As a point of reference, the thermal conductivity of liquid ^{3}He at 3 mK is approximately equal to that of pure copper at the same temperature.

9.4 Submillikelvin Refrigeration

To study the behavior of ^{3}He or any other material below a few millikelvin, it has been necessary to use additional cooling mechanisms beyond that of dilution refrigeration. There are primarily two methods to achieve lower temperatures, one being adiabatic demagnetization of nuclear spins and the other Pomeranchuk cooling.

Adiabatic demagnetization has been used extensively for very low temperature refrigeration [10, 11]. It is usually a single-cycle process. To achieve cooling by adiabatic demagnetization it is necessary to have a working magnetic material which has weakly interacting spins so that the ordering temperature is below the minimum temperature to be achieved. For submillikelvin refrigeration, the only presently successful method is demagnetization of nuclear spins in materials such as Cu or $PrNi_5$.

An alternative method used to cool ^{3}He to about 1 mK is adiabatic compression of ^{3}He along its melting line. In fact, this was the method used to originally discover the superfluid transition in ^{3}He. The method was first suggested by Pomeranchuk [12], who predicted the existence of a minimum in the solid–liquid phase boundary for pure ^{3}He ($T_{\min} = 319$ mK, $p_{\min} = 2.913$ MPa). The minimum exists because the spin ordering in the liquid occurs at higher temperatures than that in the solid. Therefore, between the ordering temperature of the liquid and that of the solid, the entropy of the solid is greater and cooling can be achieved by adiabatically compressing the liquid through the solid–liquid phase transition.

The thermodynamics of Pomeranchuk cooling are reasonably straightforward given the existence of the minimum in the solid–liquid phase boundary in ^{3}He. Using the Clausius–Clapeyron equation for the phase transition,

$$\frac{dp}{dT} = \frac{s_1 - s_s}{v_l - v_s} \tag{9.12}$$

for temperatures below the minimum the liquid state has a greater specific volume than that of the solid. Below about 40 mK, the denominator in (9.12) takes on approximately a constant value of 1.31 cm^3/mol. The entropy of each phase is dominated by the spin contribution. The liquid has an entropy that is approximately linear with temperature,

$$s_l = \frac{R}{M}\left(\frac{T}{T_F^{**}}\right)\ln 2 \tag{9.13}$$

where T_F^{**} is the pressure-dependent magnetic Fermi temperature. The entropy of the solid is nearly constant until its magnetic ordering temperature, $T_N = 1.1$ mK. The relationship for the solid entropy is more complex, involving the nuclear exchange interaction, J, that is,

$$s_s = \left(\frac{R}{M}\right)\ln 2 - \frac{1}{M}\sum_n A_n\left(\frac{J}{k_B T}\right)^{n+1} \tag{9.14}$$

where A_n are weighting factors in the summation. The behavior of the entropy of each phase is shown in Fig. 9.7.

Pomeranchuk cooling is achieved by first bringing the system to thermodynamic equilibrium at a temperature below the minimum in the solid–liquid phase boundary. This is best carried out by using a continuously operating dilution refrigerator. With the fluid compressed to just below the melting line, the Pomeranchuk cell is then

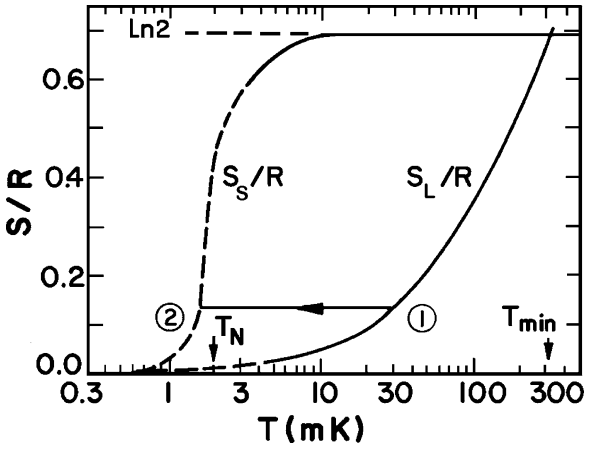

Fig. 9.7 Entropy of solid and liquid ^{3}He along the melting curve. Temperatures indicated include $T_{\min}$, the minimum in the melting curve and T_N, the spin ordering temperature in the solid

isolated from the dilution refrigerator and adiabatically compressed across the phase boundary. Temperature reductions of at least an order of magnitude are possible. For example, starting with the system at 30 mK, point ① in Fig. 9.7, adiabatic compression along line ① to ② achieves a minimum temperature of about 1 mK. Obviously, as with adiabatic demagnetization, this method is not suited to continuous refrigeration at the lower temperature. Furthermore, the end product of the cooling stage is a two-phase mixture of solid and liquid ^{3}He, which has the added difficulty of separating the physical phenomena occurring in each phase. This situation can lead to confusion when one of the phases is experiencing most unusual behavior as occurs in ^{3}He below 3 mK. As a result of these complications and the interest in studying the magnetic field dependence of ^{3}He, the most popular method for cooling ^{3}He to submillikelvin temperatures is adiabatic demagnetization.

9.5 Superfluid ^{3}He

Predictions as early as the 1960s indicated that ^{3}He would become superfluid by a mechanism similar to that occurring in superconductors. The uncertainty was based mainly on determining the transition temperature. The physical basis known as BCS-type interaction has a well established form for the transition temperature,

$$T_c = 2.28 \frac{\hbar P_F^2}{k_B m^*} \exp\left(\frac{\pi}{2} \frac{h^2}{m^*} \frac{P_F}{\langle \phi | U | P_F \rangle}\right) \tag{9.15}$$

where U is the exchange interaction and ϕ is the particle wave function. It is difficult to predict T_c from first principles because m^*, the effective mass, is primarily an experimental quantity. Since m^* enters in the denominator of the exponential argument, small changes in its value can have profound effect on T_c.

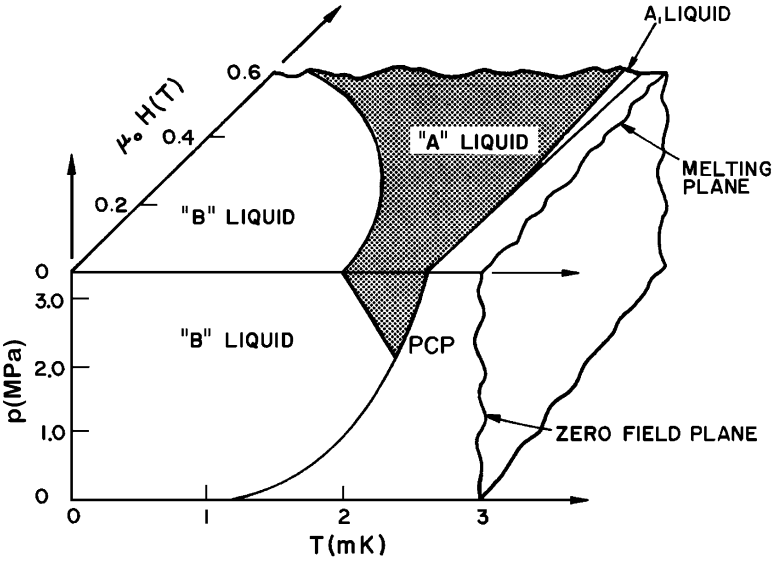

Fig. 9.8 *P-T-H* phase diagram of very-low-temperature ^{3}He

However, with liquid helium research perpetually pursuing lower temperatures, it was only a matter of time before superfluid He would be discovered.

The first observations attributed to a new phase transition in ^{3}He were made by Osheroff, Richardson and Lee [13]. Their results were eventually shown to be the first observation of the superfluid transition in ^{3}He for which they were awarded the Nobel Prize. Their experiment was an investigation of the pressure variations along the liquid–solid phase boundary using a Pomeranchuk cell. Two phase transitions were observed. The first, referred to as the A-transition, occurred at 2.65 mK and was associated with a slope change in the pressure variation of the cell, suggesting a higher-order phase transition. The lower-temperature phase transition B, occurring at 1.8 mK, was seen as a first-order transition with an associated latent heat. Since that time, an enormous amount of research has been conducted on these new phases of ^{3}He. In this brief review, it is not possible to do justice to the state-of-the-art in superfluid ^{3}He research. Fortunately, a number of excellent reviews are available in the literature [14]. The present section presents some of the interesting properties of these new phases of ^{3}He.

To begin, consider the phase diagram of ^{3}He in the very-low-temperature regime as it depends on pressure, temperature, and magnetic field; see Fig. 9.8. The dependence on magnetic field is quite unique for pure liquids. The diagram indicates the existence of primarily three phases in addition to the normal Fermi liquid occurring above T_c. The intersection point between the A, B, and normal Fermi liquid phases at zero magnetic field is referred to as the polycritical point (PCP). Note that the A phase takes precedence over the B phase with increasing magnetic field, indicating A is more strongly magnetic than B.

The theoretical description of superfluid ^{3}He is extremely complex and beyond the scope of the present discussion. Evidence suggests that three phases occur in ^{3}He because it is a magnetic superfluid that pairs in a triplet state. This fact establishes an important difference between the interactions occurring in superfluid ^{3}He and those in conventional superconductors. In the latter case the pairing is in the singlet state and consequently only one phase is present. In ^{3}He three orientations are possible for the nuclear spins, two with parallel and one with anti-parallel alignment. Since the A phases are more strongly magnetic, it is expected that they contain mostly parallel spin orientations. The B phase being less magnetic must contain a significant fraction of anti-parallel aligned spins. This effect has been shown experimentally through susceptibility measurements. The A and A, phases have magnetic properties approximately the same as the normal Fermi liquid with a temperature-independent susceptibility. The B phase has a decreasing susceptibility with temperature suggestive of an anti-ferromagnetic ordering.

Perhaps the most interesting aspects of ^{3}He in this low-temperature regime are those normally associated with superfluidity, that is, anomalous behavior in the energy transport mechanisms. As discussed in Chap. 6, superfluid ^{4}He (He II) has a number of very unique transport properties. Among these are new sound propagation mechanisms (second sound), viscosity that depends on the mechanism used for measurement, the existence of vortex lines in the bulk fluid, and extremely high heat transport capability. The latter feature makes He II a technically useful fluid. Generally, these properties are explained successfully in terms of the reasonably simple two-fluid model. It is therefore of interest to consider similar characteristics of superfluid ^{3}He.

One property that makes a superfluid very different from ordinary fluids is its unique sound propagation mechanisms. In addition to ordinary sound propagation, there is second sound and fourth sound which is propagation through a superleak. This latter sound propagation mechanism is one of several methods used to measure the superfluid density. In fact, it can be shown from the two-fluid model that the superfluid density ρ_s is related directly to the fourth and first sound velocities:

$$\frac{\rho_s}{\rho} = \left(\frac{c_4}{c_1}\right)^2 \tag{9.16}$$

Since ρ_s is an important parameter in the theory of superfluidity, experimental determinations of ρ can be compared with calculation. Such an analysis, based on a renormalized theoretical calculation, is well beyond the scope of the present discussion. However, it is important to be aware of the substantial difference between the behavior of ρ_s in ^{3}He and that for the same parameter in ^{4}He. These properties have different temperature dependencies owing to the different condensation mechanisms. In the BCS theory, which is appropriate for superfluid ^{3}He, the superfluid density goes as the order parameter squared which is approximately linear with temperature near T_c:

$$\frac{\rho_s}{\rho} \approx 1 - \frac{T}{T_c} \tag{9.17}$$

This equation is roughly consistent with experiment. By contrast, the temperature dependence of ρ_s for ^{4}He varies as $1 - (T/T_\lambda)$ [5, 6].

Now turn to the problem of viscous flow in superfluid ^{3}He. Above T_c, the viscosity of ^{3}He is that of a normal Fermi liquid, which increases with decreasing temperature as $1/T^2$. Therefore, in the millikelvin range, the viscosity is very large. The viscosity of ^{3}He decreases for temperatures below T_c; it never becomes vanishingly small. In fact, there is a minimum in the viscosity occurring around 1.6 mK for which the ratio to that of the Fermi liquid at the A transition is approximately 0.2. Therefore, although superfluid ^{3}He has a decreasing viscosity, it is still orders of magnitude more viscous than ^{4}He.

Heat transport in superfluid ^{3}He can be discussed in terms of two-fluid hydrodynamics. Therefore, the mechanism which is appropriate for describing heat flow is internal convection between the normal and superfluid components. For fine capillary tubes of diameter d, at low heat fluxes and laminar flow conditions, the dominant mechanism is the normal fluid viscous interaction with the tube walls. In this case, an effective thermal conductivity k_e, may be defined as

$$k_e = \frac{d^2(\rho s)^2 T}{32\mu_n} \tag{9.18}$$

where μ_n is the normal fluid viscosity. However, in the case of ^{3}He the value of μ_n is about four orders of magnitude larger than μ_n for ^{4}He around 1.5 K. Therefore, the effective thermal conductivity of superfluid ^{3}He in small-diameter channels should be much less than occurs in ^{4}He. To establish some rough numerical values for this property, note that the thermal conductivity of the normal Fermi liquid increases with decreasing temperature until it reaches a value of 0.1 W/m K just above T_c. Below T_c, the effective thermal conductivity in a channel of diameter 3 mm, is about 10 times higher or 1 W/m K. Although superfluid ^{3}He does not possess the phenomenally high heat conductivity capability evident in superfluid ^{4}He, it exists at much lower temperatures where its heat conductivity is comparable to that of pure metals.

In the above brief description of the properties of ^{3}He, both normal and superfluid, a number of interesting features have been reviewed. A great deal more is known about ^{3}He, however, space and theoretical limitations do not permit further analysis of this interesting system. There are a number of other unique properties of superfluid ^{3}He not described heretofore. These properties include the anisotropic nature of the system. Because of magnetic properties, the fluid can be oriented in a magnetic field. Also, superfluid ^{3}He is believed to possess some spatial correlations called "textures," referring to correlated behavior of ^{3}He over dimensions long compared to the coherence length. Needless to say, these are very new theoretical and experimental topics, which explains the substantial research effort in this very exciting field.

Questions

1. What are the unique features of the ^{3}He-^{4}He phase diagram that make possible dilution refrigeration at millikelvin temperatures?
2. Why does ^{3}He have a higher vapor pressure than ^{4}He?

References

1. D. Kramer, DOE Begins Rationing ^{3}He, *Physics Today*, Vol. 63, 23, June 2010 and D. Shea and D. Morgan, The ^{3}He shortage: Supply, Demand and Options for Congress Report to Congress Dec, 22, 2010.
2. V. Lounasmaa, *Experimental Principles and Methods Below 1 K*, Academic Press, London, 1974.
3. Y. H. Huang and G. B. Chen, A Practical Vapor Pressure Equation for Helium-3 from 0.01 K to the Critical Point, Cryogenics Vol. 46, 833 (2006).
4. P.V.E McClintock, D. J. Meredith and J. K. Wigmore, *Matter at Low Temperatures*, Blackie and Sons, Ltd, Glasgow, UK (1984).
5. K. Uhlig, ^{3}He/^{4}He dilution refrigerator with high cooling capacity and direct pulse tube pre-cooling, *Cryogenics* **Vol. 48**, 511 (2008).
6. L. D. Landau, The Theory of a Fermi Liquid, *Sov. Phys. JETP* **3**, 920 (1957); **5**, 101 (1957); **8**, 70 (1959).
7. D. M. Lee and R. C. Richardson, Superfluid ^{3}He, in *The Physics of Liquid and Solid Helium, Part II*, K. H. Bennemann and J. B. Ketterson (Eds.), Chap. 4, Wiley, New York, 1978.
8. W. F. Keller, *Helium* 3 *and Helium* 4, Plenum Press, London, 1969.
9. J. C. Wheatly, Experimental Properties of Liquid ^{3}He, in *The Helium Liquids*. J. G. M. Armitage and I. E. Farquar (Eds.), Academic Press, London, 1975.
10. K. Andres and O. V. Lounasmaa, Recent Progress in Nuclear Cooling, *Prog. Low Temp. Phys.* **8**, 221 1982.
11. V. Lounasmaa, The Pursuit of Absolute Zero, *Adv. Cryog. Eng.* **29**, 551 (1984).
12. I. Pomeranchuk, On the Theory of Liquid ^{3}He, *Zh. Eksp. Teor. Fiz.* **20**, 919 (1950).
13. D. D. Osheroff, R. C. Richardson, and D. M. Lee, Evidence for a New Phase of Solid ^{3}He, *Phys. Rev. Lett.* **28**, 885 (1972).
14. J. C. Wheatly, Superfluid Phases of Helium Three, *Phys. Today* **29**, 32 (1976).

Further Readings

W. F. Keller, *Helium* 3 *and Helium* 4, Plenum Press, London, 1969.

O. V. Lounasmaa, *Experimental Principles and Methods Below 1 K*, Academic Press, London, 1974.

P.V.E McClintock, D. J. Meredith and J. K. Wigmore, *Matter at Low Temperatures*, Blackie and Sons, Ltd, Glasgow, UK (1984).

G. K. White and P. J. Meeson, *Experimental Techniques in Low-Temperature Physics*, 4th Ed, Oxford Science Publication, 2002.

J. Wilks, *The Properties of Liquid and Solid Helium*, Clarendon Press, Oxford, 1967.

Chapter 10
Special Topics in Helium Cryogenics

In the preceding chapters, the emphasis has been on the properties of helium and its applications. However, there are numerous other topics in cryogenics which do not fall in this specific context but still have considerable relevance to the general subject of helium cryogenics. In the present chapter, three such topics are overviewed: (1) thermal insulation systems, (2) helium adsorption, and (3) magnetic refrigeration. The review of these subjects is not all-inclusive but rather represents a few areas of potential interest to the general subject of low-temperature phenomena important to the useful application of helium cryogenics.

10.1 Thermal Insulation

In the design of any cryogenic system, thermal isolation of the low-temperature environment must be achieved effectively. This is particularly true for low temperature helium systems owing to the small value of the latent heat of liquid helium and high cost per watt of refrigeration in this temperature range.

No thermal insulation system is perfect. The level of insulation can vary depending on the requirements of the application and the amount of effort applied. For very long life liquid storage tanks, the insulation is complicated and optimized to minimize the heat leak. Other systems that can tolerate a lower level of thermal isolation can have much simpler thermal insulation. However in any cryogenic application, the design and implementation of the thermal insulation system is a critical task.

There are various modes of heat transfer at play in a thermal insulation system. These involve different forms of the three principal modes of heat transfer:

1. Solid heat conduction through the structural supports, instrumentation wires and any insulating material.
2. Heat transport through any residual gas that may exist in the insulating vacuum space.

S.W. Van Sciver, *Helium Cryogenics*, International Cryogenics Monograph Series,
DOI 10.1007/978-1-4419-9979-5_10,

3. Radiant heat transfer from the surrounding to the low temperature environment.

Each of these modes is discussed below in the context of how it affects cryogenic insulation.

10.1.1 Solid Conduction

Solid conduction involves heat transport from high to low temperature through the materials of the insulating vessel. Some of these materials may be structural supports and others may be part of the insulation itself. This mode of heat transfer can be minimized by use of materials with low thermal conductivity and if necessary high strength. The relative importance of this mechanism depends on design. If the system demands a great deal of load transfer to ambient temperature, then the conduction heat leak will probably be an important contribution to the overall performance of the cryogenic system.

The conduction heat transfer can be calculated by application of Fourier's law for heat conduction,

$$\vec{q} = -k(T)\ \vec{\nabla}T \tag{10.1}$$

where *k(T)* represents the temperature dependent material thermal conductivity and $\vec{\nabla}T$ represents the temperature gradient in the direction of the heat flux, q. This property has been discussed for solid isotropic materials to a considerable extent in Chap. 2. For insulating materials, which are often anisotropic, the thermal conductivity will vary with direction as well as temperature.

Many practical problems involve one-dimensional conduction over a finite temperature difference. A commonly useful quantity in this case is the integrated or mean thermal conductivity, $\bar{k}$, which can be used for determining the total heat conduction between two fixed temperatures. The integrated thermal conductivity is defined by the expression

$$\bar{k} = \frac{1}{(T_2 - T_1)} \int_{T_1}^{T_2} k(T) dT \tag{10.2}$$

where T_2 and T_1 are the two end temperatures. In general, *k(T)* is a complex function of temperature making evaluation of (10.2) difficult. However, these thermal conductivity integrals have been tabulated for many materials of interest in cryogenics [1, 2].

For many materials at low temperatures, *k(T)* can be approximated over a limited temperature range by an expression of the form

$$k(T) = AT^n \tag{10.3}$$

Table 10.1 Integrated thermal conductivity in W/m K of several materials useful for low-temperature cryogenic storage applications [3]

Material	$\overline{k'}\Big\vert_1^4$	$\overline{k'}\Big\vert_4^{77}$	$\overline{k'}\Big\vert_{77}^{300}$
Stainless steel	0.2	4.5	12.3
G-10	0.04	0.27	0.66
Teflon	0.02	0.18	0.25
Nylon	0.005	0.13	0.28
Polystyrene	0.02	0.036	0.075
Styrofoam	0.009	0.011	0.023

where for metals in the helium temperature range $n \approx 1$ and for insulators $n \approx 3$. In that case, the integrated thermal conductivity (10.2) may be written

$$\bar{k} = \frac{A}{(n+1)} \left(\frac{T_2^{n+1} - T_1^{n+1}}{T_2 - T_1} \right) \tag{10.4}$$

Equation 10.4 indicates that as long as the thermal conductivity is a monotonically increasing function of temperature, $\bar{k}$ is dominated by the high-temperature end.

Table 10.1 gives some typical $\bar{k}$ values for materials that are common in low-temperature insulation systems. These are given for usual fixed boundary temperatures. To determine the conduction heat leak between temperatures other than those listed in Table 10.1, it is necessary to evaluate (10.2).

Some insulating foam materials have tabulated thermal conductivities that can be used for design of moderate performance cryogenic storage vessels, but normally not for the helium temperature range. The average thermal conductivity for two of these materials (polystyrene and Styrofoam) are also listed in Table 10.1. Normally, these foam materials have lower thermal conductivities than monolithic solids, with the possible exception of the very low temperature end. Note that the thermal conductivity of foam materials is a very complicated process because it involves solid conduction and conduction in the residual gas. Thus, the average thermal conductivity can vary depending on the application. For example, the thermal conductivity can increase by as much as 40% if air diffuses into the cells. This effect is even larger if light gases such as helium or hydrogen replace the air in the foam [4]. The thermal conductivity of foam can also be affected by moisture content [5]. Thus, the values for the foam insulations in Table 10.1 should be only used for approximate calculations.

10.1.2 Gas Conduction

The second important mode of heat transfer in a cryogenic storage container is conduction through the residual gas in the vacuum space surrounding the low-temperature environment. In principle, this mode can be made arbitrarily small by

reducing of the residual pressure to a very low value (typically $<10^{-3}$ Pa); however, such conditions are not always achievable. It is therefore important to be able to estimate the heat load due to a moderate vacuum condition.

To estimate the magnitude of the gas conduction heat leak, consider an ideal planer system consisting of two flat surfaces at different temperatures with a residual gas between them at pressure p. There are primarily two regimes of heat transport in the residual gas. The first represents the case where the mean free path l is short compared to the spacing between the two surfaces. Under this circumstance, the gas thermal conductivity and thus the heat leak is nearly independent of pressure except at low temperatures and high pressures (see Sect. 3.4). Gaseous conduction dominates the heat transfer for pressures in the range 1 Pa to 1 kPa. If the pressure is higher that this range free convection may further enhance the heat exchange with a process that is dependent on the geometry of the container, see Chap. 5. Such a situation would be catastrophic for a cryogenic storage vessel as it would result in a very high heat load.

For most applications pertaining to cryogenics, the residual pressure is considerably lower than this value. For lower pressures ($p < 0.1$ Pa) the heat transfer process is represented by a second regime, where the mean free path is greater than the distance between the two surfaces. The mean free path of a gas is discussed in detail in Chap. 3. This quantity is roughly equal to the inverse product of the number density, n, and the scattering cross section, σ,

$$l \approx \frac{1}{n\sigma} \sim \frac{k_B T}{\pi d^2 p} \tag{10.5}$$

assuming ideal gas behavior with k_B being Boltzmann's constant. For a residual pressure of 0.1 Pa, the mean free path for helium at 4.2 K is about 1 mm.

The regime where the mean free path is greater than the distance between the two surfaces can be evaluated in terms of molecular kinetic theory. The physical picture is that of molecules making several collision-free trips between the two surfaces before interacting with other molecules in the volume. Thus, the rate of heat transfer is more determined by the molecule-wall interaction than intermolecular behavior. In this regime, the heat transfer is approximately proportional to the absolute pressure. The molecule-wall energy exchange process is related to the extent to which the molecules come into thermal equilibrium with the wall. This process is measured in terms of an accommodation coefficient α given by [6]

$$\alpha = \frac{T_i - T_e}{T_i - T_w} \tag{10.6}$$

where T_i is the effective temperature of the incident molecule, T_e that of the emitted or reflected molecule, and T_w the wall temperature. The maximum value for α is of course unity, associated with the molecule coming into complete thermal equilibrium with the wall.

For parallel surfaces at temperatures T_1 and T_2, the heat flux by gas conduction at low pressures is given by the relationship

$$q = \frac{\alpha_0}{4}\frac{\gamma+1}{\gamma-1}\left(\frac{2R}{\pi MT}\right)^{1/2} p(T_1 - T_2) \tag{10.7}$$

Here γ is the ratio of the specific heats ($\gamma = 5/3$ for helium), and R is the universal gas constant in J/mol K, $T = (T_1 + T_2)/2$ is the average temperature and M is the molecular weight in kg/mole. The quantity α_0 is an averaged accommodation coefficient dependent on the individual accommodation coefficient and surface areas. For unequal values of α and A, the quantity α_0 must be averaged over the two surfaces, that is,

$$\alpha_0 = \frac{\alpha_1\alpha_2}{\alpha_2 + (A_2/A_1)(1-\alpha_2)\alpha_1} \tag{10.8}$$

The difficulty with applying this theory is that the value of α is known only approximately. For example, for very clean metallic surfaces near room temperature, the accommodation coefficient for helium gas is quite small because the molecules make nearly elastic collisions. A good approximate value for this regime is 0.025 [7]. At low temperatures, α increases approaching a value of about 0.6 at 20 K [8]. For many low-temperature applications, helium gas is the major contributor to gaseous conduction heat leak because most other gases condense or adsorb on the cold surfaces. For helium gas a reasonably good value to assume for average accommodation coefficients is around 0.5.

10.1.3 Radiation Heat Transfer

Thermal radiation represents the third mode of heat transfer which is of concern in cryogenic insulation systems. This mechanism is independent of residual gas pressure or structural supports. The usual method for reducing radiation heat leaks is to use one of various forms of multilayer shielding, a topic which is discussed later. In preparation for that discussion, the present section considers the basic aspects of radiant heat transfer at low temperatures.

The starting point for the description of thermal radiation heat transfer is to consider the spectral energy density associated with a black body, which is an idealized concept that assumes a body radiates the maximum energy flux as a function of wavelength. This energy flux is given by,

$$e_b(T,\lambda) = \frac{8\pi hc}{\lambda^5}\left(\frac{1}{e^{hc/\lambda k_B T} - 1}\right) \tag{10.9}$$

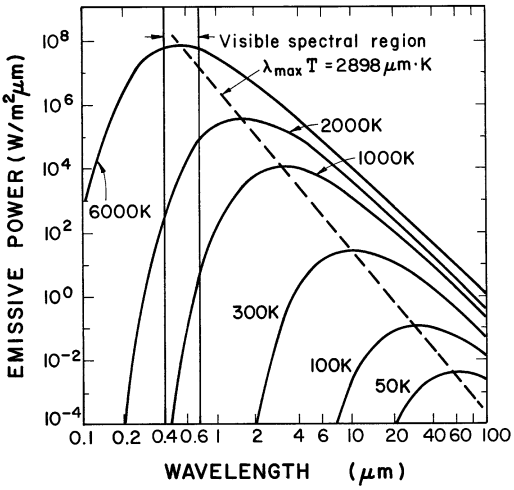

Fig. 10.1 Spectral energy density of black body radiation

where λ is the wavelength of the thermal radiation. This relationship has a well-known form shown in Fig. 10.1. At very high temperatures, the peak occurs in the range of visible spectrum, while at low temperatures the peak is shifted to longer wavelengths and has smaller amplitude. Wien's displacement law quantifies the temperature dependence of the peak wavelength:

$$\lambda_m T = 2898 \mu \text{m} \cdot \text{K} \tag{10.10}$$

Note that for surfaces at 4.2 K, the corresponding peak wavelength is 0.69 mm, which is in the far infrared. Such long wavelengths can have potentially important diffractive effects when the physical spacing between radiant surfaces approaches that of the peak wavelength [9].

For a black body the total radiant energy flux can be obtained by integration of (10.9) over all wavelengths. The integration produces what is known as the Stefan–Boltzmann law,

$$E_b = \int_0^\infty e_b(T, \lambda) d\lambda = \sigma T^4 \tag{10.11}$$

where σ is the Stefan–Boltzmann constant taking the value 5.67×10^{-8} W/m^2.

Most surfaces encountered in cryogenics do not approximate black bodies. In fact, the effort in cryogenics is usually one of minimization of the thermal radiation heat leak. If a surface is not black, its spectral energy density is smaller in proportion to its emissivity ε_λ. The emissivity is actually dependent on wavelength and is defined by the relationship

$$e_r(\lambda, T) = \varepsilon_\lambda e_b(\lambda, T) \tag{10.12}$$

where ε_λ is less than unity for nonblack surfaces.

It is often possible to make an approximation for radiant heat transfer which allows nonblack surfaces to be handled in a fairly straightforward manner. This assumption is to characterize surfaces as having constant emissivity less than unity, which is independent of wavelength. This is known as the *gray body* approximation and allows the writing of the total radiant energy flux as

$$E_r = \varepsilon \sigma T^4 \tag{10.13}$$

where the emissivity is determined for the appropriate set of conditions for the system of interest.

There are a number of implicit assumptions that enter into the *gray body* approximation. The first, already mentioned above, is that the emissivity must be wavelength independent over the range of wavelengths appropriate to the problem. Second, it is necessary to be able to equate the emissivity with the absorptivity a, which is a measure of the rate of energy absorption by the gray surface. The total absorptivity is defined by the relationship

$$E_a = aE_i \tag{10.14}$$

where E_i is the incident energy flux usually defined according to (10.13). Finally, for the gray body assumption to be reasonable, all surfaces must be diffuse scatterers of radiation. This is certainly far from the case for highly polished shields that often are present in cryogenic systems; however, it simplifies calculations considerably.

There have been numerous attempts to measure and tabulate the emissivities of different materials at low temperatures [10, 11]. Generally, these values are determined for radiant energy flux between ambient (273 or 300 K), liquid nitrogen (77 K), and liquid helium temperatures (4.2 K). A compiled graphical representation of emissivity measurements is shown in Fig. 10.2 [11]. To achieve low values of emissivity, it is necessary to have highly polished, high-conductivity surfaces made from gold, silver, copper, or aluminum. It has also been indicated [7] that since the emissivity is related to surface conductivity, it is best to polish the surfaces with a strain-free technique such as chemical etches. Finally, to estimate the radiant energy flux between surfaces of unknown emissivity, it is necessary to choose an approximate average value for ε. If the surface in question is dielectric, it is reasonable to assume black body heat transfer. If, on the other hand, the surface is a metal and polished, a conservative choice is $\varepsilon \approx 0.1$. However, as can be seen in Fig. 10.2, to achieve emissivities much less than 0.1, special care must be taken with the surface preparation.

The radiant heat transfer between parallel surfaces, shown schematically in Fig. 10.3, is a function of the properties of both surfaces. The rate at which energy is radiated from surface 1 is proportional to the emissivity ε_1, and the fourth power of the temperature T_1. A similar situation occurs for surface 2. In the simple case

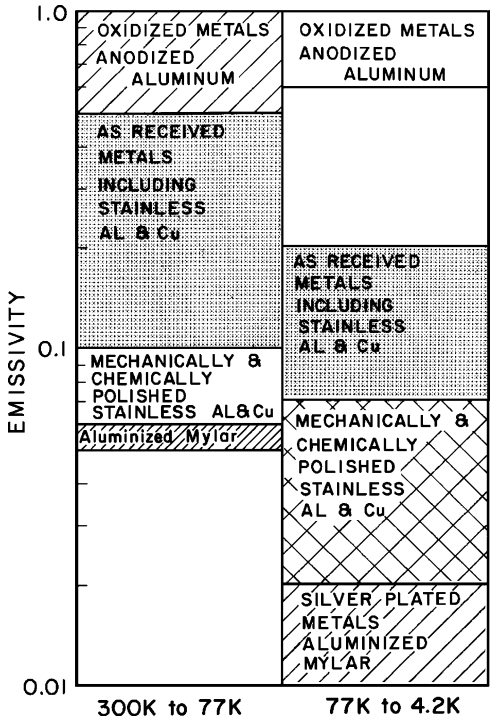

Fig. 10.2 The average emissivity of different metallic surfaces at fixed temperatures (Source: From Obert et al. [11])

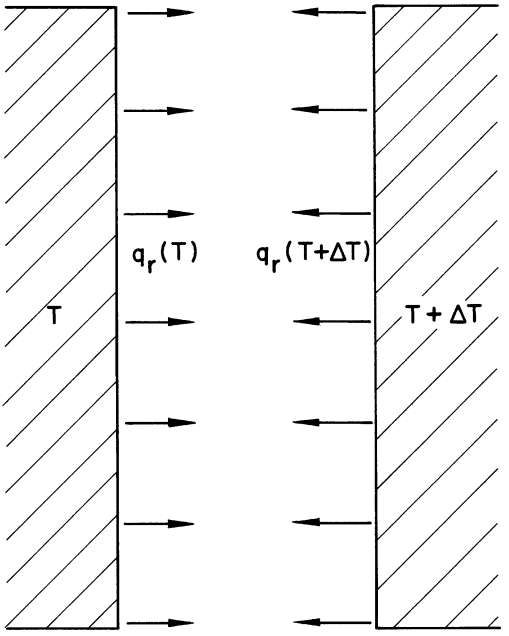

Fig. 10.3 Schematic of the radiant heat transfer process between two surfaces at different temperatures

that the surfaces can be approximated as black bodies, that is, $\varepsilon_1 = \varepsilon_2 = 1$, the net radiant heat flux is the difference between these two values:

$$q_r = \sigma\left(T_1^4 - T_2^4\right) \tag{10.15}$$

In the general case where the emissivity is considerably less than unity, the situation is more complicated. This is because the incident radiation from one surface can either be absorbed by the other or reflected back to the original surface. This problem can be solved by summing the infinite series of contributions to the radiant energy flux. The result for the net radiant heat flux for gray surfaces is

$$q_r = \left(\frac{\varepsilon_1 \varepsilon_2}{\varepsilon_1 + \varepsilon_2 - \varepsilon_1 \varepsilon_2}\right)\sigma\left(T_1^4 - T_2^4\right) \tag{10.16}$$

Note that in the special case often encountered in cryogenics where $\varepsilon_1 \simeq \varepsilon_2 \simeq \varepsilon \ll 1$, the quantity in brackets reduces to simply $\varepsilon/2$.

Example 10.1

Consider the heat leak to a vacuum insulated liquid helium container both with and without liquid nitrogen shielding. Assume that the residual vacuum is sufficiently low to be able to neglect gas conduction heat leak. Assume a fairly optimistic value for $\varepsilon = 0.05$ for both surfaces, and calculate the heat load/unit area.

Solution: Equation 10.16 yields a radiant heat leak between 77 and 4.2 K of $q_r(77\ \text{K}) \approx 50\ \text{mW/m}^2$, which for most systems is acceptable because it represents about 60 mL/h or liquid helium consumption per square meter of container surface area. If, on the other hand, the exterior surface is maintained at ambient temperature, 300 K, the heat leak is increased by approximately a factor of 300 which represents almost 3 L/h·m^2 of helium boil-off. Obviously, there is considerable benefit in liquid nitrogen shielding of liquid helium containers.

The above situation can be generalized to multiple radiation shields, which represents a fairly good approximation for aluminized mylar multilayer insulation (MLI) at low packing density, discussed below. For the case of n shields between two parallel surfaces, the radiant heat flux becomes

$$q_r = \left(\frac{\varepsilon_i \varepsilon_k}{(n-1)\varepsilon_i + 2\varepsilon_k}\right)\sigma\left(T_1^4 - T_2^4\right) \tag{10.17a}$$

where

$$\varepsilon_i \equiv \frac{\varepsilon_0 \varepsilon_s}{\varepsilon_s + \varepsilon_0 - \varepsilon_0 \varepsilon_s} \tag{10.17b}$$

and

$$\varepsilon_k = \frac{\varepsilon_s}{2 - \varepsilon_s} \tag{10.17c}$$

for which ε_0 is the emissivity of the two parallel surfaces and ε_s is that of the shields. For the special case where $\varepsilon_0 = \varepsilon_s = \varepsilon$, (10.17) can be simplified considerably:

$$q_r = \left(\frac{\varepsilon}{(n+1)(2-\varepsilon)}\right)\sigma\left(T_1^4 - T_2^4\right) \tag{10.18}$$

Note that for $\varepsilon \ll 1$, (10.18) predicts a heat leak reduced by the factor $(n + 1)^{-1}$ from that without the multilayer shields.

Example 10.2

Calculate the temperature of a thermally isolated radiation shield that is suspended between two fixed surfaces ($T_1 = 80$ K and $T_2 = 300$ K). Assume that all surfaces have a constant emissivity of 0.1.

Solution: If the shield is isolated then the only mode of heat transfer is by radiation. If we set the temperature of the shield as unknown, T_s, then the net radiant heat flux from the high temperature wall ($T_2 = 300$ K) to the shield must equal the net radiant flux from the shield to the low temperature wall ($T_1 = 80$ K),

$$q_r = \left(\frac{\varepsilon}{2}\right)\sigma\left(T_2^4 - T_s^4\right) = \left(\frac{\varepsilon}{2}\right)\sigma\left(T_s^4 - T_1^4\right)$$

Solving for T_s,

$$T_S = \left(\frac{T_1^4 + T_2^4}{2}\right)^{\frac{1}{4}} = 252.6 \text{ K}$$

It is an exercise for the student to show that the shield temperature is nearly independent of the T_1.

10.1.4 Multilayer Insulation (MLI)

Aluminized mylar with low-density fibrous insulating spacers between many layers, represents a special case of a multilayer insulation system. Since there is interlayer material present, it is no longer possible to assume that each of the n shields is isolated from the others except for the radiant heat transfer. This material is sometimes referred to as superinsulation or simply MLI (multi-layer insulation).

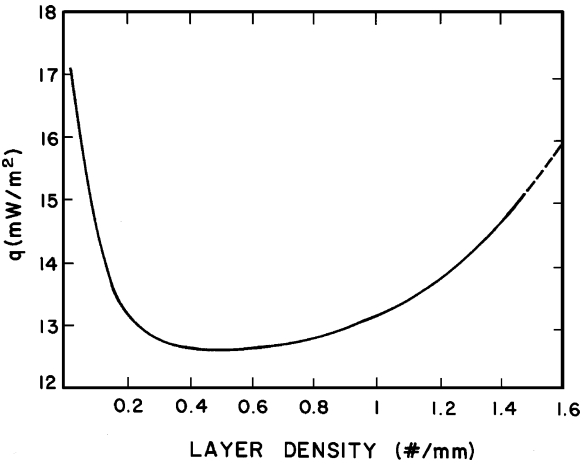

Fig. 10.4 Total heat exchange between two surfaces at 77 and 4.2 K as a function of layers of MLI (Source: Leung et al. [13])

Combined with high vacuum, MLI is the best insulating medium for low temperature systems and has become the standard for almost all cryogenic systems that operate in the liquid helium range.

With MLI there are two contributing heat transfer heat transfer mechanisms which are both functions of density and total number of shields. On the one hand, there is radiant heat transfer that decreases with increasing number of radiation shields, that is, layers of aluminized mylar. However, on the other hand, as the packing density increases, the heat transferred by conduction though the fibrous insulating spacers begins to make a larger contribution to the total heat leak. These two competing processes theoretically lead to an optimum layer density for practical multilayer insulations. Note that the solid-state conduction heat leak can be reduced by increasing the spacing between walls for the same packing density while the radiation contribution is only a function of number of layers. Therefore, the optimum number of layers should also be a function of the total insulation thickness or total number of layers.

The existence of a minimum in the layer density dependence of the heat transfer through MLI has been demonstrated experimentally [12, 13]. Plotted in Fig. 10.4 is one set of results for the heat flux through MLI between 4.2 and 77 K as a function of the numbers of layers [13]. The existence of a broad minimum near 0.5 layers/mm indicates the density where the solid-state conduction begins to play a substantial role. Note that the exact position of the minimum is not critical since a factor of two change in packing density increases the heat flux by less than 10%. Obviously, these results are not universal because the conduction and radiation contributions scale differently. However, MLI at low densities, less than 0.5 layers/mm, can be modeled fairly accurately by pure radiant heat transfer. For these results, the best choice for the emissivity of aluminized mylar is $\varepsilon = 0.011$ at 4.2 K and 0.03 at 77 K.

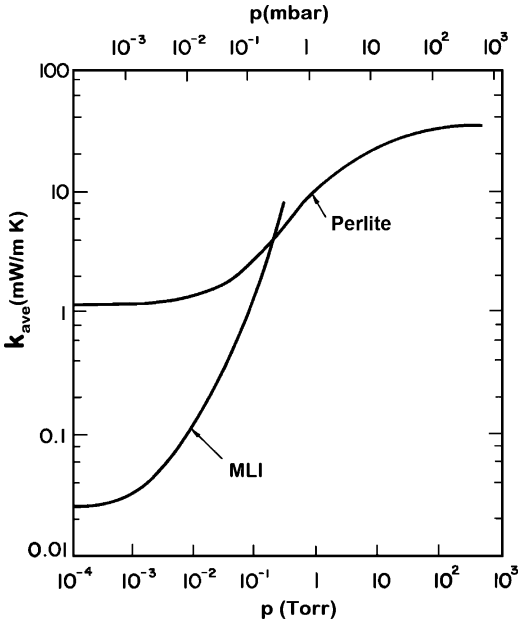

Fig. 10.5 Apparent mean thermal conductivity of glass powder and multilayer insulation versus residual gas pressure (Source: As compiled by Lady [15])

10.1.5 Powder Insulations

Glass powder insulation (the most common form is known as perlite) is also used to fill spaces between vacuum walls in insulating cryogenic vessels although it is not very common in helium systems [14]. This is because, in general, the performance of these materials is inferior to MLI. These materials generally are comprised of powders or glass microspheres with diameters in the range 10–1,000 μm. They have one clear advantage over MLI in that the material is easier to install, cheaper, and the residual vacuum requirements are not generally as stringent. However, the disadvantages of powder insulation technology are that it requires long and careful pump-down procedures and that the residual effective thermal conductivity is considerably greater than can be achieved with properly installed MLI at high vacuum. It is because of these latter two factors that powder insulations are most commonly used in large cryogenic storage tanks that contain the higher temperature cryogenic (LN_2, LNG).

The apparent thermal conductivity of perlite materials is a reasonably well-known quantity. Measurements have been carried out on the variation of this quantity with residual gas pressure. Most results are reported in the range of 77–300 K. Plotted in Fig. 10.5 are typical values for the apparent thermal conductivity of perlite versus residual gas pressure [15]. Note that minimum conductivity is achieved for pressures around 10^{-2} torr (~1 Pa) so lower pressures are not needed. For comparison, the figure also shows the apparent conductivity of superinsulation (MLI). In this case, a much

value is achievable at low pressures ($p \approx 10^{-4}$ torr or 10^{-2} Pa); however, at intermediate pressures, the benefits of superinsulation are minimal. At high pressures, $p \gtrsim 10$ Pa, superinsulation actually has higher thermal conductivity than the powders.

Recently, there has been a considerable effort at developing other porous insulations based on Aerogel, which is a very low density material containing a nano-pore structure. Some evidence suggests that these materials even in the intermediate pressure range have lower conductivities than perlite.

As a final comment, an additionally interesting problem concerns the refrigeration of radiation shields in cryogenic systems [16]. In large systems where radiation contributes substantially to the heat leak, it is possible to optimize the thermal performance by actively cooling the radiation shields. There are two main approaches to this problem. One approach, which is commonly used in cryostats that contain a stored cryogen (liquid helium storage vessels, for example) is to use the vented cryogen through tubes attached to the radiation shields. The vapor leaving the liquid container is nominally at the boiling point of the liquid and thus can intercept the radiant heat load at an intermediate temperature before venting from the cryostat.

An alternative approach that works with systems that are actively cooled is to again cool the radiation shields at intermediate temperatures but in this case with closed-cycle refrigerators. The advantage here is that improved overall thermodynamics can be achieved since radiation heat leaks from ambient temperature can be absorbed at higher temperatures, thus taking advantage of higher refrigeration efficiency. This approach often couples the conduction heat load to the intermediate cooling station for the same reasons. The thermodynamic principles needed to carry out this analysis are discussed in Chap. 8. For further details, the reader should consult references in the literature.

10.2 Helium Adsorption

Another interesting and technically significant topic related to the field of helium cryogenics is that of physical adsorption. Physical adsorption is a general term used to describe the process whereby an inert molecule comes in contact with and adheres to an inert surface or substrate. The inert character of each component is important because if substantial chemical reaction occurs, the process is referred to as chemisorption and the thermodynamics of the process are quite different. Since helium is inert and does not bond chemically to any other element, the adsorption process is described by physical mechanisms similar to those encountered in bulk condensation. It is often possible to treat the adsorbed film as an independent system, with the substrate forming the non-interactive boundaries much like walls of a container form the boundaries to bulk fluids.

Studies of adsorbed gases over the past few decades have expanded the understanding of the basic physical processes. Growth in the field can be attributed primarily to two factors. First, recent developments have introduced a number of experimental techniques for surface investigation. Several of these techniques are sensitive to less

than one atomic layer, allowing investigations of monolayer and submonolayer films. Second, scientists have discovered substrates that are regular and homogeneous and permit nearly ideal film behavior. Due to surface morphology, real surfaces tend to have considerable variability in adsorption potential which can result in inhomogeneous films. Although this situation is realistic in practice, it gives little insight into the detailed physical behavior of the film itself.

Physical adsorption has considerable technical importance in the field of cryogenics. One application is in cryopumping, a process whereby a gas is pumped from a system by exposing it to a large surface at low temperatures. This technology is used in numerous cryogenic devices and naturally occurs in liquid helium systems because the surfaces are so cold. When properly designed and used, cryopumps provide clean, oil-free vacuum systems with high capacities and essentially no moving parts. Another area of technical application for adsorption is in the separation of rarified gases. In this method, more strongly interacting molecules are adsorbed onto the substrate leaving the vapor phase enriched with the lighter more weakly bound molecules. Subsequently, the substrate can be "regenerated" by raising its temperature to desorb the heavier species. A major sector of the technology of air separation is based on this concept. Finally, adsorption is employed in a certain class of refrigerators that use the alternate condensation and evaporation of a fluid by adsorption/desorption as a process tool much like a compressor in a conventional cycle.

In addition to these technical uses, physically adsorbed layers can significantly impact the behavior of cryogenic processes and systems. For example, boiling surface heat transfer can be affected by the existence of adsorbed solid films which can interfere with the bubble nucleation process. Surface films can also impact the solid–liquid helium heat transfer process of Kapitza conductance by modifying the phonon transport. Radiative heat transfer can also be affected by variation of emissivity due to cryo-deposits on the surfaces. Finally, the adsorption of gas onto cold surfaces can represent a significant heat load to the system that can result in loss of stored cryogen. This topic was discussed in the context of the accommodation coefficient for molecular-kinetic heat exchange. All these factors make knowledge of the physical adsorption process important for proper understanding of the behavior of low-temperature systems.

10.2.1 Adsorption Thermodynamics

To begin, consider a simple thermodynamic description of the adsorption process. A closed container, shown in Fig. 10.6a, has N_v molecules in the vapor state at temperature T_v and an equilibrium pressure p. Assume that T_v is high enough that the molecules do not adhere in any significant numbers to the container walls, which are also at T_v. One of the container walls forms the adsorption substrate at a temperature T_s that can be independently regulated relative to T_v. Of interest are the physical processes that take place as the substrate temperature is reduced below T_v. Initially, as T_s decreases, the pressure will decrease also in rough proportion

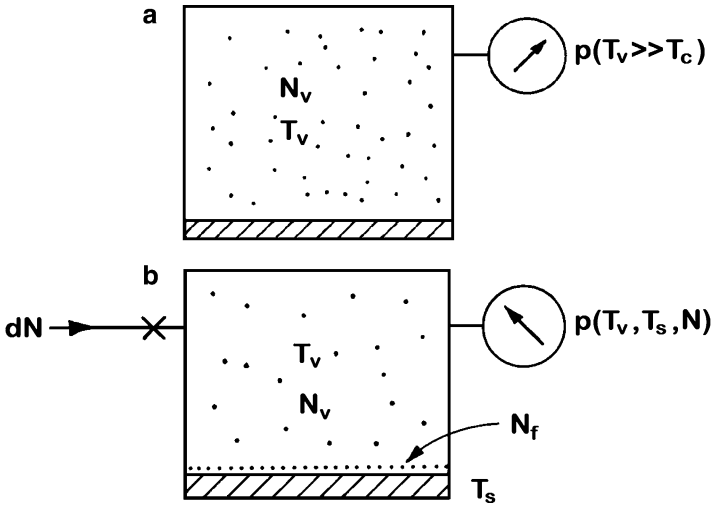

Fig. 10.6 Schematic representation of adsorption. (**a**) A closed volume with N_v, molecules in the vapor phase. The number of molecules adsorbed, N_f, is small compared to N_v because $T_s \gg T_c$. (**b**) The same volume with $T_s \lesssim T_c$ so appreciable adsorption occurs

because the vapor temperature will be some thermodynamic average of T_s and T_v. However, once T_s reaches a temperature of the order of the critical temperature of the vapor species, ~5 K in the case of ^{4}He, a substantial quantity of the gas will begin to adhere to the substrate.

The mechanism whereby this adherence occurs is the van der Waals interaction between the oscillating electric dipoles. A number of approximate potentials exist to model this interaction. One of these is the Lennard-Jones (LJ) 12-6 potential, which was introduced in Chap. 3 to describe interactions in real gases. In the case of an ideal two-dimensional planar surface comprised of substrate atoms, it is possible to write a modified form of the LJ potential for a gas atom a distance d above the plane [17],

$$U(d) = 4\pi\varepsilon n_s \left(\frac{\sigma^{12}}{45d^9} - \frac{\sigma^6}{6d^3} \right) \tag{10.19}$$

where n_s represents the density of substrate atoms and σ and ε are the Lennard-Jones parameters for the gas–substrate atom interaction.

Now consider the impact of introducing a small quantity of gas dN to the system. This situation is illustrated in Fig. 10.6b. If T_s is sufficiently low, some of the gas will be adsorbed, increasing the total particle number on the substrate by dN_f. The remainder will stay in the vapor such that $dN_v = dN - dN_f$. For a closed system in which this extra gas is introduced reversibly, the chemical potentials of each phase must be equal, $\mu_f = \mu_v$. This condition establishes a relationship between the entropy of each phase:

$$\left(\frac{\partial S_f}{\partial N_f} \right)_{E,A,V} = \left(\frac{\partial S_v}{\partial N_v} \right)_{E,A,V} \tag{10.20}$$

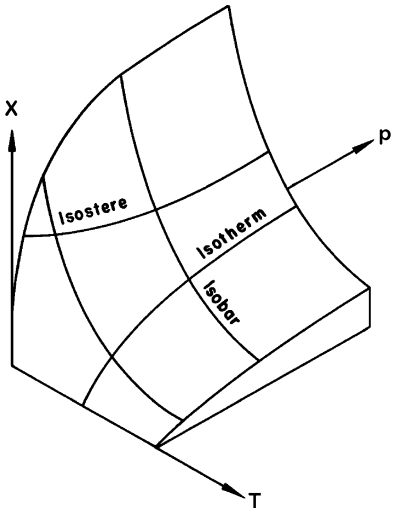

Fig. 10.7 An adsorption equilibrium surface. Lines of constant surface coverage are called isosteres

The behaviors of the two phases are related inherently through thermodynamics. For example, detailed information about the state of the film can be extracted from measurements of pressure of the equilibrium vapor phase.

In bulk matter, the behavior of the system is determined by an equation of state, a relationship between pressure, temperature, and volume. By analogy, in a film system an equation of state exists relating the three surface relevant parameters: spreading pressure φ, temperature T, and coverage or capacity x. However, under most conditions it is not possible to measure the film spreading pressure directly so that it must be inferred from bulk vapor pressure determinations. The most common situation is to construct an equation of state relating bulk vapor pressure, temperature, and capacity. Such a relationship is shown schematically in Fig. 10.7 which represents a surface equilibrium of an adsorption system. Note that processes occurring at constant capacity are referred to as "isosteric" by analogy with isochoric or constant volume processes in bulk systems.

One of the most important parameters in an adsorption system is the isosteric heat of adsorption, q_{st}. This quantity is defined as the amount of energy required to bring a molecule from the film into its equilibrium vapor. In the limit of zero coverage and at absolute zero, the isosteric heat is simply the single-particle binding energy to the substrate. As the film grows, this value decreases until for very thick films $q_{st} \rightarrow h_{fg}$, the heat of vaporization of a bulk condensate comprised of film molecules. These values form the limits for q_{st}. However, the detailed structure of this quantity can give considerable information about the thermodynamic state of the film.

The thermodynamic definition of q_{st} is given in terms of the entropy change at constant coverage:

$$q_{st} = -T\left(\frac{\partial S}{\partial N_f}\right)_{T,p,A} \tag{10.21}$$

By holding T, p, and A constant the variation of q_{st} is essentially along a constant coverage isostere; see Fig. 10.7. Substituting the relationship for equilibrium between the film and vapor, (10.20), we can rewrite (10.21) as a function of individual component entropies,

$$q_{st} = -T\left[\left(\frac{\partial S_f}{\partial N_f}\right)_{T,A} - \left(\frac{\partial S_v}{\partial N_v}\right)_{T,p}\right] \tag{10.22}$$

An alternate definition for the isosteric heat is given in terms of a temperature derivative of the equilibrium vapor pressure. This expression, which can be derived explicitly from (10.22) and is analogous to the Clausius-Clapeyron equation, is a function of easily measurable quantities:

$$q_{st} = k_B T^2 \left(\frac{\partial(\ln p)}{\partial T}\right)_{N_f,A} \tag{10.23}$$

In the simplest case where q_{st} is a constant, integration of (10.23) establishes an experimental form of the equilibrium vapor pressure,

$$\frac{p}{p_0} = e^{-q_{st}/k_B T} \tag{10.24}$$

where p_0 is a constant of integration. This expression identifies the importance that the isoteric heat plays in determining the ultimate pressure of an adsorption system.

The traditional method used for measurement of q_{st} is by vapor pressure isotherms. The behavior of the isotherms depends strongly on the type of substrate material and adsorbed gas. Substrate materials considered range from nearly ideal single-crystal surfaces to more practical inhomogeneous surfaces composed by polycrystalline metals or insulators. In addition, a given surface can be modified by first pre-plating the substrate with a more strongly adsorbed gas which then forms the new substrate for subsequent adsorption. Experimental data exist for numerous systems including almost all commonly available gaseous elements and a number of compounds. The temperature range of investigation in these studies is determined mostly by the strength of the gas–substrate interaction.

Most substrates encountered in practical adsorption problems are inhomogeneous, composed of polycrystalline or amorphous materials. Because of their non-uniformity, only qualitative models are available to describe their behavior. For inhomogeneous substrates the vapor pressure isotherm follows the general form shown in Fig. 10.8. Initially, the vapor pressure is quite low because the first layer is bound strongly. However, as the film builds thickness, the pressure increases rapidly until it asymptotically approaches that of the bulk liquid, p_s. An expression can be derived to compare with the results of Fig. 10.8 by assuming a layer-dependent form of q_{st} in (10.24). Considering only the attractive term in the van der Waals expression (10.19), we obtain the Frenkel–Halsey–Hill equation [17].

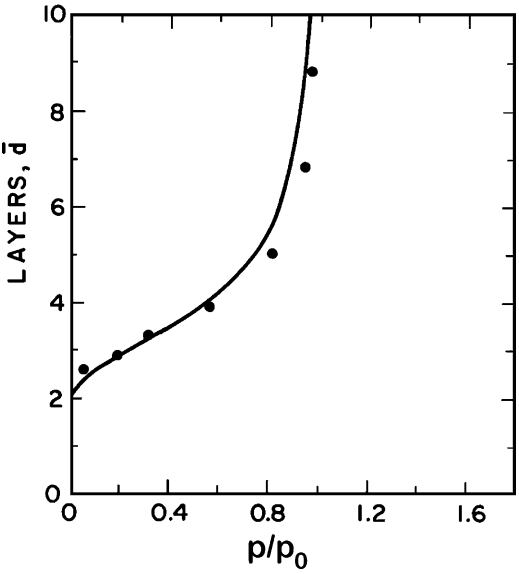

Fig. 10.8 An adsorption isotherm for a mylar substrate representing typical inhomogeneous character. The curve is based on the Frenkel–Halsey–Hill expression (10.25) (Source: Reprinted from Dash [17])

$$\frac{p}{p_s} = \exp\left(\frac{-\alpha}{k_B T \bar{d}^3}\right) \tag{10.25}$$

where α represents the strength of the attractive potential on the bare substrate and should be approximately equal to q_s, at low coverage, and d is the number of atomic layers. A comparison between the adsorption of ^{4}He on a mylar surface and that derived from (10.25) is made in Fig. 10.8. Theory and experiment are in qualitative agreement although the theory is not particularly sensitive to the detailed nature of q_{st}.

The limiting value of q_{st} is determined from the slope of low-coverage isotherms. One can also obtain information on the isosteric heat of adsorption by measuring the temperature dependence of the vapor pressure at constant coverage. For example, plotted in Fig. 10.9 is the absolute pressure versus T^{-1} for ^{4}He adsorbed on a copper sponge substrate. Note that the general form of (10.24) is obeyed. Furthermore, by extrapolation to zero coverage, it is possible to deduce an effective q_{st} for the substrate. These data yield a value $q_{st}/k_B \sim 160$ K. A number of different measurements of q_{st} for ^{4}He at low coverage are listed in Table 10.2. Note that the values of q_{st} for submonolayer ^{4}He are at least an order of magnitude larger than the latent heat of vaporization for helium, ~10 K. As a result, there can be a significant amount of adsorption of ^{4}He even at temperatures above T_c. However, the total quantities adsorbed are strong functions of temperature and are small because the process has an exponential dependence.

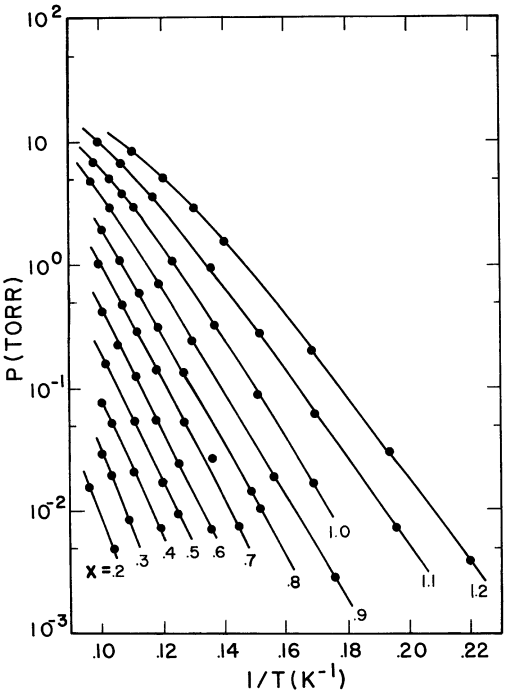

Fig. 10.9 Temperature dependence of the vapor pressure for constant coverage films on copper sponge. x refers to fractional monolayer coverage (Source: Reprinted from Princehouse [18])

Table 10.2 Isosteric heat of adsorption at low coverage for ^{4}He on various substrates

Substrate	q_{st}/k_B (K)	References
Copper	160	[18, 19]
Argon plated TiO_2	230	[20]
Exfoliated graphite	143–156	[21, 22]
Zeolite (13X)	220	[24]

As more gas is adsorbed on the surface the vapor pressure increases quite strongly. This effect can be seen most clearly in Fig. 10.8. Initially, the equilibrium vapor pressure is quite low due to the large value of q_{st}. However, as N_f increases, q_{st} decreases until for films having an equivalent thickness of four to six atomic layers the vapor pressure is essentially that of the bulk liquid or solid. The quantity of adsorbed gas necessary to complete one monolayer is an important parameter. Not only is this parameter an effective method of determining the surface area of the substrate but it also can be used as a fiducial point for estimating the density of submonolayer films. A number of methods exist for measuring monolayer completion. The most direct is to measure the vapor pressure isotherm. Above layer completion, the average position of the next absorbed gas molecule must be further from the substrate, and thus the molecule experiences a weaker binding. In an ideal

Table 10.3 ^{4}He capacities of various adsorbent materials

Substrate	Monolayer capacity (STP-cm^3/m^2)	Area (m^2/g)	References
Sintered Cu sponge (~μm^3 particles)	0.24	0.41	[18]
Zeolite 13X	0.29	527	[19, 23]
Exfoliated graphite	0.36	25	[22, 24]
Vycor glass	0.41	130	[25]

system the value of q_{st} would decrease discontinuously. However, most substrates are inhomogeneous and the layers are compressible so that, more commonly, q_{st} undergoes a change in slope at layer completion. The precise value of layer completion is also quite temperature dependent, owing to thermal excitations in the film, and therefore is defined only approximately for any substrate.

Listed in Table 10.3 are measured values for monolayer capacities of different substrates. Note that the capacity per unit area of substrate does not vary greatly from substrate to substrate. This is because the surface area is determined primarily by the hard sphere radius of the adsorbed molecule. On the other hand, there are wide variations of effective surface areas per gram of substrate material. Considerable benefit for cryopumping can be obtained by use of one of the high-surface-area materials. It should be pointed out that high adsorption capacity does not necessarily imply good cryopumping characteristics because the latter is a rate-dependent process. The rate at which adsorption occurs in high-surface-area materials is mostly a function of gas flow hydrodynamics within the material, a characteristic not necessarily desirable for high-speed cryopumps.

Vapor pressure isotherms are most commonly of the type described above, having a smoothly varying relationship between N_f and p. However, for some substrates that are very uniform this dependence is not observed. In these systems a discontinuous slope change in the vapor pressure isotherm occurs at monolayer completion. Further adsorption occurs on the second layer with a correspondingly lower value of q_{st}. This process continues until layer completion where a second step in the isotherm occurs. In the ideal case this mechanism for layer growth would continue indefinitely until the thermal excitations of the molecule of the order of k_BT blur the distinction between individual layers.

10.2.2 Physical Properties of Helium Films

Through the introduction of large-surface-area uniform substrates, it has become possible to investigate a number of interesting quasi-two-dimensional phases occurring mostly in the first one or two layers. The models that describe the physical processes emphasize the two-dimensional nature of the system. At low densities, much less than one atomic layer, helium adsorbed on graphite behaves much as a two-dimensional quantum gas. At high temperatures, its specific heat

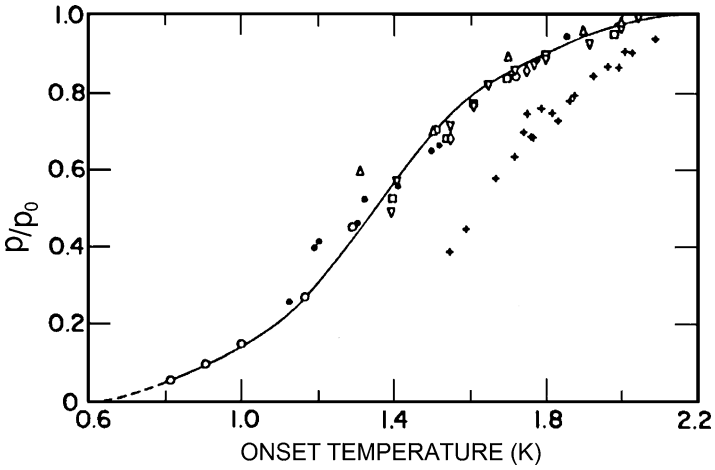

Fig. 10.10 Superfluid onset temperatures of ^{4}He films on different substrates and measured by different techniques (Source: From Herb and Dash [26])

asymptotically approaches a constant value of $C \approx Nk_B$, while at lower temperatures, quantum effects brought on by statistical correlations reduce the specific heat in a manner similar to the bulk fluids. At intermediate surface coverages, behavior occurs which can be correlated with regularity in the adsorbed gas. This effect is brought on by the adsorbed gas being affected by the periodicity of the substrate. At still higher coverages up to layer completion, the adsorbed gas sometimes behaves much as a two-dimensional solid with low-temperature specific heat varying as T^2, consistent with a two-dimensional Debye model. For these high coverages, melting transitions in the specific heat are observed at intermediate to high temperatures above which fluid-like behavior occurs. An interesting artifact of surface phases in adsorption systems is the occurrence of two-dimensional solids even though bulk helium does not solidify unless considerable external pressure is applied. In this case, the adsorption interaction compresses the molecules on the substrate to densities similar to those that occur in the bulk solid. These high densities allow the formation of long range order and crystal structure.

Of interest in unsaturated ^{4}He films is the question of when does superfluidity manifest itself. Clearly as was discussed in Chap. 6, thick saturated films display superfluidity in the form of film mobility (Rollin Film) and heat transport. For the case of unsaturated helium films of more than a few atomic layers, superfluidity is observed both in the λ-transition in the specific heat [24] as well as the onset of mobility [26]. The latter case is displayed in Fig. 10.10, which is a plot of the onset of superfluidity as a function of pressure ratio. Note the depression of the onset temperature with reduced film thickness as measured by the vapor pressure.

As was stated early on in this section, gas separation, cryopumping and adsorption refrigeration are the main applications for physical adsorption in cryogenic systems. In the first case the desired characteristics of the adsorbent are light weight, small heat

capacity, and large surface area. Typical materials used are activated charcoal, silica gel, activated alumina, or molecular sieves. The specific area of these materials are in the range 300–1,200 m^2/g and bulk densities less than 1 g/cm^3. No particular concern is given to surface uniformity. Applications generally call for designing an adsorption "bed" which provides good adsorption characteristics yet still allows for bulk flow. This application depends strongly on details of design.

In terms of cryopumping applications of adsorption, the choice of substrate material and configuration is more dependent on specific application. If high-speed pumping is required, the surface must not restrict the flow of gas. Therefore, the most common design is to use a planar metallic surface. To achieve substantial total pumping capacity before regeneration, this type of surface is necessarily quite large, a fact that leads to problems with reducing the radiation heat leak to warm surrounding surfaces. A number of standard techniques are available for providing radiation shields that allow high flow rates of gas. If high pumping speed is not necessary, use can be made of numerous high-surface-area materials, called "getters," thermally well anchored to a low-temperature heat sink. Getters of this type often are sealed into closed helium dewars to maintain good vacuum quality over an extended period of time.

Example 10.3

Calculate the vapor pressure of a three layer helium film adsorbed on a copper substrate at 4.2 K. Use the Frenkel–Halsey–Hill equation and assume $q_{st}/k_B = 160$ K. Compare the result with Fig. 10.8. Now use the same expression to estimate the vapor pressure of a monolayer film.

It is only necessary to calculate the ratio of the pressures,

$$\frac{p}{p_0} = e^{-\left(\alpha/k_B T d^3\right)}$$

For three layers (d = 3), this expression yields $p/p_0 = 0.24$, which is close to the value in Fig. 10.8. Now for d = 1 film, one calculates $p/p_0 = 2.8 \times 10^{-17}$, which is a physically unrealistic value but still emphasizes the strength of the adsorption process.

10.3 Magnetic Refrigeration

The use of the spin entropy of a magnetic system for cooling was first suggested in 1925 by Debye and Giauque [27–29]. It was then implemented by a number of groups in the 1930s. Today, magnetic refrigeration has been developed into a well-established technique for a number of specialized applications. The present section reviews this topic. We begin with a description of the physics of magnetic materials that is relevant to low temperature cooling. This discussion should provide the necessary understanding of the relevant properties of this special class of low-temperature materials.

Emphasis is given to the properties of some representative materials that have or are being used in magnetic coolers. Finally, some discussion of the practical aspects of magnetic refrigeration is presented with comments on the state of the art. The treatment is intended to introduce the microscopic and macroscopic aspects of paramagnetic cooling systems. For details, the reader should consult one of several recent publications on the subject.

There are essentially two distinct classes of magnetic refrigerators. One type of refrigerator operates down to the mK temperature range and is based on the electron spin states of paramagnetic materials. This refrigerator type will be emphasized here. The other type of magnetic refrigerator uses the nuclear spins of metallic elements to achieve temperatures in the μK range and as a result is more an expertise of low temperature physics.

10.3.1 Paramagnetic Materials

The paramagnetic salts are most commonly used in magnetic refrigerators. These materials have a number of characteristics in common. They are comprised of multi-component ionic molecules, one ion of which is magnetic. The magnetic ion is sufficiently dilute within the material that at high temperature it approximates a free non-interacting spin system. The strength of interaction determines the ordering temperature, below which the materials usually become diamagnetic. The ordering temperature of most paramagnetic salts is in the range below 1 K.

The theory of paramagnetic spin systems is developed around the statistical behavior of free magnetic ion systems. Any free magnetic molecule has two types of magnetic moment associated with its electron orbital structure. The first, due to orbital motion of the electron, is given the quantum number L. The other, resulting from uncompensated electron spins, has a quantum number S. The total angular momentum number J is the resultant of these two individual magnetic moments. In general, atoms have nonzero values of L and S. However, certain ions, particularly magnetic Fe^{3+} and Cr^{3+} and Gd^{3+}, have effectively an inert-gas orbital structure, so that $L = 0$, but they have uncompensated electron spins, such that $J = S$.

There are m_i different quantum numbers associated with each spin state of the atom, where m_i can take on values from $-J$ to J. Therefore, within each atom there are $2J + 1$ individual energy levels. Without the application of an external magnetic field, these levels are degenerate meaning that there is no distinction or energy level difference between them. However, in an external field this degeneracy is lifted, shifting the energy levels by an amount given by,

$$\varepsilon_i = -g\mu_B\mu_0 H m_i \tag{10.26}$$

where μ_B is the Bohr magneton which is a ratio of fundamental constants, $\mu_B = eh/4\pi m_e = 0.927 \times 10^{-23}$ J/T with e/m_e being the charge-to-mass ratio of an electron. The magnetic field is that which is felt locally by the atom and can be substantially

different from the applied magnetic field from external sources. The quantity g in (10.26) is known as the Landé g factor [30]. For many paramagnetic coolants with $L = 0$, $g = 2$.

For a material like gadolinium sulfate with $g = 2, J = 7/2$, the eight individual energy levels within the magnetic system have a level separation, $\Delta\varepsilon = 2\mu_B\mu_o H$, directly proportional to the magnetic field. At absolute zero in an applied magnetic field, all ions will occupy the lowest energy level. However, at finite temperature, some of the ions will be excited into higher levels based on their statistical distribution. Equating that energy level difference to the thermal energy of the ions, $k_B T$, one can show the significance of thermal excitation to the population of different levels.

$$\frac{\mu_0 H}{T} \approx \frac{k_B}{2\mu_B} \sim 0.75\left[\frac{T}{K}\right] \tag{10.27}$$

This relationship more or less establishes the boundary between the two regimes of ordering in a magnetic ion subsystem. The low-field, high-temperature regime occurs when the ratio $\mu_0 H/T \ll 0.75\ T/K$. In this regime, the magnetic ions essentially are disordered with the level spacing being small compared to $k_B T$. Since this is a disordered state, it is of higher entropy. On the other end of the spectrum, the high-field, low-temperature regime, $\mu_0 H/T \gg 0.75\ T/K$, corresponds to the majority of the spins occupying the lowest energy level. This is a lower entropy state for the spins.

Since the magnetic ion system consists of indistinguishable particles, it is appropriate to describe the behavior using Boltzmann statistics. The starting point for statistical analysis is the definition of a partition function, Z. For a magnetic ion system, the assumption is made that the total partition function is a product of the internal nonmagnetic part and the magnetic contribution,

$$Z_{total} = Z_{\text{int}} Z_B \tag{10.28}$$

In a magnetic ion system Z_B essentially is due to the Zeeman effect, the magnetic splitting in an external field. It can be shown that the Zeeman contribution to the partition function is [28],

$$Z_B = \frac{\sinh\left(J + \frac{1}{2}\right)a}{\sinh(a/2)} \tag{10.29}$$

where the parameter $a = g\mu_B\mu_0 H/k_B T$ is a measure of the ordering.

The low-temperature thermal properties of a magnetic ion system are considerably different from other more ordinary materials. Although these systems possess phonon excitations, a more dominant mechanism contributing to their thermal behavior at low temperature is due to the crystal field splitting of the ionic energy levels within the lattice [30]. Recall (Chap. 2) that the phonon specific heat is

proportional to T^3 at low temperatures. On the other hand the crystal field splitting, also referred to as the Stark effect, is caused by the ionic electric fields establishing different energy levels analogous to those from the magnetic Zeeman effect. The level splitting is small, typically on the order of 10–100 mK, and consequently only becomes important at low temperatures.

To derive an expression that adequately describes the Stark effect, we begin by making some simplifying assumptions concerning the structure of the energy levels. Often, crystal field splitting has associated with it two levels separated by an energy δ, with each level having a degeneracy g_n that is not lifted by the crystal field. In this case, we can write the partition function associated with the internal system as,

$$Z_{\text{int}} = g_0 + g_1 e^{-\delta/k_B T} \tag{10.30}$$

where g_0 and g_1 are the degeneracies of the ground and first excited states. The product of the two contributions to the partition function can be used to calculate the thermodynamic properties of the magnetic ion system.

The total entropy of such a system of spins is therefore made up of two terms,

$$S = N_m k_B T \left(\frac{\partial \ln Z}{\partial T}\right)_H + N_m k_B \ln Z \tag{10.31}$$

where N_m is the number of magnetic ions. Equation 10.31 can be differentiated to yield the specific heat and other thermodynamic variables. For example, the internal energy of the magnetic ion system is a function of the total partition function,

$$E = N_m k_B T^2 \left(\frac{\partial \ln Z}{\partial T}\right)_H + \mu_0 HM \tag{10.32}$$

The specific heat capacity at constant magnetization is just the temperature derivative of the internal energy, $C_M = (\partial E/\partial T)_M$. It therefore follows from (10.32) that the constant magnetization heat capacity is

$$\frac{C_M}{N_m k_B} = \frac{1}{N_m k_B}\left(\frac{\partial E}{\partial T}\right)_M = \frac{\delta^2}{k_B^2 T^2}\frac{(g_0/g_1)e^{\delta/k_B T}}{\left[1 + (g_0/g_1)e^{\delta/k_B T}\right]^2} \tag{10.33}$$

This expression, known as the Schottky equation, is plotted in Fig. 10.11 for different ratios of g_0/g_1. Note that the maximum in the Schottky heat capacity is approximately $½Nk_B$, which is very large compared to the other solid-state contributions at low temperatures. Note that N_m is the number of magnetic ions, which is generally much less than N, the total particle number. Also, typically, $\delta/k_B \approx 100$ mK so that this term dominates the zero field heat capacity at lower temperatures, $T < 1$ K.

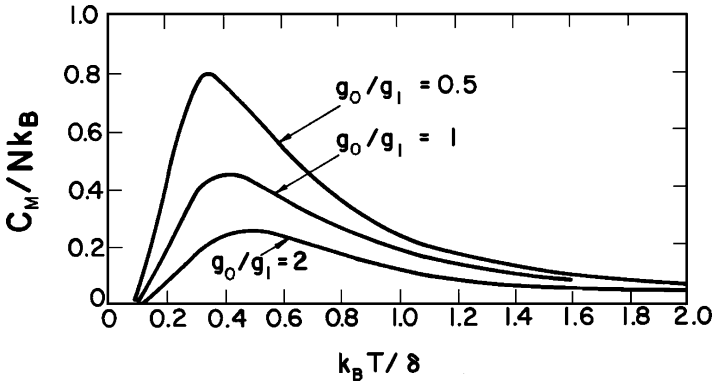

Fig. 10.11 Schottky heat capacity of a magnetic ion sub-system whose lowest energy level in the absence of any external magnetic fields is split into two states with degeneracies g_0 and g_1 (Source: From Zemansky [30])

For many magnetic refrigeration applications, the operating temperature is significantly above the Schottky anomaly temperature, δ/k_B. In this regime it is possible to take a high-temperature limiting form of (10.33) which yields

$$C_M = \frac{A}{T^2} \tag{10.34}$$

where A, the specific heat coefficient, has a value

$$A = N_m k_B \frac{g_0/g_1}{(1 + g_0/g_1)^2} \left(\frac{\delta}{k_B}\right)^2 \tag{10.35}$$

It is important to bear in mind that the above analysis applies to a system of N_m magnetic ions. Typically, in paramagnetic salts the magnetic ion number is much smaller than the total number of particles in the crystal. Therefore, if the heat capacity per unit mass or unit volume is desired, it is necessary to take into consideration the total molecular weight of the ionic salt.

The other important contribution to the specific heat of a magnetic ion system is that due to phonon excitations which at low temperatures, see Chap. 2. At low temperatures, this contribution may be approximated by the Debye model,

$$C_{\text{ph}} = 234 N k_B \left(\frac{T}{\Theta_D}\right)^3 \quad \text{for} T \ll \Theta_D \tag{10.36}$$

where N is the total atomic number and Θ_D is the Debye temperature typically >100 K.

We can compare the relative importance of the phonon and Schottky heat capacities based on the above discussion. Assuming for example that $g_0/g_1 = 0.5$ and taking the ratio of (10.34) to (10.36), we obtain

$$\frac{C_{\text{ph}}}{C_M} = 936\left(\frac{N}{N_m}\right)\left(\frac{T}{\Theta_D}\right)^3\left(\frac{k_B T}{\delta}\right)^2 \tag{10.37}$$

For a magnetic material like iron ammonium alum with $\delta/k_B = 242$ mK, $\Theta_D = 250$ K, and $N/N_m \simeq 50$, the above ratio at T = 1 K takes on the numerical value $C_{\text{ph}}/C_M = 0.052$. Therefore, the phonon contribution to the specific heat is already a minor (~5%) contributor at 1 K and becomes smaller as the temperature decreases, since the ratio goes as T^5. As a consequence, it is possible to neglect the phonon term for low temperature, T < 1 K applications. However, for many systems it must be included, particularly at high temperatures.

We now consider the magnetic properties of the paramagnetic materials. These are also given in terms of the magnetic partition function. For example, the magnetization can be obtained from a derivative of Z with respect to the applied magnetic field,

$$M = N_m k_B T\left(\frac{\partial \ln Z}{\partial \mu_0 H}\right) = N_m g \mu_B J B_J(a) \tag{10.38a}$$

where the quantity $B_J(a)$ is the Brillouin function,

$$B_J(a) = \frac{1}{J}\left[\left(J+\frac{1}{2}\right)\coth\left(J+\frac{1}{2}\right)a - \frac{1}{2}\coth\frac{1}{2}a\right] \tag{10.38b}$$

where as a reminder $a = g\mu_B\mu_0 H/k_B T$. In the limit of large a, there is a high degree of magnetic ordering and the magnetization approaches a constant value,

$$M = Ng\mu_B J \text{ for } g\mu_B\mu_0 H \gg k_B T \tag{10.39}$$

while at small values of a, the magnetic system is weakly ordered and the Brillouin function becomes linear with a. In this regime it is shown easily that the magnetization can be expressed as

$$M = \frac{\mu_0 \gamma_C H}{T} \text{ for } g\mu_B B \ll k_B T \tag{10.40a}$$

where γ_C is the Curie constant defined by expansion of the Brillouin function,

$$\gamma_C = \frac{N_m g^2 \mu_B^2 J(J+1)}{3k_B} \tag{10.40b}$$

Listed in Table 10.4 are specific heat coefficients for several paramagnetic materials along with other relevant properties.

Table 10.4 Selected properties of magnetic refrigerant materials[a]

Material	Specific volume (cm^3/g·ion)	Curie constant γ_C (J·K/g ion T^2)	Debye temperature Θ_D (K)	A (J K/g·ion)
$2Ce(NO_3)_3{\cdot}3M\ g(NO_3)_2{\cdot}24H_2O$	366	0–3.17[b]	60	5×10^{-5}
$Cr_2(SO_4)_3{\cdot}K_2SO_4{\cdot}24H_2O$	273	18.4	–	0.15
$Fe_2(SO_4)_3(NH_4)2SO_4{\cdot}24H_2O$	282	43.8	250	0.108
$Gd_2(SO_4)_3{\cdot}8H_2O$	124	78	105	–
$Gd_3Ga_5O_{12}$	48	78	203	0.13

[a]See Refs. [29–33]
[b]Anisotropic material

10.3.2 Thermodynamics of Magnetic Refrigeration

The thermodynamic principles by which magnetic cooling can be achieved are seen easily by analogy with a fluid system. For the sake of simplicity, assume that the magnetic system is composed of a solid material so that pressure–volume work is negligible. In this case, the combination of the first and second laws of thermodynamics can be written

$$T\ dS = dE - \mu_0 H\ dM \tag{10.41}$$

where M is the magnetization of the material. Thus, the second term on the right-hand side is magnetic work done on the system by direct analogy to $p\ dV$, the work done in a fluid system.

Adiabatic demagnetization is analogous to isentropic expansion in a fluid system. The important parameter that controls this process is the isentropic coefficient, which for a magnetic system is the derivative of the temperature with respect to applied field at constant entropy:

$$\mu_m = \frac{1}{\mu_0}\left(\frac{\partial T}{\partial H}\right)_s \tag{10.42}$$

Note the similarity between (10.42) and the isentropic expansion coefficient defined in Chap. 8. Normally, μ_m is referred to as the magneto-caloric coefficient. Table 10.5 presents a comparison between parameters and coefficients relevant to magnetic and fluid refrigeration systems.

It is straightforward to show that μ_m is a function of the temperature dependence of the magnetization of the spin system,

$$\mu_m = -\frac{T}{C_H}\left(\frac{\partial M}{\partial T}\right)_H \tag{10.43}$$

Table 10.5 Comparison of parameters and coefficients in magnetic and fluid refrigeration systems

	Fluid	Magnetic
Extensive variable	V	M
Intensive variable	p	$\mu_0 H$
Work	$p\ dV$	$-\mu_0 H\ dM$
Isentropic coefficient	$\mu_s = \left(\frac{\partial T}{\partial p}\right)_s$	$\mu_s = \left(\frac{\partial T}{\partial H}\right)_s$

The application of (10.43) for a particular magnetic refrigeration system requires knowledge of two quantities, C_H and the temperature dependence of M. where the constant field heat capacity is

$$C_H = T\left(\frac{\partial S}{\partial T}\right)_H \tag{10.44}$$

Returning to the relationship for the magneto-caloric coefficient and considering a weakly interacting magnetic system obeying the Curie law, we find that μ_m takes on a simplified form,

$$\mu_m = \frac{M}{C_H} \tag{10.45}$$

which is analogous to the isentropic expansion coefficient for an ideal gas.

The other term needed to establish the behavior of a magnetic refrigeration system is C_H, the specific heat at constant magnetic field. A relationship for this quantity can be derived through application of the first and second laws of thermodynamics for a magnetic system (10.41). Defining the constant magnetization specific heat as

$$C_M = T\left(\frac{\partial S}{\partial T}\right)_M = \left(\frac{\partial E}{\partial T}\right)_M \tag{10.46}$$

then (10.41) can be recast into the form

$$T\ dS = C_M dT - \mu_0 H\ dM \tag{10.47}$$

Further restricting (10.47) to a constant magnetic field process, the expansion of the temperature differential defines the specific heat at constant field:

$$C_H = T\left(\frac{\partial S}{\partial T}\right)_H \tag{10.48}$$

It follows that C_H may be written

$$C_H = C_M - \mu_0 H \left(\frac{\partial M}{\partial T}\right)_H \tag{10.49}$$

As discussed above, the constant magnetization specific heat C_M is made up to several independent contributions. The relative importance of each contribution depends on the type of magnetic material involved and the temperature range over which cooling is to be achieved. Neglecting the phonon term, we obtain a simplified expression for the magneto-caloric coefficient:

$$\mu_m = \frac{\mu_0 \gamma_C H T}{A + \gamma_C \mu_0^2 H^2} \tag{10.50}$$

Subject to the above set of assumptions, this expression can be employed to determine the final temperature achieved by adiabatic demagnetization of a magnetic material. Here we simply integrate (10.50) over a finite change in field and temperature,

$$\int_{T_i}^{T_f} \frac{dT}{T} = \int_{\mu_0 H_i}^{\mu_0 H_f} \frac{\mu_0 \gamma_C H T}{A + \gamma_C \mu_0^2 H^2} d(\mu_0 H) \tag{10.51}$$

which by demagnetization to zero applied field, $H_f = 0$, results in the expression

$$\frac{T_i}{T_f} = \left(1 + \frac{\gamma_C \mu_0^2 H_i^2}{A}\right)^{1/2} \tag{10.52}$$

Example 10.4

Calculate the final temperature due to demagnetization of iron ammonium alum from 0.1 T initially at 1 K.

Inserting the appropriate values from Table 10.4: $A = 0.108$ J · K/mol and $\gamma_C = 43.8$ J ·K/mol into (10.52), the ratio of temperatures for $\mu_0 H_i = 0.1$ T becomes $T_i/T_f = 2.25$. Therefore, with the material initially at 1 K the final temperature as a result of adiabatic demagnetization would be $T_f = 0.45$ K. In practice, demagnetizing fields much larger than 0.1 T allow lower final temperatures, but the simplified expression derived above does not apply in that case since we have used the low field approximate solution.

Another way of approaching this problem is to consider the entropy in magnetic ion systems. In the limit of small magnetic field, $g\mu_B\mu_0 H \ll k_B T$ and for $T \gg \delta/k_B$ the spin entropy can be shown to obey the relationship [30]

$$S = N_m k_B \left(\ln(2J+1) - \frac{2(A + \mu_0 \gamma_C H^2)}{RT^2}\right) \tag{10.53}$$

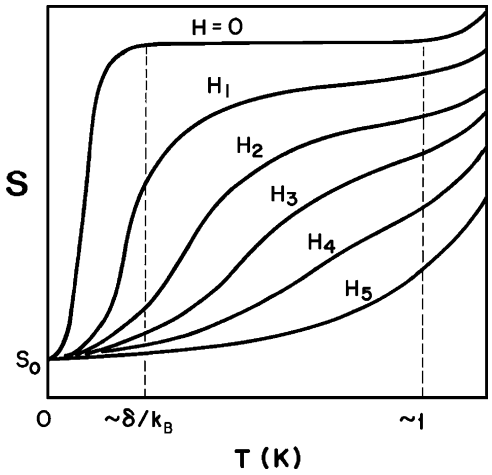

Fig. 10.12 Temperature–entropy diagram for a magnetic material

where J is the total angular momentum quantum number. Generally, except at very low temperatures ($T \ll 1\ K$), the first term in (10.53) is the dominant contribution to the spin entropy. This situation is desirable for magnetic cooling because the entropy change between the magnetized and demagnetized materials is what produces the cooling.

In the high magnetic field limit, $g\mu_B\mu_0 H \gg k_B T$, a considerably different situation occurs. Here the magnetic moments of the dipoles approach complete alignment with the magnetic field. The magnetic field is imposing a greater degree of order on the system, thus lowering the entropy. In the extreme case the spin entropy approaches zero, leaving the only remaining term associated with the Stark effect and the lattice, the latter of which can be neglected at low temperatures. In this limit, the principal behavior of the entropy is obtained by integration of the heat capacity (10.33). This analysis leads to an exponentially decaying entropy for the limit where $\delta/k_B \gg T$,

$$S = N_m k_B \left(1 + \frac{\delta}{k_B T}\right) \frac{g_0}{g_1} e^{-\delta/k_B T} \tag{10.54}$$

As the exact calculation of the entropy in a magnetic ion subsystem is dependent on choice of materials and operating range, it will not be carried out here. However, in order to calculate the final temperature of an adiabatic demagnetization, one needs to equate (10.53) with (10.54) and solve for the final temperature. This is a tedious, but straightforward calculation.

A schematic representation of the entropy of a magnetic ion subsystem is shown in Fig. 10.12. At high temperatures, $T \gg \delta/k_B$ and $T \gg g\mu_B\mu_0 H/k_B$, the entropy difference between the magnetized and unmagnetized state decreases because the

magnetic field is not very effective at magnetizing the sample. On the other hand, at very low temperatures, $T \ll \delta/k_B$ and $T \gg g\mu_B\mu_0 H/k_B$, the entropy difference decreases because the crystal field orders the system independent of the applied magnetic field. There is a range, indicated by the dashed lines in Fig. 10.12, over which the entropy difference $\Delta S \sim Nk_B \ln(2J+1)$, thereby allowing for efficient magnetic cooling. Obviously, the exact temperature range over which this region occurs depends on the particular paramagnetic material in question.

10.3.3 Continuous Magnetic Refrigerators

With the above survey of the thermodynamics of magnetic cooling, we now turn to the practical problems associated with achieving continuous refrigeration with magnetic materials. In this discussion emphasis is placed on continuous refrigeration rather than single-cycle adiabatic demagnetization, which was outlined above. The material that goes into a magnetic refrigerator must have a number of unique characteristics which set it apart from materials for other applications. Some of these characteristics have been introduced above, but a complete summary includes the following:

1. Magnetic refrigeration materials should have a small electronic and lattice specific heat. The energy used to cool the electrons and lattice is wasted and only reduces the efficiency of the cycle.
2. The magnetic level splitting due to the crystal field Stark effect, δ/k_B, should be below the range of operating temperatures. Otherwise, the entropy change with magnetization is reduced.
3. The magnetic contribution to the entropy should be large to allow more thermal energy to be cycled through the demagnetization process.
4. To achieve good thermal exchange with the systems to be refrigerated, it is desirable that the magnetic material have good heat transfer characteristics. Whenever possible, magnetic refrigeration materials should have a high thermal diffusivity.
5. Any material to be used in a device must be able to be fabricated into the configurations necessary for effective operation.

The principles of idealized closed-cycle magnetic refrigeration are similar to those for systems using fluids as working media. The most thermodynamically efficient cycle is the Carnot cycle which is a combination of isothermal and isentropic processes. This cycle can be achieved in a magnetic ion subsystem by a method shown schematically in Fig. 10.13, which is an actual T-S diagram for gadolinium sulfate. In this example, the Carnot cycle is shown as operating between two isothermal reservoirs at 15 and 1.7 K. This particular temperature range is attractive for magnetic refrigeration because helium gas–liquid cycles are limited to rather low thermodynamic efficiencies compared to the Carnot cycle. Also the maximum magnetization field of 10 T is a practical limitation because it allows

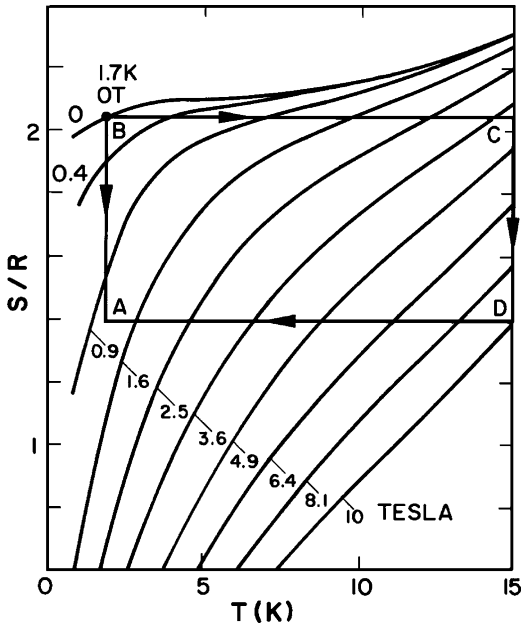

Fig. 10.13 Thermodynamic cycle executed by $Gd_2(SO_4)_3 \cdot 8H_2O$ in a magnetic Carnot cycle (from Steyert[30])

for the use of state-of-the-art but not prohibitively expensive superconducting magnet technology.

Consider the methods whereby Carnot refrigeration in a magnetic system can be achieved. A schematic diagram of the system is shown in Fig. 10.14. Apart from the reservoirs, the refrigerator consists of three principal components: the working material made of a magnetic salt, a magnet for aligning the spins of this material, and two thermal switches, one to either reservoir for exchange between the working material and isothermal baths. The Carnot cycle is a four-step process of magnetization, demagnetization, and heat exchange to the isothermal reservoirs.

The methods by which the Carnot cycle can be achieved are seen best by referring to the cycle ABCD in Fig. 10.13. With the thermal switch 1 (TS 1) closed and the working material in good contact with the heat reservoir (HR), the magnetic field is applied up to a maximum of 10 T represented by point D. Here the spins have the maximum alignment at this temperature.

Next, TS 1 is opened, isolating the magnetic material, and the field is decreased slowly, cooling the working material to point A at 1.7 K. Note that this point is not at zero field. Thermal switch 2 (TS 2) is then closed and the working material comes into the thermal equilibrium with the heat source. This step, which occurs isothermally, must be accompanied by a further slight demagnetization of the material to point B at which point all the heat has been transferred. Thermal switch 2 is then opened and the working material is magnetized slowly back to the high temperature represented by point C. Once the working material reaches the heat reservoir temperature, TS 1 is closed and further magnetization occurs isothermally to point D, completing the cycle. This process, as represented in Fig. 10.13, is able

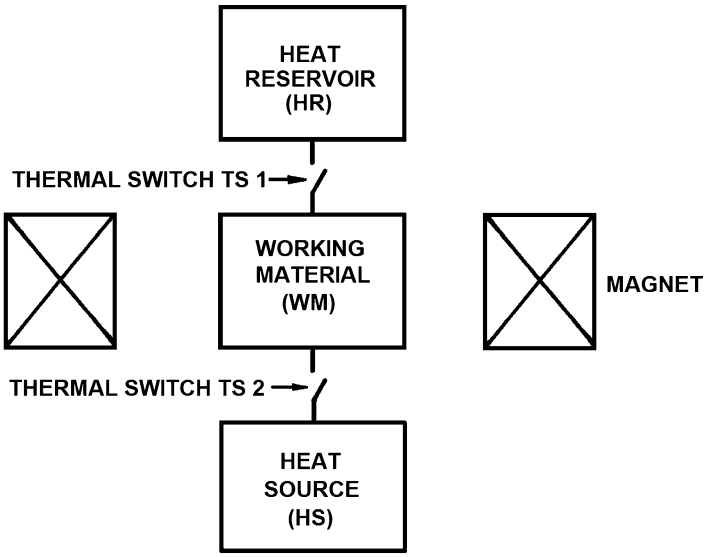

Fig. 10.14 Schematic diagram of magnetic Carnot refrigerator (Source: From Steyert [32])

to pump 27 J per liter of material per cycle, which if achievable at modest frequencies around 1 Hz could provide a rather high cooling rate in a very small volume. Of course, the difficulty in achieving this kind of cooling power lies in the practical aspects of creating a magnetic refrigerator.

In recent years there have been several devices built that are intended to bring the above concepts to realization on a practical scale [33–37]. In most cases the devices were developed to operate in the low-temperature region, $T < 4.2$ K, and to provide cooling power at the low end of the order of 1 W. Materials employed are either gadolinium sulfate or gadolinium gallium garnet (GGG), $Gd_3Ga_5O_{12}$. The latter material has shown superior thermal properties. In one particular case, a prototype refrigerator has been operated between 1.8 and 4.2 K with a cooling power of 1.2 W and an achieved figure of merit in the range of 45% [37].

10.3.4 Nuclear Demagnetization

To produce much lower temperatures with magnetic refrigeration it soon becomes inefficient to use paramagnetic salts as the working media because their spins will already be aligned. At these temperatures, which can span into the submillikelvin regime, it is possible to use the unpaired magnetic moment associated with the nuclei. The nuclear magnetic moment μ_N is smaller than the Bohr magneton by the ratio of nucleon to electron mass ($m_n/m_e = 1{,}840$). Thus, the nuclear spins can be aligned only by very high magnetic fields at low temperatures. This method was

first applied in 1956 by Simon and Kurti at Oxford where spin temperatures in the neighborhood of 10 μK were achieved through adiabatic demagnetization of the nuclei of a paramagnetic salt. However, the spin temperatures are not the same as the lattice temperatures and entropy must be transferred from one system to the other. The time constant that controls this process, called the spin–lattice relaxation time, can be large at very low temperatures, providing a severe hindrance to the ultimately achievable a microkelvin lattice temperature. In recent times, it has become more advantageous to achieve nuclear demagnetization using nuclei of metallic elements. In those systems the density of magnetic moments is much greater and the spin–lattice relaxation time shorter, allowing for minimum actual bulk temperatures. Record minimum bulk temperature of ~100 pK (10^{-10} K) have been achieved by multistage devices for which the last stage is nuclear demagnetization [38].

Questions

1. Explain why the apparent thermal conductivity of MLI has a minimum at a particular layer density. Sketch a graph of k_{app} vs. layer density. How would the graph be different if thickness of the MLI blanket were half as great, but the same number of layers used? Be as quantitative as possible.
2. If you wanted to improve heat exchange between two surfaces at low temperature, what would be the best gas to use? Why?

Problems

1. A 100 L spherical liquid helium Dewar consists of an inner vessel with a liquid nitrogen cooled shield surrounding the inner vessel. Both the helium vessel and nitrogen shield are suspended in a vacuum vessel. Assume that the emissivity of all surfaces is 0.1.

   (a) Calculate the heat load and liquid nitrogen consumption at 77 K.
   (b) Calculate the heat load at 4.2 K and liquid helium consumption.

   Neglect any contribution to the heat leak due to structural supports.
2. A liquid helium vessel (outer surface = 300 K) is surrounded by two, thermally insulated radiation shields. Assume that all surfaces have emissivities = 0.05. Calculate the temperature of the two shields and the heat leak per unit area to 4.2 K.
3. Calculate the pressure corresponding to a mean free path of 10 mm for a helium molecule at 80 K. Estimate the apparent thermal conductivity of helium gas under these conditions (Hint: you may assume that this is a free molecular flow condition). Let the spacing between walls be 10 mm.
4. Assume a monolayer of helium molecules forms a hexagonal closed packed structure. Use the hard core radius of a helium molecule to calculate the amount of gas at STP necessary to form one complete layer at low temperature. Compare your result with the data in Table 10.3.

References

1. Kittel, et al, Cryogenic Heat Transfer, Chapter 3 in *Handbook of Cryogenic Engineering*, ed. J. G. Weisend II, Taylor Francis, Philadelphia, 1998.
2. J. W. Ekin, *Experimental Techniques for Low Temperature Measurements*, Oxford University Press, 2006, pp. 514–5.
3. Values obtained from Cryocomp®.
4. R. F. Barron, *Cryogenic Systems*, 2nd Ed., Clarendon Press, Oxford, 1985.
5. J. E. Fesmire, et al, Cryogenic Moisture Uptake in Foam Insulation for Space Launch Vehicles, AIAA Conference Proceedings (2008).
6. E. H. Kennard, *Kinetic Theory of Gases*, McGraw–Hill, New York, 1938.
7. G. K. White, *Experimental Techniques in Low Temperature Physics*, 3 rd ed., Clarendon Press, Oxford, 1979.
8. R. J. Corrucini, Gaseous Heat Conduction at Low Pressures and Temperatures, *Vacuum* **7**–**8**, 19 (1959).
9. E. G. Cravalho, C. L. Tien, and R. P. Caren, Effect of Small Spacings on Radiative Transfer Between Two Dielectrics, *Transactions of ASME,* paper 67-HT-21 (1967).
10. P. F. Dickson and M. C. Jones, Infrared Spectral Reflectances of Metals at Low Temperatures, *Cryogenics* **8**, 24 (1968).
11. W. Obert, J. R. Coupland, D. P. Hammond, T. Cook, and K. Harwood, Emissivity Measurements of Metallic Surfaces Used in Cryogenics Applications, *Adv. Cryog. Eng.* **27**, 293 (1982).
12. K. D. Timmerhaus, Conductive Heat Transfer, in *Heat Transfer at Low Temperatures,* W. Frost (Ed.), Chap. 2, Plenum Press, New York, 1975.
13. E. M. Leung, R. W. Fast, H. L. Hart, and J. R. Heim, Techniques for Reducing Radiation Heat Transfer Between 77 K and 4.2 K, *Adv. Cryog. Eng.* **25**, 489 (1980).
14. R. H. Kropschot and R. W. Burgess, Perlite for Cryogenic Insulation, *Adv. Cryog. Eng.* **8**, 425 (1963).
15. E. R. Lady, Cryogenic Insulation, in *Cryogenic Engineering,* E. R. Lady (Ed.), Chap. 7, Engineering Summer Conference, University of Michigan, 1965.
16. Y. M. Eyssa and O. Okasha, Thermodynamic Systemization of Thermal Radiation Shields for a Cryogenic Apparatus, *Cryogenics* **18**, 305 (1978).
17. J. G. Dash, *Films on Solid Surfaces*, Academic Press, New York, 1975.
18. D. W. Princehouse, High-Resolution Heat Capacity Study of ^{4}He Adsorbed on Bare Copper, *J. Low Temp. Phys.* **8**, 287 (1972).
19. J. G. Daunt and E. Lerner, Adsorption of ^{3}He and ^{4}He on Various Substrates Below 30 K, *J. Low Temp. Phys.* **8**, 79 (1972).
20. W. A. Steele and J. G. Aston, Heats of Adsorption of Hydrogen and Helium on Prepared Surfaces, *J. Am. Chem. Soc.* **79**, 2393 (1957).
21. A. A. Antoniou, Adsorption of ^{4}He on Graphitized Carbon in the Submonolayer Region Between 2 and 15 K*, J. Chem. Phys.* **62**, 779 (1975).
22. R. L. Elgin and D. L. Goodstein, Thermodynamic Study of the ^{4}He Monolayer Adsorbed on Grafoil, Phys. Rev. **A 9**, 2657 (1974).
23. J. G. Daunt and C. Z. Rosen, Multilayer Adsorption of ^{3}He and ^{4}He on Zeolite from 4 to 80 K, *J. Low Temp. Phys.* **3**, 89 (1970).
24. M. Bretz, J. G. Dash, D. C. Hickernell, E. O. McLean, and O. E. Vilches, Phases of ^{3}He and ^{4}He Monolayer Films Adsorbed on Basel-Plane Oriented Graphite, *Phys. Rev. A* **8**, 1589 (1973).
25. D. F. Brewer, Some Thermal, Magnetic, and Flow Properties of Adsorbed He and He3-He4 Mixtures, *J. Low Temp. Phys.* **3**, 205 (1970).
26. J. A. Herb and J. G. Dash, Mass Transport of ^{4}He Films Adsorbed on Graphite, *Phys. Rev. Lett.* **29**, 846 (1972).

27. P. Debye, Einige Bemerkungen zur Magnetisieurung bei Taefer Temperature, *Ann. Phys*. **81**, 1154 (1926).
28. W. F. Giauque, Paramagnetism and the Third Law of Thermodynamics. Interpretation of the Low Temperature Specific Heat of Gadolinium Sulfate, *J. Am. Chem. Soc*. **49**, 1870 (1927).
29. W. F. Giauque and D. P. MacDogall, Attainment of Temperatures Below 1º Absolute by Demagnetization of $Gd_2(SO_4)_3 \cdot 8H_2O$, *Phys. Rev*. **43**, 768 (1933).
30. M. W. Zemansky, *Heat and Thermodynamics*, 5th ed., Chap. 14, McGraw–Hill. New York, 1968.
31. R. P. Hudson, *Principles and Application of Magnetic Cooling*, Chap. V, North Holland Publishing, Amsterdam, 1972.
32. W. A. Steyert, Magnetic Refrigeration, in *Liquid Cryogens*, Vol. 11, K. D. Williamson, Jr. and F. J. Edeskietz (Eds.), Chap. 6, CRC Press, Boca Raton, FL, 1983.
33. W. P. Pratt, S. S. Rosenblum, W. A Steyert, and J. A. Barclay, A Continuous Demagnetization Refrigerator Operating Near 2 K and a Study of Magnetic Refrigerants, *Cryogenics* **17**, 689 (1977).
34. R. Beranger, G. Bon Mardion, G. Claudet, C. Delpuech, A. F. Lacaze, and A. A. Lacaze, A Gadolinium Gallium Garnet Double Acting Reciprocating Magnetic Refrigerator, *Adv. Cryog. Eng*. **27**, 703 (1982).
35. A. F. Lacaze, A. A. Lacaze, R. Beranger, and G. Bon Mardion, Thermodynamic Aspects of a Double Acting Reciprocating Magnetic Refrigerator, *Proceedings of the 9th International Cryogenics Engineering Conference*, pp. 14–17, Butterworths, London, 1982.
36. A. F. Lacaze, R. Beranger, G. Bon Mardion, G. Claudet, and A. A. Lacaze, Double Acting Reciprocating Magnetic Refrigerator: Recent Improvements, *Adv. Cryog. Eng*. **29**, 573 (1984).
37. Y. Hakuraku and H. Ogata, A Rotary Magnetic Refrigerator for Superfluid Helium Production, *J. Appl. Phys.* Vol. 60, 3266 (1986).
38. J. T. Tuoriniemi and T. A. Knuuttila, Nuclear Cooling and Spin Properties of Rhodium down to Picokelvin Temperatures, Physica B, Volume 280, 474 (2000).

Further Readings

Cryogenic Insulation

R. F. Barron, *Cryogenic Systems*, 2nd Ed., Clarendon Press, Oxford, 1985.
E. H. Kennard, *Kinetic Theory of Gases*, McGraw–Hill, New York, 1938.
R. B. Scott, *Cryogenic Engineering*, Princeton Press, Princeton, NJ, 1959.
G. K. White, *Experimental Techniques in Low Temperature Physics*, 3 rd ed., Clarendon Press, Oxford, 1979.
F. P. Incropera and D. P. Dewitt, *Fundamentals of Heat Transfer*, Wiley, New York, 1981, Chapter 13.

Helium Adsorption

J. G. Dash, *Films on Solid Surfaces*, Academic Press, New York, 1975.
K. Wilson, Adsorption, in *Cryogenic Fundamentals*, G. G. Haselden (Ed.). Academic Press, London, 1971.
G. Davey, Cryosorption Pumping, in *Advanced Cryogenics*, C. A. Bailey (Ed.), Plenum Press, New York, 1971.

Magnetic Refrigeration

R. P. Hudson, *Principles and Application of Magnetic Cooling*, Chap. V, North Holland Publishing, Amsterdam, 1972.
G. K. White and P. J. Meeson, *Experimental Techniques in Low Temperature Physics*, 4 rd ed., Clarendon Press, Oxford, 2002.
M. W. Zemansky, *Heat and Thermodynamics*, 5th ed., Chap. 14, McGraw–Hill. New York, 1968.

Appendix 1
Compressibility Factor for Helium

S.W. Van Sciver, *Helium Cryogenics*, International Cryogenics Monograph Series,
DOI 10.1007/978-1-4419-9979-5,

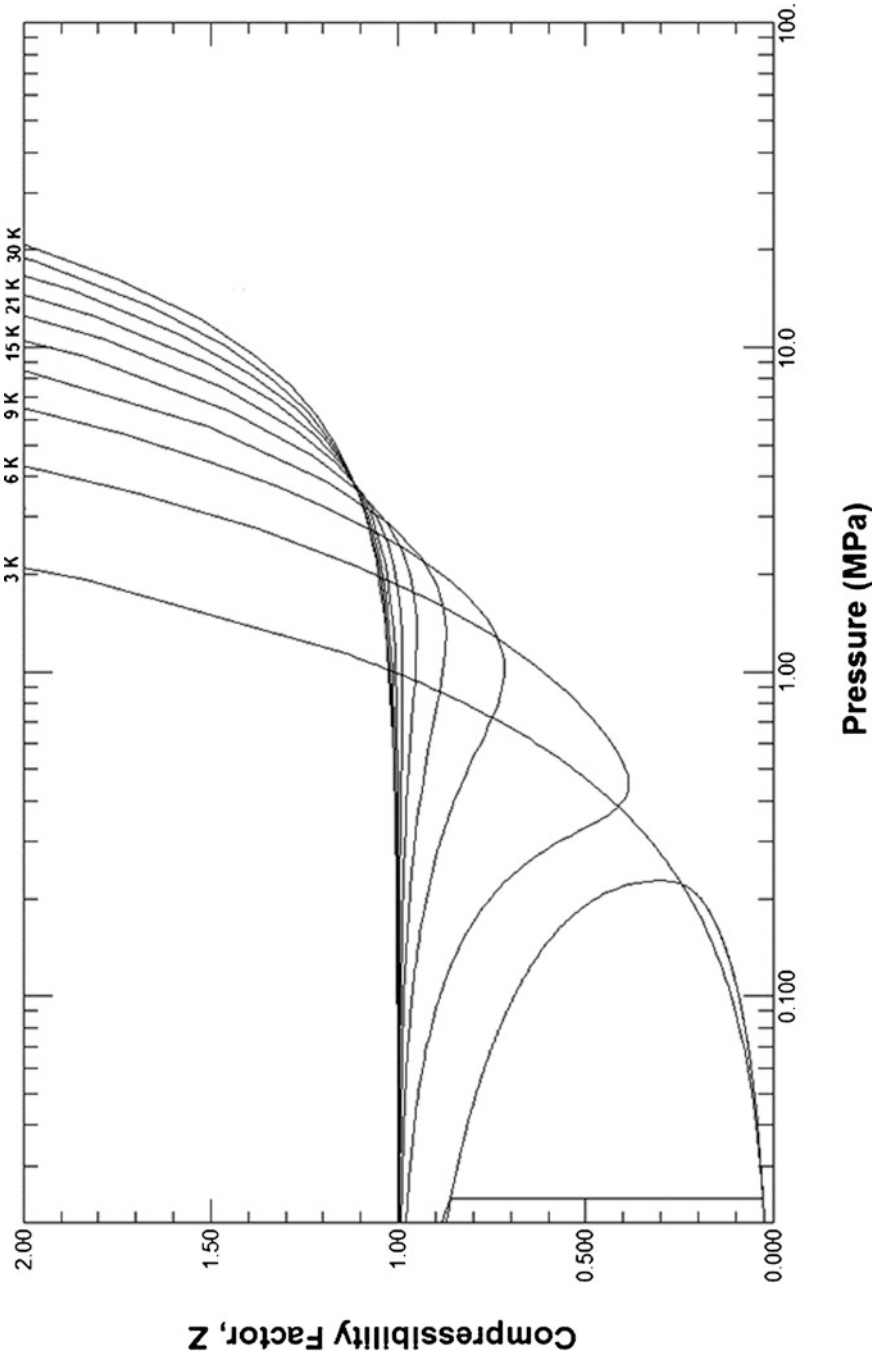
3 K
6 K
9 K
15 K
21 K
30 K
2.00
1.50
1.00
0.500
0.000
0.100
1.00
10.0
100
Compressibility Factor, Z
Pressure (MPa)

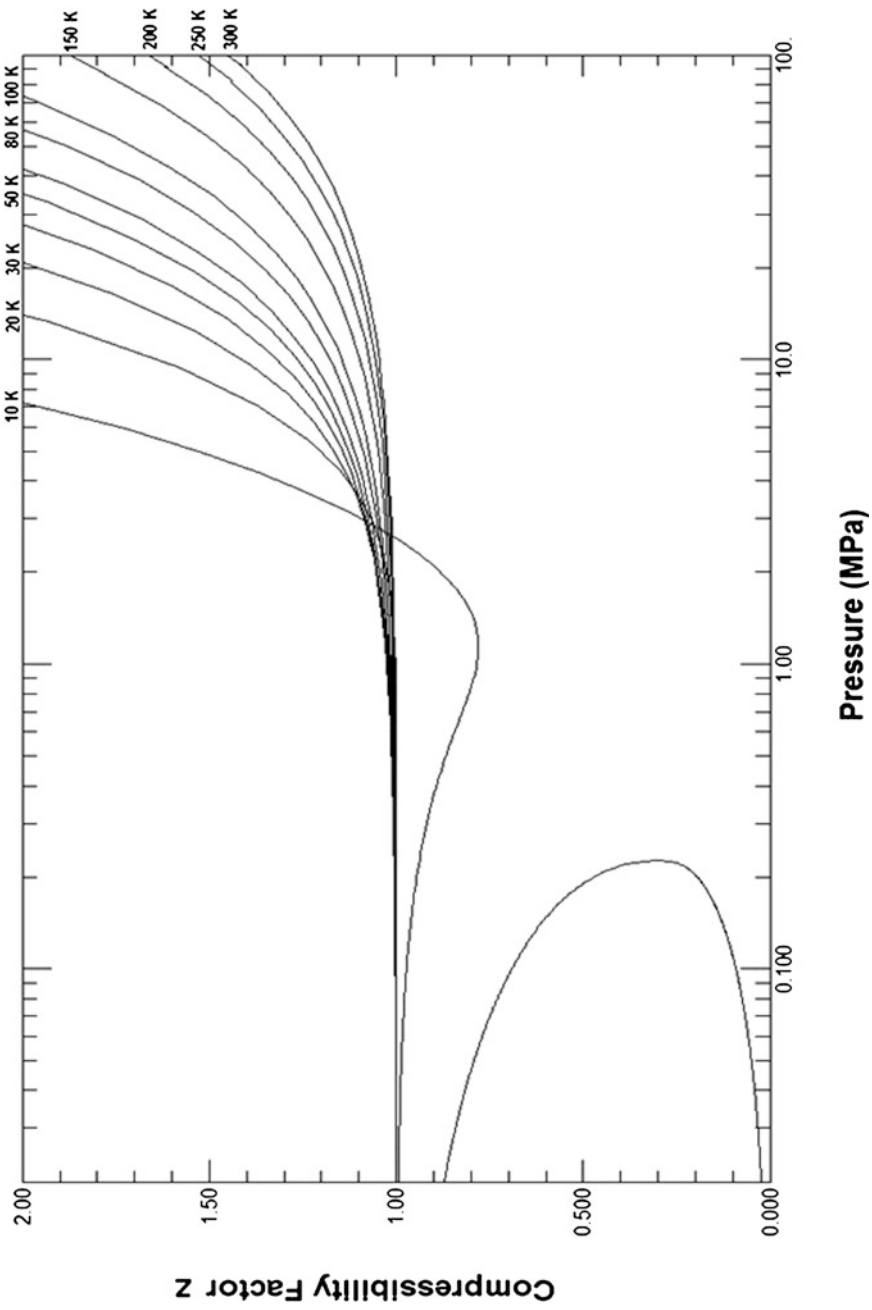
150 K
200 K
250 K
300 K
10 K
20 K
30 K
50 K
80 K
100 K
2.00
1.50
1.00
0.500
0.000
0.100
1.00
10.0
100
Compressibility Factor z
Pressure (MPa)

Appendix 2
Properties of Liquid Helium

Appendix A2.1 Properties of helium at saturated vapor pressure

T(K)	p_{svp}(Pa)	ρ_L(kg/m^3)	ρ_v(kg/m^3)	h(kJ/kg)	s(kJ/kg K)	h_{fg}(kJ/kg)	σ(mN/m)	κ(1/MPa)	β(1/K)	μ(μPa s)	k(mW/m K)
1.0	15.57	145.157	0.008	0.0127	0.0163	20.083	0.3489	0.1214	0.000185		
1.2	81.48	145.162	0.033	0.0518	0.0510	21.024	0.3439	0.1219	−0.000579		
1.4	282.00	145.199	0.098	0.1579	0.1308	21.861	0.3365	0.1223	−0.001738		
1.6	746.36	145.278	0.230	0.3923	0.2839	22.533	0.3268	0.1254	−0.003211		
1.8	1,638.41	145.416	0.455	0.8422	0.5437	22.977	0.3151	0.1284	−0.005283		
2.0	3,129.26	145.654	0.794	1.6420	0.9578	23.046	0.3016	0.1341	−0.009960		
2.1768	5,041.80	146.150	1.192	2.9490	1.5740	22.796	0.2880	0.1466	−0.051060		
2.2	5,335.15	146.150	1.251	3.0900	1.6380	22.461	0.2865	0.1424	0.010264	2.60404	13.630
2.4	8,354.10	145.494	1.828	3.6780	1.8860	22.623	0.2700	0.1470	0.033190	3.04356	14.500
2.6	12,372.07	144.429	2.549	4.1610	2.0680	22.906	0.2522	0.1589	0.045730	3.28415	15.265
2.8	17,551.76	143.035	3.433	4.6620	2.2400	23.132	0.2334	0.1756	0.057890	3.44756	15.946
3.0	24,047.07	141.354	4.499	5.1950	2.4080	23.255	0.2138	0.1940	0.070030	3.56870	16.550
3.2	32,009.97	139.442	5.767	5.7870	2.5810	23.265	0.1935	0.2162	0.082680	3.63809	17.087
3.4	41,594.70	137.267	7.267	6.4480	2.7600	23.146	0.1728	0.2449	0.096970	3.61874	17.548
3.6	52,956.31	134.813	9.033	7.1830	2.9460	22.870	0.1518	0.2826	0.113800	3.47190	17.937
3.8	66,247.39	132.050	11.111	7.9980	3.1400	22.406	0.1309	0.3337	0.134870	3.37654	18.247
4.0	81,619.69	128.929	13.564	8.8990	3.3400	21.724	0.1101	0.4053	0.162220	3.28009	18.481
4.2	99,233.46	125.372	16.487	9.9010	3.5510	20.790	0.0896	0.5112	0.200050	3.17862	18.644
4.4	119,269.30	121.252	20.035	11.0200	3.7740	19.537	0.0697	0.6803	0.256600	3.07087	18.754
4.6	141,930.40	116.339	24.489	12.3100	4.0180	17.829	0.0506	0.9831	0.351500	2.95366	18.843
4.8	167,429.50	110.162	30.445	13.8400	4.2960	15.397	0.0324	1.3840	0.544370	2.81969	18.973
5.0	196,003.90	100.890	39.327	15.9200	4.6640	11.726	0.0153	4.1530	1.207200	2.63572	19.300
5.1953	227,462.30	69.641	69.641	21.9500	5.7680	0.000	0.0000				

Appendix A2.2 Pressure 0.1 MPa

T(K)	ρ(kg/m^3)	h(kJ/kg)	s(kJ/kg K)	C_p(kJ/kg K)	C_v(kJ/kg K)	μ(μPa s)	k(mW/m K)
1.0	146.90	0.697	0.016	0.102	0.102		
1.2	146.90	0.737	0.051	0.322	0.322		
1.4	146.90	0.843	0.132	0.787	0.787		
1.6	147.00	1.075	0.287	1.614	1.612		
1.8	147.20	1.522	0.548	2.959	2.953		
2.0	147.50	2.319	0.966	5.249	5.227		
$T_\lambda = 2.168$	148.00	3.56	1.56	27.88	25.67		
2.2	148.00	3.719	1.631	3.777	3.765	2.715	13.859
2.4	147.40	4.257	1.866	2.282	2.173	3.140	14.746
2.6	146.30	4.696	2.042	2.233	2.029	3.364	15.529
2.8	145.00	5.147	2.209	2.308	1.978	3.515	16.226
3.0	143.30	5.623	2.373	2.496	2.017	3.634	16.844
3.2	141.40	6.150	2.543	2.784	2.135	3.715	17.383
3.4	139.10	6.739	2.721	3.108	2.253	3.718	17.838
3.6	136.50	7.395	2.909	3.463	2.353	3.585	18.204
3.8	133.50	8.128	3.107	3.874	2.432	3.456	18.469
4.0	129.90	8.952	3.318	4.396	2.495	3.327	18.624
4.2	125.40	9.902	3.550	5.161	2.547	3.181	18.651
$T_{svp} = 4.2163$	125.01	9.987	3.570	5.243	2.551	3.168	18.648
$T_{svp} = 4.2163$	16.533	31.81	8.510	9.015	3.240	1.241	9.004
4.4	14.940	32.37	8.872	8.056	3.217	1.274	9.275
4.6	13.640	33.92	9.215	7.436	3.194	1.312	9.586
4.8	12.620	35.36	9.523	7.027	3.175	1.350	9.901
5.0	11.780	36.74	9.803	6.735	3.159	1.389	10.216
5.2	11.070	38.06	10.06	6.517	3.146	0.000	10.528
6	9.028	43.05	10.96	6.011	3.120	1.579	11.736
7	7.426	48.89	11.86	5.724	3.111	1.761	13.161
8	6.344	54.54	12.61	5.575	3.111	1.935	14.491
9	5.555	60.06	13.26	5.485	3.113	2.100	15.729
10	4.949	65.52	13.84	5.426	3.115	2.258	16.889
12	4.074	76.29	14.82	5.353	3.118	2.557	19.025
14	3.468	86.95	15.64	5.310	3.120	2.835	20.983
16	3.023	97.54	16.35	5.282	3.120	3.097	22.811
18	2.680	108.1	16.97	5.264	3.121	3.345	24.543
20	2.408	118.6	17.52	5.250	3.121	3.582	26.198
22	2.187	129.1	18.02	5.240	3.121	3.808	27.792
24	2.003	139.6	18.48	5.232	3.120	4.025	29.333
26	1.848	150.0	18.90	5.226	3.120	4.235	30.831
28	1.716	160.5	19.28	5.221	3.120	4.437	32.290
30	1.601	170.9	19.64	5.218	3.120	4.634	33.716
40	1.200	223.0	21.14	5.206	3.119	5.542	40.444
50	0.961	275.0	22.30	5.201	3.118	6.360	46.678
60	0.801	327.0	23.25	5.198	3.118	7.116	52.552
70	0.686	379.0	24.05	5.196	3.117	7.827	58.149

(continued)

Appendix A2.2 (continued)

T(K)	ρ(kg/m^3)	h(kJ/kg)	s(kJ/kg K)	C_p(kJ/kg K)	C_v(kJ/kg K)	μ(μPa s)	k(mW/m K)
80	0.601	431.0	24.75	5.195	3.117	8.503	63.518
90	0.534	482.9	25.36	5.195	3.117	9.152	68.697
100	0.481	534.9	25.91	5.194	3.117	9.778	73.713
125	0.385	664.7	27.07	5.194	3.116	11.090	85.663
150	0.321	794.6	28.01	5.193	3.116	12.500	96.937
175	0.275	924.4	28.81	5.193	3.116	13.850	107.679
200	0.241	1,054	29.51	5.193	3.116	15.140	117.982
225	0.214	1,184	30.12	5.193	3.116	16.390	127.917
250	0.193	1,314	30.66	5.193	3.116	17.600	137.535
275	0.175	1,444	31.16	5.193	3.116	18.780	146.877
300	0.160	1,574	31.61	5.193	3.116	19.930	155.973

Appendix A2.3 Pressure 0.2 MPa

T(K)	ρ(kg/m^3)	h(kJ/kg)	s(kJ/kg K)	C_p(kJ/kg K)	C_v(kJ/kg K)	μ(μPa s)	k(mW/m K)
1.0	148.50	1.374	0.016	0.104	0.104		
1.2	148.50	1.414	0.052	0.328	0.328		
1.4	148.50	1.522	0.134	0.797	0.796		
1.6	148.60	1.757	0.290	1.631	1.628		
1.8	148.90	2.208	0.554	2.990	2.979		
2.0	149.30	3.015	0.977	5.323	5.285		
$T_\lambda = 2.158$	149.90	4.185	1.537	25.010	22.860		
2.2	149.90	4.375	1.625	3.419	3.406	2.846	14.135
2.4	149.30	4.885	1.847	2.195	2.097	3.260	15.048
2.6	148.30	5.306	2.016	2.153	1.972	3.471	15.860
2.8	147.10	5.738	2.175	2.209	1.918	3.613	16.590
3.0	145.70	6.192	2.332	2.387	1.966	3.733	17.247
3.2	143.90	6.695	2.494	2.653	2.087	3.834	17.830
3.4	141.90	7.255	2.664	2.943	2.209	3.881	18.337
3.6	139.70	7.874	2.841	3.246	2.310	3.809	18.710
3.8	137.10	8.555	3.025	3.570	2.390	3.675	19.053
4.0	134.10	9.305	3.217	3.940	2.451	3.557	19.304
4.2	130.70	10.140	3.420	4.395	2.499	3.432	19.459
4.4	126.60	11.070	3.638	5.014	2.540	3.298	19.512
4.6	121.60	12.160	3.880	5.984	2.579	3.147	19.470
4.8	114.80	13.530	4.170	7.942	2.623	2.964	19.352
5.0	102.80	15.680	4.608	16.580	2.696	2.683	19.294
$T_{svp} = 5.0356$	98.60	16.387	4.749	24.548	2.722	2.593	19.439
$T_{svp} = 5.0356$	40.36	27.842	7.023	34.804	3.040	1.721	14.136
5.2	32.030	31.140	7.669	14.290	3.081	1.670	12.791
6	21.260	38.840	9.057	7.737	3.096	1.734	12.768
7	16.260	45.850	10.140	6.519	3.095	1.882	13.834
8	13.450	52.110	10.980	6.064	3.100	2.036	15.040

(continued)

Appendix A2.3 (continued)

T(K)	ρ(kg/m^3)	h(kJ/kg)	s(kJ/kg K)	C_p(kJ/kg K)	C_v(kJ/kg K)	μ(μPa s)	k(mW/m K)
9	11.560	58.050	11.680	5.828	3.106	2.188	16.203
10	10.180	63.800	12.280	5.685	3.112	2.337	17.308
12	8.271	74.990	13.300	5.520	3.119	2.622	19.368
14	6.994	85.930	14.150	5.429	3.123	2.891	21.274
16	6.071	96.720	14.870	5.372	3.125	3.146	23.066
18	5.370	107.400	15.500	5.334	3.125	3.389	24.769
20	4.818	118.100	16.060	5.306	3.125	3.621	26.403
22	4.371	128.700	16.560	5.286	3.125	3.844	27.979
24	4.001	139.200	17.020	5.271	3.125	4.059	29.507
26	3.690	149.700	17.440	5.259	3.124	4.266	30.993
28	3.424	160.300	17.830	5.249	3.124	4.467	32.443
30	3.194	170.700	18.190	5.242	3.124	4.661	33.861
40	2.395	223.000	19.700	5.219	3.122	5.564	40.563
50	1.916	275.200	20.860	5.209	3.120	6.379	46.783
60	1.598	327.200	21.810	5.203	3.119	7.134	52.650
70	1.370	379.200	22.610	5.200	3.119	7.843	58.242
80	1.199	431.200	23.310	5.198	3.118	8.518	63.608
90	1.066	483.200	23.920	5.197	3.118	9.165	68.785
100	0.960	535.100	24.470	5.196	3.118	9.791	73.799
125	0.768	665.000	25.630	5.194	3.117	11.100	85.746
150	0.641	794.900	26.570	5.194	3.117	12.510	97.019
175	0.549	924.700	27.370	5.193	3.117	13.860	107.759
200	0.481	1,055.000	28.070	5.193	3.116	15.150	118.062
225	0.427	1,184.000	28.680	5.193	3.116	16.400	127.996
250	0.385	1,314.000	29.230	5.193	3.116	17.610	137.614
275	0.350	1,444.000	29.720	5.193	3.116	18.790	146.955
300	0.321	1,574.000	30.170	5.193	3.116	19.930	156.050

Appendix A2.4 Pressure 0.5 MPa

T(K)	ρ(kg/m^3)	h(kJ/kg)	s(kJ/kg K)	C_p(kJ/kg K)	C_v(kJ/kg K)	μ(μPa s)	k(mW/m K)
1.0	152.80	3.365	0.016	0.109	0.109		
1.2	152.80	3.407	0.054	0.346	0.346		
1.4	152.90	3.520	0.140	0.838	0.836		
1.6	153.10	3.767	0.304	1.705	1.697		
1.8	153.40	4.238	0.579	3.117	3.088		
2.0	154.00	5.081	1.021	5.604	5.510		
$T_\lambda = 2.127$	154.80	6.024	1.477	39.540	30.460		
2.2	154.80	6.301	1.605	2.696	2.681	3.308	15.561
2.4	154.20	6.743	1.798	1.985	1.900	3.685	16.538
2.6	153.50	7.125	1.951	1.976	1.830	3.852	17.424
2.8	152.50	7.513	2.095	1.993	1.774	3.962	18.236
3.0	151.40	7.920	2.235	2.151	1.839	4.075	18.982
3.2	150.10	8.373	2.381	2.385	1.972	4.209	19.665

(continued)

Appendix A2.4 (continued)

T(K)	ρ(kg/m^3)	h(kJ/kg)	s(kJ/kg K)	C_p(kJ/kg K)	C_v(kJ/kg K)	μ(μPa s)	k(mW/m K)
3.4	148.50	8.874	2.533	2.629	2.101	4.338	20.283
3.6	146.80	9.424	2.690	2.864	2.208	4.387	19.937
3.8	145.00	10.020	2.851	3.093	2.291	4.244	20.421
4.0	142.90	10.660	3.016	3.321	2.354	4.133	20.836
4.2	140.60	11.350	3.183	3.558	2.402	4.020	21.180
4.4	138.10	12.090	3.355	3.815	2.439	3.909	21.453
4.6	135.40	12.880	3.531	4.104	2.470	3.797	21.655
4.8	132.40	13.730	3.712	4.440	2.497	3.685	21.789
5.0	129.00	14.660	3.901	4.846	2.523	3.573	21.861
5.2	125.20	15.680	4.101	5.354	2.548	3.458	21.879
6	102.10	21.420	5.121	10.040	2.689	2.942	21.179
7	59.44	33.930	7.047	11.650	2.946	2.443	17.870
8	41.34	43.780	8.366	8.505	3.031	2.412	17.670
9	32.87	51.560	9.285	7.241	3.068	2.488	18.308
10	27.76	58.470	10.010	6.635	3.090	2.592	19.111
12	21.60	71.080	11.160	6.065	3.116	2.824	20.810
14	17.89	82.920	12.080	5.796	3.129	3.061	22.495
16	15.35	94.340	12.840	5.641	3.135	3.294	24.131
18	13.49	105.500	13.500	5.541	3.137	3.520	25.717
20	12.05	116.500	14.080	5.472	3.138	3.740	27.259
22	10.90	127.400	14.600	5.422	3.138	3.952	28.762
24	9.957	138.200	15.070	5.384	3.137	4.159	30.229
26	9.171	149.000	15.500	5.354	3.137	4.359	31.664
28	8.503	159.600	15.890	5.331	3.136	4.554	33.071
30	7.929	170.300	16.260	5.312	3.135	4.744	34.452
40	5.940	223.100	17.780	5.257	3.130	5.631	41.030
50	4.756	275.500	18.950	5.231	3.127	6.437	47.180
60	3.968	327.800	19.900	5.218	3.125	7.185	53.005
70	3.405	379.900	20.710	5.210	3.123	7.890	58.568
80	2.982	432.000	21.400	5.205	3.122	8.561	63.914
90	2.653	484.000	22.010	5.202	3.121	9.206	69.077
100	2.390	536.000	22.560	5.199	3.120	9.829	74.080
125	1.914	665.900	23.720	5.196	3.119	11.130	86.010
150	1.597	795.800	24.670	5.195	3.118	12.540	97.272
175	1.370	925.700	25.470	5.194	3.118	13.880	108.005
200	1.199	1,056.000	26.160	5.193	3.117	15.170	118.303
225	1.066	1,185.000	26.780	5.193	3.117	16.420	128.233
250	0.960	1,315.000	27.320	5.193	3.117	17.620	137.847
275	0.873	1,445.000	27.820	5.193	3.117	18.800	147.184
300	0.801	1,575.000	28.270	5.193	3.117	19.940	0.156

Appendix A2.5 Pressure 1.0 MPa

T(K)	ρ(kg/m^3)	h(kJ/kg)	s(kJ/kg K)	C_p(kJ/kg K)	C_v(kJ/kg K)	μ(μPa s)	k(mW/m K)
1.0	158.70	6.578	0.020	0.133	0.133		
1.2	158.80	6.627	0.064	0.393	0.391		
1.4	159.00	6.753	0.160	0.919	0.911		
1.6	159.30	7.021	0.338	1.842	1.820		
1.8	159.80	7.530	0.636	3.384	3.320		
2.0	160.80	8.471	1.128	6.538	6.243		
$T_\lambda = 2.068$	161.40	9.020	1.398	39.200	25.520		
2.2	161.40	9.388	1.571	2.026	2.003	4.215	15.604
2.4	160.80	9.753	1.730	1.730	1.652	4.497	16.671
2.6	160.20	10.09	1.868	1.777	1.661	4.569	17.655
2.8	159.60	10.44	1.997	1.761	1.602	4.607	18.574
3.0	158.70	10.80	2.121	1.900	1.683	4.689	19.433
3.2	157.70	11.20	2.250	2.115	1.829	4.842	20.234
3.4	156.50	11.64	2.385	2.331	1.967	5.039	20.978
3.6	155.30	12.13	2.524	2.530	2.082	5.217	21.508
3.8	153.90	12.65	2.665	2.712	2.171	5.090	22.134
4.0	152.40	13.21	2.809	2.882	2.238	4.962	22.698
4.2	150.80	13.81	2.954	3.045	2.290	4.837	23.203
4.4	149.10	14.43	3.099	3.206	2.330	4.716	23.648
4.6	147.30	15.09	3.245	3.369	2.363	4.599	24.033
4.8	145.40	15.78	3.392	3.539	2.391	4.487	24.360
5.0	143.30	16.51	3.540	3.718	2.416	4.379	24.631
5.2	141.10	17.27	3.690	3.909	2.439	4.276	24.848
6	130.90	20.75	4.311	4.849	2.531	3.901	25.217
7	114.10	26.41	5.180	6.584	2.659	3.506	24.643
8	93.31	33.93	6.181	8.248	2.806	3.215	23.462
9	74.62	42.33	7.170	8.341	2.932	3.083	22.862
10	61.35	50.42	8.023	7.819	3.013	3.066	22.888
12	45.58	65.06	9.361	6.898	3.094	3.172	23.747
14	36.76	78.28	10.38	6.370	3.128	3.345	24.974
16	31.07	90.68	11.21	6.060	3.145	3.537	26.308
18	27.04	102.6	11.91	5.863	3.153	3.735	27.671
20	24.02	114.2	12.52	5.728	3.156	3.933	29.039
22	21.65	125.5	13.06	5.631	3.157	4.129	30.399
24	19.73	136.7	13.55	5.558	3.156	4.322	31.747
26	18.14	147.8	13.99	5.502	3.155	4.512	33.081
28	16.81	158.7	14.40	5.458	3.153	4.698	34.401
30	15.66	169.6	14.77	5.422	3.152	4.880	35.706
40	11.72	223.2	16.32	5.316	3.143	5.740	42.014
50	9.397	276.1	17.50	5.268	3.137	6.531	48.003
60	7.850	328.7	18.45	5.242	3.133	7.269	53.721
70	6.743	381.0	19.26	5.226	3.130	7.967	59.211
80	5.912	433.2	19.96	5.217	3.128	8.633	64.504
90	5.264	485.3	20.57	5.210	3.126	9.273	69.627
100	4.745	537.4	21.12	5.206	3.125	9.892	74.600
125	3.806	667.5	22.28	5.199	3.122	11.190	86.478

(continued)

Appendix A2.5 (continued)

T(K)	ρ(kg/m^3)	h(kJ/kg)	s(kJ/kg K)	C_p(kJ/kg K)	C_v(kJ/kg K)	μ(μPa s)	k(mW/m K)
150	3.178	797.4	23.23	5.196	3.121	12.590	97.709
175	2.728	927.3	24.03	5.195	3.120	13.930	108.421
200	2.390	1,057.0	24.72	5.194	3.119	15.210	118.704
225	2.126	1,187.0	25.34	5.193	3.119	16.450	128.623
250	1.915	1,317.0	25.88	5.193	3.118	17.650	138.228
275	1.742	1,447.0	26.38	5.192	3.118	18.820	147.558
300	1.597	1,576.0	26.83	5.192	3.118	19.960	156.645

Appendix A2.6 Pressure 1.5 MPa

T(K)	ρ(kg/m^3)	h(kJ/kg)	s(kJ/kg K)	C_p(kJ/kg K)	C_v(kJ/kg K)	μ(μPa s)	k(mW/m K)
1.0	163.80	9.685	0.028	0.169	0.168		
1.2	164.00	9.744	0.080	0.448	0.445		
1.4	164.20	9.883	0.187	1.007	0.996		
1.6	164.60	10.18	0.380	2.012	1.973		
1.8	165.30	10.74	0.710	3.818	3.669		
2.0	166.80	11.89	1.310	10.310	8.875		
$T_\lambda = 2.003$	166.90	11.92	1.326	31.620	18.990		
2.2	166.80	12.36	1.536	1.654	1.624	5.198	16.101
2.4	166.30	12.67	1.673	1.586	1.515	5.335	17.249
2.6	165.70	12.99	1.803	1.634	1.540	5.276	18.317
2.8	165.20	13.31	1.924	1.593	1.471	5.228	19.324
3.0	164.40	13.64	2.037	1.730	1.565	5.277	20.275
3.2	163.60	14.01	2.155	1.935	1.718	5.448	21.172
3.4	162.70	14.42	2.279	2.138	1.862	5.702	22.012
3.6	161.70	14.86	2.406	2.322	1.981	5.993	22.792
3.8	160.50	15.34	2.536	2.486	2.074	5.903	23.519
4.0	159.40	15.85	2.668	2.634	2.146	5.748	24.188
4.2	158.10	16.40	2.800	2.773	2.201	5.600	24.800
4.4	156.70	16.96	2.932	2.905	2.245	5.457	25.354
4.6	155.30	17.56	3.064	3.035	2.281	5.321	25.852
4.8	153.80	18.18	3.196	3.166	2.311	5.192	26.295
5.0	152.20	18.82	3.328	3.299	2.339	5.070	26.685
5.2	150.50	19.50	3.460	3.436	2.365	4.953	27.023
6	143.00	22.48	3.992	4.040	2.462	4.548	27.904
7	131.70	26.96	4.681	4.952	2.584	4.152	28.124
8	118.50	32.44	5.411	6.006	2.706	3.858	27.677
9	103.90	38.93	6.175	6.925	2.821	3.655	27.024
10	89.98	46.11	6.930	7.337	2.922	3.546	26.587
12	68.77	60.71	8.262	7.145	3.054	3.524	26.683
14	55.39	74.56	9.330	6.713	3.117	3.626	27.478
16	46.58	87.62	10.20	6.369	3.148	3.776	28.535
18	40.37	100.10	10.94	6.121	3.163	3.945	29.698
20	35.75	112.20	11.57	5.943	3.170	4.122	30.909
22	32.15	123.90	12.13	5.812	3.172	4.302	32.140

(continued)

Appendix A2.6 (continued)

T(K)	ρ(kg/m^3)	h(kJ/kg)	s(kJ/kg K)	C_p(kJ/kg K)	C_v(kJ/kg K)	μ(μPa s)	k(mW/m K)
24	29.26	135.40	12.63	5.711	3.172	4.482	33.378
26	26.88	146.80	13.09	5.634	3.171	4.661	34.618
28	24.88	158.00	13.50	5.572	3.169	4.838	35.854
30	23.18	169.10	13.89	5.522	3.167	5.012	37.085
40	17.36	223.40	15.45	5.372	3.156	5.847	43.119
50	13.93	276.80	16.64	5.303	3.148	6.624	48.930
60	11.65	329.60	17.60	5.265	3.141	7.352	54.526
70	10.02	382.10	18.41	5.242	3.137	8.043	59.928
80	8.792	434.50	19.11	5.228	3.133	8.704	65.156
90	7.834	486.70	19.73	5.219	3.131	9.339	70.228
100	7.066	538.80	20.28	5.212	3.129	9.955	75.161
125	5.677	669.00	21.44	5.203	3.125	11.240	86.971
150	4.745	799.00	22.39	5.198	3.123	12.640	98.159
175	4.076	928.90	23.19	5.195	3.122	13.970	108.842
200	3.572	1,059.00	23.88	5.194	3.121	15.250	119.105
225	3.179	1,189.00	24.49	5.193	3.120	16.480	129.009
250	2.864	1,318.00	25.04	5.192	3.119	17.680	138.602
275	2.606	1,448.00	25.54	5.192	3.119	18.840	147.923
300	2.391	1,578.00	25.99	5.192	3.119	19.980	157.003

Appendix A2.7 Pressure 2.0 MPa

T(K)	ρ(kg/m^3)	h(kJ/kg)	s(kJ/kg K)	C_p(kJ/kg K)	C_v(kJ/kg K)	μ(μPa s)	k(mW/m K)
1.0	168.40	12.70	0.035	0.198	0.197		
1.2	168.50	12.77	0.095	0.503	0.500		
1.4	168.70	12.92	0.214	1.126	1.112		
1.6	169.20	13.25	0.433	2.290	2.218		
1.8	170.20	13.91	0.817	4.570	4.216		
$T_\lambda = 1.932$	171.60	14.74	1.258	31.000	15.730		
2.0	171.80	14.92	1.351	1.926	1.926	5.664E-06	15.358
2.2	171.50	15.24	1.502	1.429	1.394	6.172E-06	16.654
2.4	171.00	15.52	1.624	1.511	1.447	6.111E-06	17.875
2.6	170.40	15.83	1.751	1.525	1.446	5.904E-06	19.021
2.8	169.90	16.14	1.867	1.463	1.367	5.776E-06	20.107
3.0	169.30	16.44	1.972	1.602	1.471	5.817E-06	21.139
3.2	168.50	16.78	2.082	1.799	1.627	6.035E-06	22.118
3.4	167.80	17.16	2.197	1.993	1.774	6.364E-06	23.043
3.6	166.90	17.58	2.316	2.167	1.895	6.774E-06	23.911
3.8	166.00	18.03	2.437	2.321	1.991	6.720E-06	24.723
4.0	164.90	18.51	2.560	2.459	2.065	6.534E-06	25.478
4.2	163.90	19.01	2.683	2.585	2.123	6.355E-06	26.176
4.4	162.70	19.54	2.806	2.704	2.170	6.186E-06	26.817
4.6	161.50	20.09	2.929	2.819	2.209	6.025E-06	27.403
4.8	160.20	20.67	3.051	2.933	2.242	5.874E-06	27.934
5.0	158.90	21.26	3.173	3.047	2.273	5.730E-06	28.412

(continued)

Appendix A2.7 (continued)

T(K)	ρ(kg/m^3)	h(kJ/kg)	s(kJ/kg K)	C_p(kJ/kg K)	C_v(kJ/kg K)	μ(μPa s)	k(mW/m K)
5.2	157.50	21.89	3.295	3.163	2.301	5.596E-06	28.839
6	151.30	24.61	3.781	3.652	2.408	5.131E-06	30.080
7	142.30	28.59	4.394	4.333	2.539	4.690E-06	30.754
8	132.10	33.29	5.021	5.074	2.662	4.367E-06	30.738
9	120.90	38.74	5.662	5.814	2.773	4.137E-06	30.345
10	109.30	44.88	6.307	6.420	2.870	3.985E-06	29.875
12	88.17	58.35	7.534	6.892	3.016	3.866E-06	29.463
14	72.39	72.05	8.590	6.766	3.101	3.902E-06	29.847
16	61.22	85.34	9.478	6.517	3.146	4.010E-06	30.649
18	53.13	98.14	10.230	6.288	3.169	4.150E-06	31.639
20	47.04	110.50	10.880	6.101	3.180	4.307E-06	32.717
22	42.29	122.60	11.460	5.954	3.185	4.471E-06	33.841
24	38.48	134.40	11.970	5.838	3.186	4.638E-06	34.989
26	35.34	145.90	12.430	5.745	3.186	4.807E-06	36.148
28	32.71	157.30	12.860	5.671	3.184	4.975E-06	37.313
30	30.47	168.60	13.250	5.609	3.181	5.142E-06	38.480
40	22.84	223.70	14.830	5.424	3.168	5.953E-06	44.265
50	18.35	277.40	16.030	5.335	3.157	6.715E-06	49.905
60	15.37	330.50	17.000	5.287	3.149	7.435E-06	55.378
70	13.23	383.20	17.810	5.258	3.143	8.119E-06	60.687
80	11.62	435.70	18.510	5.239	3.139	8.774E-06	65.844
90	10.36	488.00	19.130	5.227	3.136	9.405E-06	70.860
100	9.355	540.30	19.680	5.218	3.133	1.002E-05	75.749
125	7.526	670.50	20.840	5.206	3.128	1.129E-05	87.480
150	6.296	800.60	21.790	5.199	3.126	1.268E-05	98.618
175	5.412	930.50	22.590	5.196	3.124	1.401E-05	109.267
200	4.746	1,060.0	23.290	5.194	3.122	1.528E-05	119.505
225	4.226	1,190.0	23.900	5.193	3.121	1.651E-05	129.391
250	3.809	1,320.0	24.440	5.192	3.120	1.770E-05	138.971
275	3.466	1,450.0	24.940	5.192	3.120	1.886E-05	148.281
300	3.180	1,580.0	25.390	5.192	3.119	2.000E-05	157.352

Appendix A2.8 Pressure 2.5 MPa

T(K)	ρ(kg/m^3)	h(kJ/kg)	s(kJ/kg K)	C_p(kJ/kg K)	C_v(kJ/kg K)	μ(μPa s)	k(mW/m K)
1.0	172.50	15.640	0.041	0.220	0.220		
1.2	172.60	15.720	0.107	0.569	0.566		
1.4	172.80	15.890	0.244	1.304	1.280		
1.6	173.50	16.280	0.501	2.734	2.583		
1.8	175.00	17.090	0.976	5.937	5.042		
$T_\lambda = 1.855$	175.90	17.500	1.195	29.960	12.640		
2.0	176.00	17.780	1.342	1.412	1.404	6.878	15.783
2.2	175.70	18.040	1.468	1.287	1.248	7.050	17.147
2.4	175.10	18.300	1.582	1.465	1.405	6.757	18.438
2.6	174.60	18.620	1.708	1.441	1.373	6.412	19.656

(continued)

Appendix A2.8 (continued)

T(K)	ρ(kg/m^3)	h(kJ/kg)	s(kJ/kg K)	C_p(kJ/kg K)	C_v(kJ/kg K)	μ(μPa s)	k(mW/m K)
2.8	174.00	18.920	1.821	1.365	1.287	6.243	20.816
3.0	173.50	19.200	1.919	1.501	1.393	6.329	21.923
3.2	172.80	19.520	2.022	1.690	1.549	6.645	22.977
3.4	172.10	19.880	2.130	1.877	1.696	7.088	23.977
3.6	171.40	20.270	2.242	2.044	1.818	7.608	24.921
3.8	170.60	20.690	2.357	2.191	1.915	7.557	25.808
4.0	169.70	21.140	2.473	2.321	1.992	7.334	26.639
4.2	168.70	21.620	2.589	2.440	2.052	7.122	27.412
4.4	167.70	22.120	2.705	2.551	2.102	6.922	28.128
4.6	166.70	22.640	2.821	2.657	2.143	6.733	28.788
4.8	165.60	23.180	2.936	2.762	2.179	6.555	29.393
5.0	164.40	23.740	3.051	2.866	2.213	6.387	29.945
5.2	163.20	24.330	3.165	2.971	2.244	6.230	30.445
6	157.80	26.880	3.620	3.405	2.361	5.693	31.974
7	150.10	30.570	4.188	3.984	2.501	5.189	32.991
8	141.60	34.850	4.759	4.588	2.631	4.824	33.280
9	132.30	39.740	5.335	5.189	2.746	4.562	33.115
10	122.50	45.210	5.911	5.740	2.843	4.379	32.743
12	103.30	57.520	7.030	6.461	2.992	4.194	32.111
14	87.03	70.680	8.044	6.627	3.087	4.171	32.122
16	74.51	83.850	8.924	6.528	3.142	4.239	32.657
18	65.02	96.750	9.684	6.362	3.173	4.351	33.473
20	57.72	109.30	10.35	6.198	3.189	4.487	34.430
22	51.97	121.60	10.93	6.055	3.196	4.636	35.461
24	47.32	133.50	11.45	5.935	3.199	4.791	36.531
26	43.49	145.30	11.92	5.836	3.199	4.950	37.624
28	40.27	156.90	12.35	5.753	3.197	5.110	38.730
30	37.52	168.30	12.75	5.685	3.195	5.270	39.843
40	28.16	224.00	14.35	5.471	3.179	6.057	45.413
50	22.66	278.10	15.56	5.366	3.167	6.806	50.897
60	19.00	331.40	16.53	5.308	3.157	7.516	56.251
70	16.38	384.30	17.34	5.273	3.150	8.193	61.469
80	14.40	436.90	18.05	5.250	3.145	8.843	66.553
90	12.86	489.40	18.66	5.235	3.140	9.470	71.512
100	11.61	541.70	19.22	5.224	3.137	10.080	76.354
125	9.353	672.10	20.38	5.209	3.132	11.350	88.000
150	7.832	802.20	21.33	5.201	3.128	12.730	99.083
175	6.738	932.10	22.13	5.197	3.126	14.050	109.694
200	5.911	1,062.00	22.82	5.194	3.124	15.320	119.905
225	5.266	1,192.00	23.43	5.193	3.123	16.540	129.770
250	4.747	1,322.00	23.98	5.192	3.122	17.730	139.334
275	4.322	1,451.00	24.48	5.192	3.121	18.880	148.633
300	3.966	1,581.00	24.93	5.191	3.120	20.010	157.693

Appendix 3
He II Heat Conductivity Function

Appendix A3 Turbulent He II heat conductivity function, $f^{-1}(T,p)$, kW^3/m^5 K

TEMP (K)	SVP	0.1 MPa	0.25 MPa	0.5 MPa	1 MPa	1.5 MPa	2 MPa	2.5 MPa
1.4	396.88	389.91	374.74	356.23	343.23	322.94	291.98	279.18
1.42	492.09	483.16	464.00	440.23	421.71	394.09	352.60	331.46
1.44	607.04	595.63	571.54	541.13	515.08	477.78	422.59	389.82
1.46	745.02	730.50	700.32	661.55	625.36	575.38	502.50	453.88
1.48	909.64	891.23	853.58	804.33	754.62	688.14	592.62	522.84
1.5	1,104.84	1,081.57	1,034.78	972.45	904.87	817.11	692.86	595.36
1.52	1,334.81	1,305.52	1,247.60	1,169.02	1,078.03	963.05	802.68	669.54
1.54	1,603.96	1,567.21	1,495.81	1,397.13	1,275.74	1,126.23	920.88	742.74
1.56	1,916.77	1,870.84	1,783.17	1,659.73	1,499.25	1,306.30	1,045.52	811.63
1.58	2,277.66	2,220.49	2,113.27	1,959.50	1,749.17	1,502.09	1,173.75	872.13
1.6	2,690.81	2,619.91	2,489.35	2,298.61	2,025.27	1,711.38	1,301.68	919.55
1.62	3,159.86	3,072.31	2,914.01	2,678.47	2,326.23	1,930.69	1,424.35	948.79
1.64	3,687.69	3,580.03	3,388.95	3,099.42	2,649.33	2,155.11	1,535.63	954.68
1.66	4,275.95	4,144.16	3,914.56	3,560.40	2,990.12	2,378.07	1,628.42	932.58
1.68	4,924.68	4,764.10	4,489.55	4,058.54	3,342.20	2,591.24	1,694.78	879.06
1.7	5,631.79	5,437.10	5,110.43	4,588.75	3,696.87	2,784.58	1,726.45	792.94
1.72	6,392.53	6,157.71	5,771.08	5,143.29	4,042.96	2,946.41	1,715.47	676.33
1.74	7,198.86	6,917.20	6,462.18	5,711.32	4,366.75	3,063.84	1,655.15	535.73
1.76	8,038.89	7,703.03	7,170.71	6,278.62	4,652.08	3,123.42	1,541.29	382.86
1.78	8,896.31	8,498.36	7,879.58	6,827.27	4,880.66	3,112.10	1,373.74	234.57
1.8	9,749.90	9,281.59	8,567.29	7,335.65	5,032.79	3,018.70	1,157.98	111.09
1.82	10,573.23	10,026.21	9,207.86	7,778.62	5,088.44	2,835.73	906.67	31.12
1.84	11,334.63	10,700.85	9,771.03	8,128.11	5,028.94	2,561.60	640.58	1.49
1.86	11,997.49	11,269.75	10,222.94	8,354.22	4,839.10	2,203.13	388.07	
1.88	12,521.14	11,693.80	10,527.32	8,426.88	4,510.05	1,777.95	181.76	
1.9	12,862.33	11,932.24	10,647.41	8,318.24	4,042.50	1,316.21	50.37	
1.92	12,977.62	11,945.21	10,548.69	8,005.91	3,450.25	860.57	2.39	
1.94	12,826.67	11,697.28	10,202.53	7,476.91	2,763.44	462.82		
1.96	12,376.63	11,161.98	9,590.84	6,732.33	2,030.59	174.52		

(continued)

Appendix A3 (continued)

TEMP (K)	SVP	0.1 MPa	0.25 MPa	0.5 MPa	1 MPa	1.5 MPa	2 MPa	2.5 MPa
1.98	11,607.65	10,327.35	8,711.42	5,792.32	1,317.94	27.72		
2	10,519.24	9,202.22	7,583.96	4,700.74	703.69	0.00		
2.02	9,137.17	7,822.67	6,255.61	3,528.19	263.46			
2.04	7,520.03	6,257.67	4,805.26	2,371.58	41.55			
2.06	5,763.86	4,612.16	3,344.14	1,347.17	0.00			
2.08	4,002.59	3,024.66	2,009.69	572.35				
2.1	2,400.26	1,655.30	947.80	129.50				
2.12	1,129.61	657.73	276.12	1.99				
2.14	328.41	125.60	18.18					
2.16	21.57	0.35						

Appendix 4
Temperature-Entropy Diagrams for Helium

Appendix A4 Normal fluid viscosity and laminar flow heat conductivity function

T(K)	$\mu_n(10^{-7}$ Pa.s)	g(T) (W/m^3 K) $\times 10^{-13}$
1.20	21.35	3.08
1.22	20.35	4.03
1.26	18.67	6.77
1.28	17.97	8.67
1.30	17.35	11.03
1.32	16.80	13.94
1.34	16.33	17.47
1.36	15.91	21.77
1.38	15.54	26.96
1.40	15.22	33.18
1.44	14.70	49.30
1.46	14.48	59.71
1.48	14.30	71.88
1.50	14.13	86.16
1.52	13.99	102.85
1.54	13.86	122.20
1.56	13.74	144.94
1.60	13.54	201.08
1.62	13.45	235.78
1.64	13.37	275.56
1.66	13.29	321.19
1.68	13.22	373.07
1.70	13.16	432.22
1.72	13.11	499.82
1.74	13.06	576.22
1.76	13.03	661.50
1.78	13.00	758.24
1.80	13.00	865.32
1.82	13.02	984.22
1.84	13.05	1,118.40

(continued)

Appendix A4 (continued)

T(K)	$\mu_n(10^{-7}$ Pa.s)	g(T) (W/m^3 K) $\times 10^{-13}$
1.86	13.12	1,263.00
1.88	13.22	1,420.90
1.90	13.36	1,591.30
1.92	13.54	1,775.30
1.94	13.78	1,972.20
1.96	14.07	2,178.60
1.98	14.44	2,391.80
2.00	14.88	2,617.60
2.02	15.40	2,846.10
2.04	16.03	3,075.70
2.06	16.77	3,310.70
2.10	18.67	3,777.20
2.12	19.87	3,999.40
2.14	21.29	4,229.60
2.16	23.03	4,456.50
2.18	25.25	4,677.10

Appendix 5
T-S Diagrams in He II Region

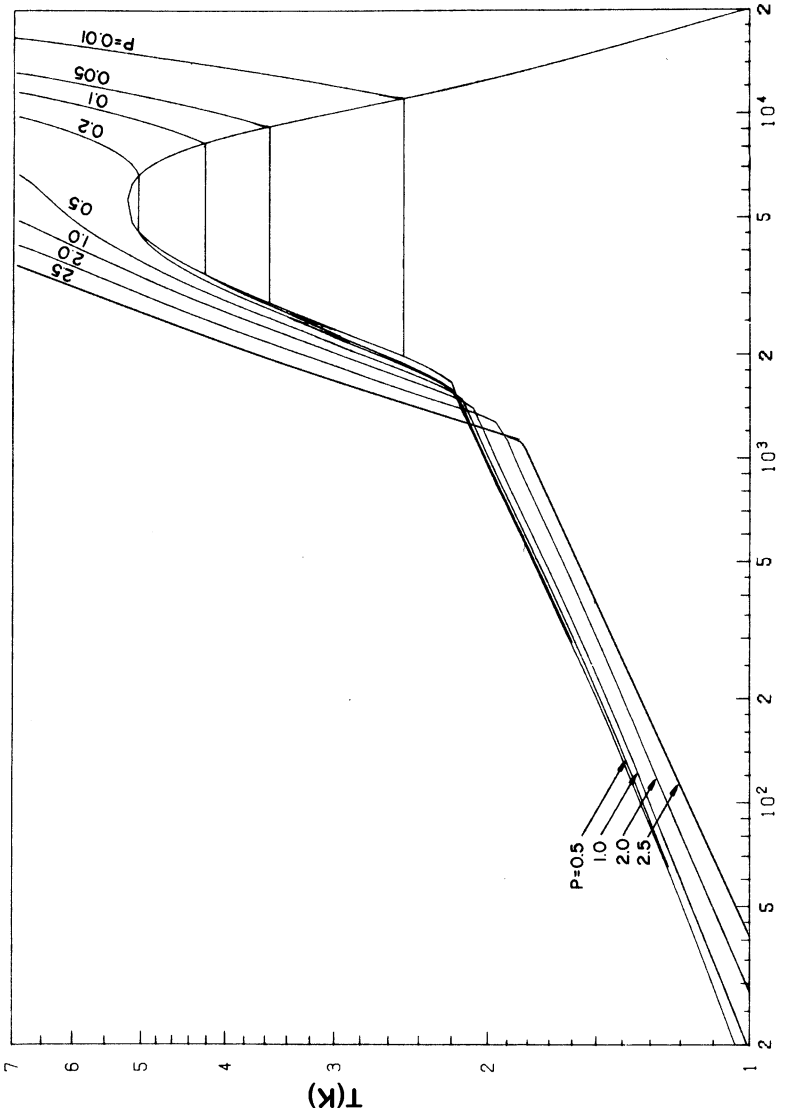

Helium T–S diagram showing isobars. Pressure P is in MPa

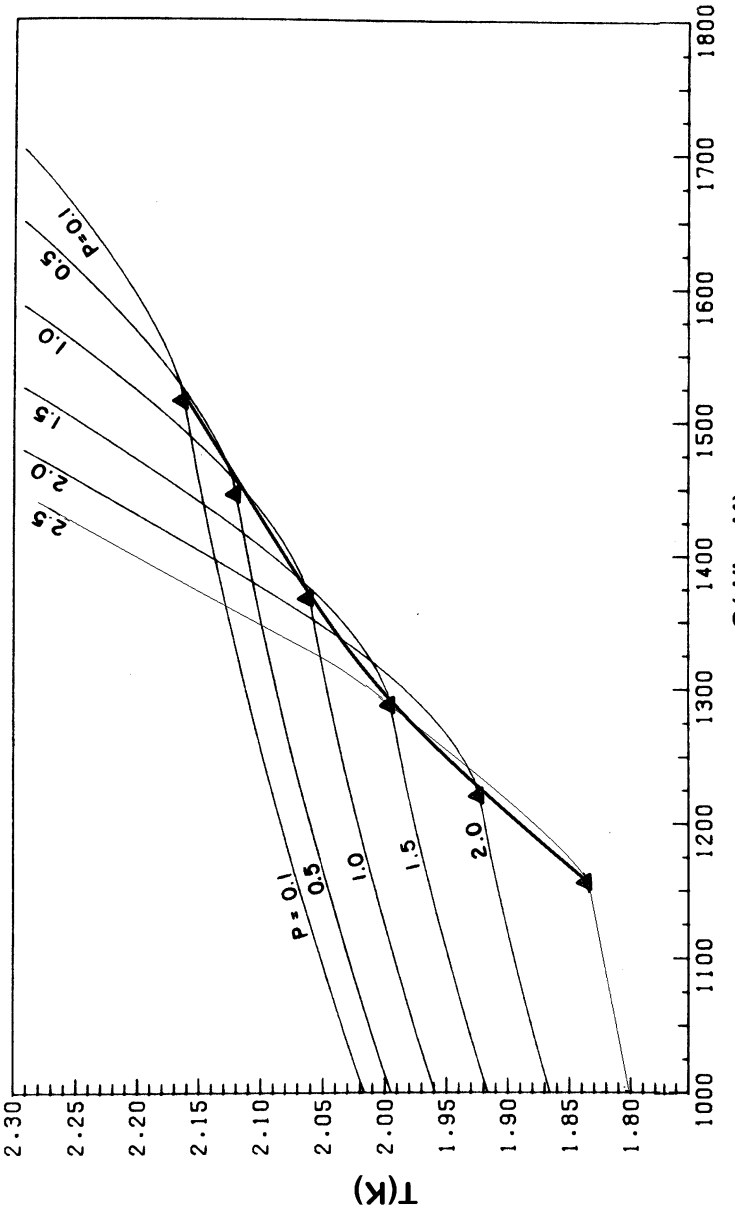

Helium T–S diagram showing isobars crossing λ-line: Δ represent λ-point and pressure P is in MPa

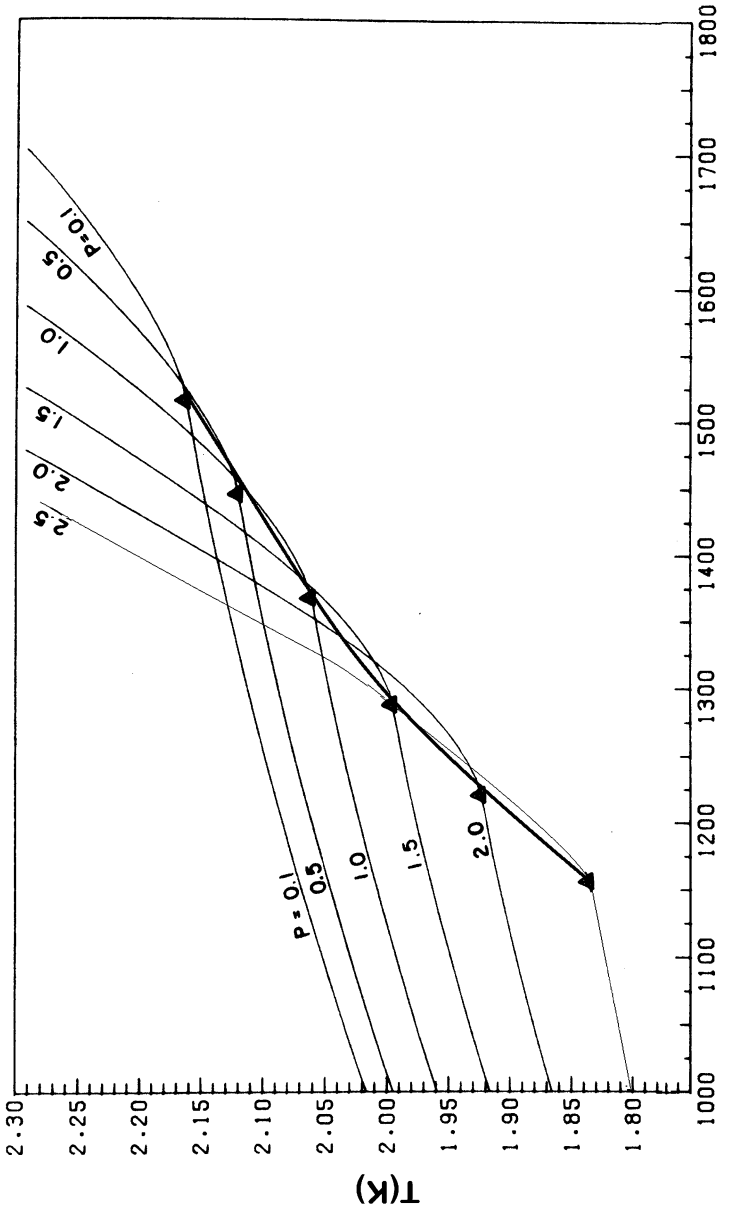

Helium *T*–*S* diagram showing isenthalps. Enthalpy *H* is in kJ/kg

Appendix 6
Helium T-S Diagrams

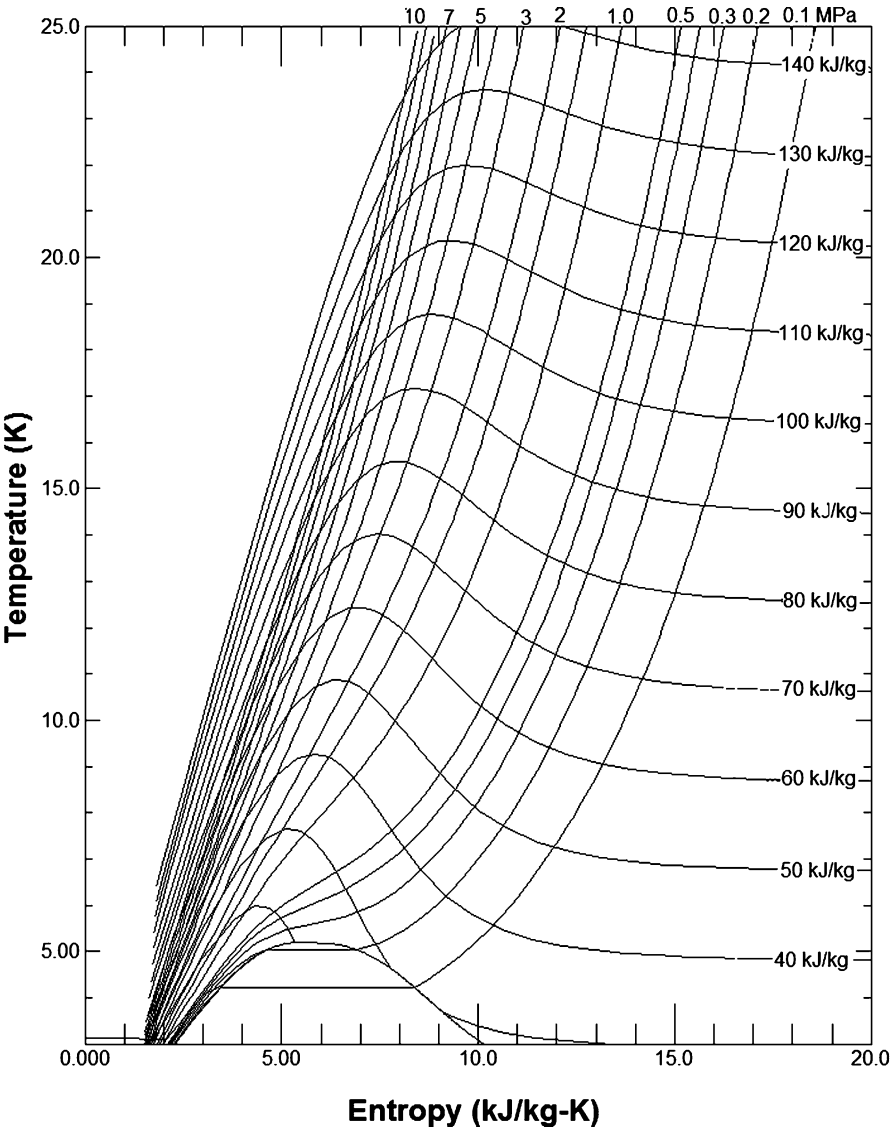

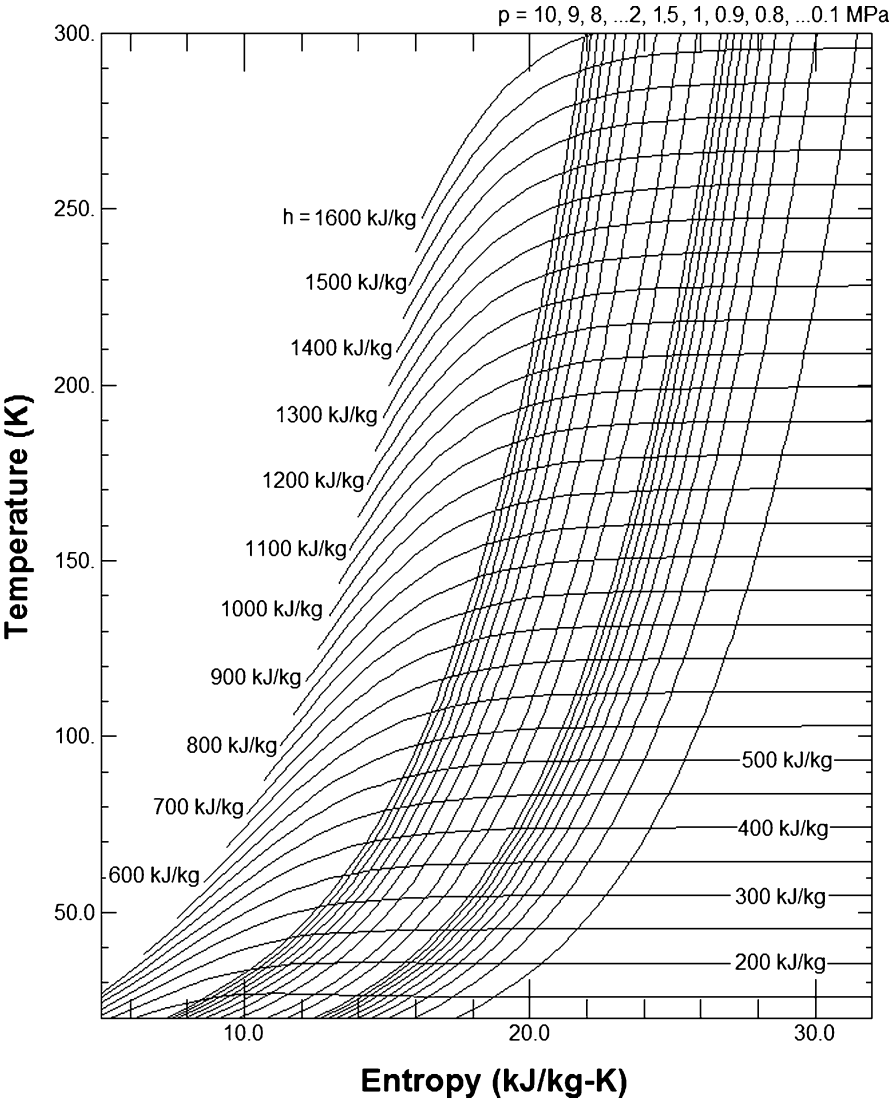
p = 10, 9, 8, ...2, 1.5, 1, 0.9, 0.8, ...0.1 MPa
300.
250.
200.
150.
100.
50.0
Temperature (K)
h = 1600 kJ/kg
1500 kJ/kg
1400 kJ/kg
1300 kJ/kg
1200 kJ/kg
1100 kJ/kg
1000 kJ/kg
900 kJ/kg
800 kJ/kg
700 kJ/kg
600 kJ/kg
500 kJ/kg
400 kJ/kg
300 kJ/kg
200 kJ/kg
10.0
20.0
30.0
Entropy (kJ/kg-K)

Conversion Factors

Unit/unit system	SI	CGS	English
Length	1 m	100 cm	3.281 ft
Area	1 m^2	10^4 cm^2	10.76 ft^2
Volume	1 m^3 (10^3 L)	10^6 cm^3	35.31 ft^3
Mass	1 kg	1,000 g	2.205 lb_m
Density	1 kg/m^3	10^{-3} g/cm^3	6.243×10^{-2} lb_m/ft^3
Velocity	1 m/s	100 cm/s	3.281 ft/s
Force	1 N	10^5 dynes	0.2248 lb_F
Pressure	1 Pa	10 $dynes/cm^2$	1.45×10^{-4} lb_f/in^2
	10^{-5} bar	9.869×10^{-6} atm	
		7.501×10^{-3} torr	
Temperature	1 K	1 K	9/5°R
Energy	1 J	10^7 erg	9.479×10^{-4} Btu
Heat transfer rate	1 W	10^7 erg/s	3.412 Btu/hr
Heat transfer coefficient	1 W/m^2 K	10^{-4} W/cm^2 K	0.176 Btu/hr ft^2°R
Viscosity	1 Pa s	10 poise	5.8×10^{-6} lb_f hr/ft^2
Thermal conductivity	1 W/m K	10^{-2} W/cm K	0.578 Btu/hr ft°R

Physical Constants

Universal gas constant	$R = 0.0823$ L atm/mole K; 8.31 J/mole K
Speed of light in vacuum	$c = 2.998 \times 10^{8}$ m/s
Avogadro's number	$N_o = 6.024 \times 10^{23}$ molecules/mole
Boltzmann constant	$k_B = 1.38 \times 10^{-23}$ J/K molecule
Planck's constant	$h = 6.625 \times 10^{-34}$ J s/molecule
Stefan-Boltzmann constant	$\sigma = 5.67 \times 10^{-8}$ W/m^2 K^4
Electron mass	$m_e = 9.11 \times 10^{-31}$ kg
Proton mass	$m_p = 1.67 \times 10^{-27}$ kg
Permeability constant	$\mu_o = 1.26 \times 10^{-6}$ H/m
Permittivity constant	$\varepsilon_o = 8.85 \times 10^{-12}$ F/m
Bohr magneton	$\mu_e = 0.927 \times 10^{-23}$ J/T
Elementary charge	e $= 1.60 \times 10^{-19}$ Coul
Gravitational acceleration	$g = 9.807$ m/s^2

Index

About the Author

Dr. Van Sciver is a Distinguished Research Professor and John H. Gorrie Professor of Mechanical Engineering at Florida State University. He is also a Program Director at the National High Magnetic Field Laboratory (NHMFL). Dr. Van Sciver joined the FAMU-FSU College of Engineering and the NHMFL in 1991, initiating and teaching a graduate program in magnet and materials engineering and in cryogenic thermal sciences and heat transfer. He also led the NHMFL development efforts of the cryogenic systems for the NHMFL Hybrid and 900 MHz NMR superconducting magnets. Between 1997 and 2003, he served as Director of Magnet Science and Technology at the NHMFL. Dr. Van Sciver is a Fellow of the ASME and the Cryogenic Society of America and American Editor for the journal *Cryogenics*. He is the 2010 recipient of the Kurt Mendelssohn Award.

Prior to joining Florida State University, Dr. Van Sciver was Research Scientist and then Professor of Nuclear Engineering, Engineering Physics and Mechanical Engineering at the University of Wisconsin-Madison from 1976 to 1991. During that

time he also served as the Associate Director of the Applied Superconductivity Center. Dr. Van Sciver received his Ph.D. in Low Temperature Physics from the University of Washington-Seattle in 1976. He received his BS degree in Engineering Physics from Lehigh University in 1970.

Dr. Van Sciver is author of over 200 publications and patents in low temperature physics, liquid helium technology, cryogenic engineering and magnet technology. The first edition of *Helium Cryogenics* was published by Plenum Press (1986). The present work is an update and expansion of that original project.